Ludden J. N., Gradstein, F. M., et al., 1990
Proceedings of the Ocean Drilling Program, Initial Reports, Vol. 123

4. SITE 765[1]

Shipboard Scientific Party[2]

HOLE 765A

Date occupied: 7 September 1988

Date departed: 7 September 1988

Time on hole: 20 hr 45 min

Position: 15°58.54′S, 117°34.49′E

Bottom felt (rig floor, m; drill pipe measurement): 5731.9

Distance between rig floor and sea level (m): 10.5

Water depth (drill pipe measurement from sea level, m): 5721.4

Total depth (rig floor, m): 5741.5

Penetration (m): 9.6

Number of cores (including cores with no recovery): 1

Total length of cored section (m): 9.6

Total core recovered (m): 9.69

Core recovery (%): 101

Oldest sediment
Depth (mbsf): 9.6
Nature: Interbedded, graded nannofossil ooze, turbidites
Earliest age: Pleistocene
Latest age: -
Measured velocity (km/s): 1.5

HOLE 765B

Date occupied: 7 September 1988

Date departed: 11 September 1988

Time on hole: 3 days 3 hr 15 min

Position: 15°58.54′S, 117°34.49′E

Bottom felt (rig floor, m; drill pipe measurement): 5728.2

Distance between rig floor and sea level (m): 10.5

Water depth (drill pipe measurement from sea level, m): 5717.7

Total depth (rig floor, m): 6123.8

Penetration (m): 395.6

Number of cores (including cores with no recovery): 41

Total length of cored section (m): 395.6

Total core recovered (m): 270.92

Core recovery (%): 68

Oldest sediment cored:
Depth (mbsf): 395.6
Nature: Clayey calcareous chalk
Earliest age: middle Miocene
Latest age: middle Pliocene
Measured velocity (km/s): 2.1

HOLE 765C

Date occupied: 11 September 1988

Date departed: 23 September 1988

Time on hole: 12 days 6 hr

Position: 15°58.54′S, 117°34.49′E

Bottom felt (rig floor, m; drill pipe measurement): 5728.2

Distance between rig floor and sea level (m): 10.5

Water depth (drill pipe measurement from sea level, m): 5717.7

Total depth (rig floor, m): 6692.1

Penetration (m): 963.9

Number of cores (including cores with no recovery): 65

Total length of cored section (m): 613.7

Total core recovered (m): 373.35

Core recovery (%): 60

Oldest sediment cored:
Depth (mbsf): 935.6
Nature: Dark brown siltstone with manganese inclusions
Earliest age: late Berriasian to Valanginian
Latest age: -
Measured velocity (km/s): 2.01 (at 896.1 mbsf)

Basement:
Depth (mbsf): 935.6
Nature: Aphyric pillow basalt with glassy margins, altered

HOLE 765D

Date occupied: 23 September 1988

Date departed: 17 October 1988

Time on hole: 24 days 7 hr

Position: 15°58.54′S, 117°34.49′E

Bottom felt (rig floor, m; drill pipe measurement): 5724.3

Distance between rig floor and sea level (m): 10.5

Water depth (drill pipe measurement from sea level, m): 5713.8

Total depth (rig floor m): 6919.2

Penetration (m): 1194.9

Number of cores (including cores with no recovery): 27

Total length of cored section (m): 247.0

Total core recovered (m): 78.7

Core recovery (%): 31

Basement:
Depth (m): 947.9
Nature: Pillow and massive basalts
Measured velocity (km/s): 5.58

Principal results: The early tectonic and paleoceanographic history of the Indian Ocean is poorly understood. For this reason, Leg 123 Site 765 was drilled in the northeastern Indian Ocean, off northwestern Australia for the following objectives:

[1] Ludden, J. N., Gradstein, F. M., et al., 1990. *Proc. ODP, Sci. Results*: 123: College Station, TX (Ocean Drilling Program).
[2] Shipboard Scientific Party is as given in list of participants preceding the contents.

1. To elucidate the paleoceanography, sedimentology, and magmatic processes related to the rifting of the early Indian Ocean.
2. To constrain the rift to drift tectonic history of one of the Earth's oldest oceanic basins.
3. To improve the late Mesozoic time scale, particularly with reference to the Southern Hemisphere.
4. To provide a geochemical reference section of old oceanic crust, incorporating the bulk composition of the sediments and basement, for use in geochemical and petrological, global mass-balance models.

Site 765 is located on a magnetic anomaly, interpreted as local marine magnetic anomaly M26, that according to the geomagnetic time scale is of late Oxfordian age. Backtracking predicts an initial ridge-crest water depth of about 2800 m, which is comparable to that of normal oceanic crust. The site is about 15 km seaward of the geophysical ocean/continent boundary separating Australia from the Argo Abyssal Plain, and approximately 350 km south of the Java Trench.

Holes 765A, 765B, and 765C, located at 15°58.541'S, 117° 34.495'E, in a water depth of 5723 m, were continuously cored for Cenozoic and Cretaceous, fine-grained, abyssal sediments. Oceanic basement was reached at 931 mbsf in Hole 765C. Average sediment recovery was 68%. The *JOIDES Resolution* then was moved approximately 30 m, where Hole 765D was drilled and cased through 924 m of sediments into volcanic basement. This hole then was continuously cored another 259 m into remarkably fresh basalt. Average core recovery in Hole 765D was 31%. Both Holes 765C and 765D were logged extensively using sonic, litho-density, and geochemical tools. Site 765 is the deepest cased drill hole in the oceans. With its reentry cone on the seafloor, this site is in perfect shape for future scientific operations.

Using combined nannofossil, foraminifer, radiolarian, and dinoflagellate biostratigraphy, visual core descriptions, assisted by multivariate analysis of smear-slide data and sedimentary paleomagnetics, we distinguished seven successive stratigraphic units. From basement to the seafloor, these are as follows:

1. Unit I: 0–189.1 mbsf, clayey calcareous turbidites, massive slumps and debris flows, and siliceous ooze of late Miocene to Pleistocene age.
2. Unit II: 189.1–474.1 mbsf, calcareous turbidites with minor clay and a massive debris flow containing basaltic pebbles of early to late Miocene age.
3. Unit III: 474.1–591.7 mbsf, varicolored zeolitic clay, redeposited calcareous sediments, and dark claystones of Cenomanian-early Miocene age, with stratigraphic hiatuses.
4. Unit IV: 591.7–724.1 mbsf, siliciclastic and mixed lithology turbidites, nannofossil chalk, calcareous claystone, and zeolitic clay of early Aptian-Cenomanian age.
5. Unit V: 724.7–859.2 mbsf, varicolored and dark gray radiolarian and rhodochrosite claystone of Barremian-early Aptian age.
6. Unit VI: 859.2–892.2 mbsf, nannofossil chalk and varied minor lithtologies of Valanginian-Hauterivian age.
7. Unit VII: 892.9–931.2 mbsf, brown-red silty claystone and reddish-brown to greenish claystone of Berriasian-Valanginian age; the basal contact between claystone and basalt is marked by a few centimeters of basalt hyaloclastite altered to celadonite floating in a matrix of red claystone and white sparry calcite cement. Altered volcanic ash layers occur higher up in Unit VI.

In general, the upper one-half of the sedimentary section recovered at Site 765 is dominated by calcareous turbidites, funneled down canyons that cut the edge of the deep continental margin plateaus, whereas the lower half is dominated by hemipelagic clays and claystones.

Geochemical variations, using major and trace elements, are significant and can be related to dilution of clay-related elements by $CaCO_3$ and SiO_2. Nonetheless, a "bulk" geochemical composition of the sediments can be calculated, and individual turbidites may be geochemically fingerprinted. The principal clay minerals in the sediments represent volcanic alteration products, with the onset of rapid sedimentation in the early Miocene exhibiting a wide variety of volcanic minerals from different source regions along the margin. All sediments display evidence of deposition below the carbonate compensation depth (CCD), although the (approximately 4 km deep) seafloor may have been above the CCD in the late Valanginian-Hauterivian, when nannofossil chalk was laid down. The same relationships are present in the Atlantic Ocean. Organic carbon content is low, as expected in abyssal sediments, with a rapid excursion to higher values near the Aptian-Albian boundary (consistent with global trends). Mesozoic microfossil assemblages are typical for middle latitudes; many radiolarian taxa are endemic.

Physical properties of sediments, measured on board the ship, reflect a downhole compaction curve, interrupted by intervals of variable physical properties in the stratigraphically condensed units of the Upper Cretaceous and lower Tertiary. This variation matches a series of high-reflectivity zones in the seismic record. Magnetic susceptibility tracks iron oxides and is high in the upper Pliocene and the mid-Cretaceous metalliferous shale units.

Detailed petrophysical well-logging recorded over 1100 m of geochemical data, 750 m of lithoporosity data, and 750 m of sonic velocity data. Steady compaction trends in the Miocene agree with the trends observed from shipboard physical measurements. Asymmetry in the spectrometric log patterns using thorium/uranium (Th/U) and uranium/potassium (U/K) can be related to the presence of clay layers in the carbonate-dominated graded sequences. The activated spectrometry record correlates with X-ray fluorescence (XRF) results in sedimentary samples in terms of calcium/silicon (Ca/Si).

Excellent regional biostratigraphic, lithostratigraphic, and seismostratigraphic correlations to DSDP Site 261, 250 km to the north, suggest that the Late Jurassic age of the basal sediments over the Argo Abyssal Plain may have to be revised upward by 20 m.y. Opening of the Indian Ocean thus may have been Early Cretaceous, rather than Late Jurassic, with important consequences for the early evolution of the Indian Ocean and the destruction of Tethys.

Holes 765C and 765D penetrated 28 and 271 m, respectively, into volcanic basement. Twenty-two volcanic units were distinguished, based on lithological and geochemical variations. The main lithologies recovered were pillow basalt (54%), massive basalt (28%), diabase (4%), autoclastic breccia (6%), and tectonically brecciated pillow basalt (8%).

Despite being one of the oldest sections of oceanic basement cored, i.e., Lowermost Cretaceous, rock preservation is excellent. Fresh glass is present in pillow margins and within hyaloclastite breccia. Low-temperature alteration has affected the entire volcanic section, which is veined with calcite, celadonite, smectite, iron-oxyhydroxides, and rare zeolites. There is no lithological indication of gradation at the base of the hole into higher temperature alteration assemblages. Nonetheless, in spite of the low-temperature alteration and associated geochemical fronts parallel to the veins, much of the basaltic section is only slightly altered.

Geochemical data indicate that the lavas are typical (although somewhat evolved) mid-ocean ridge basalt (MORB) tholeiites. The lavas are dominantly aphyric or sparsely phyric, with rare samples having up to 10% phenocrysts. Plagioclase is the dominant phenocryst, while clinopyroxene is the only mafic phenocryst in many lavas. Olivine, when observed, is highly altered and appears xenocrystic. In the upper 50 m of basalt, frequent xenocrysts of calcic plagioclase and clinopyroxene occur.

Preliminary, shipboard XRF data indicate at least eight geochemical cycles, recognized by systematic trends in zirconium, yttrium, titanium, chromium, and other elements; zirconium ranges from 110 ppm in the most evolved magmas to 70 ppm in the more primitive magmas of each cycle. Distinct negative correlations between zirconium and aluminum and calcium indicate control of magma evolution by plagioclase and clinopyroxene fractionation.

A series of basaltic pebbles from the Miocene sedimentary debris flow described above also were described petrographically, and a subset was analyzed by XRF. Most of these samples are basaltic with two oceanic andesites. The basalts are olivine and plagioclase phyric and range geochemically from normal-MORB to enriched-MORB compositions. In terms of petrography and geochemistry, these basalts are distinct from those drilled at Site 765. There, provenance is probably a series of basement highs at the mouth of the Swan submarine canyon on the Exmouth Plateau.

Hole 765D was cased to provide a stable site for coring and logging, and for a series of geophysical experiments. Lithoporosity, sonic, and geochemical logs were run in the hole with no operational problems. The chemical log also was run through the casing in the sedimentary section (as was the sonic log) to investigate the integrity of the cement behind the casing. High sonic velocities indicate broad correlations with massive flow intervals and the diabase. Potassium anomalies can be correlated with brecciated zones containing smectite and celadonite.

A vertical seismic profile (VSP) experiment was attempted in basement. This met with little success, probably because of weak signals at depths to basement of 7 km. The VSP recordings were continued through the casing in the sedimentary section, and reasonable seismic signals were recorded despite a considerable amount of noise from the pipe.

Two borehole televiewer (BHTV) runs recorded breakouts in the basement. Complete basalt cores were mapped before splitting for fracture patterns for comparison with BHTV results processed onshore. The single-packer permeability experiment was partially successful and indicated low permeability in this old oceanic crust. The double-packer experiment, which was constructed to quantify the stress measurements, failed because of a malfunctioning packer tool.

BACKGROUND AND SCIENTIFIC OBJECTIVES

Background and Site Selection

Site 765 is located in the southern Argo Abyssal Plain on the oldest oceanic crust in the Indian Ocean. This site was originally designated AAP1B and was proposed in a revision of Ocean Drilling Program (ODP) proposal 121B, submitted to the JOIDES Planning Committee in May 1986 (von Rad et al., 1986). Site surveys for this proposal were conducted by the Australian Bureau of Mineral Resources (BMR) research vessel *Rig Seismic* during Legs 55 and 56 (Exon and Williamson, 1988). During these two cruises, some operations were concerned with the definition of sites that would pass ODP Safety Panel criteria. The northern part of the outer Exmouth Plateau and the Argo Abyssal Plain were investigated by multi- and single-fold seismic surveys, and dredge hauls were performed during the second part of Leg 56. The areas involved in the seismic survey for Site 765 are shown in Figure 1. These areas were (1) Lines 27, 26, and 24, across Emu Spur to the west of the Swan Canyon to Site AAP1B (Site 765 in Fig. 1) and (2) Lines 21 and 22, from the Wombat Plateau east to Echidna Spur and northeast to Site 765. The program of Leg 56 also included a grid of lines over the proposed area of Site 765. Three of the ODP Leg 122 sites were located on the Wombat Plateau, and seismic surveys for these sites also were conducted during BMR *Rig Seismic* Cruise 56. The final location proposed for Site 765 is along Line 56/23C, near its intersection with Line 56/22 (Fig. 2).

The proposed site indicated an approximately 900-m-thick sedimentary section, overlying a strong, gently dipping reflector with hyperbolic patterns, inferred as the top of Upper Jurassic ocean crust.

Additional support for drilling in the southwestern Argo Abyssal Plain was provided by a second proposal submitted to JOIDES by Gradstein (1986). This proposal emphasized the stratigraphic and paleoceanographic objectives related to the origin of the Indian Ocean of Site 765, and proposed a companion site (AAP2 in Fig. 2), located to the northwest of Site 765 on *Atlantis II* Line 93-14. This site was on inferred marine magnetic anomaly M25 and had as its major objectives: (1) high-resolution, multiple biomagnetostratigraphy, as compared to AAP1B; (2) dating of M25 in the Argo Abyssal Plain; and (3) three-dimensional, quantitative paleontological distribution models obtained by comparison of AAP1B with AAP2. This latter idea was ultimately rejected by the JOIDES Planning Committee.

Because Site 765 is located on an abyssal plain on old oceanic crust that is being subducted beneath the Sunda Arc, it was proposed as a "global geochemical reference site," by Langmuir and Natland (1986). These sites are located near the subducting margins of the oceanic plates and require sampling of complete sections of the sedimentary sequence and a representative section of oceanic basement for geochemical purposes. This proposal was strongly supported by the JOIDES Lithosphere Panel and ultimately endorsed by the JOIDES Planning Committee. At the time the proposal was written it was anticipated that the Argo Abyssal Plain site would be complemented by other deep-ocean crust sites on the West Pacific margin.

The requirement to drill a representative section of oceanic crust was a significant addition to the proposed drilling strategy in the Argo Abyssal Plain. The JOIDES Indian Ocean Panel recommended separating the Exmouth Plateau and Argo Abyssal Plain drilling into two legs to achieve all objectives; Leg 122 was to drill five or six sites on the Wombat Plateau, and Leg 123 would drill the deep abyssal plain site (Site 765) and one of the Exmouth sites (initially EP-9A on the Wombat Plateau).

Given the deep crustal objectives of Leg 123 and the proposal to establish a deep reentry site on the Argo Abyssal Plain, several logging and geophysical experiments were proposed for Site 765. These included complete logging of the basement and sediment section, a vertical seismic profile, porosity determinations in basement, hydrofracturing of basement, and BHTV runs into basement.

The final location of Site 765 (shown in Fig. 2) is 0.25 mi southeast of proposed Site AAP1B. A beacon was dropped at 1830L (local time) on 7 September 1988; exact coordinates are 15°58.55′S, 117°34.51′E. The seismic profile for the site is shown in Figure 3. Site 765 lies in a water depth of 5725 m on Mesozoic ocean crust at the southern edge of the Argo Abyssal Plain, and within 75 km of the ocean/continent boundary. Estimated sediment thickness for Site 765 was 950 m, with 250 m of oceanic basement penetration planned.

Scientific Objectives

Specific objectives planned for Site 765 were as follows:

1. To compare the sedimentation, tectonic events, and seismostratigraphic sequences of the Argo Abyssal Plain with those on the northwestern Australian continental margin and correlative geological settings in the North and South Atlantic oceans and along the margins.
2. To improve the Mesozoic, and particularly the Upper Jurassic to Lower Cretaceous, magnetobiostratigraphy for mid-(paleo)latitudes and the geological time scale.
3. To achieve a better understanding of the early opening history of the Indian Ocean and its implications for the destruction of the Tethys Ocean.
4. To determine the nature of magmas associated with final stages of rifting of a continental margin and the formation of the oldest Indian Ocean crust.
5. To provide a "geochemical reference site" in sediments and oceanic basement for use in global mass-balance calculations.
6. To apply new logging techniques, such as vertical seismic profiling and hydrofracture experiments, for stress analysis and determination of the regional stress pattern of the eastern Indian Ocean.

GEOLOGIC SETTING

The Argo Abyssal Plain is an extremely flat, about 5.7 km deep, abyssal plain located north of the Exmouth Plateau and west of the Scott Plateau (Fig. 4). To the north, it is bounded by the Java Trench and is underlain by the oldest known oceanic crust in the Indian Ocean. Since the Cenozoic, the Argo Abyssal Plain crust has been slowly consumed by the convergence of

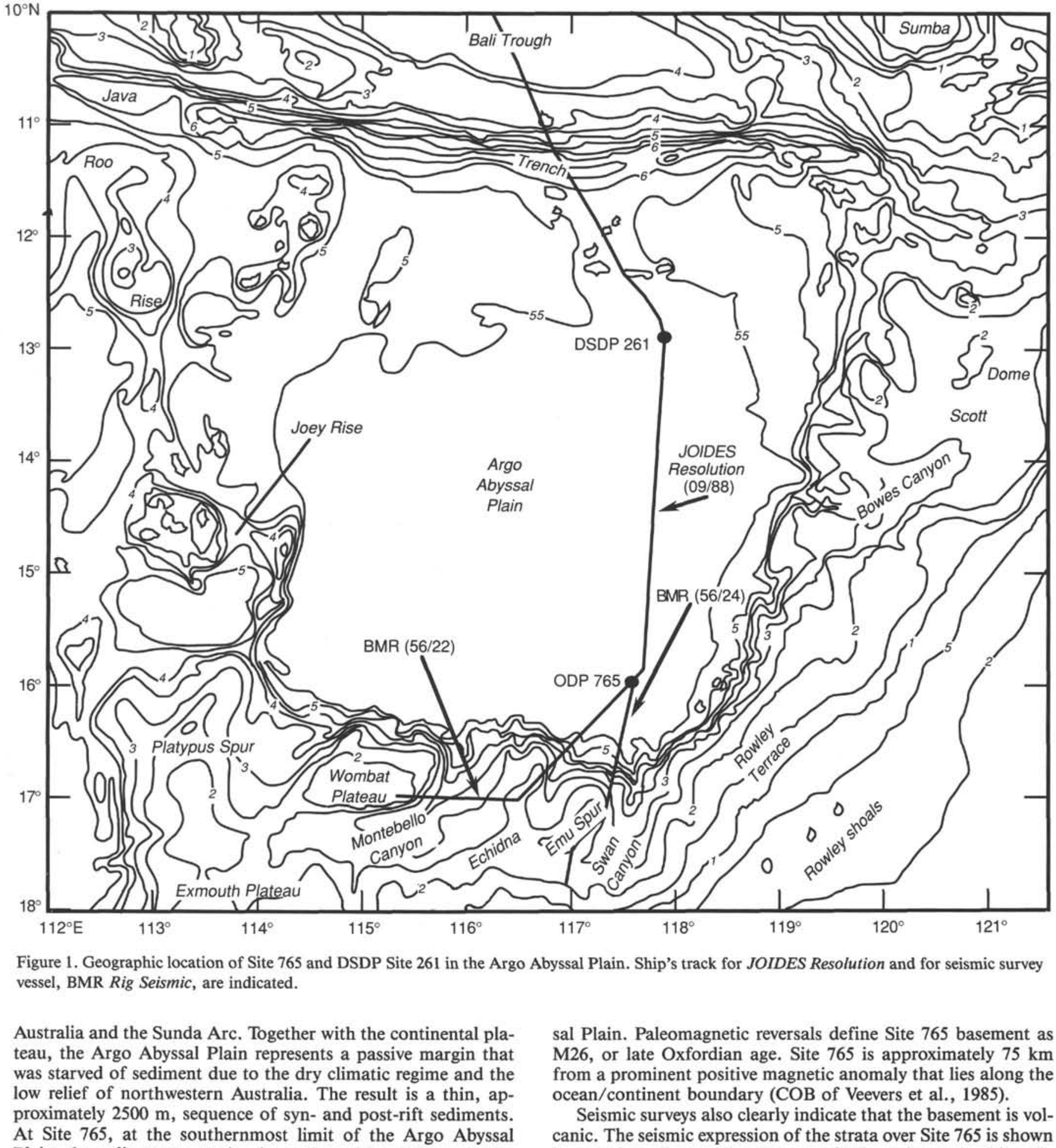

Figure 1. Geographic location of Site 765 and DSDP Site 261 in the Argo Abyssal Plain. Ship's track for *JOIDES Resolution* and for seismic survey vessel, BMR *Rig Seismic*, are indicated.

Australia and the Sunda Arc. Together with the continental plateau, the Argo Abyssal Plain represents a passive margin that was starved of sediment due to the dry climatic regime and the low relief of northwestern Australia. The result is a thin, approximately 2500 m, sequence of syn- and post-rift sediments. At Site 765, at the southernmost limit of the Argo Abyssal Plain, the sedimentary section is condensed into 900 m overlying oceanic basement.

In the Argo Abyssal Plain, marine magnetic surveys (Larson 1975; Heirtzler et al., 1978; Veevers et al., 1985; Fullerton et al., 1989) clearly show that the basement is oceanic. The magnetic anomalies generally trend N70°E. Correlation of these anomalies with the Hawaiian and Keathley marine magnetic anomaly sequences (from the Pacific and the Atlantic oceans, respectively), in addition to the accepted Late Jurassic age of basal sediments in DSDP Site 261, indicates the presence of M25 to M16 marine magnetic lineations and isochrons in the Argo Abyssal Plain. Paleomagnetic reversals define Site 765 basement as M26, or late Oxfordian age. Site 765 is approximately 75 km from a prominent positive magnetic anomaly that lies along the ocean/continent boundary (COB of Veevers et al., 1985).

Seismic surveys also clearly indicate that the basement is volcanic. The seismic expression of the strata over Site 765 is shown in a section of Australian Bureau of Mines site survey Line 56-23 (see Fig. 3, "Background and Scientific Objectives" section, this chapter). A 2-s two-way traveltime penetration of approximately 900 m of relatively soft sediments defines flat-lying sedimentary reflectors that contrast with the characteristic hyperbolic reflectance of oceanic basement. Site 765 is situated over a smooth basement surface that contrasts with the rougher, block-faulted terrain on either side.

DSDP Site 261 (Veevers, Heirtzler, et al., 1974), drilled during Leg 27, is located approximately 320 km to the north of Site 765 (Fig. 4). Information from this site was used to predict li-

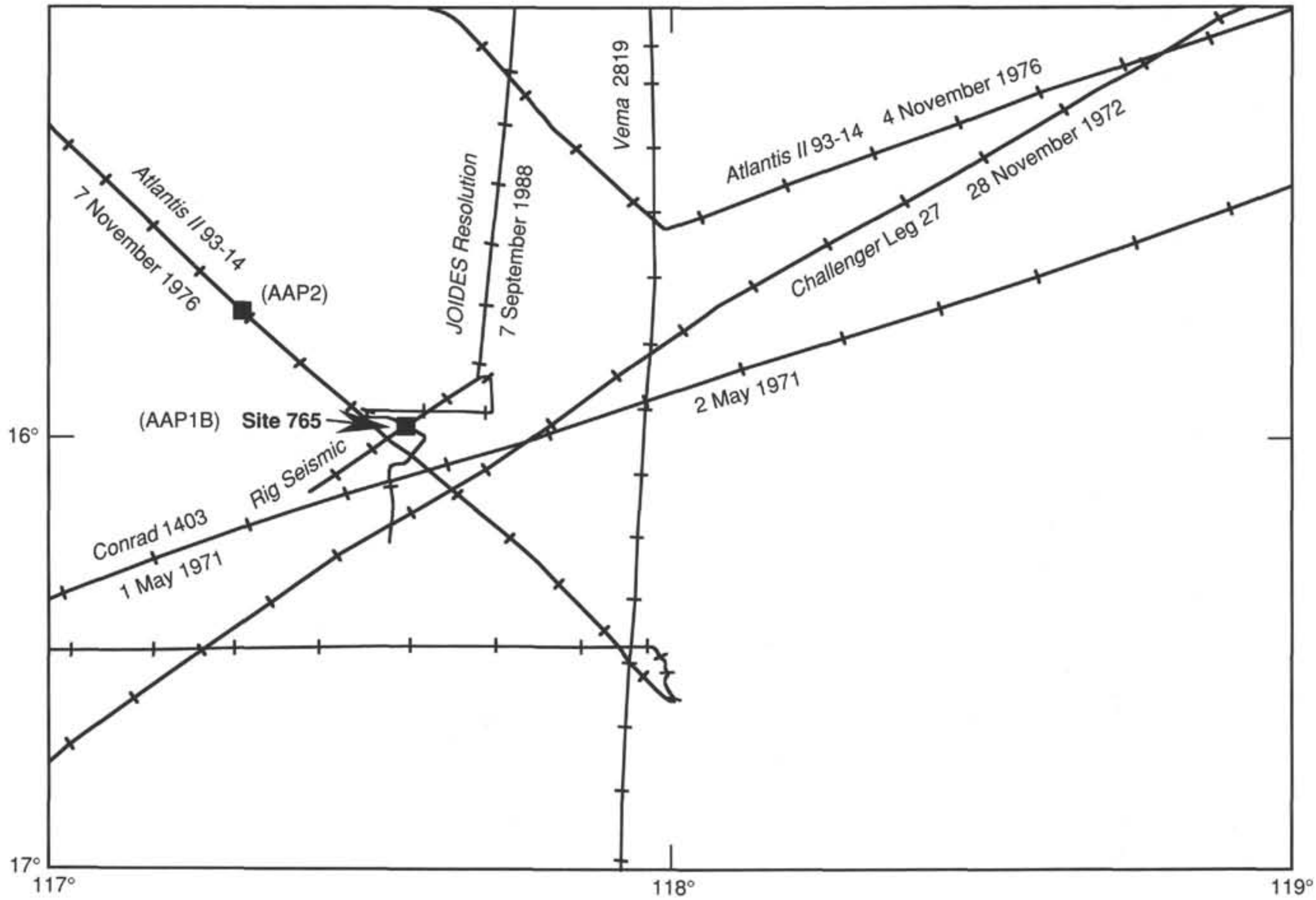

Figure 2. Site-survey information for Site 765 and proposed Site AAP2, showing exact location of Site 765.

thologies at Site 765. Recovery of sediments at DSDP Site 261 was, on average, less than 23%. The age of the section is ambiguous because of imprecise magnetostratigraphy and an incomplete biostratigraphic record. A controversial site biostratigraphy gives basal sediment ages of Valanginian to Oxfordian/Kimmeridgian. Magnetostratigraphic lineation interpretations place DSDP Site 261 at M23, in the upper Kimmeridgian. Tholeiitic basalts drilled at the base of this hole are typical MORBs, but are overlain by a sill of more evolved iron-titanium (Fe-Ti) basalt (Robinson and Whitford, 1974).

To place the geology of the Argo Abyssal Plain in a regional framework, we have included an east-to-west schematic cross section from the Australian continental margin toward the abyssal plain (Fig. 4B). The location of the section is shown in Figure 4A. This cross section is based on seismic data and stratigraphic interpretations from exploratory wells and dredges (von Stackelberg et al., 1980; von Rad and Exon, 1982). The main features of the geological development of the plateau are as follows: the sediments beneath the Exmouth Plateau were deposited in an extension of the Carnarvon and Canning basins that formed a Tethyan embayment in Gondwana open to the north and that received detrital sediments from the south and east until Early Cretaceous time. In the central plateau region, at least 3000 m of mainly Upper Jurassic to Lower Cretaceous paralic and shallow-marine detrital sediments, derived from the south and east, covered the Triassic to Middle Jurassic block-faulted surface. About 200 m of hemipelagic shallow-marine sediments were deposited in the mid-Cretaceous, followed by 500 to 1000 m of Upper Cretaceous to Cenozoic eupelagic carbonate sediment. The Exmouth Plateau Arch and landward Kangaroo Syncline probably warped to their present form during the Miocene, by which time the central plateau had subsided to bathyal depth.

The northern Exmouth Plateau experienced a Cretaceous to Cenozoic evolution similar to that of the central plateau. However, 1 to 3 km of probable Triassic to Lower Jurassic shelf carbonates were deposited north of the "North Exmouth hingeline," during a time when the central Exmouth Plateau was being eroded (e.g., on the Wombat Plateau drilled during ODP Leg 122; see cross-section B-B′ in Fig. 6 of the "Background and Introduction" chapter, this volume). In Jurassic time, break-up occurred along the northeastern rim of Gondwana and quickly led to formation of an abyssal oceanic graben north of the Exmouth and Wombat plateaus in the present Argo Abyssal Plain. This was followed in the Early Cretaceous by separation of Australia and India, when seafloor spreading was initiated in the present Gascoyne and Cuvier Abyssal plains to the west of these plateaus.

From earliest Cretaceous onward, more than 500 m of calcareous claystone accumulated in these sediment-starved, deep, continental margin grabens (cross-section C-C′ in Fig. 7 of the "Background and Introduction" chapter, this volume); these sediments presumably were derived from the southeast. Since then, more than 400 m of zeolitic clay, siliceous clay, and calcareous ooze turbidites have been deposited. Backtrack curves for DSDP Sites 260 and 261 indicate initial mid-ocean ridge depths near 2500 m, near the world average; cooling of normal ocean crust thus can account for most of the present-day ocean depths along the northwestern Australian margin.

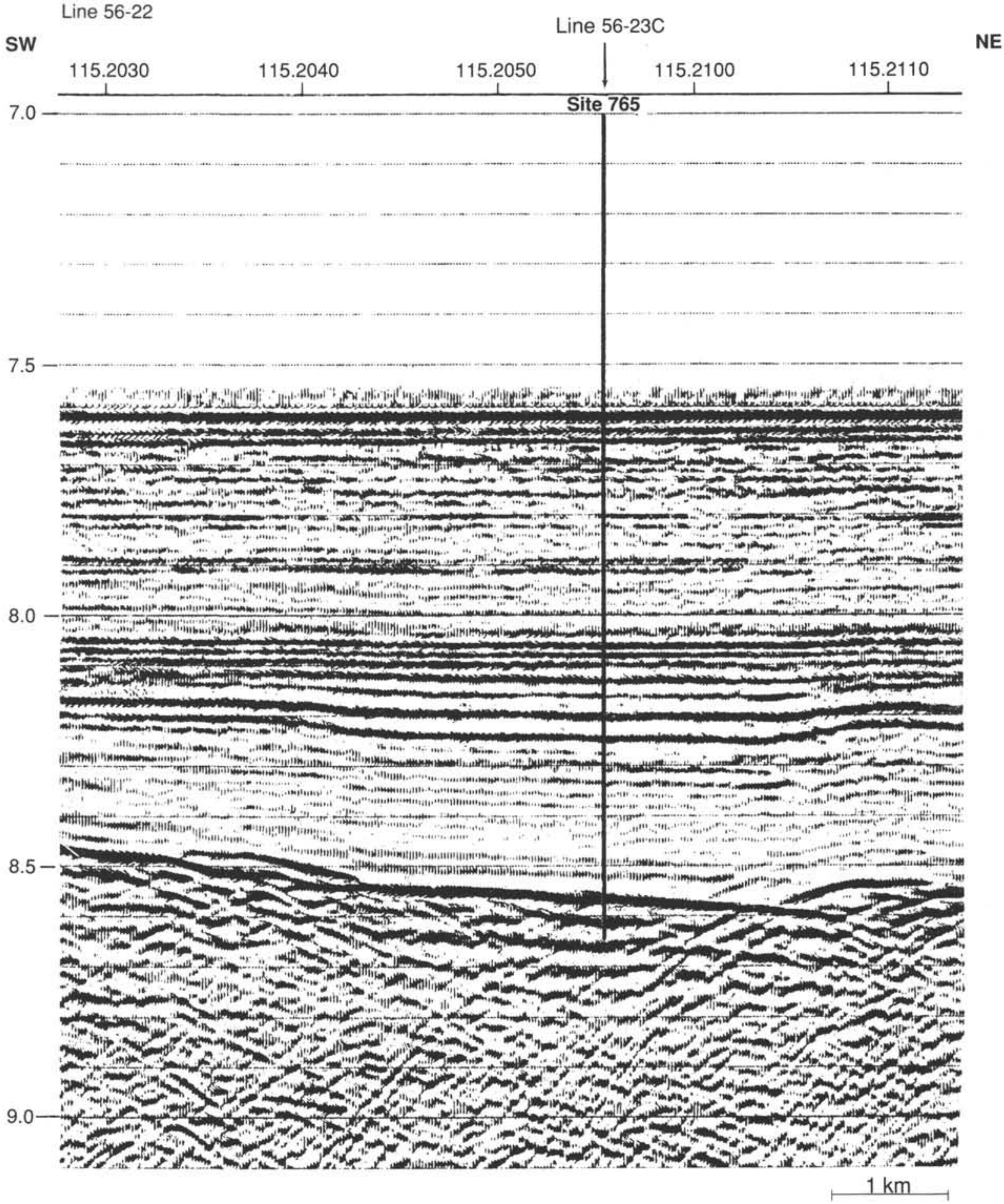

Figure 3. Multifold seismic profile over Site 765 along Line 56-22 of BMR *Rig Seismic*. Acoustic basement is at approximately 900 to 950 m. BMR *Rig Seismic* Line 56-23C intersects the section at the site position.

OPERATIONS

Introduction

On 1 September 1988 at 1500L (local time), 1 day ahead of schedule, the *JOIDES Resolution* weighed anchor and left the Johor anchorage in Singapore for Leg 123 in the Argo and Gascoyne Abyssal plains off northwestern Australia.

Under pleasant sailing conditions, the ship proceeded on a southeasterly course at an average speed of 11.8 kt through the Java Sea to the Strait of Lombok, which separates the islands of Bali and Lombok. At 0300L on 5 September, the ship turned out of the strait, on a heading of 152°, into the Indian Ocean toward DSDP Site 261. Details of the ship's track are shown in Figures 1 and 2 of the "Underway Geophysics" chapter (this

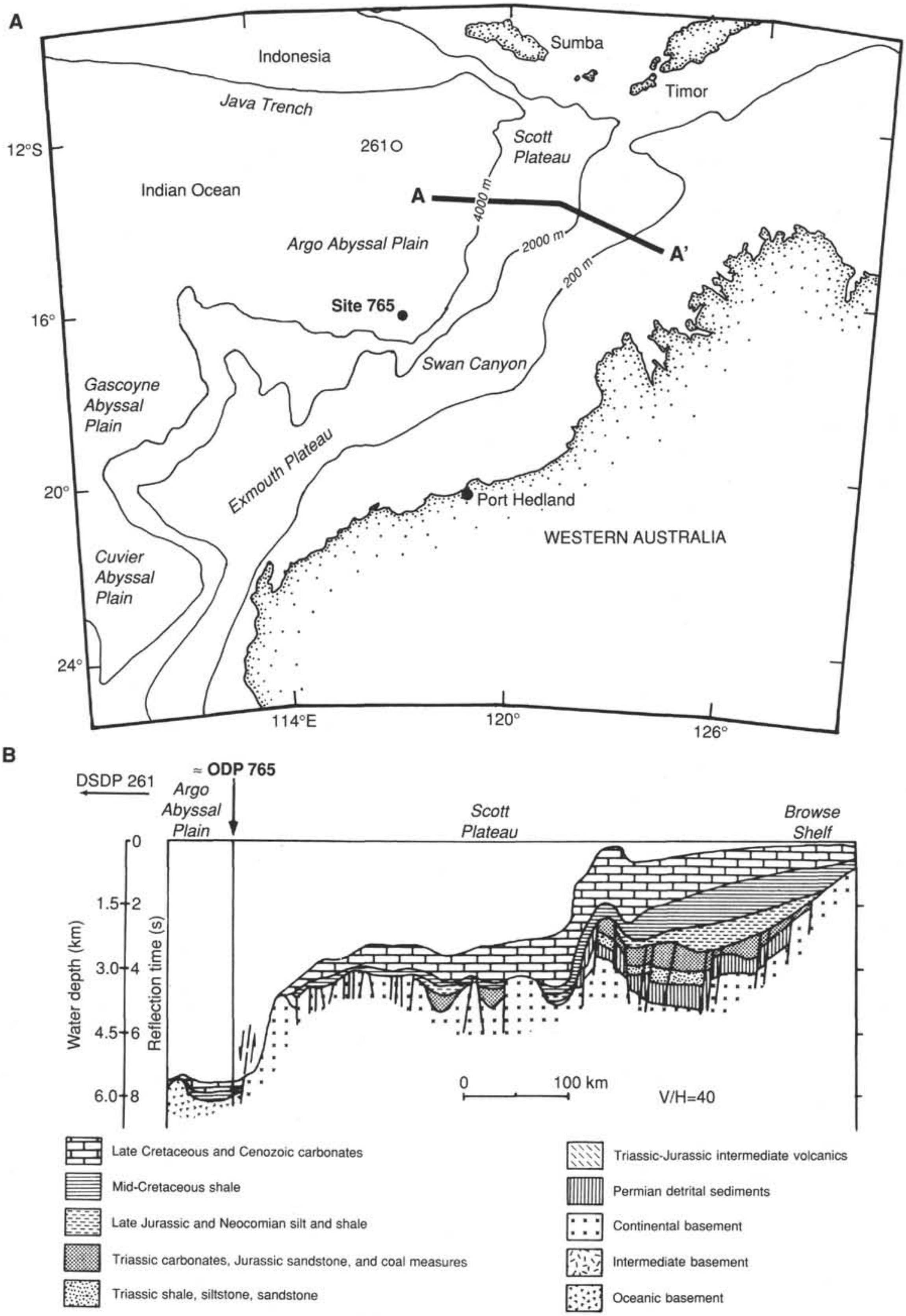

Figure 4. A. Location of Site 765 and DSDP Site 261, Argo Abyssal Plain, and line of Cross section A-A'. B. Schematic geologic cross section over the Scott Plateau into the Argo Abyssal Plain, with projected geographic position of Site 765, on the Argo Abyssal Plain, in front of the continental slope escarpment.

volume). A magnetometer was deployed at 0400L on 5 September. The newly installed 3.5-kHz sonic recording unit operated perfectly, with an excellent record of the upper 70 m of sediment.

Our operations plan was to spend three-quarters of operational time at the Argo Abyssal Plain Site 765 and one-quarter at the Gascoyne Abyssal Plain Site 766.

Strategy

Our objective at Site 765 was to core and log a complete sedimentary section and at least 250 m of basement. To maximize recovery, combined advanced hydraulic piston corer/extended-core barrel (APC/XCB) coring was planned until refusal, followed by rotary core barrel (RCB) coring to basement. Limited penetration of basement was planned (1) to allow logging of the sediment/basement interface and (2) to guarantee basement recovery in case of eventual drilling failures in later holes. Our comprehensive drilling program and the anticipated soft sediment section deep in the hole was thought to require that a second hole be drilled and the sedimentary section cased into basement. Following this engineering challenge, we believed that drilling would proceed to maximum basement depths allowable within the time frame and that logging and geophysical experiments could proceed in stable hole conditions. Logging of the sedimentary section was to be completed after coring the sediment section in the first hole and, when possible, through the casing in the second hole.

Three Schlumberger logging runs (velocity, resistivity, and caliper), a lithodensity tool (LTD), neutron-porosity tool, and natural gamma-ray tool, as well as a new Lamont-Doherty Geological Observatory (LDGO) heat-flow logging tool were to be used. In addition, a vertical seismic profile and stress experiments using permeability and hydrofracture were to be conducted during Leg 123. Table 1 summarizes the operations executed for Leg 123 and shows accumulated time for the sequence of operations.

Site Survey and Geophysics

Much of the planning for Site 765 was based on the results of drilling at DSDP Site 261 (12°56.83′S, 117°53.56′E) in the northern Argo Abyssal Plain. Despite the poor recovery at Site 261, important stratigraphic correlations were required between this site and the proposed drilling target. As only poor quality single-channel seismic data existed to tie the stratigraphic record of the two sites, we decided to shoot a 176-nmi seismic line between the two sites. This required a 17-nmi detour from our planned heading to Site 765.

At 0220L on 6 September, the ship arrived on location 6 nmi north of Site 261. Our heading was changed to 184°, the ship was slowed to 5 kt, and two 80 in.^{3} water guns were deployed. By 0324L, the ship was above Site 261, in a water depth of 5656 m. The underway seismic record indicated approximately 0.65 s two-way traveltime to basement, and a clear mid-sediment depth reflector, interpreted as the hiatus between the Miocene and the mid-Cretaceous (reflector L), was easily identifiable. At 0500L, the ship's speed was increased to 8 kt, on a heading of 186°; our location was now 13°05.11′S, 117°53.83′E and water depth was 5678 m. The seismic record proved satisfactory at this speed; good seismic records were maintained to the location of Site 765.

At 0100L on 7 September, at 15°51.55′S, 117°41.54′E, we changed our heading to 224° to coincide with the track of the *Rig Seismic* Line 56-22. After steaming for 30 min, speed was reduced to 5 kt and a 14-kHz beacon was deployed. Using the match between the shipboard underway seismic line and Line 56-22, we reached an area of flat basement (see Figs. 5D and 6, "Underway Geophysics" chapter, this volume) that had been previously selected as the location for Site 765. The precise location was confirmed later by global positioning system (GPS) navigation as 15°58.55′S, 117°34.51′E, in a water depth of 5738 m (sonar) and 5728.2 m (drill string).

To complete the seismic survey, the ship steamed 1 nmi on the same heading, then was turned and sailed on a reciprocal heading of 48° over the site. Seismic gear was retrieved at 0410L on 7 September, and the ship was positioned above the beacon. Locations of the seismic survey lines for Site 765 are given in Figure 6 of the "Underway Geophysics" chapter (this volume). Unfortunately, contact with the beacon was lost. The ship's position was maintained in the area using transit satellites and dead reckoning navigation until 1630L, when global positioning data allowed us to return the ship to the location of the original beacon drop. During this time, the rig crew ran drill pipe. At 1630L on 7 September, a second beacon was deployed (16 kHz) and successfully acquired. Figure 5 depicts a breakdown of operational time for the first 6.3 days of Leg 123.

Table 1. Operations summary, Site 765.

Operation	Date (1988)	Days cumulate
Transit		
Leave Singapore	1 Sept	0
Singapore to DSDP Site 261	6 Sept	4.5
DSDP Site 261 to Site 765	7 Sept	5.5
Holes 765A, 765B, 765C		
Locate Site 765	7 Sept	5.6
First Bit	7 Sept	6.4
Jet-in test	7 Sept	6.6
APC 173 mbsf—sediments	8 Sept	7.6
XCB 173 to 395 mbsf—sediments	10 Sept	9.1
Round trip RCB	11 Sept	9.9
RCB 540 m—sediments	18 Sept	16.2
RCB 30 m—volcanic crust	18 Sept	17.1
Condition hole	19 Sept	17.8
Schlumberger logging (SS tool)	21 Sept	20.2
Trip out	22 Sept	20.7
Hole 765D		
Ready reentry cone	22 Sept	21.3
Lower cone to seafloor	22 Sept	21.8
Jet in and release cone	23 Sept	22.3
Drill 940 m for casing string	25 Sept	23.9
Condition hole	25 Sept	24.9
Trip up	26 Sept	25.3
Makeup 82 joints casing pipe	27 Sept	27.0
Set casing	29 Sept	28.4
Trip for RCB	30 Sept	29.1
Drill out casing shoe	30 Sept	29.3
Core 250 m volcanic crust (3 drill bits)	9 Oct	37.9
Round trip packer	10 Oct	38.9
Schlumberger logging (2 tools)	12 Oct	40.7
Pre-fracture borehole televiewer	12 Oct	41.3
Vertical seismic profiling	13 Oct	42.4
Schlumberger logging (LDT)	14 Oct	42.8
Hydrofracture single packer, BHTV	14 Oct	44.5
Round trip for double packer	15 Oct	45.9
Hydrofracture double packer, BHTV	17 Oct	47.4
Trip out	17 Oct	47.9

Holes 765A and 765B

The upper sedimentary section was cored using the APC and XCB coring systems. The first APC core arrived on deck at 2230L on 7 September (Tables 1 and 2). Core 123-765A-1H was completely filled with gray nannofossil ooze, indicating the bit was below the mud line. A jet-in test was performed to 135 mbsf to determine how deep to set the conductor pipe before another attempt to define the mud line.

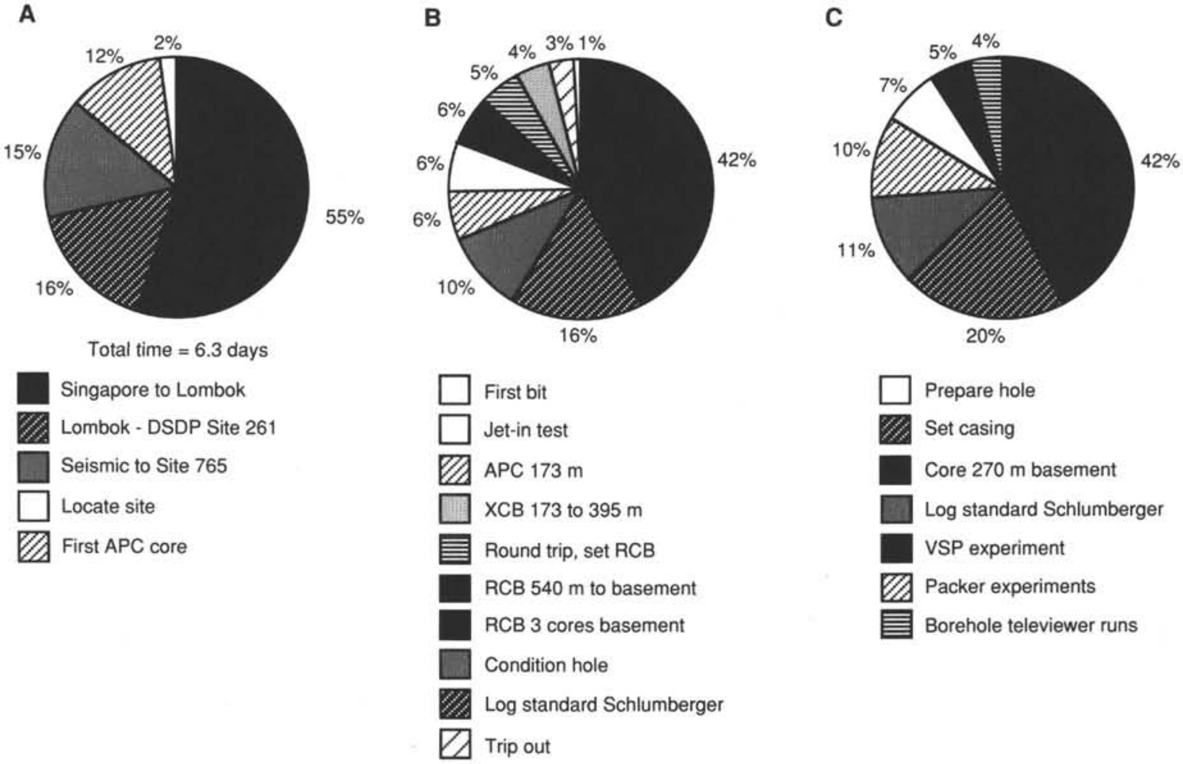

Figure 5. A. Time lapsed during transit to Site 765. B. Time lapsed during operations at Holes 765A, 765B, 765C. C. Time lapsed during operations at Hole 765D.

Core 123-765B-1H established the mud line at a water depth of 5728.2 m (gamma-ray log data later verified the mud line at 5723 mbsf). APC coring continued to 173.3 mbsf (Core 123-765B-18H) and terminated on 9 September. Pipe was removed from the hole and the XCB system picked up. Upon reentry, coring continued to 395.6 mbsf (lower middle Miocene; Cores 123-765B-19X to -41X), which was reached on 10 September at 1600L. Hole deviation from vertical at the bottom was approximately 5.9°. Sediment recovery was approximately 100% when using the APC system in the softer upper 173.3 m of the hole, but decreased to an average of 43% for the 222.3 m cored using the XCB (Fig. 6).

Hole 765C

Poor recovery in the last five cores of Hole 765B (Table 2) resulted from obstruction of the core barrel by pebbles, wood, and clay plugs. As it was clear that recovery would not improve downsection using the XCB, we decided to remove pipe and begin RCB coring. A long-toothed bit was used to improve cutting of clays and/or mudstones.

Hole 765C was spudded at 1700 on 11 September and washed to 350.2 mbsf. Core 123-765C-1R was on deck at 0005L on 12 September. The bottom of Core 123-765C-5R is 3 m below the depth reached by Core 123-765B-41X (Fig. 6). Recovery was much improved, and the RCB bit easily cut and cored the alternating lithified sandy carbonate and clay beds of the lower Miocene sediments. Hole deviation was measured at 4° to 5° and was observable in the angle of the sediment laminae in the cores.

Coring continued with moderate to good recovery using the RCB system (Fig. 7). Miocene turbidites gave way to Oligocene olistostromes containing highly disturbed sedimentary units (dominantly clays) and volcanic pebbles. Eocene sediments were cored at approximately 520 mbsf on the evening of 13 September, and clays of the Tertiary/Cretaceous boundary were drilled in the early morning of 14 September (Core 123-765C-22R). Drift measurements placed the hole deviation from vertical at 4° at 400 mbsf and 6.5° at 580 mbsf. Recovery of four to five sections per core was considered good using the RCB system. Cores 123-765C-20R to -25R contained swelling clays that underwent up to 15% expansion. To reduce the swelling and deformation of these cores in the cut core liners, cores were washed in the laboratory with seawater. Because many Cretaceous cores contained basalt pebbles in sedimentologically unusual positions (commonly on the top of the core), we concluded that the middle Tertiary debris flow (?basalt conglomerate) at approximately 480 mbsf, was shedding material into the hole during drilling of the older units.

On 16 September, during retrieval of claystone Core 123-765C-45R from 777 mbsf, the pipe became stuck—the result of swelling clays in the hole. After approximately 30 min, the pipe was worked free; mud was then circulated, and the hole was wiped. Coring of the claystone sequence continued with good to excellent recovery. Drift measurements showed that hole deviation from vertical was 10°. Using shipboard velocity measurements on the Cretaceous claystone, basement depths were revised to between 925 and 950 mbsf. After compensating for hole drift, a depth of 935 to 940 mbsf was indicated. This was confirmed when on 18 September, Core 123-765C-62R was retrieved with 35 cm of altered basalt in the core catcher. This basalt was overlain by almost 5 m of red claystone, indicating that the sediment/basement contact had been retrieved; exact basement depth for Hole 765C was established at 935.6 mbsf.

Core recovery steadily improved through the basal Cretaceous claystone and the average recovery for RCB Cores 123-765C-1R through -62R was 62.3%, compared with the total of 68% for all APC, XCB, and RCB cores combined. A final drift shot showed an 11° deviation from vertical in the lowermost part of the hole. Total RCB drill bit time was 30 hr, with most sediment cores cut in less than 30 min.

After several hours of cleaning the hole with mud circulation and wiping, three more basement cores were cut. Two of these cores were drilled to allow for logging of the sediment/basalt in-

Table 2. Coring summary, Site 765.

Core	Date (1988)	Time (L)	Depth (mbsf)	Length cored (m)	Length recovered (m)	Recovery (m)	Recovery (%)
123-765A-1H	7 Sept	1045	0	9.6	9.6	9.69	101.0
765B-1H	8 Sept	0445	0	9.3	9.3	9.30	100.0
2H	8 Sept	1610	9.3	18.8	9.5	9.48	99.8
3H	8 Sept	0715	18.8	28.5	9.7	9.74	100.0
4H	8 Sept	0840	28.5	38.1	9.6	9.63	100.0
5H	8 Sept	0945	38.1	47.8	9.7	9.72	100.0
6H	8 Sept	1105	47.8	57.4	9.6	9.71	101.0
7H	8 Sept	1210	57.4	67.1	9.7	9.87	102.0
8H	8 Sept	1420	67.1	76.8	9.7	9.74	100.0
9H	8 Sept	1530	76.8	86.4	9.6	9.81	102.0
10H	8 Sept	1640	86.4	96.0	9.6	9.86	103.0
11H	8 Sept	1745	96.0	105.6	9.6	9.84	102.0
12H	8 Sept	1905	105.6	115.2	9.6	9.78	102.0
13H	8 Sept	2010	115.2	124.8	9.6	10.00	104.1
14H	8 Sept	2125	124.8	134.5	9.7	9.59	98.8
15H	8 Sept	2240	134.5	144.2	9.7	9.88	102.0
16H	8 Sept	2355	144.2	153.9	9.7	9.81	101.0
17H	9 Sept	0105	153.9	163.6	9.7	10.05	103.6
18H	9 Sept	0220	163.6	173.3	9.7	9.80	101.0
19X	9 Sept	0345	173.3	183.0	9.7	6.84	70.5
20X	9 Sept	0500	183.0	192.7	9.7	8.23	84.8
21X	9 Sept	0615	192.7	202.4	9.7	8.22	84.7
22X	9 Sept	0730	202.4	212.1	9.7	6.99	72.0
23X	9 Sept	0845	212.1	221.8	9.7	3.50	36.1
24X	9 Sept	0955	221.8	231.5	9.7	6.26	64.5
25X	9 Sept	1110	231.5	241.2	9.7	1.11	11.4
26X	9 Sept	1225	241.2	250.9	9.7	5.65	58.2
27X	9 Sept	1355	250.9	260.6	9.7	4.56	47.0
28X	9 Sept	1525	260.6	270.2	9.6	3.84	40.0
29X	9 Sept	1700	270.2	279.9	9.7	2.30	23.7
30X	9 Sept	1825	279.9	289.6	9.7	1.41	14.5
31X	9 Sept	2020	289.6	299.3	9.7	7.58	78.1
32X	9 Sept	2205	299.3	309.0	9.7	4.70	48.4
33X	9 Oct	0000	309.0	318.7	9.7	7.27	74.9
34X	9 Oct	0145	318.7	328.3	9.6	2.47	25.7
35X	9 Oct	0330	328.3	337.9	9.6	2.66	27.7
36X	9 Oct	0530	337.9	347.5	9.6	3.98	41.4
37X	9 Oct	0730	347.5	357.1	9.6	3.01	31.3
38X	9 Oct	0930	357.1	366.7	9.6	1.99	20.7
39X	9 Oct	1140	366.7	376.4	9.7	1.27	13.1
40X	9 Oct	1400	376.4	386.0	9.6	0.68	7.1
41X	9 Oct	1710	386.0	395.6	9.6	0.74	7.7
765C-1R	12 Sept	0005	350.2	359.6	9.4	0.46	4.9
2R	12 Sept	0150	359.6	369.3	9.7	4.02	41.4
3R	12 Sept	0345	369.3	379.0	9.7	3.88	40.0
4R	12 Sept	0605	379.0	388.6	9.6	4.83	50.3
5R	12 Sept	0820	388.6	398.3	9.7	5.88	60.6
6R	12 Sept	1025	398.3	408.0	9.7	5.56	57.3
7R	12 Sept	1335	408.0	417.7	9.7	5.40	55.7
8R	12 Sept	1620	417.7	427.3	9.6	6.17	64.3
9R	12 Sept	1900	427.3	436.5	9.2	7.27	79.0
10R	12 Sept	2105	436.5	446.0	9.5	6.55	68.9
11R	12 Sept	2310	446.0	455.2	9.2	6.04	65.6
12R	13 Sept	0115	455.2	464.6	9.4	6.96	74.0
13R	13 Sept	0320	464.6	474.1	9.5	3.44	36.2
14R	13 Sept	0650	474.1	483.7	9.6	1.83	19.0
15R	13 Sept	0855	483.7	493.2	9.5	1.38	14.5
16R	13 Sept	1140	493.2	502.4	9.2	6.27	68.1
17R	13 Sept	1400	502.4	511.9	9.5	5.76	60.6
18R	13 Sept	1610	511.9	521.3	9.4	7.36	78.3
19R	13 Sept	1805	521.3	530.8	9.5	4.55	47.9
20R	13 Sept	2120	530.8	540.4	9.6	2.49	25.9
21R	13 Sept	2320	540.4	550.1	9.7	0.66	6.8
22R	14 Sept	0135	550.1	559.7	9.6	7.16	74.6
23R	14 Sept	0340	559.7	569.3	9.6	6.78	70.6
24R	14 Sept	0555	569.3	579.0	9.7	5.72	58.9
25R	14 Sept	0850	579.0	588.3	9.3	6.66	71.6
26R	14 Sept	1105	588.3	597.5	9.2	5.76	62.6
27R	14 Sept	1305	597.5	607.0	9.5	2.49	26.2
28R	14 Sept	1505	607.0	616.4	9.4	4.06	43.2
29R	14 Sept	1725	616.4	625.9	9.5	8.31	87.5
30R	14 Sept	2000	625.9	635.3	9.4	8.12	86.4
31R	15 Sept	0000	635.3	645.0	9.7	5.43	56.0
32R	15 Sept	0225	645.0	654.7	9.7	4.53	46.7
33R	15 Sept	0445	654.7	664.4	9.7	3.35	34.5
34R	15 Sept	0645	664.4	674.1	9.7	5.45	56.2
35R	15 Sept	0900	674.1	683.3	9.2	5.50	59.8
36R	15 Sept	1210	683.3	693.0	9.7	8.12	83.7
37R	15 Sept	1425	693.0	702.5	9.5	5.24	55.1
38R	15 Sept	1640	702.5	711.7	9.2	9.92	108.0
39R	15 Sept	1840	711.7	720.9	9.2	6.29	68.3
40R	15 Sept	2050	720.9	730.4	9.5	6.71	70.6
41R	15 Sept	2315	730.4	739.8	9.4	0.77	8.2
42R	16 Sept	0235	739.8	749.1	9.3	6.80	73.1
43R	16 Sept	0435	749.1	758.5	9.4	8.53	90.7
44R	16 Sept	0635	758.5	768.2	9.7	5.63	58.0
45R	16 Sept	0910	768.2	777.8	9.6	8.84	92.1
46R	16 Sept	1320	777.8	787.4	9.6	2.93	30.5
47R	16 Sept	1545	787.4	796.9	9.5	7.17	75.5

Table 2 (continued).

Core	Date (1988)	Time (L)	Depth (mbsf)	Length cored (m)	Length recovered (m)	Recovery (m)	Recovery (%)
765C-48R	16 Sept	1755	796.9	806.3	9.4	9.88	105.0
49R	16 Sept	2030	806.3	815.6	9.3	7.64	82.1
50R	16 Sept	2300	815.6	825.0	9.4	8.07	85.8
51R	17 Sept	0130	825.0	834.5	9.5	7.77	81.8
52R	17 Sept	0505	834.5	844.1	9.6	4.65	48.4
53R	17 Sept	0725	844.1	853.5	9.4	10.24	108.9
54R	17 Sept	0945	853.5	863.0	9.5	5.97	62.8
55R	17 Sept	1145	863.0	872.5	9.5	5.69	59.9
56R	17 Sept	1500	872.5	881.7	9.2	6.00	65.2
57R	17 Sept	1710	881.7	891.2	9.5	9.17	96.5
58R	17 Sept	2035	891.2	897.9	6.7	7.57	113.0
59R	17 Sept	2250	897.9	907.5	9.6	8.71	90.7
60R	18 Sept	0100	907.5	916.9	9.4	7.46	79.3
61R	18 Sept	0330	916.9	926.4	9.5	7.63	80.3
62R	18 Sept	0605	926.4	935.8	9.4	5.09	54.1
63R	18 Sept	1415	935.8	945.3	9.5	5.76	60.6
64R	18 Sept	2030	945.3	954.7	9.4	0.50	5.3
65R	19 Sept	0225	954.7	963.9	9.2	2.50	27.2
765D-1R	30 Sept	2210	947.9	955.1	7.2	2.60	36.1
2R	1 Oct	0345	955.1	964.4	9.3	3.59	38.6
3R	1 Oct	0930	964.4	973.7	9.3	3.00	32.2
4R	1 Oct	1410	973.7	983.2	9.5	0.43	4.5
5R	1 Oct	2020	983.2	992.4	9.2	10.32	112.2
6R	2 Oct	0110	992.4	1002.0	9.6	2.02	21.0
7R	2 Oct	0845	1002.0	1011.5	9.5	4.52	47.6
8R	2 Oct	1355	1011.5	1020.9	9.4	0.97	10.3
9R	2 Oct	1750	1020.9	1030.2	9.3	3.10	33.3
10R	2 Oct	2215	1030.2	1039.4	9.2	1.12	12.2
11R	4 Oct	0755	1039.4	1045.1	5.7	1.02	17.9
12R	4 Oct	1520	1045.1	1054.4	9.3	3.21	34.5
13R	4 Oct	2255	1054.4	1063.9	9.5	2.96	31.1
14R	5 Oct	0555	1063.9	1073.0	9.1	2.45	26.9
15R	5 Oct	1145	1073.0	1082.5	9.5	1.64	17.2
16R	5 Oct	1645	1082.5	1091.7	9.2	1.95	21.2
17R	6 Oct	0040	1091.7	1101.1	9.4	3.03	32.2
18R	6 Oct	0620	1101.1	1110.3	9.2	3.61	39.2
19R	6 Oct	1225	1110.3	1119.5	9.2	2.49	27.0
20R	6 Oct	1825	1119.5	1129.0	9.5	2.04	21.5
21R	8 Oct	0620	1129.0	1138.6	9.6	1.50	15.6
22R	8 Oct	1050	1138.6	1147.8	9.2	2.95	32.0
23R	8 Oct	1810	1147.8	1157.1	9.3	3.18	34.2
24R	8 Oct	2230	1157.1	1166.5	9.4	5.93	63.1
25R	9 Oct	0315	1166.5	1176.0	9.5	2.60	27.3
26R	9 Oct	0825	1176.0	1185.4	9.4	2.74	29.1
27R	9 Oct	2359	1185.4	1194.9	9.5	3.73	39.2

terface with the Schlumberger logging strings; the third core was to accommodate hole fillings (cavings) when logging in the open hole. The excellent core recovery of 5.7 m in Core 123-765C-63R was not repeated in Cores 123-765C-64R and -65R; both of these latter cores contained only 3 m of total recovery. Coring in Hole 765C terminated at 0230L on 19 September, and conditioning of the hole began before logging.

Logging in Hole 765C

Pipe was pulled up to 180 mbsf to wipe the hole; no obstruction was encountered. When lowered, the bit touched bottom at 40 m above total depth below seafloor, indicating 40 m of debris fill. Three slugs of mud were circulated to remove this fill, after which the bit was released. On 19 September at 1700L, logging operations started with the seismostratigraphy (SST) tool and the LDGO temperature tool. Logging from 150 to 480 mbsf produced a full set of data, but at 480 mbsf the tool was obstructed by cavings from the lower Miocene debris flows. The tool was retrieved, and pipe was lowered to 760 mbsf without obstruction, then pulled back to 500 mbsf, where the SST tool was lowered again. Unfortunately, the tool again was obstructed, this time at the end of the pipe. Because the pipe appeared to move freely, we concluded that the pipe was plugged and that circulation was proceeding only through the bit release slots 20 cm above the end of the core barrel. After several attempts to remove the plug with the logging tool, we were able to release it by allowing a 500-lb, 40-ft-long, inner barrel to fall freely down to the end of the drill string.

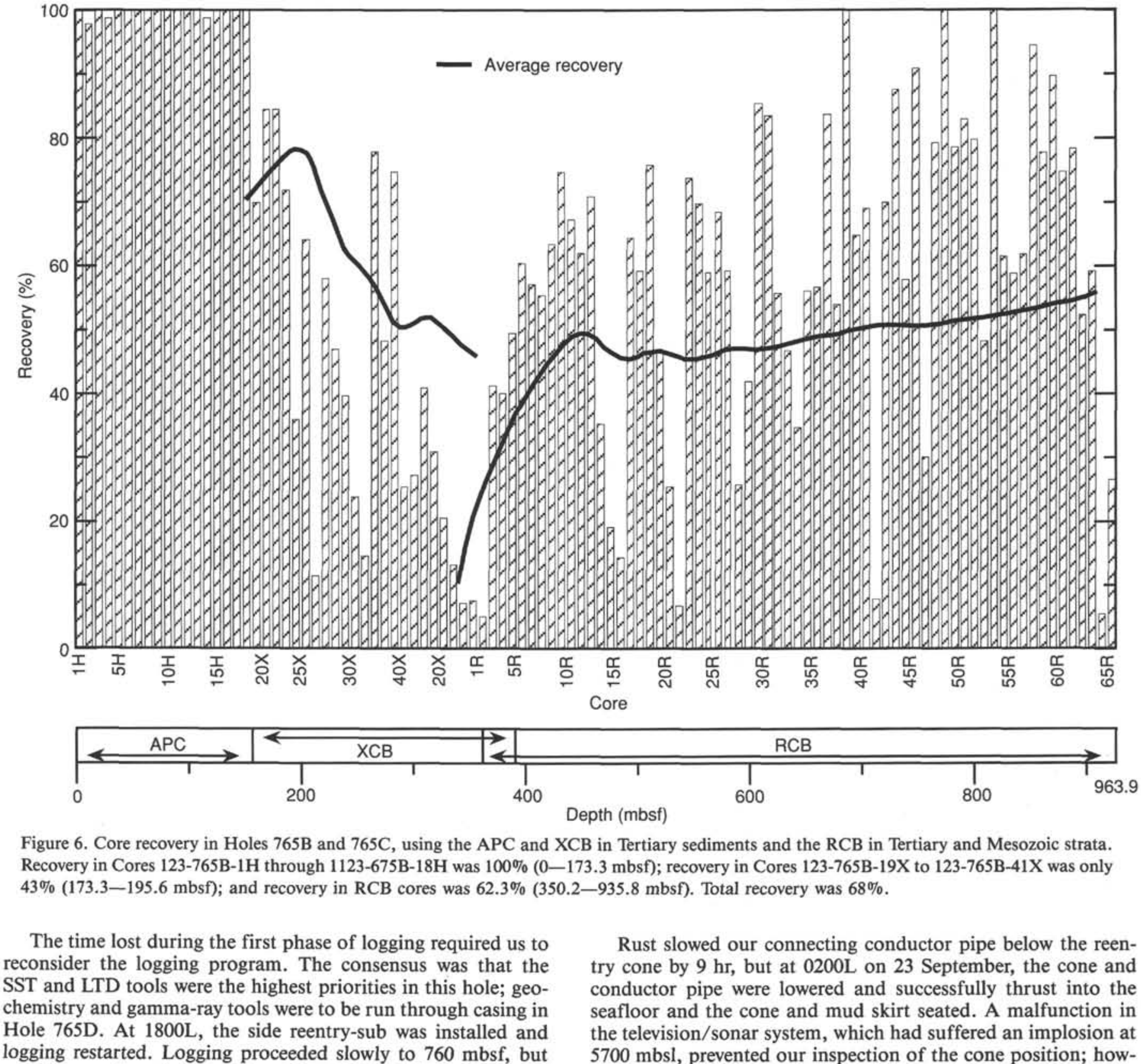

Figure 6. Core recovery in Holes 765B and 765C, using the APC and XCB in Tertiary sediments and the RCB in Tertiary and Mesozoic strata. Recovery in Cores 123-765B-1H through 1123-675B-18H was 100% (0—173.3 mbsf); recovery in Cores 123-765B-19X to 123-765B-41X was only 43% (173.3—195.6 mbsf); and recovery in RCB cores was 62.3% (350.2—935.8 mbsf). Total recovery was 68%.

The time lost during the first phase of logging required us to reconsider the logging program. The consensus was that the SST and LTD tools were the highest priorities in this hole; geochemistry and gamma-ray tools were to be run through casing in Hole 765D. At 1800L, the side reentry-sub was installed and logging restarted. Logging proceeded slowly to 760 mbsf, but was hampered continuously by a plugged bit. This plugging was probably caused when the pipe scraped sediment from the wall of the hole because it inclined 10° from vertical and the high differential pressure between the heavy, mud-filled hole and the seawater-filled pipe. At 0830L on 21 September, we decided to unplug the pipe again using the free-falling inner barrel and then to log the 180- to 450-mbsf interval with the LTD tool but without the side-entry sub before terminating logging within the 60-hr time limit set for this operation in Hole 765C. At midnight, logging was terminated and pipe was returned to the surface in preparation for spudding Hole 765D.

Hole 765D

Hole 765D was the major engineering challenge of Leg 123. Our objective was to case the hole through the sediment section and into basement. The cased hole would then be cemented, and a permanent coring and logging laboratory established. Summaries of our operations are given in Figure 5.

Rust slowed our connecting conductor pipe below the reentry cone by 9 hr, but at 0200L on 23 September, the cone and conductor pipe were lowered and successfully thrust into the seafloor and the cone and mud skirt seated. A malfunction in the television/sonar system, which had suffered an implosion at 5700 mbsl, prevented our inspection of the cone position; however, tugging at the cone revealed that it was emplaced solidly. Drilling a casing hole to basement with a 14¾ in. reaming bit (Fig. 8) began immediately, and on 25 September at 0630L, basalt was reached at 947.9 mbsf. Basement penetration rate of 3 m/hr with the reamer bit was continued for 22 m to provide a rathole to seat the 937-m-long, 11¾ in. casing string, after which the hole was conditioned for 3 hr. Following a third reaming operation, only 3 m of fill was encountered in the rathole. The hole was filled with 10.5-lb/gal mud containing 3% KCl, and the pipe returned to the surface. Hole 765D is located at 15°58.55′S, 117°34.51′E.

During 26 and 27 September, 937 m of casing string was prepared, and the hole successfully reentered on 28 September at 1245L. The casing shoe was 5 m into basement rock. No resistance was encountered while the casing was set downhole and latched in the 16¾ in. conductor pipe of the reentry cone. Latching was accomplished at 1800L, and the drill string disengaged at 1840L. Cement then was pumped between the casing and the

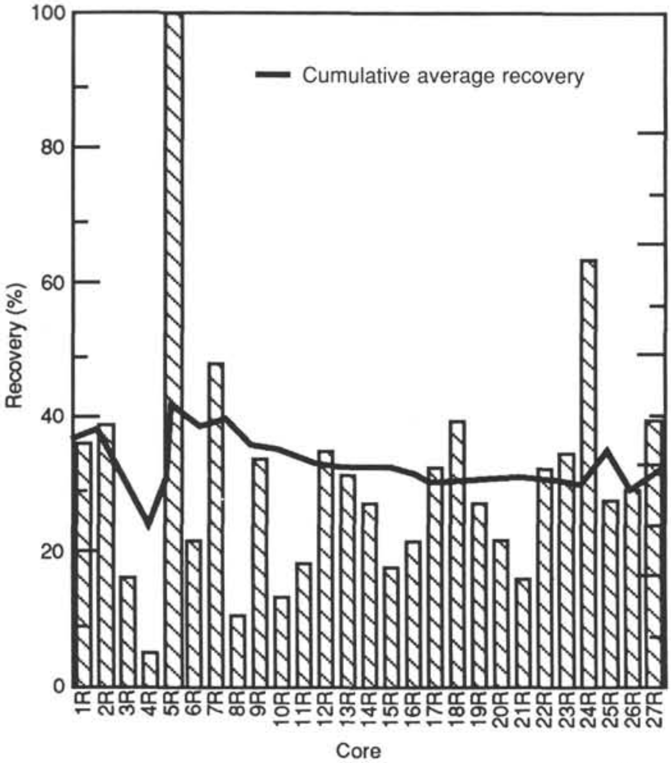

Figure 7. Core recovery using the RCB in volcanic ocean crust in Hole 765D; total recovery was 31% of 259.1 m cored (935.8–1194.9 mbsf).

wall of the hole. Pipe was returned to the surface, and the hole reentered with a tricone coring bit to drill out the flapper valve and aluminum plug in the casing shoe and the cement plug filling the rathole below. The casing shoe was drilled out in 2 hr, and casing operations were completed at 1800L on 30 September.

Basement Coring in Hole 765D

Coring started at 947.9 mbsf in Hole 765D at 1840L on 30 September; at 2220L, Core 123-765D-1R arrived on deck with two sections of basalt recovered (Fig. 7). Coring continued uninterrupted until the evening of 3 October, when because of increasing hole torque we deemed it prudent to pull the bit after 33 hr of rotating time (Cores 123-765D-1R through -10R). Including the three cores from Hole 765C, we had drilled 13 cores or 119.6 m of basalt. A total of 40.43 m had been recovered, which was equivalent to a recovery rate of 34%.

A second bit was changed on 6 October after 42 hr of rotating time and after having cut Cores 123-765D-11R to -20R. Core recovery with this bit varied, but averaged around 30%; rotating time per core was about 1 hr more than for the previous bit. Except for the first few basalt cores, no plastic liners were used in the core barrel. In our experience, the plastic liner prevented broken rock fragments from entering the core barrel and, more often than not, the liner became badly damaged during coring.

On 7 October at 1940L, Hole 765D was reentered using a third coring bit (Cores 123-765D-21R through -27R), and at 0620L on 8 October, Core 123-765D-21R arrived on deck from a depth of 1138.6 mbsf. Recovery improved substantially in Cores 123-765D-24R and -25R, reaching more than 60% (Fig. 7); overall basalt recovery in Hole 765D averaged 31%. Coring in Hole 765D terminated at 1200L on 9 October, when Core 123-765D-27R was recovered from 1194.9 mbsf, 247 m below the sediment/basalt contact. The third bit used in basalt arrived back on deck with Core 123-765D-27R at 0200L on 10 October.

Figure 8. Photograph of the 14-3/4 in. RCB bit used to drill Hole 765D and prepare it for casing; circular hole behind the rollers seats a water jet, which was removed before taking the picture. The smaller 11-7/16 in. XCB bit is shown for comparison; here, water jets are in place.

Figure 9 provides a graphic illustration of the four holes drilled at Site 765, including information about the deviation from vertical in Hole 765C and the type and number of cores obtained in each hole.

Logging of Hole 765D

Following the successful retrieval of the last basalt core, we began preparing to log the hole with the three Schlumberger logging tools, the vertical seismic profiler (VSP), and the single-packer part of the hydrofracture experiment. A single packer was inserted in the bottom-hole assembly, together with a 16-in. pedal-type running tool that, with its fins extended, would suspend the pipe in the conductor casing below the reentry cone and keep it stationary while we were running the VSP experiment. At 1500L on 10 October, Hole 765D was again reentered, and one stand of pipe was lowered into the casing. Uphole logging from total depth to 56 mbsf with the Schlumberger SST tool was completed at 2300L; the tool was retrieved and we began the second logging run with the geochemical tool.

Unfortunately, a problem developed at 1640L on 11 October, when this tool could not be raised above 168 mbsf inside the casing string. Although we were unclear as to why this was so, we assumed that the tool had become stuck in the casing. After extensive deliberations, we lowered a crimping tool that could be activated by a firing bar to clamp the logging cable in the drill pipe; the drill pipe could then be raised and we hoped, free the tool or break the logging cable in the weak link connecting tool and cable. Mysteriously, at 2100L the tool became unstuck on its own, after which it was quickly winched to the deck. No signs of damage to either cable or tool could be detected. The

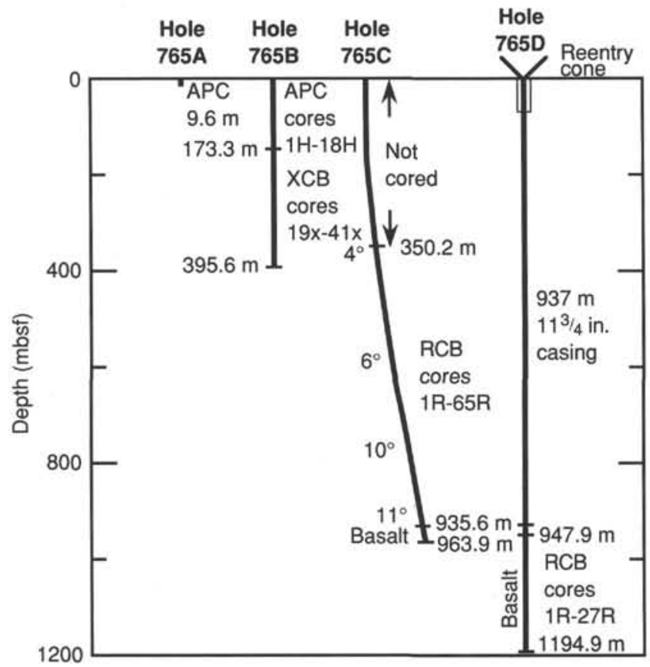

Figure 9. Holes completed at Site 765, Argo Abyssal Plain, northeast Indian Ocean.

borehole televiewer (BHTV) was run the next day (12 October) for a permeability study of the basement; this run yielded no evidence of anything unusual in the casing.

The pre-fracture BHTV run started slowly; the first tool malfunctioned at 3000 mbrf, and the second tool also experienced unexplained, erratic head rotation while in the drill pipe. While in the basement, the tool worked well, although the uphole motion was jerky because of friction between the four arms and the borehole wall. Break-outs and fracture patterns were observed, and the run was finished successfully at 1400L on 12 October.

The VSP experiment began immediately after the first BHTV run by test firing of the two water guns suspended from the rear port crane and the lowering of the hydrophone tool into the hole. The tool was tested in the drill pipe at 720 m below the rig floor (brf). Its arms were extended and retracted, and a signal was received. Unfortunately, 40 m farther down, the tool jammed in the pipe. Initially, we assumed that the arms had somehow stuck in the smooth pipe, but 2 hr later, when the tool suddenly came free and arrived on deck, we found out that two small bolts had fallen out of the oilsaver (a unit that rides on the pipe on deck and allows for pumping of water downhole with the tool's connecting cable inserted). Apparently, the VSP geophone tool had been jammed in the pipe by these two small bolts. The second VSP seismic recording tool was rigged up with a new cable connector, and shortly before midnight on 12 October, this configuration was lowered down the pipe. At 0240L on 13 October, the tool arrived at total depth, and we began shooting at stations 10 to 15 m apart, while logging uphole. Unfortunately, clamping problems combined with a too weak signal prevented us from recording in the basalt. Apparently, we should have used a stronger signal source to overcome the noise generated by the drill pipe and to penetrate the highly reflective volcanic basement. In addition, we should have stabilized the drill string by inflating the single packer, rather than resting it on the casing; this would have helped to dampen any motion. Better signal-to-noise ratio was achieved in the cased sedimentary hole, and our profiling run was deemed about 40% successful. At 1620L on 13 October, the VSP was finished, and the geophones were winched back to the ship.

After the VSP experiment, the pipe was set free from the casing string on which it had rested to stabilize the pipe and to prevent noise from being recorded. This took slightly longer than we anticipated. Pipe then was lowered into the casing, and the Schlumberger LTD tool rigged for its run. At 0100L on 14 October, the tool was lowered downhole and was back on deck at 1000L, after a successful uphole run in basalt and in the overlying, cased sediment. The LTD tool also measured the hole deviation from vertical, which we found was less than 1°.

The hydrofracture experiment using single and double packers was the last of the extensive logging operations at Site 765. Pipe was lowered with the single packer to the base of the casing string. At 1500L on 14 October, the first pressure test was performed at 6000 psi. Pressure was bled off, and this was assumed to indicate permeable basalt conditions. Next, pipe was lowered to 40 m above total depth, where the pressure test was repeated. This time, the packer did not appear to inflate, and no test could be performed. A go-devil with a pressure-measuring clock was lowered to document the lack of pressure below the packer. This tool returned, showing no inflation of pressure below the packer, which indicated that the packer might have ruptured. As a result, we decided to terminate the first permeability test. At 2350L on 14 October, the pipe was tripped to insert the straddle packer and to try to isolate permeable zones in the basalt portion of the hole.

At noon on 15 October, the packer was back on deck; we saw that it had ruptured. A double-packer (straddle-packer) configuration was inserted in the string and the pipe returned to the bottom, reentering the hole at 0400L on 16 October. After the pipe was lowered to the base of the hole, we tried to inflate the packers; despite repeated attempts, we were not successful. Although no shipboard consensus was reached, two opinions prevailed regarding why the packers failed to inflate: (1) the packers were accidentally lowered into fill at the base of the hole, and (2) an error was made during shipboard assembly of the new, slightly modified packers. During an autopsy on 18 October, we found that the packer had indeed been set into fill and that the go-devil used to activate the packer valves had been configured incorrectly. When we retrieved this tool, mud was sucked into the packer valves, causing us to fail at a further attempt to seat the go-devils.

To keep within time constraints, we decided to make the last BHTV run from the bottom of the hole to the base of the casing. Afterward, we planned to send the go-devils down one more time using a slightly modified set of keys in a final attempt to inflate the packer. The BHTV run was successful, indicating abundant evidence of recent basalt break-outs, which data were to be used for calculating the current stress vectors with depth. Unfortunately, we could get no response from the two packers set at the end of the casing; this long sand-line run also was used to grease the lower half of the line. One of the go-devils became stuck briefly, which resulted in a 0.5 hr delay, but at 1150L on 17 October, these tools were back on deck and pipe was returned to the surface. At 0005L on 18 October, after having spent more than 40 days on location at Site 765, the *JOIDES Resolution* retracted its thrusters and headed for Site 766, 460 nmi to the southwest in the proximal Gascoyne Abyssal Plain. A summary of operations at Site 765 is shown in Figure 5. Throughout our stay at Site 765, weather conditions remained perfect, with pleasant, warm temperatures, calm seas, and light to moderate winds, generally from the same northeasterly direction.

To improve the seismic resolution in basement, which was not successful using the VSP, we obtained a sonobuoy record as we were leaving Site 765. The vessel first headed slightly northeast, deployed the two 40-in.^{3} air guns, and then turned to port on a course of 240° over Site 765, toward Site 766. A sonobuoy was launched, and it recorded signals from 0100L until 0200L on 18 October, while the ship moved at a steady speed of 8 kt. At 0200L we terminated this record and pulled the seismic gear on board ship. The *Resolution*'s speed was increased to 11.5 kt.

SEDIMENT LITHOSTRATIGRAPHY

A 935-m-thick succession of Quaternary through Lower Cretaceous sediments was recovered at Site 765 (Fig. 10). A single core of Quaternary sediment was obtained from Hole 765A; drilling terminated and a new hole was drilled in an attempt to establish the mud line. Quaternary through middle Miocene sediments were cored in Hole 765B down to a depth of 395.6 mbsf. Middle Miocene through Lower Cretaceous sediments were cored in Hole 765C, after washing the interval between 0 and 350.2 mbsf. Exact lithologic correlation of the basal cores from Hole 765B with the upper cores from Hole 765C is not possible because of poor recovery; hence, correlation is based solely on matching sub-bottom depths.

The upper 173.3 m of Hole 765B was cored using the APC corer; recovery was excellent (nearly 100%), and drilling disturbance was slight. The remainder of Hole 765B was drilled using the XCB corer. Recovery was good for the first four cores but deteriorated downhole. Drilling disturbance was moderate to severe for much of the interval from 231.5 mbsf to the bottom of the hole, and recovery for several cores in this interval was less than 15%. Hole 765C was cored using the RCB corer; recovery throughout the hole averaged 60%, and drilling disturbance was minimal for most of the hole. Intervals in Hole 765C having poor recovery and/or moderate to severe drilling disturbance include those from 350.2 to 359.6, 436.5 to 493.2, 530.8 to 550.1, 730.4 to 739.8, and 777.8 to 796.9 mbsf. Volcanic basement was encountered at 935.5 mbsf and was drilled to a depth of 963.9 mbsf.

The sedimentary succession was subdivided into seven lithologic units and 18 subunits on the basis of visual core and smear slide descriptions. Thin-section descriptions, XRD analysis of clay mineralogy, cluster analysis of smear slide data, and Markov chain analysis also were used to characterize these units.

Unit I consists of 190 m Pleistocene through upper Miocene redeposited clayey calcareous sediments of pelagic origin and minor intercalated clay. Unit II is composed of 285 m of Miocene redeposited calcareous pelagic sediments and intercalated clays. Unit II sediments are similar to those in Unit I but in general contain less clay, are less variable, and are more lithified than those of Unit I. Unit III includes 117 m of lower Miocene through Cenomanian calcareous sediments interbedded with dark gray, varicolored, red, and brown claystones that are locally zeolitic. Unit IV contains 131 m of Cenomanian through lower Aptian brown, red, green, and gray claystones intercalated with calcareous (and lesser siliceous) redeposited sediments. Unit V includes 136 m of lower Aptian and Barremian dark gray and reddish-brown claystones with minor intervals of rhodochrosite sediment and of radiolarite. Unit IV consists of 34 m of Hauterivian to Valanginian reddish-brown calcareous claystone and mixed sediment, lesser noncalcareous claystones and minor radiolarites, intervals of rhodochrosite sediment, and altered ash layers. Unit VII constitutes 42 m of Valanginian to Berriasian reddish-brown and green claystones with altered ash layers and radiolarites, above brown silty claystones with calcareous shell fragments.

Calcareous sediments dominate Units I, II, III, and VI and are a subordinate component of Unit IV. Most of these calcareous sediments may have been deposited as turbidites. Units I, II, and III contain conglomeratic intervals that may have been deposited as debris flows. Calcareous sediments are uncommon in Unit V.

When interpreting the laminations in the core photographs, one should remember that hold deviation increases from 5° at about 400 mbsf to 11° at 900 mbsf.

Carbonate micronodules occur in many Site 765 sediments. These range in color from brown to green to red, and XRD analyses suggest variable compositions, including rhodochrosite, dolomite, and mixtures of the two. Further XRD results from multiple analyses of certain samples conflict with energy dispersive X-ray (EDX) analyses. The mineralogy of these nodules is not precisely known, but the evidence suggests that mineralogy varies, perhaps even with single nodules. All references in this volume to nodules of "rhodochrosite," "rhodochrosites?," "dolomite," or "rhodochrosite/dolomite," refer to these nodules.

Lithologic Units

Unit I

Cores 123-765B-1H, top to -20X-5, at 105 cm, 0–189.1 mbsf.
Age: Pleistocene to late Miocene

Unit I consists of redeposited calcareous sediments of pelagic origin with minor intercalcated clays. The calcareous sediments normally occur as graded sequences, typically with sharp, locally scoured basal contacts, and fine upward from calcareous ooze with clay to clayey nannofossil ooze. The calcareous ooze with clay is composed largely of whole and broken foraminifers, but includes a variety of calcareous with siliceous biogenic fragments. This ooze is generally fine- to medium-sand-sized at the base (Fig. 11) and silt-sized at the top. Clayey nannofossil ooze constitutes the main body of most graded sequences. This sediment is silt- to clay-sized and shows subtle grading. It is slightly to moderately bioturbated within the upper few to 20 cm; bioturbation intensity decreases downward. Darker, clayey sediment, presumably from the overlying clayey intervals, fills the burrow traces (Fig. 12).

A gradational to bioturbated boundary separates the graded sequences from interbedded clayey intervals that occur through most of the unit. These clayey intervals contain varying amounts and types of biogenic and siliciclastic components.

Uncommon reddish-gray manganiferous laminae are almost exclusively confined to the clayey intervals, or to the gradational contact between the graded sequences and clayey intervals.

Subunit IA

Cores 123-765B-1H-1, top, to 123-765B-5H-2, at 87 cm, 0–40.6 mbsf.
Age: Pleistocene

Subunit IA consists of interbedded greenish-gray and gray graded sequences and olive to dark greenish-gray clayey siliceous oozes. The graded sequences range from 10 to 200 cm thick, with clayey nannofossil ooze accounting for about 90% of most sequences. Intervals of clayey siliceous ooze range from 5 to 120 cm thick and contain abundant radiolarian fragments, with lesser amounts of spicules, diatoms, and quartz silt. Texturally, the oozes are clayey silt, with biogenic components and quartz accounting for the silt-sized material. They generally have a faintly laminated to mottled appearance.

Subunit IB

Cores 123-765B-5H-2 at 87 cm to -16H-3 at 6 cm, 40.6–147.3 mbsf.
Age: Pleistocene to late Pliocene

Subunit IB consists predominantly of five complex sequences, 6.5 to 42.5 m thick, each apparently deposited by a single event. These sequences are divided into three parts, each

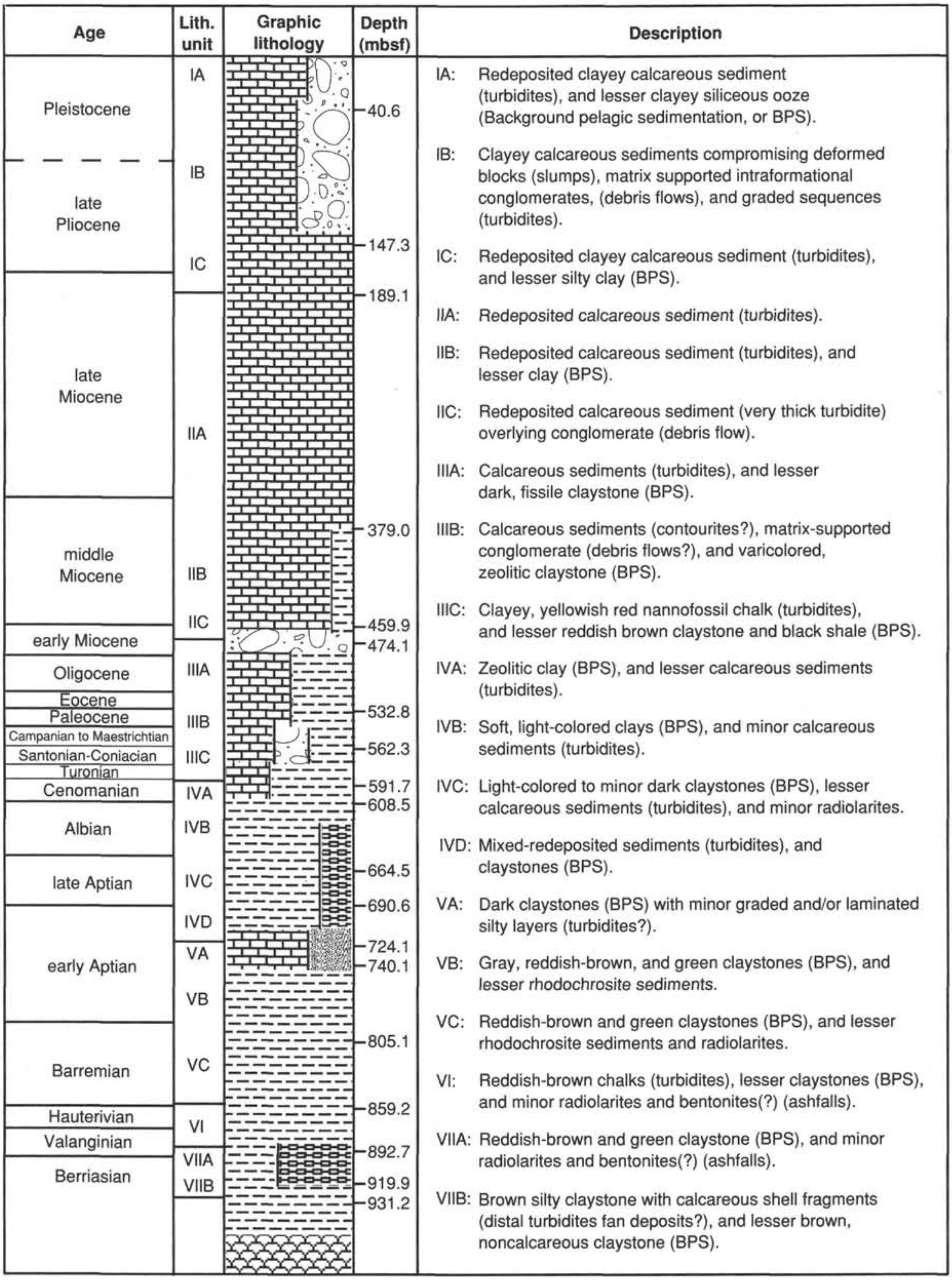

Figure 10. Lithostratigraphic column of sedimentary sequence at Site 765.

apparently formed by different sediment processes active during successive depositional stages. Graded sequences form the lowermost parts of the complex sequences. These graded sequences were deformed by flowage and shearing (Fig. 12) and may have acted as coherent blocks during transport. The middle portions of the complex sequences consist of matrix-supported intraformational conglomerate (Fig. 13). Tabular blocks (up to 175 cm in observed thickness) floating within the conglomerate commonly have deformed boundaries. Blocks consist of typical graded sequences and clayey intervals (some blocks contain

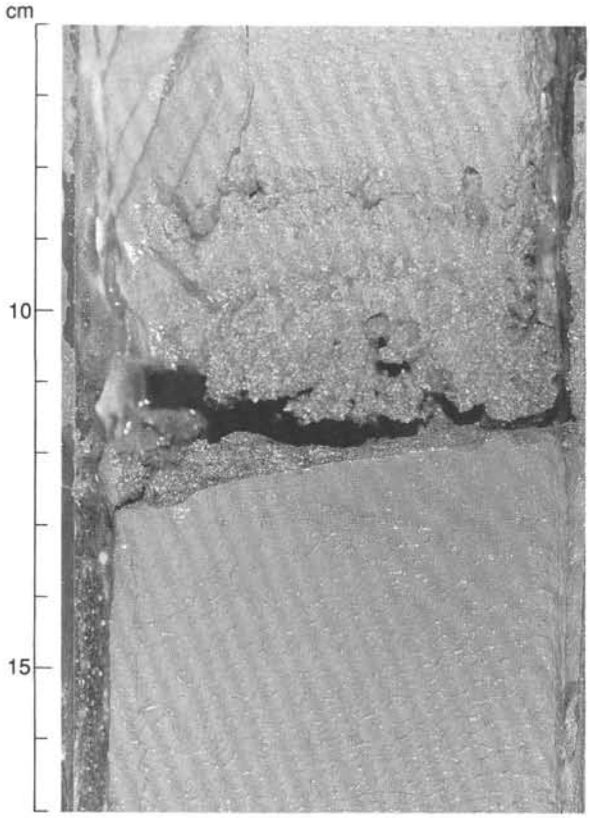

Figure 11. Subunit IA, base of calcareous graded sequence, Section 123-765B-1H-3 at 6 to 17 cm.

more than one sequence) and, in some cases, exhibit evidence of inversion during transport. The intraformational conglomerate also contains a variety of smaller clasts, including rounded reddish-brown volcanic pebbles and white and black Jurassic and Cretaceous claystones and chalks. However, the conglomerates are dominated by clasts of greenish-gray clayey nannofossil ooze like that found in the typical graded sequences of Subunit IA. These clasts are <1 to 40 cm in diameter, are rounded to deformed (Fig. 13) and tend to decrease in size stratigraphically upward. The matrix is predominantly a speckled greenish-gray clayey nannofossil ooze, but patches of coarser calcareous ooze occur as well. The speckled appearance of the conglomeratic matrix results from scattered calcareous fragments and intraformational clasts of sand- to very small pebble-size. The upper portions of the complex sequences overlie the intraformational conglomerates with gradational contacts. The upper portion of each complex sequence consists of a thick graded sequence, averaging approximately 500 cm thick and composed predominantly of speckled clayey nannofossil ooze. The scattered fragments and clasts that impart this speckled appearance decrease in size and abundance upward.

An idealized sedimentary section (Fig. 14) illustrates the previously described succession within the complex sequences, as well as the relationships of complex sequences to interbedded lithologies.

The complex sequences are interbedded with graded sequences and clayey oozes like those of Subunit IA. The basal lithology of these graded sequences (calcareous ooze) accounts for about 25% to 30% of each sequence, as opposed to about 10% of each sequence in Subunit IA. The graded sequences are generally undeformed, but a soft-sediment fault occurs in Section 123-765B-10H-5 at 25 to 34 cm, with 27 cm of vertical displacement (Fig. 15).

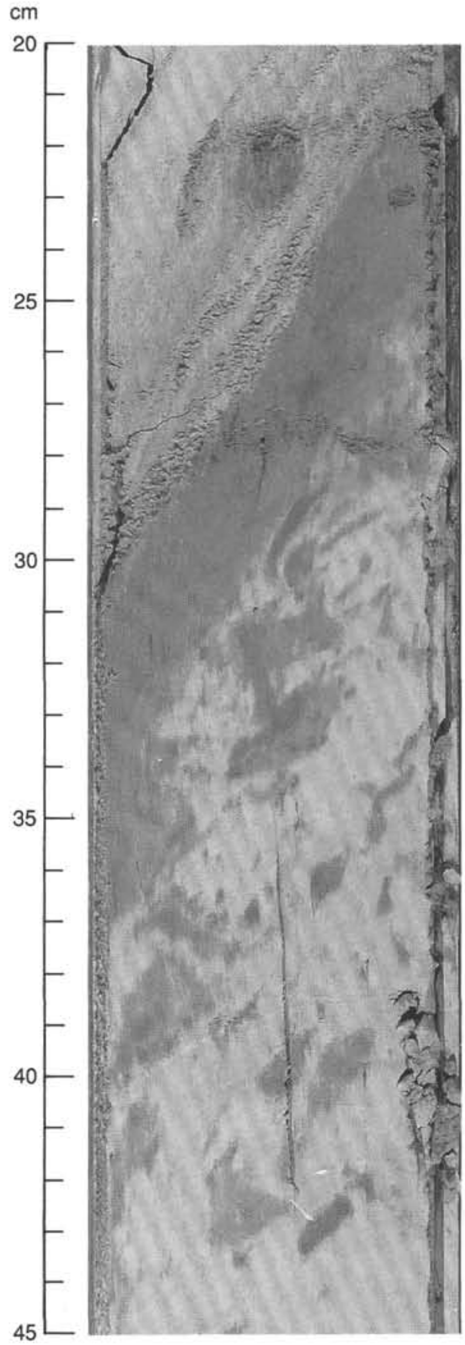

Figure 12. Subunit IB, bioturbation in upper part of graded sequence, Section 123-765B-9H-5 at 20 to 45 cm.

A distinct change in the clayey intervals is noted within this subunit. Clayey intervals as thick as 50 to 60 cm and enriched in siliceous biogenic material occur through Core 123-765B-8H. Clayey intervals are absent from Cores 123-765B-9H and -10H. Clayey intervals from Core 123-765B-11H through remainder of Unit I are characterized by very small amounts of siliceous biogenic material.

Subunit IC

Cores 123-765B-16H-3 at 6 cm to -20X-5 at 105 cm, 147.3–189.1 mbsf.

Age: late Pliocene to late Miocene[?]

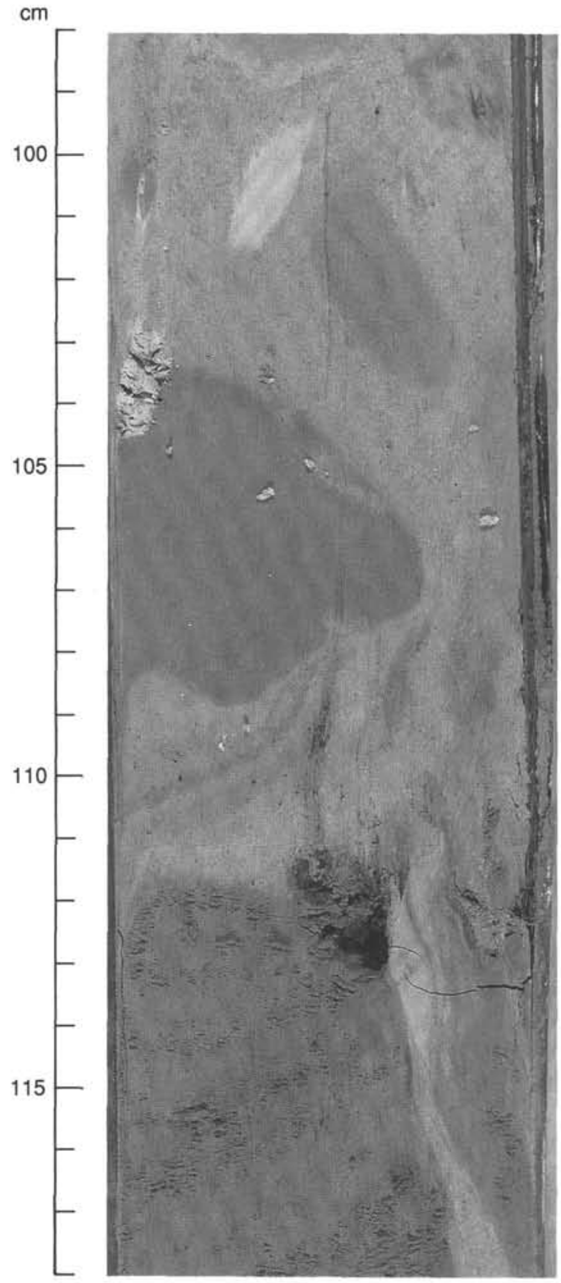

Figure 13. Subunit IB, intraformational conglomerate, Section 123-765B-6H-4 at 98 to 118 cm.

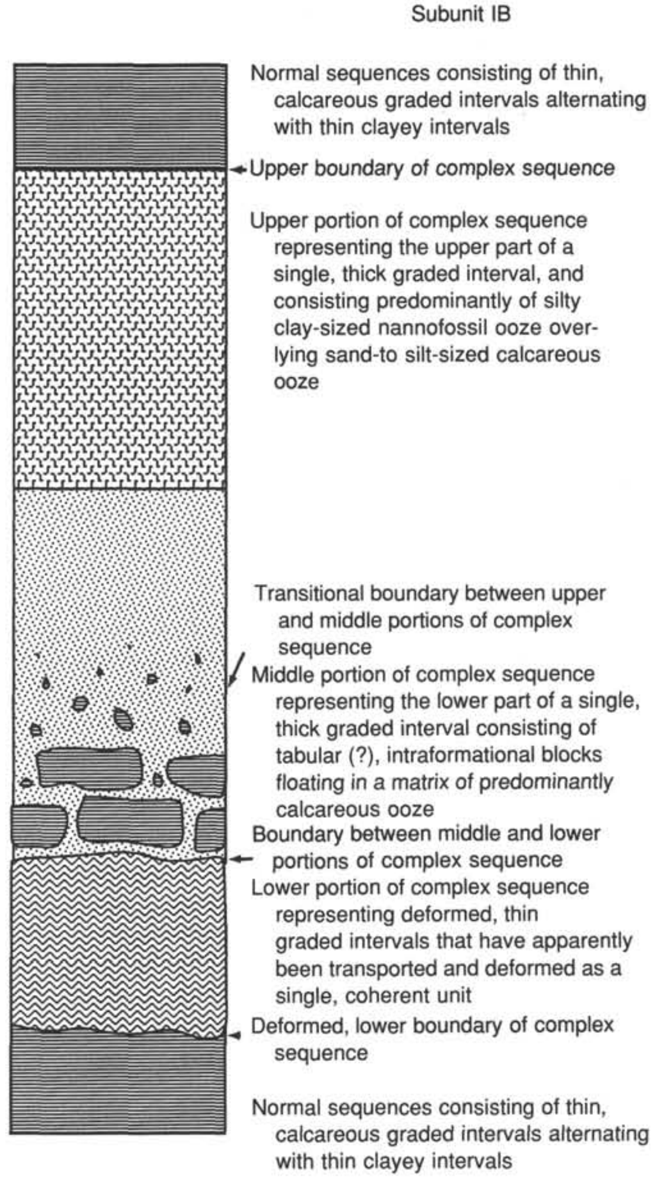

Figure 14. Idealized sedimentary section illustrating succession within complex sequences of Subunit IB.

Subunit IC consists of two kinds of gray and greenish-gray graded sequences and interbedded intervals of greenish-gray and olive gray silty clay. Thicker sequences average about 350 cm thick. These are similar to thick, speckled sequences in Subunit IB (associated with complex sequences) and include abundant intraformational pebbles toward the base. Far more common are graded sequences 5 to 65 cm thick, with interbedded intervals of silty clay <1 to 25 cm thick.

Several gradual changes occur within Subunit IC. In the upper half of the subunit (through Core 123-765B-17H) sand-sized calcareous oozes forming the basal parts of the graded sequences are generally thin and volumetrically insignificant. Basal intervals increase in thickness and are enriched in quartz sand from Core 123-765B-18H to -20X; these intervals account for about 30% to 40% of each sequence in Core 123-765B-20X. In addition, the intensity of bioturbation increases in the upper parts of the graded sequences. The relative amount of silty clay intercalated with graded sequences peaks in Core 123-765B-17H, thickness and abundance of these intervals declines throughout the rest of the subunit. Silty clay intervals are composed predominantly of clay, with variable amounts of quartz silt and nannofossils.

At the boundary between Units I and II (Section 123-765B-20X-5 at 105 cm), the quartzose base of a graded sequence overlies silty clay. Reworked clasts of the underlying silty clay are found 7 cm up into the overlying calcareous ooze. The apparent derivation of these intraformational clasts exclusively from the underlying lithology contrasts with other pebbly intervals in Unit I, which contain intraformational clasts derived from lithologies other than that *immediately below* the pebbly intervals.

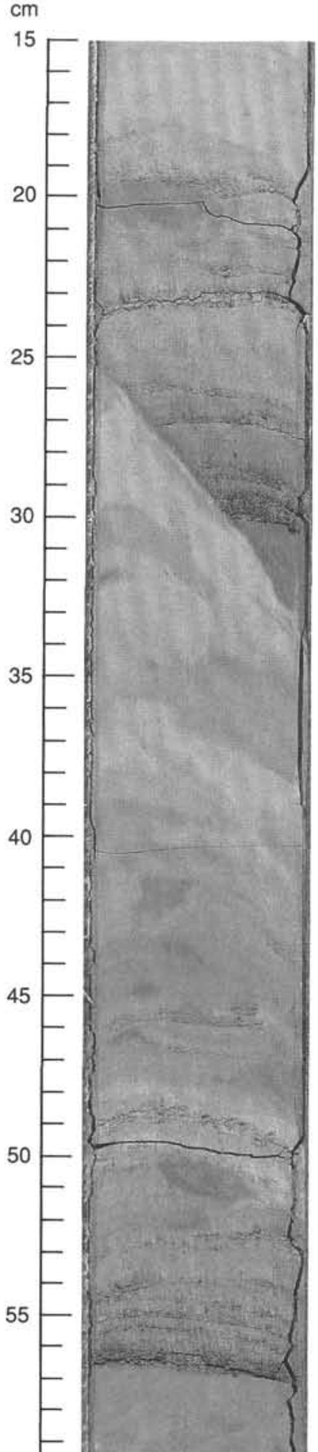

Figure 15. Subunit IB, soft-sediment fault, Interval 123-765B-10H-5, 15–62 cm.

Unit II

Sections 123-765B-20X-5 at 105 cm to -765C-14R-1 at 78 cm, 189.1–474.1 mbsf.
Age: late to early Miocene

Unit II, like Unit I, consists predominantly of graded sequences composed of redeposited calcareous sediment of pelagic origin. The fundamental difference between the two units is the percentage of $CaCO_3$. The average $CaCO_3$ content of samples from Unit II is 70%, compared with 47% in Unit I. Intraformational clasts, common in Unit I, are absent from Unit II, except for a conglomerate described at the base of the unit. Calcareous ooze, the basal lithology of the graded sequences in Unit II, is composed largely of whole and broken foraminifers, as well as additional calcareous fragments, nannofossils, and, at its base, abundant quartz sand (Fig. 16). Clasts and thin beds of coal fragments (Fig. 16) are rare. Graded sequences in this unit are typically fine to medium sand-sized at the base and fine upward to clay- or silt-sized. Nannofossil ooze with clay, as in Unit I, constitutes the bulk (about 70%) of the graded sequences throughout the unit. Interbedded clay/claystone intervals are thin or absent through the upper half of Unit II, but are common within the lower half. This difference, along with a fairly marked increase in the lithification of the sediments occurring at about the same point, is used to distinguish Subunit IIA from Subunit IIB. Subunit IIC is thin and consists of conglomerates and thick graded sequences.

Subunit IIA

Sections 123-765B-20X-5 at 105 cm to -765C-4R-1, top, 189.1–379.0 mbsf
Age: late to middle Miocene

Subunit IIA consists of greenish-gray and gray graded sequences 5 to 200 cm thick. The degree of lithification increases downward from Core 123-765B-22X to the bottom of the subunit. Recovery decreases, and drilling disturbance progressively increases, downhole. Semilithified sections, particularly calcareous chalks, are fractured, brecciated, and form drilling biscuits surrounded by less-consolidated material (Fig. 17). The apparent absence of sedimentary structures through much of this subunit is probably a direct result of drilling disturbance. Some structures are observed in the more lithified biscuits of calcareous chalk, e.g., Section 123-765B-27X-1 at 136 to 143 cm (Fig. 17), in which a massive interval is apparently reversely graded. Planar and cross-lamination is observed in some of the biscuits as well. There is a progressive decrease in the degree of bioturbation through the subunit, with the upper part of the graded sequences moderately to intensely bioturbated toward the top of Subunit IIB, and slightly to moderately bioturbated toward the bottom of the subunit. Intensity of bioturbation is commonly greatest at the top of a given graded sequence.

Subunit IIB

Sections 123-765C-4R-1, top, to -765C-12R-4 at 18 cm, 379.0–459.9 mbsf.
Age: middle Miocene

Subunit IIB consists of graded sequences 2 to 165 cm thick. The sediments are of a similar degree of consolidation throughout, and only slightly disturbed by drilling. Greenish-gray, gray, and white calcareous chalk constitutes the bases of the graded sequences and contains a variety of sedimentary structures, including massive to planar laminations that grade into thin, slightly inclined sets of cross-laminae (Figs. 18 and 19). Convolute laminations (Fig. 20) are also common. Intervals of nannofossil chalk with clay are generally massive to faintly laminated, and slightly to moderately bioturbated upward, with a variety of burrow types, as in Section 123-765C-11R-4 at 127 to 138 cm (Figs. 20 and 21). Intervals of dark greenish-gray to gray claystone alternate with the graded sequences throughout the subunit, and although these are not increasingly abundant toward

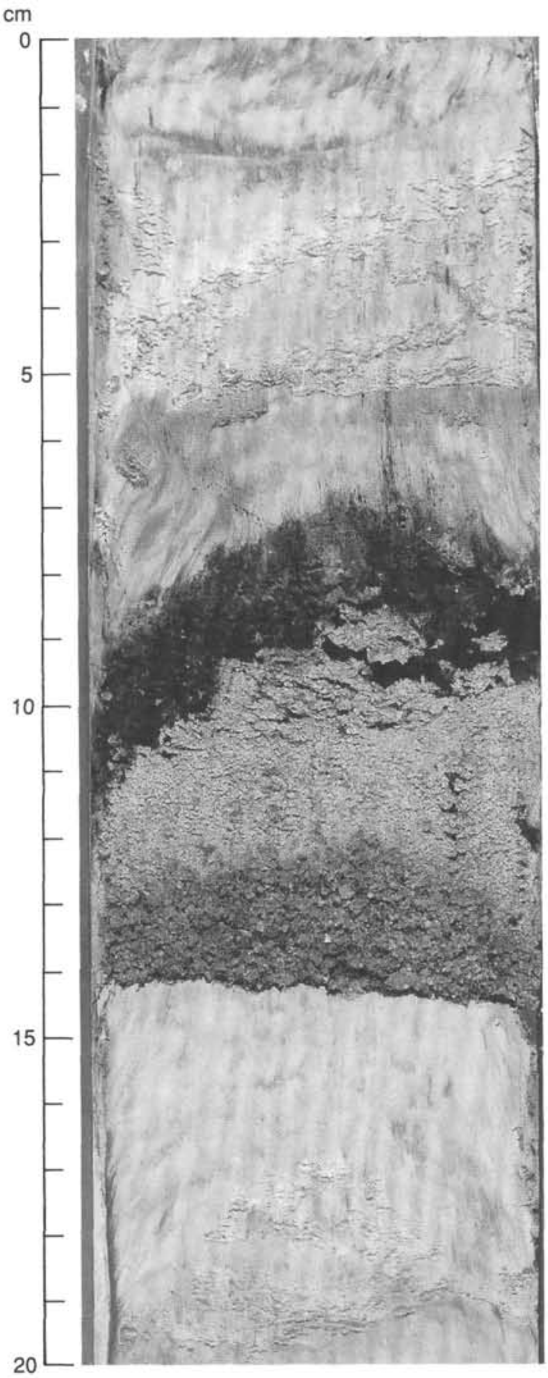

Figure 16. Subunit IIA, base of graded sequence, Interval 123-765B-12X-CC at 0–20 cm. Note quartz sand at 12.5 to 14.5 cm and coal fragments, 7.5–11.5 cm.

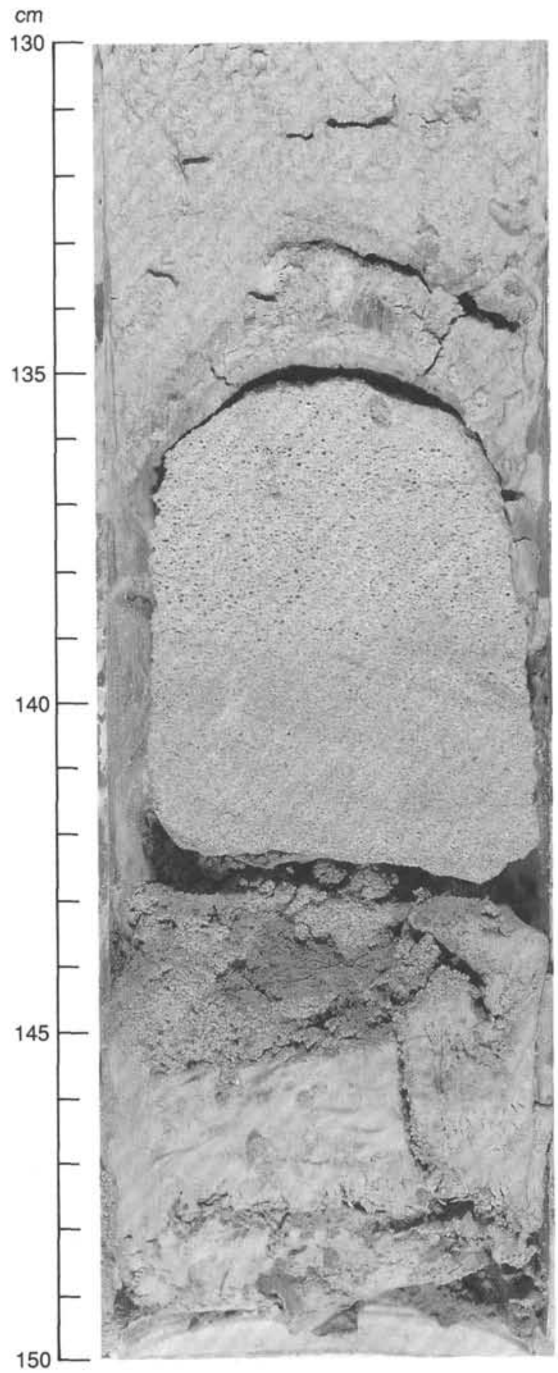

Figure 17. Subunit IIA, calcareous chalk surrounded by drilling-disturbed ooze, Interval 123-765B-27X-1, 130–150 cm.

the bottom of the subunit; maximum thickness progressively increases from 6 cm at the top to 20 cm toward the bottom. Claystones are generally mottled and characterized by authigenic dolomite, with concentrations as high as 30% in some intervals.

Subunit IIC

Sections 123-765C-12R-4 at 18 cm to -14R-1 at 78 cm, 459.9–474.1 mbsf.
Age: middle to early Miocene

Subunit IIC comprises a complex interval with a graded upper part and a highly disturbed lower part. This subunit may record multiple events, but drilling disturbance and poor recovery preclude identification of sedimentological sequence boundaries within it. The upper part of this subunit consists of greenish-gray sandy calcareous fragmented chalk that grades up into greenish-gray nannofossil chalk, whereas the lower part is matrix-supported conglomerate. This matrix consists of greenish-gray clayey chalk. The pebbles, which are rounded to subrounded and as much as 8.5 cm in diameter, display a wide vari-

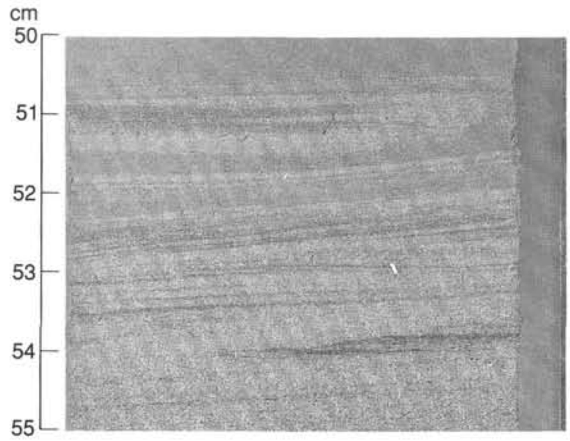

Figure 18. Subunit IIB, cross-laminated carbonate in graded sequence, Interval 123-765C-9R-1, 50–55 cm.

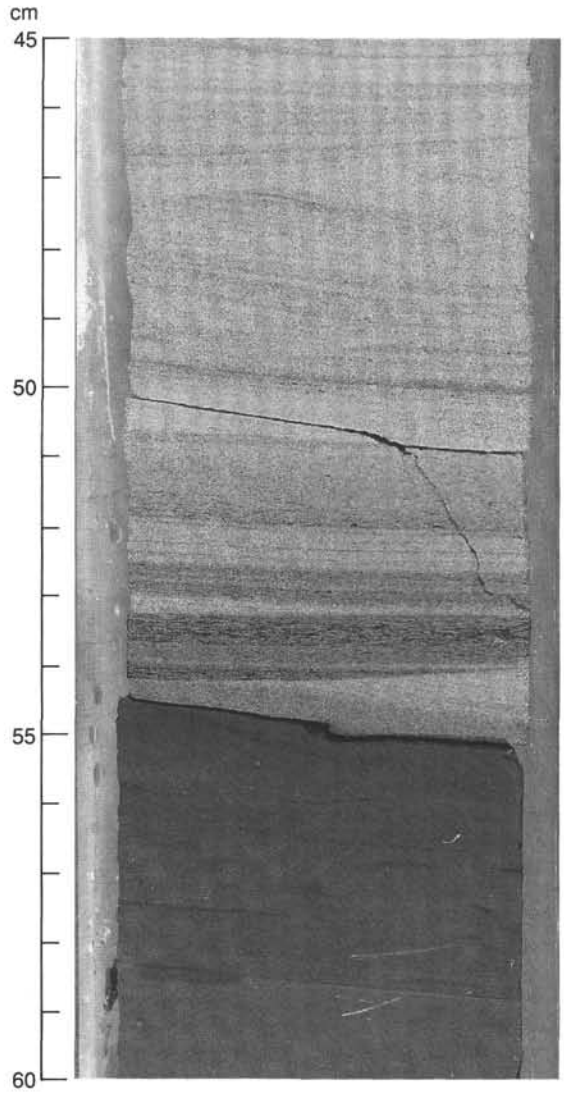

Figure 19. Subunit IB, cross-laminated carbonate in graded sequence, Interval 123-765C-11R-4, 45–60 cm.

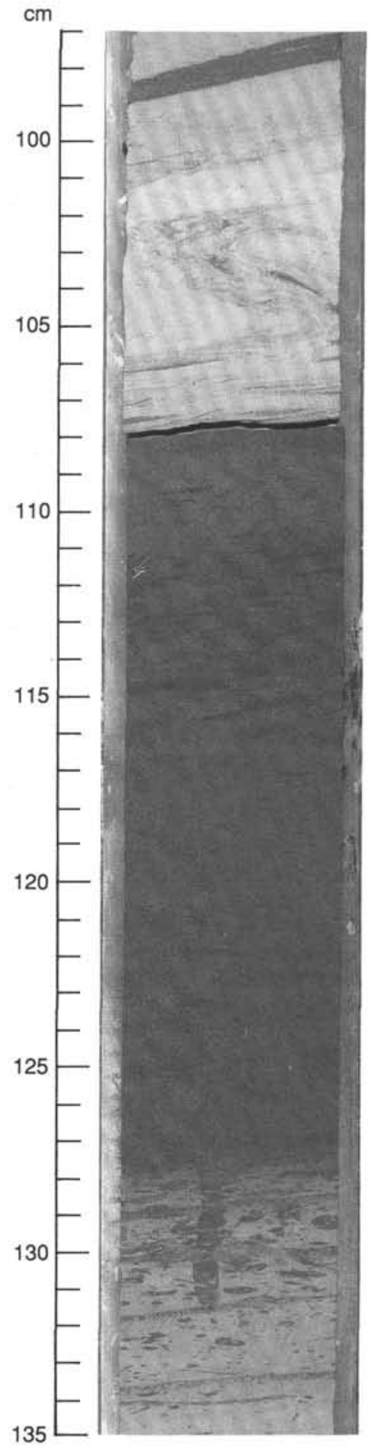

Figure 20. Subunit IB, convolute lamination and complex bioturbation, Interval 123-765C-11R-4, 97–135 cm.

ety of lithologies, including black silty claystone of Middle Jurassic age and basalt.

Unit III

Sections 123-765C-14R-1 at 78 cm and -26R-4 at 5 cm, 474.1–591.7 mbsf.
Age: early Miocene to Cenomanian

Unit III consists of interbedded claystones, graded carbonate sequences, and matrix-supported carbonate conglomerates. The

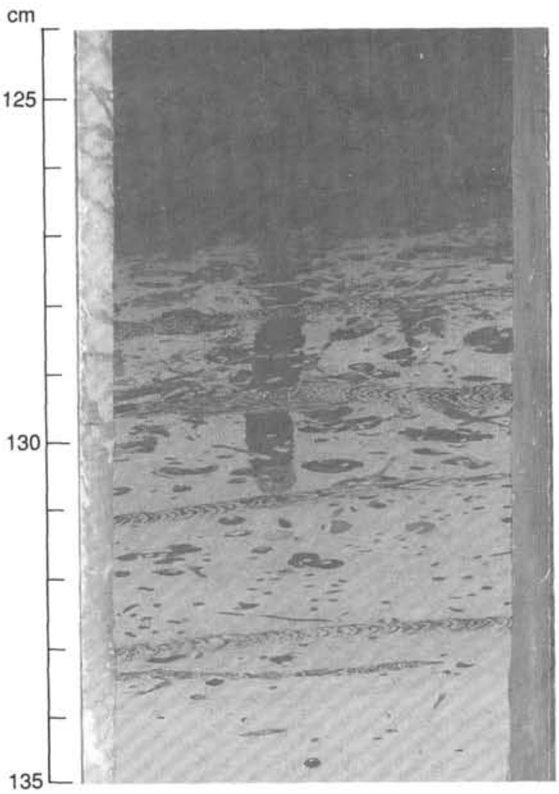

Figure 21. Subunit IIB, close-up of bioturbation in Figure 20, Interval 123-765C-11R-4, 124–135 cm.

claystones are dominantly green, gray, red, and brown in the upper part, and red and brown in the lower part. The carbonates are dominantly greenish-gray in the upper part; brown, gray, white, and red in the middle part; and yellow and red in the lower part. The succession is subdivided into three subunits, distinguished by the dominant clay colors and by the dominant sedimentary structures and compositions of the graded sequences. Unit III differs from the overlying Unit II in its greater clay content and the greater abundance of red and brown colors. Unit IV has much less carbonate material than Unit III, and the few graded carbonate sequences are much finer grained.

Subunit IIIA

Sections 123-765C-14R-1 at 78 cm to -20R-2 at 53 cm, 474.1–532.8 mbsf.
Age: early Eocene to early Miocene

This subunit is characterized by dark, moderately fissile clay intercalated with lighter colored graded sequences. Sequences consist of foraminiferal calcareous fragment ooze (commonly with quartz) that grades up into silty-clayey nannofossil ooze, and finally into clayey nannofossil ooze. The uppermost parts are bioturbated, and contacts with overlying clays are gradational. The uppermost graded sequence exceeds 5 m in thickness, but underlying sequences are thinner (10–25 cm). The proportion of clay decreases downward within graded sequences, nannofossil chalks increase, and abundant thin sandy layers occur in the basal portions. Poor recovery in Cores 123-765C-14R and -15R makes interpretation of their stratigraphy problematic.

Major sequences occur as follows: Sections 123-765C-16R-1, top, to -16R-4 at 107 cm, displaying a distinct scoured base; Sections 123-765C-17R-3, top, to -17R-4 at 87 cm; Sections 123-765C-18R-2 at 123 cm to -18R-3 at 96 cm; and Sections 123-765C-18R-4, top, to 18R-5 at 121 cm (top and base missing).

Subunit IIIB

Sections 123-765C-20R-2 at 53 cm to -23R-2 at 103 cm, 532.8–562.3 mbsf.
Age: early Eocene to latest Campanian

Subunit IIIB consists of interbedded varicolored claystone and clayey nannofossil chalk, with both lithologies containing a fair amount of clinoptilolite in the upper part of the subunit. Intercalated coarser graded sequences consisting of nannofossil and calcareous fragment chalks and quartzose siltstones and sandstones show distinct lamination or ripple cross-lamination with sharp or scoured basal contacts (Fig. 22). A coarser grained interval with a laminated basal part and climbing ripples is shown in Figure 22. In Sections 123-765C-22R-3 and -22R-4, several matrix-supported conglomerates occur, overlain by grade intervals. The most distinctive conglomerate occurs in Section 123-765C-22R-2 at 85 to 110 cm (Fig. 23). The texture is tentatively ascribed to soft pebble deformation, but intense bioturbation is also a possibility.

Toward the base of the subunit, laminated intervals are absent and grading is more obvious. Also, dominantly varicolored clays give way downward to brown to dark brown clays.

Subunit IIIC

Sections 123-765C-23R-2 at 108 cm to -26R-3 at 36 cm, 562.3–591.7 mbsf.
Age: Campanian to Cenomanian

This subunit is composed of dark brown/dark reddish brown claystone with thick intercalated graded sequences. The latter have a sand-sized basal interval with quartz and claystone pebbles (Fig. 24). They grade up to silty chalk with subrounded and flattened dark brown claystone pebbles (1 cm), and hence into yellowish to reddish clayey micritic nannofossil chalk. Distinct erosional features are obvious around Section 123-765C-23R-5 at 47–60 cm (Fig. 24). The upper contacts are commonly gradational and bioturbated, but are locally scoured by the overlying sequence. These scours erode at least parts of the bioturbated intervals (Fig. 25). Color variation reflects in clay content in nannofossil ooze and in carbonate content in clay. Distinct graded sequences occur in Section 123-765C-23R-3 at 68 cm to -23R, CC at 7 cm (Fig. 26) and Sections 123-765C-24R-2 at 70 cm to -24R-3 at 132 cm (Fig. 29).

Coarse clastic input decreases downhole, and claystone increases proportionally. This is especially true for Section 123-765C-26R-1 at 50–115 cm. In this interval centimeter thick layers of dark reddish clay alternate with black shale (Fig. 28).

Unit IV

Sections 123-765C-26R-3 at 36 cm to 40R-3 at 15 cm, 591.7 to 724.05 mbsf.
Age: Cenomanian to early Aptian

Unit IV is dominated by brown, red, and greenish-gray zeolitic claystones. Calcium carbonate content increases stratigraphically downward, coinciding with lighter colors. Reds and browns decrease, and greens and greenish-gray colors increase downward. The boundary between dominantly red and brown and dominantly gray and green colors falls within Subunit IVB (Section 123-765C-31R-2). Intercalated fine-grained carbonates are absent from the uppermost cores and increase in number, thickness, purity, and grain size downward. The lowest part of Unit IV is dominated by carbonate and lesser siliciclastic, fine-grained graded sequences and intercalcated thin dark claystones. The upper boundary is drawn at the top of the highest thick

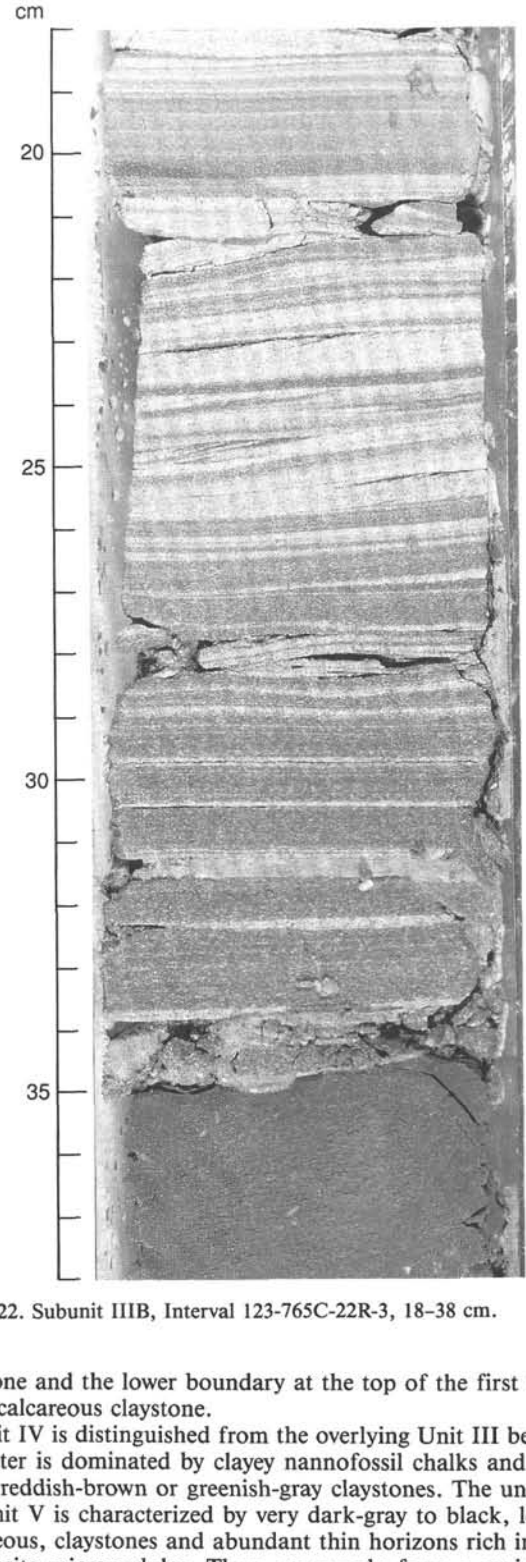

Figure 22. Subunit IIIB, Interval 123-765C-22R-3, 18–38 cm.

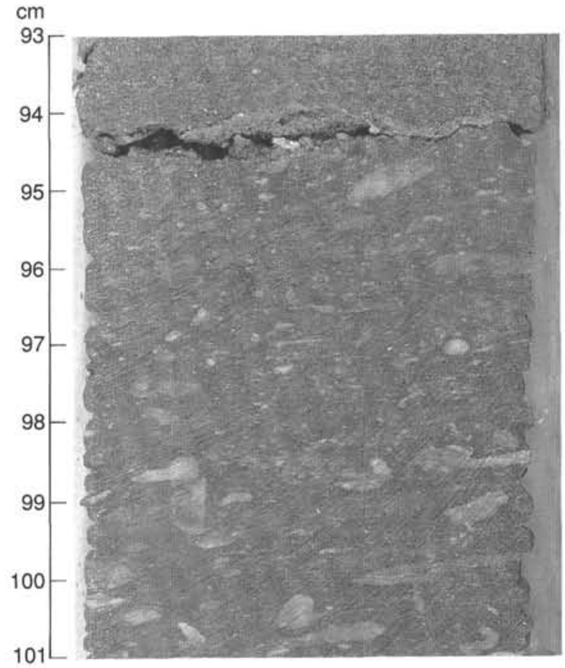

Figure 23. Subunit IIIB, Interval 123-765C-22R-3, 93–101 cm.

claystone and the lower boundary at the top of the first thick, dark, calcareous claystone.

Unit IV is distinguished from the overlying Unit III because the latter is dominated by clayey nannofossil chalks and lacks thick, reddish-brown or greenish-gray claystones. The underlying Unit V is characterized by very dark-gray to black, locally calcareous, claystones and abundant thin horizons rich in rhodochrosite micronodules. These commonly form a grain-supported fabric. This unit lacks the thick, reddish and greenish claystones and mixed carbonate and siliciclastic graded sequences common in Unit IV.

Dominant fossils in Unit IV include nannofossils, foraminifers, radiolarians, and calcispheres; the last three groups are concentrated especially in the graded sequences in Subunit IVD. Unit IV is divided into four subunits on the basis of dominant lithology, grain size, color, clay mineralogy, and distribution and character of graded sequences.

Subunit IVA

Sections 123-765C-26R-3 at 36 cm to -28R-1 at 150 cm, 591-7–608.5 mbsf.
Age: Cenomanian and late Albian

This subunit is dominated by dark red to reddish-brown zeolitic clay (Fig. 29), with lesser fine-grained red to reddish-brown carbonates. The base of the subunit was chosen arbitrarily in a transitional interval at the base of a claystone with nannofossils and at the highest occurrence of well-developed, bedding-parallel partings in claystone.

The Cenomanian/Albian boundary occurs between Section 123-765C-26R-5 at 25 to 26 cm and -27R-1 at 30 to 31 cm. This interval is dominated by red clay and red to gray nannofossil ooze and contains no obvious sedimentologic breaks.

Subunit IVB

Sections 123-765C-28R-1 at 150 cm to -34R-1 at 6 cm, 608.5–664.5 mbsf.
Age: late Albian to late Aptian

This subunit is characterized by light-colored, moderately fissile clays with minor clayey nannofossil chalks (Fig. 30). The lower boundary of this subunit is between overlying soft fissile dark grayish-green clay and underlying, harder and lighter-colored gray nannofossil claystone or clayey nannofossil chalk.

The upper part of the subunit (through the middle of Section 123-765C-31R-2) is dominated by brown and reddish-browns, with minor grays and greenish-grays. The lower part of the subunit is dominated by greenish-grays and grays, with minor yellowish-browns, browns, and reddish-browns. Color in this subunit is weakly correlated to lithology. Clay mineral composition may differ in this subunit from those in adjacent subunits. A downward decrease in kaolinite is accompanied by a strong increase in smectite, which becomes the dominant clay mineral.

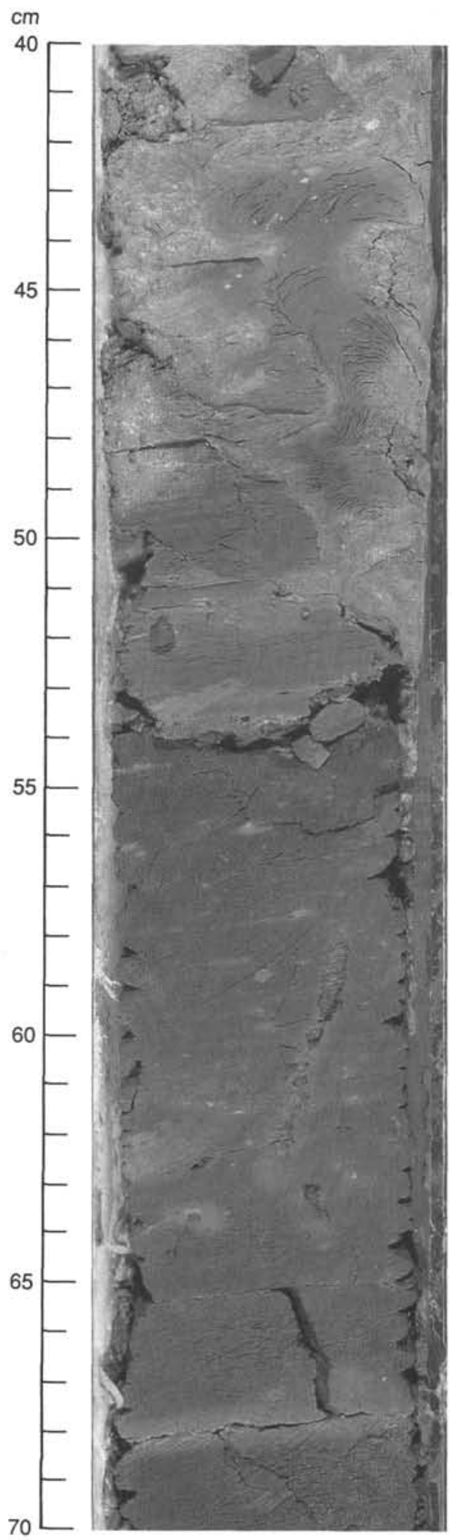

Figure 24. Subunit IIIC, Interval 123-765C-22R-5, 40–70 cm.

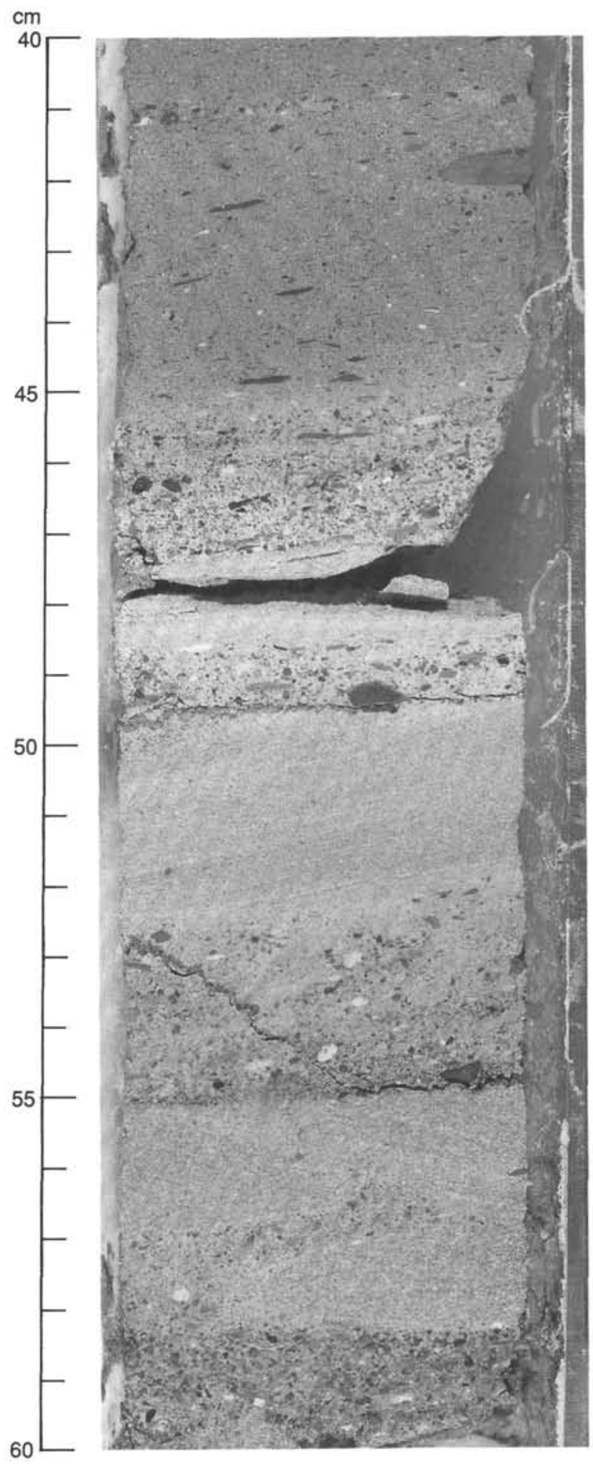

Figure 25. Subunit IIIC, coarse-grained cross-laminated base of graded sequence, Interval 123-765C-23R-5, 40–60 cm.

Clinoptilolite is dominant in two samples for Subunit IVB, but absent from Subunits IVA and IVD.

Clayey nannofossil chalks are most well-developed in Sections 123-765C-31R-1, -31R-2, and -31R-4. These chalks are entirely absent from Core 123-765C-33R, and mostly absent from Core 123-765C-29R. Radiolarian molds consisting of clinoptilolite are locally abundant in Core 123-765C-31R.

The Albian/Aptian boundary occurs between Sections 123-765C-33R-1 at 38 to 40 cm and -34R-1 at 130 to 132 cm. This thick interval is dominated by greenish-gray claystone that contains no major sedimentological breaks.

Subunit IVC

Sections 123-765C-34R-1 at 6 cm to -36R-6, top, 664.46–690.6 mbsf.

Age: late Aptian

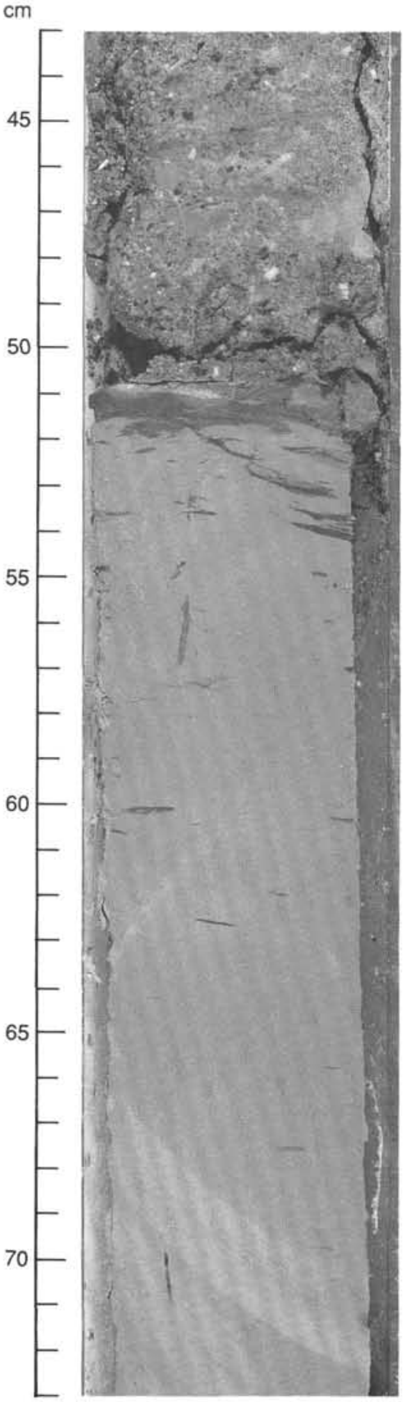

Figure 26. Subunit IIIC, Interval 123-765C-23R-3, 43–73 cm.

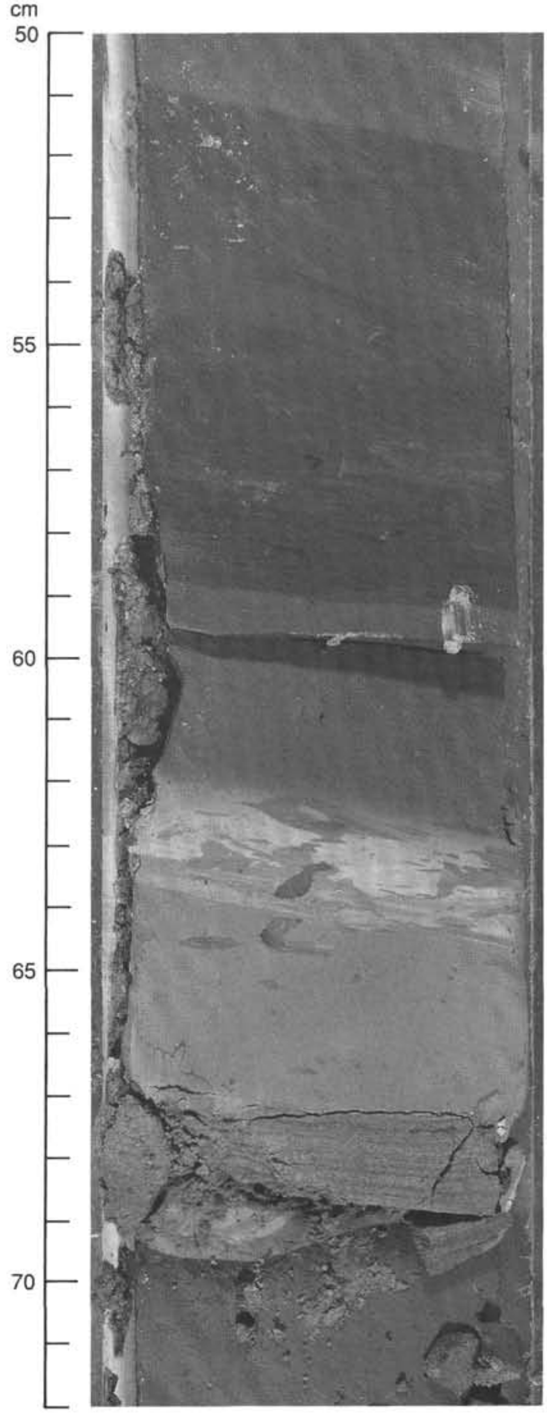

Figure 27. Subunit IIIC, Interval 123-765C-24R-2, 50–72 cm.

The lower boundary of Subunit IVC is between dusky green claystone above and graded and laminated calcareous chalk, constituting a graded sequence 8 cm thick, below (Fig. 31).

The subunit consists predominantly of light-colored, gray and green calcareous claystones, nonfissile and considerably harder than those of Subunit IVB, and fine-grained clayey chalks. Calcareous and noncalcareous black claystones occur in Sections 123-765C-34R-1 at 92 cm to -34R-2 at 12 cm, and -35R-3 at 52 cm to -35R-3 at 107 cm. Thin radiolarites occur in Sections 123-765C-35R-3 at 14 to 15 cm and -35R-4 at 11 to 14 cm. A small percentage of radiolarians disseminated in claystone occurs. Smectite is the dominant clay mineral; minor amounts of illite occur. The highest occurrence of kaolinite within this subunit is also noteworthy.

Subunit IVD

Sections 123-765C-36R-6, top, to -40R-3 at 15 cm, 690.6–724.05 mbsf.

Age: early to late Aptian

This subunit is dominated by gray and green siliciclastic (Core 123-765C-37R) and mixed carbonate-siliciclastic (lower

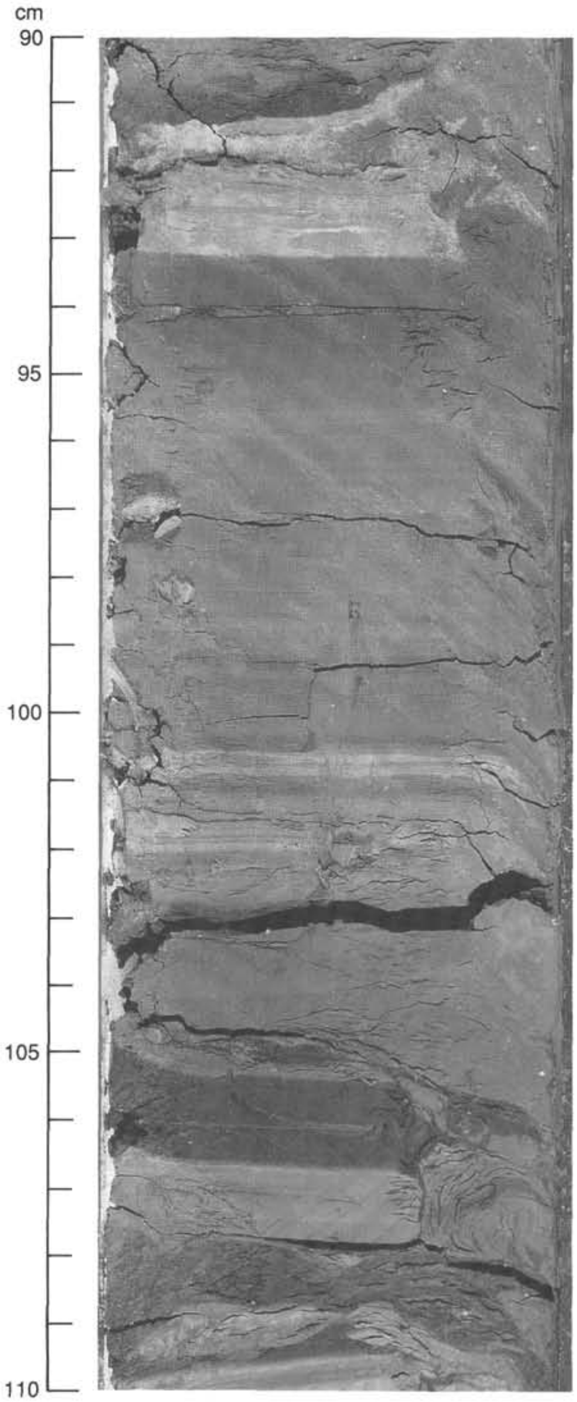

Figure 28. Subunit IIIC, Interval 123-765C-26R-1, 90–110 cm.

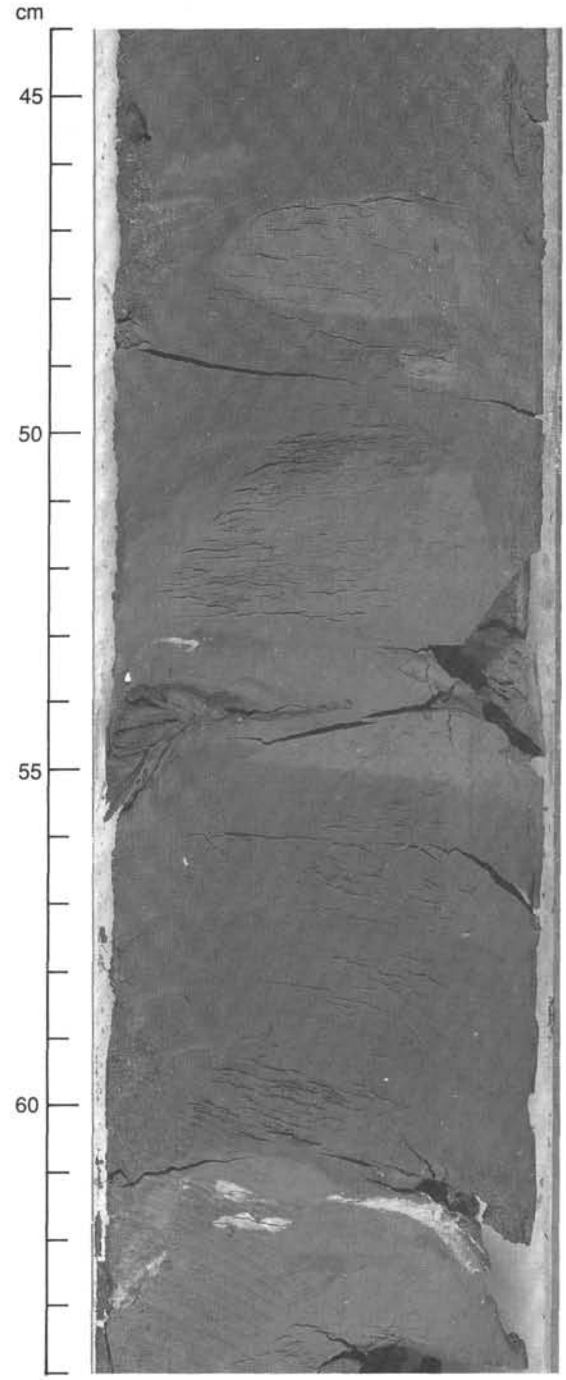

Figure 29. Subunit IVA, dark-colored zeolitic clay, Interval 123-765C-28R-1, 44–64 cm.

cores) graded sequences (Fig. 32); particles range from clay- to medium-sand-sized, but are primarily finer than sand-sized. XRD analysis shows that smectite (smectite/illite) is the dominant clay mineral, together with minor amounts of illite. Sequences range from 7 to more than 268 cm thick, but most are less than 50 cm thick. Sequences thicken downward but are coarsest in Core 123-765C-38R, in which visibly graded sand-sized basal intervals commonly exceeding 10 cm are well-represented. Graded sequences in adjacent cores typically have little or no sand-sized basal portion, although a thick sequence in Sections 123-765C-39R-1 and -39R-2 includes a 90-cm-thick silty interval that is apparently graded.

The thin, fine-grained, graded sequences in Subunit IVD typically contain four depositional units from bottom to top: (1) a sometimes-present basal massive to graded interval, commonly very thin; (2) a silty laminated zone; (3) a massive, silt- to clay-sized interval (commonly the thickest portion of the sequence); and (4) a dark-colored clay-rich cap, which may be absent.

The uppermost part of the massive unit is commonly bioturbated and the intensity of bioturbation decreases downward. The silty laminated interval above the basal coarse graded unit includes (in some graded sequences) contorted laminae, micro-erosion surfaces, and low-angle cross-laminae. The basal con-

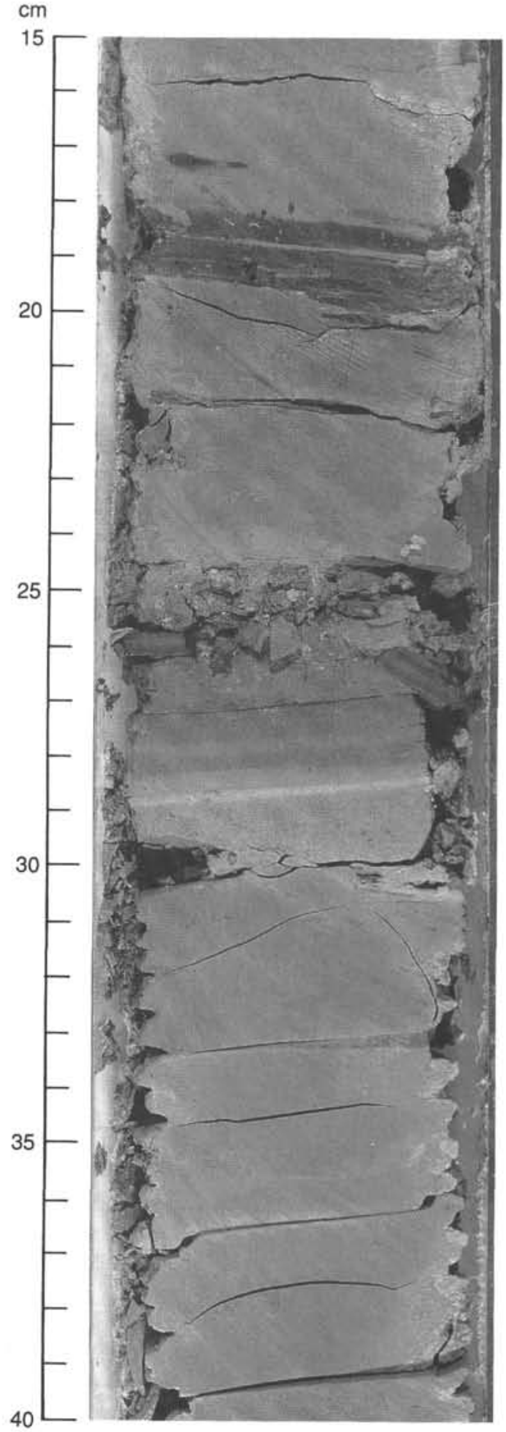

Figure 30. Subunit IVB, thin, graded, clay-rich carbonate sequence and moderately fissile claystones, Interval 123-765C-28R-3, 15–40 cm.

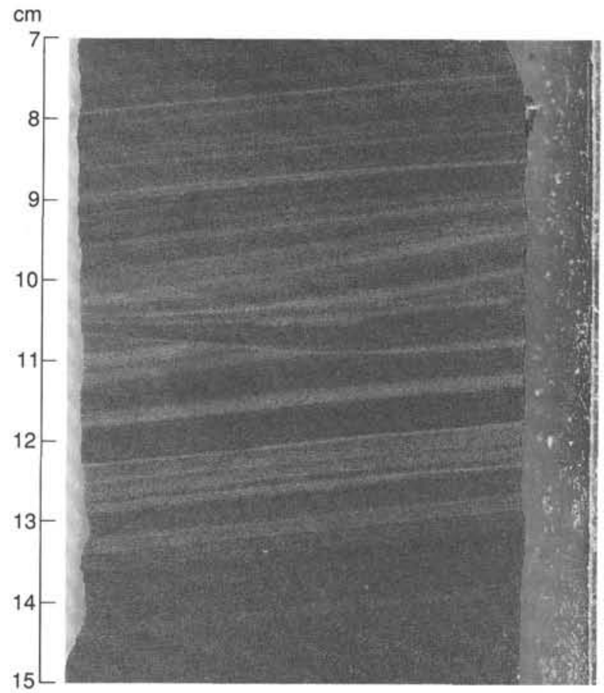

Figure 31. Subunit IVD, low-angle cross-lamination in graded sequence, Interval 123-765C-36R-2, 7–15 cm.

tacts of graded sequences are sharp (rarely scoured), and upper contacts also are sharp. Contacts between parts of a single sequence are commonly gradational.

Proportions of lithologies composing >1% of each of the four subunits of Unit IV are as follows:

Subunit IVA: claystone = 60%, nannofossil chalk = 24%, calcareous chalk = 16%.

Subunit IVB: claystone = 85%, nannofossil chalk = 11%, siltstone = 3%.

Subunit IVC: claystone = 81%, calcareous chalk = 18%.

Subunit IVD: claystone = 48%, calcareous chalk = 16%, mixed sediment = 16%, siltstone/sandstone = 12%, nannofossil chalk = 7%.

Up to 10% radiolarians occur disseminated in claystones, suggesting that at least some of the claystones in this subunit are hemipelagites.

Unit V

Sections 123-765C-40R-3, 15 cm, to 123-765C-54R-1, 119 cm, 724.1–859.2 mbsf.
Age: Barremian to Aptian.

Unit V consists of dark gray, gray, reddish-brown, and green claystones, with minor graded carbonate sequences (only in the upper part), rhodochrosite sediment and concretions, and radiolarites. This unit is distinguished from Unit IV by the abrupt appearance of dark gray claystone and a reduction in number, thickness, and grain size of graded carbonate sequences in the upper part of Unit V. Unit V differs from Unit VI by the occurrence in the latter unit of altered ash layers and abundant nannofossil chalks. Three subunits are defined based on the distributions of dark gray claystones, rhodochrosite sediment, and radiolarites.

Subunit VA

Sections 123-765C-40R-3 at 15 cm to -42R-1 at 29 cm, 724.1–740.1 mbsf.
Age: early Aptian

Subunit VA consists of a 16-m-thick, dark gray claystone having thin silty layers. Clay mineralogy from XRD analysis shows that the predominant constituents are of the illite and smectite groups. Minor phases are calcareous particles (nannofossils, micrite, calcareous fragments, and calcite), authigenic

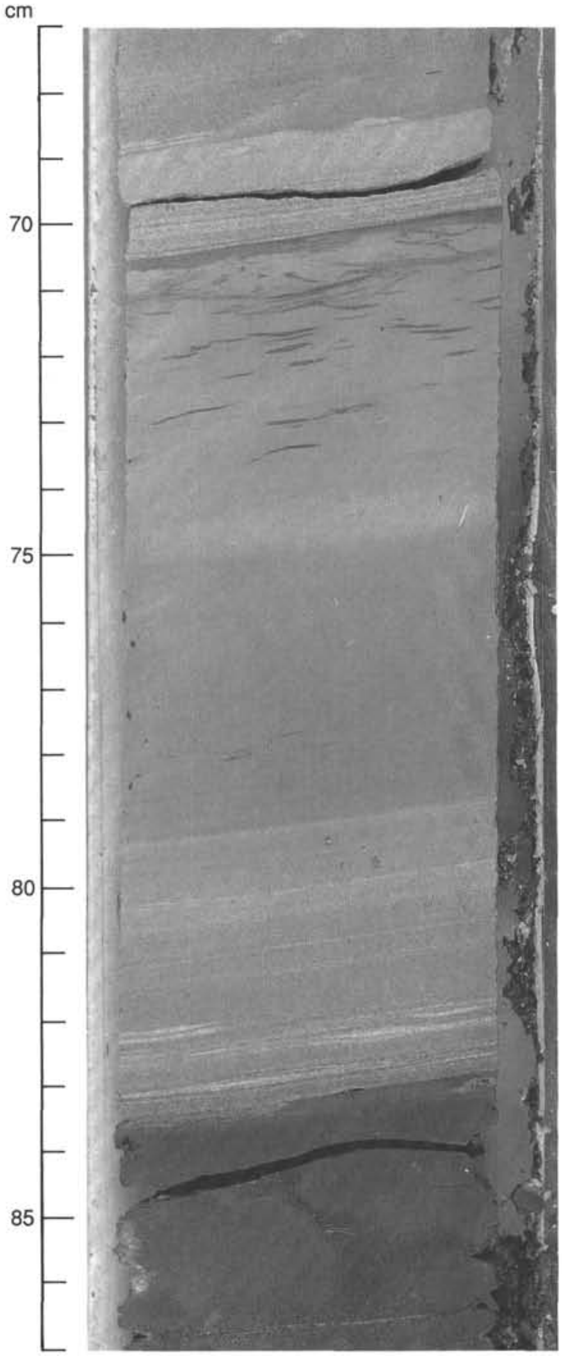

Figure 32. Subunit IVD, complete, typical carbonate graded sequence, Interval 123-765C-38R-5, 67–87 cm.

dolomite, and quartz, the proportions of which tend to increase toward the bases of the laminated and graded silty layers. These layers are sparsely intercalated through the unit and have gradational upper contacts and sharp lower contacts. XRD analysis from the base of a prominent coarser-grained interval (Section 123-765C-40R-4 at 53 cm) indicates that the mineral components are dolomite, quartz, clay, and calcite (in order of decreasing abundance) and from a laminated interval (Section 123-765C-40R-4 at 102 cm) are expanding clay (dominant) and quartz (major).

Subunit VB

Sections 123-765C-42R-1 at 29 cm to -48R-7 at 3 cm, 740.1–805.1 mbsf.
Age: Barremian to early Aptian

Subunit VB is composed predominantly of claystone, with minor rhodochrosite sediment and/or microconcretions (Pl. 1). The claystone in Subunit VB is similar to that of Subunit VA, except for its color, which is extremely variable but predominantly gray to very dark gray, dark reddish-brown, dark reddish-gray, dusky green, or grayish-green. Color banding occurs on a centimeter to decimeter scale. The claystone is commonly massive. Elongated and flattened mottles, which are mostly parallel to bedding, occur locally. These are apparently caused by diagenetic processes and/or possibly bioturbation. Mineralogy from XRD analysis of a black silty claystone in Sample 123-765C-42R-1, 42 cm, is dominantly quartz, mixed layer clays (smectite/illite) and illite and in Sample 123-765C-48R-5, 135 cm, predominantly dolomite with a lesser amount of quartz and illite/smectite. Scattered occurrences of pyrite, zeolites and organic debris were observed in smear slides. Sparse calcareous intervals, similar to those described in Subunit VA, exhibit grading, lamination, and medium-sand- to silt-sized texture.

Rhodochrosite sediment and/or microconcretions and micronodules occur throughout the entire subunit with a highest observed occurrence in Section 123-765C-42R-1 at 29 cm. Color is predominantly greenish-gray, gray, olive gray, or white. Two main types of occurrence characterize round concretions of rhodochrosite: (1) coarse-sand- to silt-sized globular masses floating in a claystone matrix (e.g., Section 123-765C-46R-2 at 63 to 64 cm; Fig. 33); and (2) concretion-supported graded intervals (e.g., Section 123-765C-46R-2 at 61.5 to 62 cm). These are lo-

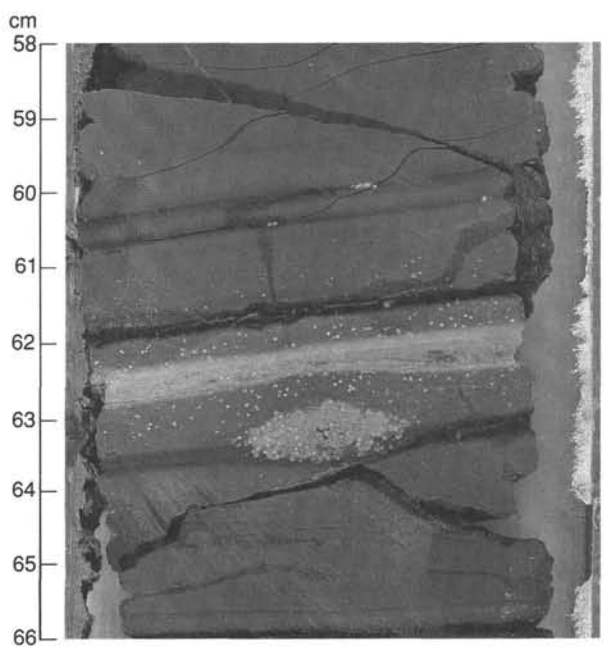

Figure 33. Subunit VB, various settings of rhodochrosite micronodules, Interval 123-765C-46R-2, 58–66 cm. Claystone-supported disseminated micronodules, Interval 123-765C-46R-2, 62–63 cm. Centimeter-thick layer of concentrated micronodules with cross-laminae, Interval 123-765C-46R-2, 63–64 cm. Accumulation within lens-shaped concretion, Interval 123-765C-46R-2, 56–66 cm.

cally intercalated within claystone, are laminated and/or cross-laminated, and are locally graded complexely with juxtaposition of fining- and coarsening-upward sequences (Fig. 34). Many rhodochrosite microconcretions contain radiolarians, either well-preserved or highly corroded; it is not clear whether radiolarians were present in some concretions (Pl. 1, Figs. 2 and 3). Some of the microconcretions resemble rhodochrosite spherules synthesized by Momoi et al. (1988) from silica gels.

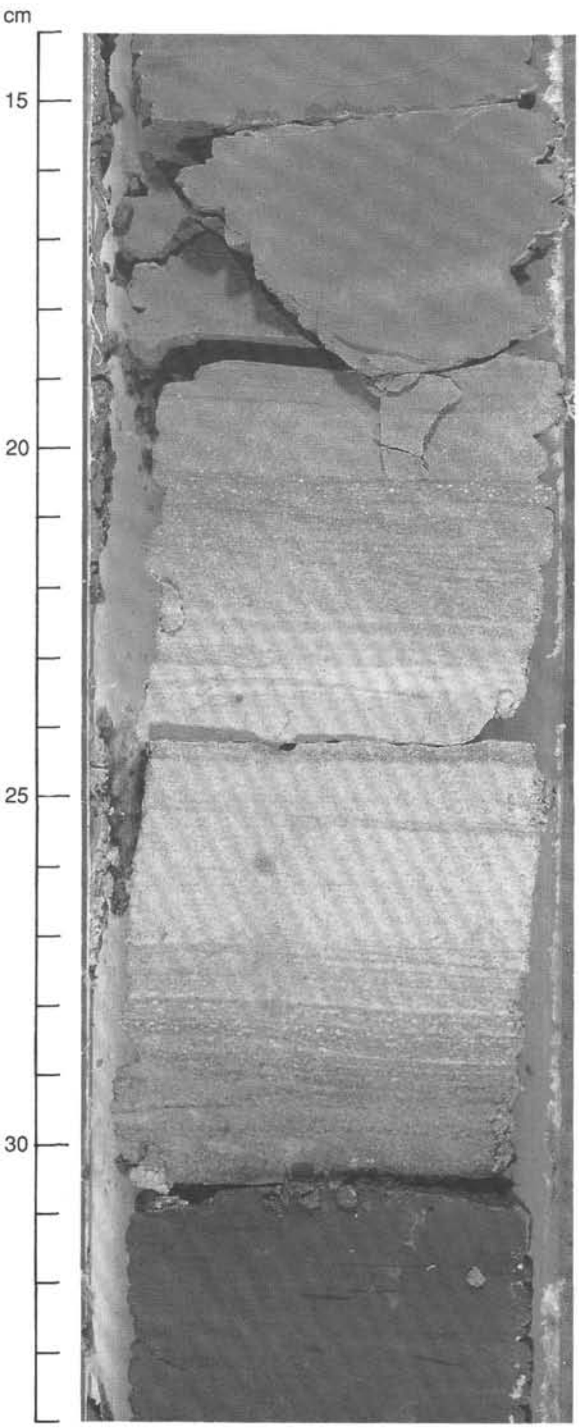

Figure 34. Subunit VB, graded intervals of micronodules with parallel and/or cross-laminae, Interval 123-765C-47R-2, 14–34 cm.

Subunit VC

Sections 123-765C-48R-7 at 3 cm to -54R-4 at 119 cm, 805.1–859.2 mbsf
Age: Barremian

Subunit VC is dominantly claystone. Rhodochrosite microconcretions and subordinate radiolarite, the highest observed occurrence of which is in Section 123-765C-48R-7 at 9 cm, occur throughout the subunit. The claystone is similar to claystone described in Subunits VA and VB, with the same diversity of color as that in Subunit VB. Closely spaced bands of alternating, similar, colors are common and are probably burrows flattened by compaction. Rhodochrosite micronodules and pyrite cubes are sparse. The most common minor constituents in Cores 123-765C-52R and -53R, in decreasing abundance, are siliceous debris, radiolarians, quartz silt, organic debris, and zeolites. Siliceous fragments and radiolarians are locally as much as 25% to 30% of the observed grains. Radiolarites occur locally as distinct greenish-gray, gray, and green layers ranging from a few millimeters to 2 cm thick. These layers are commonly graded, with a silty to medium-sand-sized texture and with parallel and/or wavy laminations (Fig. 35). Contacts are commonly sharp, but in some cases, upper contacts are gradational to clayey siltstone with radiolarians (Fig. 36). Section 123-765C-54R-1 between 41 and 70 cm displays a complex graded interval of superposed coarsening- and fining-upward sequences.

Unit VI

Sections 123-765C-54R-4, at 119 cm to -58R-2, 20 cm, 859.2–892.7 mbsf.
Age: Valanginian to Hauterivian

Unit VI is distinguished by abundant intervals of calcareous (nannofossil-bearing) claystone and calcareous mixed sediment. These calcareous sediments are the dominant lithologies in the unit and are not found in the immediately adjacent Units V and VII. These sediments are intercalated with claystones, radiolar-

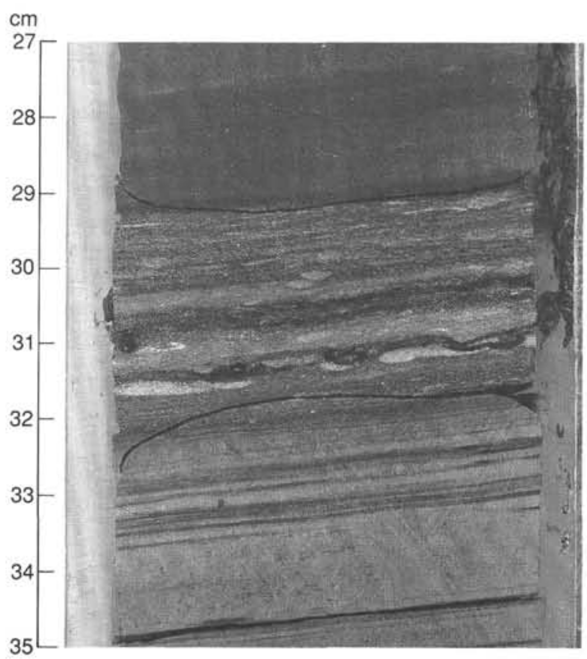

Figure 35. Subunit VC, radiolarite, Interval 123-765C-51R-5, 27–35 cm.

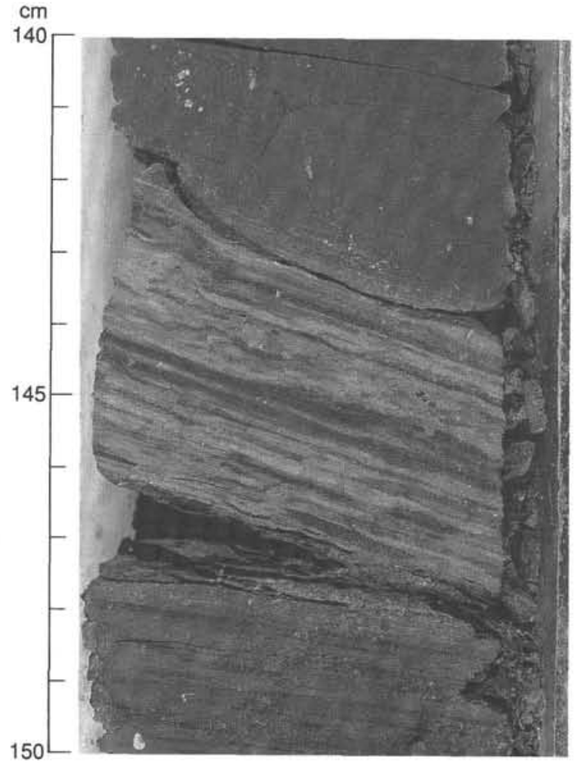

Figure 36. Subunit VC, radiolarite, Interval 123-765C-50R-5, 140–150 cm.

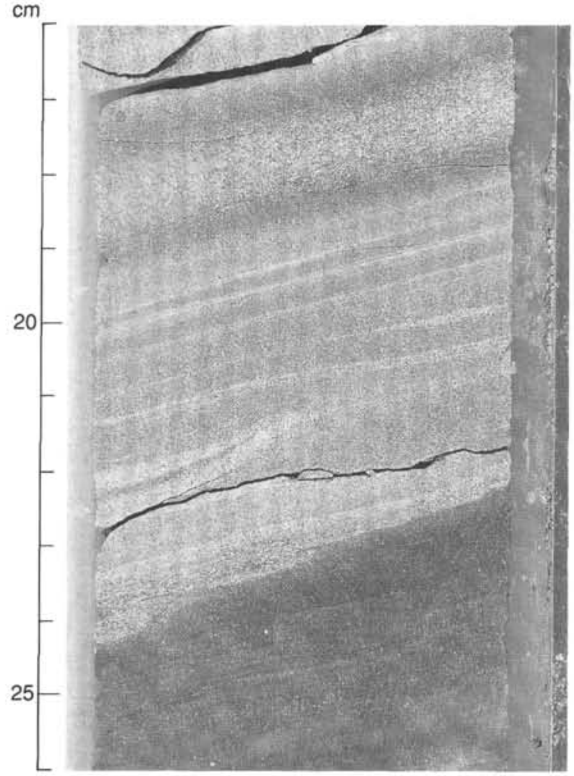

Figure 37. Unit VI, graded and channeled calcareous mixed sediment, Interval 123-765C-57R-3, 16–26 cm.

ites, and rhodochrosite-bearing sediments, like those in Units V and VII, and have altered ash layers similar to those in Unit VII. The top and base of the unit are taken, respectively, at the top of the highest and the base of the lowest calcareous interval. Unit VI is Valanginian to Hauterivian in age, based on nannofossil and radiolarian faunas found throughout the unit.

Calcareous claystone and calcareous mixed sediment constitute about two-thirds of Unit VI. These calcareous sediments are typically reddish-brown, brownish-gray, or pinkish-gray, less commonly greenish-gray or gray. Most constitute upward-fining sequences less than 5 cm to almost 3 m thick; they are typically less than 20 cm thick. Some sequences are entirely silt- to clay-sized nannofossil-bearing sediment, other intervals are coarse- to fine-sand-sized calcareous fragment-bearing sediment (Fig. 37) grading up into finer-grained nannofossil claystone. Both types of sequence typically have sharp or scoured bases, with tops graditional to claystone. Both contain parallel- and cross-laminae, small-scale channels, microflasers, and locally abundant bioturbation, including distinctive Y-shaped burrows as much as 2 cm long (Fig. 38). Other calcareous intervals, particularly in Cores 123-765C-55R and -56R, consist of nannofossil claystone that is neither demonstrably graded nor current-worked; some of these intervals can be distinguished from intercalated noncalcareous claystones by testing with HC1. In general, however, calcareous intervals are lighter-colored than noncalcareous intervals, and many exhibit inferred wispy stylolites (pressure-solution features?) at high angles to bedding. Calcareous intervals may contain bivalve (inoceramid) fragments, rhodochrosite micronodules, micrite, quartz sand or silt, radiolarians, and calcispheres, as well as minor benthic foraminifers, organic matter, pyrite, glauconite, white mica, and phosphatic debris.

Claystone, silty claystone, and clayey siltstone make up almost one-third of Unit VI. This lithology, mainly shades of reddish-brown and brownish-gray, is commonly massive and featureless, but locally may contain light or dark mottles (possible bioturbation structures), parallel or (rarely) convolute laminae. Claystones are mostly noncalcareous and contain a few percent (locally, as much as 60%) silt-sized quartz, radiolarians, and/or rhodochrosite micronodules, as well as minor organic debris and pyrite. Siltstone occurs as thin, graded laminae with scoured bases and small flaser structures. XRD analysis indicates smectite is the major component, with minor amounts of illite.

Radiolarites and altered ash layers constitute less than 5% of Unit VI. Radiolarites are white, greenish-gray, or reddish-brown, medium-sand- to silt-sized, with sharp or gradational upper contacts and scoured or sharp lower contacts (Fig. 39). Some intervals are normally graded, whereas others appear reversely graded; most are parallel or cross-laminated. Radiolarites contain minor amounts of siliceous fragments, spicules, quartz silt, clay, and/or rhodochrosite micronodules; some radiolarian tests are infilled with chalcedony. In Section 123-765C-57R-4, radiolarite laminae occur at several intervals within a 0.5-m-thick sequence of calcareous chalk. Radiolarites increase in abundance and thickness downward in Unit VI, from Core 123-765C-55R, where they constitute a few millimeter-thick layers, to Core 123-765C-57R, where more than 10 discrete intervals as much as 8 cm thick can be discerned. One altered 8-cm-thick ash layer occurs in Section 123-765C-57R-7 (Fig. 40). XRD analysis confirmed that this layer is pure smectite (Pl. 1, Fig. 6).

Unit VII

Sections 123-765C-58R-2 at 20 cm to 62R-4, 28 cm, 892.7–931.2 mbsf.
Age: Berriasian to Valanginian

The top of Unit VII is taken at the base of the lowest calcareous interval, and the base is the contact between claystone and basalt. Unit VII is distinguished by the absence of calcareous

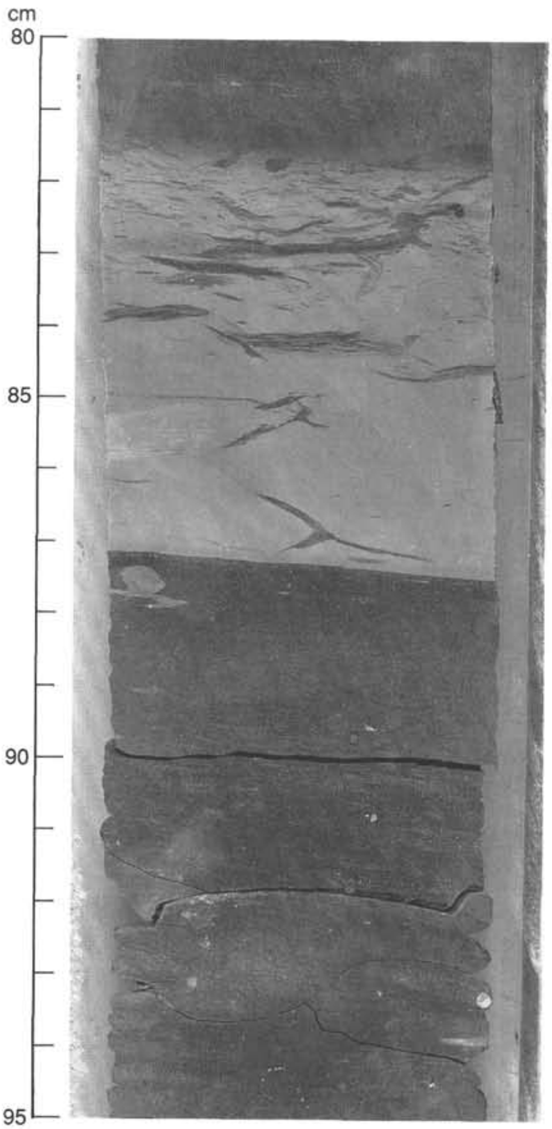

Figure 38. Unit VI, nannofossil-bearing claystone intercalated with darker colored noncalcareous claystone. Note Y-shaped burrow, Interval 123-765C-57R-2, 80–95 cm.

sediments like those that characterize Unit VI, and, in its lower half, by the presence of brown silty claystone having calcareous shell fragments, a lithology found nowhere else at Site 765. The rest of the unit consists of dark reddish-brown noncalcareous claystone, radiolarites, and altered ash layers like those found in Unit VI. Unit VII is Berriasian to Valanginian in age, based on dinoflagellate assemblages from Sections 123-765C-59R-4 and -59R-5 and radiolarian assemblages from Cores 123-765C-61R and -62R. Other fossils found in this unit include benthic foraminifers, nannofossils, bivalve mollusks, calcipheres, and belemnite fragments.

Unit VII consists of two subunits: Subunit VIIB is distinguished from VIIA by the presence of brown silty claystone with calcareous shell fragments.

Subunit VIIA

Sections 123-765C-58R-2 at 20 cm to -61R-2, 150 cm, 892.7–919.9 mbsf.
Age: Berriasian to Valanginian

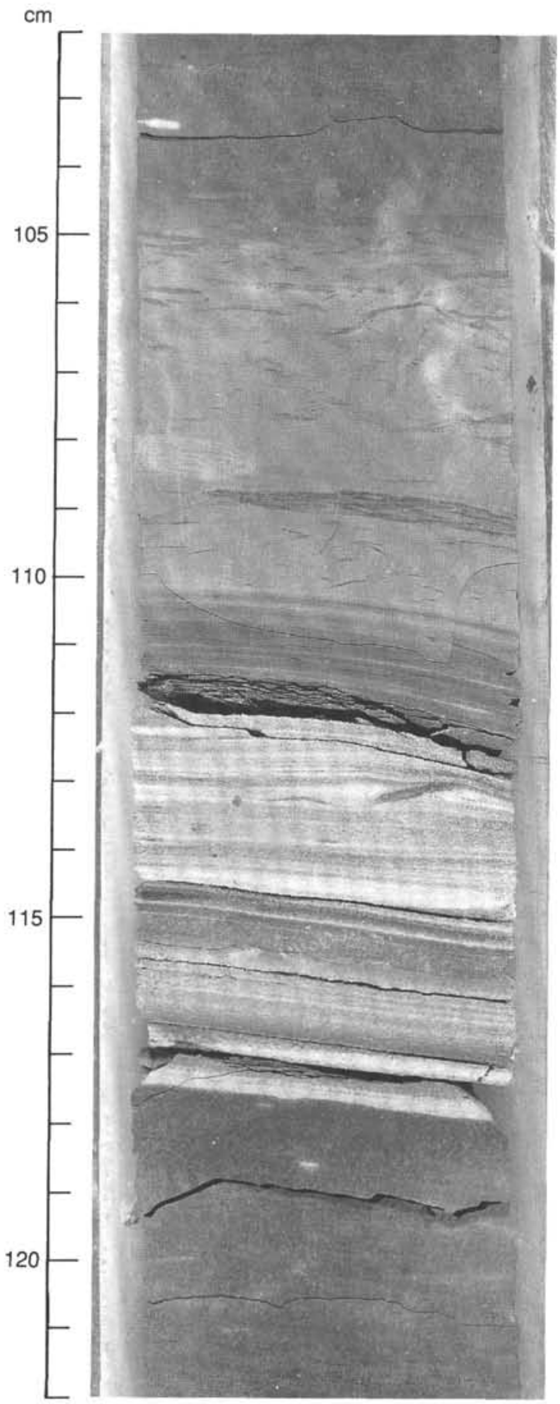

Figure 39. Unit VI, thin radiolarite layers having sharp basal contacts, gradational upper contacts, Interval 123-765C-57R-2, 102–122 cm.

Subunit VIIA consists primarily of noncalcareous claystones, dominantly reddish-brown, less commonly greenish-gray or gray to dark gray; its lower boundary is taken at the stratigraphically highest occurrence of brown silty claystone with shell fragments. Most typically, the claystone is massive and featureless, but greenish-gray color bands, streaky laminae, halos, and mottles flattened parallel to bedding occur locally and are especially common in Section 123-765C-60R-4 (Fig. 41). At least some of these mottles may represent diagenetic alteration envelopes surrounding thin seams of volcanic ash. Some intervals are charac-

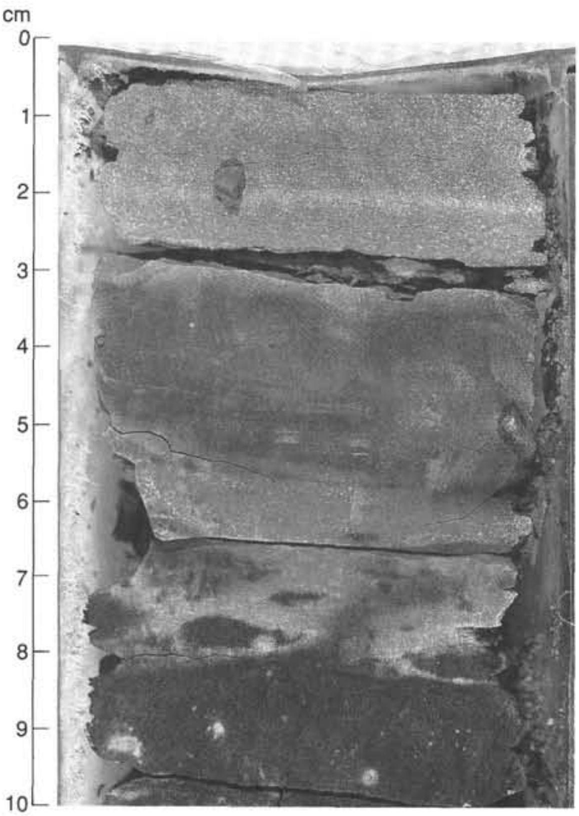

Figure 40. Unit VI, altered ash layer, Interval 123-675C-57R-7, 0–10 cm.

terized by a blocky fracture; thin intervals, particularly in Core 123-765C-59R, have well-developed fissility.

Locally, claystones contain minor silt or sand (mostly quartz, rhodochrosite micronodules, radiolarians and glass, as well as organic debris, pyrite, apatite, muscovite, and feldspar)—disseminated, or as thin laminae, or, rarely, as burrow infillings(?). XRD analyses of three claystones from Cores 123-765C-59R and -61R indicate the presence of varying amounts of rhodochrosite, quartz, predominant smectite, and minor illite. Several intervals of very dark gray, finely laminated, organic-rich(?) claystone occur in Sections 123-765C-59R-4 and -59R-5.

Subunit VIIA also contains a few percent radiolarites and altered ash beds as thin layers dispersed throughout the subunit. Radiolarites are white, gray to greenish-gray, or reddish-brown lenticular lenses or thin layers, typically a few millimeters to 1 cm thick, but as much as 15 cm thick. These layers may be graded, inversely graded, or have wavy to cross-laminae; most are sand- to silt-sized, but some are clay-rich. Boundaries are sharp to diffuse. Distinct radiolarite intervals were not observed below Core 123-765C-59R. Twenty intervals that may be altered ash layers occur in Subunit VIIA; they are greenish-gray to gray, waxy, locally mottled (bioturbated?) and have a soapy texture (Fig. 42). XRD analyses of samples from Cores 123-765C-60R and -61R indicate the presence of illite and smectite, whereas white layers consist entirely of smectite. Most horizons are a few millimeters to 1 cm thick; rare intervals as much as 11 cm thick were noted in Core 123-765C-61R.

A possible hardground is developed in reddish-brown claystone in Section 123-765C-61R-2, at 93 cm, 57 cm above the top of Subunit VIIB. It consists of an irregular, botryoidal, black, Mn-oxide crust, 1 mm thick (Fig. 43). A few 1- to 2-cm-diameter angular to subrounded white shell fragments and black MnO(?) clasts occur just beneath the crust. This layer was not

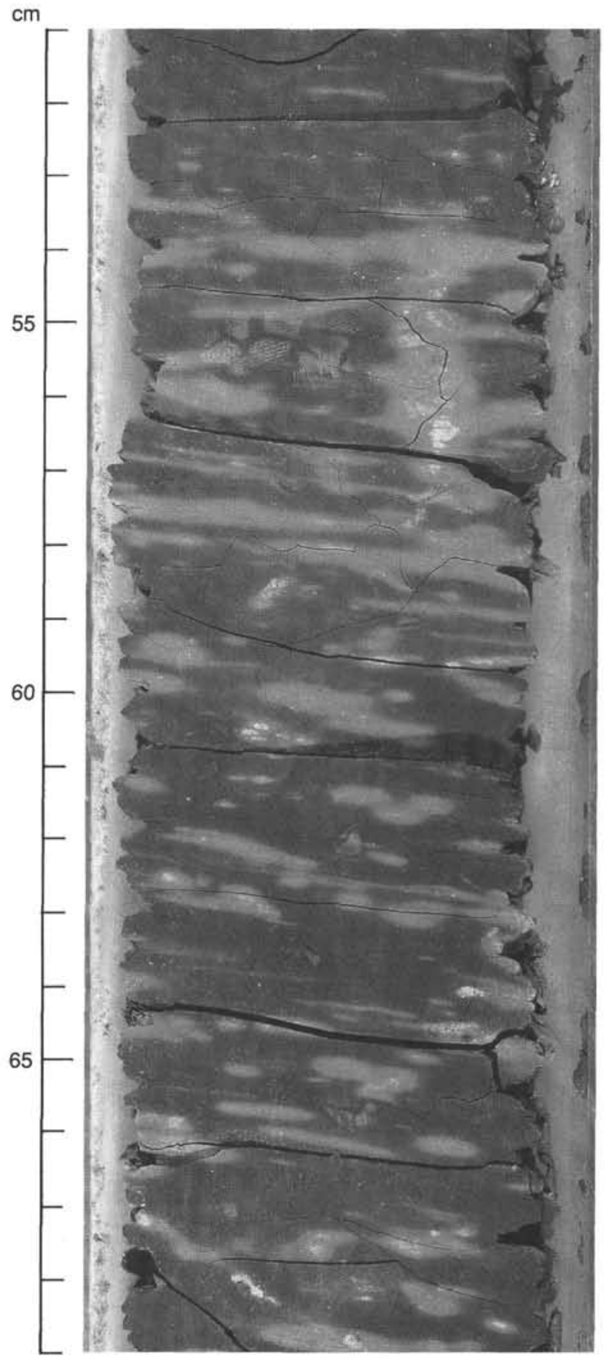

Figure 41. Subunit VIIA, mottled (ashy?) claystone, Interval 123-765C-60R-4, 51–69 cm.

chosen as a unit or subunit boundary because it occurs within a homogeneous lithologic unit (reddish-brown claystone, noncalcareous, and locally slightly silty). A concentration of silt-sized radiolarians occurs directly beneath the hardground.

Subunit VIIB

Sections 123-765C-61R-3, top, to -62R-4 at 28 cm, 919.9–931.2 mbsf.
Age: Berriasian

The base of Subunit VIIB is at the sediment/basalt contact in Core 123-765C-62R. This subunit consists largely of a single lithology, a brown to red silty claystone, locally a clayey silt-

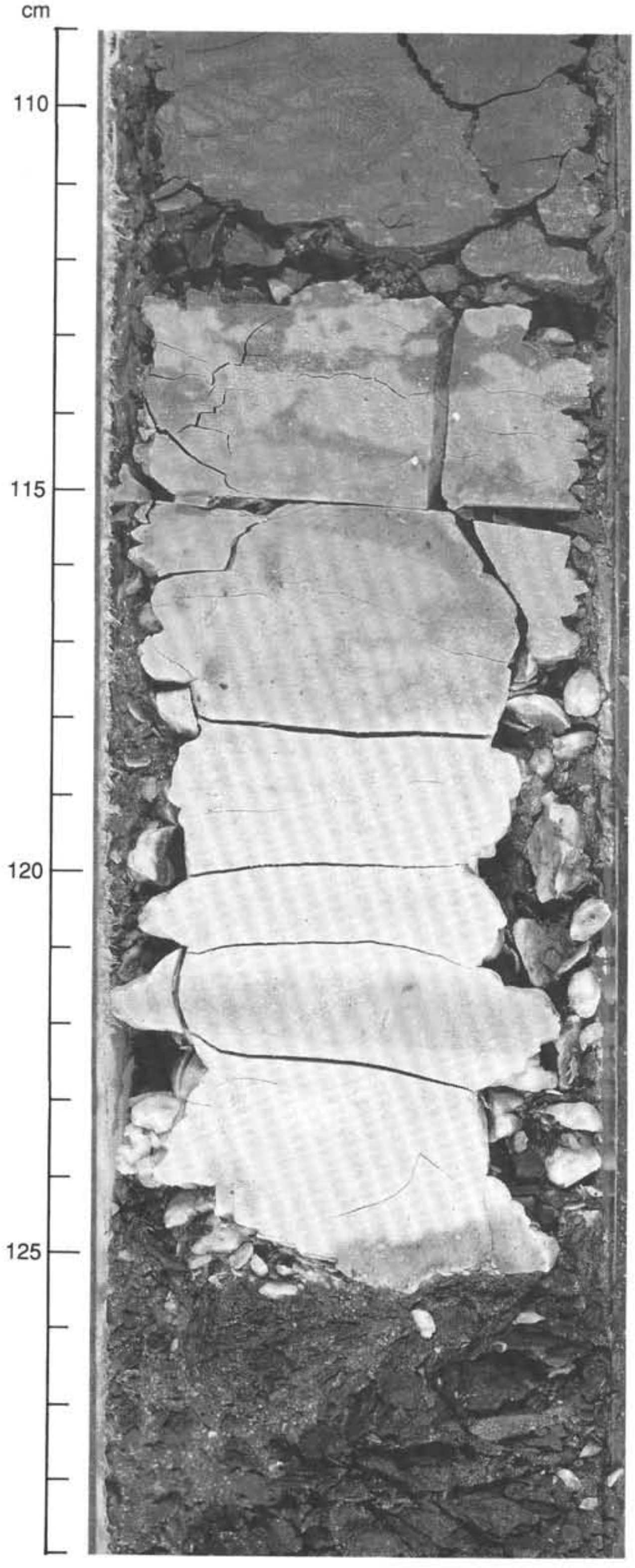

Figure 42. Subunit VIIA, altered ash layer, Interval 123-765C-60R-5, 109–129 cm.

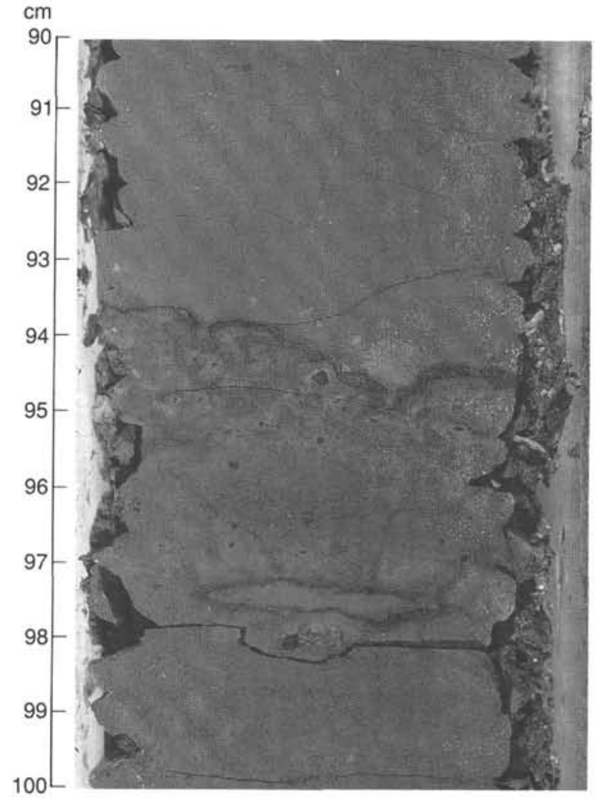

Figure 43. Subunit VIIA, possible hardground (manganese oxide crust) underlain by brown clayey radiolarite and overlain by brown claystone, Interval 123-765C-61R-2, 90–100 cm.

stone or sandstone, predominantly calcareous but with thin noncalcareous intervals (e.g., Section 123-765C-61R-4 at 78 to 90 cm). The silt- and sand-sized material is dominantly shell debris with lesser quartz. White calcareous shell debris (principally inoceramid prisms, also other molluscan and belemnite fragments) occurs disseminated throughout this subunit; this material is mostly sand-sized (Fig. 44), but bivalve cross sections as much as 1 cm in diameter occur in Section 123-765C-62R-2 at 0 to 10 cm. Locally, shell debris concentrations constitute 30% to 50% of the sediment and form a fabric of closely spaced whitish wispy laminae and lenses; many shell fragments are pitted (etched?) and aligned parallel to bedding. Black MnO nodules are also disseminated throughout the claystone; these are predominantly a few millimeters or less in diameter, but reach 1 cm in diameter in Core 123-765C-62R. A thin interval of greenish-gray sediment in Section 123-765C-61R-3 at 16 to 20 cm consists almost entirely of calcispheres. Also, several intervals of red of light green calcareous claystone occur in Sections 123-765C-61R-4, -61R-5, and -62R-1; these intervals contain etched nannofossils. The clay mineral composition does not differ significantly from the units above; smectite is dominant, and illite forms a minor constituent.

The lower part of Subunit VIIB (Section 123-765C-62R-3 at 35 cm to -62R-4 at 28 cm) consists of brown, noncalcareous claystone. The basal contact between claystone and basalt is marked by a few centimeters of basalt hyaloclastite, altered to celadonite, floating in a matrix of red claystone and white sparry calcite cement (Fig. 45).

SEDIMENTOLOGY

Introduction

Various techniques were used to decipher the sedimentation history of Site 765, including Markov chain analysis of facies transitions, XRD analysis of clay and other minerals, and multivariate analysis of smear-slide data, in addition to the standard descriptive procedures employed by the shipboard sedi-

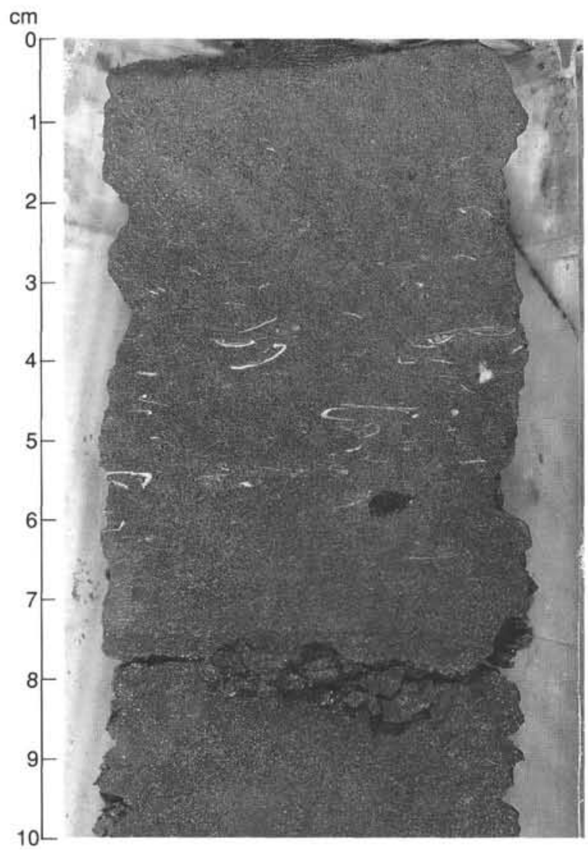

Figure 44. Subunit VIIB, cryptically laminated, mollusk claystone or molluscan clay mixed sediment. Note whole shells of thin-walled bivalves. Rock contains abundant silt- to sand-sized *Inoceramus* debris, Interval 123-765C-62R-2, 0–10 cm.

mentologist. This chapter presents brief summaries of methodology and major findings of these three techniques, a summary of the sedimentation history, and a discussion of trends in sedimentation through time.

Markov Chain Analysis

Markov Chain Analysis is a variety of transition-frequency analysis (Davis, 1973). The technique has been applied previously to geological systems by Read (1969), Gingerich (1969), Selley (1970), Miall (1973), and Walker (1979). In this procedure, the first step is to identify all lithofacies (or lithologies) that occur in the section to be studied. One then constructs a matrix consisting of all observed transitions between successive facies. This analytical method does not account for facies *thickness* data. The *transition frequency matrix* is converted to a *transition proportion matrix* by first converting counts to decimal frequencies (by dividing each element in the matrix by the grand total number of transitions) and then row-normalizing the elements by dividing each by its row total (Davis, 1973). This eliminates the dependency of the matrix elements on the overall frequency of lithofacies in the sequence.

Expected transition probabilities are calculated and transformed in the same way. Expected transition probabilities depend strictly on the frequency of occurrence of lithologies. Therefore, the expected frequency for an element in the *expected transition frequency matrix* is simply the product of the frequencies of the two lithofacies involved. The expected transition proportions can now be compared to observed transition proportions. If expected proportions are subtracted from observed proportions, then a *difference matrix* is produced. In the difference matrix, positive numbers indicate which transitions occur more often than expected, and negative numbers correspond to transitions that occur less often than expected (Walker, 1984; Harper, 1984). These nonzero differences summarize the extent to which the observed facies sequence has first-order memory: the identity of a given facies influences that of the succeeding facies (de Raaf et al., 1965; Davis, 1973; Walker, 1979, 1984). To a first approximation, this method identifies the most typical cycle(s) observed in the sequence. This is not the same as the *ideal* cycles of many scientists (e.g., Cant and Walker, 1976; Duff et al., 1967, pp. 6–8 and Table 1). Ideal cycles are commonly formulated explicitly to include *all* facies observed within the cyclic sequences, each placed where it is believed to occur most typically. In contrast, what are here referred to as *typical* cycles are those that derive from Markov chain analysis. Generally, these cycles do not include all facies or all transitions observed to occur within the cyclic sequences, but rather only those facies and facies transitions that exhibit memory (as defined above).

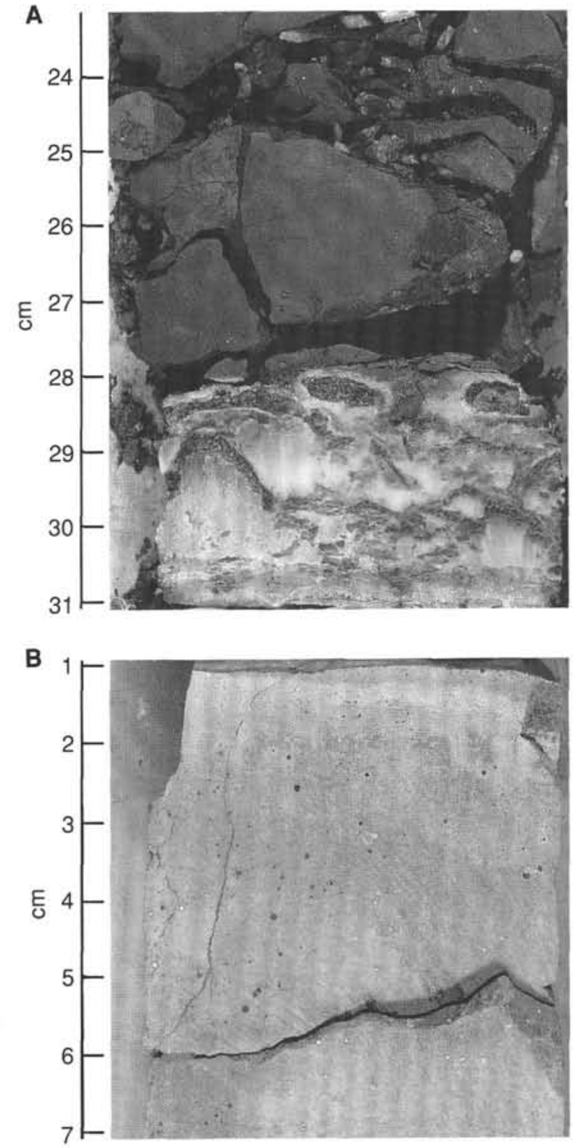

Figure 45. Subunit VIIB, claystone/basalt contact. Basalt hyaloclastite altered to celadonite floats in a matrix of red claystone and white sparry calcite cement, A. Interval 123-765C-62R-4, 24–31 cm. B. Interval 123-765C-62R-4, 1–7 cm.

It is desirable to estimate the probabilities that these differences are statistically significant, and Harper (1984) provided a method for doing this. This method involves calculating probabilities for each nonzero cell in the difference matrix and is facilitated by programs written by Cedric Griffiths (C. Griffiths, pers. comm., 1988). Here, only those transitions significant at the 0.1 level are included in summary diagrams, but complete difference matrices and difference probability matrices are available as a data base from ODP.

Most Markovian analyses of sediments do not recognize multistory lithologies (transitions from a facies to itself, or *autotransitions*). This procedure causes theoretical statistical problems, which were addressed by Carr (1982). However, any attempt to get around this statistical problem by recognizing multistory lithologies causes even graver geological problems. That is, in some facies autotransitions are quite apparent (e.g., nannofossil chalks with bioturbated tops), whereas in others they generally are not observable (clay or massive foraminiferal ooze). Thus, the attempt to count autotransitions would result in a severe bias. Autotransitions were excluded from this analysis.

In cyclic sequences, some transitions occur far less often than expected by chance alone, and others occur far more often. The transitions for which the observed frequency is significantly greater than the expected frequency are those that tend to repeat in the sedimentary cycles. Transitions that occur far less often than expected from random chance are equally informative about the nature of the depositional processes at work in the sedimentary environment. These two classes of transitions are referred to as "what does happen" and "what does not happen," respectively. If no transitions occur significantly more or less often than predicted, then there is no observed cyclicity of sedimentation.

Twelve facies were recognized in cyclic sequences at Site 765 (Fig. 46). These facies either correspond directly to lithologies recognized in ODP terminology or to groups of related lithologies. Several of these are extremely uncommon in the cyclic sequences, and commonly four to seven facies participate in cyclic sedimentation in a given interval. The nine intervals subjected to Markov chain analysis are listed in Table 3. These include three analyses of consecutive intervals in Subunit IIB, which allow for evaluation of the degree of consistency of turbidite character within one of the lithologic units. All Markov chains for the nine units studied appear in Figure 46. Frequency matrices, difference matrices, and probability matrices are available from the ODP data repository.

Seven of the nine analyses were performed on the expanded Miocene to Pleistocene turbidite sequence. The resultant typical cycles are of two types: (1) those consisting of carbonate lithofacies plus clay, and (2) those consisting of both carbonate and siliciclastic lithofacies. This dichotomy in turn reflects changes in the nature of the source sediment (and possibly in the source area) with time. Subunits IA, lower part of IIA, and IIB are characterized by carbonate-dominated cycles. Of these, the Pliocene-Pleistocene cycles are the simplest, consisting of either massive or laminated coarse-grained carbonate (facies A and C), followed by nannofossil ooze (facies D) and capped by clayey siliceous ooze (facies I). The simplicity of these cycles may be in part artificial, because drilling disturbance of very soft, young oozes may obliterate sedimentary structures, which would allow discrimination between facies A, B, C, and L (massive, cross-laminated, laminated, or convolute). The typical cycle includes a closed loop: A-D-I-A. This indicates that massive coarse-grained carbonates almost always form cycle bases and that siliceous oozes nearly always form cycle tops: energy levels of turbidites are consistent and are rarely erosive. Similar cycles in Subunits IIA (lower part) and IIB vary in detail, but document essentially uniform deposition of carbonate turbidites in which the various coarse facies commonly occur singly or in pairs within a single turbidite. The full Bouma sequence is almost never developed. The most significant deviation is the absence of massive coarse-grained carbonate (facies A) from the typical cycle of the bottom part of Subunit IIB. Typical turbidite bases here consist of cross-laminated (facies B) or convolute laminated (facies L) silt- to sand-sized carbonate.

A mixed carbonate-siliciclastic cycle typifies Subunit IC. In this cycle, a thin unit of quartzose sandstone (facies H) or siltstone (facies G) forms the turbidite base. Facies H, where it occurs, is succeeded by the typical carbonate turbidite, but facies G is succeeded only by facies D and E. This difference arises because facies H commonly occurs as a coarse basal portion of facies A in high-energy turbidites, whereas facies G forms the bases of low-energy turbidites in which facies H, A, B, C, and L are missing. A closed cycle consisting of A-C-D-E-A represents intermediate-energy turbidites that lack the sandy base.

The typical cycles of Subunit IIA (upper part) also contain both carbonate and siliciclastic components, but in this interval they form two separate cycles. Typical A-D or C-D carbonate cycles are interbedded with H-G siliciclastic cycles. Both are capped with clay (facies E), and the carbonate cycles predominate. This is why facies E appears only below facies A in the diagram of typical cycles. In all of these Cenozoic sequences, the diagrams of "what does not happen" are dominated by transitions that are forbidden because they derive from energy transitions that scarcely ever occur (e.g., A-E, or D-B). Most of the remaining transitions that tend not to occur relate to the overwhelming dominance of either turbidite tops or bases by certain facies. For example, in Subunit IA, facies I almost never precedes facies D because most of the turbidites in this interval have coarse bases.

Five intervals in the Paleogene and Mesozoic sections at Site 765 are suitable for Markov chain analysis. To date, two of these have been analyzed; the other three will be studied later. One of the two intervals already analyzed is the Aptian Subunit IVD. This is a turbiditic sequence within a larger Lower Cretaceous section dominated by claystones. The typical cycle here resembles that of Subunit IIA (upper): both contain siliciclastic and carbonate cycles. In Subunit IVD, carbonate cycles predominate slightly, whereas in Subunit IIA (upper) they predominate overwhelmingly. Because carbonate and siliciclastic cycles occur in subequal proportions in Subunit IVD, the typical cycle consists of a standard carbonate cycle (A-B-D-E or A-C-D-E) linked to a siliciclastic cycle consisting of H-G-E. The two are linked by facies E (claystone) because facies E is almost invariably preceded by either the complete carbonate cycle or the complete siliciclastic cycle, but rarely by a mixture of the two or by coarse basal units without overlying fine units (facies D or G). Thus, there are apparently two distinct sources for these turbidites: a carbonate source and a siliciclastic source. An additional complication, which is not apparent in the Markov chain analysis, is that the carbonate facies in this subunit are unusually rich in quartz, suggesting that the carbonate and siliciclastic sources fed the same canyon(s), allowing them to mix within some turbidite flows.

The other interval analyzed is Subunit IIIB. These cycles do not look like typical turbidites and were interpreted as possible contourite deposits. Two discrete cycles come from the analysis: a closed cycle of facies B and C (cross-laminated and laminated coarse-grained carbonate) and a fine-grained, closed, mixed siliciclastic and carbonate cycle (G-D-E-G) with an alternative coarser cycle (H-D-E). Facies H, B, and C are rare, and volumetrically, the sequence is dominated by the closed fine-grained cycle G-D-E-G. The siltstones are commonly laminated and thus are equivalent to facies C in terms of flow regime. This cycle is similar to those of Subunits IA and IIA (lower) and resembles

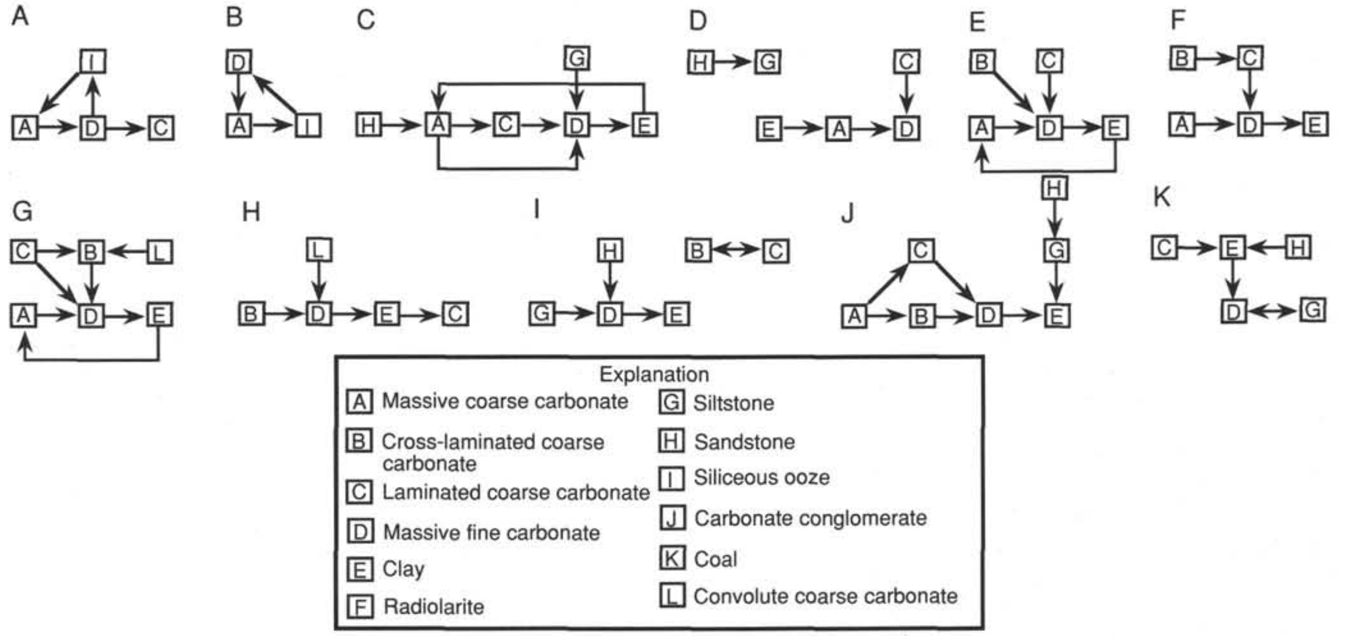

Figure 46. Flow charts illustrating transitions that occur statistically significantly more often ("what happens"), or less often ("what does not happen"), for selected intervals dominated by graded sequences. A. Subunit IA: what happens. This is the simplest cycle. A closed loop consists of massive coarse carbonate (A), to nannofossil ooze (D), to clayey siliceous ooze (I); an alternative sequence base is laminated coarse carbonate (C). Most sequences in this subunit follow one or the other of these two patterns; the loop with facies A is closed because its component facies are much more common than facies C. Clayey siliceous ooze occupies the cycle top, a position filled by clay or claystone (E) in all other units analyzed. The paucity of siliceous fauna and flora in clays below Subunit A may be diagenetic or primary. B. Subunit A: what does not happen. This loop is the exact reverse of the closed loop in Figure 46A, reflecting the fact that these transitions correspond to "forbidden" energy transitions. For example, during deposition of graded sequences, high-energy conditions that would deposit massive sand-sized carbonate ooze cannot be followed by extremely low-energy conditions accompanying siliceous ooze deposition without passing through conditions that would deposit nannofossil ooze. C. Subunit IC: what happens. This cycle is more complex than that of Subunit IA, primarily because carbonate and siliciclastic facies can co-occur. Facies H (sandstone) occurs at the sequence base, where it constitutes a coarse, quartz-rich end-member of facies A (massive coarse carbonate). Likewise, facies G (siltstone) can substitute for facies C (laminated coarse carbonate) below nannofossil ooze. D. Subunit IIA (upper part): what happens. This interval is typified by two alternate cycles; one siliciclastic and one calcareous. The facies involved are those that are common throughout the Cenozoic at this site. The significant point is that cycles tend to be either siliciclastic or calcareous, but not both. This is marked contrast to the typical cycle of Subunit IC. E. Subunit IIA (lower part): what happens. The lower part of Subunit IIA differs markedly from the upper part. In this interval, cycles are calcareous, and facies A most commonly forms cycle bases, although either facies B or C can substitute. The three facies do not tend to occur together within a single cycle. F. Subunit IIB (top third): what happens. This simple cycle resembles that of the lower part of Subunit IIA, but differs in that facies B and C tend to occur together, with B below C, as cycle bases. Facies A also occurs as cycle bases, and is not strongly associated with either of the other two coarse carbonate facies. G. Subunit IIB (middle third): what happens. The flow chart for this interval appears different from that of the overlying top portion of Subunit IIB, but they are in fact very similar. The major differences are the addition of facies L as a possible cycle base, and a more complex set of transition relationships between the four coarse carbonate facies. H. Subunit IIB (bottom third): what happens. In contrast to the similarity between the middle and upper portions of Subunit II, this basal portion presents a different picture. The coarse massive facies A is missing from the cycle, and the remaining three coarse carbonate facies (B, C, and L) substitute as cycle bases. I. Subunit IIIB: what happens. Like the basal portion of Subunit IIB, the typical cycle of Subunit IIIB lacks the massive facies A. However, the reason is different in this case. Here, facies H (quartzose sandstone) occupies the cycle bases (finer-grained cycles have siltstone bases; facies G). A discrete autocycle consisting of facies B and C reflects a tendency in this subunit for these two facies to be interlaminated within thick, carbonate-rich cycles. J. Subunit IVD: what happens. The typical cycle of this subunit resembles closely that of upper Subunit IIA. Both share the characteristic, unusual at this site, of having co-occurring but distinct siliciclastic and calcareous cycles. The carbonate cycles in this subunit are more complex than those of upper Subunit IIA, because in this interval one or the other of the two laminated coarse carbonate facies (B and C) commonly occurs between the basal facies A and overlying facies D. The complex cycles of Subunits IIA (upper) and IVD suggest that multiple sources of turbidites (both siliciclastic and carbonate) existed during deposition of these intervals. In contrast, turbidites found in other intervals could have been derived from a single source area. K. Subunit IVD: what does not happen. Three factors are responsible for the disfavored transitions. The C-E and H-E transitions are uncommon because the energy transitions (very high energy directly to very low energy) are not common in density flows. The E-D transition is uncommon because facies D rarely forms cycle bases (i.e., low-energy events are rare). The D-G and G-D transitions are uncommon because turbidites composed of mixed siliciclastic and carbonate sediments are uncommon in this interval.

Table 3. Sections subjected to Markov chain analysis.

Lithologic unit	Core, section, interval (cm)
Subunit IA	123-765B-1H (top) to 123-765B-5H-2, 87
Subunit IC	123-765B-16H-3, 6 to 123-765B-20X-5 at 105
Subunit IIA (upper)	123-765B-20X-5, 105 to 123-765B-24X-CC, 28 (base)
Subunit IIA (lower)	123-765B-31X-1 (top) to 123-765B-33X-CC, 38 (base)
Subunit IIB (upper)	123-765C-4R-1 (top) to 123-765C-6R-1, 110
Subunit IIB (middle)	123-765C-6R-1, 110 to 123-765C-9R-2, 100
Subunit IIB (lower)	123-765C-9R-2, 100 to 123-765C-12R-4, 118
Subunit IIIB	123-765C-22R-1 (top) to 123-765C-23R-2, 103
Subunit IVD	123-765C-36R-5, 150 to 123-765C-40R-1, 145

that of Subunit IIB to a lesser extent. The basal part of Subunit IIB shares with Subunit IIIB the conspicuous absence of facies A from the typical cycle. Significantly, however, facies A accounts for 6% of the facies occurrences in basal Subunit IIB, whereas it is entirely absent from Subunit IIIB. This difference supports the inference that the graded sequences of Subunit IIIB were not formed by the same depositional process responsible for the majority of the graded sequences at Site 765.

X-Ray Diffraction Studies

XRD analyses were completed on bulk samples and on samples using the fraction finer than 2 μm from Holes 765B and 765C. Samples were dried and weighed. For powder diffraction analyses, samples were ground and then analyzed using the shipboard method (see "Explanatory Notes" chapter, this volume). For clay mineralogy either powder residues or bulk samples were used. The preparation method is similar for both types of samples, except for the sieving step as follows. Samples were treated with distilled water to disaggregate the components and then were separated into the fractions >38 μm, 2 to 38 μm, and <2 μm. This separation was obtained by sieving with a 38-μm mesh sieve, followed by a 3-min centrifuging step. The suspension was decanted and again centrifuged for 15 min. The resulting suspension was assumed to contain the fraction finer than 2 m. This suspension was washed through a 0.6-μm filter. The method led to a good orientation of the clay minerals. A piece of the filter was mounted on an XRD tray using petroleum jelly. Finally, the samples were analyzed on both nonglycolated and glycolated bases.

XRD analyses give only qualitative estimates of mineral composition. Therefore, results were plotted using the relative peak intensity of each mineral as follows: for bulk samples the strongest peak (the dominant mineral) was assigned a value of 40%, followed by up to two major components, each with 20% each; minor components (up to four) were assigned values of 5%; samples containing only one mineral (e.g., washing residues) were plotted as 100% for this mineral.

For the clay minerals, a similar method was used, with the difference that the total composition always equaled 10.

Results of the powder diffraction analysis are plotted in Figure 47; Table 4 lists groups of distinct mineral assemblages obtained in Holes 765B and 765C by the XRD method. Results confirm trends identified from study of smear slides. For comparison, some major components seen in smear slides are displayed in Figure 48. Results of the clay mineral analysis are plotted in Figure 49.

Powder-diffraction analyses were performed (1) to refine the findings of the smear-slide studies with respect to the detrital component, and (2) to determine the mineralogical composition of the various diagenetic minerals, microconcretions, and layers found in Hole 765C.

Clay-mineral analyses were performed (1) to identify long-term trends in mineralogical composition during basin evolution, (2) to identify significant differences in clay-mineral composition of turbidites and background sedimentation, and (3) to describe the mineralogy of suspected volcanic ash-rich layers in the lower part of Hole 765C.

Major Findings

Bulk Samples

Based on XRD results of bulk samples, five groups were defined. Group 1 (Fig. 47A) includes nonexpandable clay and mica. Mica was observed throughout the sequence; it is most abundant in turbidites, but is always present, even if other common detrital components are not. A major trend in this group is the appearance of kaolinite and palygorskite in the upper 500 m of Holes 765B and 765C, whereas expandable clay occurs in considerable amounts only below 500 mbsf. The distribution of kaolinite, which is a good indicator for continental sediment supply and is formed by weathering of "granitic" rocks under tropical conditions (the Australian Shield being the primary inferred source), occurs primarily in the Tertiary graded sequences. However, the paleolatitude reconstructions of the area through the Tertiary and Upper Cretaceous are not tropical. The inferred Upper Cretaceous paleolatitude of the area is about 35°S (see "Paleomagnetics" section, this chapter), which suggests that the primary source of the kaolinite may have been an unknown landmass to the north.

The distribution of palygorskite (an authigenic Mg-rich clay mineral) coincides approximately with the rapidly deposited Miocene interval in which Mg is enriched (see "Sediment Inorganic Geochemistry" section, this chapter), as does the distribution of authigenic dolomite. The oldest occurrence of significant amounts of palygorskite is found in Core 123-765C-15R, which coincides with the major change in sediment accumulation rate from low to high over the interval from Oligocene into Miocene.

Group 2 (Fig. 47A) includes detrital carbonates. Calcite is a major component in the upper 500 m of the sequence; aragonite occurs in only two samples (Cores 123-765C-5R and -13R; "Sediment Inorganic Geochemistry" section, this chapter). Calcite occurs predominantly in turbidites, and smear-slide data (Fig. 47B) indicate that almost all calcite is of biogenic origin (primarily nannofossils). The calcite content decreases downhole with the decrease in turbidites. Furthermore, as seen in smear slides, much of the calcite in the lower part of the succession consists of micrite.

Group 3 (Fig. 47C) includes a variety of diagenetic minerals. The occurrence of clinoptilolite (zeolite in the smear-slide plot, Fig. 48C) is preferentially linked to the occurrence/diagenetic alteration of radiolarians (see "Biostratigraphy" section, this chapter), but the distribution of dolomite, rhodochrosite, and other carbonates is not yet completely understood. Note that clinoptilolite occurs as high as Core 123-765C-19R (Eocene), whereas phillipsite, the common zeolite in Tertiary deep-marine sediments, was not detected. Diagenetic replacement of radiolarian skeletons by zeolite is generally an expression of undersaturation of sediment pore waters with respect to silica; the absence of clinoptilolite (and other zeolites) in the deeper part of the sequence reflects the high radiolarian and silica contents of the sediment (see "Sediment Inorganic Geochemistry" section, this chapter).

In the upper part of the sequence, dolomite occurs as scattered small idiomorphic rhombs, (smear-slide observation, see Fig. 48C), whereas in the lower part of Hole 765C (Cores 123-765C-40R to -58R) dolomite(?) occurs as comparatively large spherulitic crystalline masses that form concretions or layers. Many concretions may consist of mixtures of dolomite and rhodochrosite, a common sediment constituent over the same interval (Pl. 1, Figs. 1 and 4). The XRD patterns for these two min-

Table 4. Groups of distinct mineral assemblages obtained in Holes 765B and 765C using XRD.

Characteristic mineral content of Groups 1 through 5, distinguished in the XRD study of samples of Cores 123-765B-10H to 123-765C-62R

Group 1 Nonexpandable clays		Occurrence	Occurrence smear slides	
	Palygorskite	(see Fig. 47A)	Clay	(see Fig. 48D)
	Kaolinite		Mica	

(for comparison expandable clay and mica also are plotted in Fig. 47A). XRD analysis of the sediment-fraction <2 μm (clay minerals) on both nonglycolated and glycolated bases.

Group 2 Carbonates		Occurrence	Occurrence smear slides	
	Calcite	(see Fig. 47B)	Nannofossils	(see Fig. 48A)
	Aragonite		Micrite	
Group 3 Diagenetic minerals		Occurrence	Occurrence smear slides	
	Rhodochrosite	(see Fig. 47C)	(Rhodochrosite see Fig. 48C)	
	Dolomite		Dolomite	
	Clinoptilolite		Zeolite	
Group 4 Silica		Occurrence	Occurrence smear slides	
	Radiolarians*	(see Fig. 47D)	Radiolarians	(see Fig. 48B)
	Quartz		Quartz	

*Distinction between terrigenous quartz (QUARTZ) and replacement quartz/chert (RADIOLARIANS) is based on thin-section and smear-slide data.

Group 5 Minor minerals		Occurrence
	Goethite	(see Fig. 47E)
	Manganite	
	Fluorapatite	
	Barite	
	Unknown	

erals do not always match the expected patterns, suggesting that some concretions may consist of mixed Mg- and Mn-carbonates. Thin-section studies reveal rhodochrosite-replaced skeletons of radiolarians and diatoms in these dolomite/rhodochrosite crystals/microconcretions (Pl. 1, Figs. 2 and 3). This suggests that the carbonates are probably a late diagenetic replacement product of early diagenetic chert.

Group 4 (Fig. 47D) consists of silica. Quartz is common throughout the sequence (see also smear-slide data in Fig. 48B); however, above Core 123-765C-40R, quartz is mainly confined to turbiditic intervals, whereas downhole most of the quartz is authigenic (diagenetic replacement of radiolarian skeletons; Fig. 48B). The strong quartz pattern in Figure 47D is misleading (as is the mica pattern) because it reflects more the absence of calcite (the overwhelming presence of the latter in most samples overprints all other minerals) than an increase in the quartz content.

Group 5 (Fig. 47E) includes minor minerals found locally. These are manganite (as small manganese nodules observed in Cores 123-765C-61R and -62R); barite, as crystals up to 2 mm long (Pl. 1, Fig. 5) that occur in association with diagenetic dolomite/rhodochrosite; graphite(?), clearly indicated in several samples by the powder search program used on board ship (however, it is unlikely that significant amounts of graphite are present); and goethite, found in strongly weathered nodules that originally may have been basalt pebbles.

Clay Minerals

Various clay minerals are abundant constituents in all samples (Fig. 48D), and their distribution pattern is uniform (Fig. 49).

There are five distinct clay mineral assemblages at Site 765 (Fig. 50). The lowermost assemblage (E), from 912 to 610 mbsf, is predominantly smectite, with illite constituting from 0% to 50% of the sample. Smectite dominates the clay-mineral pattern in all Lower Cretaceous samples, and its occurrence is independent of sediment color or type. The overlying assemblage (D), which ranges from 610 to 484.9 mbsf, can be divided into two subunits: the lower one consists of smectite, which is dominant over kaolinite, and illite; the upper one consists of kaolinite, which dominates over smectite, and illite. The clay mineralogy changes dramatically at 484.9 mbsf (the base of assemblage C). Assemblage C consists of palygorskite and chlorite, with possible illite and kaolinite. The presence of illite and kaolinite cannot be confirmed until the samples are heated to 550°C. Above 367.6 mbsf (base of assemblage B), there is a complex clay assemblage dominated by palygorskite and containing significant amounts of kaolinite, smectite, and sepiolite. Chlorite is absent above 367.6 mbsf. The increase in sepiolite above 367.6 mbsf may be gradational. Assemblage B is Late Cretaceous/early Tertiary in age and is confined to an interval of increased turbidite sedimentation characterized by a substantial amount of redeposited rounded quartz of inferred continental origin. The abundance of kaolinite, a product of continental weathering, supports this interpretation. The deepest occurrence of kaolinite is as a constituent of turbidites near the Lower/Upper Cretaceous boundary. From 195.7 mbsf (base of assemblage A) to the top of the section, the clay-mineral assemblage is dominated by kaolinite, with equal to lesser amounts of smectite and illite.

Based on the glycolated patterns, most of the smectite is estimated to contain <5% to 20% illite layers. The smectite is either terrigenous or an alteration product of volcanic and terrigenous material. Sediment layers composed of nearly 100% smectite were interpreted as altered volcanic ash deposits. The abundance of smectite in the lowermost clay assemblage and its high Fe and Mg content suggest that a significant amount was derived from the alteration of mafic igneous material (see "Sed-

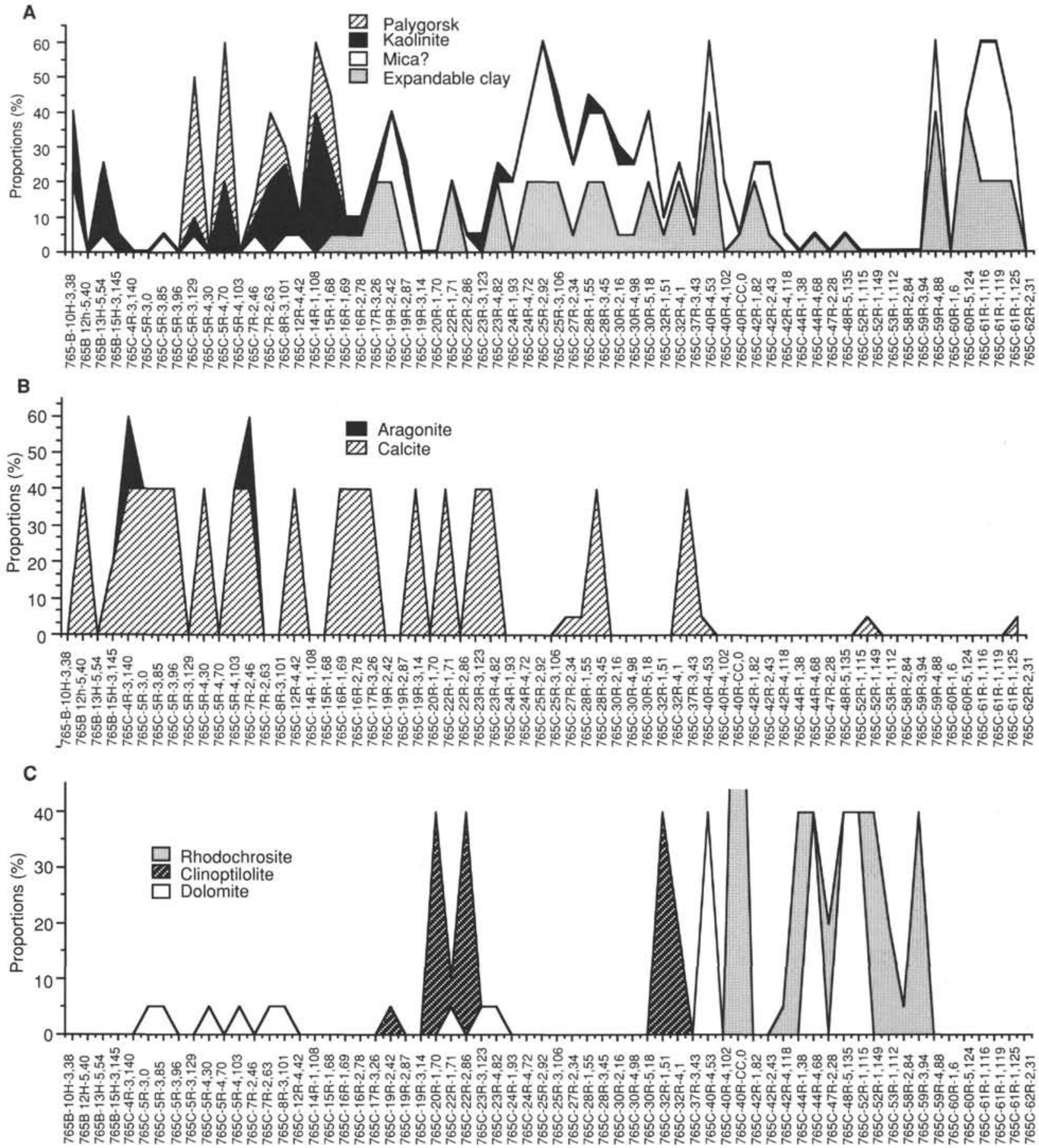

Figure 47. Distribution patterns of minerals in XRD analyses of bulk samples from Holes 765B and 765C. A. Clay minerals. B. Calcite and aragonite. C. Diagenetically formed minerals. D. Quartz and quartz-replaced radiolarians (according to thin sections). E. Minor minerals.

iment Inorganic Geochemistry" section, this chapter). The source of the smectite may be volcanic rocks of basement highs outcropping in the vicinity of Site 765; this inference is supported by the clay-mineral chemistry. However, the large volume of smectite required to form the Lower Cretaceous sedimentary cover of the Argo Abyssal Plain may exceed that available from this source. An alternative explanation is the possible formation of smectite by alteration of detrital illite (providing the necessary aluminum) and dissolution of radiolarian tests.

Altered ash layers in Cores 123-765C-57R to -60R show a clay-mineral composition similar to the dark reddish or brownish claystone surrounding them, but they contain predominantly, or are entirely composed of, smectite (Pl. 1, Fig. 6) that is low in Al and high in Fe and Mg. Such a composition, together with

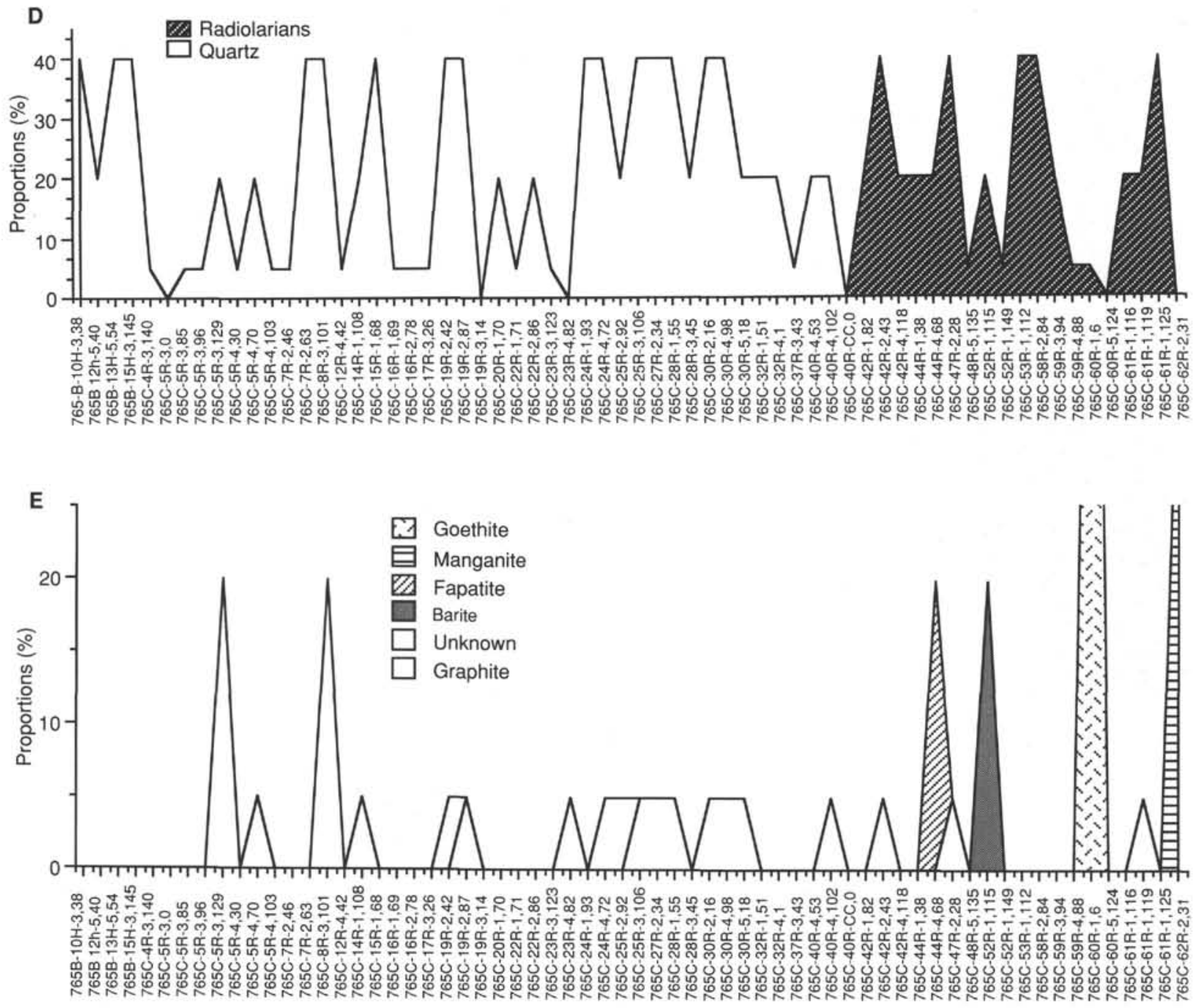

Figure 47 (continued).

abundant smectite pseudomorphs of rectangular minerals, suggests a volcanic origin for these layers.

Multivariate Analyses of Smear-Slide Data

About 500 smear slides were prepared during the lithologic description of the cores. There are about 150 samples for Hole 765B and about 350 samples for Hole 765C. For the multivariate analyses of smear-slide data, correlation and cluster analysis methods were used (calculation of Q-mode product moment correlation coefficient matrices, followed by a "weighted pair group" [average linkage] cluster analysis; Davis, 1973; Steinhausen and Langer, 1977; Schott, 1984; see smear-slide data).

To keep the large data tables clearly arranged and to avoid too high weightings during cluster analysis, the original data matrices were subdivided stratigraphically into two parts for Hole 765B and into six parts for Hole 765C. These parts were clustered and rearranged into new matrices, which contain the most representative samples of the groups defined by the preceding cluster analyses. Elements of the groups of the final cluster analyses (dendrogram for Hole 765C, see Fig. 51) and the corresponding elements of the previous clusters were related to their sample numbers to show the distribution of the groups within Holes 765B and 765C (see Figs. 52 and 53).

All smear-slide data for each hole used in these analyses are organized in a data-bank file, together with additional information about sample number, nomenclature, grain size, and cluster-group numbers for each sample. The calculated clusters can be sorted and related to their grain size and nomenclature. The cluster-to-grain size relationship generally shows good correlations; i.e., the groups can be sorted by grain size. The cluster-to-nomenclature relationship mostly shows correlations good enough to relate the cluster groups to their main lithologies. Causes of deviation for both relationships may be found by further, more detailed investigations.

To get a clear graphic picture of the distribution of the groups within the whole sedimentary column cored in Site 765, a new method was developed and used for graphic representation of the cluster-analysis results. This method is based on the relative frequency of the calculated reaction groups. Although the number of different groups within a single section may depend on sampling, the average distribution of the groups over two or three cores reflects well the relative frequency of the main lithologies within a given range. The average percentages of the main groups appearing in one to two cores were plotted vs. depth (see Fig. 54). This graphic representation shows the general lithologic features of the entire hole. Frequency and/or group changes cor-

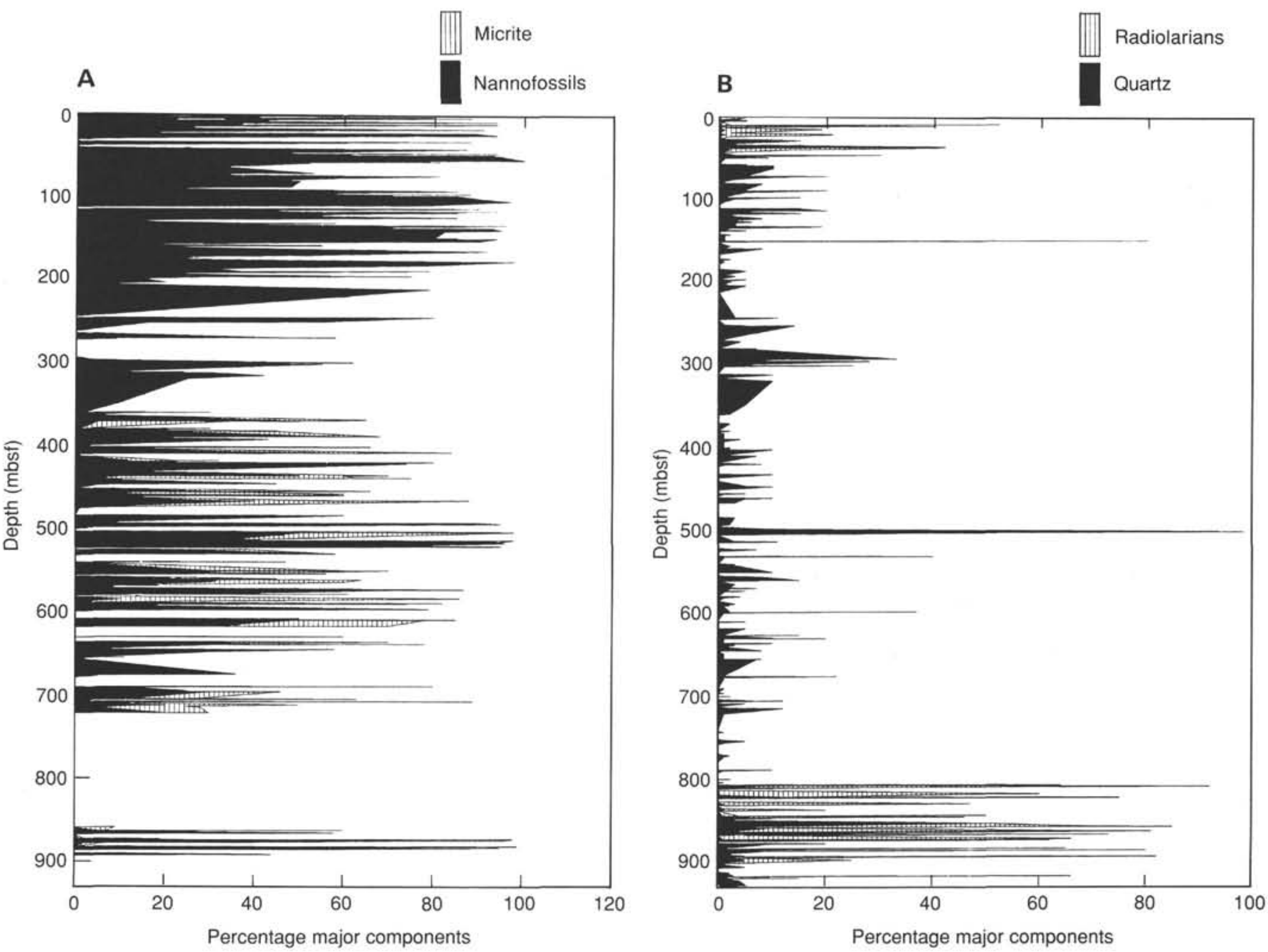

Figure 48. Distribution patterns of minerals in samples from Holes 765B and 765C. A. Biogenic and diagenetic $CaCO_3$ (smear-slide data). B. Quartz (mainly in turbidites) and radiolarians. C. Diagenetic minerals. D. Mica and relative amounts of clay.

respond well to the described lithologic unit and subunit boundaries (see Fig. 10, "Sediment Lithostratigraphy" section, this chapter). Most of these boundaries and the main lithologies are well displayed in the diagram.

Sedimentation History

As outlined in the "Introduction" chapter (this volume), Jurassic break-up along the northeastern rim of Gondwana quickly led to formation of an abyssal oceanic graben north of the Exmouth and Wombat plateaus in the present Argo Abyssal Plain. From Earliest Cretaceous time onward, less than 1000 m of clayey sediments accumulated in this abyssal environment. Using the Berriasian age (142 Ma) for basement and the present water depth of 5728 m at Site 765, a backtrack curve can be calculated (see "Trends in Sedimentation" section, this chapter). This curve, which is well established empirically and theoretically, shows the subsidence track, corrected for sediment loading and compaction, of ridge-crest sediment through time as it moves away from the spreading-ridge axis. Site 765, apparently starting near 2800 m in Berriasian time, subsided rapidly to more than 5 km by middle Cretaceous time. The area has subsided more slowly since the middle Cretaceous, with post-middle Cretaceous subsidence totaling about another 700 m.

At Site 765, on the Argo Abyssal Plain, Lower Cretaceous claystones rest directly on basalt, presumably of about the same age. Claystone is the dominant lithology in the Lower Cretaceous, although lesser calcareous and mixed-sediment turbidites dominate some intervals. Minor lithologies include rhodochrosite-rich sediments, radiolarites, and bentonites(?). The relative importance of calcareous sediments, mostly turbidites, increases upward in the middle to upper Aptian. A pronounced upward increase in calcareous turbidite deposition occurs at about the Paleogene to Neogene boundary; turbidites remain dominant to the present.

Lower Cretaceous

Neocomian

The original sediment/basement contact appears to be preserved intact; red clays at the base of Subunit VIIB commingle with fragile hyaloclastic basalt breccia formed above the uppermost basalt flow.

The dominant lithology in Subunit VIIB (Berriasian) is a silty claystone with abundant calcareous shell fragments. These shell fragments are largely inoceramid mollusk prisms that are typically pitted (etched and/or bored), aligned parallel to bed-

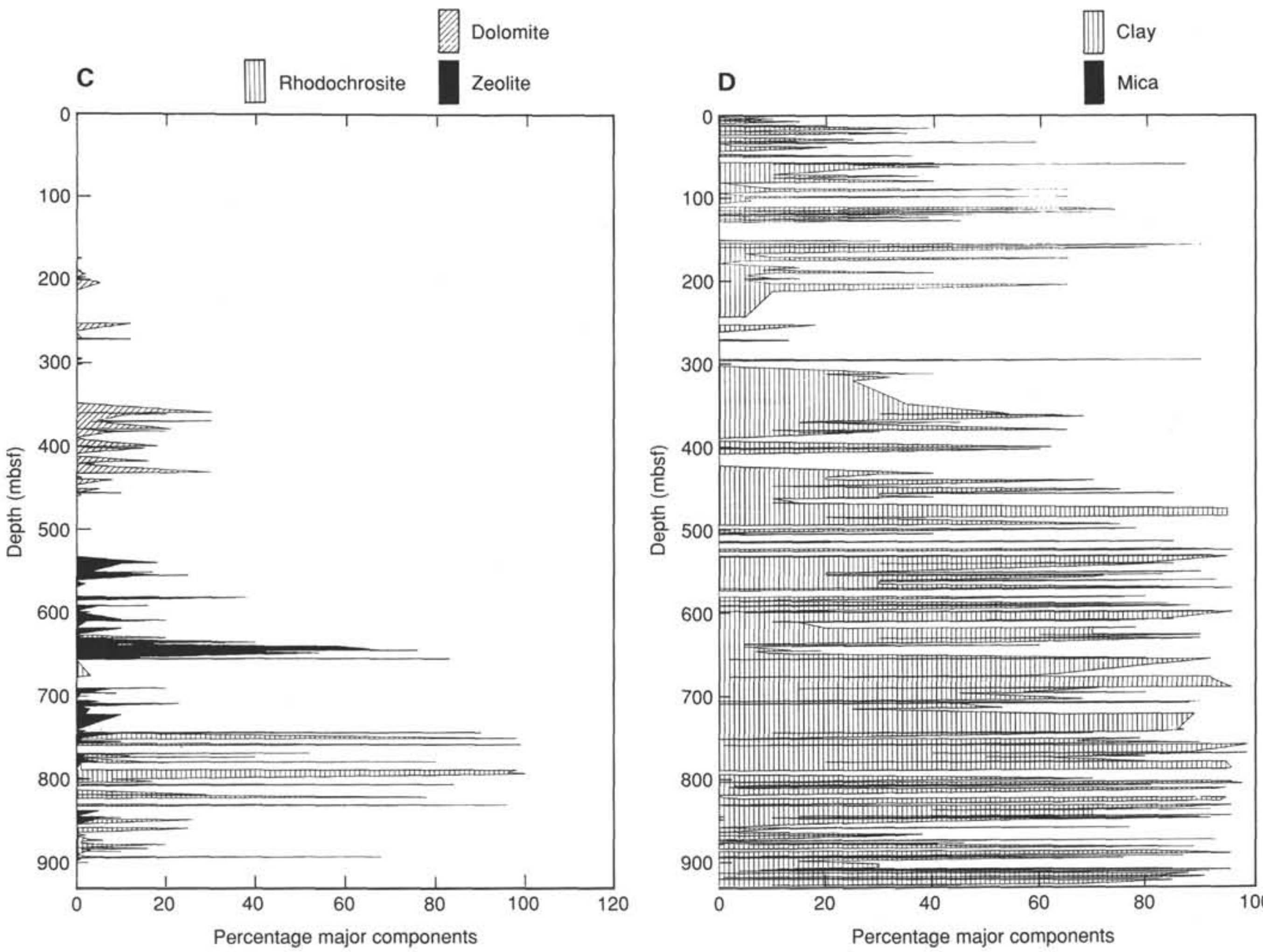

Figure 48 (continued).

ding, and locally concentrated into white wispy layers and lenses a few millimeters thick. Silt- to sand-sized shell material generally makes up 20% to 50% of this lithology and may constitute as much as 90% of the white wispy layers and lenses. The reddish-brown of the clay matrix indicates deposition in an oxidizing environment, and the alignment of the shell fragments suggests the influence of currents during deposition; the discontinuity of the shelly layers may reflect local disruption by bioturbation.

Manganite (recognized by shipboard XRD analysis) occurs as widely disseminated millimeter- to centimeter-sized nodules elongated parallel to bedding. Textural evidence suggests that these nodules grew *in-situ*, because they can be seen in thin section to incorporate calcareous shell fragments similar in size and shape to those in the surrounding sediment. These fragments are concentrated in the outer rims of the nodules. In addition, some nodules are surrounded by halos of fine-grained, disseminated manganite. Minor lithologies in Subunit VIIB include thin intervals of nannofossil-bearing claystone, laminae and lenses of fine-grained limestone, and a 1.5-m-thick interval of noncalcareous brown claystone that directly overlies volcanic basement. The nannofossil-bearing claystone contains as much as 20% carbonate, mostly badly etched specimens of the large nannofossil *Watznaueria manivitae* and calcareous fragments. In contrast to the reddish-brown of the surrounding sediments, some intervals of this claystone have a greenish-gray or bluish-gray color, suggesting deposition and/or diagenesis under reducing conditions.

Fine-grained limestones consist almost exclusively of calcispheres and 1- × 10-μm needles (probably fragments of calcispheres) concentrated into millimeter-sized clasts and nodular laminae separated by clayey partings.

Etching of nannofossils and mollusk debris suggests that Berriasian sediments at Site 765 were deposited below the lysocline. Nannofossils and radiolarians may have lived within the depositional basin, or may have been carried in from elsewhere. The abundance of inoceramid fragments suggests that these epiplanktonic or epifaunal forms lived within the basin.

The calcareous silty claystones may represent distal fan or delta deposits in a rift basin partially isolated from Tethys. The nannofossil-bearing claystones could be background hemipelagic deposits, as could the noncalcareous basal claystone. Alternatively, the basal claystone could have formed as distal fan or delta deposits, originally containing carbonate material like the overlying brown silty claystone, which has been leached after deposition.

Noncalcareous claystones, silty claystones, and clayey siltstones become abundant in Subunit VIIA (lower Valanginian to upper Berriasian), less common in Unit VI (lowermost Hauterivian to upper Valanginian), and predominant in Unit V (upper to middle early Aptian to Barremian). These lithologies may be "background" hemipelagic deposits that accumulated beneath

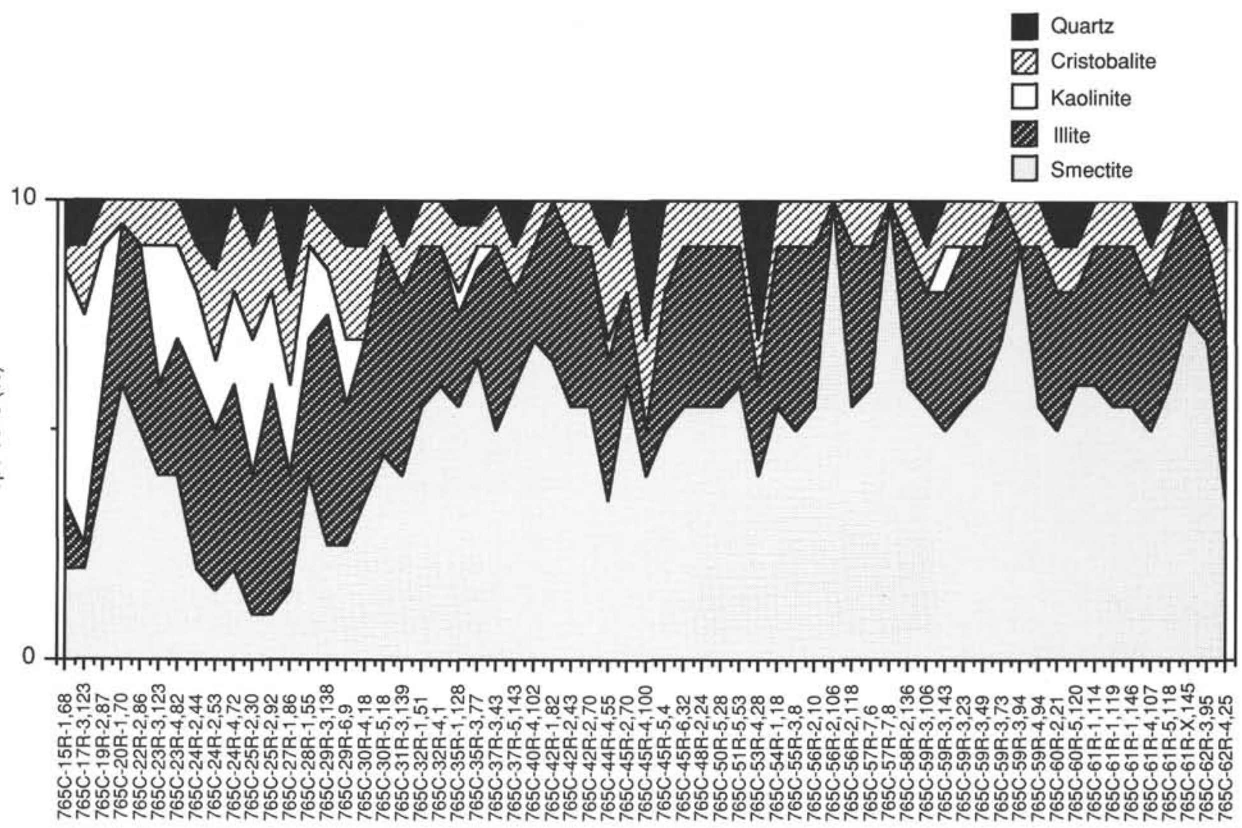

Figure 49. Distribution pattern of clay minerals (<2 μm) in samples from Hole 765C.

the CCD. However, the isolated occurrences of parallel and possible convolute laminae in these lithologies suggests that they may represent, at least in part, siliciclastic mass-flow deposits; for example, fine-grained distal turbidites.

Greenish-gray to gray claystones, provisionally interpreted as bentonites, occur in Units VI and VII. They appear waxy and have a soapy texture. The recognition of degraded glass shards and feldspar crystals (in smear slides and thin sections) and of montmorillonitic (smectitic) clays (in XRD analyses) supports their interpretation as altered volcanic ashes. Similar bentonites in claystones of Neocomian age at Site 761 were interpreted as ash layers and may be correlated with those of Site 765. Layers at both sites may have been derived from the Roo Rise volcanic epilith (west of the Wombat Plateau) and/or the large volcanic structure of the Wallaby Plateau (south of the Exmouth Plateau; Leg 122 Shipboard Scientific Party, unpubl. data); both of these features were active in the Early Cretaceous. Site 761 ash layers contain smectite (determined by shipboard XRD analysis) but they are white, pale brown or pink, not greenish-gray, and contain sepiolite, biotite, and Mn micronodules not found in Site 765 altered ash layers.

Agglutinated foraminifers are locally abundant in the altered ash layers and claystones of Units VI and VII; these foraminifers are bathyal to abyssal forms and may be an autochthonous fauna. Their occurrence supports the interpretation of a deep-water depositional environment at Site 765 during the Early Cretaceous.

Unit VI consists largely of calcareous claystone and mixed sediment, with lesser noncalcareous claystone, radiolarite, rhodochrosite sediment, and altered ash layers. The calcareous sediments may be allochthonous and may have been deposited by mass-flow processes, predominantly turbidity currents. Thick calcareous intervals with coarse bases exhibit a succession of sedimentary structures approximating a classical turbidite sequence: sand-sized calcareous sediment, massive, graded, and with a scoured basal contact, grades upward into parallel- and cross-laminated sand- to silt-sized calcareous claystone and then into silt- to clay-sized, parallel-laminated and bioturbated nannofossil claystone (e.g., calcareous sequence in Section 123-765C-57R-3 at 0 to 26 cm).

Finer-grained calcareous intervals commonly do not exhibit such a complete succession of sedimentary structures, and, particularly in Cores 123-765C-55R and -56R, they may be massive and featureless with no obvious evidence of grading or current-working. These intervals are similar in color and composition to the upper parts of the coarse-grained graded sequences described above and are thought to be distal turbidites. Their prominence in the upper half of Unit VI suggests that the source of allochthonous calcareous sediments deposited at Site 765 became increasingly distant and/or fine-grained throughout the time of deposition of Unit VI (Hauterivian-Valanginian).

Unit VI calcareous claystones and mixed sediments contain abundant nannofossils, with lesser inoceramid fragments, calcispheres, benthic foraminifers, micrite, and calcareous fragments. The nannofossil assemblages of Unit VI display little or no evidence of reworking, and thus contrast with the younger assemblages of the Neogene; the latter show a significant degree of mixing and probably were derived from a variety of sources. Unit VI nannofossils were likely redeposited soon after their initial accumulation.

Unit VI turbidites may have been derived from the south. A possible source for the calcareous sediments in Unit VI is the Wombat Plateau. Site 761 on the central Wombat Plateau contains 20 m of Neocomian chalk. This chalk contains a calcisphere and nannofossil assemblage very similar to that found in Unit VI and is thought to have been deposited at upper bathyal

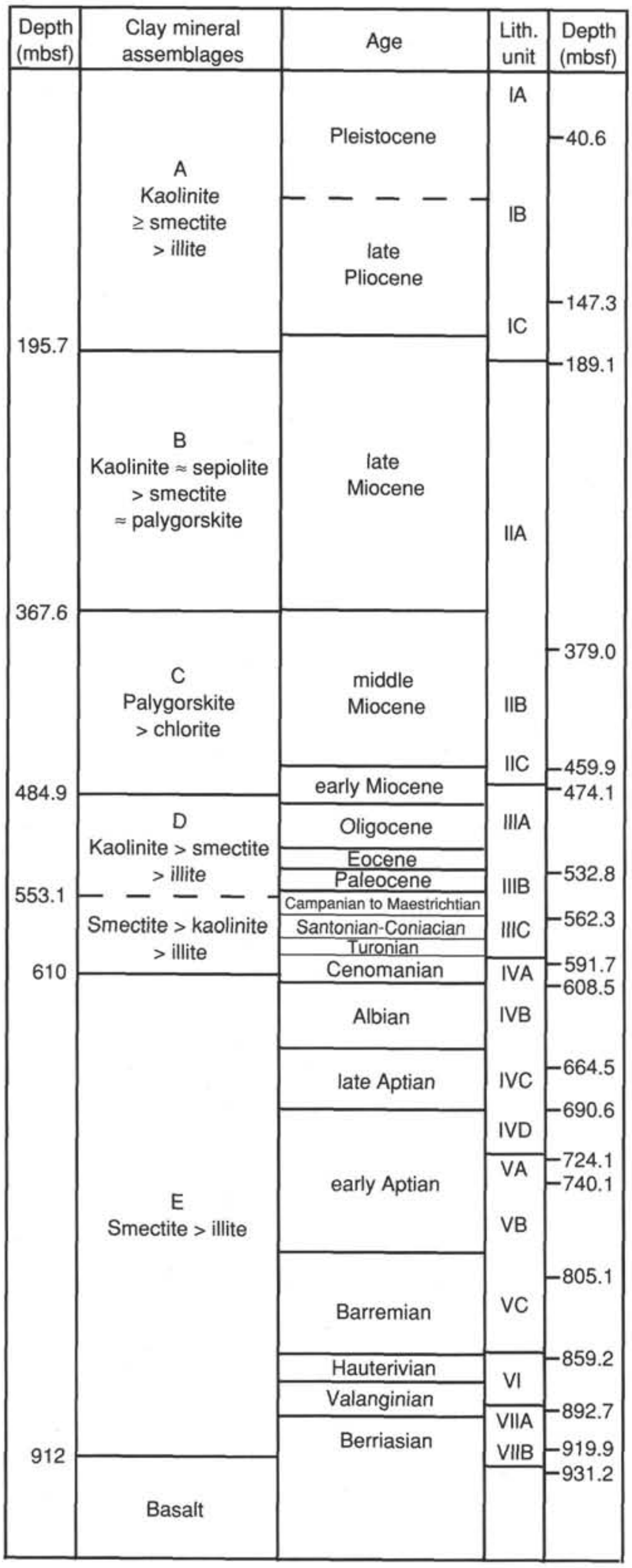

Figure 50. Clay mineral assemblages of Site 765.

depths (Leg 122 Shipboard Scientific Party, unpubl. data). The coarser parts of the calcareous turbidites in Unit VI contain as much as 20% quartz, indicating some influx from siliciclastic sources. Siliciclastic deposits predominated over most of the Exmouth Plateau during the Early Cretaceous (for example, Berriasian to Valanginian sediments at Sites 762 and 763 are silty claystones and clayey siltstones) and could have been a source for the siliciclastic sediment at Site 765.

Two unusual sediments occur in the Lower Cretaceous section, particularly in Units V and VI and, to a lesser extent, in VIIA. These are radiolarite and rhodochrosite sediment and/or concretions.

Rhodochrosite is an authigenic carbonate that occurs within claystone from Cores 123-765C-59R to -42R (Fig. 55). Two major kinds occur as follows:

1. Manganese micronodules disseminated and floating in a claystone matrix; this type of occurrence (see "Sediment Lithostratigraphy" section, this chapter, Fig. 33) is scarce to common in Cores 123-765C-59R to -42R and is interpreted to indicate *in-situ* authigenic formation. This interpretation is corroborated by the observation that, in places, micronodules decrease in size and abundance upward so that rhodochrosite sediment passes into a rhodochrosite micronodule claystone.
2. Concentrated and accumulated in graded (see "Sediment Lithostratigraphy" section, this chapter, Fig. 33; locally complex/reversed) layers and/or macronodules (concretions). In this case, the sedimentary features—parallel laminae, microrippleforms, low-angle cross-laminae, and microerosion surfaces—indicate reworking and winnowing by bottom currents. Halos of claystone with rhodochrosite micronodules commonly surround rhodochrosite sediment that is interpreted to be authigenic and *in situ* but were not observed around graded intervals with laminae and microerosion surfaces. The occurrence of rhodochrosite (associated with pyrite) in a similar context has been previously described in DSDP Leg 43, at Site 386 (Tucholke, Vogt, et al., 1979); this indicates a reducing environment.

Distinct radiolarite intervals occur between Cores 123-765C-51R and -59R. Sand- to silt-sized radiolarians form thin distinct radiolarite intervals exhibiting sedimentary features, such as parallel and/or wavy laminae (see "Sediment Lithostratigraphy" section, this chapter, Fig. 34), and grading normal and (locally) reversed. Boundaries are commonly sharp, but locally diffuse to gradational at the top (see "Sediment Lithostratigraphy" section, this chapter, Fig. 39). These characteristics clearly indicate redeposition and concentration of radiolarians by hydrodynamic processes; e.g., winnowing bottom currents or, less probably, low-density turbidity currents. Similar radiolarite sands were described from the western Atlantic, near the Bermuda Rise (DSDP Leg 43, Site 386, Tucholke, Vogt, et al., 1979). McCave (1979) suggested that deposition of the radiolarian sand beds occurred during "long blooms" and subsequent bottom current winnowing. Sequences similar to those of Site 765 can be observed in deep-water sections (of Upper Jurassic age) deposited on oceanic crust (e.g., Ligurian Alps, Italy; Barrett, 1982). This contrasts dramatically with the classic Tethyan Mesozoic ribbon radiolarites, with thicknesses of tens to hundreds of meters that have been deposited on thinned continental crust (e.g., Greece and Oman): in Hole 765C, for 80 m of section between Cores 123-765C-58R and -51R, we found a maximum of 3.5 m of radiolarite, with silica contents as high as 85% to 100%. As emphasized by many authors (e.g., Jenkyns and Winterer, 1982; Hein and Karl, 1983; Baumgartner, 1987), nothing resembling Tethyan ribbon radiolarites has ever been cored from present-day ocean basins.

Upper Lower Cretaceous

Subunit IVD (lower to upper Aptian) is dominated by graded carbonate sequences having a minor siliciclastic admixture and associated with less common graded siliciclastic sequences. Mar-

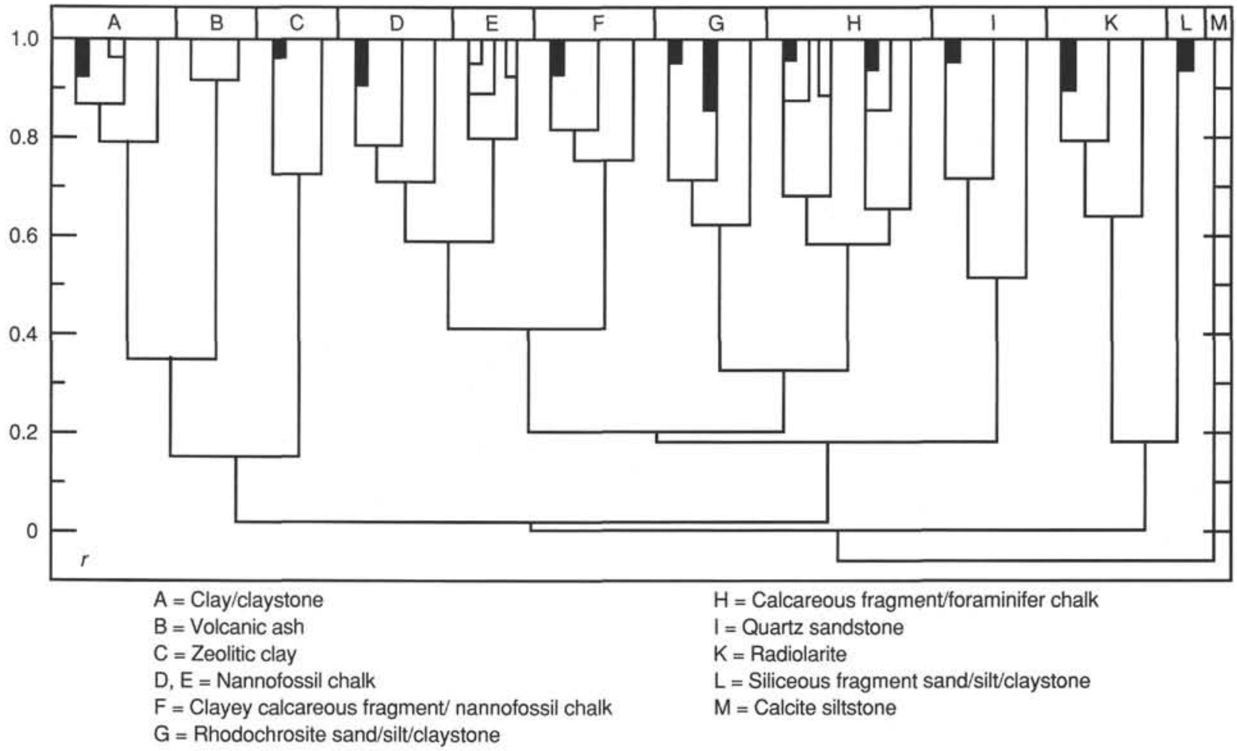

Figure 51. Dendrogram of correlation matrix, clustered by average linkage method for Hole 765C. r = correlation coefficient; A,B,... = group numbers.

kov chain analysis of the graded sequences constituting most of Subunit IVD (Section 123-765C-40R-1 at 145 cm to -36R-6, top) yields a dominant cycle whose base consists of silty to sandy quartzose foraminiferal and calcareous fragment chalk. This chalk is massive below and cross-laminated and/or laminated above and is overlain by massive clayey nannofossil chalk, which in turn is overlain by claystone. A less common siliciclastic cycle consists of sandstone (commonly laminated or cross-laminated and uncommonly with convolute laminations), overlain by siltstone (laminated to massive) and capped by claystone. These graded sequences are interpreted as turbidity current deposits, although other grain-flow mechanisms are also possible. These turbidity currents probably flowed out of one or more of the submarine canyons that incise the northern margin of the Northwest Australian shelf, which faces the Argo Abyssal Plain on the southwest, south, and southeast (see "Geologic Setting" section, this chapter).

Both detrital silica and carbonate bioclasts are abundant, demonstrating the existence of multiple sediment sources (Fig. 56). The common mixing of the two sediment types within single turbidites in Subunit IVD indicates that both sediment sources fed the same canyon(s). However, the predominance of either carbonate or siliciclastic sediment within single turbidites suggests that carbonate and siliceous sediments were not intimately commingled, but that sediments from separate sources combined during entrainment and transport. The silica consists primarily of silt- to fine-sand-sized, subangular to subrounded, detrital quartz grains. The carbonate material is dominated by nannofossils, micrite (fragmentary nannofossils?), foraminifers, and calcareous fragments, probably largely derived from foraminifers.

Paleoenvironmental evidence from foraminifers indicates that most turbidites at Site 765 had a source at bathyal depths (probably deeper than 2000 m). This suggests a slope or drowned platform environment for the turbidite source area(s).

The Exmouth Plateau, the inferred primary source area because of its proximity to Site 765, may have already been submerged to a depth of about 2000 m by the time Unit IV was deposited in the Aptian to Cenomanian (based on backtracking of burial history). The Wombat Plateau, a high, partially isolated block on the northeastern Exmouth Plateau, subsided to bathyal depths during the Aptian-Albian (Leg 122 Shipboard Scientific Party, unpubl. data). Furthermore, dredging in Swan Canyon, which lies south of Site 765 on the Northwest Australian shelf margin (von Stackelberg et al., 1980), yielded Lower Cretaceous pelagic sediments, including silty quartzose claystone similar to that found in turbidites at Site 765. Thus, the presumed source areas may have been bathyal during Unit IV deposition.

Subunit IVD overlies 16 m of dark gray claystone, with minor laminated and graded silty layers that may be distal turbidites. Thus, Subunit IVD is interpreted to record either the initiation of fan construction in this area of the Argo Abyssal Plain, or lateral migration of an existing fan, perhaps by fan-lobe switching, to initiate turbidite sedimentation in the vicinity of Site 765.

Subunits IVC to IVA closely resemble each other and consist of claystones with minor clayey nannofossil chalks and silty to sandy foraminiferal calcareous fragment chalks. Claystones in Subunit IVA and the upper part of Subunit IVB are predominantly red and brown, whereas those in the lower part of Subunit IVB and in Subunit IVC are predominantly green and gray. This color difference clearly represents a change from reduced to oxidized sediment, but the cause of this change is unknown. However, black to dark gray claystones occur in the upper Aptian Subunit IVC, and these may have formed in a similar environment to that of Atlantic black shales of similar age. Carbonates in Subunits IVA to IVC are graded. Basal portions are commonly calcareous fragments and foraminifer chalks. These have massive bases that are overlain by laminated, cross-laminated, or convolute laminated intervals and are capped by massive nan-

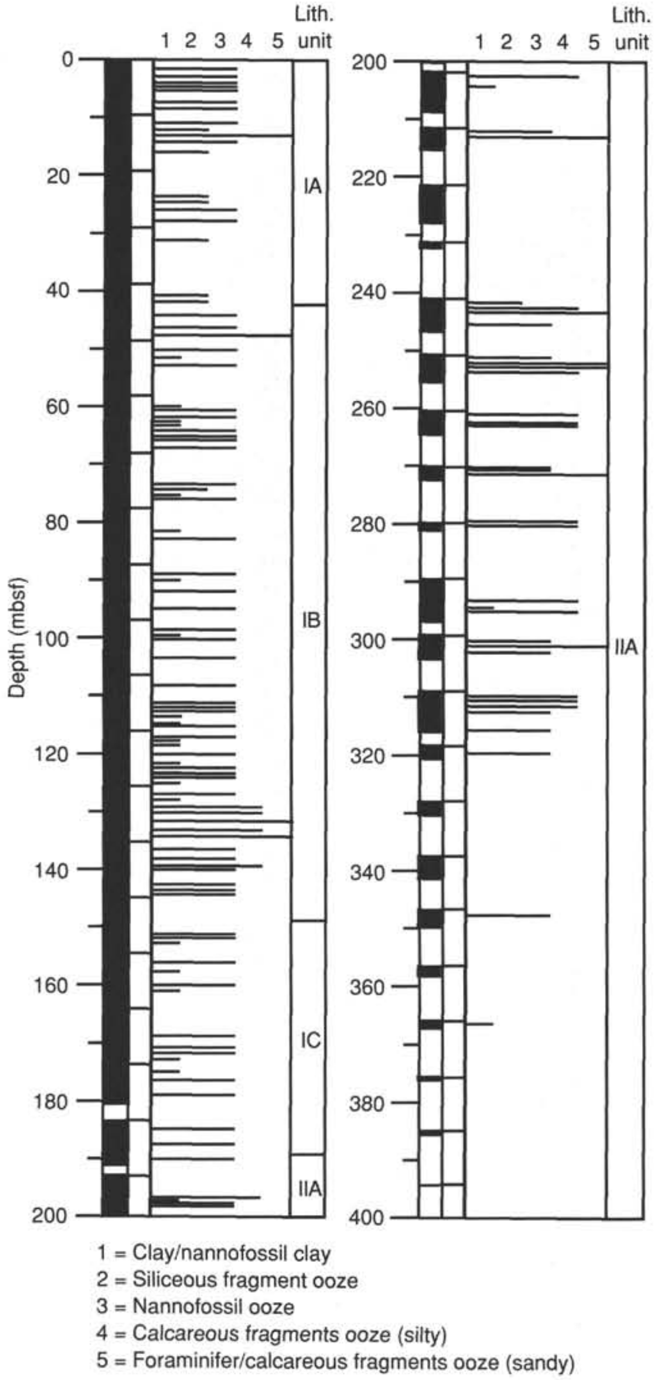

Figure 52. Distribution of cluster elements for Hole 765B. Group number is shown for each sample. Numbers are related to main lithologies.

nofossil and clayey nannofossil chalks. These sequences closely resemble inferred turbidites of Subunit IVD and are also interpreted as turbidites. The turbidites are coarsest and exhibit the greatest variety of sedimentary structures in Subunit IVD. Those in the lower part of Subunit IVC are less prominent; overlying ones are rare, thin, and fine-grained. This indicates a gradual reduction in the intensity of turbidite deposition with time and may represent either fan-lobe switching or fan abandonment, or downcutting into clayey sediments in the source area. A reduction or elimination of the supply of coarser than clay-sized sediment would remove those sediments capable of forming the easily-recognized basal portions of turbidites. In this case, only laminated claystones and massive nannofossil chalks, which dominate Subunits IVA to IVC, would be deposited.

Unit IV is overlain by an interval characterized by a renewal of turbidite sedimentation in the Campanian-Cenomanian.

Upper Cretaceous and Paleogene

The Upper Cretaceous and Paleogene sediments are condensed and also incomplete. They are dominated by graded sequences, matrix-supported carbonate conglomerates, and claystone-rich intervals around the Cenomanian-Turonian and in the Paleocene. The coarser detrital material consists mainly of biogenic fragments; terrigenous components are rare. Autochthonous claystone layers consist of varying amounts of smectite/illite, illite, and kaolinite. Clinoptilolite (replacing radiolarian skeletons) is a significant component in some intervals.

Subunit IIIC (Campanian to Cenomanian) consists mainly of two lithologies. Clayey chalk with yellowish red colors form graded sequences. Basal parts of these sequences contain sand-sized quartz and red flattened sandstone pebbles. Foraminifers (all deep-water forms) and radiolarians dominate the detrital material toward the top of coarser-grained intervals. The upper fine-grained intervals consist almost entirely of nannofossils. These graded sequences are interpreted as turbidites, based on sedimentary structures. Some of the coarser-grained basal parts, where the clasts are matrix-supported and neither sorting nor grading is visible, can be explained as debris flows evolving to turbidites. Erosional contacts are obvious, and red claystone pebbles can be explained as reworked material from the autochthonous claystones intercalated between the turbidites. The claystones are (1) reddish-brown; (2) consist of a mixture of illite, smectite/illite, and kaolinite; and (3) are devoid of any coarser detrital material. They closely resemble modern deep-sea red clays. Turbidites become more abundant relative to claystone from base to top in this subunit. A few distinct layers of black, faintly laminated shale occur near the Turonian/Cenomanian boundary. Smear slides from these layers contain a significant amount of zeolite (clinoptilolite) and less abundant organic material. These shales can be interpreted as the local expression of the global Cenomanian/Turonian Boundary Event (CTBE), a period of enhanced carbon burial in almost all marine environments.

Subunit IIIB (lower Eocene to uppermost Campanian) consists of interbedded varicolored claystone and clayey nannofossil chalk, with intercalated coarser graded sequences. This subunit is condensed and incomplete (poor recovery).

The claystones are a mixture of smectite/illite, illite, and variable amounts of kaolinite (the latter was not detected in the Eocene interval). Eocene claystones contain a fair amount of clinoptilolite, probably formed by the replacement of radiolarian skeletons. The Eocene was a time of enhanced silica deposition on a global scale; thus, the clinoptilolite spike can be explained as the local expression of this phenomenon.

The intercalated, coarser-graded sequences are either chalks rich in calcareous biogenic fragments, interpreted as turbidites, or quartzose siltstones and sandstones with distinct parallel or ripple cross-lamination and sharp basal contacts, tentatively explained as having been formed by contour currents.

Subunit IIIB contains the Cretaceous/Tertiary boundary; however, the biostratigraphic resolution is not good enough to determine the exact position of this boundary. In Interval 112-765C-22-3, 85–110 cm (which, according to the nannofossil data, contains the Cretaceous/Tertiary boundary), a distinctive matrix-supported conglomerate occurs. The structure may be explained as bioturbation that was deformed while the sediments were still soft.

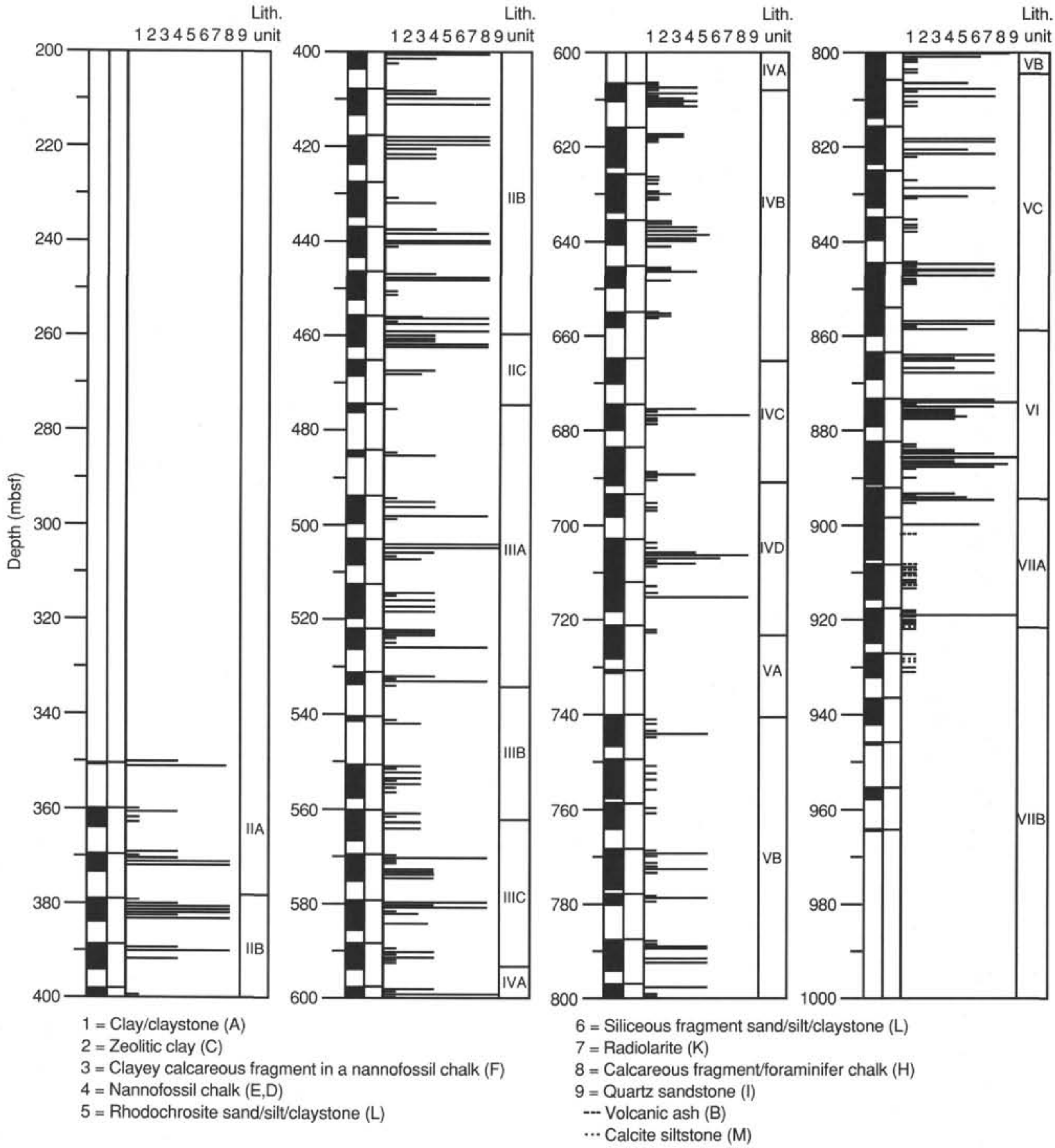

Figure 53. Distribution of cluster elements for Hole 765C. Group number is shown for each sample. Numbers are related to main lithologies. Corresponding cluster numbers from the dendrogram (Fig. 51) are given in brackets.

Subunit IIIA

This subunit also exhibits intercalations of dark claystones and lighter-colored graded sequences. The claystones consist of varying amounts of smectite/illite and kaolinite and minor amounts of illite. Detrital elements are minor clinoptilolite and quartz (?biogenic). The high amount of kaolinite, compared to the previous subunits, reflects an increase in continental detritus, probably windblown from the Australian Shield.

Graded sequences dominate this subunit and consist largely of foraminiferal fragments and nannofossils, with minor amounts of quartzose material that becomes more abundant in the lower part of the subunit. The contacts with overlying claystones are gradational but generally obscured by bioturbation.

A reconstruction of the depositional environment and an evaluation of potential source areas for the detrital components remain vague as a result of poor core recovery. All subunits resemble each other; however, increased mass transport without

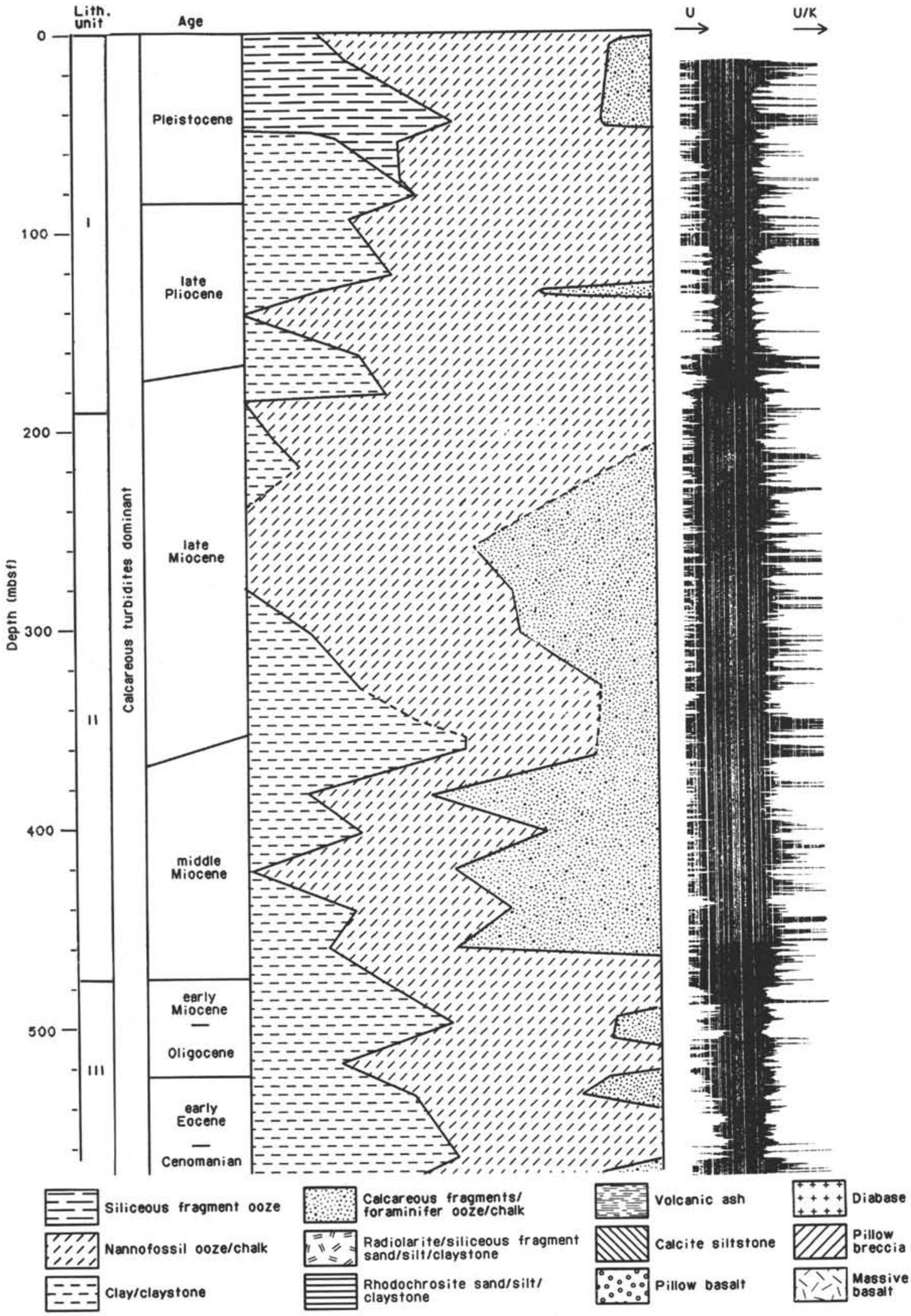

Figure 54. Stratigraphy of Site 765, with stratigraphic representation of principal lithologies using multivariate analysis of all smear-slide lithologic data in more than 500 samples. Downhole K and U/K anomalies that assist in lithostratigraphy were obtained from spectrometer logs. Graphic representation of distribution of the main lithologies through Site 765 is based on Figures 52 and 53. The average, relative frequency of the groups (in relation to their lithologies) for one to three cores in each point is given, sorted by grain size (fining to the left).

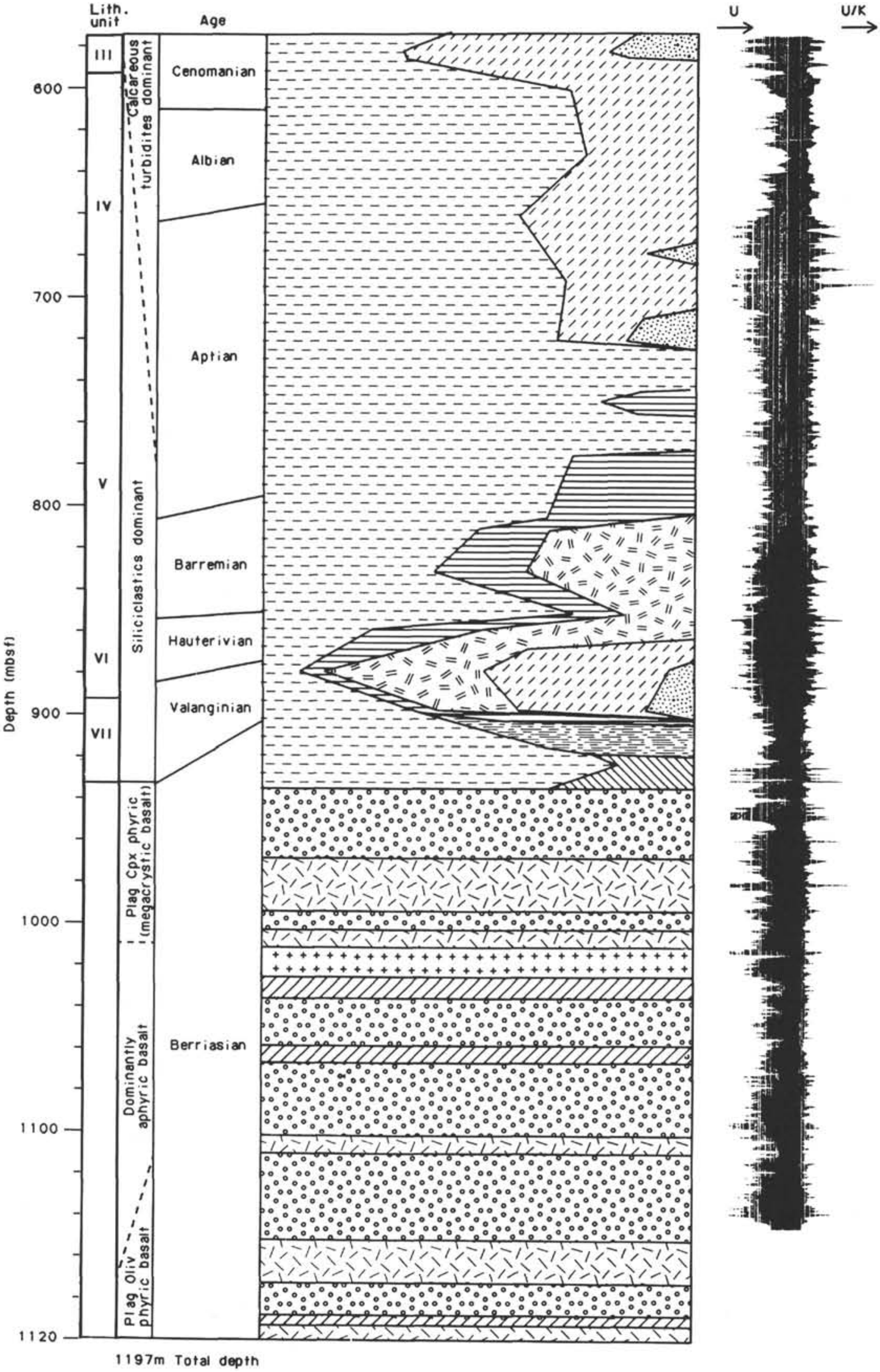

Figure 54 (continued).

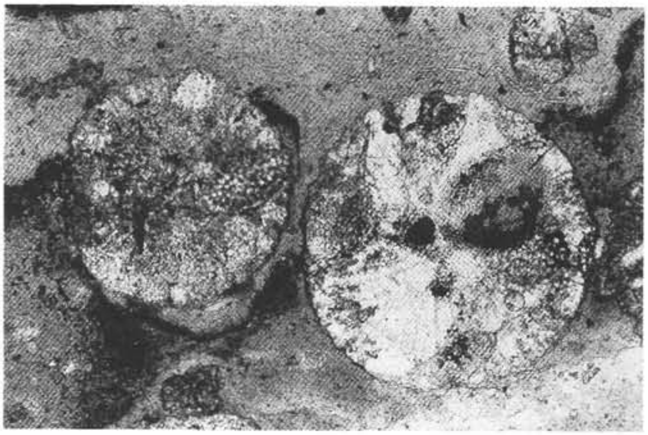

Figure 55. Rhodochrosite (?) concretions having distinctive radial texture contain radiolarian ghosts; inclusion of recognizable microfossils indicates replacive growth of these concretions (Sample 123-765C-42R-3, 110 cm).

Figure 56. Sand-sized basal interval of a calcareous turbidite. Dominant constituents are calcispheres, quartz, and glauconite (Sample 123-765C-36R-2, 24 cm).

significant terrigenous influx in the Campanian may indicate slope instabilities. Times of global highstands of sea level are reflected in the decrease in abundance of graded sequences near the Cenomanian/Turonian boundary; at that time, most detritus was trapped in shallow-water areas.

Two major paleoceanographic events recorded from other ocean basins can be detected; however, they are not as pronounced in other basins, for example, in the Atlantic Ocean. The CTBE is expressed as thin black shale layers with intercalated radiolarian and zeolite sands, a common expression of this event. Further studies are needed to confirm the major positive ^{13}C excursion as well as the marine nature of the organic material, together with a significant increase in trace metal content, always associated with this event. The second event—the Lower Campanian Event (LCE), typically characterized by a spike of siliceous sediments—has a local expression in radiolarian-rich turbidites. Further studies of the autochthonous red clays (e.g., isotopes, trace metals) are needed to confirm the presence of this event in the Indian Ocean.

Neogene

The Neogene paleobathymetry and sedimentation history of Site 765 is dominated by sediment gravity flows deposited at abyssal depths. Turbidites predominate, but debris flows occur locally. The Neogene sediment gravity flows are composed predominantly of pelagic, calcareous material, deposited well below the CCD. Estimates for paleowater depth through the Neogene, obtained from the backtracking curve, range from 5600 to 5800 m, compared to a modern CCD of about 4500 m. Interbedded clayey intervals are interpreted as resulting from background pelagic and hemipelagic sedimentation (BPS), although a turbidite contribution resulting from post-depositional leaching of calcareous components cannot be discounted. The clayey intervals are almost carbonate-free and consistently contain a very fine sand-sized to coarse silt-sized component of quartz and volcanic glass. This component, which may represent windblown detritus, is absent from the fine-grained turbidite tops. This observation supports the interpretation of the clayey intervals as pelagites and/or hemipelagites. The Neogene comprises Units I and II and the upper part of Subunit IIIA.

Unit II includes most of the Miocene series and consists predominantly of calcareous turbidites with minor debris flows. Subunit IIC (lowermost middle Miocene to uppermost lower Miocene) consists of a very thick turbidite overlying a debris flow and contrasts markedly with the underlying thick- to very thick-bedded claystones and calcareous turbidites of Subunit IIIA. The debris flow is a matrix-supported polymict conglomerate that contains intraformational clasts, as well as altered volcanics and Jurassic claystones.

Subunits IIA (upper Miocene and uppermost middle Miocene) and IIB (middle Miocene) consist of thin- to thick-bedded calcareous turbidites. Pelagic and hemipelagic dolomitic claystones are progressively less common upward in Subunit IIB, and they are absent from Subunit IIA. This progression coincides with coarser grain sizes in basal portions of younger turbidites (supported by Markov chain analysis) and an increase in quartz sand within the turbidite bases. This results in the formation of carbonate cycles in the lower part of Subunit IIA and mixed carbonate-siliciclastic cycles in the upper part. Based on qualitative comparison of core photos and barrel sheets, higher frequency cycles of bed thickness and relative coarseness are suggested by differences between adjacent cores, but an overall pattern is not immediately obvious. Individual turbidites display a variety of incomplete "Bouma sequences." The most common sequences appear to be "BCDE," "BCD," and "CDE" types.

Variability within Unit II is probably related to evolutionary changes within a turbidite depositional system (e.g., submarine fan, slope apron). A prominent, but diachronous (lower upper Oligocene to lower Miocene), unconformity, overlain by an extensive upper Oligocene to middle Miocene progradational cycle, was described by Apthorpe (1988) for the northwest shelf of Australia. This unconformity may be genetically related to Unit II on the Argo Abyssal Plain. The apparent coarsening upward of turbidites through the Miocene can be viewed as progradation within a turbidite system, but may also represent additional source materials resulting from incision of canyons and channels responsible for distribution of sediment off the shelf. The predominance of moderately complete turbidites is consistent with a middle to outer fan setting, according to current submarine fan models. A point worth consideration is that current fan models are based primarily on observations of terrigenous depositional systems. Hydraulic conditions within turbidity currents, consisting primarily of biogenic grains and parameters such as deceleration and transport distances for these currents, may be considerably different than for those of terrigenous systems.

Lithologic Unit I combines the Pleistocene, Pliocene, and uppermost Miocene and consists of calcareous turbidites, debris flows, and slumps. Unit I displays greater variability within the sediment gravity flows when compared to Unit II. Unit I also contains a higher proportion of pelagic and hemipelagic clayey intervals and higher proportions of clay within the calcareous intervals themselves. Most major lithologic changes within this interval do not correlate well with proposed series or stage boundaries.

Subunit IC (upper Pliocene to uppermost Miocene) consists of thin- to thick-bedded calcareous turbidites and thin-bedded pelagic and hemipelagic intervals of silty clay. Basal portions of some turbidites in Subunit IC include substantial amounts of quartz sand. There is no obvious difference between the turbidites in cores directly adjacent to the boundary separating Units I and II. However, the turbidites in Unit I become progressively finer-grained upward (increasingly distal), and the pelagic and hemipelagic intervals become increasingly common and thicker. This trend is interrupted locally by very thick-bedded turbidites with conglomeratic bases. In addition, the occurrence of siliciclastic material in Subunit IC turbidites yields a typical cycle very different from those of other parts of Units I and II. The typical cycle of Subunit IIA also is a mixed carbonate-siliciclastic cycle, but differs from that of Subunit IC in that the carbonate and siliciclastic components form separate subcycles, whereas in Subunit IC these are commingled.

Subunit IB (Pleistocene to upper Pliocene) consists predominantly of large, composite sediment gravity flows. Five such flows were observed, each one including a generally deformed but coherent slumped section at the base, a debris flow, and a single, very thick-bedded turbidite. These composite flows are separated by thin- to thick-bedded turbidites and generally thin-bedded pelagic and hemipelagic siliceous oozes and clays. A distinct change was noted between the Pliocene pelagic and hemipelagic silty clays and the Pleistocene clayey siliceous oozes.

Subunit IA (Pleistocene) is dominated by thick-bedded calcareous turbidites and thin- to thick-bedded pelagic and hemipelagic clayey siliceous oozes. Markov chain analysis indicates simple and low-variability cycles consisting of either massive or laminated coarse-grained carbonate, overlain by nannofossil ooze, overlain by clayey siliceous ooze.

A gradual change toward increasingly distal turbidites through Subunit IC apparently signals either the end of fairly consistent turbidite deposition over the Argo Abyssal Plain or, at least, a shift in the locus of deposition away from Site 765. Distal turbidites are replaced by more variable and thicker sediment gravity flows, particularly through Subunit IB. This transition suggests fundamental differences controlling the occurrence and characteristics of sediment gravity flows in Units I and II. The abundance of slumps, debris flows, and very thick-bedded turbidites, reaching a maximum thickness of 42.6 m, suggests a trend toward less frequent, possibly catastrophic, events. The marked difference in calcium carbonate content between Units I and II implies a new source, or at least an additional component to the previous one, presumably consisting of material being transported off the northwest shelf. One possible scenario involves a combination of sources, combining what was being funneled off the northwest shelf with material sloughing off the shelf margin and canyon walls. Barber (1988) described several phases of subduction of the Australian Plate beneath the Banda Sunda Arc along the Timor Trough. Although the timing of these phases of subduction is not well constrained, they may coincide roughly with the onset of thicker, chaotic sediment gravity flows observed in the lower part of Unit I at Site 765. The burial history at Site 765 indicates uplift in this area of the Argo Abyssal Plain at about the same time. The apparent decreased frequency of sediment gravity flows extends into the upper Pleistocene, as recorded by the thin- to thick-bedded pelagic and hemipelagic intervals in Subunit IA. The turbidites are still quite variable in thickness, but are more consistent in character and considerably thinner than the larger, chaotic flows of Subunit IB.

TRENDS IN SEDIMENTATION

Introduction

In the "Background and Introduction" chapter (this volume), a brief overview was presented of the regional and global paleoceanographic and geological settings that influenced sedimentation patterns in the Argo Abyssal Plain. In this section, we review this pattern and offer a preliminary interpretation of the trends observed.

Methods

Shipboard analysis began with backtracking of Site 765 to determine the initial ridge-crest depth below sea level, the subsidence track of the basement/sediment interface, and that of the successively younger sedimentary units that once formed the paleoseafloor. We used the short F77 program BTRACK, written by Z. Huang (Dalhousie Univ., Halifax, Nova Scotia) and the empirical equations for age-since-formation of the oldest ridge-crest volcanics vs. water depth for the 0- to 70-Ma and 70- to 160-Ma intervals (Sclater et al., 1985). The program corrects for basement loading caused by sediment build-up and the compaction of the sediments proper, to arrive at an age/depth curve for basement and each sedimentary unit below the paleoseafloor. Values entered are present-day water depth at a site, sediment thickness above basement at time, *t*, and average density of the sediment column. Both values entered and retrieved for each site analyzed are shown in Table 5.

The Earliest Cretaceous ridge-crest depth for Site 765 was 2834 m, which falls within the uncertainty envelope for the average global ridge-crest depth.

Next, the paleowater depth for each time-successive sedimentary unit in Site 765 was used as input in version 3.0 of programs DEPOR and BURSUB (Stam et al., 1986). These F77 programs calculate the subsidence and burial rates of the sedimentary units through time in centimeters per 1000 yr and the increase in burial depths below sea level. Corrections are applied for increased compaction of the sedimentary units through time with deeper burial and changes in elevations of sea level relative to today. Values entered into BURSUB are age of each sedimentary unit in Ma, depth below the seafloor or below rotary table, paleowater depth, height of sea level through time relative to the

Table 5. Input and output data for backtracking at Site 765.

Input data		Output data	
Present water depth = 5723 m Basement depth (bsf) = 932 m Ave. sed. density = 1.7 g/cm^3 Age of basement = 139 Ma		Present unsedimented water depth = 6383 m Theoretical, present unsedimented water depth = 6050 m Offset = 33 m	
		Paleodepth (m)	
Time (Ma)	Sediment thickness (m)	Unsedimented	Sedimented
0	932	6383	5723
4.5	762	6357	5817
6	762	6348	5808
11	562	6316	5918
17	458	6274	5950
23.5	442	6224	5911
37	407	6102	5814
52	407	5932	5644
62	382	5794	5524
70	372	5740	5477
94	324	5180	4951
100	324	5018	4789
113	267	4617	4428
119	127	4398	4308
127	73	4045	3994
133	39	3690	3663
139	0	2833	2833

Table 6. Sedimentation and burial history at Site 765.

Age (Ma)	Depth (m)	Paleo water depth (m)	Eustatic sea level (m)
0	0	5723	0
4.5	170	5818	9
6.0	170	5809	12
11	370	5919	20
17	474	5950	26
23.5	490	5912	36
37	525	5815	55
52	525	5645	70
62	550	5524	80
70	560	5477	95
94	608	4951	98
100	608	4789	90
113	665	4429	50
119	805	4309	30
127	859	3994	27
133	893	3663	25
139	932	2834	30

Depth-porosity (decompaction function combined) lithologies: 'power law' =
alpha beta
0.6098 0.2419

present, lithology and grain density of each unit, decompaction parameters alpha and beta of each unit, and the shape of the decompaction function. Program DEPOR calculated this decompaction function, which is the statistically most-acceptable best fit, if any, for the measured porosity vs. depth values in the cores for each principal lithology. The best fit can be linear, exponential or a power function that either goes to zero porosity at maximum depth or levels off to a small value. At the high end of the porosity scale (i.e., the surface porosities), the best-fit functions do not exceed empirically observed average surface porosities that are realistic for each lithology.

The decompaction parameters calculated in DEPOR are entered into BURSUB, together with the age-depth/water-depth and lithology data. For decompaction, each sedimentary unit is moved up its own porosity/depth curve to determine its porosity at successively shallower burial depths back through time. For each step back in time, the thickness of the water column needed to fill the increased porosity at this time is added to the measured unit thickness to provide the restored thickness. The restored thicknesses are used to calculate restored sedimentation rates and rates of burial (Table 6 and Fig. 57).

Site 765 displays high initial subsidence rates, which decreased rapidly with time. If known turbidite- and debris-flow deposits are removed from the abyssal sedimentary column, less than 25% of the column would remain, representing inferred true hemipelagic and/or pelagic deposits. The Hauterivian calcareous (nannofossil) claystone of Unit VI may reflect a deepening of the CCD, from a position at or above the ridge crest at 2800 m in the latest Berriasian/Valanginian. Evidence that Berriasian/Valanginian sediments accumulated at or near the CCD is provided by strongly etched inoceramid shell fragments and sparse nannofossil assemblages in the basal red siltstone and claystone of Unit VII. The present-day depth of the CCD below 4 km is much deeper than the inferred depth of the Cretaceous CCD.

Initial Mesozoic sedimentation rates were relatively high, varying from 1 to 4 cm/k.y. Post-Aptian sedimentation rates are sharply lower (by a factor of two or more), compared with earlier rates. This may reflect the relatively rapid rise of global sea level from Barremian to Turonian time, which flooded continental margins, diminished coastal relief, and led to an expanded zone of sediment trapping around the continents. The rise in CCD probably resulted from decreasing influx of carbonate to the oceans, which further reduced abyssal carbonate sedimentation. Extreme sediment starvation with fluctuating sediment influx on the Argo Abyssal Plain lasted from middle Cretaceous until Oligocene time.

In mid-Tertiary time, abyssal sedimentation rates increased by a factor of 2 to 6. This change may reflect the progressive lowering of sea level (by as much as tens of meters) with global climatic cooling. By the Eocene, rising sea levels caused the continental shelves to prograde seaward and accentuated canyon cutting at the shelf edge. Increased canyon cutting may have promoted transport of continental clastics to the abyssal plain. The catastrophic nature of Miocene abyssal sedimentation (characterized by massive debris flows) was perhaps enhanced by continental margin uplift from the Oligocene/Miocene Alpine orogeny, including formation of the Sunda Arc. Increased productivity of cold Antarctic bottom waters, particularly since the onset of southern glaciation in the middle Miocene, led to increased contour-current activity that contributed to redistribution of lower slope sediments and caused formation of local hiatuses along continental margins. Pliocene hiatuses in Site 765 sediments may be the result of such erosion. Further studies, particularly on the sedimentary structures at Site 765 and of regional seismostratigraphy, will lead to a more refined model for the relation between Mesozoic and Cenozoic paleoceanography and abyssal sedimentation patterns.

BIOSTRATIGRAPHY

Introduction

Site 765 is situated on the southern Argo Abyssal Plain in a water depth of 5725 m. Of the four holes drilled at this site, only cores from the first three went into the sedimentary sequence. Only a single core was obtained from Hole 765A, which was dated as undifferentiated Quaternary. A summary of the preliminary biostratigraphic results of this hole, from which we recovered a predominately turbiditic, Quaternary to middle Miocene sequence, is presented in Figure 58.

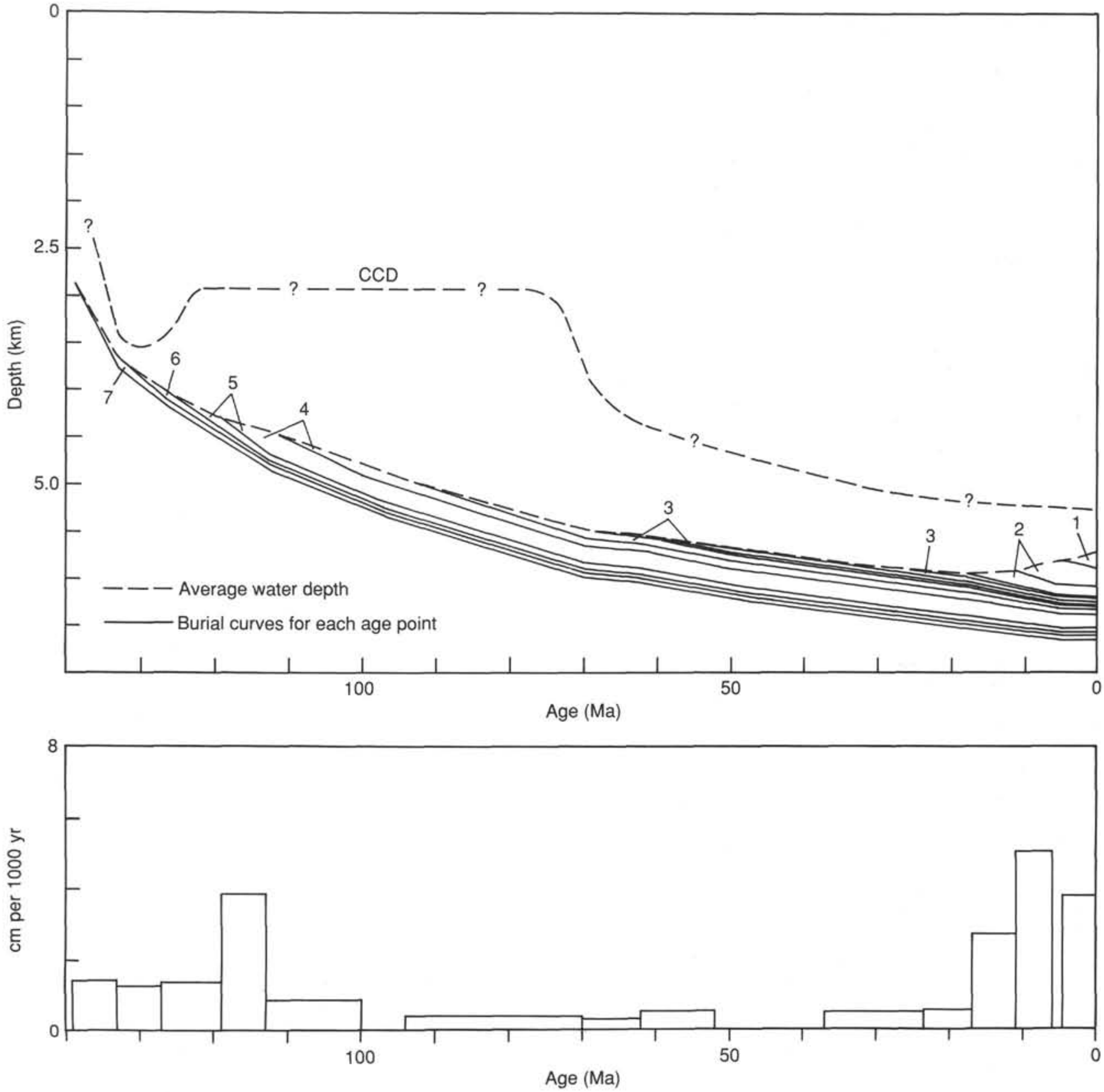

Figure 57. Decompacted sedimentation rates and burial curves for Site 765. Numbers refer to successive lithologic units. The carbonate compensation depth (CCD) track is tentative.

Coring in Hole 765C commenced at 350.2 mbsf using the RCB and terminated at a depth of 964 mbsf after penetrating approximately 30 m of basaltic basement. Hole 765C yielded a middle Miocene to Berriasian sequence. Following a thick Neogene sequence, the Paleogene and Upper Cretaceous sequences are relatively condensed and contain several significant hiatuses. However, the lower Albian to Berriasian sequence is thicker and is probably more complete. A preliminary biostratigraphic summary of this hole is presented in Figure 59.

In the Quaternary, foraminifers and radiolarians provide the biostratigraphic detail. However, radiolarian markers become poorly preserved below this level and provide little further biostratigraphic information until the Lower Cretaceous. Age determination for the remainder of the Cenozoic is provided by planktonic foraminifer and nannofossil markers. Detailed resolution over this period is constrained by the turbiditic style of sedimentation. Most foraminiferal and nannofossil samples are distinctly size-sorted and contain abundant evidence of reworking; this naturally limits the use of last occurrence datums. Dinoflagellate assemblages are present in the Neogene, but the lack of a suitable zonation for this time period limits their usefulness in age determination; these assemblages were not recorded from either the Paleogene or Upper Cretaceous sequences.

Foraminifers and nannofossil assemblages were obtained from most Upper Cretaceous stages but poor preservation, low diversity, and reworking limit the maximum obtainable biostratigraphic resolution.

There are extensive intervals devoid of calcareous planktonic microfossils in the Lower Cretaceous, but dinoflagellate cysts and radiolarians become increasingly abundant. The latter, to-

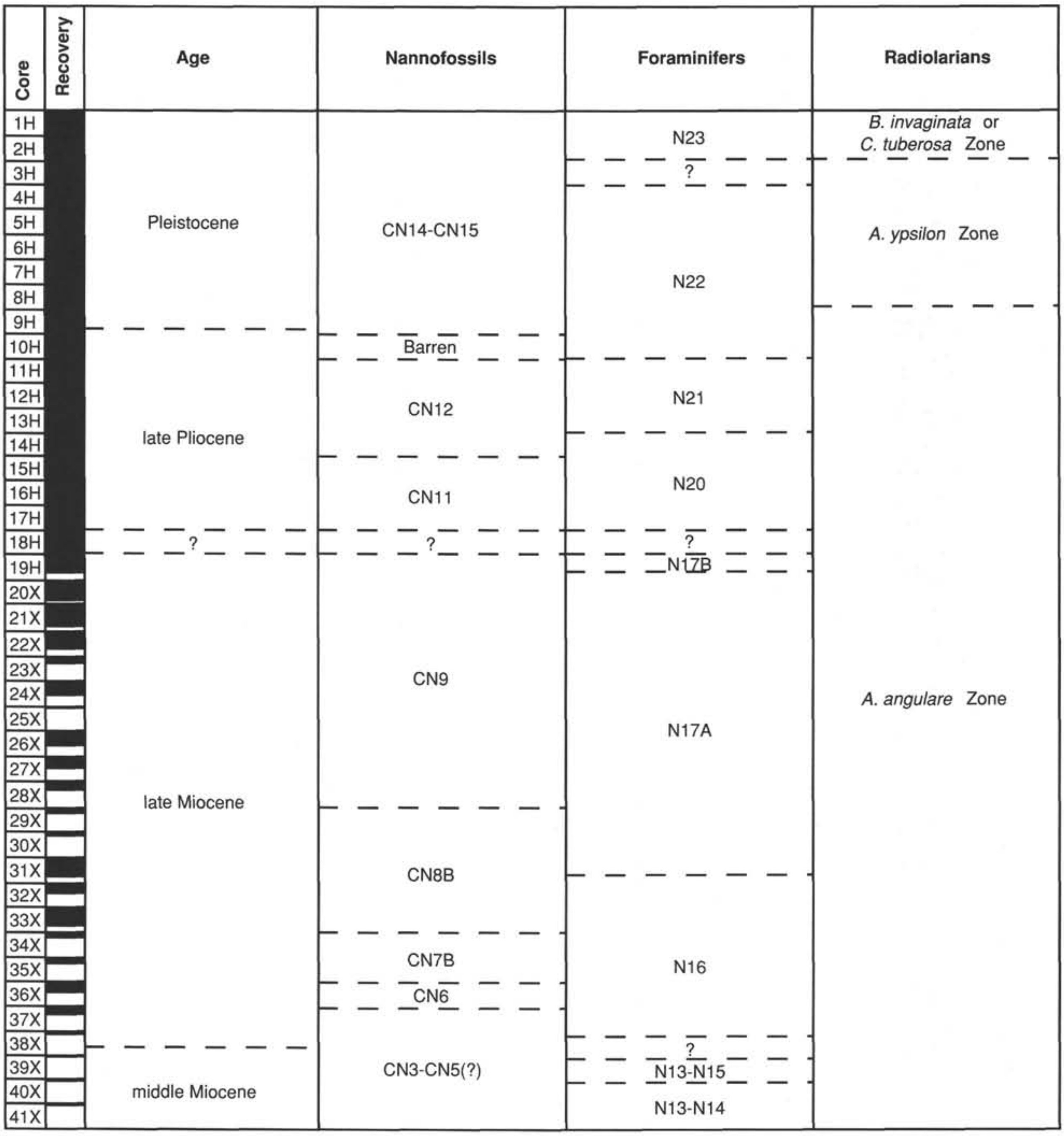

Figure 58. Biostratigraphic summary of Hole 765B.

gether with sporadic nannofossil assemblages, provide the main biostratigraphic control to the base of the Cretaceous.

In the following discussion "LO" and "FO" refer to the last and first occurrence of a taxon, respectively.

Planktonic Foraminifers

The application of planktonic foraminiferal biostratigraphy to Site 765 is constrained by the allochthonous nature of the assemblages and the large amount of reworking encountered in many of the samples. Planktonic foraminifers were recovered from sands apparently transported downslope as turbidites or other mass flows and deposited as graded units. The coarser sands contain sorted assemblages of large-size specimens; whereas the finer parts of the graded beds host mainly small-sized juvenile forms, many of which are difficult to classify. Dissolution has affected shell preservation to a limited extent. The poorest preserved assemblages encountered at this site (middle Miocene) include specimens having thick overgrowths of sparry calcite.

Planktonic foraminiferal analysis was based mainly on core-catcher samples, which, depending on lithology, contain microfaunas of varying composition and preservation. In the condensed Paleogene and Upper Cretaceous intervals, additional samples were taken from different levels within selected cores.

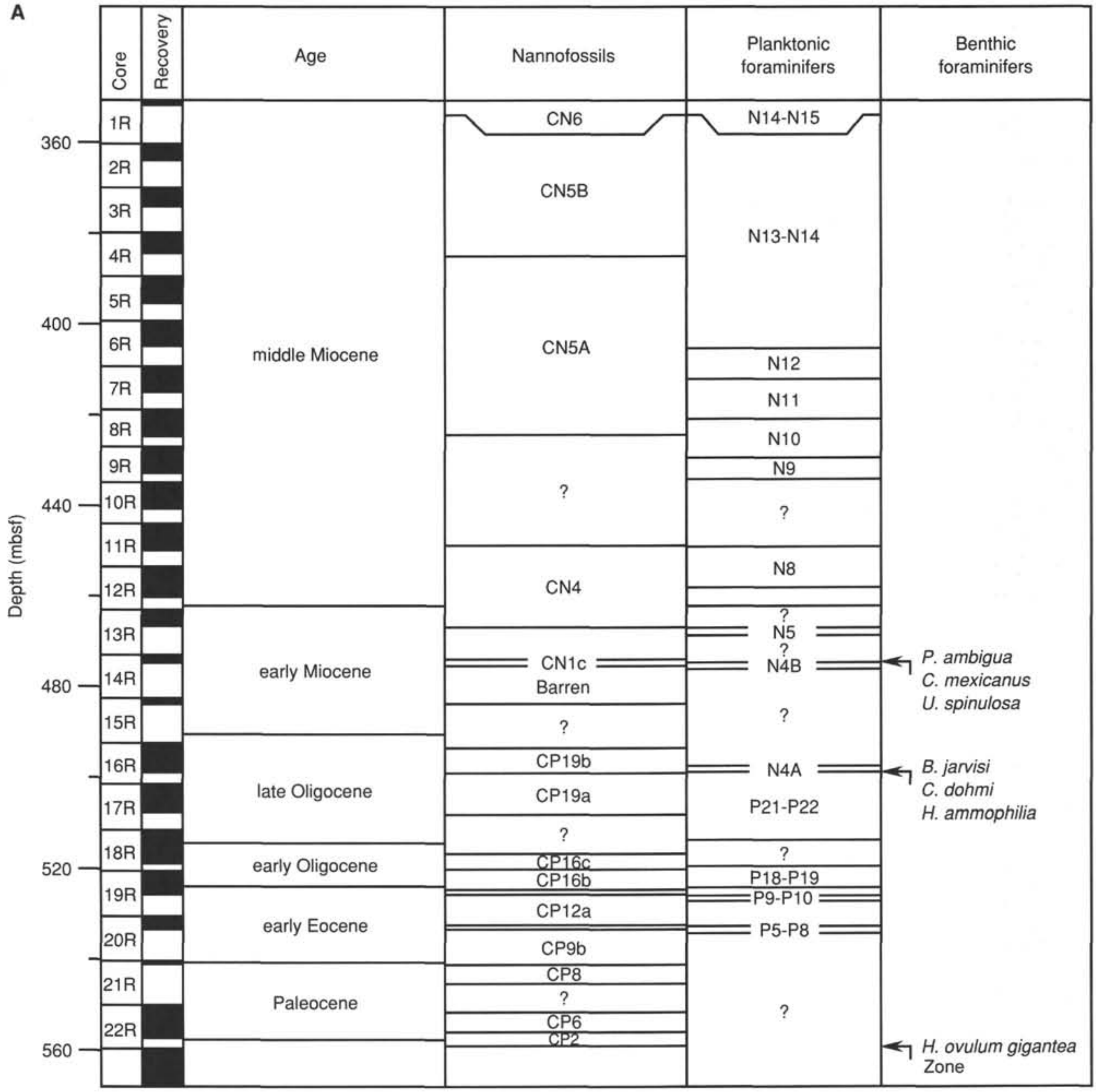

Figure 59. A. Biostratigraphic summary of Cenozoic sequence in Hole 765C. B. Biostratigraphic summary of Upper Cretaceous sequence in Hole 765C. C. Biostratigraphic summary of the Lower Cretaceous sequence in Hole 765C.

Neogene

The Neogene includes the interval from 0 to approximately 480 mbsf. The fauna is diverse and typical of the tropical Indo-Pacific. During shipboard study, taxonomic discrimination of species followed Kennett and Srinivasan (1983), and zonation was slightly modified from Blow (1969), as described in the "Explanatory Notes" chapter (this volume). A large part of the Neogene is represented in the succession. However, a significant faunal break is apparent within Core 123-765B-18H, where the lower Pliocene may be missing. The lower Neogene is also condensed, but the extent of disconformities is unclear because of broad sampling intervals.

Holocene to Upper Pleistocene

Samples 123-765A-1H, CC; 123-765B-1H, CC; and 123-765B-2H, CC, contain assemblages dominated by small-size foraminifers, including *Bolliella adamsi* and pink *Globigerina rubescens*, which suggest that the upper 18.8 m of sediment belongs to the Holocene and upper Pleistocene Zone N23. Specimens are well preserved and show no evidence of significant dissolution. The size range of the material is attributed to current sorting.

Lower Pleistocene

Zone N22, which is based on the co-occurrence of *Globorotalia truncatulinoides* and *Globorotalia tosaensis*, includes the

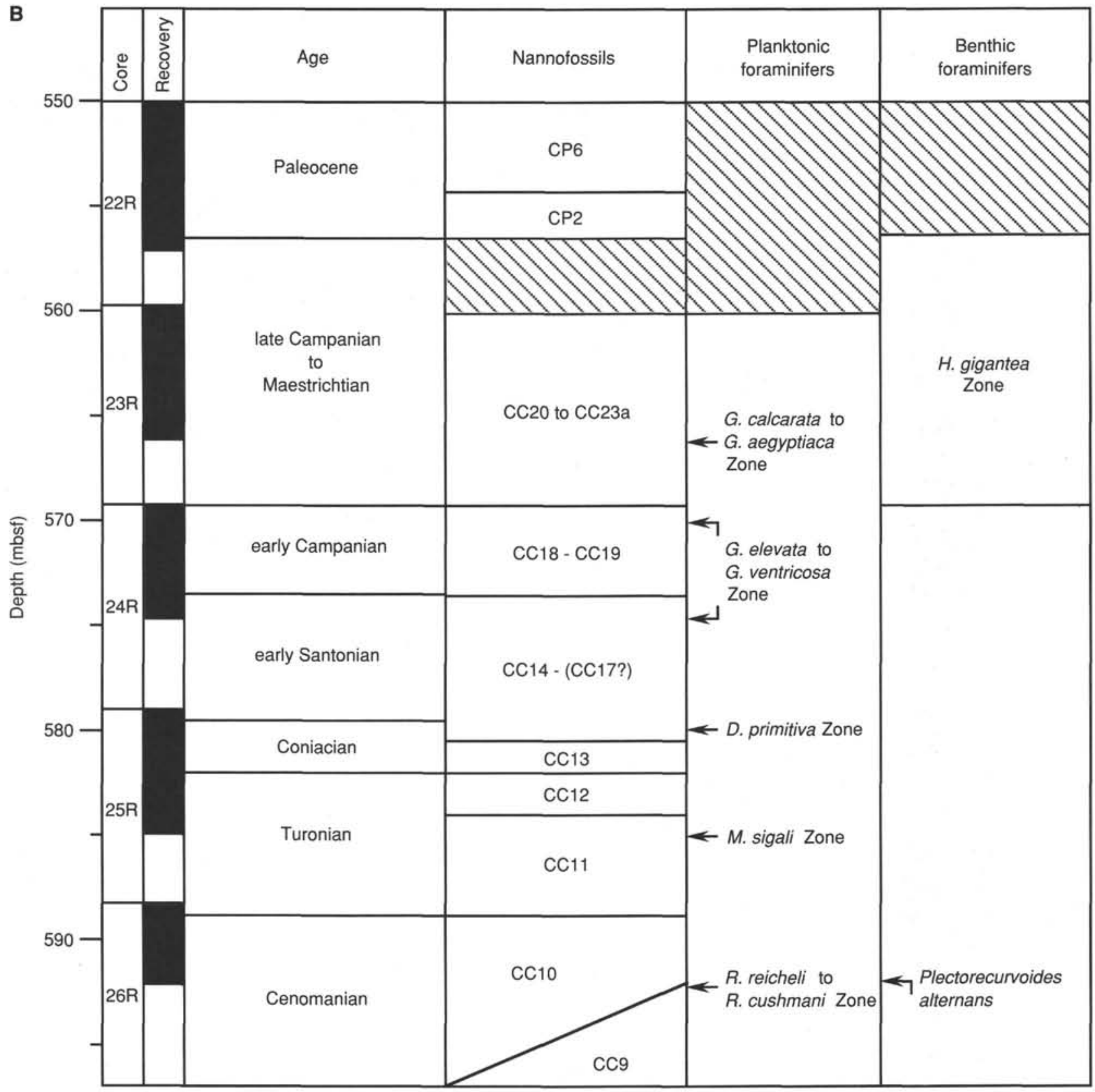

Figure 59 (continued).

interval between 28.4 and 96.1 mbsf (Samples 123-765B-3H, CC, to -10H, CC). The significant faunal events present here are (1) the LO of *Globorotalia tosaensis* in Sample 123-765B-3H, CC; (2) the LO of *Globigerinoides fistulosus* in Sample 123-765B-3H, CC; the LO of *Globigerinoides extremus* in Sample 123-765B-4H, CC; the LO of *Sphaeroidinellopsis seminulina* s.l. in Sample 123-765B-5H, CC; the LO of *Dentoglobigerina altispira* in Sample 123-765B-6H, CC; the FO of *G. fistulosus* in Sample 123-765B-8H, CC; and the FO of *G. truncatulinoides* in Sample 123-765B-10H, CC. The faunal succession suggests that reworking of Pliocene material occurred and that LO datums should be used with caution. Although *G. fistulosus* and *G. extremus* are known to have LO datum levels within Zone N22, the extinction levels of *S. seminulina* and *D. altispira altispira* are located in the upper Pliocene (Berggren et al., 1985b; Kennett and Srinivasan, 1983). *Globigerinoides fistulosus* has a later FO in the Site 765 succession than elsewhere, where it is known to range from the upper Pliocene Zone N21 (Kennett and Srinivasan, 1983).

Pliocene

Upper Pliocene Zone N21 includes the interval between 105.6 and 124.9 mbsf (Samples 123-765C-11H, CC to -13H, CC), based on the occurrence of *G. tosaensis* preceding the first appearance of its descendent species, *G. truncatulinoides*. Significant faunal events within the interval are the LO of *Globorotalia margaritae* in Sample 123-765B-11H, CC; the LO of *Globigerina decoraperta* in Sample 123-765B-11H, CC; the FO of *Neogloboquadrina dutertrei* in Sample 123-765B-12H, CC; the LO of *Globigerina nepenthes* in Sample 123-765B-12H, CC; the LO of *Globigerina apertura* in Sample 123-765B-12H, CC; the LO of *Neogloboquadrina humerosa* in Sample 123-765B-12H, CC; the FO of *Globorotalia inflata* in Sample 123-765B-13H, CC; and the FO of *G. tosaensis* in Sample 123-765B-13H, CC. The

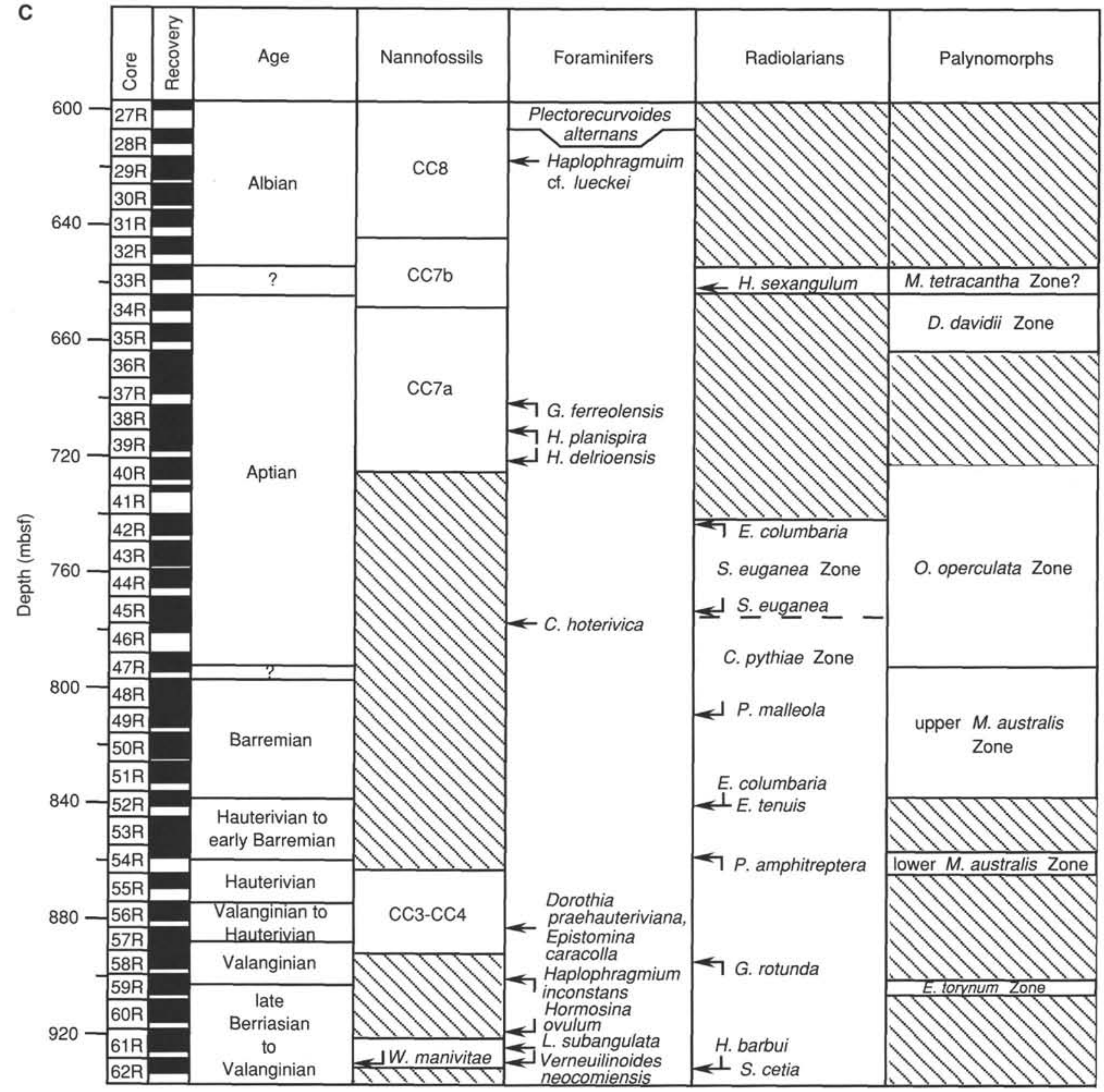

Figure 59 (continued).

last appearances recorded here for *G. margaritae* and *G. nepenthes* are anomalously high compared to their extinction levels (below the FO of *G. tosaensis*, within Zone N20) indicated on the Berggren (1985b) datum scale.

The interval between approximately 134.4 and 163.6 mbsf (Samples 123-765B-14H, CC, to -17H, CC) contains assemblages attributed to the middle Pliocene Zone N20, based on the occurrence of *Globorotalia crassaformis* below the FO of *G. tosaensis*. Significant faunal events within this interval include the LO of *Globoquadrina venezuelana* in Sample 123-765B-14H, CC; the FO of *Sphaeroidinella dehiscens* in Sample 123-765B-15H, CC; the change down-sequence from dextral to sinistral coiling in *Pulleniatina* spp. between Samples 123-765B-15H, CC, and 123-765B-16H, CC; the LO of *Globoquadrina dehiscens* in Sample 123-765B-16H, CC; the FO of *G. margaritae* in Sample 123-765C-17H, CC; and the FO of *G. crassaformis* in Sample 123-765C-17H, CC. The first appearance of *S. dehiscens* (which usually is taken to mark the base of lower Pliocene Zone N19) above the FO datum for *G. crassaformis* confirms Vincent's (1977) observation that the evolution of *Sphaeroidinella* from *Sphaeroidinellopsis* was diachronous in the Indian Ocean. Berggren et al. (1985b) located the LO of *G. dehiscens* within the upper Miocene. The presence of rare *G. dehiscens* in Sample 123-765B-16H, CC, suggests that reworking of Miocene sediment occurred here.

The lower Pliocene Zone N19 and the uppermost Miocene Zone N18 were not identified from core-catcher samples studied here. These units may be present within Core 123-765B-18H, or an unconformity may exist within this core.

Miocene

Upper Miocene Zone N17B is represented in the interval between 173.1 and 179.8 mbsf (Samples 123-765B-18H, CC, and -19X, CC), based on the co-occurrence of *Globorotalia plesio-*

tumida and *Pulleniatina primalis* and the absence of *Globorotalia tumida*. Significant faunal events recorded here include the LO of *Globorotalia juanai* in Sample 123-765B-19X, CC; the LO of *Globorotalia lenguaensis* in Sample 123-765B-19X, CC; and the FO of *Pulleniatina primalis* in Sample 123-765B-19X, CC.

A thick section in Hole 765B between 191 and 296.7 mbsf (Samples 123-765B-20X, CC, to -31X, CC) belongs to Zone N17A of the upper Miocene, based on the occurrence of *G. plesiotumida* below the FO of *Pulleniatina primalis*. The evolution of *G. plesiotumida* from *G. merotumida* (which marks the Zone 17A to Zone 16 boundary) involves a gradual change in chamber shape, and the distinction between the taxa (and the zones) is subjective. Significant faunal events recorded within the interval are the LO of *Globorotalia paralenguaensis* in Sample 123-765B-20X, CC; the FO of *G. juanai* in Sample 123-765B-21X, CC; the FO of *Globorotalia cibaoensis* in Sample 123-765B-21X, CC; the change down-sequence from dextral to sinistral coiling in *Neogloboquadrina acostaensis* in Core 123-765B-24X; the FO of *Candeina nitida* in Sample 123-765B-27X, CC; the FO of *N. acostaensis* in Sample 123-765B-28X, CC; and the FO of *G. plesiotumida* in Sample 123-765B-31X, CC. The FOs of *G. juanai* and *N. acostaensis* have been recorded at lower levels elsewhere (in Zone N16; Kennett and Srinivasan, 1983). Because assemblages from the lower part of the interval are poorly preserved, it is difficult to document the full stratigraphic range of many of the species in the Hole 765B succession.

Upper Miocene Zone N16 includes the interval between approximately 303.9 and 358.6 mbsf (Samples 123-765B-32X, CC, to -38X, CC). The poorly preserved assemblages contain *G. merotumida* and lie below the FO of forms interpreted to be *G. plesiotumida*. *Globigerinoides extremus* is present throughout the interval, which suggests that only the upper part of Zone N16 is represented here. The assemblages contain *G. nepenthes*, *Globigerinoides obliquus*, *Globigerinoides quadrilobatus*, *Orbulina universa*, *Orbulina bilobata*, sinistral *Globorotalia menardii*, *G. dehiscens*, *D. altispira*, and *S. seminulina*, but lack *N. acostaensis* (the first evolutionary appearance of which defines the base of Zone N16).

The interval that includes Samples 123-765B-39X, CC, to -41X, CC, of Hole 765B (approximately 367.6–386.3 mbsf) and Samples 123-765C-1R, CC, to -6R, CC, of Hole 765C (approximately 350.5–403.8 mbsf) contains poorly preserved assemblages that have been placed within Zones N13 to N15 of the middle Miocene. The occurrence of *Globorotalia mayeri* in Sample 123-765B-40X, CC, suggests that this level is no higher than Zone N14. In Hole 765C, *G. nepenthes* is common in the highest core-catcher Sample 123-765C-1R, CC, but is not recorded below this level. This indicates that the upper core of Hole 765C penetrated no lower than Zone N14. Sample 123-765C-3R, CC, contains the LOs of *G. mayeri* and *Cassigerinella chipolensis* recorded in Hole 765C, which suggest that this level lies no higher than Zone N14. Sample 123-765C-5R, CC, contains the LO of *Globigerinoides subquadratus*, a species that ranges no higher than middle Miocene (Zone N15).

Middle Miocene Zone N12 is represented in Sample 123-765C-7R-2, 126–128 cm (at 410.8 mbsf), which contains *Globorotalia fohsi*, the index species whose total range defines the zone. Rare *Globorotalia peripheroacuta* is also present, together with a typical middle Miocene assemblage that includes *O. universa*, *Globigerina druryi*, *G. subquadratus*, *Globorotalia siakensis*, *G. dehiscens*, *D. altispira*, and *S. seminulina* s.l.

An assemblage that includes *Globorotalia praefohsi*, *G. peripheroacuta*, and *Globorotalia peripheroronda* defines middle Miocene Zone N11 in Sample 123-765C-8R-2, 76–78 cm (at 420 mbsf). *Globorotalia praemenardii* and *Globorotalia lenguaensis* also occur at this level.

Middle Miocene Zone N10 includes the interval from 423.5 to 428.4 mbsf (Samples 123-765C-8R, CC, and -9R-1, 113–114 cm) and is characterized by the occurrence of *G. peripheroacuta* and *G. praemenardii* below the FO of *G. praefohsi*. Sample 123-765C-9R, CC (at 434.4 mbsf) probably belongs within Zone N9, because it contains the lowest record of *Orbulina* and has primitive *G. peripheroronda* as the only representative of the *Globorotalia fohsi* lineage. Samples from Core 123-765C-10R lack zonal indexes but belong either to Zone N9 or to Zone N8, based on stratigraphic position.

Zone N8 lies near the boundary between the lower and middle Miocene and includes the interval between 451.9 and 462 mbsf (Samples 123-765C-11R, CC, and 123-765C-12R, CC). Assemblages are characterized by the occurrence of *Globigerinoides sicanus* and the absence of *Orbulina*. The occurrence of *Praeorbulina glomerosa* in Sample 123-765C-11R, CC, but not in Sample 123-765C-12R, CC, suggests that the lower sample lies near the base of the zone.

Lower Miocene Zone N5 is represented in Sample 123-765C-13R, CC (at 467.9 mbsf) by a well preserved assemblage of *Globoquadrina binaiensis*, *Catapsydrax dissimilis*, *Catapsydrax unicavus*, and diverse *Globigerinoides* (including *G. triloba*, *G. immaturus*, *G. altiapertura*, and *G. obliquus*).

The lowest Miocene Zone N4B includes Sample 123-765C-14R, CC (at 475.4 mbsf), which contains a poorly diverse assemblage of small forms that includes *G. triloba* and *Globorotalia kugleri*. A similar assemblage from Sample 123-765C-15R, CC (at 484.9 mbsf) also includes *G. kugleri* and may belong to Zone N4B or to the uppermost Oligocene Zone N4A.

Paleogene

Compared to the Neogene, the Paleogene succession in Hole 765C is condensed and includes the interval between approximately 498 and 560 mbsf. Recovered Oligocene assemblages are, in general, well-preserved and diverse; however, the Eocene fauna is poorly preserved and contains few identifiable forms. The taxonomy of Bolli and Saunders (1985) and Toumarkine and Luterbacher (1985) has been followed here, as well as the zonation charted by Berggren (1969).

Oligocene

The uppermost Oligocene Zone N4A includes Sample 123-765C-16R-4, 94–96 cm, taken from a coarse sand at the base of a turbiditic unit (at 498.6 mbsf). The co-occurrence of *Globigerinoides primordius* and *Globigerina angulisuturalis* identifies the zone. Other species represented here include *Globigerina praebulloides* (the precursor species of *G. primordius*), *Globoquadrina binaiensis*, *Globigerina ciperoensis*, and *Catapsydrax unicavus*.

The lowest occurrence of *G. binaiensis* in Hole 765C is in Sample 123-765C-16R, CC (at 499.3 mbsf), which also contains *G. praebulloides* but lacks *G. primordius*. This level is included within Zone P22 of the upper Oligocene. Samples 123-765C-17R, CC, and -18R-1, 4–9 cm (508–512 mbsf) also may belong to Zone P22 or to Zone P21, based on the occurrence of *G. angulisuturalis*.

The lower Oligocene includes Samples 123-765C-18R, CC, and -19R-2, 57–58 cm (519.1–523.4 mbsf), which contain *Globigerina increbescens*, *Globigerina ampliapertura*, and *Globigerina tapuriensis* that are indicative of Zones P18-P19. The presence of *Pseudohastigerina barbadoensis* in Sample 123-765C-18R, CC, also suggests that this interval is no higher than Zone P19.

Eocene

Lower Eocene assemblages were identified in four samples. A major faunal break occurs in Core 123-765C-19R, and much of the middle and upper Eocene may be missing. The highest recovered Eocene assemblage is from Sample 123-765C-19R, CC (at 525.6 mbsf), which contains a poorly preserved assemblage dominated by the *Acarinina spinuloinflata*/*Acarinina bullbrooki* lineage. The occurrence of these species together with *Morozovella caucasica* and *Morozovella aragonensis* indicates that the sample lies within Zones P9 to P10. The microfauna recovered from three Core 123-765C-20R samples contains few identifiable elements. The presence of common *Morozovella subbottinae* and rare *Morozovella aragonensis* in Sample 123-765C-20R-2, 52–53 cm (at 532.8 mbsf) suggests that this level lies within Zones P7-P8; the occurrence of *Morozovella lensiformis* in Sample 123-765C-20R-2, 80–81 cm (at 533 mbsf) indicates a level no lower than Zone P6; and the presence of *Acarinina soldadoensis* in Sample 123-765C-20R, CC (at 533.1 mbsf) places this no lower than Zone P5.

Upper Cretaceous

Upper Cretaceous microfaunas were recovered from a condensed sequence between approximately 566 and 594 mbsf in Hole 765C. Most assemblages can be correlated only broadly with the tropical zonation of Caron (1985) because of low species diversity, poor preservation, and much reworking.

The youngest recovered assemblage comes from Sample 123-765C-23R, CC (at 566.3 mbsf) and contains relatively diverse heterohelicids, including *Heterohelix planata*, *Heterohelix pseudotessera*, *Pseudotextularia elegans*, and *Gublerina cuvillieri*; abundant *Rugoglobigerina rugosa* and *Rugoglobigerina milamensis*; a restricted *Globotruncana* association of *G. arca*, *G. linneiana*, *G. bulloides*, and *G. ventricosa*; and *Rosita fornicata*. This assemblage is indicative of the upper Campanian to lower Maestrichtian (around the *Globotruncana calcarata* to *Globotruncana aegyptiaca* Zone of Caron, 1985). Rare specimens that resemble *Globotruncanella havanensis* and *Globotruncanella petaloidea* also occur here and may indicate an early Maestrichtian, rather than late Campanian, age for the sample.

Core 123-765C-24R (569.3–579 mbsf) contains low-diversity assemblages, including *G. arca*, *G. linneiana*, *G. bulloides*, *G. ventricosa*, and *Rosita fornicata*. The heterohelicid component of the fauna is restricted to *Heterohelix reussi* and, toward the top of the core, *H. pseudotessera* and *H. planata*. This assemblage suggests an early to middle Campanian age. *Globotruncana ventricosa*, which marks the base of the middle Campanian *G. ventricosa* Zone of Caron (1985), is known to range from at least the Santonian in the western Australian region (Belford, 1981).

Assemblages dominated by *Dicarinella* occur in Core 123-765C-25R. Sample 123-765C-25R-1, 103–105 cm (at 579.1 mbsf) contains *D. algeriana* and *D. canaliculata*, together with rare *Marginotruncana pseudolinneiana*, and probably belongs within the Coniacian *Dicasanella primitiva* Zone of Caron (1985). A more primitive assemblage of *Dicarinella* (*D. algeriana*, *D. imbricata*, *D. hagni*) occurs in Sample 123-765C-25R, CC (at 585.6 mbsf) and is associated with abundant *Praeglobotruncana stephani*. These species suggest that the lower portion of the core lies within the upper Turonian *Marginotruncana sigali* Zone of Caron (1985).

The upper Cenomanian is represented in Sample 123-765C-26R-4, 79–84 cm (at 593.6 mbsf) by an assemblage that includes *Rotalipora greenhornensis*, *Rotalipora reicheli*, *R. appenninica*, *P. stephani*, *Praeglobotruncana gibba*, and *Praeglobotruncana delrioensis*. This is a mixed association that contains elements belonging both to the *Rotalipora reicheli* Zone and *Rotalipora cushmani* Zone of Caron (1985). *Planomalina buxtorfi* also occurs in the sample but is probably reworked from the upper Albian.

Lower Cretaceous

Planktonic foraminiferal assemblages occur sporadically in the interval from Cores 123-765C-27R to -45R (600–777 mbsf) and are dominated by primitive *Hedbergella*. In the material studied, the LO of *Hedbergella planispira* is in Sample 123-765C-38R-3, 32–37 cm (at 705.8 mbsf), and the LO *Hedbergella delrioensis* is in Sample 123-765C-40R-1, 10–12 cm (at 721 mbsf). This suggests that Core 123-765C-40R is no lower than Aptian. The occurrence of rare *Globigerinelloides ferreolensis* in Samples 123-765C-34R, CC, and -37R-4, 50–52 cm suggests that the interval between 669.6 and 698 mbsf lies within the middle Aptian to upper Aptian.

The lowest planktonic foraminiferal assemblage recovered at this site (from Sample 123-765C-45, CC, at 776.9 mbsf) contains *Caucasella hoterivica*, *Guembelitria* sp., and *Hedbergella* sp. According to Caron (1985), *Caucasella hoterivica* ranges from the Hauterivian to lower Aptian.

Reworking

Evidence for reworking of foraminiferal assemblages occurs throughout Hole 765. Levels that contain reworked foraminifers much older than the time of deposition are listed in Table 7. Paleogene and Upper Cretaceous specimens are encountered throughout the Miocene. Reworking is conspicuous in some of the Oligocene samples, where Upper Cretaceous and lower to middle Eocene foraminifers are common. Many of the Upper Cretaceous samples contain specimens reworked from the Albian to Coniacian.

Benthic Foraminifers

Cenozoic

We examined benthic foraminifers in core-catcher samples from Hole 765B and the upper 200 m of Hole 765C (Cores 123-765C-1R to -21R). The biostratigraphic scheme of van Morkhoven et al. (1986) was used exclusively for the Cenozoic at Site 765. Preservation of core-catcher samples from Hole 765B ranges from poor to good and generally deteriorates with increasing depth. The abundance of calcareous benthic foraminifers relative to planktonic foraminifers is generally low. Altogether, only four of the 41 samples examined from Hole 756B were barren of foraminifers. These barren samples were from the radiolarian-bearing sediments near the top of the hole (Samples 123-765B-2H, CC; -4H, CC; -7H, CC; and -9H, CC).

Table 7. Depositional age and age of reworked planktonic foraminifers at Site 765.

Core	Depositional age	Age of reworked foraminifers
123-765B-22X	late Miocene	Oligocene
123-765B-30X	late Miocene	Late Cretaceous
123-765B-31X	late Miocene	Late Cretaceous
123-765B-38X	late Miocene	Late Cretaceous
123-765B-41X	middle Miocene	Late Cretaceous
123-765C-1R	middle Miocene	Late Cretaceous
123-765C-5R	middle Miocene	Late Cretaceous
123-765C-7R	middle Miocene	early Eocene; Late Cretaceous
123-765C-9R	middle Miocene	Late Cretaceous
123-765C-12R	early Miocene	Late Cretaceous
123-765C-13R	early Miocene	early-late Eocene; Late Cretaceous
123-765C-16R	late Oligocene	early-middle Eocene; Late Cretaceous
123-765C-19R	early Oligocene	early-middle Eocene; Late Cretaceous
123-765C-23R	late Campanian–early Maestrichtian	Coniacian
123-765C-24R	Campanian	Turonian; Cenomanian
123-765C-25R	Turonian	Cenomanian
123-765C-26R	Cenomanian	late Albian

Most of the foraminifer-bearing samples from Hole 765B occur in turbidite sediment and display evidence of size sorting. In 10 of the core-catcher samples (123-765B-16H, CC; -18H, CC; -21X, CC; -22X, CC; -24X, CC; -26X, CC; -28X, CC; -32X, CC; -39X, CC; and -40X, CC), only small-sized foraminifers are present, and the benthic assemblage is dominated by small specimens of *Brizalina* and *Uvigerina*. These assemblages are probably derived from upper bathyal depths. The remaining samples from Hole 765B contain diverse assemblages of upper to middle bathyal calcareous benthic foraminifers. The common background elements of these assemblages include *Bulimina aculeata*, *B. alazanensis*, *B. marginata*, *B. striata*, *Cibicidoides bradyi*, *C. cicatricosus*, *C. mundulus*, *C. pachyderma*, *C. robertsonianus*, *Globocassidulina subglobosa*, *Hoeglundina elegans*, *Laticarinina pauperata*, *Lenticulina atlantica*, *Melonis barleeanum*, *Planulina wuellerstorfi*, *Planulina* sp. 1, *Planulina* sp. 3, *Pleurostomella spp.*, *Pullenia bulloides*, *P. quinqueloba*, *Pyrgo murrhina*, *Oridorsalis umbonatus*, *Osangularia mexicana*, *Sigmoilopsis schlumbergeri*, *Siphonina pozonensis*, *Sphaeroidina bulloides*, *Stilostomella* spp., *Uvigerina hispida*, *U. hispidocostata*, and *U. peregrina*. In general, the typical deep-water species, such as *Nuttallides umbonifera*, *Melonis pompilioides*, and *Epistominella exigua,* occur only rarely and sporadically. However, a number of benthic foraminifers in Site 765 samples have stratigraphically useful LOs and compare well with the biostratigraphy of van Morkhoven et al. (1986). These are as follows:

LO *Planulina dohertyi* (N18) in Sample 123-765B-19H, CC.
LO *Plectofrondicularia parri* (N17) in Sample 123-765B-20X, CC.
LO *Planulina renzi* (N17) in Sample 123-765B-23X, CC.
LO *Cibicidoides dutemplei* (N20) and *Plectofrondicularia vaughani* (N17) in Sample 123-765B-27X, CC.
LO *Cibicidoides havanensis* (N10) in Sample 123-765B-30X, CC.
LO *Cibicidoides alazanensis* (N9) in Sample 123-765B-35X, CC.
LO *Cibicidoides barnetti* (N10) and *Siphonina tenuicarinata* (N9) in Sample 123-765B-38X, CC.
LO *Planulina mexicana* (N12) in Sample 123-765C-41X, CC.

Benthic foraminiferal assemblages in the upper 10 core-catcher samples from Hole 765C are similar to those from the bottom of Hole 765B. Samples 123-765C-1R, CC, through -10R-1, 79–81 cm, contain sorted assemblages of small-sized foraminifers. The benthic assemblage in these samples is dominated by *Brizalina*, *Uvigerina*, and small specimens of *Bulimina*. Sample 123-765C-10, CC, is barren of foraminifers.

Below Core 123-765C-11R, the benthic assemblage becomes more diverse and size-sorting is less obvious. Sample 123-765C-12R, CC, contains large specimens of *Lenticulina*, *Cibicidoides matanzaensis*, *C. mundulus*, *Laticarinina*, *Siphonina*, and *C. pachyderma*. Sample 123-765C-13R, CC, contains a more diverse assemblage, with definite lower Miocene species (*Cibicidoides mexicanus*, *Planulina ambugua*, and *Uvigerina spinulosa*). These three species have their LO in Zone N5, according to van Morkhoven et al. (1986). Core-catcher samples from Cores 123-765C-14R and -15R are barren of foraminifers, and Sample 123-765C-16R-2, 5–7 cm, contains reworked Upper Cretaceous agglutinated species. Sample 123-765C-16R-4, 94–96 cm, contains a diverse lower Miocene assemblage, and the LOs of *Cibicidoides dohmi*, *Bulimina jarvisi*, and *Hanzawaya ammophilia* were observed in this sample. Assemblages observed in samples from Cores 123-765C-17R through -21R are generally impoverished, but one sample (123-765C-18R, CC) contains an assemblage composed of stratigraphically long-ranging calcareous benthic species (*Pleurostomella*, *Oridorsalis*, *Pullenia bulloides*, *Gyroidinoides*, and *Bulimina jarvisi*), which is typical of the lower Oligocene.

Cretaceous

The highest Cretaceous benthic foraminiferal assemblage was observed in Sample 123-765C-22R, CC. This sample contains abundant terrigenous detritus, and the assemblage consists entirely of coarsely agglutinated taxa. An assemblage consisting entirely of fine-grained agglutinated taxa was reported from the Upper Cretaceous of DSDP Hole 261 (Krasheninnikov, 1974). Sample 123-765C-22R, CC, contains good specimens of *Hormosina ovulum gigantea*, together with *Rhabdammina*, *Rhizammina*, *Glomospira*, *Ammodiscus*, *Psammosphaera*, *Haplophragmoides*, and *Spiroplectammina parvissima*, and belongs in the *Haplophragmoides gigantea* Zone of Geroch and Nowak (1984). However, the presence of *S. parvissima* suggests that Sample 123-765C-22R, CC, is in the lower part of the *H. gigantea* Zone, since the LO of this species in the North Atlantic is in the lower Maestrichtian (Kuhnt and Kaminski, unpubl. data).

Upper Cretaceous calcareous benthic foraminifers occur in the interval that includes Cores 123-765C-23R to -26R. The highest level with this assemblage was found in Sample 123-765C-23R, CC. This sample still contains rare *Hormosina ovulum gigantea* and has been assigned to the *H. gigantea* Zone. The dominant species are *Nuttallides truempyi* and *Stensioina beccariiformis*, which occur with species of *Aragonia*, *Gavelinella*, *Globorotalites*, *Gyroidinoides*, *Loxostomium*, *Praebulimina*, *Osangularia*, *Reussella*, and *Stensioina pommerana*. Sample 123-765C-24R-3, 128–129 cm, contains common specimens of *Marssonella* and *Gaudryina*, in addition to the calcareous benthic foraminifers listed above. Sample 123-765C-24R, CC, is barren of foraminifers.

A different assemblage was found in Sample 123-765C-26R, CC. This sample contains an agglutinated assemblage consisting of *Ammodiscus*, *Clavulinoides*, *Gaudryina*, *Glomospira*, *Labrospira*, *Haplophragmoides*, *Marssonella*, *Plectorecurvoides alternans*, *Praecystammina*, and *Trochammina*. This sample has been assigned to the upper Albian to lower Cenomanian *P. alternans* Zone of Geroch and Nowak (1984). Sample 123-765C-27R, CC, contains an agglutinated assemblage similar to the one in 123-765C-26R, CC, but also contains *Haplophragmium* sp. cf. *H. lueckei*, which was reported by Krasheninnikov (1974) from Cores 7 and 8 of DSDP Hole 261. Sample 123-765C-29R, CC, contains only a few specimens of *Rhabdammina* and *Glomospira*, and all core-catcher samples examined from Samples 123-765C-30R, CC, to -50R, CC, are barren of foraminifers. Within this interval in Hole 765C, only two samples taken from within the cores contain any foraminifers. Samples 123-765C-37R-4, 50–52 cm, and -38R-3, 32–37 cm, were collected from turbidite layers and contain small, sorted specimens of nodosariids, *Lenticulina*, *Gyroidinoides*, *Gavelinella*, *Loxostomium*, *Pullenia*, and *Gaudryina*.

Below the barren interval, benthic foraminiferal assemblages from the dark claystones are initially sparse and display low diversity. Sample 123-765C-51R, CC, contains a single specimen of *Rhizammina*. Below this level in Hole 765C, the assemblages become increasingly more diverse with depth. Sample 123-765C-52R-3, 75–79 cm, contains species of *Ammodiscus* and *Glomospira*, along with tubular fragments. The interval from Core 123-765C-56R to the base of the sediment column in Core 123-765C-62R contains a diverse agglutinated benthic assemblage that includes *Ammodiscoides*, *Ammodiscus*, *Ammobaculoides*, *Bathysiphon*, *Glomospira*, *Glomospirella*, *Gaudryina*, *Hippocrepina*, *Haplophragmium*, *Haplophragmoides*, *Hormosina*, *Hyperammina*, *Kalamopsis*, *Lagenammina*, *Marssonella*, *Paratrochamminoides*, *Plectorecurvoides*, *Psammosphaera*, *Pseudobolivina*, *Pseudoreophax*, *Reophax*, *Rhabdammina*, *Rhizammina*, *Saccammina*, *Spiroplectammina*, *Subreophax*, *Textularia*, *Trochammina*, *Turritellella*, *Uvigerinammina*, and *Verneuilinoides*. However, two of the 18 samples examined from Cores 123-765C-52R to -62R contain calcareous benthic foraminifers. The first sample (123-765C-56R, CC) contains a mixed assemblage of calcareous and agglutinated benthic foraminifers that includes *Dorothia praehauteriviana*, an index species for the lower Valanginian (Moullade, 1984). The second sample (123-765C-61R-5, 58–60 cm) contains rare nodosariids and lenticulinids that include the species *Lenticulina subangulata*, a species known from the Valanginian of DSDP Site 416 in the eastern North Atlantic (Sliter, 1980). Other stratigraphically important occurrences in this interval include the FO of *Verneuilinoides neocomiensis* in Sample 123-765C-61R, CC, which defines the base of the *V. neocomiensis* Zone of Geroch and Nowak (1984); the LO of *Trochammina quinquiloba* in Sample 123-765C-60R-2, 37–40 cm; the LO of *Haplophragmium inconstans* in Sample 123-765C-59R-2, 121–125 cm, which is placed in the upper Valanginian, and the FO of *Hormosina ovulum* in Sample 123-765R-60R, CC, which occurs in the Hauterivian, according to the biostratigraphic scheme of Geroch and Nowak (1984). Interestingly, the benthic assemblage from sediments directly overlying basement (Sample 123-765C-62R-4, 25–27 cm) contains the species *Hippocrepina depressa* and *Trochammina abrupta*. The reported FO of these deep-water benthic species in the Carpathians is in the Hauterivian and lower Barremian, respectively (Geroch and Nowak, 1984), but their earlier presence in Hole 765C may be due to earlier subsidence of the Argo Basin.

Calcareous Nannofossils

Abundance and Preservation

The presence of calcareous nannofossils throughout the Site 765 section may be directly related to the presence of graded carbonate sequences, which for the most part are thought to represent turbiditic flow deposits. The site is presumed to have been situated below the CCD for all, or most, of its depositional history. Carbonate present within the sediments thus is most probably redeposited from adjacent slope or shelf areas lying above the CCD. Calcareous nannofossils are always present in the graded carbonate intervals and generally make up a significant proportion of the sediment. Within individual graded units, however, there may be some variation in abundance, diversity, and quality of preservation. Generally, the coarser-grained basal units of the flow deposits contain sparse nannofossil assemblages of relatively low diversity and poor preservation. This contrasts with foraminiferal and radiolarian residues that are more abundant, diverse, and well-preserved at the turbidite bases. Toward the top of the graded units the lithology is predominantly nannofossil ooze containing abundant, high diversity, and well-preserved nannofossil assemblages. Intervals completely barren of nannofossils are commonly observed at the top of the graded units, and these are thought to represent true abyssal sedimentation, devoid of calcareous material as a result of the position of this site beneath the CCD. Alternately, some of these horizons may simply represent the leached tops of sediment flow deposits. In the Cenozoic turbidite sediments, the nannofossil assemblages commonly exhibit significant degrees of reworking, which often results in an inability to recognize finer biostratigraphic subdivisions. A number of the coarser debris deposits also include lithified clasts that contain calcareous nannofossils of Middle Jurassic and Late Cretaceous age. The mixing of assemblages in the Mesozoic sediments is less pronounced or apparently absent and must reflect deposition by less erosive sediment flows.

Cenozoic Biostratigraphy

The first core of Hole 765A was presumed to have missed the mud line, and thus only one core was retrieved. Sample 123-765A-1H, CC, contains a mixed nannofossil assemblage that indicates a Pleistocene age by the common presence of *Calcidiscus macintyrei*, *Gephyrocapsa oceanica*, *Gephyrocapsa caribbeanica,* and *Pseudoemilinia lacunosa*. No differentiation based on the Pleistocene zones of Gartner (1977) is possible.

The youngest turbidite cored in Hole 765B is in Core 123-765B-1H, which contains a nannoflora assemblage that indicates a Pleistocene age. The absence of *Emiliania huxleyi* and presence of *G. oceanica* at the top of Core 123-765B-1H and in Sample 123-765B-1H, CC, suggest that both samples are between the *Helicopontosphaera selli* and the *G. oceanica* zones of Gartner (1977). Reworked Pliocene, Miocene, Paleocene, and Cretaceous specimens are fairly common and well preserved. Apparent mixing of upper Pliocene and Pleistocene nannofossil assemblages does not allow for differentiation of Gartner's zones (1977).

A Pleistocene age has also been also given for turbiditic sediment in Sections 123-765B-2H, CC, through -9H, CC, based on the appearance and absence of the above-mentioned species. Again, no differentiation of Gartner's (1977) Pleistocene zones is possible in these cores because of mixed assemblages. Extensive reworking of well-preserved Pliocene and Miocene flora, particularly discoasters, can be seen in Samples 123-765B-5H, CC; -6H, CC; and -7H, CC.

Sample 123-765B-10H, CC, is essentially barren of calcareous nannofossils, while Samples 123-765B-11H, CC, through -14H, CC, have been placed in Zone CN12 (*Discoaster brouweri* Zone), based on the presence of abundant *P. lacunosa* and absence of *G. oceanica*. This signifies an age of late Pliocene. Okada and Bukry (1980) did not specifically use the first appearance of *P. lacunosa* as a zonal marker; however, Perch-Nielsen (1985) reported that the first appearance of this species closely coincides with the base of Zone CN12. Fairly common reworking of middle Pliocene sphenoliths, discoasters, and reticulofenestrids makes the distinction of Zone CN12 difficult.

Samples 123-765B-15H, CC, through -17H, CC, have been placed in Zone CN11 (*Reticulofenestra pseudoumbilica* Zone) as indicated by the lack of *P. lacunosa* (except in Sample 123-765B-15H, CC) and presence of abundant and well-preserved *R. pseudoumbilica*, *Sphenolithus abies,* and *Sphenolithus neoabies*. This suggests an age of early Pliocene. A slight overlap in the ranges of *P. lacunosa* and *R. pseudoumbilica* can be observed in Sample 123-765B-15H, CC.

In Hole 765B, upper Miocene sediment begins in Sample 123-765B-18H, CC, and continues to the base of the hole in Sample 123-765B-41X, CC. Samples 123-765B-18H, CC, through -28X, CC, have been placed in the *Discoaster quinqueramus* Zone (CN9), as indicated by the presence of the nominative species *D. quinqueramus* and the lack of *Discoaster asymmetricus*, *Ceratolithus acutus*, and *C. rugosus*. The absence of Zone CN10 indicates a significant hiatus or a highly condensed section in the lower Pliocene (approximately 1.9 Ma according to Berggren et al., 1985a) between Samples 123-765B-17H, CC, and -18H, CC. Samples 123-765B-21X, CC, through -28X, CC, and samples taken from within these cores contain primarily poorly preserved, low-diversity nannofossil assemblages. This poor preservation continues through the underlying Subzone CN8b, and thus its separation from Zone CN9 is difficult.

Subzone CN8b (*Discoaster neorectus* Subzone) begins in Section 123-765B-29X, CC, and continues through Section 123-765B-33X, CC. This is indicated by the lack of *D. quinquera-*

mus in Section 123-765B-29X, CC, and the presence of *Discoaster pentaradiatus* and *D. neorectus* in Sections 123-765B-29X, CC, through -33X, CC. Preservation improves and assemblage diversity increases toward the base of this subzone. Subzone CN7b (*Catinaster calyculus* Subzone) is easily recognized and begins in Sample 123-765B-34X, CC, and continues through Samples 123-765B-35X, CC. This is signified by the lack of *D. neorectus* and the common presence of *C. calyculus*; however, there is an unexplainable lack of *Discoaster hamatus*, the last appearance of which defines the top of Zone CN7. Preservation is fairly good in this subzone.

Middle Miocene sediment occurs in the underlying Sample 123-765B-36X, CC, which is the only sample placed in Zone CN6 (*Catinaster coalitus* Zone). This is suggested by the presence of *C. coalitus* and the absence of *C. calyculus*. Preservation is poor in this section. Poor preservation and depauperate assemblages continue through the rest of Hole 765B. Sections 123-765B-37X, CC, through -41X, CC, have been tentatively placed in undifferentiated Zones CN3 through CN5, based on the presence of *Calcidiscus macintyrei* and the absence of *Sphenolithus heteromorphus*.

Hole 765B was terminated after Core 123-765B-41X because of low recovery levels with the XCB coring system as the sediments became progressively more lithified. Coring in Hole 765C was resumed in middle Miocene sediments at 350.2 mbsf using the RCB coring system. The first section of Hole 765C, Section 123-765C-1R, has been placed in Zone CN6, as indicated by the presence of species listed above. Sample 123-765C-2R, CC, contains sparse, undiagnostic nannofossils, while Samples 123-765C-3R, CC, and 123-765C-4R, CC, contain an assemblage that includes *Discoaster kugleri* and excludes *C. coalitus* and thus are placed in Subzone CN5b (*D. kugleri* Subzone).

Foraminiferal data suggest that Samples 123-765C-5R, CC, through -8R, CC, are between Zones N13 and N9, which lie entirely in Subzone CN5a (*Coccolithus miopelagicus* Subzone) according to Bolli et al. (1985). Nannofossil species from this interval include common *Cyclicargolithus floridanus*, *S. heteromorphous*, and *Discoaster exilis*. *Cyclicargolithus floridanus* and *S. heteromorphous* may be reworked, as indicated by their scattered appearance, or they may extend higher here than in other areas. Although Bukry (1973) and Perch-Nielsen (1985) indicated that the first appearance of *Discoaster exilis* extends below the base of Zone CN5, foraminifers markers indicate that the first appearance of this species in Hole 765C occurs very near the base of this subzone. Therefore, this datum hasd been used to mark the base of Subzone CN5a (Fig. 65), which occurs in the interval between Samples 123-765C-5R, CC, and -8R, CC.

Only sparse and undiagnostic nannofossils can be seen in Samples 123-765C-9R, CC, and -10R, CC, and thus no age determination is possible. Samples 123-765C-11R, CC, through 123-765B-13R, CC, have been placed in Zone CN4 (*S. heteromorphous* Zone) based on the presence of *S. heteromorphous* and *C. macintyrei*.

Lower Miocene sediment, found in Sample 123-765C-14R, CC, has been assigned to Subzone CN1c (*Discoaster druggi* Subzone), based on the presence of *D. druggi* and the absence of *Sphenolithus belemnos*. This indicates a significant unconformity or highly condensed section between Samples 123-765C-13R, CC, and 123-765C-14R, CC, of at least 4.4 Ma, according to Berggren et al. (1985b).

Sample 123-765C-15R, CC, is barren, while upper Oligocene sediment can be found in Sample 123-765C-16R, CC. The latter has been placed in Subzone CN19b (*Dictyococcites bisectus* Subzone), based on the presence of *Sphenolithus ciperoensis* and the absence of *S. distentus*. *Sphenolithus distentus* is found along with *S. ciperoensis* in Sample 123-765C-17R, CC, and thus this sample has been placed in Subzone CN19a (*Cyclicargolithus floridanus* Subzone). Lower Oligocene marker species are found in Sample 123-765C-18R, CC, which has been placed in Subzone CP16C (*Reticulofenestra hillae* Subzone), based on the presence of *R. umbilica* and common *Helicopontosphaera reticulata* and the absence of *Ericsonia formosa* and *S. distentus*. This suggests a condensed section or unconformity between Cores 123-765C-17R and -18R of approximately 4.4 Ma, according to Berggren et al. (1985a).

Sample 123-765B-19R, CC, is barren of calcareous nannofossils; however, both Samples 123-765B-19R-1, 105–106 cm, and -19R-2, 108–109 cm, have been placed in Subzone CP16b (*E. formosa* Subzone), based on the presence of *R. umbilica*, *E. formosa*, and *Isthmolithus recurvus* and the absence of unreworked *Discoaster barbadiensis* and *D. saipanensis*. Farther down in this core, lower Eocene sediment is found in Sample 123-765B-19R-3, 112–113 cm, which has been placed in Subzone CP12a (*Discoasteroides kuepperi* Subzone), based on the presence of *Discoaster sublodoensis* and *D. kuepperi* and the absence of *Nannotetrina quadrata*. This indicates an unconformity between Sections 123-765B-19R-2 and -19R-3, which spans at least 13.7 Ma, according to Berggren et al. (1985b). Lower Eocene sediment is again found in Sample 123-765B-20R, CC, which has been placed in Subzone CP9b (*Discoaster binodosus* Subzone), based on the presence of *Tribrachiatus orthostylus* and absence of *Discoaster lodoensis*.

Core 123-765C-21R possesses a nannoflora of upper Paleocene age and has been placed in Zone CP8 (*Discoaster multiradiatus* Zone NP9; Martini, 1971), based on the presence of *Fasciculithus tympaniformis*, *Toweius eminens*, *Chiasmolithus bidens*, *Discoaster nobilis*, *Discoaster mohleri*, and rare *Discoaster multiradiatus* in Sample 123-765C-21R-1, 16–17 cm. The lower part of the core (Sample 123-765C-21R, CC) is barren. The interval from Sample 123-765C-22R-1, 149–150 cm, to Sample 123-756C-22R-4, 108–109 cm, yields a well-preserved lower to lower upper Paleocene flora ranging in age from Zone CP6 (*Discoaster mohleri* Zone NP7) to Zone CP2 (*Chiasmolithus danicus* Zone NP3).

The co-occurrence of *F. tympaniformis*, *T. eminens*, *Heliolithus kleinpellii*, and very rare *D. mohleri* in Samples 123-765C-22R-1, 149–150 cm, to -22R-2, 1–2 cm, places the upper part of Core 123-765C-22R in Zone CP6 (NP7). The presence of *Cruciplacolithus tenuis* and *Chiasmolithus danicus* in Sample 123-765C-22R-4, 108–109 cm, indicates Zone CP2 (NP3) for the lower part of this core. Samples taken from throughout Section 123-765C-22R-5, including the core catcher, are barren of calcareous nannofossils. Reworked Upper Cretaceous species are present in all productive samples from Core 123-765C-22R; however, it is only in Sample 123-765C-22R-1, 23–24 cm, that these elements become dominant to the exclusion of Paleocene specimens.

Mesozoic Biostratigraphy

Throughout this account of Mesozoic nannofossil biostratigraphy, the zones of Sissingh (1977) will be referred to by the abbreviation CC.

Cores 123-765C-23R to -26R are Late Cretaceous in age. Sample 123-765C-23R-1, 17–18 cm, is the first sample to contain a purely Upper Cretaceous nannoflora, of which *Quadrum trifidum*, *Reinhardtites levis*, *Quadrum gothicum*, and *Ceratolithoides aculeus* are characteristic of the *Quadrum trifidum* and the *Tranolithus phacelosus* Zone (CC23) of late Campanian to early Maestrichtian age. Since *Aspidolithus parcus constrictus*, a species whose last appearance marks the Campanian/Maestrichtian boundary, is still present, the sample might be assigned a Campanian age. Therefore, strata of earliest Paleocene through Maastrichtian age are either missing or are heavily condensed and represented by the barren interval in Section 123-765C-22R-5.

The interval between Sample 123-765C-23R-2, 20 cm, and Sample 123-765C-23R, CC, is late Campanian in age (*C. aculeus* Zone CC20 to *Q. trifidum* Zone CC22) because of the presence of *C. aculeus*, *Q. gothicum*, *Reinhardtites levis*, *A. parcus constrictus*, and *Eiffellithus eximius*.

The early Campanian (*Aspidolithus parcus* Zone CC18 and *Calculites ovalis* Zone CC19) is represented by the presence of *Reinhardtites anthophorus*, *E. eximius*, *Marthasterites furcatus*, *A. parcus*, and *A. parcus constrictus*, as is observed in Sample 123-765C-24R-1, 147–147 cm, to Sample 123-765C-24R-3, 57–58 cm. *Ceratolithoides aculeus*, whose first appearance characterizes the base of the overlying *C. aculeus* Zone (CC20), is not present. The lower part of Section 123-765C-24R-4 to the base of Core 123-765C-24R consists of a nannoflora of Santonian age (*Micula decussata* Zone CC14 to *R. anthophorus* Zone CC15 or *Calculites obscurus* Zone CC17?). Diagnostic fossils are *Quadrum gartneri*, *M. decussata*, *R. anthophorus*, and *M. furcatus*, including *Lithastrinus septenarius* in Sample 123-765C-24R, CC. Because the genera *Lucianorhabdus* and *Calculites* are rare or even absent, it is not clear whether the overlying *L. maleformis* and *C. obscurus* zones (CC16 and CC17) are absent or simply unrecognizable due to environmental factors. A reworked *Calculites obscurus/ovalis*-rich assemblage is observed in the Neogene (Sample 123-765C-13R, CC). This might suggest a hiatus at Site 765 between the upper lower Santonian *R. anthophorus* Zone (CC15) and the lower Campanian *A. parcus* Zone (CC18).

Core 123-765C-25R is Turonian to earliest Santonian age (*Q. gartneri* to *M. decussata* Zone [CC11 to CC14]), based on the occurrences of *E. eximius* (Sample 123-765C-25R-3, 138–139 cm), *M. furcatus* (Sample 123-765C-25R-2, 46–47 cm), and *M. decussata* (Sample 123-765C-25R-1, 13–14 cm). These intervals have been placed in the *L. maleformis* (CC12), *M. furcatus* (CC13), and *M. decussata* (CC14) zones, respectively. Samples 123-765C-25R-4, 140–150 cm, to 123-765C-26R-1, 25–26 cm, are assigned an early Turonian age (*Q. gartneri* Zone CC11) because of the presence of *Q. gartneri*, *Eiffelithus turriseiffelii*, *Eprolithus floralis*, and *Lithastrinus moratus*.

Samples 123-765C-26R-1, 128–129 cm, to -26R-5, 25–26 cm, contain *Corollithion kennedyi*, a well-defined marker, which gives these beds a Cenomanian age (*Microrhabdulus decoratus* Zone [CC10] and upper part of the *E. turriseiffelii* Zone CC9).

The interval from Section 123-765C-26R-5 to -62R-1 is of Early Cretaceous age. The first occurrence of *Corollithion kennedyi* in Sample 123-765C-26R-5, 25–26 cm, approximates the Zone CC9/CC10 boundary (in the absence of *Microrhabdulus decoratus*), which is situated within the lower Cenomanian. The FO of *Eiffelithus turriseiffeli* in Sample 123-765C-27R-1, 89–90 cm, marks the boundary between the *Prediscosphaera columnata* Zone (CC8) and *E. turriseiffelii* Zone (CC9), which is of late Albian age. The Cenomanian/Albian stage boundary thus falls between Samples 123-765C-26R-5, 25–26 cm, and -27R-1, 30–31 cm.

The interval between Sample 123-765C-27R-1, 89 cm, and Sample -32R-1, 110 cm, lies within the *P. columnata* Zone (CC8), which is of Albian age. The FO of *P. columnata* marks the base of the zone. The CC8 Zone designation for this interval is also confirmed by the FO of *Tranolithus phacelosus*, which can be observed in Sample 123-765C-28, CC. In addition, the interval includes the LOs of *Vagalapilla* cf. *matalosa*, *Flabellites biforaminis*, *Hayesites albiensis* (Sample 123-765C-28R-1, 146 cm), and *Bukrylithus ambiguus* (Sample 123-765C-28R, CC). The underlying *Chiastozygus litterarius* Zone (CC7, Subzone B; upper Aptian to lower Albian) is found between Samples 123-765C-32R-1, 110–111 cm, and -34R, CC. The zone was defined using the FO of *Hayesites albiensis* (in the absence of *Micrantholithus obtusus*), which was recorded in Sample 123-765C-34R, CC. The FO of *Eprolithus floralis* also approximates the zonal base, and this is recorded in Sample 123-765C-34R, CC. The Albian/Aptian boundary falls within Zone CC7B and is thus situated in the interval between Samples 123-765C-32R-1, 110–111 cm, and -34R, CC.

The interval from Sample 123-765C-34, CC, to Sample 123-765C-40R-3, 2–3 cm, is of early Aptian age (CC7A) and is characterized by nannofossil assemblages containing *Rhagodiscus angustus* and, more rarely, *Chiastozygus litterarius*. This interval also includes the FO of *Flabellites biforaminis* (Sample 123-765C-37R-4, 7–8 cm) and rare occurrences of *Nannoconus* sp. (Sample 123-765C-36R, CC), and *Conusphaera mexicana* (Samples 123-765C-36R, CC and 123-765C-34R, CC). The remaining samples from Sections 123-765C-40R-3 and -40R-4 yielded low-diversity assemblages dominated by *Watznaueria barnesae* and *Watznaueria fossacincta,* and no age designation is possible. There follows an interval of dark green and gray claystones devoid of calcareous matter and thus barren of nannofossils.

The next productive sample, Sample 123-765C-55R, 41–42 cm, yielded *Cruciellipsis cuvillieri*, indicating a Berriasian to Hauterivian age. The barren interval thus may include at least the *Lithraphidites bollii* and *Micrantholithus hoschulzii* Zones (CC5 and CC6), which cover the uppermost Hauterivian and Barremian. A more diagnostic flora is found in Sample 123-765C-56R-3, 142–143 cm, with the presence of *C. cuvillieri* (Berriasian to upper Hauterivian), *Speetonia colligata* (Valanginian to Hauterivian), and *Tegumentum striatum* (Valanginian-Hauterivian), suggesting a Valanginian to Hauterivian age (CC2 to CC4). The lack of the Valanginian marker species, *Tubodiscus verenae* (reported from DSDP Site 261), may indicate a Hauterivian only age for this sample. Relatively abundant and diverse nannofossil assemblages are found down to Section 123-765C-58R-1, and the lowest assemblage in this interval includes *C. cuvillieri*, *Seribiscutum salebrosum*, *T. striatum*, and *Assipetra infracretacea*, which similarly indicates a Valanginian to Hauterivian age. This interval is stratigraphically somewhat problematic because of the absence of key marker species that are usually used to divide the earliest Cretaceous period, for example, *T. verenae*, *Diadorhombus rectus*, *Calcicalathina oblongata*, *L. bollii*, and *Nannoconus* spp.

The deepest productive samples from Site 765 come from Cores 123-765C-61R and -62R and yield only etched assemblages of *Watznaueria manivitae*, a large coccolith species that is strongly constructed and thus very resistant to dissolution. The biostratigraphic value of this species is rather limited as it ranges from Callovian to Valanginian. However, Cooper (1984) noted that *Watznaueria manivitae* occurs most abundantly in the upper Tithonian and becomes rarer across the Jurassic/Cretaceous boundary. This statistical observation may not be applicable at this site due to the geographic separation from the area of research in Mediterranean Tethys, although an equivalent statistical trend was recorded from DSDP Site 261.

The assemblages recovered from the Lower Cretaceous of Hole 765C are distinct from those of the better-known European and Atlantic areas in a number of ways:

1. Most of the short-range marker species used by biostratigraphic schemes for this time interval (e.g., Thierstein, 1973; Sissingh, 1977) are not observed (see above).
2. Typical Mediterranean-Tethyan nannofloral components, particularly nannoconids and *Conusphaera mexicana*, are absent or extremely rare (i.e., one or two specimens).
3. A number of taxa have significantly differing ranges. Particularly striking is the common and consistent occurrence of *Vagalapilla* cf. *matalosa* through the entire Hauterivian to Albian sequence. This species has been reported having an FO in the upper Barremian. In the Aptian it was used as a zonal marker (Roth, 1978).

4. The assemblages are generally of lower diversity and dominated by *Watznaueria* spp.

These nannofloral variations illustrate clearly the effects of provincialism at this time.

Determination of Nannofossil Age for Cenozoic Debris Flow Clasts

The Cenozoic graded carbonate sequences include a number of intervals that contain pebble-sized, matrix-supported clasts that are different in color, lithology, and degree of lithification from the surrounding and adjacent Cenozoic sediments. A number of these clasts from Cores 123-765B-6H, -7H, -13H and -28X, and Core 123-765C-13R were examined and yielded nannofossil assemblages that indicate Mesozoic ages.

Sample 123-765B-6H-7, 25–26 cm (white chalk clast) yielded an extremely abundant, diverse, and well-preserved assemblage of Late Cretaceous age. Marker species present in the sample include *Aspidolithus parcus constrictus*, *Reinhardites levis*, *Arkhangelskiella cymbiformis*, and *Prediscosphaera grandis* and indicate a latest Campanian age (*Tranolithus phacelosus* Zone, CC23, subzone A). Sample 123-765C-13R-2, 93–94 cm (brown claystone clast) also contained an Upper Cretaceous assemblage, including the species *Quadrum gartneri*, *Gartnerago obliquum*, and *Lithastrinus moratus*, indicating an early Turonian age (*Q. gartneri* Zone CC11).

The remaining clasts examined yielded lower abundance and lower diversity assemblages that are of Middle Jurassic or Middle to Late Jurassic age. Sample 123-765B-13H-5, 101–102 cm (black claystone clast) contained the most diverse and well-preserved Jurassic assemblage, which indicates an early Bajocian age (*Watznaueria britannica* Zone; Bown et al., 1988). Age diagnostic nannofossils include *Lotharingius contractus*, *Watznaueria britannica*, *Retecapsa incompta*, and *Carinolithus superbus*. These nannofossil marker species also are present in Sample 123-765B-13H-5, 109–110 cm (black claystone clast). Sample 123-765B-28X, CC (black claystone clast) contains a similar assemblage, but lacks the presence of *W. britannica* and thus has been dated as Aalenian to early Bajocian age (*Lotharingius contractus* Subzone; Bown et al., 1988). Sample 123-765C-13R-1, 33–34 cm (black silty claystone clast) yielded an assemblage that includes *Stephanolithion hexum* and *Hexapodorhabdus cuvillieri*, which suggest a late Bathonian to Callovian age (*Ansulosphaera helvetica* Zone to *Stephanolithion bigotii* Zone; Bown et al., 1988).

The remaining clasts examined yielded low-diversity and relatively poorly preserved assemblages and could only be assigned a broader age range; Sample 123-765B-6H-1, 124–125 cm (Bajocian to Bathonian, based on the presence of *Lotharingius velatus*), Sample 123-765B-7H-2, 18–19 cm (Middle to Late Jurassic), and Sample 123-765B-7H-2, 84–85 cm (Middle to Late Jurassic, based upon the abundant occurrence of *W. britannica* and *Zeugrhabdotus erectus*).

The presence of these transported blocks of Mesozoic sediments within the Cenozoic debris deposits is of particular interest and reveals the time of exposure and range of strata being eroded on the adjacent shelf area at this time. In addition, these blocks represent important age dates, confirming the presence of at least Aalenian to Callovian Jurassic sediments in the Swan Canyon area.

Palynology

Preservation and Abundance

Dinoflagellate cyst assemblages are scattered in Neogene samples, and are absent from Paleogene and Upper Cretaceous samples, but are present in Early Cretaceous samples. Neogene assemblages typically have very low abundances and low diversities. By contrast, Lower Cretaceous assemblages are mostly abundant and diverse. The preservation in all assemblages is excellent.

Neogene

Neogene dinoflagellate assemblages were recovered from 16 out of 41 core-catcher samples in Hole 765B and in one sample out of 14 Neogene core-catcher samples in Hole 765C. However, as yet, there is no Southern Hemisphere or tropical Neogene dinoflagellate zonation with which to compare these assemblages, and thus it is not possible to determine ages reliably for assemblages from this time interval at Site 765. Assemblages of Pliocene to Holocene age are typically dominated by *Impagidinium* spp. and *Tuberculodinium vancampoae,* while those of Miocene age are characterized by *Polysphaeridium zoharyi*, *Hystrichokolpoma rigaude*, and *Operculodinium* spp. However, there are several widely accepted palynological datums that do constrain the ages to some extent. *Systematophora placantha*, which has an LO in the upper Miocene (Williams and Bujak, 1985; McMinn, unpubl. data), is present in Cores 123-765B-31X, -35X, and -36X. Similarly *Acacia* pollen, which appears in the lower Miocene (Stover and Partridge, 1973), is present in Core 123-765C-6R.

Paleogene to Upper Cretaceous

No palynological assemblages were recovered from this interval.

Lower Cretaceous

Dinoflagellate cyst assemblages recovered from Samples 123-765C-33R-1, 38–40 cm; -34R-1, 130–132 cm; and -35R, CC, contain *Diconodinium davidii* and *Pseudoceratium turneri* and thus are equivalent to the upper Aptian *D. davidii* Zone of Helby et al. (1987). The uppermost of these cores, however, shows a decline in abundance of *D. davidii* in association with abundant *Canninginopsis intermedia*. Helby et al. (1987) considered this latter species to be restricted to the overlying *Muderongia tetracantha* Zone and therefore, this assemblage is probably intermediate between the two zones and of earliest Albian age. Spores and pollen are relatively abundant in these samples and are equivalent to the upper Aptian to lower Albian *Crybelosporites striatus* Zone (Helby et al., 1987).

Cores 123-765C-36R to -39R are barren of palynomorphs. Samples taken from Cores 123-765C-40R to -46R (i.e., Samples 123-765C-40R-4, 138–140 cm; -41R-1, 58–60 cm; -41R, CC; -42R-2, 117–119 cm; -42R, CC; -43R-1, 111–112 cm; -43R, CC; -44R-1, 100–102 cm; -44R, CC; -45R-1, 102–104 cm; -45R, CC; and—46R, CC) contain *Odontochitina operculata* but lack *D. davidii* and *Pseudoceratium turneri* and, therefore, are equivalent to the lower Aptian *Odontochitina operculata* Zone (Helby et al., 1987). According to Helby et al. (1987), the Aptian/Barremian boundary is coincident with the boundary between the *O. operculata* and *Muderongia australis* zones. The LO of the *M. australis* Zone, which is characterized by the absence of *O. operculata* and an abundance of *Herendeenia postprojecta*, is found in Sample 123-765C-47R-3, 139–140 cm, and a similar assemblage is also present in Samples -49R, CC; -50R, CC; -51R, CC; and -52R-1, 150–151 cm.

The *M. australis* Zone can be divided informally into an upper and lower interval by the extinction of *Phoberocysta neocomica* and the appearance of *Herendeenia postprojecta*. Assemblages from the lower interval (upper Hauterivian to lower Barremian) are present in Samples 123-765C-54R-4, 49–50 cm, and -54R, CC. An undiagnostic assemblage containing only

Kiawaradinium scrutillinum, which has a upper Berriasian to middle Hauterivian range, is present in Sample 123-765C-58R-2, 25–26 cm.

The lowest intervals that contain palynological assemblages are from Samples 123-765C-59R-4, 105–112 cm, and -59R-5, 8–9 cm. Species present in these samples include *Cassiculosphaera magna*, *Cyclonephelium densebarbartum*, *Tubotuberella vlamingii*, *Apteodinium granulatum*, and common *Egmontodinium torynum*. This assemblage implies an age equivalent to the upper Berriasian to lowest Valanginian *E. torynum* Zone (Helby et al., 1987) and the Valanginian *Kaiwaradinium scrutillinum* Zone of Backhouse (1988). The age determined by correlation with the zonation of Helby et al. (1987) is considered the more appropriate of the two zonations to Site 765, as the zonation of Backhouse (1988) is strongly influenced by local facies changes, with many of the species ranges being shorter than those documented by Helby et al. (1987).

Reworking

Jurassic reworking is common throughout most of the section. This involves predominantly spores and pollen of an undifferentiated Jurassic age, although the presence of the dinoflagellate *Wanea digitalis* in Cores 123-765B-14H,-18H, -21X, -31X, and -39X suggests that at least some of the reworking is of Middle Jurassic age. Rare pollen grains of Permian age are present in Cores 123-765B-11X and -14X and in Core 123-765C-59R; rare Triassic pollen grains are present in Cores 123-765B-10X and -14X.

Radiolarians

This section is based on the examination of all core-catcher samples plus additional samples selected during normal sampling of the cores (a total of 150 samples was studied). Abundance and preservation of radiolarians are graphically represented in Figure 60A for Hole 765B (Table 8), and in Figure 60B (with Table 9) for Hole 765C.

Quaternary Biostratigraphy of Hole 765B

Abundant and well-preserved Quaternary radiolarians recovered from the topmost nine cores of Hole 765B allow for a detailed upper Quaternary biostratigraphy. Cores 123-765B-1H through Section 123-765B-2H, CC, can be assigned to the *Buccinosphaera invaginata* Zone or the *Collosphaera tuberosa* Zone (Sanfilippo et al., 1985), based on well-preserved and highly diverse assemblages that include *C. tuberosa*, *Disolenia quadrata*, *Euchitonia furcata*, *Spongaster tetras*, *Amphirhopalum ypsilon*, *Spongocore puella*, *Dictyocoryne profunda*, *Octopyle stenozona*, *Giraffospyris angulata*, *Lamprocyclas martialis*, *Theocorythium trachelium trachelium*, *Lithopera bacca*, *Eucyrtidium hexagonatum*, and *Theopilium tricostatum*. These assemblages are characteristic of the low-latitude (±30°) Indian Ocean. The residues also contain rare diatoms and arthropod remains, as well as silica-filled, reworked older Quaternary radiolarians. Since *B. invaginata* was not found, the Holocene cannot be differentiated from the uppermost Pleistocene. The presence of *C. tuberosa*, however, indicates an age younger than 400,000 yr for Cores 123-765B-1H and -2H.

Cores 123-765B-3H through -8H, CC, have been assigned to the *A. ypsilon* Zone (Sanfilippo et al., 1985), based on the presence of *Lamprocyrtis nigriniae* and the absence of *C. tuberosa*. These highly diverse assemblages (especially Sample 123-765B-8, CC) include common *A. tachelium*, *Pterocanium praetextum*, *Callimitra elisabethae*, *Clathrocanium diadema*, and *Tetrapyle octacantha*. This assignment correlates well with preliminary paleomagnetic data that show the Jaramillo normal interval to range from Section 123-765B-8H-3 to the top of Core 123-765B-9H, indicating an age younger than 1 Ma. Rare, reworked *Pterocanium prismatium* and *Anthocyrtidium angulare* in Cores 123-765B-3H through -4H document reworking of older Quaternary sediment in turbidites. Reworked Pliocene (*Didymocyrtis avita*) is found in Sample 123-765B-8H, CC.

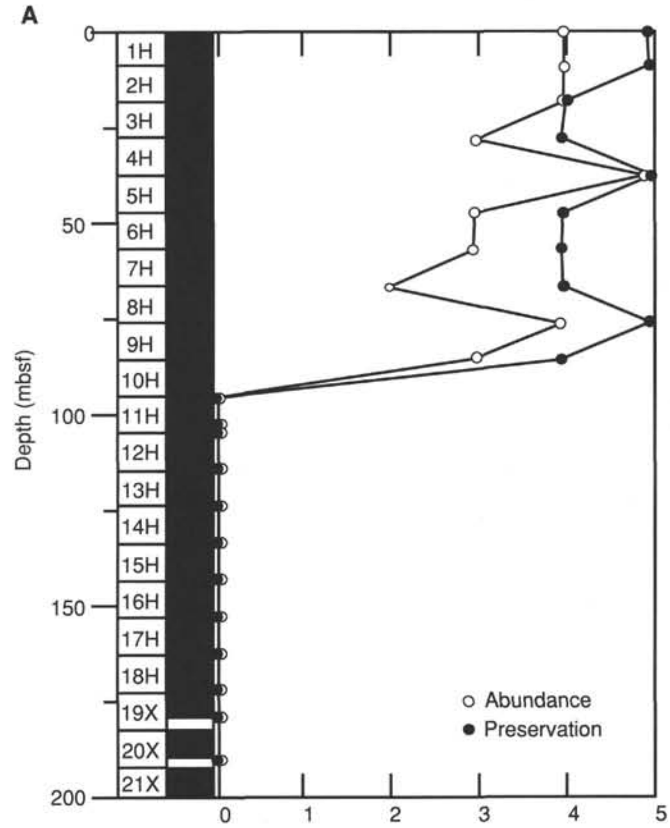

Figure 60. A. Abundance and preservation of radiolarians in Hole 765B, based on core-catcher and selected samples. Key: 0 = barren/preservation indeterminable; 1 = very rare/very poor; 2 = rare/poor; 3 = few/moderate; 4 = common/good; 5 = abundant/very good. Only samples that score at least 3/3 (few/moderate) are biostratigraphically useful. For definitions of abundance and preservation of radiolarians see "Explanatory Notes" chapter (this volume). B. Abundance and preservation of radiolarians in Hole 765C, based on core-catcher and selected samples. Same key as in Figure 60A.

Sample 123-765B-9H, CC, has been assigned to the *Anthocyrtidium angulare* Zone (Sanfilippo et al., 1985), based on the common occurrence of *A. angulare* and the absence of *Lamprocyrtis nigriniae*; these species indicate an age of less than 1.6 Ma. Accordingly, the top of the Olduvai normal polarity interval seems to be located near the base of Core 123-765B-9H (see "Sediment Paleomagnetism" section, this chapter).

All remaining core-catcher samples of Hole 765B were found to be barren of radiolarians. Sieved acid residues contain only sand-sized, subrounded detrital quartz, biotite, muscovite, green hornblende, and zircon.

Cretaceous

Core-catcher Samples 123-765C-1R, CC, through -20R, CC, are all barren except for Sample 123-765C-11R, CC, which contains rare and poorly preserved indeterminate Paleogene radiolarians.

Cores 123-765B-21R through -27R contain scattered rare and moderately preserved radiolarians that are clearly reworked. Sample 123-765C-21R, CC, contains *Foremanina* sp. known from

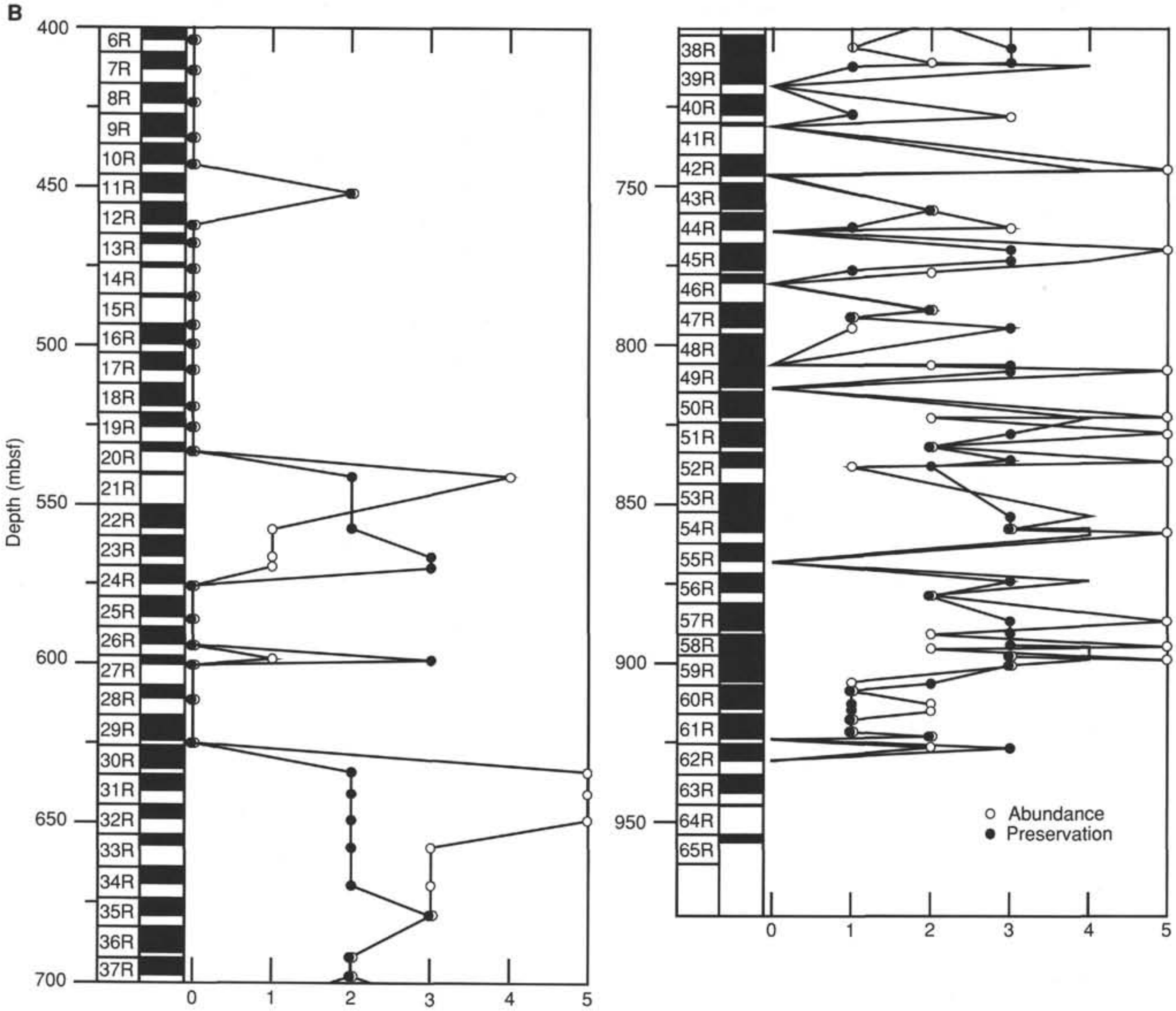

Figure 60 (continued).

the Upper Cretaceous (Campanian). Sample 123-765C-22R, CC, contains *Sethocapsa leiostraca*, known from the Lower Cretaceous. Samples 123-765C-24R-1, 0–1 cm, and 123-765C-27R-1, 87–88 cm, contain reworked assemblages typical of the upper Hauterivian to lower Barremian recovered farther downhole (Cores 123-765C-54R through -57R). These observations suggest that a relatively thin Cretaceous sequence was being eroded during the Latest Cretaceous and earliest Paleogene, probably by downcutting turbidites. Cores 123-765C-30R through -44R contain mostly undeterminable radiolarians that have been generally replaced by carbonates (rhodochrosite) or zeolites. In Sample 123-765C-33R, CC, the middle Cretaceous *Halesium sexangulum* was recorded. Radiolarian ghosts made of rhodochrosite are common to abundant in Cores 123-765B-30R through -34R, whereas the residues of Cores 123-765B-40R and 123-765B-42R through -44R contain abundant rhodochrosite spherules that must have formed partly *in situ* as concretions. However, some occur in laminated, size-sorted layers that suggest winnowing and/or redeposition.

The interval between Samples 123-765C-42R, 140–150 cm, and -45R-5, 52–55 cm, yielded an abundant, moderately preserved, and diverse assemblage assignable to the lower *Sethocapsa euganea* Zone (Schaaf, 1985), indicating an early Aptian age. Species include *Stichocapsa euganea*, *Eucyrtis columbaria*, *Parvicingula malleola*, *Mirifusus chenodes*, *Foremanella hipposidericus*, and *Stephanastrum inflexum*.

Cores 123-765B-49R through -62R contain a continuous section with moderately to well-preserved, sometimes abundant radiolarians, indicating late Barremian to late Berriasian age. Detailed evolutionary lineages can be observed. The assemblages may be composed mainly of undescribed species endemic to this area. Radiolarian dating is hampered by the paucity of "cosmopolitan" marker species with ranges known from other oceans (Schaaf, 1985; Sanfilippo and Riedel, 1985). Some of these samples are discussed below in more detail.

Sample 123-765C-49R-2, 39–43 cm, is characterized by the lowest occurrence of ?*Parvicingula malleola,* together with the occurrence of *Pseudodictyomitra lilyae*, *Eucyrtis tenuis*, *Eucyrtis columbaria*, and *Sethocapsa leiostraca*. This assemblage is characteristic of the upper Barremian (combining several sources of known ranges).

The FOs of *Eucyrtis tenuis* and *E. columbaria* were found in Sample 123-765C-52R-2, 68–71 cm, indicating a late Hauterivian to early Barremian age.

Table 8. Abundance, preservation, and determination of radiolarians in Hole 765B.

Core, section, interval (cm)	Depth (mbsf)	NA	NP	Abundance	Preservation
123-765B-1H-1, 0–1	0.00	4	5	C	VG
1H-CC, 0	9.15	4	5	C	VG
2H-CC, 0	18.74	4	4	C	G
3H-CC, 0	28.37	3	4	F	G
4H-CC, 0	37.94	5	5	A	VG
5H-CC, 0	47.62	3	4	F	G
6H-CC, 0	57.31	3	4	F	G
7H-CC, 0	67.01	2	4	R	G
8H-CC, 0	76.65	4	5	C	VG
9H-CC, 0	86.37	3	4	F	G
10H-CC, 0	96.06	0	0	barren	
11H-5, 150	103.50	0	0	barren	
11H-CC, 0	105.55	0	0	barren	
12H-CC, 0	115.17	0	0	barren	
13H-CC, 0	124.94	0	0	barren	
14H-CC, 0	134.36	0	0	barren	
15H-CC, 0	144.13	0	0	barren	
16H-CC, 0	153.71	0	0	barren	
17H-CC, 0	163.64	0	0	barren	
18H-CC, 0	173.14	0	0	barren	
19X-CC, 0	179.83	0	0	barren	
20X-CC, 0	191.02	0	0	barren	
21X-CC, 0	200.55	0	0	barren	
22X-CC, 0	208.94	0	0	barren	
23X-CC, 0	215.10	0	0	barren	
24X-CC, 0	227.71	0	0	barren	
25X-CC, 0	232.13	0	0	barren	
26X-CC, 0	246.40	0	0	barren	
27X-CC, 0	255.03	0	0	barren	
28X-CC, 0	264.06	0	0	barren	
29X-CC, 0	272.03	0	0	barren	
30X-CC, 0	280.90	0	0	barren	
31X-CC, 0	296.68	0	0	barren	
32X-CC, 0	303.89	0	0	barren	
33X-CC, 0	315.83	0	0	barren	
34X-CC, 0	320.82	0	0	barren	
35X-CC, 0	330.57	0	0	barren	
36X-CC, 0	341.52	0	0	barren	
37X-CC, 0	349.87	0	0	barren	
38X-CC, 0	358.60	0	0	barren	
39X-CC, 0	367.61	0	0	barren	
40X-CC, 0	376.68	0	0	barren	
41X-CC, 0	386.30	0	0	barren	

(For NA and NP see "Explanatory Notes," this volume.)

Sample 123-765C-54R, CC, shows the LO of *Podocapsa amphitreptera*. The last appearance of this species elsewhere is known to be in the upper Valanginian. Considering the biostratigraphic data of nannofossils and palynomorphs, however, this datum occurs here in the upper Barremian to lower Hauterivian. Reworking is unlikely as this species continuously occurs in all samples down to the bottom of the sedimentary section. Moreover, an undescribed descendant species of *A. amphitreptera* can be observed starting in Sample 123-765C-54R-4, 21–24 cm, suggesting that this species has its evolutionary last appearance higher than its last appearance observed elsewhere.

The LO of *Obesacapsula rotunda* is observed in Sample 123-765C-58R-3, 89–93 cm, indicating an age not younger than late Hauterivian.

The lowest sample yielding determinable radiolarians was Sample 123-765C-62R-1, 53–56 cm. It shows the co-occurrence of *Sethocapsa* sp. aff. *S. cetia* with *Holocryptocanium barbui* (*sensu* Baumgartner, 1984), indicating a late Berriasian to early Valanginian age. The latter species is known to range from early Albian to early Cenomanian (Schaaf, 1985; Sanfilippo and Riedel, 1985), but Baumgartner (1984) found that it ranged down to his Unitary Association 12, which is dated as late Berriasian in Locality 46 of Baumgartner (1984; Trattberg, near Salzburg,

Table 9. Abundance, preservation, and determination of radiolarians in Hole 765C, based on selected samples.

Core, section interval (cm)	Depth (mbsf)	NA	NP	Abundance	Preservation
123-765C-1R-CC, 0	350.48	0	0	barren	
2R-CC, 0	363.41	0	0	barren	
3R-CC, 0	373.00	0	0	barren	
4R-CC, 0	383.63	0	0	barren	
5R-CC, 0	392.88	0	0	barren	
5R-3, 128–130	394.30	0	0	barren	
6R-CC, 0	403.76	0	0	barren	
7R-CC, 0	413.35	0	0	barren	
8R-CC, 0	423.53	0	0	barren	
9R-CC, 0	434.35	0	0	barren	
10R-CC, 0	443.00	0	0	barren	
11R-CC, 0	451.91	2	2	R	P
12R-CC, 0	461,99	0	0	barren	
13R-CC, 0	467.88	0	0	barren	
14R-CC, 0	475.74	0	0	barren	
15R-CC, 0	484.92	0	0	barren	
16R-CC, 0	493.75	0	0	barren	
16R-1, 55–58	499.29	0	0	barren	
17R-CC, 0	507.98	0	0	barren	
18R-CC, 0	519.11	0	0	barren	
19R-CC, 0	525.63	0	0	barren	
20R-CC, 0	533.11	0	0	barren	
21R-CC, 0	540.91	4	2	C	P
22R-CC, 0	557.30	1	2	VR	P
23R-CC, 0	566.30	1	3	VR	M
24R-1, 0	569.30	1	3	VR	M
24R-CC, 0	574.89	0	0	barren	
25R-CC, 0	585.55	0	0	barren	
26R-CC, 0	594.19	0	0	barren	
27R-1, 87–88	598.37	1	3	VR	M
27R-CC, 0	599.93	0	0	barren	
28R-CC, 0	610.94	0	0	barren	
29R-CC, 0	624.80	0	0	barren	
30R-CC, 0	634.42	5	2	A	P
31R-CC, 0	640.71	5	2	A	P
32R-CC, 0	649.43	5	2	A	P
33R-CC, 0	658.08	3	2	F	P
34R-CC, 0	669.64	3	2	F	P
35R-CC, 0	679.28	3	3	F	M
36R-CC, 0	692.40	2	2	R	P
37R-CC, 0	698.08	2	2	R	P
38R-3, 79–80	706.29	1	3	VR	M
38R-6, 104–108	711.04	2	3	R	M
38R-CC, 0	712.13	4	1	C	VP
39R-CC, 0	717.86	0	0	barren	
40R-CC, 0	727.50	3	1	F	VP
41R-CC, 0	731.04	0	0	barren	
42R-3, 140–150	744.20	5	4	A	G
42R-CC, 0	746.42	0	0	barren	
43R-CC, 0	757.50	2	2	R	P
44R-4, 18–19	763.18	3	1	F	VP
44R-CC, 0	764.07	0	0	barren	
45R-1, 107–111	769.27	5	3	A	M
45R-2, 26–28	769.96	5	3	A	M
45R-4, 52–56	773.22	4	3	C	M
45R-CC, 0	776.91	2	1	R	VP
46R-CC, 0	780.58	0	0	barren	
47R-2, 23–24	789.13	2	2	R	P
47R-2, 25–31	789.15	2	2	R	VP
47R-3, 102–105	791.42	1	1	VR	VP
47R-CC, 0	794.52	1	3	VR	M
48R-7, 4–8	805.94	0	0	barren	
48R-CC, 0	806.54	2	3	R	M
49R-2, 39–43	808.19	5	3	A	M
49R-3, 69–75	809.99	2	4	R	G
49R-CC, 5–9	813.90	0	0	barren	
50R-4, 108–112	821.18	2	4	R	G
50R-5, 144–148	823.04	5	4	A	G
50R-CC, 0	823.62	2	4	R	G
51R-2, 20–22	826.70	2	4	R	G
51R-3, 6–9	828.06	5	3	A	M
51R-CC, 0	832.50	2	2	R	P
52R-2, 68–71	836.68	5	3	A	M
52R-CC, 0	838.80	1	2	VR	P
53R-CC, 0	853.94	4	3	C	M
54R-4, 0–1	858.00	3	3	F	M

Table 9 (continued).

Core, section interval (cm)	Depth (mbsf)	NA	NP	Abundance	Preservation
123-765C-54R-4, 21-24	858.21	5	4	A	G
54R-CC, 0	859.41	5	4	A	G
55R-CC, 0	868.66	0	0	barren	
56R-2, 7-8	874.07	4	3	C	M
56R-CC, 0	878.50	2	2	R	P
57R-4, 51-53	886.71	5	3	A	M
57R-CC, 0	890.75	2	3	R	M
58R-3, 31-34	894.51	5	3	A	M
58R-3, 89-93	895.09	5	4	A	G
58R-4, 0	895.70	2	4	R	G
58R-4, 88-92	896.52	2	4	R	G
58R-5, 143-147	898.63	5	4	A	G
58R-CC, 0	898.68	3	3	F	M
59R-1, 32-35	898.22	5	4	A	G
59R-1, 66-68	898.56	3	4	C	G
59R-1, 123-126	899.13	5	4	A	G
59R-2, 121-125	900.61	3	3	F	M
59R-CC, 0	906.54	1	2	VR	P
60R-1, 128-130	908.78	1	1	VR	VP
60R-4, 148-150	913.48	2	1	R	VP
60R-CC, 0	914.89	2	1	R	VP
61R-1, 75-79	917.65	0	0	barren	
61R-1, 91-95	917.81	1	1	VR	VP
61R-2, 50-53	918.90	0	0	barren	
61R-2, 96-100	919.36	2	3	R	M
61R-4, 73-75	922.13	0	0	barren	
61R-4, 87-89	922.27	1	1	VR	VP
61R-4, 91-93	922.31	0	0	barren	
61R-5, 52-55	923.42	2	2	R	P
61R-CC, 0	924.40	0	0	barren	
62R-1, 52-56	926.92	1	3	VR	M
62R-1, 53-56	926.93	2	3	R	M
62R-4, 25-27	931.15	0	0	barren	

(For NA and NP, see "Explanatory Notes," this volume.)

Austria). *Sethocapsa cetia* is known to make its last appearance in the lower or upper Valanginian (lower, Sanfilippo and Riedel, 1985; upper, Schaaf, 1985), which corresponds to the top of Unitary Association 13 of Baumgartner (1984). Although the assemblage of this sample is of low diversity, there are several other species, like *Thanarla conica*, that have never been reported from Upper Jurassic strata and thus clearly indicate a Neocomian age for this sample. This age, together with considerations about sedimentation rates (see below), suggests an Earliest Cretaceous age for the oceanic crust at this site.

Macrofossils

Bivalves

Inoceramid shell debris associated with gravity flow deposits of late Miocene to late Berriasian age was found at Site 765. In Sample 123-765B-28X, CC, a conglomerate containing a 3-cm-sized fragment of a 5-mm-thick inoceramid shell was found. Sand-sized inoceramid prisms were found in washed residues of Samples 123-765C-25R, CC, and 123-765C-44R-4, 18-19 cm. These prisms also constitute a significant part of the sand fraction in Cores 123-765C-61R and -62R. Centimeter-sized, thin-shelled bivalves occur as a concentrated layer (lumachella) in Sample 123-765C-62-2, 2-6 cm. Some of these specimens show epifaunal overgrowths by probable serpulid worm tubes.

Belemnites

Two fragments of belemnites were observed in the basal part of Hole 765C. The first, poorly preserved fragment, from Sample 123-765C-61R, CC, is part of the apical region split along the "de Klaehn'sche" interface. Since the central part along the apical line is heavily corroded and the apex is not preserved, it is difficult to give any generic assignment. However, because of the slender shape of the fragment, it may belong to the belemnopseid genus *Hibolithes*.

The second fragment, from Sample 123-765C-62R-2, 30-35 cm, is a laterally deformed piece of the alveolar region of a duvaliid belemnite. Although the guard is not completely preserved, a generic assignment to either *Duvalia* sp. or *Produvalia* sp. seems likely because of to the high degree of lateral compression. Belemnite assemblages, consisting of *Produvalia* aff. *neyrivensis*, have been described from the uppermost Tithonian of Antarctica (Mutterlose, 1986) and a further *Produvalia* sp. from the Valanginian of Antarctica (Crame and Howlett, 1988).

Preliminary Paleoenvironmental Interpretation

The presence of calcareous microfossils in the sediments of Hole 765 may be directly related to the occurrence of carbonate graded sequences that represent the deposits of mass flows. Sedimentary intervals occurring between the graded sequences are interpreted as abyssal deposits and are invariably devoid of carbonate as a result of their deposition beneath the CCD. The allochthonous nature of these carbonate sediments is confirmed by the significant degree of microfossil reworking that was observed, particularly in the Neogene sequences. Miocene/Pliocene mass-flow deposits include pervasive reworked Jurassic dinoflagellates and spores and pollen (Callovian age can be assigned where short-ranging taxa are present) and clasts within the Miocene debris flows, which contain calcareous nannofossil assemblages of Aalenian, Callovian (Jurassic), and Turonian and Campanian (Late Cretaceous) age. Reworking from directly underlying and stratigraphically contiguous sediments is apparent throughout the Tertiary sequence. These sediment mass flows (predominantly turbidites) were thus significantly erosive, cutting through Mesozoic sedimentary sequences in their source area.

The depth from which these flows originated may be inferred from the included benthic foraminifers, the ratio of planktonic to benthic foraminifers, and the ratio of included dinoflagellates to spores and pollen. In the Cenozoic interval, the majority of productive samples contained bathyal benthic foraminiferal assemblages having no evidence of "larger" complex forms that would indicate a provenance within the photic zone. Neogene palynological preparations yielded virtually no spores or pollen, inferring a depositional environment far removed from continental influence. The abundance of spores and pollen is low in the Neocomian sediments, but is significantly higher in the Aptian/Albian. Thus, the source area during the Aptian/Albian interval must have seen increased terrestrial influx, and this may be significant for interpreting the high sedimentation rate that was observed at this time. The lowermost two cores include the occurrence of abundant inoceramid fragments and rarer thin-walled bivalves. The observed bivalves include probable byssate forms that may have been pseudoplanktonic, together with forms that may have been benthic. The valves and fragments of valves are sorted within the sediment, indicating reworking. Calcispheres, also present in this interval, are considered indicative of deep shelf conditions, but their presence in great numbers is often thought to reflect environmental stress. The presence of only highly etched nannofossils, the virtual absence of calcareous foraminifers, and the corroded appearance of the bivalve fragments suggests that the site was near or already below the CCD at this earliest period of its sedimentary history. Agglutinated foraminifers, which are thought to be *in situ* in the background clay, indicate a bathyal to abyssal water depth.

Biogeographic Observations for the Lower Cretaceous

The Lower Cretaceous sequence is characterized by red claystones with subordinate, interbedded sandy layers composed of radiolarians, detrital quartz or rhodochrosite spherules. In Cores 123-765C-49R through -59R in particular, these layers are radiolarites, composed of between 50% and 80% radiolarians. They are likely to have resulted from periodic fluctuations in bottom currents that winnowed and redistributed the radiolarians. Some of the beds may represent low-density turbidites. Substantial differences in radiolarian assemblages can be observed between the two major lithologies.

The claystone assemblages are moderately to well preserved (radiolarians are clay-filled); the abundance is low to very low, and the diversity also is very low. In most assemblages, 80% to 90% of the specimens are either *Holocryptocanium barbui* and *Thanarla conica* or similar, cosmopolitan forms. The remainder of the assemblage is composed of only a few species. The claystone assemblage is interpreted as an autochthonous, oceanic faunal association, reflecting low-fertility conditions in a basin that is paleoceanographically isolated from the world ocean. The number of species is about 50 to 100 times lower than in typical Tethyan assemblages (e.g., Oman, Umbria; Baumgartner, unpubl. data). The sand assemblages are usually less well preserved (radiolarians are quartz cement filled), the abundance is high and the diversity is higher than in the clays, but still low compared to Tethyan assemblages. A few, probably endemic species make up 70% to 80% of the assemblages, with the remainder constituting only 10 to 15 species. The predominant species change every few cores. "Cosmopolitan" species account for less than 10% of the taxa and probably less than 1% of the specimens. Species typical of the clay assemblage form a constant background in sand assemblages. The radiolarians of the radiolarite layers are thought to be penecontemporaneously displaced from an area of possible upwelling near the continental slope.

Pantanelliids are absent from claystone assemblages and very rare in sand assemblages. "*Parvicingula*"-type forms dominate "*Ristola*"-type forms. Pessagno and Blome (1986) suggested that low abundance and diversity of pantanellids and high abundance of "*Parvicingula*"-type nassellarians characterize the "northern Tethyan" faunal realm. We interpret this faunal provincialism to be an expression of the degree of paleoceanographic restriction of the Early Cretaceous Argo Basin, with respect to more central water masses. The following taxa, which are abundant and diverse in Tethyan assemblages of the Neocomian, were not found on the Argo Abyssal Plain: Hagiastridae, *Podobursa* sp., *Emiluvia* sp., *Triactoma* sp., *Ristola* sp., *Syringocapsa agolarium*, *Alievum helenae*, *Cecrops semptemporatus*, *Crolanium pythiae*, and *Dibolachras tythopora*.

Calcareous nannofossil assemblages also exhibit significant biogeographic differences from those observed in southern Europe. They are generally of lower diversity and lack a number of groups that typify Tethyan assemblages at this time, for example, *Nannoconus* and *Conusphaera*. This suggests floral provincialism, which may be explained by various factors, such as water depth, temperature, or basin configuration causing paleoceanographic restriction.

Backtracking of the sediment units and basement/sediment level in Site 765 establishes a ridge-crest depth for the basal sediments near 2800 m, which is near the global average. Water depth rapidly increased to 4 km in the Hauterivian/Barremian, and more slowly to more than 5 km in the Late Cretaceous and Cenozoic. Thus, all sediments in Site 765 are abyssal. The Lower Cretaceous calcareous foraminifers in Site 765 are without exception known from abyssal sediments in the North Atlantic Ocean, although the taxonomic diversity is limited compared to the Atlantic. For example, Sample 123-765C-51R, CC, contains common to abundant *Dorothia praehauteriviana* and *Lenticulina subangulata*, and rare *Ramulina spandeli* and *Epistomina caracolla*, previously also described from the Neocomian Blake-Bahama Formation in the western North Atlantic, and coeval abyssal strata in the eastern North Atlantic (e.g., Gradstein, 1978; Sliter, 1980). *Caucasella hoterivica* in Sample 123-765C-45R, CC, is widely known from Barremian to lower Aptian, neritic to bathyal sediments in Europe, North Africa, and circum-North Atlantic sites; further study may determine if these specimens in Site 765 were resedimented from the shallower northwestern Australian continental margin, or were eupelagic at the site. The same is true for the hedbergellid assemblages found in the interval from Cores 123-765C-27R to -45R. Although more detailed analysis is needed, the Lower Cretaceous calcareous foraminiferal assemblage is much impoverished compared to Tethyan, lower-latitude assemblages. Both depth of deposition on the seafloor, leading to dissolution of more thin-walled taxa, and the middle latitude position of the site in the Southern Hemisphere may have contributed to the impoverished character of the calcareous foraminiferal fauna.

The Cretaceous agglutinated foraminiferal assemblages are similar to those described from the Carpathian and Alpine flysch troughs of central Europe. The Lower Cretaceous assemblages also have been described from the abyssal sediments of the North Atlantic Ocean. A number of the species, however, exhibit differing stratigraphic ranges, occurring in older sediments at this site. This was as expected, because in our experience most agglutinated taxa exhibit slightly varying stratigraphic ranges from one sedimentary basin to another. More detailed study will refine the local stratigraphic ranges.

Initial observations about the paleocecology and biogeography of the microfossil groups examined in the sediment cores of Site 765 show that significant biogeographic differences exist in this area, compared to the better-known western Tethys and Atlantic realms.

Summary

At Site 765, diagnostic age data are provided by planktonic and benthic foraminifers, nannofossils, radiolarians, dinoflagellates, spores and pollen, and belemnites. The biostratigraphic information is summarized in Figures 65 and 66. There are no significant differences in the ages provided by the different fossil groups. In general, foraminifers and nannofossils provide the best age control in the Upper Cretaceous to Holocene, while radiolarians and dinoflagellates provide the best control in the Lower Cretaceous. The interpreted depths of chronostratigraphic boundaries in the summary figures are based on a synthesis of biostratigraphic data. The depth of the Barremian/Aptian boundary in Hole 765C is further constrained by identification of magnetic reversal M0 in Core 123-765C-47R (see "Sediment Paleomagnetism" section, this chapter).

SEDIMENT PALEOMAGNETISM

The lithologic succession at Site 765 consists of three main lithologic-age units: (1) a thick series of Neogene light gray calcareous turbidites; (2) a Paleocene and Upper Cretaceous variegated claystone, overlying mid-Cretaceous dark gray claystone, and (3) a Lower Cretaceous reddish-brown claystone. The magnetic characteristics and magnetic polarity zonation of each of these main units are described separately.

Neogene

Susceptibility

The determination of low-field susceptibility is useful for estimating the total magnetic content of a specimen and as an important monitor of any chemical changes affecting the magnetic minerals (Tarling, 1983). Susceptibility is expressed as the dimensionless ratio "K" of the magnetization acquired per unit volume per unit applied field.

Within the Neogene calcareous turbidite series, distinctive peaks in susceptibility (Fig. 61) correspond to clay-rich intervals of the pelagic host sediment and of the bioturbated mixing zones at the tops of the turbidites. This susceptibility response, therefore, provides a simple method to display graphically the frequency of turbidites.

Susceptibility Units

Three "susceptibility units" can be distinguished within the Neogene series on the basis of the average susceptibility values and of the contrast between the turbidite and pelagic clay peaks (Fig. 62; Table 10).

Susceptibility Unit S-1 consists of the upper 104 m of the sediments (Core 123-765B-1H to the lower part of Core 123-765B-11H) and is characterized by weak susceptibility and low pelagic clay peaks (K generally less than 10×10^{-6} cgs). In sharp contrast, susceptibility Unit S-2 has intense sharp peaks (K = 30 to 70×10^{-6} cgs), corresponding to the greenish clay-rich intervals, and is approximately 170 m thick (lower part of Core 123-765B-11H through the upper part of Core 123-765B-19X; 104–176 mbsf). The change from the high contrasts of Unit S-2 to the generally low susceptibility of Unit S-1 is probably the result of a reduction in thickness and clay content of the pelagic intervals. The change takes place approximately at the hiatus between the Pliocene and Pleistocene, and appears to correspond to the seismic reflector separating seismic Units 1 and 2 (see "Seismic Stratigraphy" section, this chapter).

Susceptibility Unit S-3 is another low-contrast, low-level susceptibility unit that corresponds to the thick Miocene turbidite series (lower part of Core 123-765B-19X through the middle of Core 123-765C-14R; 176–475 mbsf). The sharp boundary between Unit S-3 and overlying Unit S-2 is located approximately at the hiatus between the Miocene and Pliocene (see "Biostratigraphy" section, this chapter). This boundary also corresponds to the seismic reflector between seismic Units 2 and 3 and is in

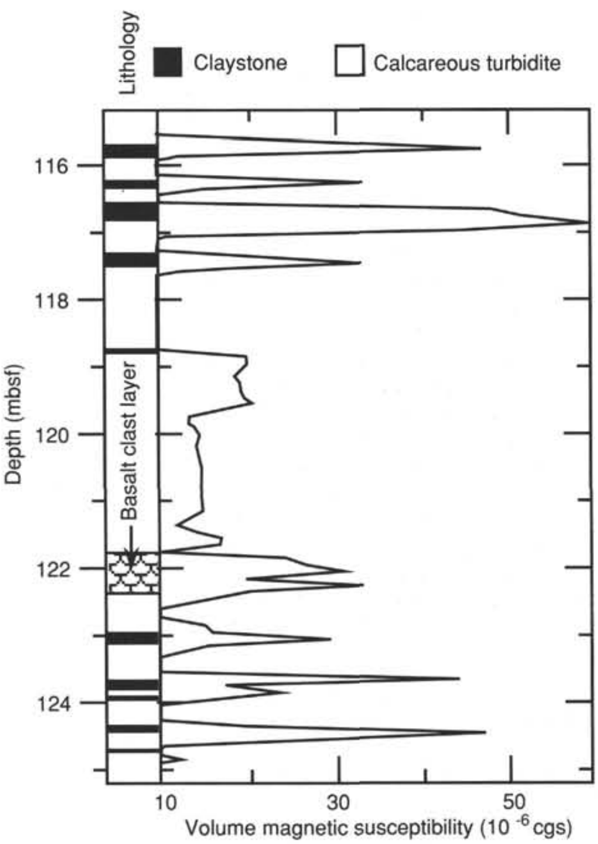

Figure 61. Susceptibility plot of Core 123-765B-13H. Peaks in susceptibility correspond to clay-rich intervals, low susceptibilities correspond to calcareous turbidite beds. K = dimensionless ratio of magnetization acquired per cubic centimeter per unit field (expressed in Gauss/Oersted; to convert to SI units, divide by 4π).

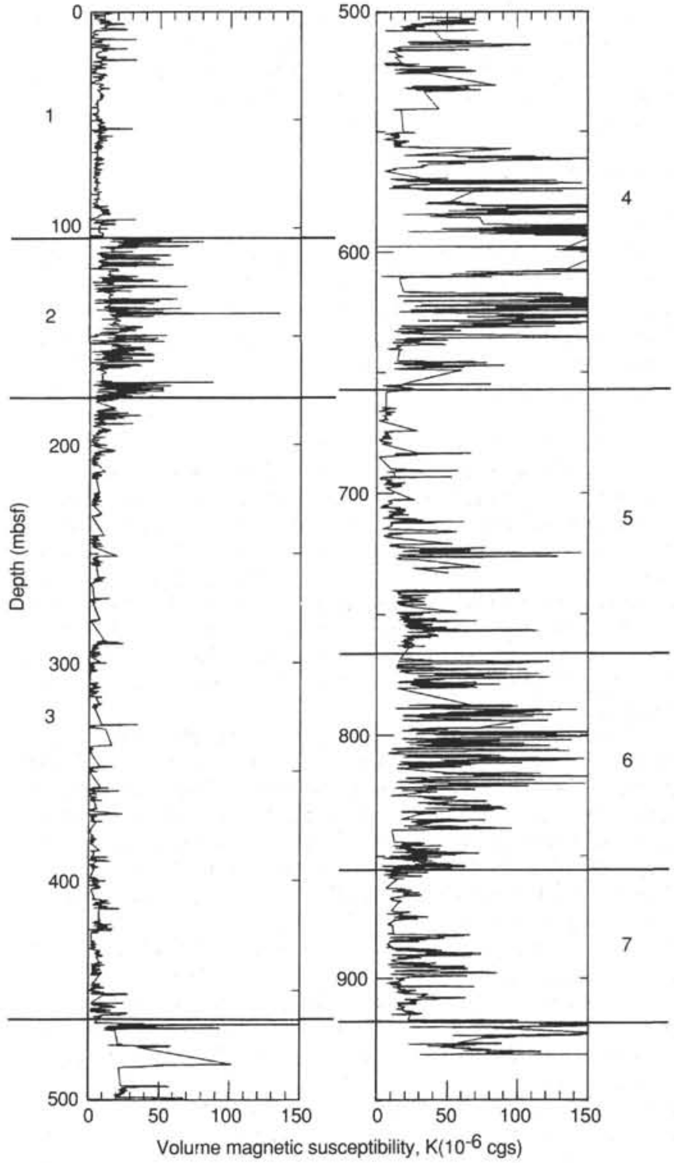

Figure 62. Stratigraphic plot of susceptibility measurements at Site 765. Susceptibility units are distinguished by the average susceptibility value and by the relative magnitude and frequency of peaks.

Table 10. Susceptibility units, Site 765.

Susceptibility unit	Core	Depth (mbsf)	Age (Ma)	Lithologic units
S-1	123-765B-1H to -11H	0–104	Pleistocene	IA-IB
S-2	765B-11H to -19X	104–176	Pliocene	IB-IC
S-3	765B-19X to 765C-14R	176–470	Miocene	IC-IIIA
S-4	765C-14R to -33R	470–655	early Teritary to Late Cretaceous	IIIA-IVB
S-5	765C-33R to -45R	655–769	Albian-Aptian	IVB-VB
S-6	765C-45R to -53R	769–854	Barremian	VB-VC
S-7	765C-54R to -62R	854–931	Haut.-Val.	VC-VIIB

the gradational boundary between lithologic Units IB and IC (see "Sediment Lithostratigraphy" section, this chapter). The base of susceptibility Unit S-3 is the debris flow marking the hiatus between the Paleogene and the Neogene and the boundary between lithologic Units II and III.

Magnetostratigraphy

Pleistocene

Hole 765A (Core 123-765A-1H). Natural remanent magnetization (NRM) directions of Core 123-765A-1H show a uniform, present-field normal polarity; but, after alternating field (AF) demagnetization at 5 and 10 mT, a short, reversed-polarity zone can be recognized at the top of Section 123-765A-1H-5 (6–6.5 mbsf). The NRM intensity ranges from 0.1 to 10 mA/m (= 10^{-6} emu/cm^3 in cgs units), with the higher intensities from dark gray ash-rich zones (Fig. 63A).

Hole 765B (Cores 123-765B-1H to -10H). NRM intensity of the light gray calcareous turbidites that dominate the cores is generally weak and ranges from 0.1 to 1 mA/m, except for a few intercalated pelagic sediment layers that have intensities greater than 1 mA/m. AF demagnetization of the cores yielded stable directions of magnetization (Fig. 63B) and enabled us to identify the polarity pattern. Polarity chronozones were assigned according to the nannofossil and foraminifer biostratigraphy and the magnetic polarity time scale (see "Explanatory Notes" chapter, this volume) (Fig. 64).

Within the Brunhes normal-polarity zone, there are at least three short reversed-polarity zones in the interval from the lower portion of Core 123-765B-1H to the top of Core 123-765B-2H (Fig. 64). These short zones are probably some of the magnetic field excursions recognized within the latest Pleistocene (Tarling, 1983). The highest reversed-polarity zone, located in Section 123-765B-1H-7 (9–9.2 mbsf), has been correlated to the zone recognized in Hole 765A in Section 123-765A-1H-5 (6.0–6.5 mbsf); the apparent difference in depths results from nonrecovery of the uppermost sediments in Hole 765A.

The Brunhes/Matuyama boundary may be located at 35 cm below the top of Section 123-765B-5H-5, although several spikes with reversed polarity are recognized above the boundary (some of these may represent excursions). Because of the disturbance from debris flows and slump breccias, no reliable paleomagnetic data were obtained from Core 123-765B-6H and the upper half of Core 123-765B-7H. The normal-polarity zone recognized from Core 123-765B-8H to the bottom of Core 123-765B-9H may be a greatly thickened Subchron C1r-1n (Jaramillo). A normal-polarity zone located from the bottom of Core 123-765B-9H to Core 123-765B-10H may be Chron C2n (Olduvai). The reversed-polarity zone from the bottom of Core 123-765B-10H to Core 123-765B-11H can be identified as Chron C2r, although present field overprint persists in several portions of the cores even after 10 mT demagnetization.

Pliocene (Cores 123-765B-10H to -18H). Calcareous turbidites are dominant in the Pliocene cores. NRM intensities range from 0.1 to 1 mT/m for Cores 123-765B-10H and -11H, similar to the Pleistocene cores. Below these cores, NRM intensities increase by approximately one order of magnitude. Polarity zones were evident upon AF demagnetization at 10 mT. Debris flow structures were recognized in several cores, especially Sections 123-765B-11H-5 to -12H-2, making it impossible to obtain reliable paleomagnetic records.

Below the upper disturbed zones, Core 123-765B-12H exhibits a normal polarity, which can be correlated to Subchrons C2r-1n or C2r-2n of late Pliocene age (Fig. 68). Core 123-765B-13H has three distinctive reversed-polarity zones that correlate with three subchrons in Chron C2Ar. Core 123-765B-14H displays normal polarity, with a short reversed-polarity zone at the bottom, which correlates to normal-polarity Chron C2An and to Subchron C2A-1r or C2A-2r, respectively. Two reversed zones are clearly identified in Core 123-765B-15H. The short normal zone between these zones might be Subchron C2Ar. Core 123-765B-16H and the upper one-third of Core 123-765B-17H exhibit a normal polarity and have been assigned to Subchron C3.1n. The underlying normal polarity of Core 123-765B-17H, therefore, correlates with Chron C3.2n. Because there is no paleontological age for Core 123-765B-18H and a hiatus is probable, it is uncertain whether the normal-polarity zone of Core 123-765B-18H is Chron C3.3n or Chron C3An.

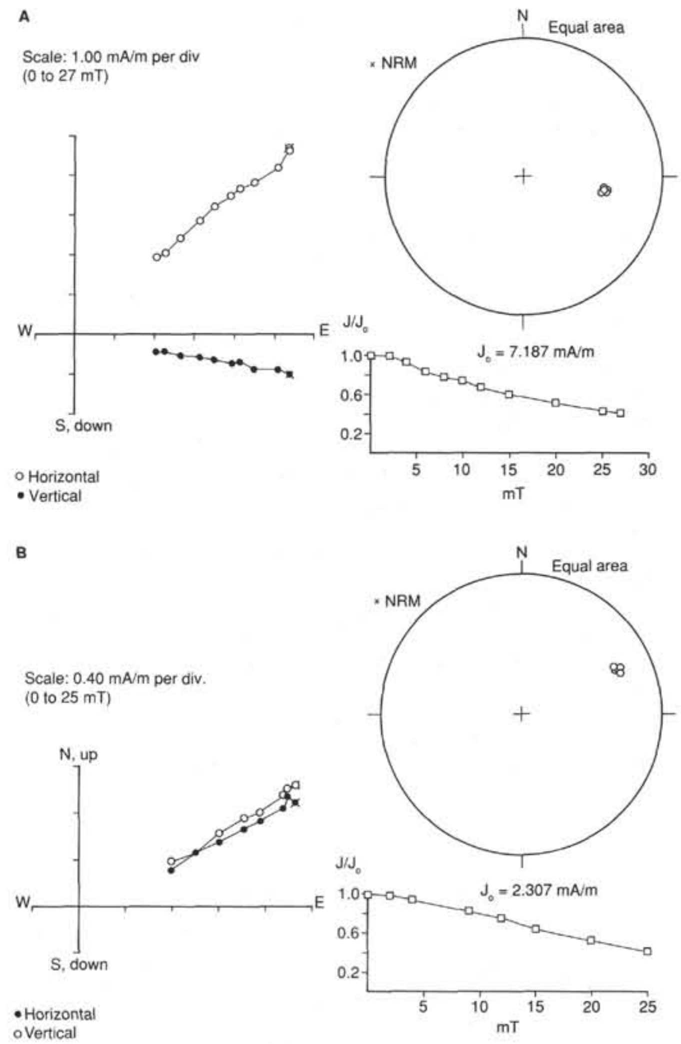

Figure 63. Effects of progressive AF demagnetization: A. Pleistocene ash-rich layer (Sample 123-765A-1H-4, 62—64 cm). The direction of magnetization remains stable through the NRM, 2, 4, 8, 10, 12, 15, 20, and 25 mT steps, and the negative intensity indicates normal polarity because the site is in the Southern Hemisphere. B. Pleistocene nannofossil claystone (Sample 123-765B-3H-3, 80—82 cm). Stable directions with positive inclination indicates reversed polarity. In vector plots (left diagram in set), inclination (open circles; up, down) is a projection of the magnetization vector onto the east-west axis; declination (solid circles) is the projection of the magnetization vector onto the horizontal plane. In the equal- plots (upper right diagram), open circles indicate vectors with negative (upward) inclinations; however, the stable direction of magnetization for these samples causes these open circles to cluster densely over each other. Intensity plot (lower right diagram) is the ratio of intensity at each demagnetization step to the NRM intensity.

Miocene (Cores 123-765B-18H through -41X, and 123-765C-1R through -13R). The middle and upper Miocene sections at Site 765 consist of 300 m of calcareous turbidites. The Pliocene/Miocene boundary can be placed within Core 123-765C-18H, but it is apparently represented by a hiatus. Most of the lower middle and lower Miocene is absent. Therefore, the Miocene section should span polarity Chrons C3A through C5B (see "Explanatory Notes" chapter, this volume). Because of the extremely rapid reversal rate during this interval, these Miocene cores (Cores 123-765B-18H to -13R) may potentially include more than 30 brief polarity chrons.

Magnetic Properties. For the Miocene cores, reversed polarity was assigned to any interval displaying either consistent positive inclinations, or a dominance of positive inclinations interspersed among negative inclinations. Normal polarity was assigned to intervals having positive inclinations and relatively stable directions upon demagnetization. A polarity assignment of "indeterminant" or "questionable" was given to intervals having no consistent trends in inclinations, or displaying unstable directions during demagnetization. Using these criteria, most of the cores appeared to consist of reversed or uncertain polarity, with only a minor amount of normal polarity present in short segments. These results are inconsistent with the expected 50/50 ratio of normal to reversed polarity for the middle and late Miocene and also display an unusually high reversal frequency. Therefore, we suspect that some intervals of normal polarity have been overprinted with reversed polarity or could not be resolved in these weakly magnetized sediments. It is also possible that 24-hr storage of the sediments before splitting and paleomagnetic analysis may have caused significant rotation of the magnetic grains toward the shipboard ambient field. In addition, the procedure of banging the wire-sliced core onto the preparation table to separate the halves may have imparted a resistant "shock" remanence to these cores. The very weakly magnetized discrete samples from these cores could not be accurately measured using either the Minispin or cryogenic magnetometer; therefore, there is no independent check upon the polarity assignments.

The average intensity of NRM magnetization is approximately 5 mA/m, with many intervals having magnetizations less than 0.1 mA/m. Upon 10 mT AF demagnetization, intensities generally decreased by one-half. A curious phenomenon was observed in the XCB cores of Hole 765B. A dramatic decrease in magnetic intensity by one to two orders of magnitude occurs from the upper portion to the lower portion of each core; we suspect that this must be an artifact induced by this type of drilling procedure, perhaps a progressive acquisition of shock remanence, the presence of abundant rust flakes in the uppermost portions of each XCB core induced by the high-pressure washing, or exposure to the magnetized core barrel. Neither the HPC cores of Hole 765B nor the RCB cores of Hole 765C exhibited this systematic decrease in intensity.

Within an individual calcareous turbidite, a progressive decrease in intensity was observed from top to bottom, with the basal sandy portion exhibiting unstable or anomalous magnetization. In some instances, an apparent change in polarity occurred at the scoured basal contact of the turbidite or within the turbidite at the depth of significant bioturbation from the surface, perhaps reflecting the reworking of the uppermost portion of the turbidite during a succeeding interval of opposite polarity.

Magnetostratigraphy. Polarity chrons within the middle and late Miocene could be tentatively assigned to some of the polarity zones, based upon the nannofossil and foraminifer biostratigraphy (Fig. 64). The lack of a distinctive polarity pattern precludes independent correlation with the magnetic polarity time scale. In some intervals, age assignments from the nannofossil and foraminifer zones differ by one or two polarity chrons (see "Biostratigraphy" section, this chapter). Polarity Chrons C3Ar and C3Br probably extend from the base of Core 123-765B-18H to approximately Core 123-765B-27X. Chron C4Ar probably includes Cores 123-765B-28X to -33X. The remainder of Hole 765B and the top 12 cores of Hole 765C have been assigned to Chrons C5r though C5Br. Because of the irregular magnetic behavior of some intervals, these polarity chron assignments are considered preliminary until they can be checked with discrete samples.

No reliable paleolatitude data could be obtained from the Neogene sediments.

Paleogene–Late Cretaceous

Susceptibility

The relatively condensed sedimentation of the Paleogene and Late Cretaceous is characterized by high average susceptibility values (K generally 50 $\times$ 10^{-6} cgs) with peaks commonly exceeding 100 $\times$ 10^{-6} cgs. This interval is recognized as susceptibility Unit S-4 and extends approximately from the middle of Core 123-765C-14R to the top of Core 123-765C-33R (470–655 mbsf) (Fig. 64). This high susceptibility is caused by iron enrichment within the reddish and variegated claystones.

In contrast, susceptibility Unit S-5, from Core 123-765C-33R to the top of Core 123-765C-45R (655–769 mbsf) has a relatively low susceptibility, with K averaging about 10 to 20 $\times$ 10^{-6} cgs and with few peaks. This unit corresponds to the dark gray claystones of the Aptian. The upper portion of Unit S-5 has a reduced average susceptibility relative to the lower portion; this change in character is probably caused by the greater importance of calcareous turbidite beds within the upper portion.

Magnetostratigraphy

Oligocene (Cores 123-765C-15R to -18R)

The light gray and reddish-brown clay has a strong NRM intensity that ranges from 1 to 100 mA/m. Overprints of present magnetic field were sufficiently removed by 10 mT AF demagnetization to identify normal and reversed polarity zones.

The four Oligocene cores (Cores 123-765C-15R to -18R) have rapidly changing sedimentation rates caused by a few thick turbidites, which makes it difficult to assign polarity chrons to the distorted polarity pattern. Therefore, the polarity chron assignments are based entirely upon the bio-magnetostratigraphy time scale (see "Explanatory Notes" chapter, this volume) (Fig. 64).

Eight reversed-polarity zones were recognized in the four cores. Planktonic foraminifers suggest correlation with Chron C6C (despite poor recovery in Core 123-765C-15R). Accordingly, the polarity zones in Core 123-765C-16R may be correlated with Chrons C7 or C7A, and the three reversals recorded in Core 123-765C-17R may be correlated with Chron C8r, Subchron C9-1r, and Chron C9r. Because of the small hiatus between Cores 123-765C-17R and -18R, the polarity zones in Core 123-765C-18R may be correlative with Chron C12-C12r.

Eocene-Paleocene-Latest Cretaceous (Cores 123-765C-18R to -24R)

The dark gray and greenish-gray clay intercalated with reddish pelagic sediments has a strong and stable magnetization, with NRM intensities of about 1 to 100 mA/m.

Recovery for Eocene and Paleocene cores (Cores 123-765C-19R to -21R) was extremely poor and renders it essentially impossible to identify a polarity pattern. In addition, slow sedimentation of the lower Maestrichtian to Campanian sediments makes assigning the polarity chron difficult.

Paleontological data indicate a hiatus within Core 123-765C-19R between the lower Oligocene and lower to middle Eocene

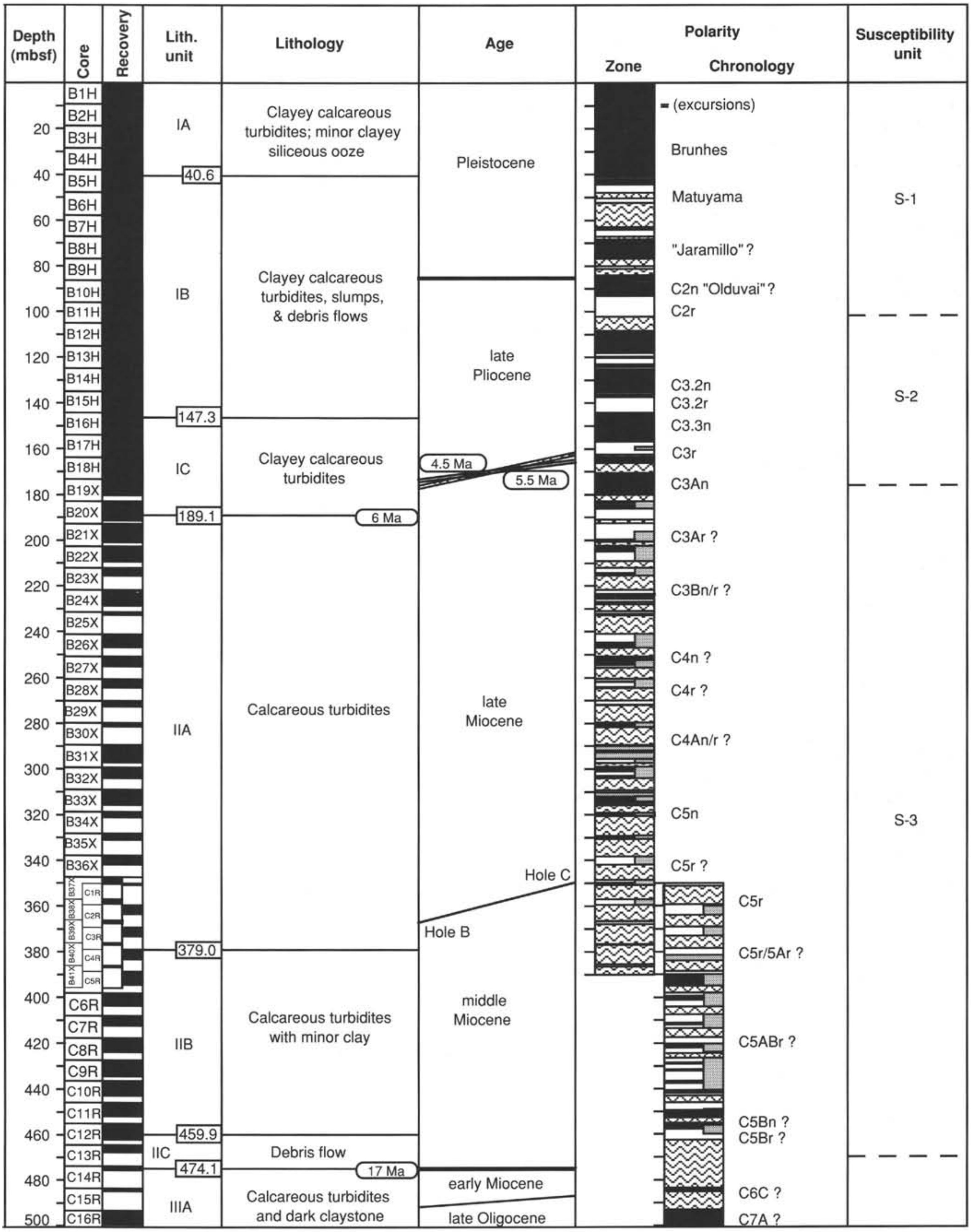

Figure 64. Magnetostratigraphy of Site 765 with possible polarity chron assignments.

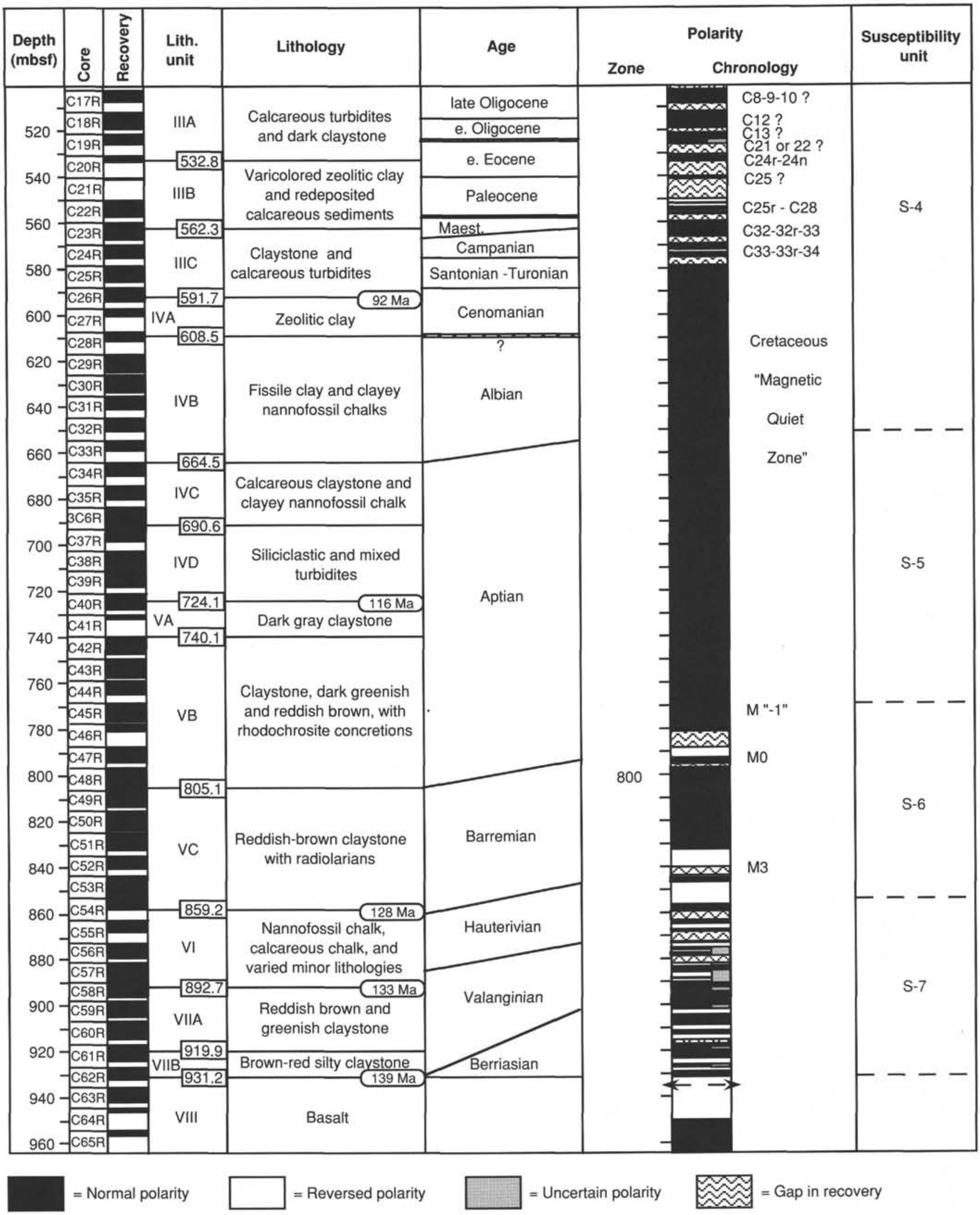

Figure 64 (continued).

sediments. Therefore, the normal-polarity zone of the lower Oligocene portion of this core may be assigned to polarity Chron C13n, and the underlying reverse-polarity zone of the middle Eocene may be assigned to Chrons C21r or C22r (Fig. 64). The reversed-polarity zone of Core 123-765C-20R (early Eocene) may be Chron C24r, and the normal-polarity zone of Core 123-765C-21R (late Paleocene) may be Chron C25n. Several polarity zones recorded in Core 123-765C-22R may correspond to the early Paleocene polarity pattern of Chrons C25r, C26n, C26r, C27n, C27r, and C28n, from top to bottom.

Core 123-765C-23R is earliest Maestrichtian to latest Campanian; thus, the reversed-polarity zones located at the upper part of the core (in the middle of Section 123-765C-23R-2) are probably correlative with Chrons C32.1r or C32r. Accordingly, the reversed polarity zone within Sections 123-765C-24R-2 and -24R-3 may be Chron C33r of Campanian age.

Cretaceous Quiet Zone (Cores 123-765C-24R to -45R)

All cores from the lower part of Core 123-765C-24R to the middle of Core 123-765C-45R display constant normal polarity, which can be assigned to the Cretaceous magnetic quiet zone.

Lower Cretaceous (Reddish-Brown Claystones; Cores 123-765C-45R to -62R). Lower Cretaceous (Valanginian-earliest Aptian age) sediments, dominated by reddish-brown radiolarian claystone, extend 160 m from the basalt basement to the middle of Core 103-765C-45R. Within this claystone are intervals of marl (nannofossil-rich clayey chalk), greenish-gray to black claystone, radiolarian-rich horizons, rhodochrosite- and dolomite-rich silts, fining-upward calcareous turbidites, and dark reddish-brown silty claystone (near the base of the section). The relative abundance of these minor constituents was used to distinguish lithologic Units VB, VC, VI, VIIA, and VIIB (see "Sediment Lithostratigraphy" section, this chapter), although the overall facies and magnetic character remain very similar. The reddish coloration indicates that hematite is present and may be an important carrier of magnetization. Greenish-gray mottling within the red claystones suggests (1) that the original depositional environment was oxidizing while hematite formed near the sediment/water interface, and (2) that post-depositional reduction occurred around burrow fillings or buried organic concentrations. Therefore, after removing secondary overprints, the hematite should be a major carrier of characteristic magnetization and a reliable indicator of the magnetic polarity at the time of sediment deposition.

Shipboard measurements on all cores were performed for susceptibility at 10-cm intervals and for magnetization (NRM and after 10 and 15 mT of AF demagnetization) at 5-cm intervals. A total of 248 oriented minicores were collected at approximately 50-cm intervals for shore-based progressive thermal demagnetization. When this section was prepared, preliminary results from several of these minicores were available for use in identifying possible magnetic polarity zones.

Susceptibility

The reddish-brown claystone has a relatively high average susceptibility value, with a K of approximately 50×10^{-6} cgs, but with peaks exceeding 100×10^{-6} cgs. Susceptibility Unit S-6 extends from Cores 123-765C-45R to -53R (769–854 mbsf) (Fig. 62).

Below Core 123-765C-53R, the sediment is rich in nannofossil-claystone turbidites and thus has a lower average susceptibility. The basal brownish silty claystone also has a low susceptibility. These lowermost sediments (854–931 mbsf) make up susceptibility Unit S-7.

Magnetic Behavior

The reddish-brown claystone has a strong magnetization with NRM intensities averaging between 10 and 100 mA/m. NRM inclinations were generally negative, indicating a significant overprint by the present magnetic field (Fig. 65).

Claystones having a high hematite content, especially the dark reddish-brown claystone and silty marl in the lowest portion of the hole (Cores 123-765C-55R to -62R), did not respond significantly to AF demagnetization. The directions of magnetization displayed only slight rotations during decreases in magnetic intensities by 10% to 50% of NRM intensity. In contrast, the intercalated intervals of grayish-green claystone displayed major shifts in direction and intensity of magnetization. These directional shifts commonly indicate a characteristic polarity different from the host reddish-brown claystone. However, average inclinations from reversed-polarity intervals were shallower than those of normal-polarity intervals, and the declinations of adjacent reversed- and normal-polarity zones differed by only 120° to 160°. This lack of antipodality between polarities is another indication of the presence of a persistent secondary overprint that could not be removed by AF demagnetization.

Reddish-colored pelagic sediments required progressive thermal demagnetization to remove secondary overprints from the primary directions of magnetization (Steiner, 1977; Ogg, 1981; Lowrie and Heller, 1982). In a study of coeval reddish claystones of the same facies at nearby DSDP Site 261, Jarrard (1974) observed only normal polarity after applying 5 mT AF demagnetization. Thermal demagnetization of a suite of samples from this same interval revealed both normal and reversed polarities, consistent with the M-sequence age of the sediments (Ogg and Warnick, unpubl. data).

Progressive thermal demagnetization was applied to several pilot minicores. Upon heating above 300°C, a normal-polarity overprint, presumably from the present magnetic field, was removed (Fig. 66). Stable and nearly antipodal directions of normal and reversed polarity generally were present from 450° through 650°C, with intensities of magnetization typically being about 10% to 30% of NRM intensities. From such typical behavior, the primary or characteristic magnetization may have been carried both by hematite, formed from early oxidation at the sediment/water interface, and by magnetite, as indicated by the similar magnetic directions of greenish-gray intervals. The secondary overprint is probably carried by goethite and/or multiple-generation hematite.

Magnetostratigraphy

Orientation Relative to Apparent Dip; Rotation of Australia

As noted above, Hole 765C deviated from vertical, causing a 10° to 11° apparent dip of the recovered sediments. Measurement of several sediment intervals displaying uniform apparent dip indicated that the dip direction was oriented 40° (±10°) counterclockwise to the "normal-polarity" declination of NRM carried by the red claystones, which is considered to be dominated by a secondary overprint of present field. The ubiquitous presence of an apparent dip throughout the Lower Cretaceous sediments enabled us to orient each minicore with respect to this uniform dip direction, thereby establishing a declination of all discrete samples with respect to each other and to the "N40°W" direction of hole deviation. This procedure of minicore orientation was used at other DSDP sites (Morgan, 1979; Ogg, 1986, 1987, 1988) and is illustrated in Figure 67.

Upon thermal demagnetization, the mean declination of such oriented minicores relative to the azimuth of apparent dip was approximately 0° for samples of normal polarity and approximately 180° for samples of reversed polarity (Ogg and Kodama, unpubl. data). We also observed that the declination of characteristic direction from a typical normal-polarity minicore was rotated 15° to 30° counterclockwise relative to the declination of the NRM direction. From these preliminary results, we concluded that (1) the Lower Cretaceous portion of Hole 765C de-

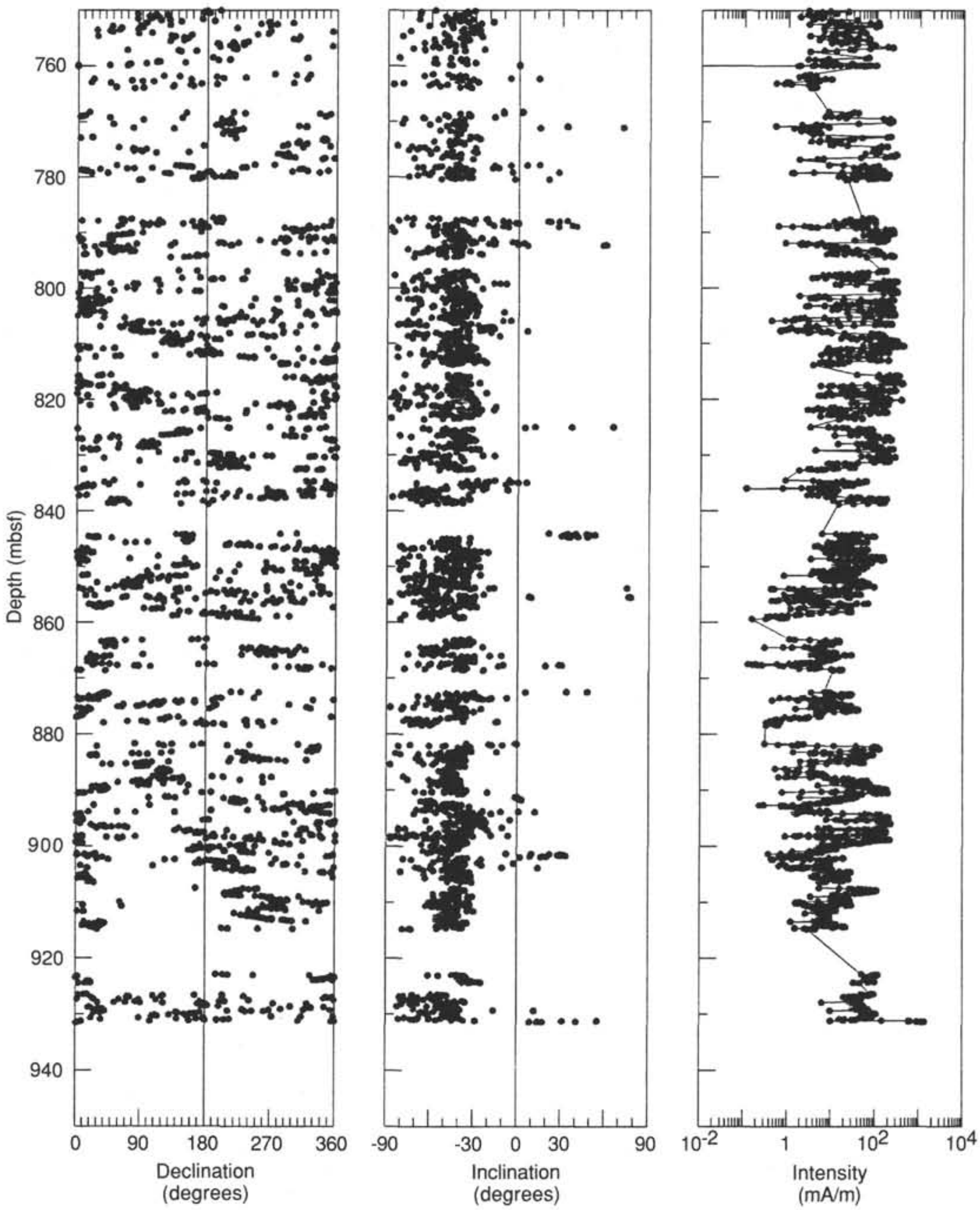

Figure 65. Stratigraphic plot of NRM declinations, inclinations, and intensities of the Early Cretaceous portion of Site 765.

viated 10° to 11° from vertical in a direction that fortuitously slanted toward Early Cretaceous "North," and (2) the azimuth of Early Cretaceous "North" is a minimum of 30° counterclockwise from present-day North, therefore implying that this region of northwestern Australia has rotated at least 30° counterclockwise since the Early Cretaceous. This counterclockwise rotation is consistent with paleogeographic reconstructions of Gondwana (Embleton, 1981), although the magnitude is less than expected. Early Cretaceous paleomagnetic poles indicate that Australia has rotated approximately 90° (±20°) counterclockwise with respect to the present longitude meridians (see "Background and Introduction" chapter, this volume). If the *removed* vector between NRM and the attainment of characteristic magnetization (i.e., the secondary overprint of presumably present-day field) is used, then the computed counterclockwise rotation agrees much better with the predicted rotation.

Interpretation of Polarity

The characteristic magnetizations of minicores, as obtained from progressive thermal demagnetization, can be used as a control on the interpretation of polarity from shipboard close-spaced measurements of magnetization of the cores. The counterclockwise rotation of Australia since the Early Cretaceous, as noted above, helped us to interpret the shipboard measurements, even if we could not obtain characteristic magnetic directions. If, upon progressive AF demagnetization, the magnetic declination of an interval displays rotation in a counterclockwise direction, then this interval probably has normal polarity. Similarly,

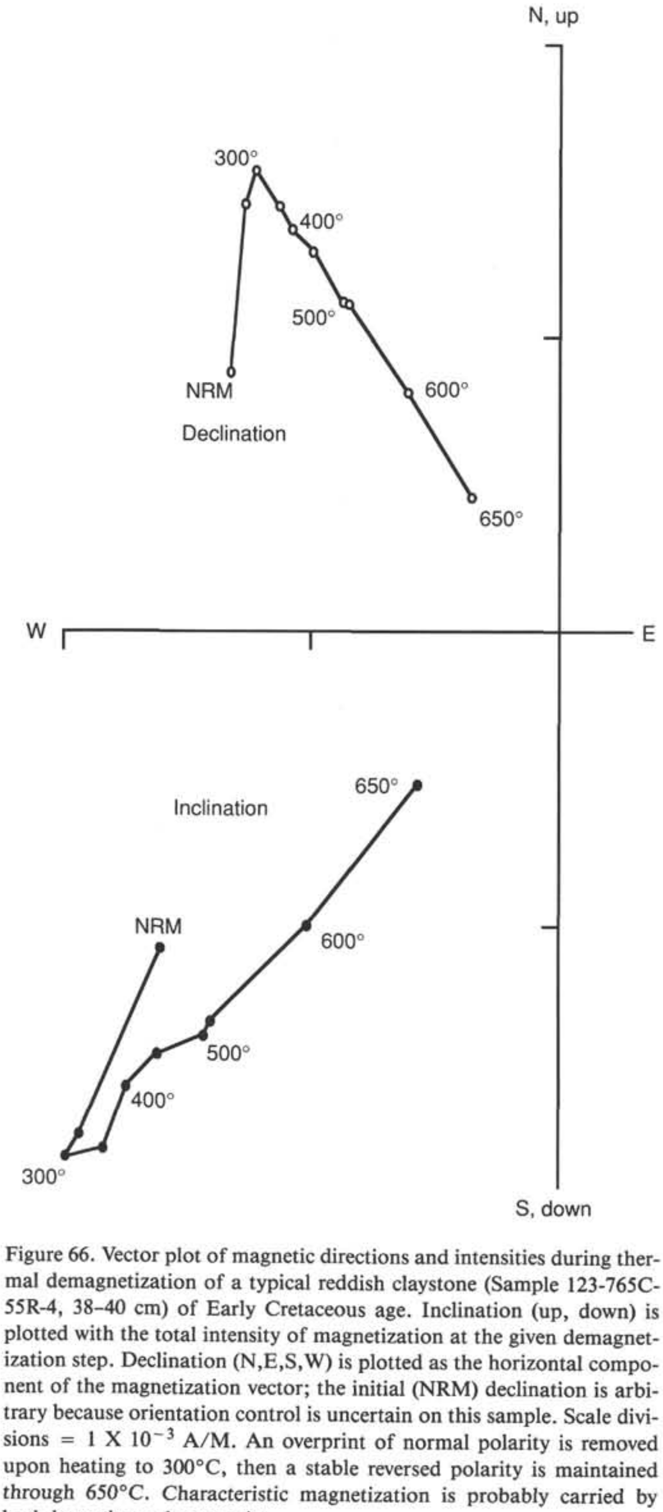

Figure 66. Vector plot of magnetic directions and intensities during thermal demagnetization of a typical reddish claystone (Sample 123-765C-55R-4, 38–40 cm) of Early Cretaceous age. Inclination (up, down) is plotted with the total intensity of magnetization at the given demagnetization step. Declination (N,E,S,W) is plotted as the horizontal component of the magnetization vector; the initial (NRM) declination is arbitrary because orientation control is uncertain on this sample. Scale divisions = 1×10^{-3} A/M. An overprint of normal polarity is removed upon heating to 300°C, then a stable reversed polarity is maintained through 650°C. Characteristic magnetization is probably carried by both hematite and magnetite.

intervals displaying clockwise rotations possibly have reversed polarity. By combining results from minicores with shipboard measurements, the limits of polarity zones can be more precisely delimited.

In some cases, the apparent change in polarity occurred within the upper portion of a turbidite, perhaps indicating the depth of bioturbation and resetting of magnetization during the succeeding time of opposite polarity. The gray, coarse-grained, rhodochrosite-dolomite-bearing basal portions of turbidites generally displayed unstable magnetization or anomalously steep inclinations.

The assignment of polarity *chrons* from the magnetic polarity time scale to the polarity *zones* observed in the sediments is another realm of speculation. The M-sequence polarity pattern was correlated to biostratigraphic datum levels and zonations in the Atlantic and western Tethyan faunal provinces (see "Explanatory Notes" chapter, this volume; Ogg, 1988). At Site 765C, several key taxa of this Atlantic-Tethys province, especially nannofossils and calpionellids, are not present. In addition, the lowest and highest occurrences of other taxa are poorly contrained. As a result, the available biostratigraphy does not provide a precise age framework for unambiguously correlating most of the observed magnetic polarity zones with the Atlantic-Tethys magneto-biostratigraphic time scale.

Polarity Zonation

The stratigraphic column of tentative polarity interpretations of the Lower Cretaceous section of Site 765 is shown in Figure 64.

The highest reversed-polarity zone of the Lower Cretaceous is a narrow, but clearly defined, event that occupies 40 cm of core from Sections 123-765C-45R-2, 114 cm, to Section 123-765C-45R-3, 7 cm, of Aptian age. This event probably is not Chron M0, but rather a possible representation of an earlier brief polarity chron that was previously observed in magnetostratigraphic studies of sediments (Jarrard, 1974; Keating and Helsley, 1978a, 1987b; Lowrie et al., 1980; Vandenberg and Wonders, 1980; Khramov, 1982). This event may correspond to a narrow magnetic anomaly "CL" in the Pacific, as modeled by Hilde et al. (1976) and designated M"-1" in some Atlantic magnetic profiles (Vogt and Einwich, 1979). The informal designation M"-1" has been tentatively assigned to this short reversed-polarity zone.

Chron M0r has been assigned to the 4-m-thick, reversed-polarity zone extending approximately from Section 123-765C-47R-1, 95 cm, through Section 123-765C-47R-4, 66 cm. The Barremian/Aptian stage boundary, which occurs prior to Chron M0 (Channell et al., 1979; Ogg, 1988), thus is within the lower portion of Core 123-765C-47R or within the uppermost portion of Core 123-765C-48R.

Chron M3r, and possibly Chron M1r, are tentatively assigned to the interval of predominantly reversed-polarity extending from Section 123-765C-51R-5, 131 cm, through the upper half of Core 123-765C-54R. The age of M1r-M3r is middle Barremian, which is consistent with biostratigraphy and average sedimentation rates extrapolated for this portion of the sediment column (see "Biostratigraphy" section, this chapter).

Polarity chrons cannot be reliably assigned to the polarity zones of the Hauterivian and Valanginian sediments because of the limited biostratigraphic age control. The pattern of polarity zones, as interpreted from the shipboard analyses and the preliminary results from shorebased analysis of selected minicores, does not have a distinctive "fingerprint" to enable us to correlate unambiguously the magnetic polarity time scale of this age interval. There are a minimum of 11 reversed-polarity zones within Cores 123-765C-55R through -62R; therefore, it is probable that most of the polarity zones through M13 (basal Valanginian) or older are present.

The basal sediments directly overlying the basalt basement are apparently of normal polarity. The upper pillow flows of the basalt section are of reversed polarity, presumably corresponding to the marine magnetic anomaly designated "M26" by Fullerton et al. (1989). Therefore, it is probable that there is a hiatus between the basalt flows and the overlying reddish-brown claystone and dark brown silty marl. Below the uppermost 15 m

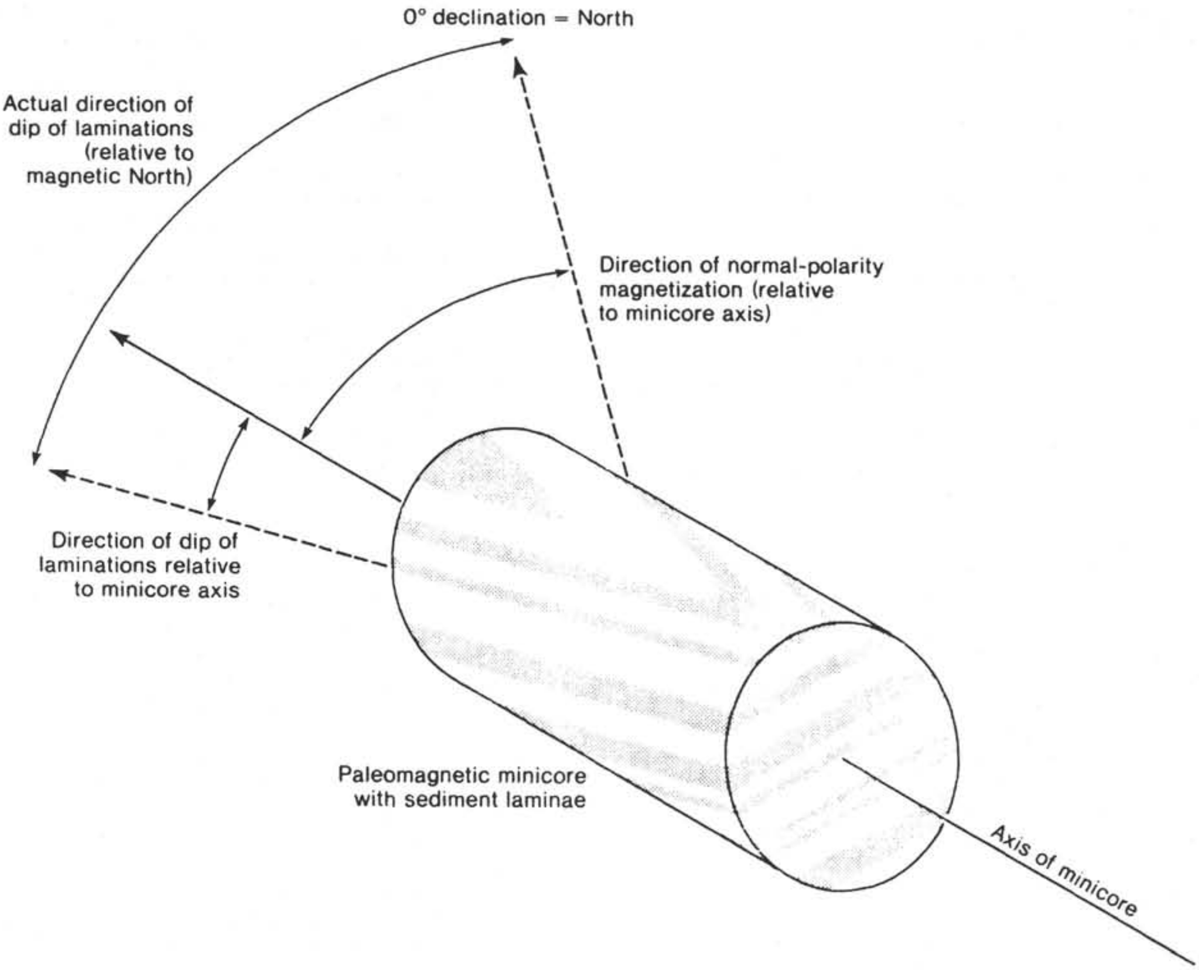

Figure 67. Orientation procedure for a minicore using dipping laminae. The azimuth of apparent dip of the laminae relative to the axis of the minicore provides a relative orientation for each sample. This direction was used as "field correction" on the sample orientations. The declination of normal-polarity characteristic magnetization in this coordinate system (with respect to the direction of apparent dip) enables one to determine the azimuth of the deviation of the drill hole from vertical (with respect to paleonorth). This azimuth, and the measured deviation of the hole, is then used as a "structural correction' for the direction of characteristic magnetization to obtain the true inclination of the ancient magnetic field (from Ogg, 1987).

of flows, the basalt is of normal polarity (see "Basalt Paleomagnetism" section, this chapter), suggesting that only a portion of this reversed-polarity chron is present. As a preliminary interpretation, it is probable that the corresponding polarity chrons of the basalt are actually within the M16 to M13 set, which spans the transition from Berriasian into Valanginian.

All of these M-sequence polarity chron assignments are subject to revision after thermal demagnetization studies on most of the minicores.

Paleolatitudes

Mean Inclination of NRM

The present latitude of Site 765 is 16.0°S, which corresponds to a magnetic dipole inclination of −29.8°. The average inclination of the NRM directions from the Lower Cretaceous section is approximately −41°, using a visual fit through clusters of NRM inclinations (Fig. 67). The difference between the present inclination and the NRM average inclination is probably due to three factors: the deviation of the hole from vertical, the presence of steeper-inclination normal-polarity components of Cretaceous age in the NRM, and possible vertical overprints induced by drilling (reviewed by the DSDP Leg 89 Shipboard Scientific Party in 1986; see also "Basalt Paleomagnetism" section, this chapter).

The hole deviates approximately 10.5° from vertical (10° at Core 123-765C-45R; 11° at Core 123-765C-57R) toward approximately N30-40°W (±5°) with respect to the NRM direction, as discussed above. To compensate for the magnitude and direction of hole deviation and to compute the true average NRM inclination, a correction factor consisting of the hole deviation multiplied by the cosine of the angular difference between the direction of hole deviation and direction of NRM (hence, 10.5° cos(35°) = approximately 7°) must be subtracted from the observed NRM average inclination of −41°. The true NRM average inclination is therefore −48° (± approximately 3°), or about 18° steeper than the present-day dipole magnetization. This steeper than expected inclination of NRM may have been by several factors, including (1) presence of steep Early Cretaceous components within the NRM, (2) a slight primary dip of the *in-situ* sediments (shipboard measurements of apparent dips were up to 15°), and (3) vertical components of NRM induced during drilling. Drilling-produced vertical overprints on sediment and basalt cores have been observed at several other drill sites (see review by DSDP Leg 89 Shipboard Scientific Party,

1986) and also were observed in the basalt cores of Site 765 (see "Basalt Paleomagnetism" section, this chapter).

Early Cretaceous Paleolatitude

Mean inclinations for each core were estimated from characteristic directions of the pilot suites of minicores from Cores 123-765C-44R through -62R. There is no significant trend with depth for these inclinations, implying that the paleolatitude of the Argo Abyssal Plain was fairly constant throughout the Early Cretaceous.

The mean inclination for the minicore suite is approximately −43° for normal-polarity samples. Reversed-polarity samples displayed a slightly shallower inclination, indicating that a secondary overprint persisted through the demagnetization procedure. Application of AF demagnetization to the thicker turbidite beds in the cores yielded a progressive decrease in inclination from the base to the top of the bed; this phenomenon could indicate inclination shallowing from compaction effects with finer grain sizes, or the varying response to AF demagnetization.

Application of the statistical procedure of Kono (1980a, 1980b) for computing true mean inclinations from drill-core paleomagnetic data yielded a mean inclination of approximately −46°. The direction of the deviation of Hole 765C from vertical is toward the Early Cretaceous "north." Therefore, to correct for the apparent dip of bedding, the 10.5° deviation must be subtracted from the true mean inclination. The corrected mean inclination of approximately −56.5° corresponds to an Early Cretaceous paleolatitude of approximately 37°S. This value should be considered as a preliminary estimate until a complete evaluation is made of the entire suite of 248 minicores collected from this interval. This paleolatitude of 37°S is consistent with the preliminary paleomagnetic results from Lower Cretaceous sediments of Site 766 (this volume). However, the paleolatitude is about 8° *north* of the Early Cretaceous paleolatitude of 45° predicted from paleogeographic reconstructions for this site (see "Background and Introduction" section, this chapter) and is 16° *south* of the paleolatitude derived from paleomagnetism of Lower Cretaceous deep-sea sediments in western Timor (Wensink et al., 1987).

Summary of Lower Cretaceous Paleomagnetism

Lower Cretaceous reddish-brown claystones have hematite as a major carrier of magnetic remanence and required progressive thermal demagnetization to obtain a reliable magnetic stratigraphy and paleolatitude information. A preliminary polarity interpretation derived from a pilot suite of minicores, from analysis of the rotation of magnetic directions of the reddish sediments during AF demagnetization, and from the magnetic polarity displayed by greenish-gray intervals was used to identify several polarity zones (Fig. 64). Polarity chron M"-1" was identified within the Aptian. Polarity Chrons M0r and M3r could be assigned to the polarity pattern in lithologic Units VB and VC, implying that the Aptian/Barremian boundary is near the base of Core 123-765C-47R. Polarity chrons could not be unambiguously assigned to the underlying set of reversed-polarity zones, but the pattern is consistent with the Valanginian-Hauterivian magnetic polarity time scale. Hole 765C deviates from vertical toward the WNW with respect to present north, therefore the observed magnetic inclinations are approximately 10° to 11° shallower than actual inclinations. The Early Cretaceous paleolatitude for this site is approximately 37°S.

SEDIMENT-ACCUMULATION RATES

Cenozoic

Sedimentation rates were estimated from an age-vs.-depth plot for Holes 765A, 765B, and 765C (Fig. 68). The data are well-constrained, as the curve is defined by a total of 30 well-defined chronostratigraphic events (Table 11). These events include nannofossil and planktonic foraminiferal datum levels (first and last occurrences) and radiolarian zones. Absolute ages follow the Cenozoic time scale outlined in the "Explanatory Notes" chapter (this volume).

Average sedimentation rates for the Neogene of Site 765 are uniformly high (26.6 m/m.y.), with the exception of a few prominent hiatuses or intervals of markedly reduced deposition (Fig. 68). Nannofossil and foraminiferal zones (see "Biostratigraphy" section, this chapter, Figs. 58 and 59) indicate hiatuses or highly condensed sections in the lower Pliocene and lower Miocene.

Compared to those in the Neogene, average Paleogene rates are considerably lower (1.8 m/m.y.). The microfossil sequence indicates a hiatus in the middle Oligocene and a distinct unconformity in Core 123-765C-19R that separates the lower Oligocene from the lower Eocene (see "Biostratigraphy" section, this chapter, Fig. 59A).

Cretaceous

The sediment-accumulation rate (age-depth) curve for the Cretaceous of Hole 765C was established using 39 chronostratigraphic events (Table 12). The resulting curve (Fig. 69) suggests continuous deposition from the late Berriasian to the Maestrichtian. To establish the age-depth curve, we mainly used zones based on planktonic microfossils and several magnetic polarity reversals in the Barremian to Aptian part of Hole 765C. The numeric ages of the microfossil zones were taken from the Cretaceous time scale and zonal schemes given in the "Explanatory Notes" chapter (this volume).

The calculated sediment-accumulation rates are variable, with the highest rate in the Aptian (14 m/m.y.) and the lowest rate in the upper Albian to lower Cenomanian (0.25 m/m.y.). The age-depth curve is roughly divided into six segments from the Berriasian to the Maestrichtian. The sediment-accumulation rate in the Upper Cretaceous part the curve is 1.7 m/m.y. and is constrained using planktonic foraminifers and nannofossil zones. Nannofossil zones in the upper Turonian to Maestrichtian have estimated durations between 1.0 and 2.5 Ma and provide the best chronostratigraphic resolution. An inflection point in the curve is placed at approximately 595 mbsf, which is about 3 m below the boundary between lithologic Subunits IIID and IVA. The upper Albian to lower Cenomanian interval is condensed and one or more hiatuses may be present, but these cannot be completely resolved with the biostratigraphic data. The sediment-accumulation rate increases in the Albian portion of the curve, although this rate (approximately 4.2 m/m.y.) is somewhat less well-constrained because it is based on the ranges of just two nannofossil taxa. The age-depth curve again changes slope near 660 mbsf. This change in the sediment-accumulation rate occurs near the boundary between lithologic Subunits IVB and IVC, which has been placed near the top of Core 123-765C-34R at about 665 mbsf.

In the Aptian to Barremian interval of Hole 765C, the age-depth curve is well-constrained using palynomorphs, planktonic foraminifers, and magnetic polarity reversals. The sediment-accumulation rate in this part of the curve is approximately 14 m/m.y. A late Aptian age for Samples 123-765C-33R, CC, through -35R, CC, is supported by the presence of the *G. algeriana/H. gorbachikae* and *D. davidii* zones. The base of the Aptian can be accurately determined by means of magnetic polarity reversals. The top of magnetic Chron M0 (118 Ma) has been placed near the base of Core 123-765C-45R or within Core 123-765C-46R, and the base of M0 occurs near the base of Core 123-765C-47R. Magnetic polarity reversals assigned to M3 occur near the base of Core 123-765C-51R and approximately 2 m below the top of Core 123-765C-53R. Below Core 123-765C-53R,

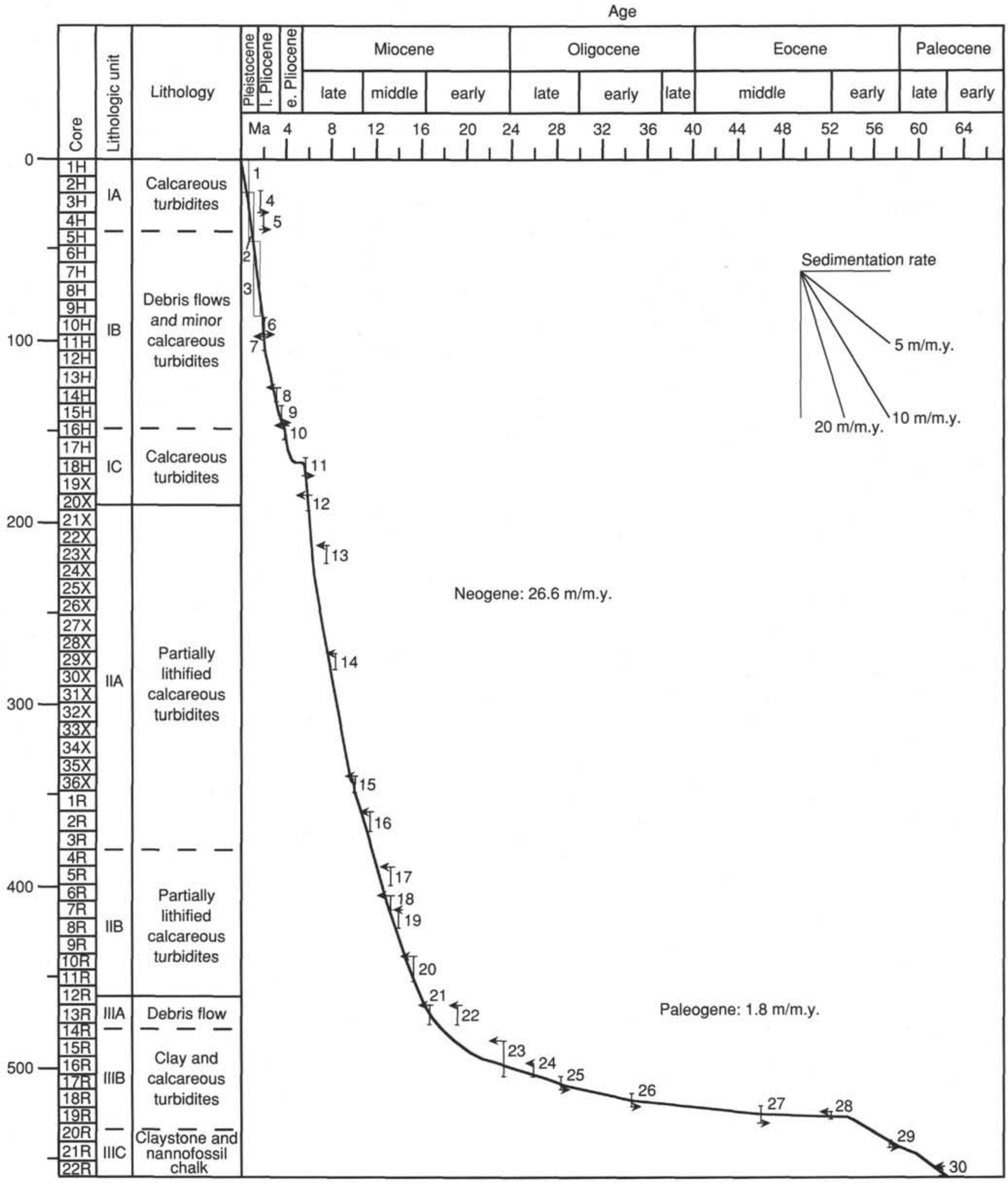

Figure 68. Cenozoic depth vs. age curve, Hole 765C.

the paleomagnetic data generated on board ship do not give identifiable patterns.

Below Core 123-765C-53R (approximately 850 mbsf) the age-depth curve is less well-constrained, although it can be extended linearly to about 915 mbsf. Palynomorphs and radiolarians provide the best age constraints in the Berriasian to Hauterivian, and the age-depth curve has been drawn using these points. Range end points for selected benthic foraminiferal species are also given to compare their stratigraphic ranges in Hole 765C with those of other microfossils.

Two microfossil ages that are in apparent conflict are the last occurrence (LO) of the radiolarian *S. cetia* and the LO of the ra-

Table 11. Cenozoic chronostratigraphic events, Site 765.

Number	Datum levels/zones	Interval	Age (Ma)
1	*C. tuberosa* Zone	765B-1H, Top to 765B-2H, CC	0–0.6
2	*A. ypsilon* Zone	765B-2H, CC to 765B-5H, CC	0.6–1.0
3	*A. angulae* Zone	765B-5H, CC to 765B-9H, CC	1.0–1.6
4	LO *G. fistulosus*	765B-2H, CC to 765B-3H, CC	1.6
5	LO *G. extremus*	765B-3H, CC to 765B-4H, CC	1.8
6	LO *D. brouweri*	765B-9H, CC to 765B-10H, CC	1.9
7	FO *G. truncatulinoides*	765B-10H, CC to 765B-11H, CC	1.9
8	FO *G. toseaensis*	765B-13H, CC to 765B-14H, CC	3.1
9	LO *R. pseudoumbilica*	765B-14H, CC to 765B-15H, CC	3.5
10	S.D. coiling *Pulleniatina*	765B-15H, CC to 765B-16H, CC	3.8
11	LO *D. quinqueramus*	765B-17H, CC to 765B-18H, CC	5.6
12	FO *P. primalis*	765B-19X, CC to 765B-20X, CC	5.8
13	FO *N. humerosa*	765B-22X, CC to 765B-23X, CC	7.5
14	FO *D. quinqueramus*	765B-28X, CC to 765B-29X, CC	8.2
15	FO *C. calyculus*	765B-35X, CC to 765B-36X, CC	10.0
16	FO *C. coalitus*	765C-1R, CC to 765C-2R, CC	11.3
17	FO *D. kugleri*	765C-4R, CC to 765C-6R, CC	13.1
18	FO *G. fohsi*	765C-7R-2 to 765C-8R-2	13.1
19	FO *G. praefohsi*	765C-8R-2 to 765C-8R, CC	13.9
20	FO *O. suturalis*	765C-9R, CC to 765C-11R, CC	15.2
21	FO *G. sicana*	765C-12R, CC to 765C-13R, CC	16.6
22	FO *S. heteromorphous*	765C-12R, CC to 765C-13R, CC	17.1
23	FO *D. druggi*	765C-14R, CC to 765C-16R, CC	23.2
24	FO *G. primordius*	765C-15R, CC to 765C-16R-4	25.8
25	LO *S. distentus*	765C-16R, CC to 765C-17R, CC	28.2
26	LO *R. umbilica*	765C-17R, CC to 765C-18R, CC	34.6
27	LO *M. aragonensis*	765C-18R, CC to 765C-19R, CC	46.0
28	FO *D. sublodoensis*	765C-19R-2 to 765C-19R-3	52.6
29	LO *Fasiculithus* sp.	765C-20R, CC to 765C-21R-1	57.4
30	FO *F. typaniformis*	765C-22R-2 to 765C-22R-4	62.0

diolarian *P. amphitreptera*. Both species have been reported to range to the late Valanginian, but in Hole 765C the LO of *S. cetia* is in Section 123-765C-62R-1, whereas *P. amphitreptera* ranges up to Section 123-765C-57R-4, suggesting a younger age for the LO of *P. amphitreptera* in this area. One line can be drawn that is constrained by the base of Chron M3, the LO of *P. amphitreptera*, and the *E. torynum* Zone. This line yields a calculated sediment-accumulation rate of 5.0 m/m.y. Another line can be fit through the base of Chron M3, the top of the sampling error associated with *S. cetia*, and the first occurrence (FO) of the benthic foraminifer *V. neocomiensis*. This line yields a calculated sediment-accumulation rate of 6.1 m/m.y. Our suggested age-depth model is halfway between these two limits and yields a calculated sediment-accumulation rate of 5.6 m/m.y.

The age of the sediment overlying basement at Site 765 has been determined as late Berriasian or slightly younger, based on the presence of the radiolarian species *H. barbui* in Sample 123-765C-62R-1, 53–56 cm. We favor a slightly increased sediment-accumulation rate for Cores 123-765C-61R and -62R because of the presence of abundant detrital material (about 30% by volume) in lithologic Subunit VIIB, although the biostratigraphic data neither support nor contradict a linear rate to the base of the sediment column.

SEDIMENT INORGANIC GEOCHEMISTRY

Interstitial-Water Chemistry

Introduction

A total of 40 interstitial-water (IW) samples were taken at Site 765. No *in-situ* samples were taken. Because the steepest concentration gradients are commonly observed in the uppermost sediment, the strategy was to sample the uppermost 100 mbsf in detail, taking an IW sample every core. Two whole-round core samples, 3 cm long, were taken from the topmost, relatively undisturbed sediment (0.5 and 1.5 mbsf) to define better the gradients near the sediment/seawater interface. In addition, an attempt was made to sample the bottom water, but no sample was obtained because of a faulty water sampler. Below 100 mbsf the normal sampling procedure was followed; an IW sample was taken approximately every third core, depending on the amount of core recovered. During APC and XCB coring of Holes 765A and 765B, the lithology was not visible through the core liner and so samples were randomly chosen; usually samples were taken midcore at the base of the third interval, 145–150 cm. Whole-round core samples, 5 cm long, provided sufficient IW (>20 cm^3) throughout most of Hole 765B (to 367.6 mbsf). During rotary drilling of Hole 765C, we could see the core through the liner, and samples from noncemented intervals were selected to maximize IW yield and solid vs. fractured core and clayey vs. sandy lithologies were taken to avoid possible contamination. Whole-round core samples, 10 cm long, were required for all of Hole 765C. Many deeper samples from Hole 765C yielded less than 5 cm^3 of IW, even after squeezing for more than 2 hr at 40,000 psi. Established ODP sample squeezing and analytical methods were used (see "Explanatory Notes" chapter, this volume). IW analytical results are summarized in Table 13. Some analyses were not performed on deeper samples because of the small IW volumes recovered.

Salinity and Chloride

Salinity decreases with sediment depth from values near those of IAPSO seawater (35.5 ‰) to 32.2 ‰ at 441.0 mbsf (Fig. 70A). The decrease in salinity is mostly a result of sulfate reduction and depletion of magnesium ion (see "Sulfate and Magnesium" section, this chapter) Below 441.0 mbsf the salinity is far more variable, ranging from 19.8 to 35.9 ‰. Several of the minor fluctuations in salinity below 441.0 mbsf correlate with sulfate and magnesium variations, but the major changes correlate directly with the chloride ion concentration. The correlation between salinity and chloride suggests the IW was diluted by essentially pure H_2O, since the chloride ion is generally considered conservative in pelagic marine sediments, having no significant sinks or sources. Chloride concentration can be affected by brines or the decomposition of gas hydrates, but no evidence for either was found at Site 765. With the exception of two samples, chloride concentration is more or less constant at a value within about 1% of normal seawater (559 mM) to a depth of 585.0 mbsf (Fig. 70B). Below 585.0 mbsf the chloride ion exhibits unusually large and scattered decreases that correlate with the low salinities. Seven IW samples have unusually low salinities and chloride concentrations that range from approximately 53% to 97% of normal seawater (Table 14). The IW samples occurring between the low salinity/chloride samples have salinities and chloride concentrations within 1% of normal seawater.

There are several possible explanations for the seven unusually low salinity samples observed at Site 765.

1. The IW samples were contaminated by either freshwater in the laboratory or drilling mud (salinity = 15 ‰).
2. The IW was diluted by freshwater that entered the sediment at some stage of burial from an outside source. The large elevation of the adjacent Australian continental margin may have provided a hydrostatic head capable of moving low-salinity waters through fractured basement rock into sediments of the Argo Abyssal Plain.
3. The IW was diluted with relatively pure water that resulted from one or more of the following diagenetic processes: (1) dewatering of expandable clay minerals as a result of clay mineral transformations during burial or during squeezing in the hydraulic press in the laboratory; (2) production of water from diagenetic reactions, such as the silica phase transformations; (3) osmotic membrane filtration of IW by the clay minerals during burial compaction.

Table 12. Microfossil zones and occurrences used to construct the Cretaceous sediment-accumulation rate curve for Hole 765C.

Chart #	Zone or event	Core, section, interval (cm)	Chronostratigraphy	Age (Ma)	Reference
N	*T. phacelosus*	123-765C-23R-1	latest Camp.-earliest Maest.	73–75.5	Sissingh (1977)
1 BF	*H. ovulum gigantea*	22R, CC	late Campanian-Maestricht.	80–66.4	Geroch and Nowak (1984)
2 N	*C. aculeus*	23R, CC	middle Campanian	79–80.5	Sissingh (1977)
3 PF	*G. elevata.*	24R-1	early Campanian	81–84.5	Caron (1985)
4 N	*B. parca-C. obscurus*	24R-1 to 24R-3	early Campanian	81–83.5	Sissingh (1977)
5 N	*C. obscurus*	24R-4	latest Sant.-earliest Camp.	83.5–84.5	Sissingh (1977)
6 PF	*D. primitiva*	25R-1	late Coniacian	87.5–88	Caron (1985)
7 N	*M. decussata*	25R-1	early Santonian	86.5–87.5	Sissingh (1977)
8 N	*M. furcatus*	25R-2	Coniacian	88.7–88.5	Sissingh (1977)
9 N	*E. eximius*	25R-3	late Turonian	88.5–89.5	Sissingh (1977)
10 N	*G. gartneri*	25R-4, 75–26R-1, 25	early–mid Turonian	89.5–91	Sissingh (1977)
11 PF	*M. sigali*	25R, CC	late Turonian	88.5–89.5	Caron (1985)
12 N	*M. decoratus*	26R-1, 28–26R-5, 105	lte Cenomanian	91–92	Sissingh (1977)
13 PF	*R. cushmani*	26R-4	latest Cenomanian	91–93	Caron (1985)
14 BF	LO *P. alternans*	26R, CC	early Cenomanian	~94	Geroch and Nowak (1984)
15 N	*E. turrieseiffelii*	26R, CC–27R-1	late Albian–early Cenoman.	92–100	Sissingh (1977)
16 N	*P. columnata*	27R-1, 75–32R-1, 27	Albian	100–111	Sissingh (1977)
17 N	FO *T. phacelosus*	28R, CC	Albian	~104	Perch-Nielsen (1985)
18 N	*C. litterarius-P. columnata*	32R-2, 30–39R, CC	Aptian–early Albian	111–119	Sissingh (1977)
18 a P	FO *C. intermedia*	33R-1, 38	earliest Albian	~113	Helby et al. (1987)
19 P	*D. davidii*	34R-1 & 35R, CC	late Aptian	113–115	Helby et al. (1987)
20 PF	*G. algeriana-H. gorbachikae*	34R, CC	late Aptian	113–115	Caron (1985)
21 P	*O. operculata*	40R, CC & 45R, CC	early Aptian	115–118	Helby et al. (1987)
22 PF	occ. *C. hoterivica*	45R, CC	Barremian–early Aptian	116–130	Kent and Gradstein (1985)
23 P	u. *M. australis*	47R-1, 50R, CC, 52R, CC	late Barremian	118–125	Helby et al. (1987)
24 R	LO *P. lilyae*	49R-2	mid late Barremian	~121	Schaaf (1985)
25 R	FO *E. tenuis*	52R-2	Valanginian/Hauterivian	~131	Sanfilippo and Riedel (1985)
26 P	l. *M. australis*	54R-4–54R, CC	latest Valang.–e. Barrem.	125–128	Helby et al. (1987)
27 N	*N. columi-C. oblongata*	55R-1, 42–58R-1, 131	l. Berriasian–e. Hauteriv.	128–144	Sissingh (1977)
28 N	FO *S. colligata*	56R-3, 142	early Valanginian	130	
29 BF	occ. *D. praehauteriviana*	56R, CC	Valanginian	131.5–138.5	Gradstein (1983)
30 R	LO *P. amphitreptera*	57R-4	late Valanginian	~134	Schaaf (1985)
31 BF	*Haplophragmium inconstans*	59R-2–62R-4	early Tithon.–late Valang.	150–133	Gradstein (1983)
32 P	*E. torynum*	59R-4–59R-5	e. Valanginian–l. Berrias.	137–139	Helby et al. (1987)
33 BF	FO *Hormosina ovulum*	60R, CC	mid Hauterivian	<130	Geroch and Nowak (1984)
34 BF	FO *Hippocrepina depressa*	62R-4	mid Hauterivian	<130	Geroch and Nowak (1984)
35 R	LO *S. cetia*	62R-1	late Valanginian	~134	Schaaf (1985)
36 BF	FO *V. neocomiensis*	61R, CC	Valanginian or younger	~138.5	Geroch and Nowak (1984)
37 BF	occ. *L. subangulata*	61R-5, 58	early Valanginian	<138.5	Sliter (1980)
38 R	FO *H. barbui*	62R-1	middle Berriasian	<142.5	Baumgartner (1984)
A PM	Top of Chron M0	47-1-95 or higher	earliest Aptian	118	Berggren et al. (1985a)
B PM	Bottom of Chron M0	47R-4, 66	basal Aptian	~118.5	Ogg (unpubl. data)
C PM	Top of Chron M3	51R-5, 131	upper mid-Barremian	~123	Ogg and Steiner (unpubl. data)
D PM	Bottom of Chron M3	53R-1, 76	lower mid-Barremian	~125.5	Ogg and Steiner (unpubl. data)

N = nannofossil; BF = benthic foraminifer; PF = planktonic foraminifer; P = palynomorphs; R = radiolarian; PM = paleomagnetics.

Contamination by freshwater in the laboratory can be ruled out because of the extreme care taken in processing the samples, especially after the first low-salinity sample was analyzed. Presently, there is no evidence to support Possibility 2, which invokes extensive lateral migration of freshwater. Low chloride concentrations, observed at several hemipelagic DSDP sites, are usually explained by infiltration of continentally derived freshwater as these sites are associated with permeable sandstone aquifers (Gieskes, 1981).

During rotary drilling of Hole 765C, each core was exposed to both surface seawater and drilling mud. Surface seawater was continuously pumped through the drill hole, and pulses of drilling mud were periodically sent down to clear out drill-bit cuttings. The drilling mud used at Site 765 consisted of a gel made by mixing 13.6 kg bentonite, 113 g NaOH, and 113 g Na_2CO_3 in 159 dm^3 of freshwater. This gel was then diluted 50% with surface seawater. In the deeper parts of Hole 765C, 10 to 50 bbl (159 dm^3/bbl) of drilling mud was pumped downhole per core. Drilling mud was observed periodically to flow out of the core liner after the core was laid out on deck. Despite the exposure of the cores to drilling fluids, we argue below that the IW samples were not contaminated by drilling fluids.

Compositions of surface seawater and drilling mud were determined to evaluate possible contamination of IW samples (Table 13). Differences in salinity, chloride, silica, and calcium contents of the drilling fluids and IW samples are significant and can be used as tracers to evaluate possible contamination. We assume that the IW originally had a salinity and chloride content of normal seawater and that, although salinity can decrease slightly as a result of sulfate reduction, chloride ion is conserved. The lower chloride concentrations are a result of dilution, not chloride removal by diagenetic reactions, as no chloride-bearing solid phases were detected at Site 765. Clearly, the IW samples were not contaminated with surface seawater (salinity = 35.2 ‰), because contamination could never produce a decrease in salinity or chlorinity. In the case of Sample 123-765C-39R-3, 140–150 cm (716.2 mbsf), having a chloride concentration nearly one-half that of normal seawater, the IW sample would require 80% contamination by the drilling mud. This amount of contamination would require the IW to have unreasonably high calcium, magnesium, and silica concentrations of 85 and 45 mM and 1090 μM, respectively. In the six other low-salinity samples, the amount of drilling mud necessary to explain the low chloride concentrations would require that the IW samples have much higher calcium concentrations than expected from the calcium profile at Site 765. Therefore, drilling fluid and laboratory contamination can be ruled out, and these low salinities appear to be real. This conclusion is consistent with

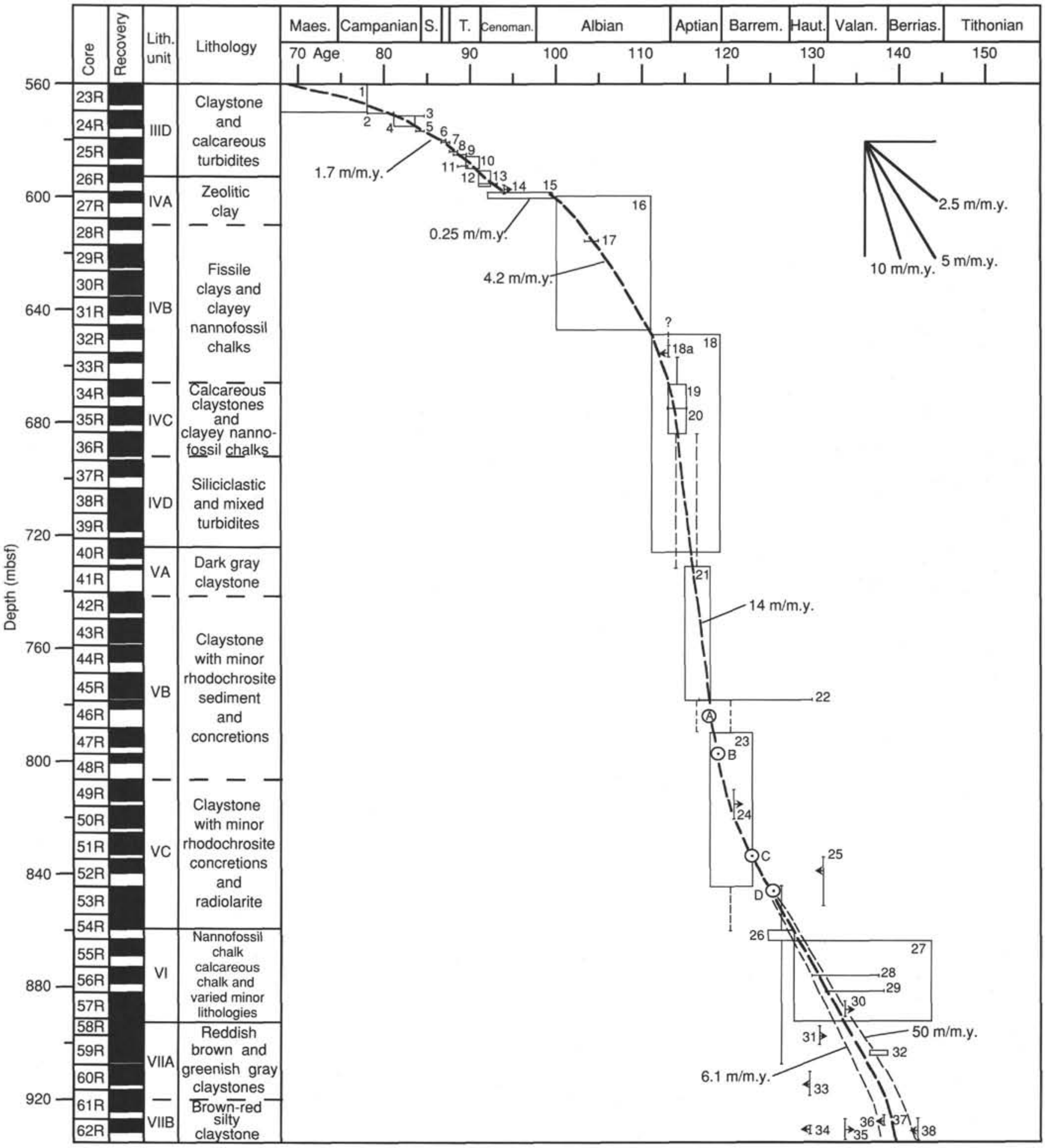

Figure 69. Cretaceous depth vs. age curve, Hole 765C.

the observation that the low-salinity IW samples have been intercalated with normal-salinity samples of similar lithology and porosity that underwent nearly identical processing in the laboratory.

The most likely explanation for the low chloride concentrations is the addition of H_2O to the IW from diagenetic processes. One possible process is expulsion of excess H_2O from the interlayer sites of expandable clay minerals (smectite) during burial compaction.

$$\text{smectite} \cdot nH_2O = \text{smectite} \cdot (n - x)H_2O + xH_2O. \quad (1)$$

In addition, several diagenetic reactions can produce H_2O, such as the transformation of opal-A or opal-CT to quartz (Eq. 2 be-

Table 13. Interstitial-water data, Site 765.

Core, section, interval (cm)	Depth (mbsf)	IW Vol (cm^3)	pH	Alk (mM)	Sal (‰)	Mg (mM)	Ca (mM)	Mg/Ca	Cl (mM)	SO_4 (mM)	PO_4 (μM)	NH_4 (mM)	Silica (μM)	Mn (μM)	Sr (mM)	K (mM)
123-765A-1H-1, 53–56	0.5	14	8.0	3.94	35.5	51.9	10.1	5.13	565	27.7	4.8	0.2	628	43.7	0.12	11.4
765A-1H-3, 145–150	4.5	48	7.6	5.52	36.0	51.5	10.3	5.02	566	25.3	4.2	0.3	808	34.4	0.15	12.3
765B-1H-1, 147–150	1.5	45	7.3	4.35	35.5	51.6	10.5	4.92	564	26.4	4.4	0.2	686	57.1	0.12	11.5
765B-2H-3, 145–150	13.8	40	7.8	7.50	35.2	50.9	10.2	5.01	566	23.1	14.0	0.5	778	72.7	0.16	11.4
765B-3H-3, 145–150	23.3	60	7.8	8.14	35.0	50.6	9.7	5.20	559	21.6	11.6	0.7	820	50.9	0.17	11.7
765B-4H-3, 145–150	33.0	60	7.8	6.96	35.3	50.6	8.3	6.11	554	20.1	7.9	0.6	636	23.1	0.19	11.7
765B-5H-3, 145–150	42.6	47	7.6	7.53	35.5	50.2	7.8	6.47	567	19.9	6.4	0.6	827	21.3	0.20	10.7
765B-6H-3, 145–150	52.3	52	7.5	8.13	35.3	49.8	7.4	6.75	567	18.7	6.9	0.8	827	20.7	0.23	10.5
765B-7H-3, 145–150	61.9	40	7.5	8.64	35.0	48.8	7.2	6.82	565	16.7	7.7	1.0	739	8.3	0.28	10.1
765B-8H-3, 145–150	71.6	55	7.5	9.13	34.5	48.6	7.1	6.86	564	15.6	9.8	0.8	812	4.0	0.31	9.5
765B-9H-3, 145–150	81.3	60	7.5	8.63	34.2	47.9	6.7	7.17	553	14.5	7.7	0.9	667	3.3	0.33	9.4
765B-10H-3, 145–150	90.9	42	7.6	7.55	34.5	46.3	6.0	7.67	560	13.5	6.4	0.9	510	4.4	0.37	9.7
765B-12H-3, 145–150	110.1	50	7.7	5.40	33.5	44.0	5.5	7.99	560	12.5	1.4	1.0	213	6.9	0.42	9.2
765B-15H-3, 145–150	139.0	27	7.7	3.84	32.5	39.5	6.7	5.91	560	10.6	0.9	1.0	197	3.9	0.64	8.4
765B-18H-3, 145–150	168.1	46	7.6	2.99	33.0	35.8	8.1	4.44	563	10.0	0.6	1.1	182	3.4	0.87	7.8
765B-21X-2, 145–150	195.7	37	7.6	2.48	32.5	32.7	10.4	3.15	560	9.1	1.1	1.2	236	0.5	1.11	7.9
765B-24X-3, 145–150	226.3	35	7.8	2.78	32.2	31.3	11.5	2.73	557	9.0	0.5	1.6	174	0.5	1.41	7.7
765B-27X-2, 145–150	253.9	25	7.6	2.27	33.0	29.3	11.3	2.59	558	7.6	0.9	1.6	403	0.5	1.62	7.5
765B-31X-3, 140–150	294.1	28	7.7	2.30	33.0	28.7	12.0	2.40	563	7.1	0.9	1.7	255	0.5	1.89	7.3
765B-36X-2, 140–150	340.9	59	7.8	2.48	32.0	28.2	13.4	2.10	558	8.0	0.0	2.0	201	0.8	2.09	7.3
765B-39X-1, 86–91	367.6	20	7.4	2.71	32.5	26.5	14.4	1.84	545	6.0	0.5	1.9	276	0.5	1.79	7.2
765C-4R-3, 140–150	383.5	14	7.5	1.89	32.7	31.4	12.5	2.51	558	7.8	0.0	1.5	213	—	1.82	7.8
765C-7R-4, 75–85	413.3	19	7.5	0.81	32.3	31.6	13.3	2.38	556	8.0	0.0	1.4	163	2.7	1.71	7.8
765C-10R-3, 140–150	441.0	18	7.4	1.57	32.3	31.4	13.4	2.34	564	8.0	0.0	1.6	150	2.7	1.47	7.4
765C-15R-1, 115–125	484.9	12	7.9	2.57	33.8	40.0	18.3	2.19	552	16.6	0.0	1.0	94	—	1.00	5.6
765C-18R-3, 140–150	516.4	20	7.5	3.56	33.0	35.4	20.0	1.77	575	9.8	0.0	0.8	270	18.0	0.68	6.0
765C-22R-2, 140–150	553.1	16	7.3	3.03	33.9	34.1	23.9	1.43	558	12.4	—	0.9	452	—	0.48	6.4
765C-25R-4, 140–150	585.0	8	7.1	—	34.0	36.8	25.8	1.43	556	15.4	—	0.6	306	—	0.37	5.3
765C-28R-2, 140–150	610.0	4	7.2	—	31.1	36.1	30.0	1.20	518	13.6	—	0.9	492	—	0.37	4.3
765C-31R-2, 130–140	638.2	8	7.3	—	32.5	35.3	31.4	1.12	538	14.6	—	0.6	611	—	0.29	4.5
765C-34R-3, 115–125	668.6	6	7.2	—	34.4	32.0	33.2	0.96	565	16.0	—	0.6	478	—	0.28	5.4
765C-37R-3, 140–150	697.5	5	7.1	1.73	34.6	34.0	34.3	0.99	5.62	15.6	—	0.7	566	—	0.26	4.6
765C-39R-3, 140–150	716.2	6	7.4	1.49	19.8	18.9	18.5	1.02	296	10.9	—	0.2	378	—	0.14	2.4
765C-42R-3, 140–150	744.3	3	7.5	—	27.9	27.8	33.1	0.84	435	13.0	—	0.8	150	—	—	—
765C-45R-3, 140–150	772.7	4.9	7.5	1.60	34.6	32.9	41.0	0.80	571	16.2	—	0.5	133	—	—	—
765C-48R-3, 140–150	801.4	2	7.6	—	29.0	31.9	30.9	1.03	464	16.9	—	—	—	—	—	—
765C-51R-3, 140–150	829.5	4	7.3	0.92	35.9	28.6	44.0	0.65	582	15.5	—	0.0	102	—	0.27	—
765C-54R-3, 140–150	858.0	5	7.1	1.50	35.0	26.5	45.4	0.58	572	14.3	—	0.5	167	—	0.27	3.0
765C-57R-3, 140–150	886.2	4.8	7.2	—	34.4	28.9	43.3	0.67	572	14.9	—	0.0	215	—	0.26	3.0
765C-60R-3, 140–150	912.0	1.5	7.5	—	27.6	24.2	28.7	0.63	429	11.7	—	—	—	—	—	—

low), the transformation of smectite to illite (Eq. 3), and the degradation of organic matter (Eq. 4).

$$SiO_2 \cdot nH_2O = SiO_2 + nH_2O, \tag{2}$$

$$\text{smectite} \cdot nH_2O = \text{illite} + nH_2O, \tag{3}$$

$$\text{organic matter} = CO_2 + H_2O. \tag{4}$$

The problem is that the above reactions do not typically produce sufficient H_2O to explain the unusually large salinity variations at Site 765. There is too little organic matter to make much water, and the preliminary X-ray diffraction results (see "Sediment Mineralogy," this section) suggest most of the clay is smectite, with relatively minor amounts of interlayer illite (<5% to 40%). In addition, the sediment contains discrete illite that is probably detrital, rather than diagenetic, in origin. Although the opal-CT to quartz transformation occurs at a sediment depth corresponding to the low-salinity samples, the amount of water released is insufficient. A more likely source of H_2O is from the partial dewatering of smectites (Eq. 1) that results from the increasing pressures deeper in the hole, where porosity is lower and the IW volume is more easily diluted. Smectite is abundant in samples below 600 mbsf. The problem is that porosities are still high in the low-salinity samples, ranging from 40% to 60% (see "Sediment Physical Properties" section, this chapter). The possibility that water was introduced by dewatering of the clay minerals during sample squeezing seems unlikely because most samples from Hole 765C were squeezed under approximately the same conditions. In addition, there is no correlation between the amount of dilution and differences in the clay mineralogy of the sediment samples. Thus, the origin of the low-salinity samples remains unclear and requires more detailed future study.

If one assumes that the IW samples were diluted by freshwater, then concentrations can be corrected to nondilution values. The result is an increase in all values and reversals of trends in sulfate, calcium, and magnesium. Dilution-corrected values are generally more consistent with trends in concentration profiles, suggesting that the steady-state concentrations were perturbed by adding freshwater. Because there is no evidence for presently active depletion reactions in these samples, dilution probably occurred within the last 1 m.y., based on the approximate time for diffusion to smooth out the sharp concentration gradients observed, unless the clay minerals are excluding vertical ionic transport and gradients were maintained by osmotic membrane filtration.

pH and Alkalinity

The pH varies from a high of 8.0 at 0.5 mbsf to a low of 7.1 in three samples below 585.0 mbsf (Fig. 70C). The pH is generally less variable and higher in the upper 340.9 mbsf. Alkalinity has two maxima, one at 13.8 mbsf and the other at 71.6 mbsf, and then decreases exponentially to an asymptotic value near the alkalinity of seawater (2.3 mM) at 367.6 mbsf (Fig. 70D). Alkalinity decreases sporadically below 367.6 mbsf. Alkalinity maxima correlate with a high average organic matter content in the uppermost 80 m of sediment (see "Organic Geochemistry"

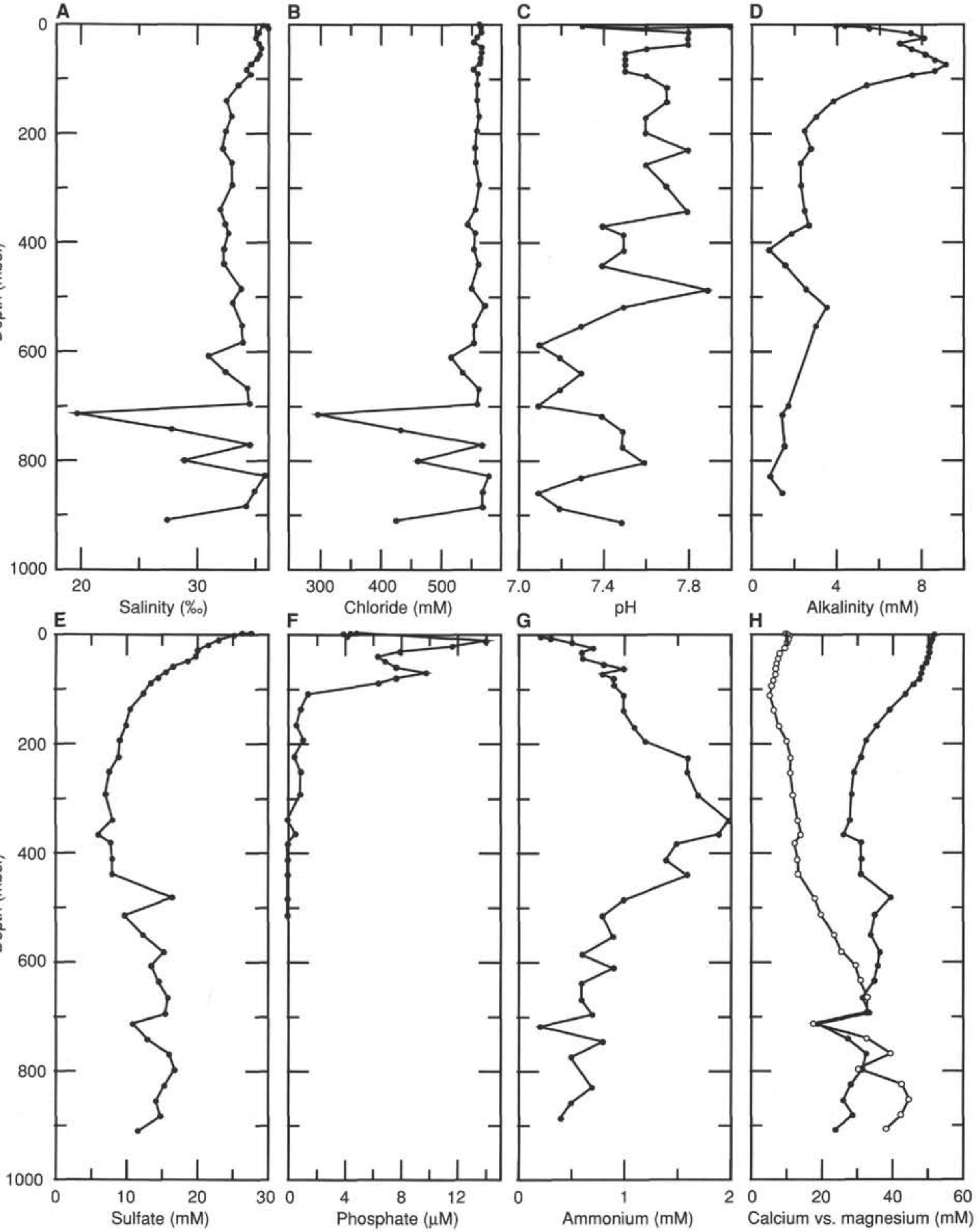

Figure 70. Interstitial-water composition as a function of depth, Site 765. A. Salinity. B. Chloride ion. C. pH. D. Alkalinity. E. Sulfate ion. F. Phosphate. G. Ammonium. H. Calcium (open circles) and magnesium (closed circles).

section, this chapter). The higher alkalinity is a result of bicarbonate production by the sulfate-reducing bacteria during organic matter degradation (see "Sulfate," this section) and is commonly observed in organic-rich (>0.5 wt% organic carbon) marine sediments (Gieskes, 1983).

Sulfate

Sulfate concentrations decrease exponentially from concentrations slightly less than seawater at 0.5 mbsf to an asymptotic value of about 7 mM at 441.0 mbsf (Fig. 70E). The rapid de-

Table 14. Low-salinity samples from Site 765.

Core, section, interval (cm)	Depth (mbsf)	Salinity (g/kg)	Chlorinity (mM)	H_2O dilution (%)
123-764B-39X-1, 86–91	367.7	32.5	545	3
765C-28R-2, 140–150	610.0	31.1	518	8
31R-2, 130–140	638.2	32.5	538	4
39R-3, 140–150	716.2	19.8	296	47
42R-3, 140–150	744.3	27.9	435	22
48R-3, 140–150	801.4	29.0	464	17
60R-3, 140–150	912.0	27.6	429	23

crease in sulfate is typical of rapidly deposited, organic-rich sediments, where sulfate-reducing bacteria reduce sulfate to H_2S and produce CO_2 (Gieskes, 1981). The general reaction can be written as,

$$53SO_4^{=} + C_{106}H_{263}O_{110}N_{16}P = 39CO_2 + 67HCO_3^- + 16NH_4^+ + 53HS^- + 39H_2O + HPO_4^{=}. \quad (5)$$

Sulfate increases sporadically below 441.0 mbsf to a maxima of 16.9 mM at 801.0 mbsf and then decreases to 11.7 mM at 912.0 mbsf. The higher sulfate values correlate with lower contents of organic carbon in sediments between 500 and 650 mbsf (see "Organic Geochemistry" section, this chapter). The sediment below 484.9 mbsf may not have had sufficient organic matter to deplete the sulfate to the same extent as the overlying sediment. It is less clear why the relatively high sulfate values continue below 650 mbsf, since these sediments are high in organic carbon. One possible explanation is differences in the type of organic carbon; organic carbon at depths below 650 mbsf is largely terrestrial, rather than marine, in origin (see "Organic Geochemistry" section, this chapter).

Phosphate

Phosphate strongly correlates with alkalinity, having two maxima at 13.8 and 71.6 mbsf of 14 and 10 μM, respectively. Phosphate values decline rapidly to <2 μM from 110.1 to 367.6 mbsf, and then are essentially zero below 367.6 mbsf (Fig. 70F). High phosphate concentrations are common near the sediment/seawater interface of organic-rich sediments, because of the preferential metabolism of phosphate by sulfate-reducing bacteria (Eq. 5). Phosphate-bearing minerals, such as francolite, a carbonate fluorapatite, $Ca_5(PO_4,CO_3)_3(F,OH)$, have been detected in carbonate nodules in Sample 123-765B-6H-3, 145–150 cm.

Ammonium

Ammonium values increase sporadically from 0.2 mM at 0.5 mbsf to a maximum of 2.0 mM at 340.9 mbsf, and then decrease sporadically to 0.4 mM at 886.2 mbsf (Fig. 70G). The ammonium maximum corresponds to the sulfate minimum; in general, the sulfate and ammonium profiles mirror one another. Ammonium, like phosphate, is released preferentially during degradation of organic matter (Eq. 5), and the ammonium maximum normally occurs below the phosphate maximum (Gieskes, 1983). Ammonium has two minor maxima at 13.8 and 71.6 mbsf that correlate with the alkalinity maxima. Ammonium is known to rapidly exchange for interlayer cations in clay minerals (Rosenfield, 1981), and some of the increase in magnesium below the ammonium maximum may be related to intake of ammonium by clays in exchange for magnesium.

Calcium, Magnesium, Manganese, and Strontium

Calcium content is initially constant in the uppermost 13.8 mbsf at a concentration (10.5 mM) near that of seawater, then decreases to a minimum of 5.5 mM at 110.1 mbsf (Fig. 70H). Calcium increases moderately from 110.1 to 195.7 mbsf, then increases more slowly to 441.0 mbsf. Finally, below 441.0 mbsf, the calcium gradient steepens to a maximum concentration of 45.4 mM. The initial decrease in calcium is typical of rapidly accumulating, organic-rich sediments, where a rapid increase in alkalinity results in carbonate precipitation (Gieskes, 1981). Depletion of calcium can result from either calcite or dolomite precipitation.

$$Ca^{2+} + CO_3^{=} = CaCO_3, \quad (6)$$

$$Ca^{2+} + Mg^{2+} + 2CO_3^{=} = CaMg(CO_3)_2. \quad (7)$$

The increase in calcium below 110.1 mbsf is probably from dolomite replacing calcite,

$$2CaCO_3 + Mg^{2+} = CaMg(CO_3)_2 + Ca^{2+}, \quad (8)$$

as well as calcium released during alteration of volcanic material and basement basalt. The alteration of volcanic material in the sediment and underlying basalt basement rock of Layer 2 results in the release of calcium and the intake of magnesium, and may explain why calcium increases and magnesium decreases with sediment depth, a pattern commonly observed in oceanic sediments (Gieskes, 1983).

Initially, magnesium decreases only slightly in the uppermost 13.8 mbsf, but then decreases more rapidly between 13.8 and 110.1 mbsf (Fig. 70H). Below 110.1 mbsf, magnesium decreases exponentially to an asymptotic value of 26.5 mM at 367.6 mbsf. Below 367.6 mbsf, magnesium increases to a maximum of 40 mM at 484.9 mbsf, and then decreases sporadically with depth to 24.2 mM at 912.0 mbsf. The two major reactions consuming magnesium are dolomitization (Eqs. 7 and 8) and alteration of volcanic material within the sediment and basement basalt.

Dolomite was observed in sediment from throughout Hole 765B, especially at the base, and from the top of Hole 765C (see "Sediment Mineralogy," this section). Volcanic material is thought to occur at Site 765 as well, especially below 744.2 mbsf. Magnesium decreases more rapidly than calcium increases in the upper 484.9 mbsf (Fig. 71), suggesting that the dolomite reaction (Eq. 7) predominates, with the necessary calcium diffused in from above and below. Below 484.9 mbsf, calcium and magnesium have a linear relationship, suggesting that the intake of magnesium is directly related to the release of calcium, either by dolomitization (Eq. 8) or alteration of volcanic material. Initially, the Mg/Ca ratio increases rapidly from 5 to 8 in the upper 110.1 mbsf. A higher Mg/Ca ratio should favor dolomitization (Eq. 8). The Mg/Ca ratio decreases rapidly below 110.1 mbsf to about 2 at 226.3 mbsf, and then decreases more gradually to a minimum of 0.6 at 912.0 mbsf (Fig. 72A).

Manganese has a sharply defined maximum of 73 μM at 13.8 mbsf (Fig. 72B). The manganese maximum corresponds to the alkalinity maximum, suggesting that manganese is released during early diagenesis, possibly from the reduction of manganese oxides in the sulfate-reduction zone. Rhodochrosite ($MnCO_3$) occurs in the sediment from 13.8 mbsf, suggesting rhodochrosite is presently precipitating at depth in the sediment. Manganese decreases exponentially to about 5 μM at 61.9 mbsf and declines to <1 μM below 168.1 mbsf, except for higher values between 413.3 and 516.4 mbsf. Manganese was not determined in IW samples below 516.4 mbsf. Rhodochrosite was found in a number of samples from Site 765 (see "Sediment Mineralogy," this section).

Strontium increases rapidly from near-seawater values at 0.5 mbsf to a maximum of 2.1 μM at 340.8 mbsf (Fig. 72C). Below 340.8 mbsf, strontium decreases rapidly to an almost con-

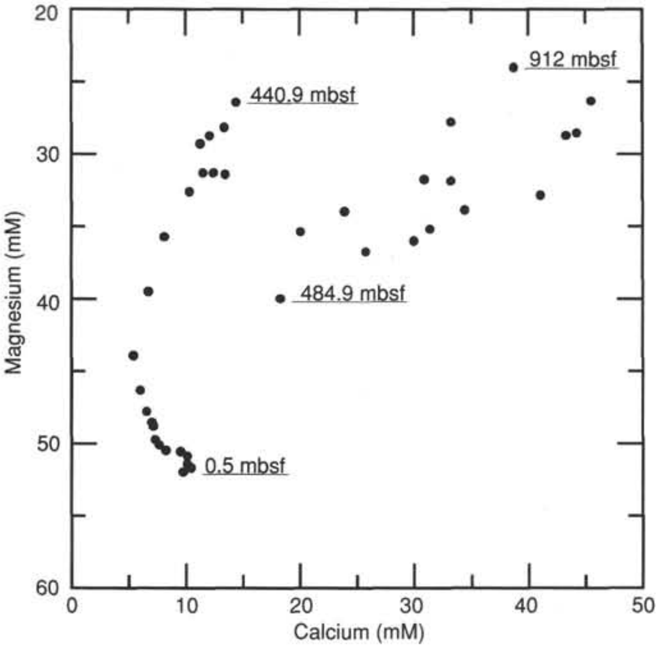

Figure 71. Plot of calcium vs. magnesium, Site 765.

stant asymptotic value of about 0.3 μM from 584.9 to 886.1 mbsf (except for the diluted sample at 716.2 mbsf). The strontium maximum correlates with sediment having a relatively high aragonite content. Strontium is most likely being introduced to the IW during recrystallization of the aragonite to calcite or dolomite.

In summary, it appears that there are several zones of carbonate precipitation at Site 765. Rhodochrosite is precipitating in the uppermost 13.8 m of sediment, followed by dolomite precipitation to 484.9 mbsf. In addition, calcite may be precipitating in the uppermost 100 mbsf.

Silica and Potassium

Silica concentration is highest (603–827 μM) in the uppermost 71.6 mbsf, where there are abundant radiolarian tests (see "Biostratigraphy" section, this chapter). Below 71.6 mbsf, silica concentration decreases rapidly to 94 μM at 484.9 mbsf (Fig. 72D). Below 484.9 mbsf, a second silica maxima of 611 μM occurs at 638.2 mbsf, below which silica decreases to a range of 102 to 215 μM at the bottom of Site 765. The silica profile reflects the solubilities of different silica phases. Radiolarian tests are originally composed of hydrous, amorphous silica (opal-A), which is unstable and highly soluble, having a solubility of around 1000 μM. Opal-A radiolarian tests can recrystallize to either opal-CT or quartz. Upon deeper burial, opal-CT will recrystallize eventually to quartz. The silica transformations, opal-A to opal-CT to quartz, are usually gradational with increasing sediment depth, since they depend on sediment composition as well as temperature (Kastner, 1979). The solubility of quartz is about 100 μM, and the solubility of opal-CT lies somewhere in between that of opal-A and quartz (Kastner, 1979). At Site 765, opal-A radiolarians are abundant in the high silica zone of the uppermost 100 mbsf, opal-CT is abundant from 668.6 to 716.2 mbsf within the second silica maximum, and diagenetic quartz is abundant below 744.3 mbsf, where the silica concentration is low. Radiolarians are fairly abundant between 550 and 900 mbsf, and have been replaced by opal-CT and quartz (see "Biostratigraphy" section, this chapter).

Potassium has a maximum near the sediment/seawater interface at values above IAPSO seawater. Potassium decreases expo-

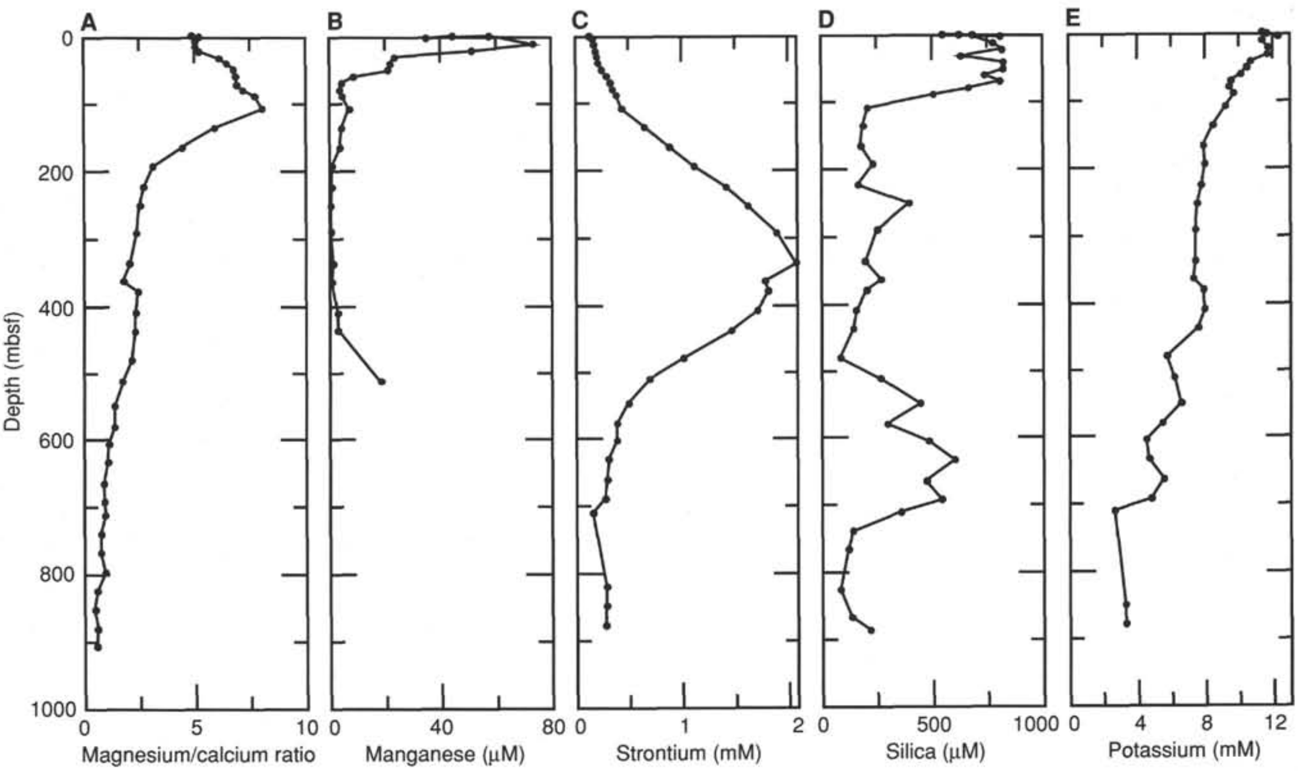

Figure 72. Interstitial-water composition as a function of a depth, Site 765. A. Ratio of magnesium to calcium. B. Manganese. C. Strontium. D. Silica. E. Potassium.

nentially to an asymptotic value of about 7 mM at 367.5 mbsf, followed by a slight increase, and then decreases sporadically to 3.0 mM at 886.1 mbsf (Fig. 72E). The trend of decreasing potassium is similar to other DSDP sites and is from the intake of potassium by alteration reactions in the sediment and basement basalt (Gieskes, 1981). Smaller-scale variations in the potassium profile are unclear; the minimum value at 716.2 mbsf is from dilution of the IW.

Conclusions

The sediment at Site 765 can be divided into two parts: an upper part (0–484.9 mbsf) in which the IW trends are fairly straightforward and commonly observed in other oceanic sedimentary sections (e.g., Gieskes, 1981), and a lower part (484.9–912.0 mbsf) in which there are ambiguous IW trends. In the upper part, diagenesis is driven in large part by the degradation of organic matter by sulfate-reducing bacteria. The result is an increase in alkalinity, phosphate, and ammonium; a sharp decrease in sulfate; and a small decrease in salinity, with chloride remaining essentially constant. The increase in alkalinity results in supersaturation with respect to carbonate minerals, and their precipitation is supported by gradients in calcium, magnesium, and manganese. The relatively high phosphate concentration can result in francolite precipitation, while ammonium may exchange with magnesium on clay minerals. If a source for iron exists, then precipitation of pyrite is expected, as well as iron carbonates (ankerite was observed in Sample 123-765C-7R-4, 75–85 cm).

In the lower part of Site 765 (484.9–912.0 mbsf), the IW trends are far less obvious. The increase in both sulfate and magnesium is unusual, but such an increase has been observed at other sites (Gieskes, 1981). The increase in sulfate probably results from lower organic matter contents, and higher magnesium may be from less extensive dolomitization as well as exchange with ammonium. The most puzzling feature of the lower part of Site 765 is the unusually low salinities, especially the sharp chloride gradients observed. Although the samples appear to have had simple freshwater dilution, the source of this freshwater is problematic. No other truly pelagic basins are known that have such low salinities. The silica profile is fairly straightforward throughout and correlates well with the known silica phases present at Site 765.

Two distinct sets of trends above and below 484.9 mbsf can be understood in terms of the sedimentation history at Site 765. From the base of the section to the middle Cretaceous, the sedimentation rate ranges from approximately 4 to 14 m/m.y. The sedimentation rate slowed to only 1.8 m/m.y. from the middle Cretaceous through the Paleogene, and then increased dramatically during the Neogene to a rate of about 26.6 m/m.y. (see "Sediment Accumulation Rates" section, this chapter). The sudden change in the sedimentation rate from 1.8 to 26.6 m/m.y. correlates well with the break in the IW profiles at 484.9 mbsf. Slow deposition would have allowed the lower section to have been in diffusional contact with the overlying seawater for a long period of time (middle Cretaceous through Paleogene); whereas rapid sedimentation during the Neogene would have rapidly removed the underlying sediments from diffusional contact with the overlying seawater. The more-or-less constant Neogene sedimentation rate resulted in what may be a steady-state condition for the section above 484.9 mbsf.

Sediment Mineralogy

Introduction

Sediment composition and mineralogy were determined at Site 765 to relate IW profiles to diagenetic reactions occurring in the solid phases. IW squeeze cakes were separated into three grain sizes: >38 μm, 2 to 38 μm, and <2 μm. In most samples a 2-μm-size fraction also was obtained. The methods used to separate the bulk sediment and to obtain XRD patterns and elemental analyses by XRF are discussed in the "Explanatory Notes" chapter (this volume). Here, illite is used to describe discrete detrital illite and does not include illite layers occurring in mixed layers of illite/smectites. Smectite is used to describe mixed layer illite/smectite. The mixed layer illite/smectites from Site 765 are predominantly composed of smectite layers, with most samples containing <5% to 20% illite layers.

Results

Preliminary mineralogy of the IW squeeze-cake sediment samples is summarized in Table 15 and Figure 73.

Clay Mineralogy

There are five distinct clay mineral assemblages at Site 765. The lowermost assemblage, from 912 to 610 mbsf, is predominantly smectite with illite constituting from 0% to 50% of the sample. The overlying assemblage consists of smectite, kaolinite, and illite; from 610 to 553.1 mbsf smectite is the dominant clay mineral and from 553.1 to 484.9 mbsf kaolinite is the dominant clay mineral. The clay mineralogy changes dramatically at 484.9 mbsf, consisting of palygorskite and chlorite, with possible illite and kaolinite. The presence of illite and kaolinite cannot be confirmed until the samples are heated to 550°C. Palygorskite and chlorite are the dominant clay minerals from 484.9 to 367.6 mbsf. At 367.6 mbsf there is a complex clay assemblage dominated by palygorskite and containing significant amounts of kaolinite, smectite, and sepiolite. From 340.9 to 195.7 mbsf the clay minerals are dominated by approximately equal amounts of kaolinite and sepiolite, with palygorskite and smectite present in minor amounts; chlorite is absent above 367.6 mbsf. The increase in sepiolite above 367.6 mbsf may be gradational. From 195.7 mbsf to the top of the section the clay mineral assemblage is dominated by kaolinite, with equal to lesser amounts of smectite and illite.

Carbonate Minerals

Calcite dominates the carbonate mineralogy from the top of the site to 744.3 mbsf. Below 744.3 mbsf, a significant amount of calcite was also observed in the form of calcispheres at 886.2 mbsf. Generally, the carbonate content is highly variable throughout Site 765 (see "Organic Geochemistry" section, this chapter). The calcite consists of low-Mg coccoliths and foraminifer tests. The foraminifers are both planktonic and benthic species that generally occur in the >38-μm-size fraction. The coccoliths are mostly in the 2- to 38-μm-size fraction. Scattered dolomite is found in minor amounts in the upper 226.3 mbsf, but is abundant from 226.3 to 441.0 mbsf. Dolomite rhombs are common in the 2- to 38-μm-size fraction, and appreciable dolomite is present in the <2- and ≪2-μm-size fractions. Aragonite occurs in the >38-μm-size fraction in minor amounts throughout the uppermost 484.9 mbsf as benthic foraminifers. Rhodochrosite was observed in the uppermost 13.8 mbsf, and as coalesced spheres in the >38-μm-size fraction at 772.7 mbsf. Ankerite was observed in the 2- to 38-μm-size fraction at 413.3 mbsf.

Silica Phases

The uppermost 90.9 mbsf contains abundant, well-preserved opaline radiolarian tests in the >38-μm-size fraction. Broken radiolarian tests are common in the 2- to 38-μm-size fraction. Minor amounts of more resistent opal-A sponge spicules were observed deeper in the sediment to 253.9 mbsf. Opal-CT is most abundant from 668.6 to 716.2 mbsf. Opal-CT is thought to occur in trace to minor amounts at Site 765. However, the presence

Table 15. Sediment composition and mineralogy, Site 765.

Core, section, interval (cm)	Depth (mbsf)	Color	Fraction composition		Clay mineralogy (<2 μm)						CaCO$_3$ (%)	Carbonate		
			>38 μm	2-38 μm	Kaol	Smect	Illite	Palyg	Sepio	Chlor		Arag	Dolo	Rhodo
123-765A-1H-1, 53-56	0.5										68.3	Minor		
765A-1H-3, 145-150	4.5										68.5	Minor		
765B-1H-1, 147-150	1.5										71.1	Minor		
765B-2H-3, 145-150	13.8	Gray	Rads, mica, om	Rads, qtz	—	—	—				0.8		Trace	Minor
765B-3H-3, 145-150	23.3										0.4			
765B-4H-3, 145-150	33.0	Lt gray	Rads, forams	Nannos, rads, qtz	—	—	—				56.6	Minor		
765B-5H-3, 145-150	42.6										56.2			
765B-6H-3, 145-150	52.3	Gry/grn	Rads, forams, pyr, phos	Nannos, rads, qtz	—	—	—				62.1		Trace	
765B-7H-3, 145-150	61.9										62.1			
765B-8H-3, 145-150	71.6	Gry/grn	Rads, forams, mica, om	Nannos, qtz	—	—	—				70.9	Minor	Trace	
765B-9H-3, 145-150	81.3										71.8			
765B-10H-3, 145-150	90.9	Grn/gry	Forams, rads, pyrite, om	Nannos, qtz	—	—	—				57.9			
765B-12H-3, 145-150	110.1	Gry/whi	Forams	Nannos, qtz	—	—	—				72.2		Trace	
765B-15H-3, 145-150	139.0	Lt grn	Forams, qtz, pyr, om	Nannos, qtz	—	—	—				9.9		Minor	
765B-18H-3, 145-150	168.1	Lt grn	Forams, om	Nannos, qtz	—	—	—				70.0			
765B-21X-2, 145-150	195.7	Whi/grn	Forams, pyr	Nannos, qtz	—	—	?	—	—		80.9	Minor	Trace	
765B-24X-3, 145-150	226.3	Whi/tan	Forams, pyr	Dolo, nannos	—	—	?	—	—		89.1	Minor	Abund	
765B-27X-2, 145-150	253.9	Brn/grn	Forams	Nannos, chrt	—	—	?	—	—		69.2	Minor	Abund	
765B-31X-3, 140-150	294.1	Gry/grn	Forams, om	Nannos, dolo	—	—	?	—	—		79.8	Minor	Abund	
765B-36X-2, 140-150	340.9	Grn/whi	Forams, coal, pyr, qtz	Dolo, nannos	—	—	?	—	—		78.7	Minor	Abund	
765B-39X-1, 86-91	367.6	Whi/tan	Forams	Dolo, nannos	—	—	?	—	—	—	95.1	Minor	Abund	
765C-4R-3, 140-150	383.5	Gray	Forams	Qtz, nannos, dolo	?		?	—		—	71.6	Minor	Abund	
765C-7R-4, 75-85	413.3	Green	Forams, pyr	Anker, qtz, nannos	?		?	—		—	40.1	Minor	Abund	
765C-10R-3, 140-150	441.0	Gray	Forams	Nannos, dolo	?		?	—		—	50.9	Minor	Abund	
765C-15R-1, 115-125	484.9	Green	Qtz, om	Nannos, qtz, felds	—	—	—				2.3			
765C-18R-3, 140-150	516.4	Orange	Forams	Nannos	—	—	—				76.5			
765C-22R-2, 140-150	553.1	Whi/gry	Forams, mica, clinop	Nannos		—	—				68.6			
765C-25R-4, 140-150	585.0	Brn/org	Forams, qtz	Nannos	—	—	—				63.8			
765C-28R-2, 140-150	610.0	Tan	Forams	Nannos, qtz	—	—	—				16.2			
765C-31R-2, 130-140	638.2	Org/brn	Forams, clinop	Nannos		—	—				26.3			
765C-34R-3, 115-125	668.6	Green	Cemented clay	Nannos		—	—				21.7			
765C-37R-3, 140-150	697.5	Tan	Forams, pyr	Nannos		—	—				51.9			
765C-39R-3, 140-150	716.2	Gry/brn	Forams, pyr	Nannos		—	—				20.6			
765C-42R-3, 140-150	744.3	Green	Rads, pyr	Qtz		—	—				0.6			
765C-45R-3, 140-150	772.7	Red/brn	Rads, rhodo	Qtz, volithic, felds		—	—				3.6			Minor
765C-48R-3, 140-150	801.4	Brown	Cememted clay, pyr, om	Qtz		—	—				1.0			
765C-51R-3, 140-150	829.5	Brown	Cemented clay, om	Chert, qtz, felds		—	—				1.4			
765C-54R-3, 140-150	858.0	Tan	Rads	Qtz		—	—				0.3			
765C-57R-3, 140-150	886.2	Whi/gry	Calcispheres, pyr	Nannos, qtz		—	—				28.2			
765C-60R-3, 140-150	912.0	Red/brn	Rads, qtz, mica	Qtz		—	—				0.4			

Rads = radiolarians; om = organic material; forams = foraminifers; pyr = pyrite; phos = phosphate; qtz = quartz, clinop = clinopyroxene; rhodo = rhodochrosite; nannos = nannofossils; dolo = dolomite; chrt = chert; felds = feldspar.

of opal-CT is uncertain because the shape of the 4.11 Å peak on the XRD patterns is unusual and may not represent opal-CT. Scanning electron microscopy will help to verify the presence of opal-CT. Diagenetic microcrystalline to cryptocrystalline quartz is abundant below 744.3 mbsf, especially in the <2-μm-size fraction.

Additional Diagenetic Minerals

The hydrogen sulfide produced during sulfate reduction can react with reduced iron to form pyrite (FeS_2; Berner, 1970). Pyrite is scattered in minor to trace amounts throughout the sediment at Site 765. It occurs most commonly in the >38-μm-size fraction as microcrystalline clusters (framboids), and in places as pyritized burrows and radiolarian tests. Small calcareous nodules from 52.3 mbsf were observed; these contained significant francolite. Clinoptilolite was observed at 553.1 and 638.2 mbsf as the molds of the interior of radiolarian tests. Large barite crystals ($BaSO_4$) were observed in Sample 123-765C-52R-1, 115 cm. High barium concentrations are common in clayey, siliceous sediments.

Elemental Analysis of Clay Separates from Hole 765C

XRF analyses of 10 major and 13 trace elements were performed on six clay-size separates from Hole 765C (Tables 16 and 17). No chemical treatments, such as phosphate dispersant or acid (HCl), were used in processing these samples. The clay was ground in an agate mortar and pestle, dried overnight at 110°C, cooled in a desiccator, and weighed into quartz crucibles. Then, the samples were ignited to 1030°C for 2.5 hr, cooled in a desiccator, and weighed again to calculate weight loss on ignition (LOI). Two samples, both representing the ≪2-μm-size fraction, partially fused to the base of the quartz crucible, and some quartz contamination was unavoidable. The ignited sample (550 mg) was added to 6 g of flux and fused into a glass bead, which was then run on the XRF for major elements. The remaining sample was mixed with a polymeric binder, pressed at 5 to 7 tons into a pellet, and run on the XRF for trace elements (see "XRF Analyses" section, "Explanatory Notes" chapter, this volume). Of the six clay separates analyzed, one sample was from the palygorskite > chlorite zone, one from the kaolinite > smectite > illite zone, one from the smectite > kaolinite > illite zone, and three were from the lowermost smectite > illite zone. The analyses are low in aluminum (11.62-21.15 wt%), high in iron (8.43 to 10.57 wt% Fe_2O_3), and similar in magnesium (3.18 to 4.00 wt% MgO), except for the palygorskite/chlorite sample, which is relatively low in iron (5.81 wt%) and high in magnesium (8.50 wt%).

Origin of the Clay Minerals

Kaolinite is an abundant clay mineral in three of the five clay assemblages at Site 765. Kaolinite is normally interpreted as terrigenous, transported as suspended matter in rivers or high-altitude winds, and is usually indicative of a low-latitude source area, since it is formed in highly weathered soil horizons commonly found in tropical climates. However, the paleolatitude at Site 765 ranged from about 40°S, based on the basement paleomagnetism (see "Basement Paleomagnetism" section, this chapter), to its current latitude of 17°S. Therefore, in addition to that from the Australian continent, kaolinite may have been transported from landmasses to the north as windborne dust. Illite has also been interpreted as terrigenous at Site 765. Chlorite is often associated with weathering of continental landmasses in

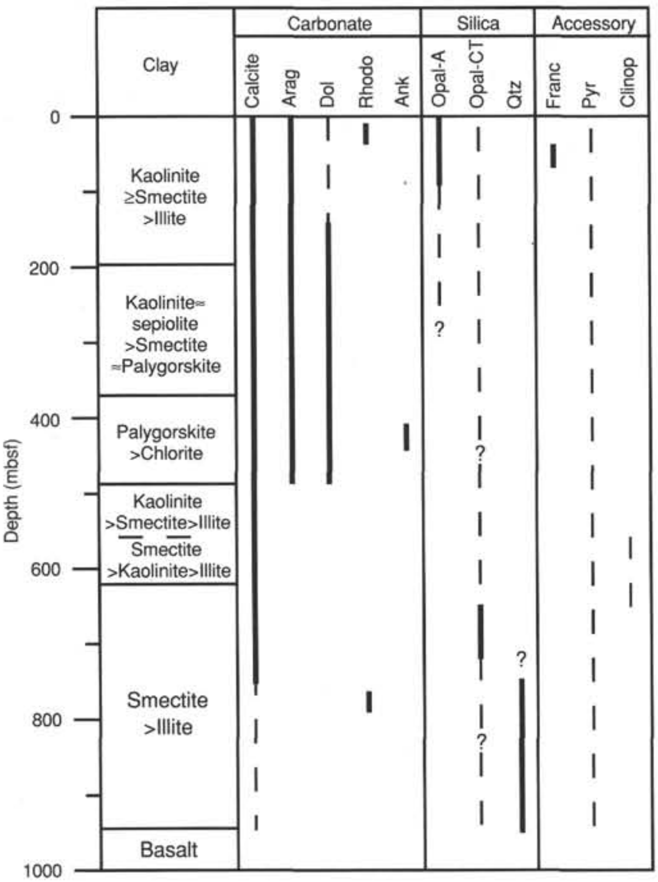

Figure 73. Mineralogy of sediments from Site 765, based on XRD. Arag = aragonite, Dol = dolomite, Rhodo = rhodochrosite, Ank = ankerite, Qtz = quartz; Franc = francolite (carbonate fluorapatite), Pyr = pyrite, and Clinop = clinoptilolite.

high latitudes (polar to subpolar) that have metamorphic terranes. The chlorite at Site 765 is thought to be diagenetic, rather than detrital, in origin, since it is confined to one clay assemblage, where it is associated with a magnesium-rich diagenetic clay mineral, palygorskite.

Smectite is abundant in all but one of the five clay mineral assemblages. Based on the glycolated XRD patterns, most of this smectite is estimated to contain <5% to 20% illite layers. Sediment layers composed of nearly 100% smectite have been interpreted as altered volcanic ash deposits (bentonites; see "Sedimentology" section, this chapter). The abundance of smectite in the lowermost clay assemblage and its low aluminum and high iron and magnesium contents suggest that a significant amount was derived from the alteration of mafic igneous material.

Palygorskite and sepiolite are both magnesium-rich clays that are often associated with one another. At Site 765, these two clay minerals occur in two separate assemblages: palygorskite was found associated with chlorite only, and in the overlying assemblage, sepiolite and kaolinite are associated with subordinate amounts of palygorskite and smectite. Usually, palygorskite and sepiolite form under conditions characterized by high magnesium and silica concentrations. They form in both marine and lacustrine environments, and also are usually found in sediments of Miocene age or older. The origin of palygorskite and sepiolite in pelagic environments still is not well understood. These clays are often found associated with dolomite, diagenetic opal-CT or quartz cherts, and volcanogenic sediments (von Rad and Rösch, 1972). The required excess silica may be derived from solution of unstable radiolarian tests or alteration of volcanic glass. The required magnesium can be supplied by diffusion from the overlying seawater, assuming that sedimentation rates are not too high, so that residence times near the sediment/seawater interface are sufficient. Palygorskite and sepiolite are commonly observed in Upper Cretaceous to Paleogene marine sediments, which represent a time of relatively slow sedimentation rates. For example, at Site 765 the sedimentation rate during the Late Cretaceous to Paleogene is an order of magnitude slower than either the underlying Lower to middle Cretaceous or overlying Neogene sediments. However, the palygorskite-sepiolite clay mineral assemblages at Site 765 occur above

Table 16. Elemental composition of clay-size fraction from Hole 765C.

Core, section, interval (cm)	Depth (mbsf)	Major oxides (wt%) SiO_2	TiO_2	Al_2O_3	Fe_2O_3	MnO	MgO	CaO	Na_2O	K_2O	P_2O_5	Total	LOI	$CaCO_3$ (wt%)	Size fraction (μm)
123-765C-7R-4, 75–85	413.3	52.61	0.70	16.74	5.81	0.07	8.50	12.19	0.26	1.71	0.05	98.63	17.90	17.9	<2
15R-1, 115–125	484.9	59.68	1.06	21.15	8.63	0.04	3.18	0.59	2.18	1.87	0.06	98.44	10.49	<2.3	≪2
28R-2, 140–150	610.0	56.99	0.96	16.85	10.26	0.56	3.93	5.57	1.20	3.28	0.11	99.70	9.68	7.7	<2
42R-3, 140–150	744.3	68.18	0.80	14.15	9.01	0.05	3.35	0.73	1.01	2.41	0.05	99.74	5.95	<0.6	<2
48R-3, 140–150	801.4	67.97	0.94	11.62	10.57	0.08	3.24	1.42	1.00	2.04	0.45	99.34	5.75	<1.0	<2
60R-3, 140–150	912.0	65.78	0.63	14.43	8.43	0.19	4.00	1.12	2.79	1.70	0.19	99.26	8.35	<0.4	≪2

LOI = Loss on ignition.

Table 17. Trace-element composition of clay-size fraction from Hole 765C.

Core, section, interval (cm)	Depth (mbsf)	Trace-element composition (ppm) Nb	Zr	Y	Sr	Rb	Zn	Cu	Ni	Cr	V	TiO_2	Ce	Ba	Size fraction (μm)
123-765C-7R-4, 75–85	413.3	7.6	97.8	11.9	966.6	81.0	82.2	23.3	35.4	116.6	125.1	0.5	40.5	117.8	<2
15R-1, 115–125	484.9	11.1	172.5	20.2	325.8	79.3	276.6	26.8	65.6	156.8	215.9	0.9	87.1	75.1	≪2
28R-2, 140–150	610.0	11.7	123.5	23.1	175.7	99.2	209.1	114.6	97.0	65.1	112.7	0.7	84.1	814.5	<2
42R-3, 140–150	744.3	12.5	149.9	20.4	90.0	68.7	97.5	179.3	47.1	46.1	160.4	0.7	145.8	343.8	<2
48R-3, 140–150	801.4	13.0	121.5	42.0	93.1	47.6	78.6	34.9	216.9	26.2	84.1	0.7	107.2	43.0	<2
60R-3, 140–150	912.0	10.5	103.9	32.7	97.4	51.3	155.6	130.7	107.7	37.8	92.7	0.5	110.5	1073.4	≪2

the condensed section. A possible explanation is that Upper Cretaceous to Paleogene sediments occurring upslope were redeposited in the Argo Basin during the early Neogene. Redeposition is supported by the dominance of turbidite sequences throughout the Neogene at Site 765 (see "Sedimentology" section, this chapter).

Origin of the Diagenetic Carbonates

The sediment from 484.9 to 195.7 mbsf contains the abundant magnesium-rich diagenetic minerals dolomite, palygorskite, and sepiolite. The exponential decrease of IW magnesium to a sediment depth corresponding to this magnesium-rich assemblage suggests one or more of these minerals are forming presently at depth in the sediment. In addition, some of the dolomite may have formed elsewhere and been redeposited at Site 765. Rhodochrosite may be precipitating now at depth, as it occurs in the sediment at a depth that corresponds to the maximum IW manganese concentration (13.8 mbsf). Rhodochrosite occurring deeper in the section is probably no longer forming, because the alkalinity, and presumably the manganese concentration, are much lower at these greater depths. The occurrence of ankerite at 413.3 mbsf is not unexpected because the sediment was reducing and iron was available.

Silica Diagenesis

The abundant radiolarian tests in the uppermost 90 mbsf are still composed of the originally precipitated opal-A; however, the abundant radiolarian tests below 550 mbsf are mostly composed of quartz. There, silica underwent the solution/precipitation transformation of opal-A to quartz, most likely passing through the intermediate silica phase, opal-CT. These silica phase transformations have been observed in many other pelagic sediments. The abundant quartz that occurs below 744.3 mbsf is probably from the recrystallization of what was originally biogenic silica, but may also contain significant amounts of eolian quartz. The occurrence of quartz and opal-CT in the <2- (and particularly the $\ll 2$-) μm-size fraction demonstrates the intimate association of these silica phases with the clay minerals.

Bulk Sediment Geochemistry

Introduction

A total of 73 samples from Site 765 were analyzed by XRF for major and trace elements (see Tables 18 to 20). This data set represents the first extensive and high-quality sediment geochemical data yet obtained aboard the *JOIDES Resolution*. A detailed description of sample preparation and machine operating conditions appears in the "Explanatory Notes" chapter (this volume). Trace element values are reported in parts per million for dry (to 110°C) sample powders (Table 20). Major element values are reported in weight percent for ignited (to 1000°C) samples, and thus represent volatile-free compositions that should total 100% (Table 19). The weight percent (wt%) LOI and both organic and inorganic carbon contents are reported for each sample in Table 18. Replicate analyses of the sediment standard SCO-1 (Cody shale) indicate an average relative precision of about 1.5% for major elements, and about 2.5% for trace elements (see Table 21).

Sediment samples for XRF analysis were taken at a frequency of one every few cores down Holes 765B and 765C, with a prominent sampling gap between Cores 123-765B-33X and -11R (~310–440 mbsf). In addition, some individual cores were subsampled (Cores 123-765B-2H, -15H, and -11R). We tried to take samples that are representative of the major lithologies cored. In general, the upper half of Site 765 is dominated by calcareous turbidites, while the lower half is dominated by clays and claystones. Samples were taken from various positions within the turbidites and from clays of various color. Table 18 includes brief sample descriptions.

The most obvious feature of the sediment geochemistry is its variability. Indeed, for most elements, there is substantial variability at all scales, from the centimeter scale of a single turbidite to the kilometer scale of the entire sedimentary column. Thus, this discussion is structured by scale. It begins with the large-scale lithology-dependent features, then examines just the clay lithologies, and finally focuses on two individual turbidites.

Large-Scale Geochemical Variability

Sediments can be viewed as rock mixtures. Most of the geochemical variability of the Site 765 sediments can be understood in terms of mixing. The components that dominate the sediment geochemistry are calcium carbonate and silica. Since calcium carbonate and silica typically are fairly pure phases, with little trace element substitution (with the exceptions of strontium and magnesium in calcium carbonate), their presence has the effect of diluting the other more metal-rich constituents in the sediments (i.e., clays, manganese, and iron hydroxides). Indeed, with few exceptions (which will be discussed later), all the metals analyzed in the Site 765 sediments exhibit linear mixing trends with both calcium carbonate and silica, which may be interpreted as dilution trends. For example, Figure 74 shows a plot of TiO_2 vs. calcium carbonate for all Site 765 sediments analyzed. Two trends may be identified in this plot. The first is that of calcium carbonate dilution, whereby an end-member with about 1.2 wt% TiO_2 mixes with calcium carbonate that has essentially no TiO_2, forming a tight linear array. The second trend is that of silica dilution. To illustrate this, the "noncarbonate" ($<$ 6 wt% calcium carbonate) fraction is plotted vs. SiO_2 (Fig. 74). Again, these data form a linear array that would result from mixing a 1.2 wt% TiO_2 end-member with pure silica.

Because most of the geochemical variation in the sediments is closely linked to calcium carbonate and silica variations, it is important to understand the systematics of calcium carbonate and silica at Site 765. In general, calcium carbonate is most abundant in the upper half of the site, where calcareous turbidites dominate (Fig. 75). However, for any given turbidite sequence, calcium carbonate may vary from near 80 wt% at the coarse turbidite base, which is commonly composed of foraminifer sands, to almost 0 wt% in the clay interval that characterizes the tops of turbidites. In other words, almost the entire range in calcium carbonate throughout Site 765 also is present at the scale of an individual turbidite. As most metals vary inversely with calcium carbonate, these too may exhibit almost their entire range on the scale of an individual turbidite. For example, Figure 76 shows the enormous TiO_2 variation in a single graded sequence from Core 123-765B-15H.

Silica variations in Site 765 are slightly more complicated. In the carbonates that predominate in the upper half of the site, silica behaves as any other metal not taken into carbonate and exhibits a dilution trend (Fig. 77). However, in the clays, silica increases with depth (Fig. 77). Silica in the clays remains below 65 wt% in the turbidite tops that characterize the upper 650 m of Site 765, while it varies between 65 and 75 wt% in the clays and claystones that dominate the lower 300 m. This increase in silica coincides with an increase in the abundance of radiolarians in the interval between 650 and 900 mbsf.

Based on calcium carbonate and silica systematics, the behavior of most metals may be summarized simply. In the upper half of Site 765, metal abundances vary on the scale of single turbidite units in response to calcium carbonate variations. In

Table 18. Sediment samples analyzed by XRF, Site 765.

Core, section, interval (cm)	Depth (mbsf)	$CaCO_3$ (wt%)	Organic carbon (wt%)	LOI	Color	Lithology	Comments
123-765B-							
1H-4, 48–50	5.0	55.23	0.63	32.50	5Y 6/2	Nannofossil ooze	Upper turbidite
2H-3, 94–106	13.2	56.06	0.51	32.21	5Y 7/1	Nannofossil ooze	Turbidite base
2H-3, 123–135	13.5	3.42	0.82	11.50	10Y 4/1	Nannofossil ooze	Upper turbidite
2H-4, 7–19	13.9	5.41	0.98	12.50	10Y 4/1	Nannofossil ooze	Upper turbidite
2H-4, 31–43	14.1	67.81	0.74	36.77	10Y 7/1	Nannofossil ooze	Middle turbidite
2H-4, 91–103	14.7	81.38	0.13	40.33	10Y 6/1	Nannofossil ooze	Middle turbidite
2H-4, 131–143	15.1	1.00	0.67	9.75	10Y 3/1	Nannofossil ooze	Turbidite top
2H-6, 138–140	18.2	0.58	0.72	10.52	5Y 4/1	Clay	Turbidite top
3H-1, 33–35	19.1	70.64	0.22	37.00	10H 7/1	Nannofossil ooze	Middle turbidite
4H-6, 20–22	36.2	2.42	0.91	11.15	10R 4/1	Nannofossil ooze	Purple bands
5H-7, 40–42	47.5	74.47	0.13	37.90	10H 7/1	Foraminifer sand	Turbidite base
7H-3, 38–43	60.8	70.31	0.58	35.60	5Y 6/1	Clayey ooze	Top of slump
8H-6, 85–90	75.5	46.90	0.29	27.25	5Y 6/2	Nannofossil clay	Upper turbidite
9H-6, 104–106	85.3	55.31	0.66	30.65	5GY 6/1	Nannofossil clay	Middle turbidite
10H-5, 84–88	93.2	4.83		7.41	5B 6/1	Clay	Turbidite top
11H-2, 40–44	97.9	61.89	0.15	30.10	5Y 6/1	Nannofossil ooze with clay	
12H-4, 44–48	110.5	69.81	0.04	34.00	5Y 7/1	Nannofossil ooze	
12H-6, 105–110	114.2	0.50	0.27	7.80	5Y 5/1	Clay	Turbidite top
13H-2, 138–143	118.1	60.89	0.31	31.50	5Y 6/2	Nannofossil ooze	
14H-4, 83–87	130.1	62.31	0.12	30.60	5Y 7/1	Nannofossil ooze	
15H-2, 76–88	136.8	60.00	0.30	30.59	5Y 7/1	Foraminifer sand	Turbidite base
15H-2, 88–100	136.9	0.50	0.29	8.26	5Y 4/1	Nannofossil ooze	Purple bands
15H-2, 115–127	137.2	63.47	0.05	32.73	5Y 7/1	Nannofossil ooze	Upper turbidite
15H-3, 1–13	137.5	59.64	0.24	31.70	10Y 8/1	Nannofossil ooze	Middle turbidite
15H-3, 20–32	137.7	73.22	0.08	36.64	5Y 7/1	Calc. fragment sand	Turbidite base
15H-3, 32–44	137.8	1.17	0.29	8.56	5GY 5/1	Nannofossil ooze	Turbidite top
15H-5, 23–27	140.7	36.49	0.31	20.80	5GY 6/1	Nannofossil ooze	Middle turbidite
15H-5, 49–54	141.0	58.81	0.19		5Y 7/1	Nannofossil ooze	Upper turbidite
15H-5, 116–121	141.7	58.48	0.11	30.60	5GY 7/1	Nannofossil ooze	Middle turbidite
15H-7, 52–56	144.0	57.48	0.13	29.80	5Y 7/1	Foraminifer sand	Turbidite base
16H-1, 42–46	144.6	57.23	0.13	29.50	5Y 7/1	Calc. fragment sand	Fine conglomerate
17H-5, 63–65	160.5	51.98	0.08	24.20	5Y 6/1	Foraminifer sand	Turbidite base
20X-2, 125–129	185.8	74.72		35.70	5Y 8/1	Nannofossil ooze	Purple bands
22X-1, 94–97	203.3	73.80	0.07	34.30	5Y 5/1	Foraminifer sand	Turbidite base
26X-1, 69–73	241.9	91.96	0.00	41.00	5Y 7/1	Foraminifer sand	Turbidite base
26X-3, 72–77	244.9	68.89	0.13	33.20	10Y 6/1	Nannofossil ooze	Middle turbidite
27X-1, 41–46	251.3	74.89	0.26	36.10	5GY 6/1	Calc. fragment sand	
28X-1, 34–38	260.9	80.88	0.25	38.20	10Y 6/1	Calc. fragment sand	Middle turbidite
32X-2, 126–129	302.1	82.22	0.13	41.74	5GY 7/1	Foraminifer sand	Foraminifer sand w/organic material
33X-2, 71–73	311.2	68.81	0.01	34.00	5GY 7/1	Nannofossil chalk	Upper turbidite
123-765C-							
11R-1, 84–88	446.8	32.90	0.31	20.60	5Y 4/1	Nannofossil clay	Turbidite top
11R-1, 97–100	447.0	81.80	0.00	38.04	5Y 7/1	Nannofossil ooze	Middle turbidite
11R-1, 119–123	447.2	80.72	0.09	37.82	5Y 6/1	Nannofossil ooze	Middle turbidite
11R-1, 133–137	447.3	83.80	0.04	37.40	5Y 6/1	Foraminifer sand	Turbidite base
11R-4, 61–64	451.1	1.08	0.18	9.62	5B 4/1	Clay	Turbidite top
13R-2, 61–64	466.7	4.08	0	8.99	5GY 4/1	Clay cobble	Debris flow
17R-2, 66–68	504.6	54.23	0	27.68	5YR 6/6	Nannofossil ooze	Middle turbidite
22R-2, 28–32	551.9	2.42	0.04	6.94	5GY 5/1	Clay	
24R-4, 92–93	570.2	0.33	0.03	6.87	10YR 4/1	Clay	w/organic material
24R-4, 71–72	574.5	0.67	0	8.07	5YR 3/1	Clay	Turbidite top
25R-2, 92–98	581.4	0.42	0.03	7.30	5YR 3/1	Clay	Turbidite top
25R-3, 106–111	583.1	0.50	0.03	7.46	10YR 3/1	Clay	Turbidite top
26R-4, 22–28	593.0	4.83	0.02	8.43	5YR 4/4	Clay	
27R-2, 34–40	599.3	0.25	0.01	6.36	5YR 4/1	Claystone	Mottles
28R-1, 55–58	607.6	0.17	0.01	6.08	5YR 3/1	Claystone	Zeolites
28R-3, 45–53	610.5	22.24	0.11	14.88	5G 5/1	Clayey nannofossil chalk	
29R-3, 76–80	620.2	5.33	0.06	7.90	5BG 5/1	Claystone	
30R-2, 16–22	627.6	0.67	0.03	3.15	5YR 4/2	Claystone	
30R-4, 98–102	631.4	0.17	0.05	6.21	5YR 3/4	Claystone	
35R-3, 24–29	677.3	0.33	0.13	5.41	5BG 4/1	Claystone	
35R-3, 86–90	678.0	4.66	0.67	6.70	2.5Y 2/0	Calc. siltstone	Black clay
37R-3, 40–43	696.4	34.65	0.04	19.35	5Y 5/2	Calc. claystone	
39R-3, 101–105	715.7	1.00	0.04	5.19	5Y 4/1	Calc. claystone	
40R-3, 104–109	724.9	0.50	0.22	5.24	5Y 2.5/1	Claystone	w/organic material
42R-2, 41–43	741.7	0.58	0.15	4.23	5G 4/1	Claystone	Glass, opaques
44R-4, 55–59	763.6	1.08	0.29	4.80	5Y 3/1	Claystone	Concretions
45R-2, 70–75	770.4	0.67	0.09	4.34	5R 3/2	Claystone	Blue streaks
50R-1, 110–113	816.7	0.58	0.01	4.64	2.5YR 3/2	Claystone	Rhodochrosite
51R-1, 84–86	825.8	0.42	0.18	4.00	2.5Y N3	Claystone	Black stripes
58R-4, 67–71	896.4	0.33	0.01	4.41	2.5 YR 2.5/4	Claystone	Radiolarians
60R-5, 120–123	917.0				2.5 YR 3/6	Bentonite	Ash
61R-4, 92–94	922.3	9.58	0.02	10.67	2.5 YR 3/6	Bentonite	Ash
61R-5, 81–85	923.7	27.32	0	16.05	5YR 3/2	Calc. claystone	Shell fragments
62R-3, 80–84	930.2	0.50	0	4.66	5YR 3/2	Claystone	

Note: $CaCO_3$ wt% calculated from coulemetrically determined inorganic carbon. Organic carbon wt% calculated from difference between inorganic and total carbon. LOI = wt% loss on ignition to 1000°C. Color codes from visual core description and Munsell soil color chart (1975) codes. Lithologic descriptions from core description sheets. Comments include position of sample in a given turbiditic sequence.

Table 19. Concentrations of major-element oxides of sediment samples, Site 765.

Core, section, interval (cm)	SiO_2 (wt%)	TiO_2 (wt%)	Al_2O_3 (wt%)	Fe_2O_3 (wt%)	MnO (wt%)	MgO (wt%)	CaO (wt%)	Na_2O (wt%)	K_2O (wt%)	P_2O_5 (wt%)	Total (wt%)
123-765B-											
1H-4, 48-50	32.56	0.44	9.60	3.76	0.27	2.97	45.87	0.86	2.38	0.24	98.97
2H-3, 94-106	33.42	0.42	8.12	3.02	0.70	2.22	46.98	0.34	2.02	0.22	97.47
2H-3, 123-135	59.96	0.82	16.59	6.43	0.35	3.98	2.52	4.01	2.93	0.19	97.78
2H-4, 7-19	60.15	0.79	16.12	5.57	0.14	3.42	4.16	3.93	2.74	0.18	97.21
2H-4, 31-43	22.22	0.32	6.53	2.27	0.55	2.44	61.14	0.35	1.85	0.29	97.97
2H-4, 91-103	13.93	0.16	2.56	1.49	0.41	1.21	77.10	0.13	0.92	0.10	98.01
2H-4, 131-143	62.43	0.87	17.29	5.88	0.13	3.52	1.09	3.91	2.69	0.12	97.93
2H-6, 138-140	61.64	0.83	16.72	6.19	0.17	3.94	0.66	4.17	2.75	0.14	97.22
3H-1, 33-35	21.58	0.31	6.65	2.44	0.50	1.77	62.67	0.03	1.71	0.21	97.87
4H-6, 20-22	61.71	0.83	16.20	6.17	1.29	3.70	0.94	3.72	2.65	0.12	97.34
5H-7, 40-42	21.90	0.24	4.54	1.97	0.12	1.75	65.98	0.12	1.44	0.10	98.16
7H-3, 38-43	22.47	0.34	6.72	2.48	0.17	2.65	59.99	0.59	1.79	0.27	97.47
8H-6, 85-90	38.92	0.55	11.67	4.45	0.16	3.39	36.66	1.70	2.41	0.20	99.49
9H-6, 104-106	32.08	0.50	10.13	3.82	0.16	3.59	43.98	1.35	2.46	0.27	98.33
10H-5, 84-88	59.19	1.00	19.63	6.87	0.05	4.60	0.37	2.53	3.30	0.14	97.69
11H-2, 40-44	32.20	0.48	9.15	3.44	0.14	2.71	48.16	0.81	2.44	0.27	99.79
12H-4, 44-48	23.48	0.39	7.25	2.66	0.21	1.98	59.99	0.46	0.00	0.24	96.65
12H-6, 105-110	60.73	1.07	20.63	7.70	0.05	4.04	0.58	1.23	3.23	0.19	99.45
13H-2, 138-143	28.37	0.48	9.50	3.62	0.14	2.58	49.83	0.97	2.29	0.29	98.06
14H-4, 83-87	29.26	0.50	10.49	3.94	0.13	2.38	49.64	0.34	2.57	0.20	99.46
15H-2, 76-88	31.32	0.46	7.98	3.51	0.09	2.38	48.49	0.93	2.31	0.22	97.69
15H-2, 88-100	59.07	1.08	21.02	8.39	0.04	4.01	0.46	185	3.44	0.18	99.55
15H-2, 115-127	26.45	0.43	9.07	3.56	0.21	2.18	53.17	0.86	2.78	0.16	98.87
15H-3, 1-13	29.91	0.46	8.22	3.58	0.18	2.09	50.80	0.88	2.38	0.23	98.72
15H-3, 20-32	22.60	0.30	4.84	1.97	0.14	1.44	65.83	0.45	1.58	0.17	99.31
15H-3, 32-44	57.80	1.07	20.45	8.25	0.04	4.50	0.65	1.73	3.71	0.15	98.34
15H-5, 23-27	43.55	0.75	14.48	5.97	0.06	3.27	26.16	0.62	3.52	0.14	98.51
15H-5, 49-54											
15H-5, 116-121	30.11	0.51	10.98	4.01	0.11	2.34	47.16	0.82	2.59	0.16	98.79
15H-7, 52-56	33.52	0.48	9.68	3.58	0.10	2.03	45.80	0.77	2.34	0.17	98.47
16H-1, 42-46	34.59	0.47	9.15	3.46	0.11	2.02	46.33	0.57	2.23	0.15	99.08
17H-5, 63-65	50.57	0.26	3.47	2.13	0.06	0.63	38.70	0.58	1.44	0.09	97.93
20X-2, 125-129	21.30	0.35	6.40	2.58	0.06	2.56	62.50	0.17	1.49	0.19	97.60
22X-1, 94-97	26.06	0.26	2.79	2.45	0.04	2.88	61.05	0.22	0.00	0.21	95.97
26X-1, 69-73	10.78	0.10	1.12	0.36	0.03	1.87	83.18	0.12	0.49	0.11	98.17
26X-3, 72-77	26.85	0.45	8.06	2.44	0.03	4.41	53.85	0.42	1.95	0.12	98.58
27X-1, 41-46	20.42	0.34	6.35	1.94	0.03	4.53	61.75	0.44	1.64	0.16	97.60
28X-1, 34-38	15.77	0.24	4.53	1.53	0.05	3.81	70.89	0.26	1.09	0.15	98.33
32X-2, 126-129	14.71	0.26	4.82	1.80	0.02	4.97	70.76	0.37	1.31	0.13	99.15
33X-2, 71-73	25.07	0.43	8.69	2.71	0.04	4.08	54.88	0.32	2.20	0.10	98.53
123-765C-											
11R-1, 84-88	45.87	0.79	15.52	5.27	0.06	5.54	23.37	1.15	2.02	0.20	99.79
11R-1, 97-100	15.24	0.25	4.66	1.80	0.14	2.76	72.71	0.24	0.93	0.08	98.82
11R-1, 119-123	17.31	0.25	3.94	1.59	0.16	2.94	71.58	0.28	0.87	0.13	99.05
11R-1, 133-137	17.70	0.18	2.04	1.16	0.14	2.32	75.09	0.17	0.66	0.08	99.55
11R-4, 61-64	60.51	1.09	20.23	6.51	0.07	6.55	0.46	1.27	2.07	0.22	98.99
13R-2, 61-64	58.39	0.99	19.86	9.44	0.05	3.26	1.70	1.67	2.28	0.11	97.74
17R-2, 66-68	34.76	0.64	12.80	5.08	0.33	1.46	42.80	0.88	0.62	0.12	99.49
22R-2, 28-32	65.64	0.65	15.28	5.91	0.06	4.20	1.99	2.18	2.18	0.15	98.24
24R-4, 92-93	60.30	1.10	16.53	9.97	0.09	4.03	0.73	1.36	3.87	0.31	98.28
24R-4, 71-72	59.41	1.03	16.29	8.15	1.75	4.91	1.07	1.77	3.70	0.37	98.46
25R-2, 92-98	58.89	1.14	17.01	9.81	0.54	4.16	0.93	1.58	3.72	0.32	98.11
25R-3, 106-111	59.93	1.05	17.79	8.43	1.17	3.55	1.08	1.70	3.53	0.39	98.62
26R-4, 22-28	60.24	1.11	16.35	8.24	0.11	4.15	3.85	1.60	3.68	0.31	99.65
27R-2, 34-40	60.08	1.12	17.45	7.97	1.92	3.44	0.56	1.64	4.20	0.14	98.52
28R-1, 55-58	61.05	1.05	18.06	8.21	0.88	3.07	0.51	1.68	4.01	0.11	98.64
28R-3, 45-53	53.08	0.85	14.13	6.94	0.12	3.02	15.82	1.78	3.65	0.13	99.51
29R-3, 76-80	61.38	0.93	17.58	6.58	0.11	3.01	3.97	2.11	4.17	0.12	99.96
30R-2, 16-22	61.61	1.02	18.05	7.54	1.53	3.13	0.85	2.09	3.71	0.13	99.66
30R-4, 98-102	62.71	0.95	18.02	7.99	0.15	2.87	0.78	2.23	3.67	0.11	99.47
35R-3, 24-29	71.57	0.79	13.26	5.20	0.04	3.08	0.73	1.75	2.10	0.14	98.66
35R-3, 86-90	86.30	0.31	5.22	1.90	0.02	0.98	3.22	1.12	0.79	0.07	99.93
37R-3, 40-43	52.66	0.60	9.24	5.76	0.68	2.42	24.82	1.31	1.99	0.18	99.65
39R-3, 101-105	68.51	0.89	12.97	7.77	0.18	3.17	1.16	1.66	2.43	0.18	98.91
40R-3, 104-109	70.13	0.86	12.16	8.57	0.05	3.30	0.76	1.50	2.14	0.12	99.59
42R-2, 41-43	77.81	0.58	9.73	5.23	0.14	2.05	0.62	1.16	1.60	0.11	99.02
44R-4, 55-59	71.80	0.74	12.56	7.03	0.14	2.41	0.68	1.33	2.09	0.09	98.89
45R-2, 70-75	75.05	0.72	11.43	6.29	0.04	2.36	0.70	1.27	1.80	0.17	99.82
50R-1, 110-113	73.25	0.81	9.76	9.08	0.08	2.83	0.67	1.24	1.87	0.11	99.70
51R-1, 84-86	77.31	0.82	9.34	5.35	0.06	2.50	0.60	1.16	1.81	0.11	99.06
58R-4, 67-71	76.50	0.57	8.95	6.25	0.21	2.63	0.72	1.14	1.49	0.16	98.63
60R-5, 120-123											
61R-4, 92-94	62.13	0.98	14.98	4.83	0.12	4.58	7.16	1.65	2.32	0.16	98.93
61R-5, 81-85	52.97	0.82	9.71	8.35	1.82	2.67	18.43	0.85	3.16	0.14	98.92
62R-3, 80-84	68.61	0.89	10.93	8.63	2.34	2.91	0.92	1.11	2.97	0.26	99.58

See Table 18 for lithologic description of samples.

Table 20. Concentrations of trace elements in sediment samples Site 765.

Core, section, interval (cm)	Nb (ppm)	Zr (ppm)	Y (ppm)	Sr (ppm)	Rb (ppm)	Zn (ppm)	Cu (ppm)	Ni (ppm)	Cr (ppm)	V (ppm)	Ce (ppm)	Ba (ppm)
123-765B-												
1H-4, 48–50	5.3	60.7	17.6	1905.1	51.3	67.1	85.7	56.2	39.4	62.5	18.9	526.9
2H-3, 94–106	5.5	84.4	21.3	1141.9	41.3	61.4	95.8	113.2	31.4	55.4	19.2	810.8
2H-3, 123–135	11.6	143.4	26.7	198.7	113.7	162.7	227.5	155.9	75.3	141.6	39.3	1086.1
2H-4, 7–19	11.0	148.4	27.6	238.1	104.2	148.8	194.0	158.7	75.3	122.1	48.0	1042.8
2H-4, 31–43	3.8	46.2	17.0	1568.5	32.4	51.2	78.1	49.7	30.5	53.2	5.0	620.9
2H-4, 91–103	1.5	36.1	6.9	1089.4	12.9	23.9	35.6	35.0	6.0	18.5	3.1	236.0
2H-4, 131–143	12.3	162.0	25.6	150.1	109.6	125.8	263.9	115.8	73.1	129.3	45.9	862.7
2H-6, 138–140	11.8	151.6	25.8	148.6	107.9	146.9	218.0	171.0	69.2	108.7	42.8	990.8
3H-1, 33–35	3.7	40.8	15.9	1346.7	28.7	40.6	54.0	37.5	28.9	42.4	5.3	708.3
4H-6, 20–22	11.5	159.5	31.4	166.8	100.6	133.7	167.4	183.0	70.7	118.2	47.0	1263.3
5H-7, 40–42	2.9	47.4	10.1	996.9	22.0	28.2	40.6	24.2	15.4	27.7	14.3	267.9
7H-3, 38–43	4.1	49.7	14.6	1917.5	31.4	42.1	44.9	35.2	35.2	43.9	14.3	378.4
8H-6, 85–90	7.0	85.8	21.1	973.5	61.9	76.6	88.9	62.2	45.3	69.9	20.9	871.7
9H-6, 104–106	5.7	65.8	19.4	1296.7	53.2	69.7	64.3	47.2	47.0	64.5	16.4	595.2
10H-5, 84–88	14.1	197.3	28.1	117.4	135.9	120.4	88.5	83.9	105.1	131.2	49.5	685.2
11H-2, 40–44	5.3	84.9	19.4	1198.7	48.3	56.7	50.4	43.3	40.0	61.9	17.1	469.1
12H-4, 44–48	4.6	65.9	16.3	1302.2	31.9	33.1	42.2	31.6	32.3	44.7	12.0	428.3
12H-6, 105–110	15.6	221.5	32.9	200.4	133.1	118.4	87.9	66.6	103.2	126.9	55.6	644.0
13H-2, 138–143	5.8	79.2	15.4	1468.8	48.3	48.5	45.9	56.6	45.1	57.5	21.7	296.7
14H-4, 83–87	6.3	74.7	14.5	1308.4	54.4	45.6	47.3	29.1	42.8	56.7	19.5	402.6
15H-2, 76–88	5.0	93.4	18.1	1973.5	45.8	42.6	61.3	42.7	56.0	68.0	17.6	227.3
15H-2, 88–100	15.3	211.2	30.7	208.6	139.8	110.5	226.3	75.3	114.5	161.5	56.3	587.3
15H-2, 115–127	5.1	70.1	17.6	1368.1	48.8	43.7	32.3	21.8	33.4	47.1	19.2	539.3
15H-3, 1–13	5.2	94.3	20.2	1162.6	45.4	40.8	38.7	22.9	28.3	49.8	17.2	437.7
15H-3, 20–32	3.3	72.8	13.0	1016.0	24.9	27.4	50.2	19.9	28.2	35.3	10.8	248.5
15H-3, 32–44	14.8	201.9	28.9	216.4	147.8	132.5	282.3	102.6	115.9	144.1	59.4	636.0
15H-5, 23–27	9.2	122.8	20.0	1100.2	99.2	67.4	29.2	42.0	67.3	91.7	37.0	275.8
15H-5, 49–54	6.2	75.2	16.1	1291.7	57.7	50.8	37.0	26.8	47.1	60.5	21.7	497.1
15H-5, 116–121	6.7	78.0	15.1	1272.9	55.9	48.5	56.1	31.2	41.5	60.4	28.1	463.8
15H-7, 52–56	6.2	102.7	16.3	1114.7	49.2	44.3	56.0	30.2	38.9	54.4	22.8	385.0
16H-1, 42–46	6.2	99.7	15.6	1101.6	46.7	43.0	53.4	25.0	37.8	54.2	24.3	362.6
17H-5, 63–65	4.6	119.7	8.1	762.6	26.4	18.7	43.5	34.5	8.3	28.7	13.2	197.1
20X-2, 125–129	3.7	58.6	7.9	2033.4	25.4	29.8	139.0	29.6	37.3	41.6	17.0	118.3
22X-1, 94–97	2.6	98.8	6.2	2500.7	13.3	12.7	31.7	27.8	19.8	17.4	8.7	72.7
26X-1, 69–73	1.2	41.0	2.1	1583.7	5.4	4.6	22.4	0.9	0.0	3.1	1.3	58.8
26X-3, 72–77	4.6	49.1	8.5	2660.7	40.5	27.5	34.1	14.2	48.2	48.6	20.1	101.6
27X-1, 41–46	3.2	49.8	6.4	2775.1	30.3	34.7	33.3	12.5	38.2	32.2	12.7	86.4
28X-1, 34–38	2.1	36.6	5.3	3170.5	16.9	18.5	43.0	8.8	22.7	21.7	2.7	97.3
32X-2, 126–129	2.6	40.4	5.6	3106.2	18.8	17.4	35.3	12.6	22.6	24.6	8.2	110.3
33X-2, 71–73	4.5	63.9	8.5	2344.7	42.5	30.7	29.8	16.0	43.2	49.8	13.4	128.0
123-765C-												
11R-1, 84–88	10.4	129.4	21.9	684.8	64.4	89.3	104.2	71.3	89.4	98.7	42.1	125.6
11R-1, 97–100	2.7	39.5	6.2	1041.0	13.2	18.9	20.0	15.8	26.2	28.2	8.5	89.6
11R-1, 119–123	3.1	52.7	7.7	1545.1	12.3	18.3	34.6	16.4	18.6	32.7	9.4	82.2
11R-1, 133–137	1.8	45.8	4.2	1390.9	8.5	9.8	23.1	10.8	11.8	22.0	8.0	91.1
11R-4, 61–64	17.0	211.6	38.4	376.5	93.4	151.1	272.6	121.4	123.2	159.0	71.4	129.1
13R-2, 61–64	11.8	166.1	18.7	440.8	92.0	119.3	61.4	67.1	94.8	149.0	44.8	177.1
17R-2, 66–68	6.4	89.6	13.1	1097.2	37.9	59.3	30.4	46.9	51.5	90.5	27.0	173.2
22R-2, 28–32	11.3	135.2	27.1	364.5	70.5	80.0	71.5	152.9	88.7	163.2	44.5	320.8
24R-4, 92–93	17.9	209.2	49.5	126.9	116.3	132.1	59.0	97.3	62.7	121.1	86.1	167.5
24R-4, 71–72	15.4	170.1	72.5	199.2	104.6	140.8	143.8	140.7	60.2	147.6	128.2	2308.9
25R-2, 92–98	13.8	178.9	61.6	157.4	113.2	153.3	155.3	131.0	79.6	141.3	91.6	645.7
25R-3, 106–111	17.4	185.9	73.2	171.4	108.8	155.8	159.1	163.3	71.6	143.7	130.9	1754.3
26R-4, 22–28	16.0	187.3	60.3	143.2	100.4	119.8	91.4	94.2	74.2	99.8	83.5	159.9
27R-2, 34–40	16.3	179.3	25.6	223.6	109.7	127.8	131.6	121.6	55.5	137.0	112.6	2048.7
28R-1, 55–58	15.2	166.4	19.7	164.5	115.8	155.4	123.7	113.3	68.1	146.1	104.1	684.0
28R-3, 45–53	11.4	122.7	24.2	282.1	86.8	109.3	43.1	84.2	50.7	93.7	59.2	1439.7
29R-3, 76–80	13.3	150.9	21.8	167.5	120.0	140.8	223.6	96.9	64.8	141.5	76.0	422.8
30R-2, 16–22	14.9	154.0	27.6	202.2	112.1	133.6	123.8	94.1	59.5	128.6	107.2	891.3
30R-4, 98–102	12.0	139.5	19.7	221.0	110.9	127.5	84.3	88.1	58.5	115.9	78.9	181.8
35R-3, 24–29	15.9	142.5	25.6	119.8	76.4	117.7	284.6	109.4	50.2	121.5	98.5	738.2
35R-3, 86–90	3.6	0.0	11.4	85.5	31.3	40.3	30.4	21.2	36.7	45.1	10.6	305.0
37R-3, 40–43	7.9	91.1	30.7	242.7	47.2	93.6	90.5	83.6	31.2	69.7	54.1	2794.7
39R-3, 101–105	12.8	134.4	29.4	134.2	76.8	118.8	103.4	86.8	41.2	129.3	94.4	481.4
40R-3, 104–109	14.1	146.8	22.2	95.3	69.4	96.6	210.4	85.5	40.9	236.2	61.9	119.9
42R-2, 41–43	8.4	106.5	20.6	114.2	61.4	72.9	70.5	35.6	34.9	93.4	51.7	1512.9
44R-4, 55–59	12.2	144.5	18.0	95.9	71.2	104.3	156.3	60.3	45.3	139.2	57.7	386.3
45R-2, 70–75	11.2	129.9	27.8	118.5	65.1	52.4	174.4	51.1	51.1	129.1	54.2	1411.0
50R-1, 110–113	12.8	134.4	25.6	89.1	54.4	85.5	76.2	51.8	30.5	69.9	67.0	987.2
51R-1, 84–86	11.7	103.0	21.9	74.1	54.1	69.8	97.2	41.1	26.8	106.2	57.2	366.4
58R-4, 67–71	12.4	118.0	32.6	139.1	48.8	107.5	48.9	69.6	20.7	33.1	81.9	3037.9
60R-5, 120–123	12.1	193.8	8.0	146.3	6.7	180.6	26.1	256.9	12.1	634.7	14.4	189.3
61R-4, 92–94	102.5	458.8	49.3	134.7	46.8	217.3	18.9	119.3	13.4	2469.4	151.8	229.7
61R-5, 81–85	10.9	135.3	31.2	126.6	54.7	96.2	122.9	88.7	15.2	102.6	69.2	162.2
62R-3, 80–84	15.6	190.5	44.9	135.1	83.3	129.1	146.3	136.8	22.1	148.9	73.8	1171.5

See Table 18 for lithologic descriptions of samples. See Table 19 for concentrations of major elements.

Table 21. Comparison of accepted values for Cody Shale standard with average of seven replicate XRF analyses.

	SCO-1	Average (N = 7)	Standard deviation (1σ)	Standard deviation (%)
Major elements (wt%)				
SiO_2	68.62	68.22	0.12	0.18
TiO_2	0.67	0.75	0.02	2.91
Al_2O_3	14.83	15.18	0.12	0.77
Fe_2O_3	5.65	5.72	0.02	0.33
MnO	0.05	0.06	0.01	13.34
MgO	2.99	2.98	0.05	1.66
CaO	2.86	2.80	0.01	0.45
Na_2O	1.03	0.95	0.06	6.13
K_2O	3.05	3.00	0.01	0.43
P_2O_5	0.24	0.21	0.00	2.36
Trace elements (ppm)				
Nb	10	13	0.2	1.7
Zr	135	176	5.8	3.3
Y	24	24	0.8	3.3
Sr	170	164	1.6	1.0
Rb	115	115	1.1	1.0
Zn	105	107	1.7	1.6
Cu	28	27	0.6	2.1
Ni	30	34	0.8	2.4
Cr	71	64	2.3	3.6
V	135	144	2.5	1.7
Ce	63	57	4.3	7.6
Ba	590	543	12.3	2.3

SCO-1 = Cody Shale standard.

the lower half of Site 765, where calcareous turbidites give way to clays, metal abundances decrease downsection as a result of the increasing amount of silica.

A few elements behave differently from that described above. Strontium and magnesium may be important constituents in calcium carbonate and dolomite, and thus do not form negative trends with calcium carbonate. In fact, strontium defines a fairly good positive trend with calcium carbonate, although there is significant variation at high calcium carbonate concentrations (Fig. 78). Strontium is much lower in the noncarbonates and exhibits a good silica dilution trend (Fig. 78). Magnesium does not correlate with calcium carbonate (Fig. 79A), but does correlate inversely with silica in the noncarbonates (Fig. 79B). Both the strontium and magnesium contents of the carbonates are highest at about 300 mbsf (Figs. 80A and 80B), which coincides with a magnesium minimum in the IW chemistry (see "Interstitial Water Chemistry," this section). Dolomite increases in abundance in sediments from this depth range.

Manganese, barium, copper, and phosphorus do not correlate with calcium carbonate or silica. Copper ranges from 20 to 300 ppm in Site 765 sediments, but does not seem to correlate with any other factor. Barium, manganese, and phosphorus show a few similarities in their distribution in Site 765 sediments. Barium, manganese, and phosphorus (as well as organic carbon) are high in the surface sediments, but decrease with depth to about 550 mbsf (Fig. 80C-E). At about 600 mbsf, in Cores 123-765C-24R to -28R, barium, manganese, and phosphorus (as well as many of the other metals), vary tremendously from unspectacular values to values exceeding all others within the site. Other than these generalizations, the variations in barium, man-

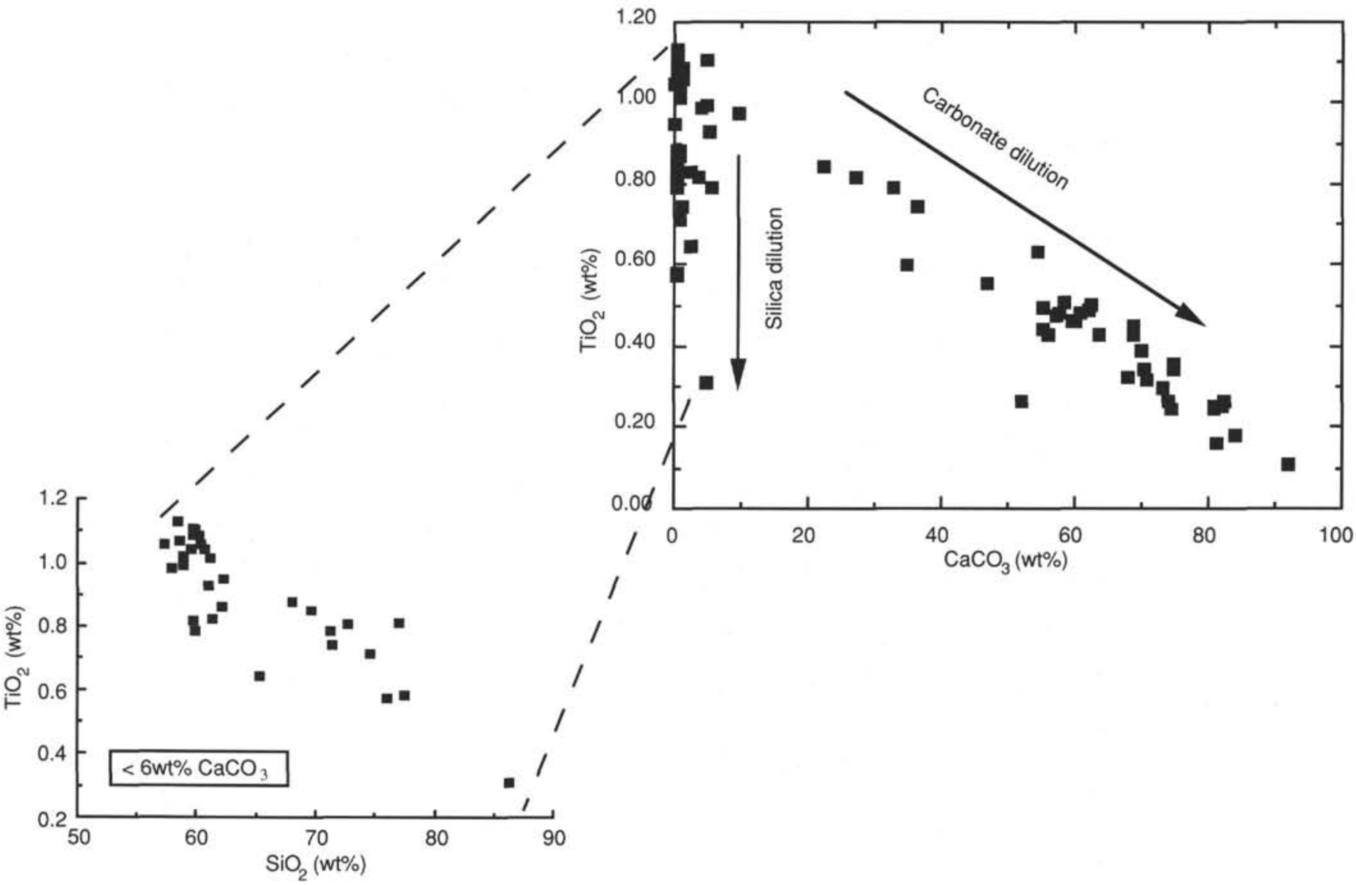

Figure 74. TiO_2 vs. $CaCO_3$ for all Site 765 samples analyzed, and TiO_2 vs. SiO_2 for a subset of low-carbonate samples (<6wt.% $CaCO_3$). Note that TiO_2 variations may be explained by dilution of an end-member having about 1.2% TiO_2 with pure $CaCO_3$ and pure SiO_2.

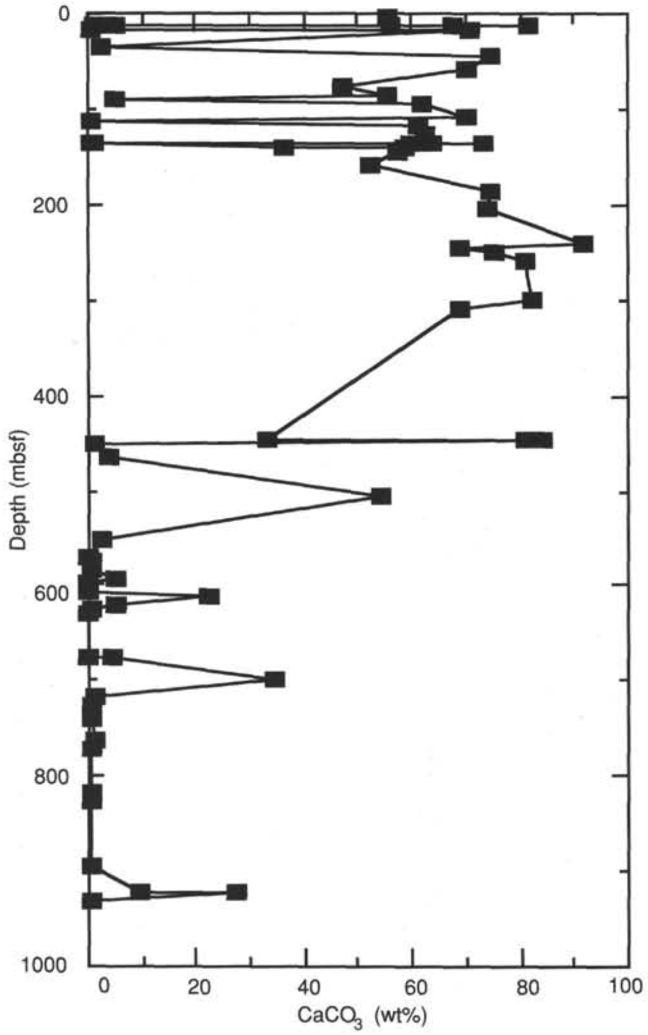

Figure 75. $CaCO_3$ variation with depth for all Site 765 samples analyzed. The high $CaCO_3$ contents of the samples from the upper 400 m reflect the predominance of calcareous turbidites in the upper one-half of Site 765.

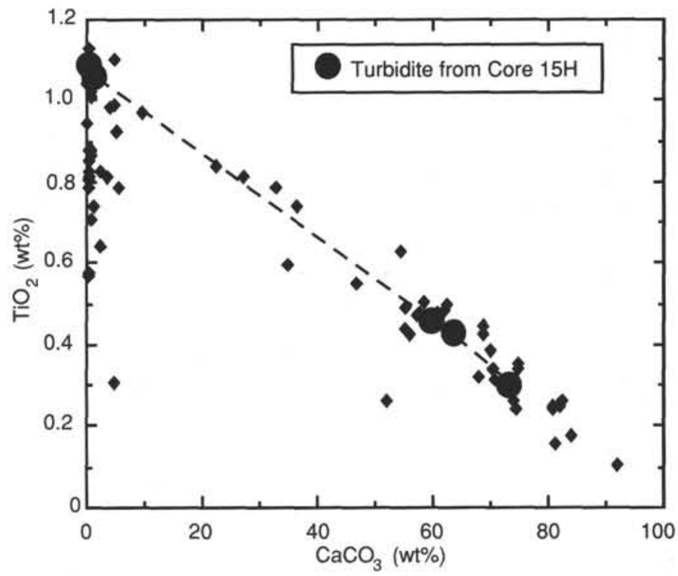

Figure 76. The TiO_2 variation in a single turbidite sequence (large filled circles) is superimposed upon the $CaCO_3$ variation in the whole site (small closed squares). Ranges are comparable, illustrating the extreme geochemical variability preserved on a small scale.

ganese, and phosphorus are otherwise scattered. Phosphorus and barium, and especially manganese, are high in the basal sediment Core 123-765C-62R, which contains manganese nodules. Barium values are high (>3000 ppm) in Core 123-765C-37R (in a carbonate-rich sample) and in Core 123-765C-58R (in a clay sample); barite has been identified within this interval, in Core 123-765C-52R.

Clay Lithologies

Although clays and claystones dominate the lithologies of the lower half of the site, clays also are present in the upper half of the site as fine-grained, dark, almost carbonate-free intervals on top of turbidite sequences, ranging in thickness from millimeters to tens of centimeters. The clays on top of the calcareous turbidites are typically dark green or dark blue green, while the clays that make up most of the Cretaceous section may be red brown, dark green, or almost black. Thus, the clays of Site 765 may be split roughly into two types: turbidite tops and the multicolored Cretaceous clays. The chemistry of these two clay types may be compared by separating out the noncarbonate fraction and backtracking the silica dilution trend. In this way, the "carbonate-free" and "silica-free" end-members of the two clay types may be compared. Only the Cretaceous clays should actually be corrected for silica addition, because the clays associated with turbidite tops are uniformly low in silica. The main result of this comparison is that these two clay end-members are remarkably similar for most elements. Figure 81A depicts a plot of zinc vs. SiO_2 for both clay types. The clay compositions tend to converge at the low-silica end of the spectrum. Thus, for zinc, and indeed for most elements, there is overlap in the clay chemistry over the approximately 130 m.y. represented by this site, and over a change in the style of deposition, from one characterized by quiet intervals between turbidity flows to one characterized by more quiescent abyssal sedimentation. Only two elements, potassium and cesium, indicate no overlap between the two clay types (Fig. 81B and 81C). Both K_2O and cesium are substantially higher in the Cretaceous clays.

Two Individual Turbidites

Although most of the geochemical variation in Site 765 sediments can be explained simply by the mixing of a single, metal-rich end-member and pure calcium carbonate and silica, there may be subtle differences in the metal-rich end-members on the scale of a single turbidite. Four samples were taken from each of two different turbidites. In both turbidites, there are linear trends in almost any given element with calcium carbonate. Silica dilution is not a factor in these cases because both turbidites have low and similar silica contents. Although the geochemical variations in the two turbidites are dominated by calcium carbonate dilution, the calcium carbonate mixing trends are slightly but significantly offset for several metals. For example, zirconium is high throughout the turbidite from Core 123-765B-15H (Fig. 82A), while nickel is much higher in the turbidite from Core 123-765B-2H (Fig. 82B). In fact, these two turbidites may be fingerprinted by a whole suite of metals. The turbidite from Core 123-765B-15H is higher in cesium, zirconium, niobium, TiO_2, Fe_2O_3, and Al_2O_3. Since Al_2O_3 is almost exclusively associated with clay minerals in marine sediments, the enrichments in these elements may be coupled to the clay mineral component in these sediments. The turbidite from Core 123-765B-2H, near the top of Site 765, is higher in nickel, zinc, barium, P_2O_5,

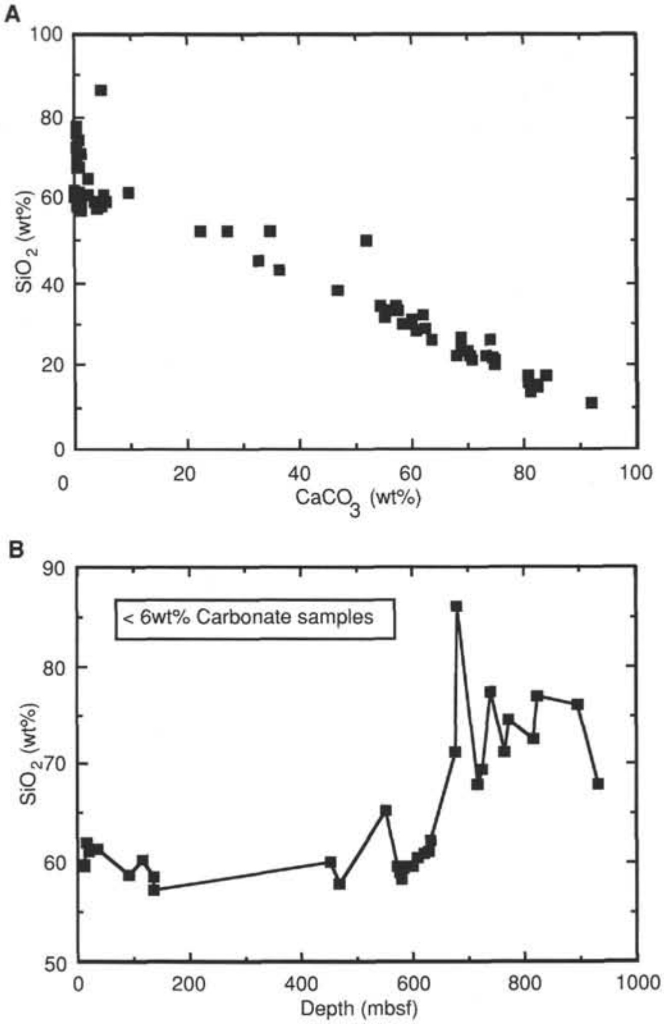

Figure 77. A. SiO_2 vs. $CaCO_3$ for all Site 765 sediments analyzed. For the carbonate-rich samples, SiO_2 displays a carbonate dilution trend similar to most other elements. B. SiO_2 increases with depth in the clay samples probably because of the abundance of radiolarians in the lower part of the site.

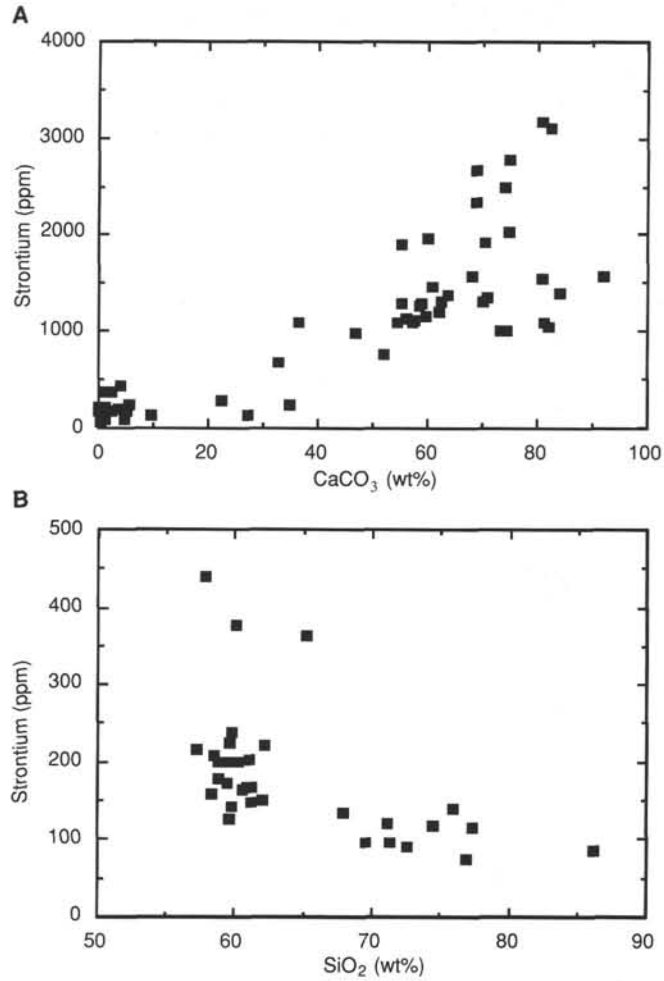

Figure 78. Strontium vs. $CaCO_3$ for all Site 765 samples analyzed. The positive trend with carbonate indicates that there is a substantial amount of strontium in the carbonates. B. Strontium vs. SiO_2 for the clay samples only. Strontium exhibits a SiO_2 dilution trend in the clays similar to other elements.

Na_2O, MnO, and organic carbon. These elements, in general, seem to be enriched in the upper 50 m of Site 765. There are also large gradients in the IW chemistry in the upper 100 m of Site 765 (see "Interstitial-Water Chemistry," this section), and the reactions that lead to these large gradients (mostly involving the breakdown of organic matter), may also be responsible for the distinctive surface sediment chemistry preserved in this upper-level turbidite in Core 123-765B-2H.

Summary

The geochemical variations in Site 765 sediments are intimately linked to lithologic variations on many different scales. The major process that affects geochemical variations in the upper half of Site 765, where calcareous turbidites dominate, is that of calcium carbonatec dilution. This process operates on the meter scale of a single graded sequence. The major process affecting geochemical variations in the lower half of the site, which is dominated by siliceous clays, is that of silica dilution. This process may operate on a scale of hundreds of meters of the entire Cretaceous section. There are slight geochemical differences between the upper turbidite clay tops and the Cretaceous clays, but, in general, the clay chemistry remained remarkably similar through time. Within these general systematics there are subtle but detectable geochemical fingerprints that may be used to distinguish individual turbidite sequences.

ORGANIC GEOCHEMISTRY

A total 401 samples were analyzed for inorganic carbon, and 179 samples were analyzed for total carbon at Site 765. The weight percent of calcium carbonate and total organic carbon were calculated from these data. A total 199 samples were analyzed by Rock-Eval pyrolysis techniques to help characterize the nature and source of organic matter. Light hydrocarbons (C_1–C_3) were monitored on the Carle GC for safety considerations. Additional light hydrocarbons (C_1–C_6) and nitrogen, carbon dioxide, carbon monoxide, and hydrogen sulfide were measured with the natural gas analyzer on 57 sediment samples. The methods used for analyses are described in the "Explanatory Notes" chapter (this volume).

Coulometric Analyses of Total and Inorganic Carbon

Data obtained from the Coulometric analyses of the sediments are summarized in Table 22. These data represent analy-

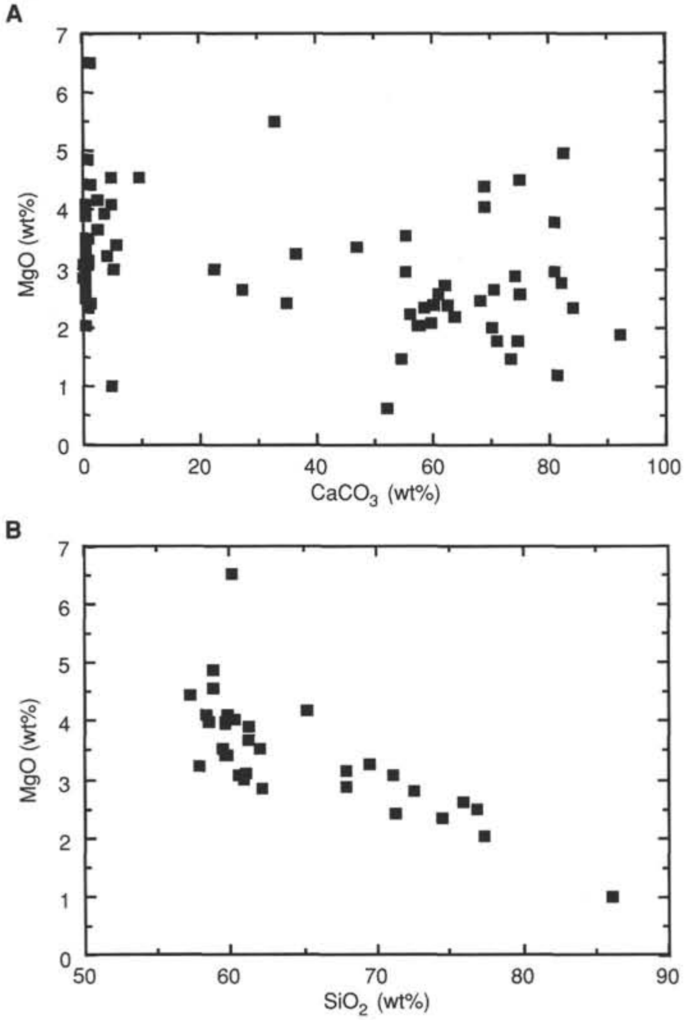

Figure 79. A. MgO vs. $CaCO_3$ for all Site 765 samples analyzed. There is no systematic relationship between MgO and $CaCO_3$. The high MgO contents of some carbonates probably reflect the presence of dolomite. B. MgO vs. SiO_2 for clay samples only. Although MgO shows no systematic relationship in the carbonates, it shows a good silica dilution trend in the noncarbonates.

ses of sediments of several different sample codes. Samples analyzed from headspace and interstitial-water squeeze cake residues were collected, usually from Sections 3 or 4 of each core, and were analyzed for inorganic (IC) and total (TC) carbon. In addition, "bomb" samples collected during shipboard sampling were taken within different lithologies and analyzed primarily for inorganic carbon. Furthermore, all shipboard samples collected for XRF analyses and selected samples for Rock-Eval pyrolysis were analyzed for inorganic and total carbon.

Calcium Carbonate

The weight percent of calcium carbonate was calculated from inorganic carbon data (wt% $CaCO_3$ = 8.33 × %IC). These data are plotted in Figure 75 and represent approximately 60 data points for 200 m of core. Four observations can be made from these data. First, calcium carbonate contents vary erratically throughout most of the sedimentary column, often between <5 and about 60 wt% over distances of less than 1 m. Second, calcium carbonate contents between 160 and 410 mbsf are consistently high, typically >50 wt% and frequently >70 wt%. Third, calcium carbonate contents at >60 wt%, and often to 80 wt%, dominate the record to depths of about 500 mbsf: only 12% of these data contain calcium carbonate of <10 wt%. Fourth, the record below about 500 mbsf, in contrast to the upper 500 m of sediment, is dominated by samples having a carbonate content of <10 wt%: fewer than 30% of the samples contain >10 wt% calcium carbonate.

The consistent presence of calcium carbonate in these sediments is unexpected because this site is below the CCD. Sedimentological examination of the cores indicate that the sedimentary column is dominated by turbidite deposition (see "Sedimentology" section, this chapter). To test if turbidite depositional sequences were responsible for the erratic variations in calcium carbonate contents, two apparent turbidite sequences were selected for additional sampling and analyses. One sequence was selected from lithologic Unit I (Sections 123-765B-2H-3 at 123–135 cm through 123-765B-2H-4 at 91–103 cm) and the other from lithologic Unit II (Sections 123-765B-15H-2 at 88–100 cm through 123-765B-15H-3 at 20–32 cm). Four samples were taken from each sequence; one in the top "dark" layer, another within the "bioturbated" zone (usually a mottled and dark green color), another in the light green/gray zone, and another in the coarse-grained material (usually a light gray color) at the base of the turbidite. In addition, samples were taken from the adjacent sediments above and below the tops and bottoms, respectively, of each sequence. The carbon data from these samples are included in Table 22.

The calcium carbonate data from both sequences indicate a marked fractionation in carbonate content between the top and base of both turbidites. Calcium carbonate and organic carbon from the turbidite sequence of Unit I, Core 123-765B-2H, are plotted in Figure 83. Data from Core 123-765B-2H show low carbonate contents (<6 wt%) in the top 40 cm of the sequence (dark and mottled green layers) that increase rapidly to near 65 wt% in the adjacent deeper interval. Calcium carbonate contents remain high (>60 wt%) in the base of the turbidite, but decrease dramatically across the lithologic boundary to the top of the underlying sequence. Similarly, calcium carbonate in the top section of Core 123-765B-15H had nearly undetectable carbonate, but this increased to approximately 60 wt% over a 15-cm depth. These data explain the erratic variations in calcium carbonate measured throughout the sediment column. The high carbonate sediments are turbidites and probably derived from the nearby Exmouth Plateau or Rowley Shoals. Sediments having very low carbonate probably represent periods of hemipelagic deposition below the CCD, with bioturbation and dissolution of carbonate from the top of the turbidite.

Organic Carbon

Organic carbon was calculated as the difference between total carbon and inorganic carbon. The organic carbon contents vary between 0 and 4.9 wt% throughout the cores, often with large variations over relatively short depth intervals, probably because of the turbidite-dominated sedimentation: organic carbon data of Figure 83 indicate the highest total organic carbon (TOC) contents in the low-carbonate intervals of the turbidite. The downhole organic carbon results obtained from calometric analysis are plotted in Figure 84A. Despite the scatter in the downhole profile, a trend is evident in these data. Organic carbon concentrations in the top 200 m of sediment were measured as high as 1.5 wt% and frequently were >0.5 wt%. Organic carbon decreased erratically to minimum values (<0.1 wt%) between 500 and 630 mbsf. Organic carbon concentrations below 630 mbsf increase, although erratically, with increasing depth in Lower Cretaceous sediments. Organic carbon contents in the "dark" sediment layers (up to 1.1 wt%) were consistently higher than those measured in the red brown and green clay-

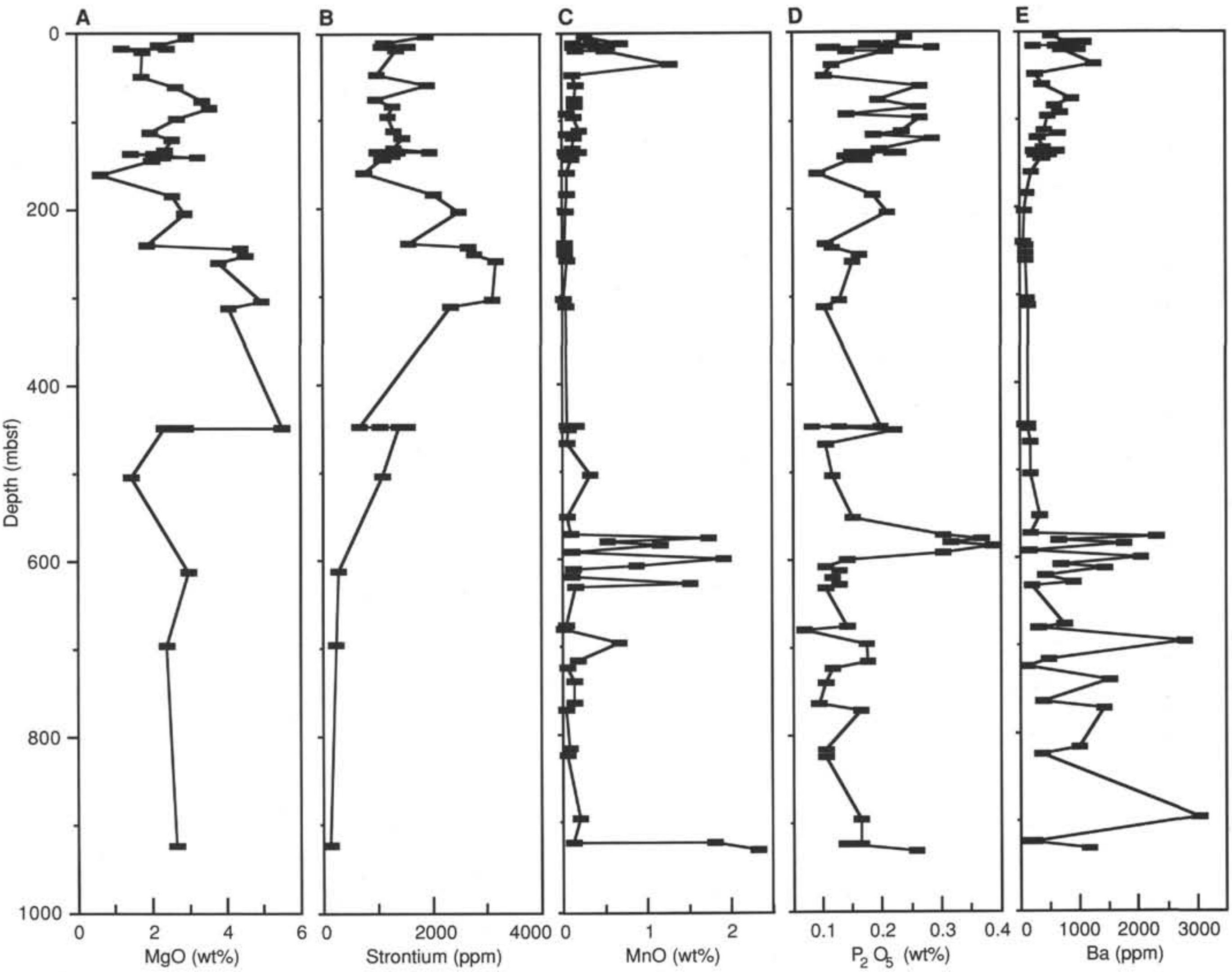

Figure 80. MgO (A) and strontium (B) vs. depth for all carbonate-rich (>20 wt.% $CaCO_3$) samples. Carbonates at about 300 mbsf have high MgO and strontium contents. MnO (C) and P_2O_5 (D), and barium (E) vs. depth for all Site 765 samples analyzed. Samples from the upper 100 m, and from about 600 mbsf have high MnO, barium, and P_2O_5 contents.

stone sediments. One sample (123-765C-45R-4, 100–101 cm) had an organic carbon content of 4.9 wt%.

Rock-Eval Pyrolysis

To help determine the nature and source of organic matter in the sediments, 199 samples were analyzed by pyrolysis techniques (Espitalié et al., 1977). Pyrolysis data are summarized in Table 23. Samples from headspace analyzes and interstitial-water squeeze cake residues were routinely analyzed initially in the top few hundred meters of sediment, and thereafter samples were chosen selectively from the deeper sediments during shipboard sampling. Rock-Eval TOC and Coulometer organic carbon were determined on several samples and provide a useful comparison of the two techniques over a wide range of calcium carbonate and organic carbon contents. Rock-Eval TOC data indicate similar trends in TOC variations with depth, similar to those found with Coulometer data (Fig. 84B). The highest TOC value (5.1 wt%) was similarly measured in an isolated thin "black" layer in Core 123-765C-45R. Rock-Eval TOC data may be generally lower than Coulemeter organic carbon in the high carbonate samples of Cenozoic sediments (no statistical comparison has been made).

To examine the nature and source of the organic matter, pyrolysis data were screened and those samples with TOC of <0.5 wt% were eliminated from further considerations. These samples, particularly those containing appreciable calcium carbonate, have erroneous oxygen indexes (OI) because of mineral matrix effects (Katz, 1983; Peters, 1986). The remaining data were plotted on a van Krevelen-type diagram (Fig. 85) and generally indicate two different groups of samples. First, several samples from Cenozoic sediments, Cores 123-765B-2H through 123-765B-8H (open squares), with relatively high hydrogen indexes (HI up to 1100) and OIs of generally >100, plot between the type II and III fields, which suggests that the organic matter in these cores is oxidized and of a terrestrial or mixed terrestrial and marine source(s). Some other samples with TOC of >0.5 wt% had very high OIs (>500) and were interpreted as reworked and extremely oxidized. A second group of samples from Cretaceous sediments, Cores 123-765C-30R through 123-765C-59R (solid squares), have consistently lower HIs than Cenozoic sediments, although two intervals (Sections 123-765C-55R-2 with 0.22 wt% TOC and 123-765C-30R-4 with 0.17 wt% TOC) had HIs of >1000, variable OIs, and cluster around the type III line, indicating that these were primarily terrestrial or-

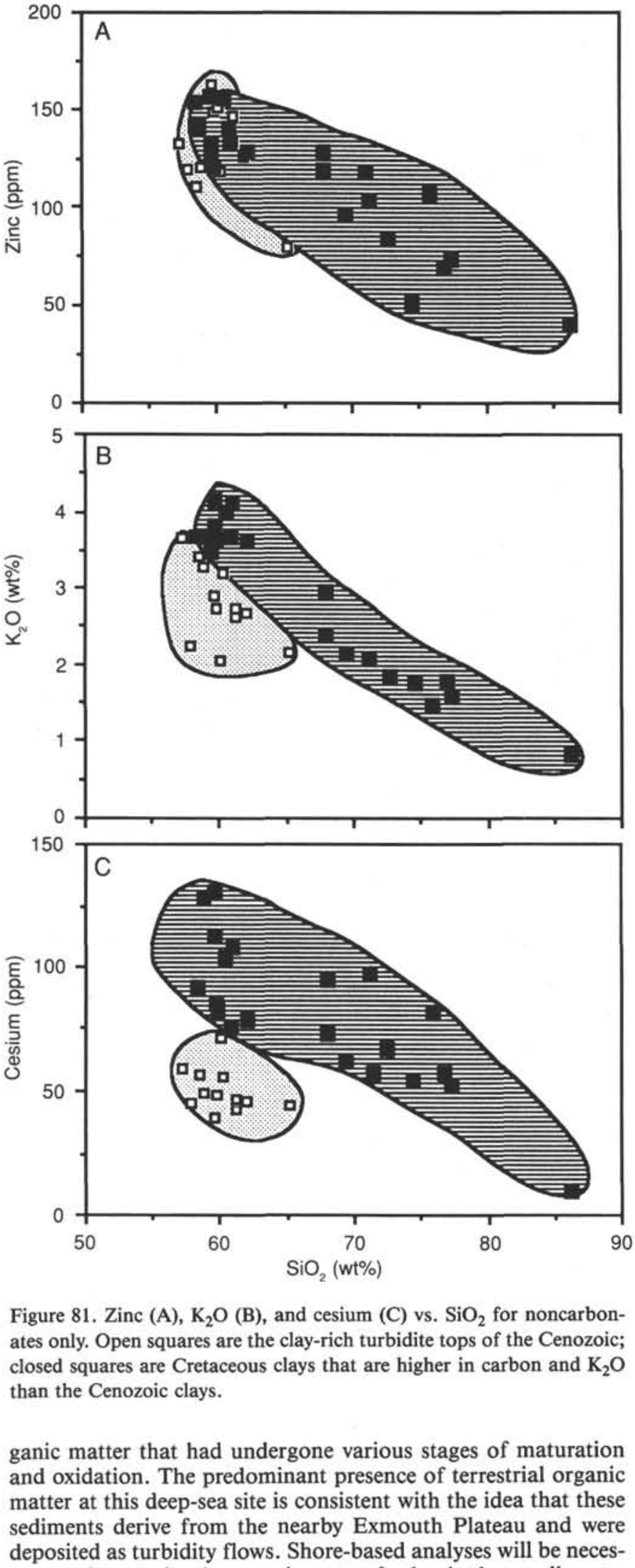

Figure 81. Zinc (A), K_2O (B), and cesium (C) vs. SiO_2 for noncarbonates only. Open squares are the clay-rich turbidite tops of the Cenozoic; closed squares are Cretaceous clays that are higher in carbon and K_2O than the Cenozoic clays.

ganic matter that had undergone various stages of maturation and oxidation. The predominant presence of terrestrial organic matter at this deep-sea site is consistent with the idea that these sediments derive from the nearby Exmouth Plateau and were deposited as turbidity flows. Shore-based analyses will be necessary to characterize the organic matter further in these sediments.

Gases in Sediments

Light hydrocarbons are not only produced in marine sediments during bacterial degradation of organic matter, but also

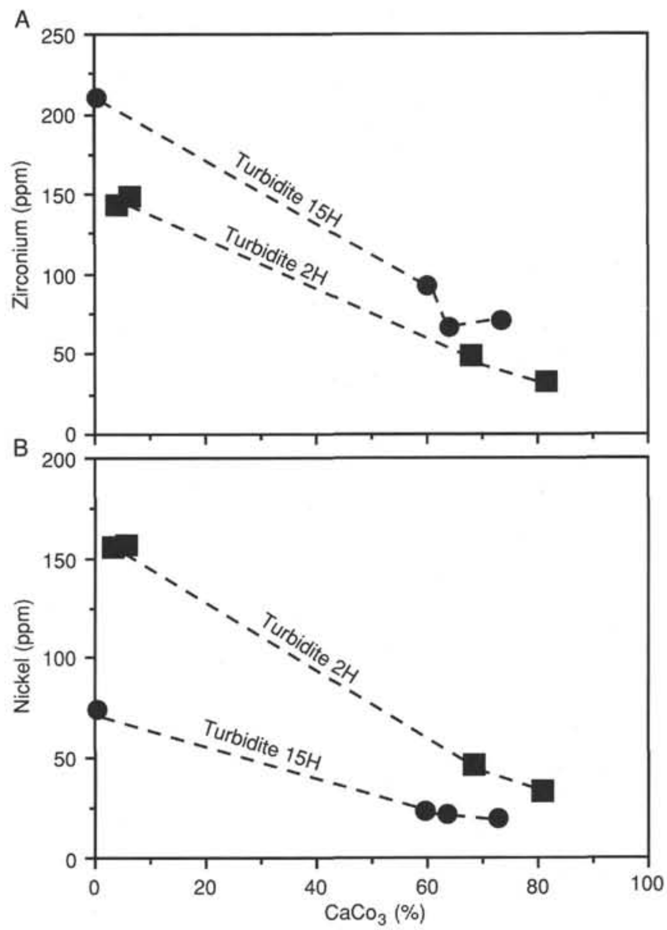

Figure 82. Zirconium (A) and nickel (B) variations in two individual turbidite sequences. Zirconium is higher for the turbidite from Core 123-765B-15, while nickel is higher for the turbidite from Core 123-765B-2H.

by the thermal degradation of deeply buried organic carbon (Claypool and Kvenvolden, 1983). The concentrations of gases (expressed as ppm by volume of headspace) measured in the sediments of Site 765 are summarized in Table 24. Concentrations of methane at this site were monotonously low throughout the cores—rarely increasing above 2 ppm (volume of headspace). Isolated occurrences of several other hydrocarbons; ethane, ethylene, propane, propylene, *n*-butane, *i*-butane, 1-butane, *i*-pentane, 1-pentane, cyclopentane, methylcyclopentane, 2-methylpentane, *n*-hexane, *i*-hexane, and cyclohexane were found throughout the hole, but did not appear to correlate with either lithology or organic carbon content. These gases probably were produced by low-temperature ($<50°C$) degradation and maturation of organic matter (Whelan and Hunt, 1980). No convincing evidence exists for thermogenic gas production at this site.

Nitrogen gas contents also were measured in sediments. Because the vacutainers were flushed with helium before heating and extraction of sedimentary gases, the oxygen content in the headspace vials was used to indicate atmospheric contamination; thus, the headspace nitrogen content could be corrected for atmospheric nitrogen. However, no evidence of excess nitrogen was found in these sediments. The headspace carbon dioxide concentrations were always in excess of the atmospheric concentration and probably result from the oxidation of organic carbon and degassing of pore waters. Carbon monoxide was detected in about two-thirds of the samples and is probably related

Table 22. Organic carbon and carbonate carbon data, Site 765.

Core, section, interval (cm)	Depth (mbsf)	Total carbon (%)	Inorganic carbon (%)	Organic carbon (%)	$CaCO_3$ (%)
123-765A-1H-1, 53–56	0.53	9.00	8.20	0.80	68.3
765B-1H-1, 96–98	0.96		1.56		13.0
765A-1H-2, 78–80	2.28		6.30		52.5
765B-1H-3, 42–44	3.42		4.28		35.7
765A-1H-3, 145–150	4.45	8.55	8.22	0.33	68.5
765A-1H-4, 38–40	4.88		0.05		0.4
765B-1H-4, 48–50	4.98	7.26	6.63	0.63	55.2
765B-1H-4, 145–150	5.95	8.53	8.10	0.43	67.3
765A-1H-4, 145–150	5.95	10.03	8.70	1.33	72.5
765B-1H-4, 147–150	5.97	9.34	8.54	0.80	71.1
765B-1H-6, 61–63	8.11		0.30		2.5
765A-1H-6, 68–70	8.18		8.68		72.3
765B-2H-1, 53–55	9.83		8.57		71.4
765B-2H-3, 65–67	12.95		0.35		2.9
765B-2H-3, 94–106	13.24	7.24	6.73	0.51	56.1
765B-2H-3, 123–135	13.53	1.23	0.41	0.82	3.4
765B-2H-3, 145–150	13.75	1.18	0.10	1.08	0.8
765B-2H-4, 7–19	13.87	1.63	0.65	0.98	5.4
765B-2H-4, 31–43	14.11	8.88	8.14	0.74	67.8
765B-2H-4, 91–103	14.71	9.90	9.77	0.13	81.4
765B-2H-4, 131–143	15.11	0.79	0.12	0.67	1.0
765B-2H-4, 145–150	15.25	1.09	0.03	1.06	0.3
765B-2H-6, 34–36	17.14		0.03		0.3
765B-2H-6, 75–78	17.55		3.52		29.3
765B-2H-6, 138–140	18.18	0.79	0.07	0.72	0.6
765B-3H-1, 33–35	19.13	8.70	8.48	0.22	70.6
765B-3H-1, 83–85	19.63		8.33		69.4
765B-3H-3, 145–150	23.25	1.23	0.05	1.18	0.4
765B-3H-4, 125–128	24.55		0.19		1.6
765B-3H-4, 145–150	24.75	1.12	0.03	1.09	0.3
765B-3H-5, 127–130	26.07		6.56		54.6
765B-3H-6, 23–26	26.53		7.94		66.1
765B-4H-3, 145–150	32.95	7.74	6.80	0.94	56.6
765B-4H-4, 0–5	33.00	1.11	0.06	1.05	0.5
765B-4H-5, 128–130	35.78		2.14		17.8
765B-4H-6, 20–22	36.20	1.20	0.29	0.91	2.4
765B-5H-2, 85–87	40.45		3.81		31.7
765B-5H-3, 145–150	42.55	7.30	6.75	0.55	56.2
765B-5H-4, 0–5	42.60	7.26	6.69	0.57	55.7
765B-5H-7, 40–42	47.50	9.07	8.94	0.13	74.5
765B-6H-3, 145–150	52.25	7.97	7.46	0.51	62.1
765B-6H-4, 0–5	52.30	7.81	6.83	0.98	56.9
765B-6H-6, 99–101	56.29		3.93		32.7
765B-7H-3, 38–45	60.78	9.02	8.44	0.58	70.3
765B-7H-3, 145–150	61.85	8.16	7.45	0.71	62.1
765B-7H-4, 0–5	61.90	9.39	8.31	1.08	69.2
765B-7H-5, 105–107	64.45		7.87		65.6
765B-8H-3, 145–150	71.55	9.48	8.51	0.97	70.9
765B-8H-4, 0–5	71.60	9.22	8.53	0.69	71.1
765B-8H-5, 139–141	74.49		5.87		48.9
765B-8H-6, 85–90	75.45	5.92	5.63	0.29	46.9
765B-9H-3, 145–150	81.25	8.70	8.62	0.08	71.8
765B-9H-4, 0–5	81.30	8.99	8.98	0.01	74.8
765B-9H-4, 89–93	82.19		8.22		68.5
765B-9H-6, 104–106	85.34	7.30	6.64	0.66	55.3
765B-10H-3, 145–150	90.85	7.22	6.95	0.27	57.9
765B-10H-4, 0–5	90.90	7.52	7.36	0.16	61.3
765B-10H-4, 119–121	92.09		0.11		0.9
765B-10H-5, 84–88	93.24		0.58		4.8
765B-11H-2, 19–21	97.69		0.07		0.6
765B-11H-2, 40–44	97.90	7.58	7.43	0.15	61.9
765B-11H-4, 0–5	100.50	7.37	6.82	0.55	56.8
765B-12H-3, 145–150	110.05	8.75	8.67	0.08	72.2
765B-12H-4, 0–5	110.10	8.61	8.14	0.47	67.8
765B-12H-4, 44–48	110.54	8.42	8.38	0.04	69.8
765B-12H-5, 69–72	112.29		1.04		8.7
765B-12H-6, 105–110	114.15	0.33	0.06	0.27	0.5
765B-13H-2, 138–143	118.08	7.62	7.31	0.31	60.9
765B-13H-4, 0–5	119.70	7.61	7.55	0.06	62.9
765B-13H-4, 54–56	120.24		7.34		61.1
765B-14H-4, 0–5	129.30	7.06	6.38	0.68	53.2
765B-14H-4, 83–87	130.13	7.60	7.48	0.12	62.3
765B-14H-6, 40–42	132.70		4.92		41.0
765B-15H-1, 41–43	134.91		9.44		78.6
765B-15H-2, 76–88	136.76	7.51	7.21	0.30	60.1
765B-15H-2, 88–100	136.88	0.35	0.06	0.29	0.5
765B-15H-2, 115–127	137.15	7.67	7.58	0.09	63.1
765B-15H-3, 0–13	137.50	7.40	7.16	0.24	59.6
765B-15H-3, 20–32	137.70	8.87	8.79	0.08	73.2
765B-15H-3, 32–44	137.82	0.43	0.14	0.29	1.2

Table 22 (continued).

Core, section, interval (cm)	Depth (mbsf)	Total carbon (%)	Inorganic carbon (%)	Organic carbon (%)	$CaCO_3$ (%)
765B-15H-3, 76–88	138.26	7.50	7.19	0.31	59.9
765B-15H-3, 145–150	138.95	1.69	1.19	0.50	9.9
765B-15H-4, 0–5	139.00	3.27	2.95	0.32	24.6
765B-15H-5, 23–27	140.73	4.69	4.38	0.31	36.5
765B-15H-5, 49–54	140.99	7.25	7.06	0.19	58.8
765B-15H-5, 116–121	141.66	7.13	7.02	0.11	58.5
765B-15H-7, 52–56	144.02	7.03	6.90	0.13	57.5
765B-16H-1, 42–46	144.62	7.00	6.87	0.13	57.2
765B-16H-4, 0–5	148.70	5.94	5.33	0.61	44.4
765B-17H-4, 0–5	158.40	3.05	2.72	0.33	22.7
765B-17H-5, 63–65	160.53	6.32	6.24	0.08	52.0
765B-17H-6, 76–78	161.40		0.28		2.3
765B-18H-4, 0–5	167.50	8.50	8.20	0.30	68.3
765B-18H-4, 145–150	168.95	8.67	8.40	0.27	70.0
765B-18H-6, 114–116	171.64		0.16		1.3
765B-19X-3, 145–150	177.75	5.60	5.03	0.57	41.9
765B-20X-2, 125–129	185.75		8.97		74.7
765B-20X-4, 0–7	187.50	5.40	4.40	1.00	36.7
765B-21X-1, 67–70	193.37		6.78		56.5
765B-21X-2, 145–150	195.65	9.93	9.71	0.22	80.9
765B-21X-3, 0–5	195.70	9.92	9.64	0.28	80.3
765B-21X-3, 138–140	197.08		8.70		72.5
765B-22X-1, 94–97	203.34	8.93	8.86	0.07	73.8
765B-22X-2, 80–82	204.70		7.44		62.0
765B-22X-3, 87–89	206.27		10.30		85.8
765B-22X-4, 0–5	206.90	8.93	8.72	0.21	72.6
765B-22X-4, 60–62	207.50		9.92		82.6
765B-23X-1, 31–34	212.41		9.06		75.5
765B-23X-2, 0–3	213.60	7.50	7.61	0.00	63.4
765B-23X-2, 40–43	214.00		9.65		80.4
765B-24X-1, 65–68	222.45		8.68		72.3
765B-24X-2, 128–131	224.58		8.96		74.6
765B-24X-3, 145–150	226.25	10.77	10.70	0.07	89.1
765B-24X-4, 0–3	226.30	8.68	8.45	0.23	70.4
765B-24X-4, 85–88	227.15		7.58		63.1
765B-25X-1, 50–53	232.00		7.50		62.5
765B-26X-1, 69–73	241.89	10.92	10.99	0.00	91.6
765B-26X-2, 101–105	243.71		8.39		69.9
765B-26X-3, 13–16	244.33		9.43		78.6
765B-26X-3, 72–77	244.92	8.40	8.27	0.13	68.9
765B-26X-3, 145–150	245.65	8.13	7.99	0.14	66.6
765B-27X-1, 41–46	251.31	9.25	8.99	0.26	74.9
765B-27X-1, 48–51	251.38		8.90		74.1
765B-27X-2, 145–150	253.85	8.75	8.31	0.44	69.2
765B-27X-3, 0–5	253.90	9.63	9.50	0.13	79.1
765B-27X-3, 64–66	254.54		7.26		60.5
765B-28X-1, 19–22	260.79		9.48		79.0
765B-28X-1, 34–38	260.94	9.96	9.71	0.25	80.9
765B-28X-2, 90–93	263.00		8.58		71.5
765B-28X-2, 145–150	263.55	9.90	9.73	0.17	81.1
765B-29X-1, 87–90	271.07		6.41		53.4
765B-29X-2, 0–5	271.70	9.62	9.30	0.32	77.5
765B-30X-1, 35–38	280.25		9.34		77.8
765B-30X-1, 95–100	280.85	10.41	10.17	0.24	84.7
765B-31X-2, 79–83	291.89		8.48		70.6
765B-31X-3, 140–150	294.00	9.72	9.58	0.14	79.8
765B-31X-4, 0–5	294.10	8.93	8.74	0.19	72.8
765B-31X-4, 10–13	294.20		9.67		80.6
765B-32X-1, 45–48	299.75		9.32		77.6
765B-32X-2, 126–129	302.06	10.00	9.87	0.13	82.2
765B-32X-2, 145–150	302.25	11.27	10.88	0.39	90.6
765B-32X-3, 29–31	302.59		9.70		80.8
765B-33X-1, 111–113	310.11		8.77		73.1
765B-33X-2, 71–73	311.21	8.27	8.26	0.01	68.8
765B-33X-4, 0–5	313.50	9.73	9.61	0.12	80.1
765B-33X-4, 84–87	314.34		9.64		80.3
765B-34X-1, 88–91	319.58		9.38		78.1
765B-34X-1, 141–146	320.11	10.17	10.00	0.17	83.3
765B-35X-1, 110–113	329.40		9.63		80.2
765B-35X-2, 0–5	329.80	9.93	9.61	0.32	80.1
765B-36X-2, 0–5	339.40	8.22	8.51	0.00	70.9
765B-36X-2, 39–41	339.79		10.40		86.6
765B-36X-2, 140–150	340.80	9.74	9.45	0.29	78.7
765B-37X-1, 42–44	347.92		10.46		87.1
765B-37X-2, 25–30	348.95	10.20	10.03	0.17	83.6
765B-37X-CC, 56–58	350.43		11.42		95.1
765B-38X-1, 0–5	357.10	9.40	9.22	0.18	76.8
765B-38X-1, 104–106	358.14		9.89		82.4
765B-38X-CC, 9–1	358.69		10.98		91.5
765B-39X-1, 35–37	367.05		9.42		78.5

Table 22 (continued).

Core, section, interval (cm)	Depth (mbsf)	Total carbon (%)	Inorganic carbon (%)	Organic carbon (%)	$CaCO_3$ (%)
765B-39X-1, 76–81	367.46	11.38	11.45	0.00	95.4
765B-39X-1, 81–86	367.51	11.54	11.42	0.12	95.1
765C-3R-3, 0–5	372.30		8.63		71.9
765B-40X-1, 0–5	376.40	9.04	8.75	0.29	72.9
765C-4R-3, 0–5	382.00		6.22		51.8
765C-4R-3, 140–150	383.40	8.69	8.60	0.09	71.6
765C-6R-4, 0–5	402.80		9.63		80.2
765C-7R-1, 145–150	409.45		7.18		59.8
765C-7R-2, 61–63	410.11		10.12		84.3
765C-7R-2, 79–81	410.29		7.32		61.0
765C-7R-2, 98–100	410.48		0.88		7.3
765C-7R-4, 75–85	413.25	4.93	4.81	0.12	40.1
765C-7R-4, 75–85	413.25		2.15		17.9
765C-8R-2, 145–150	420.65		5.88		49.0
765C-8R-4, 86–88	423.06		2.02		16.8
765C-8R-4, 98–100	423.18		7.85		65.4
765C-8R-4, 115–117	423.35		10.62		88.5
765C-9R-3, 0–5	430.30		7.08		59.0
765C-10R-2, 0–5	438.00		1.51		12.6
765C-10R-3, 140–150	440.90	6.32	6.11	0.21	50.9
765C-11R-1, 84–88	446.84	4.26	3.95	0.31	32.9
765C-11R-1, 97–100	446.97	9.77	9.82	0.00	81.8
765C-11R-1, 119–123	447.19	9.78	9.69	0.09	80.7
765C-11R-1, 133–137	447.33	10.10	10.06	0.04	83.8
765C-11R-3, 0–5	449.00		11.90		99.1
765C-11R-4, 61–64	451.11	0.31	0.13	0.18	1.1
765C-12R-3, 145–150	459.65		7.75		64.6
765C-13R-1, 0–5	464.60		9.14		76.1
765C-13R-2, 61–64	466.71	0.43	0.49	0.00	4.1
765C-14R-1, 0–5	474.10		6.13		51.1
765C-15R-1, 0–5	483.70		0.97		8.1
765C-15R-1, 115–122	484.85	0.47	0.27	0.20	2.3
765C-16R-1, 0–5	493.20		0.15		1.3
765C-16R-1, 38–41	493.58		0.06		0.5
765C-16R-1, 79–82	493.99		5.68		47.3
765C-16R-3, 95–98	497.15		6.90		57.5
765C-16R-4, 90–92	498.60		6.22		51.8
765C-17R-2, 66–68	504.56	6.41	6.51	0.00	54.2
765C-17R-2, 103–105	504.93		0.04		0.3
765C-17R-3, 0–5	505.40		0.51		4.3
765C-17R-3, 123–125	506.63		8.32		69.3
765C-18R-1, 0–5	511.90		0.14		1.2
765C-18R-3, 140–150	516.30	8.95	9.18	0.00	76.5
765C-18R-4, 0–5	516.40		9.18		76.5
765C-19R-1, 70–71	522.00		9.76		81.3
765C-19R-2, 0–5	522.80		3.58		29.8
765C-19R-2, 72–73	523.52		0.05		0.4
765C-19R-3, 47–49	524.77		0.07		0.6
765C-20R-1, 145–150	532.25		0.18		1.5
765C-21R-1, 0–5	540.40		0.14		1.2
765C-22R-2, 28–32	551.88	0.33	0.29	0.04	2.4
765C-22R-2, 140–150	553.00	0.07	8.24	0.00	68.6
765C-22R-3, 145–150	554.62		0.39		3.3
765C-23R-5, 55–60	566.25		3.89		32.4
765C-24R-1, 92–93	570.22	0.07	0.04	0.03	0.3
765C-24R-4, 0–5	573.80		6.92		57.6
765C-24R-4, 4–6	573.84		9.48		79.0
765C-24R-4, 62–65	574.42		0.28		2.3
765C-24R-4, 63–65	574.43		8.50		70.8
765C-24R-4, 71–72	574.51	0.12	0.07	0.05	0.6
765C-24R-4, 82–84	574.62		7.29		60.7
765C-25R-2, 30–31	580.80	0.10	0.06	0.04	0.5
765C-25R-2, 92–96	581.42		0.05		0.4
765C-25R-2, 96–98	581.46	0.08	0.05	0.03	0.4
765C-25R-2, 136–137	581.86		6.75		56.2
765C-25R-3, 106–111	583.06	0.09	0.06	0.03	0.5
765C-25R-4, 135–140	584.85		6.83		56.9
765C-25R-4, 140–150	584.90	7.57	7.66	0.00	63.8
765C-26R-3, 135–140	592.58		4.28		35.7
765C-26R-4, 22–28	592.92	0.60	0.59	0.01	4.9
765C-26R-4, 89–91	593.59		0.04		0.3
765C-26R-4, 90–91	593.60		0.05		0.4
765C-26R-4, 97–99	593.67	0.17	0.08	0.09	0.7
765C-26R-5, 18–19	593.93		1.50		12.5
765C-27R-1, 69–71	598.19		0.03		0.3
765C-27R-1, 86–87	598.36		0.05		0.4
765C-27R-1, 120–121	598.70		1.60		13.3
765C-27R-1, 145–150	598.95		0.38		3.2
765C-27R-2, 34–40	599.41	0.04	0.03	0.01	0.3
765C-28R-1, 55–58	607.55	0.03	0.02	0.01	0.2

Table 22 (continued).

Core, section, interval (cm)	Depth (mbsf)	Total carbon (%)	Inorganic carbon (%)	Organic carbon (%)	$CaCO_3$ (%)
765C-28R-1, 55–58	607.55		0.02		0.2
765C-28R-1, 145–150	608.45		3.97		33.1
765C-28R-2, 82–84	609.32	0.05	0.04	0.01	0.3
765C-28R-2, 115–117	609.65		1.79		14.9
765C-28R-2, 140–150	609.90		0.92		7.7
765C-28R-2, 140–150	609.90	1.94	1.95	0.00	16.2
765C-28R-3, 45–49	610.52	2.78	2.68	0.10	22.3
765C-29R-2, 145–150	619.42		4.04		33.7
765C-29R-3, 76–80	620.23				
765C-29R-3, 76–80	620.23	0.70	0.64	0.06	5.3
765C-30R-1, 77–78	626.67		0.03		0.3
765C-30R-2, 16–22	627.55	0.11	0.07	0.04	0.6
765C-30R-2, 105–106	628.44	0.05	0.05	0.00	0.4
765C-30R-4, 10–11	630.42		0.24		2.0
765C-30R-4, 18–19	630.50		0.40		3.3
765C-30R-4, 32–33	630.64		0.48		4.0
765C-30R-4, 32–34	630.64		0.53		4.4
765C-30R-4, 40–41	630.72		0.29		2.4
765C-30R-4, 49–50	630.81		0.80		6.7
765C-30R-4, 60–61	630.92		0.04		0.3
765C-30R-4, 71–72	631.03		0.03		0.3
765C-30R-4, 80–81	631.12		0.03		0.3
765C-30R-4, 98–102	631.30	0.07	0.02	0.05	0.2
765C-30R-5, 10–11	631.91		0.08		0.7
765C-30R-5, 19–20	632.00		0.16		1.3
765C-30R-5, 29–30	632.10		0.06		0.5
765C-30R-5, 40–41	632.21		0.04		0.3
765C-30R-5, 50–51	632.31		0.03		0.3
765C-30R-6, 64–65	633.93	0.02	0.05	0.00	0.4
765C-30R-6, 99–104	634.28		1.11		9.3
765C-30R-6, 110–111	634.39	1.07	1.01	0.06	8.4
765C-31R-2, 130–140	638.01	3.16	3.16	0.00	26.3
765C-31R-3, 0–5	638.18		3.01		25.1
765C-32R-2, 97–100	647.37		0.03		0.3
765C-32R-3, 0–5	647.90		0.36		3.0
765C-33R-1, 20–21	654.90	0.65	0.07	0.58	0.6
765C-33R-2, 0–5	656.18		0.07		0.6
765C-34R-2, 0–5	665.90		0.51		4.3
765C-34R-3, 115–125	668.55	2.71	2.61	0.10	21.7
765C-35R-1, 145–150	675.55		2.32		19.3
765C-35R-3, 24–29	677.35	0.17	0.04	0.13	0.3
765C-35R-3, 55–57	677.65		0.79		6.6
765C-35R-3, 86–90	677.96	1.23	0.56	0.67	4.7
765C-35R-CC, 15–16	679.43		1.29		10.8
765C-36R-5, 145–150	690.75		0.10		0.8
765C-37R-2, 143–145	695.93		2.10		17.5
765C-37R-3, 40–43	696.40	4.20	4.14	0.06	34.5
765C-37R-3, 110–115	697.10		6.59		54.9
765C-37R-3, 140–150	697.40	6.38	6.23	0.15	51.9
765C-38R-2, 145–150	705.45		0.19		1.6
765C-39R-3, 0–5	714.70		3.14		26.2
765C-39R-3, 93–94	715.63		0.40		3.3
765C-39R-3, 101–105	715.71	0.16	0.12	0.04	1.0
765C-39R-3, 140–150	716.10	2.41	2.47	0.00	20.6
765C-40R-3, 104–109	724.94	0.28	0.08	0.20	0.7
765C-40R-3, 145–150	725.35		1.21		10.1
765C-40R-3, 143–144	726.83		0.06		0.5
765C-40R-4, 149–150	726.89	0.68	0.08	0.60	0.7
765C-41R-1, 59–64	730.99		0.10		0.8
765C-42R-1, 95–97	740.75		0.07		0.6
765C-42R-2, 41–43	741.71	0.22	0.07	0.15	0.6
765C-42R-3, 88–89	743.68	0.45	0.20	0.25	1.7
765C-42R-3, 140–150	744.20	0.15	0.07	0.08	0.6
765C-42R-4, 0–5	744.30		0.09		0.8
765C-42R-4, 26–28	744.56		0.06		0.5
765C-42R-4, 30–31	744.60		0.08		0.7
765C-43R-6, 0–5	756.60		0.09		0.8
765C-44R-3, 9–10	761.59		0.08		0.7
765C-44R-3, 17–19	761.67		0.48		4.0
765C-44R-3, 106–107	762.56	0.64	0.13	0.51	1.1
765C-44R-3, 135–136	762.85	0.55	0.12	0.43	1.0
765C-44R-4, 0–5	763.00		3.27		27.2
765C-44R-1, 55–59	763.55	0.42	0.13	0.29	1.1
765C-44R-4, 63–64	763.63		0.06		0.5
765C-45R-2, 70–75	770.40	0.17	0.08	0.09	0.7
765C-45R-3, 48–49	771.68		0.98		8.2
765C-45R-3, 53–55	771.73		0.36		3.0
765C-45R-3, 140–150	772.60	0.57	0.43	0.14	3.6
765C-45R-4, 100–101	773.70	5.20	0.28	4.92	2.3
765C-45R-5, 0–5	774.20		0.65		5.4
765C-46R-1, 145–150	779.25		0.08		0.7

Table 22 (continued).

Core, section, interval (cm)	Depth (mbsf)	Total carbon (%)	Inorganic carbon (%)	Organic carbon (%)	$CaCO_3$ (%)
765C-47R-3, 55-57	790.95		0.06		0.5
765C-47R-4, 145-150	793.35		0.05		0.4
765C-48R-3, 140-150	801.30	0.52	0.12	0.40	1.0
765C-48R-4, 0-5	801.40		0.06		0.5
765C-48R-4, 36-37	801.76		0.63		5.3
765C-48R-5, 107-109	803.97		0.07		0.6
765C-49R-1, 94-95	807.24	0.64	0.13	0.51	1.1
765C-49R-1, 122-125	807.52		0.04		0.3
765C-49R-1, 141-143	807.71	0.65	0.12	0.53	1.0
765C-49R-4, 0-5	810.80		0.25		2.1
765C-50R-1, 110-113	816.70	0.08	0.07	0.01	0.6
765C-50R-2, 80-82	817.90		0.09		0.8
765C-50R-2, 145-150	818.55		0.05		0.4
765C-50R-5, 17-20	821.77		0.11		0.9
765C-50R-5, 28-30	821.88		0.16		1.3
765C-50R-3, 38-40	821.98		6.39		53.2
765C-50R-6, 51-52	823.61		0.05		0.4
765C-51R-1, 84-86	825.84	0.23	0.05	0.18	0.4
765C-51R-3, 140-150	829.40	0.17	0.17	0.00	1.4
765C-51R-5, 0-5	831.00		0.05		0.4
765C-51R-CC, 2-5	832.52		0.05		0.4
765C-52R-1, 132-133	835.82	0.37	0.07	0.30	0.6
765C-52R-2, 8-10	836.08		0.05		0.4
765C-52R-2, 134-135	837.34	0.16	0.08	0.08	0.7
765C-52R-2, 134-135	837.34		0.04		0.3
765C-52R-2, 145-150	837.45		0.04		0.3
765C-52R-3, 65-66	838.15		0.29		2.4
765C-52R-3, 83-84	838.33		0.16		1.3
765C-52R-3, 111-112	838.61		0.12		1.0
765C-53R-1, 102-103	845.12		0.07		0.6
765C-53R-3, 72-74	847.82		0.04		0.3
765C-53R-4, 27-28	848.87		0.96		8.0
765C-53R-4, 50-52	849.10		0.62		5.2
765C-53R-4, 65-66	849.25		0.79		6.6
765C-53R-6, 123-125	852.83		0.03		0.3
765C-54R-3, 140-150	857.90	0.17	0.03	0.14	0.3
765C-54R-4, 0-1	858.00		0.04		0.3
765C-54R-4, 49-50	858.49		0.04		0.3
765C-54R-4, 72-73	858.72		0.36		3.0
765C-54R-4, 110-111	859.10		0.87		7.3
765C-54R-4, 139-140	859.39		1.76		14.7
765C-55R-2, 82-84	865.32		0.18		1.5
765C-55R-3, 0-1	866.00		2.46		20.5
765C-55R-3, 7-8	866.07		2.58		21.5
765C-55R-3, 86-87	866.86		3.04		25.3
765C-56R-2, 108-110	875.08		0.17		1.4
765C-56R-2, 120-122	875.20		2.99		24.9
765C-56R-4, 9-11	877.09		2.61		21.7
765C-56R-4, 109-111	878.09		1.83		15.2
765C-56R-4, 140-141	878.40		2.27		18.9
765C-57R-3, 110-115	885.80		3.34		27.8
765C-57R-3, 140-150	886.10	3.46	3.39	0.07	28.2
765C-57R-7, 15-17	890.55		0.17		1.4
765C-58R-4, 67-71	896.37	0.05	0.04	0.01	0.3
765C-59R-3, 23-25	901.13	0.14	0.06	0.08	0.5
765C-59R-3, 49-50	901.39	0.10	0.05	0.05	0.4
765C-59R-3, 73-74	901.63	0.12	0.05	0.07	0.4
765C-59R-3, 94-95	901.84	0.10	0.04	0.06	0.3
765C-59R-3, 106-109	901.96	0.18	0.04	0.14	0.3
765C-59R-3, 123-125	902.13		0.04		0.3
765C-59R-3, 149-150	902.39	0.54	0.07	0.47	0.6
765C-59R-4, 94-95	903.34	5.01	4.90	0.11	40.8
765C-59R-4, 111-112	903.51	0.53	0.06	0.47	0.5
765C-60R-2, 61-63	909.61		0.06		0.5
765C-60R-3, 26-27	910.76		0.04		0.3
765C-60R-3, 140-150	911.90	0.07	0.05	0.02	0.4
765C-60R-4, 0-1	912.00		0.07		0.6
765C-60R-5, 98-99	914.48		0.04		0.3
765C-60R-5, 120-123	914.70	0.12	0.03	0.09	0.3
765C-61R-1, 145-146	918.35	0.10	0.04	0.06	0.3
765C-61R-2, 149-150	919.89		0.10		0.8
765C-61R-4, 58-59	921.98	1.17	1.15	0.02	9.6
765C-61R-5, 81-85	923.71	3.17	3.28	0.00	27.3
765C-61R-5, 105-106	923.95		2.32		19.3
765C-61R-5, 118-119	924.08		2.27		18.9
765C-62R-1, 120-121	927.60		4.88		40.7
765C-62R-3, 0-1	929.40		5.17		43.1
765C-62R-3, 68-70	930.08		0.03		0.3
765C-62R-3, 80-84	930.20	0.05	0.06	0.00	0.5
765C-62R-3, 84-85	930.24		0.04		0.3
765C-62R-4, 25-26	931.15	0.08	0.05	0.03	0.4

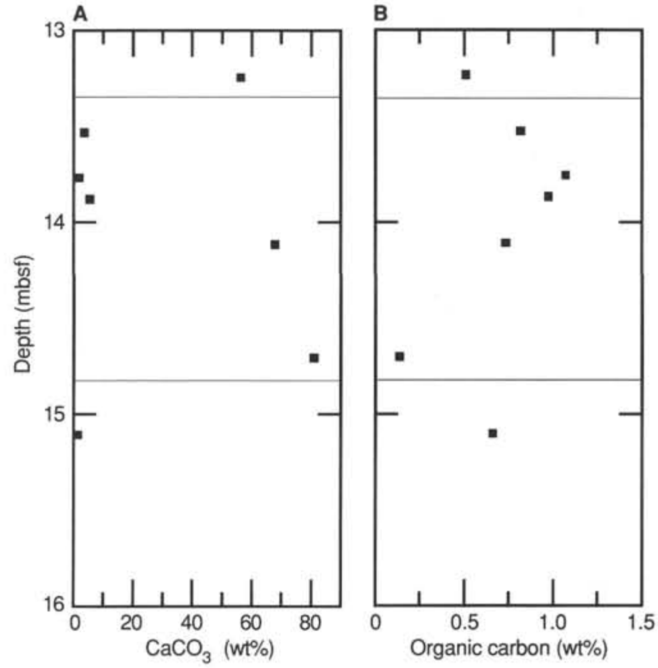

Figure 83. A. Core 123-765B-2H, wt% $CaCO_3$ vs. sub-bottom depth. B. Core 123-765B-2H, wt% organic carbon vs. sub-bottom depth.

to processes of carbon dioxide production and degassing of pore fluids. Hydrogen sulfide was measured in nine samples; most occurrences were found in the top 100 m of sediment, where the pore water sulfate gradient is steepest, indicating the location of the highest rates of sulfate reduction.

SEDIMENT PHYSICAL PROPERTIES

Introduction

The physical properties determined from sediments of Site 765 on the Argo Abyssal Plain include compressional-wave velocity (as measured using a *P*-wave logger and Hamilton frame), index properties (i.e., bulk density, grain density, porosity, and water content, as determined by a pycnometer and balance), Gamma Ray Attenuation Porosity Evaluator (GRAPE) bulk density, thermal conductivity, and vane shear strength. Four holes (Holes 765A through 765D) were cored at Site 765. Specific details concerning the coring procedures and depths can be found in the "Operations" section (this chapter). Velocities and index properties were measured for most of the cores, except those containing sensitive stratigraphic boundaries (Cores 123-765C-33R, -34R, -59R, -60R, -61R, and -62R). *P*-wave-logger velocities were measured for APC cores only. The GRAPE bulk densities were measured for both APC and XCB cores. Thermal conductivities were measured on competent material. Vane shear measurements were not obtained below 300 mbsf because of the brittle nature of the material. Values of these various physical property measurements are listed in Tables 25 through 27 and the variations of these properties with depth are illustrated in Figure 86A.

Results

Index Properties

Bulk density, grain (or matrix) density, porosity, and water content (dry basis) of samples from Holes 765A, 765B, and 765C are listed in Tables 25 to 27 and are plotted relative to depth in Figure 86. Four basic units can be identified in terms of

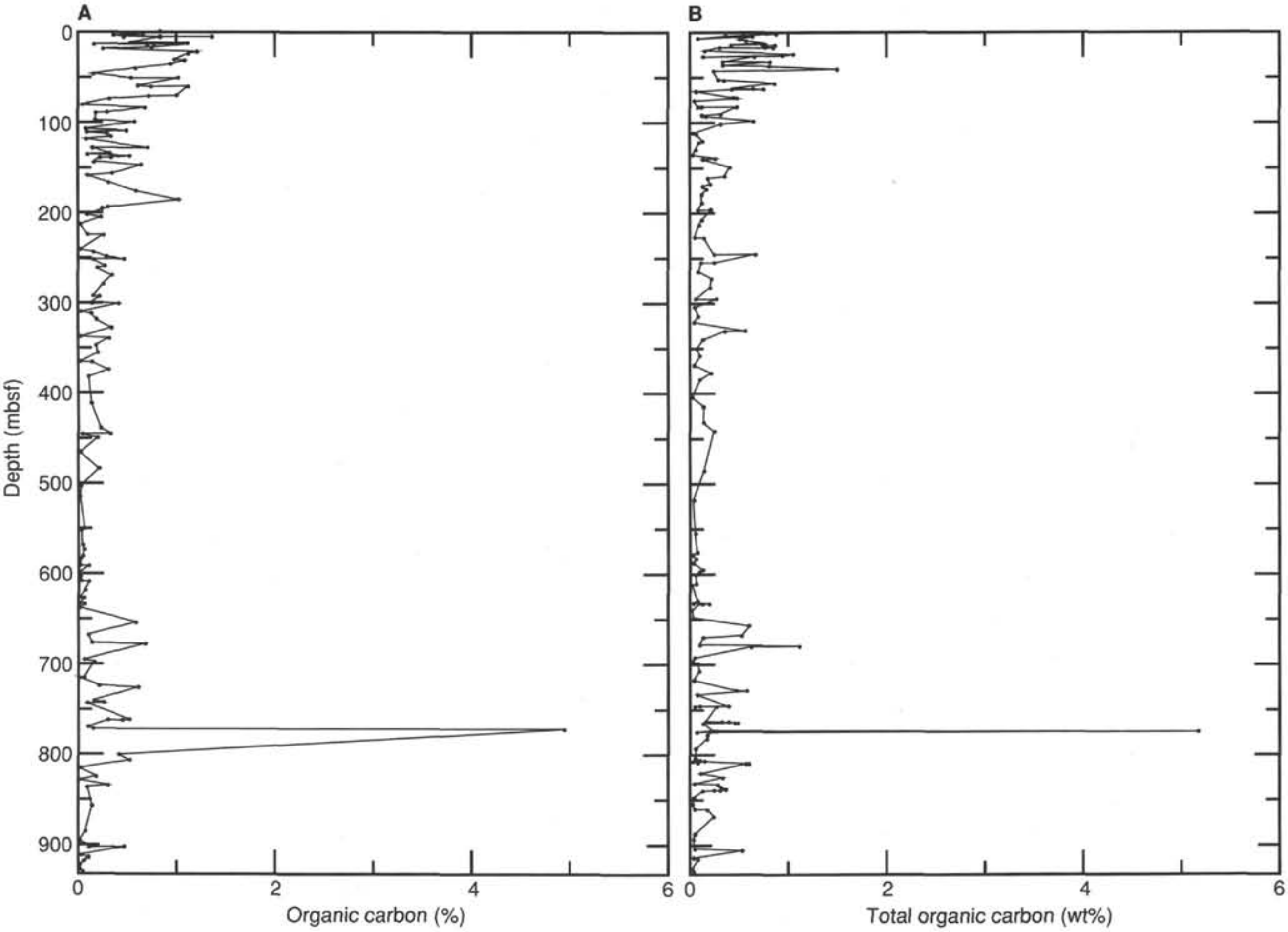

Figure 84. A. Organic carbon vs. sub-bottom depth. B. Total organic carbon (from rock evaluation analyses) vs. sub-bottom depth.

physical properties, namely, Unit A (0–80 mbsf), Unit B (80–350 mbsf), Unit C (350–590 mbsf), and Unit D (590–896 mbsf). No samples were taken from the intervals at 646–675 mbsf and 896–936 mbsf, as these represented sensitive stratigraphic boundaries.

Unit A (0–80 mbsf) consists of calcareous ooze having significant changes in the index properties. Grain density remains relatively constant with an average value of 2.62 ± 0.13 g/cm^3. A distinct decrease in water content and porosity can be observed. The former has values ranging from approximately 300% at the mudline to near 100% at 80 mbsf. The latter ranges from approximately 90% to 70% for the same interval. An increasing trend is observed for the bulk densities, with values going from approximately 1.3 to 1.6 g/cm^3 over the same 80-m interval.

Unit B (80–350 mbsf) consists of debris flows and turbidites. The physical property data show considerably less variability. The same general compaction trends are observed, i.e., decreasing water content and porosity and corresponding increase in bulk density, but to a lesser extent than those observed for Unit A. Grain densities increase slightly to 2.71 ± 0.11 g/cm^3 for the unit. An observable change in properties occurs in the interval from 265 to 290 mbsf. Bulk density decreases from approximately 2.0 g/gm^3 to a value of 1.79 g/cm^3. In addition, porosity increases from approximately 50% to 65%. The general lithology of this section consists of homogeneous clay deposits sandwiched between thinner layers of carbonate cemented sands.

Unit C (350–590 mbsf) consists of debris flows and turbidites, with the sediments showing a much higher degree of lithification. This material alternates between claystone, chalk, and cemented sandstone, with periodic intrusions of coarse sands and basalt pebbles. Index properties appear to remain constant throughout the unit, but show a high degree of variability. Grain densities have an average value of 2.70 ±0.13 g/cm^3. In addition, porosities and bulk densities have values of 46% ±10% and 2.13 ±0.19 g/cm^3, respectively. Water content decreases from roughly 35% at the top to 20% at the bottom of the unit; again, there is a high degree of variability in the measurements. This variability can be attributed to measurements performed in the layered calcareous claystone and cemented sandstones. In addition, a few measurements (465.56, 635.33, and 763.34 mbsf) were performed on the basalt pebbles.

Unit D (590–896 mbsf) consists predominantly of a dark red claystone. This claystone is not as competent as the claystones in Unit C and tends to slake or delaminate when exposed to water or when air dried. The boundary is readily distinguishable in terms of changes in physical property. Porosity increases from 41% to 61% across the boundary, and bulk density decreases from about 2.3 to 1.9 g/cm^3. In addition, water content increases from 23% to 50%. During sampling, this material had a "spongy" appearance. The profile as a whole shows normal compaction trends, i.e., decreasing water content and porosity, with a resulting increase in bulk density, as a function of increasing depth. The average grain density for the interval is 2.66 ±0.14 g/cm^3. Water content and porosity decreased from approximately 50% to 25% and 61% to 42%, respectively. Bulk density increased from 1.9 to 2.2 g/cm^3.

Table 23. Rock evalatuion analysis of sediment samples, Site 765.

Core, section, interval (cm)	Depth (mbsf)	S_1 (mg/g)	S_2 (mg/g)	S_3 (mg/g)	TOC (%)	%C	HI	OI	T (°C)	PI	S_3/S_3
123-765B-1H-1, 96–98	0.96	0.64	1.47	4.98	0.85	0.17	172	585	384	0.30	0.29
765B-1H-2, 78–80	2.28	0.38	1.25	5.15	0.52	0.13	240	990	404	0.23	0.24
765B-1H-3, 42–44	3.42	0.30	0.94	5.07	0.34	0.10	276	1491	419	0.24	0.18
765A-1H-4, 38–40	4.88	0.68	2.76	1.05	0.61	0.28	452	172	490	0.20	2.62
765B-1H-4, 145–150	5.95	0.16	0.10	3.40	0.06	0.02	166	5666	375	0.62	0.02
765A-1H-4, 145–150	5.95	0.28	1.33	3.34	0.48	0.13	277	695	417	0.17	0.39
765B-1H-6, 61–63	8.11	0.56	2.19	3.22	0.54	0.22	405	596	544	0.20	0.68
765A-1H-6, 68–70	8.18	0.42	1.65	4.47	0.55	0.17	300	812	413	0.20	0.36
765B-2H-3, 65–67	12.95	0.46	1.65	3.55	0.74	0.17	222	479	517	0.22	0.46
2H-3, 123–135	13.53	0.21	2.27	3.77	0.71	0.20	319	530	588	0.08	0.60
2H-3, 145–150	13.75	0.38	2.37	1.79	0.84	0.22	282	213	464	0.14	1.32
2H-4, 7–19	13.87	0.22	1.39	4.76	0.84	0.13	165	566	544	0.14	0.29
2H-4, 31–43	14.11	0.23	0.84	4.36	0.39	0.08	215	1117	407	0.22	0.19
2H-4, 143–150	15.23	0.56	3.52	1.38	0.74	0.34	475	186	470	0.14	2.55
2H-4, 145–150	15.25	0.45	3.39	1.28	0.81	0.32	418	158	488	0.12	2.64
2H-6, 34–36	17.14	0.37	3.02	0.74	0.28	0.28	1078	264	493	0.11	4.08
3H-1, 83–85	19.63	0.09	0.24	5.24	0.13	0.02	184	4030	399	0.28	0.04
3H-3, 145–150	23.25	0.54	1.56	2.43	1.03	0.17	151	235	407	0.26	0.64
3H-4, 125–128	24.55	0.50	2.59	3.61	0.90	0.25	287	401	548	0.16	0.71
3H-4, 145–150	24.75	0.82	3.31	2.35	1.02	0.34	324	230	471	0.20	1.40
3H-4, 145–150	24.75	0.63	2.55	1.16	0.92	0.26	277	126	504	0.20	2.19
3H-5, 127–130	26.07	0.15	0.57	4.79	0.12	0.06	475	3991	452	0.21	0.11
3H-6, 23–26	26.53	0.27	1.39	4.86	0.63	0.13	220	771	413	0.16	0.28
4H-3, 145–150	32.95	0.11	0.30	2.94	0.31	0.03	96	948	388	0.27	0.10
4H-4, 0–5	33.00	0.46	4.01	0.94	0.80	0.37	501	117	513	0.10	4.26
4H-4, 0–7	33.00	0.40	3.99	2.63	0.78	0.36	511	337	468	0.09	1.51
4H-5, 128–130	35.78	0.16	0.51	5.20	0.31	0.05	164	1677	511	0.24	0.09
4H-6, 20–22	36.20	0.29	1.78	6.30	0.78	0.17	228	807	521	0.14	0.28
5H-2, 85–87	40.45	0.14	0.32	4.57	1.46	0.03	21	313	310	0.30	0.07
5H-3, 145–150	42.55	0.13	0.40	4.03	0.21	0.04	190	1919	365	0.25	0.09
5H-4, 0–5	42.60	0.26	0.46	3.19	0.22	0.06	209	1450	329	0.36	0.14
6H-3, 145–150	52.25	0.16	0.42	3.23	0.27	0.04	155	1196	389	0.28	0.13
6H-4, 0–5	52.30	0.30	0.72	2.58	0.32	0.08	225	8.06	394	0.29	0.27
6H-6, 99–101	56.29	0.06	0.37	4.53	0.83	0.03	44	545	417	0.14	0.08
7H-3, 145–150	61.85	0.23	0.78	4.26	0.40	0.08	195	1065	403	0.23	0.18
7H-4, 0–7	61.90	0.28	2.01	4.94	0.72	0.19	279	686	418	0.12	0.40
7H-4, 0–5	61.90	0.34	1.57	2.77	0.61	0.15	257	454	413	0.18	0.56
7H-5, 105–107	64.45	0.13	0.37	3.05	0.04	0.04	925	7625	346	0.26	0.12
8H-3, 145–150	71.55	0.20	1.08	3.88	0.43	0.10	251	902	4.09	0.16	0.27
8H-4, 0–5	71.60	0.29	1.22	2.72	0.45	0.12	271	604	412	0.19	0.44
8H-5, 139–141	74.49	0.14	0.30	4.06	0.03	0.03	1000	13533	355	0.32	0.07
9H-3, 145–150	81.25	0.04	0.10	1.85	0.09	0.01	111	2055	303	0.29	0.05
9H-4, 0–5	81.30	0.14	0.03	1.55	0.06	0.01	50	2583	304	0.87	0.01
9H-4, 89–93	82.19	0.20	0.92	4.18	0.45	0.09	204	928	423	0.18	0.22
10H-3, 145–150	90.85	0.27	0.31	7.45	0.29	0.04	106	2568	404	0.47	0.04
10H-4, 0–5	90.90	0.19	0.19	2.48	0.11	0.03	172	2254	304	0.50	0.07
10H-4, 119–121	92.09	0.19	1.60	0.30	0.14	0.14	1142	214	421	0.11	5.33
11H-2, 19–21	97.69	0.17	2.35	1.31	0.62	0.21	379	211	474	0.07	1.79
11H-4, 0–5	100.50	0.21	0.40	2.48	0.29	0.05	137	855	388	0.35	0.16
12H-3, 145–150	110.05	0.04	0.02	2.10	0.02	0.00	100	10500	354	0.67	0.00
12H-4, 0–5	110.10	0.06	0.00	1.87	0.04	0.00	0	4675	304	1.00	0.00
12H-5, 69–72	112.29	0.16	0.51	2.72	0.05	0.05	1020	5440	353	0.24	0.18
13H-4, 0–5	119.70	0.08	0.10	1.73	0.10	0.01	100	1730	266	0.44	0.05
13H-4, 54–56	120.24	0.06	0.07	2.85	0.08	0.01	87	3562	387	0.50	0.02
14H-4, 0–5	129.30	0.07	0.03	2.07	0.04	0.00	75	5175	238	0.70	0.01
14H-6, 40–42	132.70	0.14	0.33	3.61	0.03	0.03	1100	12033	318	0.30	0.09
15H-1, 41–43	134.91	0.02	0.00	2.88	0.01	0.00	0	28800	281	1.00	0.00
15H-3, 145–150	138.95	0.10	0.16	2.50	0.24	0.02	66	1041	321	0.38	0.06
15H-4, 0–5	139.00	0.07	0.06	3.36	0.11	0.01	54	3054	266	0.58	0.01
16H-4, 0–5	148.70	0.15	0.34	3.32	0.38	0.04	89	873	355	0.31	0.10
17H-4, 0–5	158.40	0.14	0.31	2.85	0.33	0.03	93	863	358	0.32	0.10
17H-6, 76–78	161.40	0.12	0.69	1.61	0.16	0.06	431	1006	564	0.1	0.42
18H-4, 0–5	167.50	0.17	0.24	3.70	0.18	0.03	133	2055	282	0.42	0.06
18H-4, 145–150	168.95	0.05	0.07	2.00	0.11	0.01	63	1818	304	0.42	0.03
18H-6, 114–116	171.64	0.12	1.06	0.11	0.14	0.09	757	78	479	0.10	9.63
19X-3, 145–150	177.75	0.05	0.15	1.39	0.10	0.01	150	1390	304	0.25	0.10
20X-4, 0–7	187.50	0.08	0.08	1.00	0.10	0.01	80	1000	253	0.50	0.08
21X-2, 145–150	195.65	0.08	0.16	1.92	0.06	0.02	266	3200	335	0.33	0.08
21X03, 0–5	195.70	0.11	0.21	2.00	0.19	0.02	110	1052	304	0.34	0.10
22X-4, 0–5	206.90	0.05	0.23	2.02	0.10	0.02	230	2020	384	0.18	0.11
23X-2, 0–3	213.60	0.10	0.21	2.15	0.07	0.02	300	3070	343	0.33	0.09
24X-3, 145–150	225.25	0.05	0.03	1.44	0.03	0.00	100	4800	303	0.62	0.02
24X-4, 0–3	226.30	0.00	0.10	2.01	0.12	0.01	83	1675	292	0.50	0.04
26X-3, 143–150	245.63	0.13	0.58	3.89	0.22	0.05	263	1768	410	0.19	0.14
26X-3, 145–150	245.65	0.06	0.03	0.90	0.64	0.00	4	140	259	0.75	0.03
27X-2, 145–150	253.85	0.07	0.33	1.74	0.22	0.03	150	790	406	0.17	0.18
27X-3, 0–5	253.90	0.08	0.14	2.11	0.09	0.01	155	2344	325	0.36	0.06

Table 23 (continued).

Core, section, interval (cm)	Depth (mbsf)	S_1 (mg/g)	S_2 (mg/g)	S_3 (mg/g)	TOC (%)	%C	HI	OI	T (°C)	PI	S_3/S_3
765B-28X-2, 145-150	263.55	0.01	0.11	0.65	0.07	0.01	157	928	471	0.08	0.16
29X-2, 0-5	271.70	0.05	0.30	1.51	0.20	0.02	150	755	410	0.15	0.19
30X-1, 95-100	280.85	0.02	0.18	1.15	0.19	0.01	94	605	368	0.10	0.15
31X-3, 140-150	294.00	0.07	0.09	1.53	0.04	0.01	225	3825	313	0.44	0.05
31X-4, 0-5	294.10	0.19	0.79	1.64	0.25	0.08	316	656	417	0.19	0.48
32X-2, 145-150	302.35	0.01	0.00	0.61	0.03	0.00	0	2033	288	0.00	0.00
33X-4, 0-5	313.50	0.05	0.13	1.28	0.06	0.01	216	2133	335	0.28	0.10
34X-1, 141-146	320.11	0.02	0.00	1.02	0.03	0.00	0	3400	228	1.00	0.00
35X-2, 0-5	329.80	0.08	0.30	1.53	0.53	0.03	56	288	396	0.21	0.19
35X-2, 0-7	329.80	0.12	0.37	3.46	0.33	0.04	112	1048	347	0.25	0.10
36X-2, 0-5	339.40	0.02	0.00	0.56	0.11	0.00	0	509	260	1.00	0.00
36X-2, 140-150	340.80	0.04	0.15	1.52	0.10	0.01	150	1520	340	0.22	0.09
37X-2, 25-30	348.95	0.00	0.07	1.30	0.05	0.00	140	2600	304	0.00	0.05
38X-1, 0-5	357.10	0.05	0.12	1.45	0.08	0.01	150	1812	330	0.31	0.08
39X-1, 76-81	367.46	0.01	0.00	0.71	0.02	0.00	0	3550	225	0.00	0.00
39X-1, 81-86	367.51	0.00	0.00	0.78	0.01	0.00	0	7800	272	0.00	0.00
40X-1, 0-5	376.40	0.12	0.49	2.95	0.19	0.05	257	1552	403	0.20	0.16
765C-4R-3, 140-150	383.40	0.06	0.11	2.07	0.08	0.01	137	2587	255	0.37	0.05
6R-4, 0-5	402.80	0.00	0.01	0.00	0.00	0.00	0	0	447	0.00	0.00
7R-4, 75-85	413.25	0.07	0.17	2.22	0.11	0.02	154	2018	256	0.29	0.07
9R-3, 0-7	430.30	0.15	0.38	1.85	0.11	0.04	345	1681	379	0.29	0.20
10R-3, 140-150	440.90	0.09	0.25	2.44	0.22	0.02	113	1109	297	0.26	0.10
15R-1, 0-5	483.70	0.10	0.81	1.41	0.12	0.07	675	1175	422	0.11	0.57
15R-1, 115-122	484.85	0.04	0.50	0.86	0.12	0.04	416	716	405	0.07	0.58
18R-3, 140-150	516.30	0.00	0.00	1.28	0.01	0.00	0	12800	304	0.00	0.00
22R-2, 140-150	553.00	0.03	0.00	0.91	0.03	0.00	0	3033	286	1.00	0.00
24R-4, 62-65	574.42	0.07	0.60	1.33	0.05	0.05	1200	2660	540	0.11	0.45
24R-4, 63-65	574.43	0.04	0.00	2.53	0.02	0.00	0	12650	382	1.00	0.00
25R-2, 30-31	580.80	0.07	0.49	0.00	0.04	0.0	1225	0	379	0.12	0.00
25R-4, 140-150	584.90	0.02	0.00	1.95	0.01	0.00	0	19500	303	1.00	0.00
26R-4, 89-91	593.59	0.01	1.21	0.97	0.10	0.10	1210	970	468	0.01	1.24
26R-4, 97-99	593.67	0.14	0.74	0.55	0.07	0.07	1057	785	427	0.1	1.34
27R-1, 69-71	598.19	0.04	0.51	0.97	0.04	0.04	1275	2425	409	0.07	0.52
28R-2, 82-84	609.32	0.07	0.47	0.16	0.04	0.04	1175	400	348	0.13	2.93
28R-2, 140-150	609.90	0.02	0.00	0.61	0.00	0.00	0	0	303	1.00	0.00
30R-2, 105-106	628.44	0.12	0.59	0.10	0.05	0.05	1180	200	385	0.17	5.90
30R-4, 10-11	630.42	0.04	0.00	0.27	0.01	0.00	0	2700	329	1.00	0.00
30R-4, 18-19	630.50	0.15	1.91	0.39	0.17	0.17	1123	229	383	0.07	4.89
30R-4, 32-33	630.64	0.03	0.33	0.81	0.02	0.03	1650	4050	381	0.08	0.40
30R-4, 32-34	630.64	0.02	0.00	1.16	0.00	0.00	0	0	303	1.00	0.00
30R-4, 40-41	630.72	0.00	0.00	0.33	0.00	0.00	0	0	277	0.00	0.00
30R-4, 49-50	630.81	0.07	0.02	0.91	0.02	0.00	100	4550	303	0.87	0.02
30R-4, 60-61	630.92	0.16	0.63	0.11	0.07	0.06	900	157	453	0.21	5.72
30R-4, 71-72	631.03	0.21	0.91	0.19	0.10	0.09	910	190	453	0.19	4.78
30R-4, 80-81	621.12	0.11	0.56	0.05	0.06	0.05	933	83	364	0.17	11.20
30R-5, 10-11	631.91	0.14	0.58	0.07	0.06	0.06	966	116	354	0.19	8.28
30R-5, 19-29	632.00	0.12	0.62	0.07	0.06	0.06	1033	116	303	0.16	8.85
30R-5, 29-30	632.10	0.10	0.60	0.05	0.05	0.05	1200	100	357	0.14	12.00
30R-5, 40-41	632.21	0.16	0.42	0.17	0.07	0.04	600	242	329	0.28	2.47
30R-5, 50-51	632.31	0.14	0.62	0.05	0.06	0.06	1033	83	303	0.18	12.40
30R-6, 64-65	633.93	0.05	0.20	0.19	0.01	0.02	2000	1900	380	0.21	1.05
30R-6, 110-111	634.39	0.06	0.07	1.25	0.02	0.01	350	6250	303	0.50	0.05
31R-2, 130-140	638.01	0.02	0.00	1.04	0.00	0.00	0	0	339	1.00	0.00
32R-2, 97-100	647.37	0.02	0.15	0.96	0.01	0.01	1500	9600	478	0.12	0.15
33R-1, 20-21	654.90	0.11	0.55	0.35	0.57	0.05	96	61	384	0.17	1.57
34R-2, 0-5	665.90	0.04	0.12	2.12	0.50	0.01	24	424	318	0.25	0.05
34R-3, 115-125	668.55	0.19	0.25	2.00	0.11	0.03	227	1818	265	0.43	0.12
35R-1, 145-150	675.55	0.10	0.04	1.39	0.08	0.01	50	1737	259	0.71	0.02
35R-3, 55-57	677.65	0.10	0.76	2.21	1.08	0.07	70	204	408	0.12	0.34
35R-3, 86-90	677.96	0.07	0.32	1.51	0.59	0.03	54	255	398	0.18	0.21
36R-5, 145-150	690.75	0.01	0.34	0.10	0.03	0.02	1133	333	370	0.03	3.40
37R-2, 143-145	695.93	0.03	0.00	1.99	0.01	0.00	0	19900	292	1.00	0.00
37R-3, 140-150	697.40	0.09	0.09	1.80	0.05	0.01	180	3600	220	0.50	0.05
38R-2, 145-150	705.45	0.02	0.24	0.62	0.07	0.02	342	885	420	0.08	0.38
39R-3, 93-94	715.63	0.03	0.01	1.01	0.01	0.00	100	10100	358	0.75	0.00
39R-3, 140-150	716.10	0.01	0.03	1.45	0.02	0.00	150	7250	322	0.25	0.02
40R-4, 143-14	726.83	0.04	0.27	1.36	0.44	0.02	61	309	338	0.13	0.19
40R-4, 149-150	726.89	0.13	0.50	0.75	0.55	0.05	90	136	517	0.21	0.66
41R-1, 59-64	730.99	0.05	0.34	0.61	0.05	0.03	680	1220	378	0.13	0.55
42R-3, 88-89	743.68	0.08	0.39	0.74	0.36	0.03	108	205	350	0.17	0.52
42R-3, 140-150	744.20	0.05	0.57	0.64	0.08	0.05	712	800	453	0.08	0.89
42R-4, 0-5	744.30	0.03	0.32	1.30	0.04	0.02	800	3250	402	0.09	0.24
42R-4, 26-28	744.56	0.04	0.38	0.73	0.25	0.03	152	292	380	0.10	0.52
42R-4, 30-31	744.60	0.02	0.18	1.09	0.25	0.01	72	436	386	0.10	0.16
44R-3, 9-10	761.59	0.12	0.53	1.22	0.14	0.05	378	871	451	0.19	0.43
44R-3, 17-19	761.67	0.03	0.20	2.32	0.30	0.01	66	773	408	0.14	0.08
44R-3, 24-25	761.74	0.06	0.41	1.14	0.36	0.03	113	316	422	0.13	0.35

Table 23 (continued).

Core, section, interval (cm)	Depth (mbsf)	S_1 (mg/g)	S_2 (mg/g)	S_3 (mg/g)	TOC (%)	%C	HI	OI	T (°C)	PI	S_3/S_3
765C-44R-3, 106–107	762.56	0.12	0.41	0.96	0.46	0.04	89	208	362	0.23	0.42
44R-3, 135–136	762.85	0.07	0.37	0.54	0.43	0.03	86	125	356	0.1	0.68
44R-4, 63–64	763.63	0.13	0.30	0.93	0.10	0.03	300	930	420	0.31	0.32
45R-3, 48–49	771.68	0.06	0.22	2.80	0.22	0.02	100	1272	358	0.21	0.07
45R-3, 53–55	771.73	0.01	0.20	1.75	0.24	0.01	83	729	382	0.05	0.11
45R-3, 140–150	772.60	0.02	0.19	0.80	0.05	0.01	380	1600	353	0.10	0.23
45R-4, 100–101	773.70	0.36	8.93	2.80	5.12	0.77	174	54	412	0.04	3.18
45R-5, 0–5	774.20	0.02	0.35	1.27	0.16	0.03	218	793	411	0.06	0.27
46R-1, 145–150	779.25	0.01	0.55	0.96	0.15	0.04	366	640	470	0.02	0.57
47R-3, 55–57	790.95	0.01	0.52	0.90	0.04	0.04	1300	2250	520	0.02	0.57
48R-3, 140–150	801.30	0.00	0.22	0.64	0.03	0.01	733	2133	460	0.00	0.34
48R-4, 36–37	801.76	0.00	0.01	2.23	0.05	0.00	20	4460	412	0.00	0.00
48R-5, 107–109	803.97	0.00	0.42	0.61	0.09	0.03	466	677	514	0.00	0.68
48R-6, 62–63	805.02	0.04	0.44	0.57	0.13	0.04	338	438	501	0.08	0.77
48R-6, 105–106	805.45	0.02	0.23	1.09	0.02	0.02	1150	5450	478	0.08	0.21
48R-6, 147–148	805.87	0.08	0.45	0.98	0.06	0.04	750	1633	548	0.15	0.45
49R-1, 94–95	807.24	0.01	0.43	0.33	0.57	0.03	75	57	399	0.02	1.30
49R-1, 122–125	807.52	0.04	0.69	0.18	0.05	0.06	1380	360	502	0.06	3.83
49R-1, 141–143	807.71	0.02	0.55	0.51	0.54	0.04	101	94	398	0.04	1.07
50R-2, 80–82	817.90	0.01	0.32	0.31	0.09	0.02	355	344	382	0.03	1.03
50R-6, 51–52	823.61	0.06	0.57	0.30	0.31	0.05	183	96	479	0.10	1.90
51R-3, 140–150	829.40	0.01	0.32	0.34	0.03	0.02	1066	1133	371	0.03	0.94
51R-5, 0–5	831.00	0.00	0.00	1.02	0.26	0.00	0	392	303		0.00
51R-CC, 2–5	832.52	0.04	0.40	0.36	0.28	0.03	142	128	343	0.09	1.11
52R-1, 132–133	835.82	0.10	0.50	0.53	0.33	0.05	151	160	350	0.17	0.94
52R-2, 8–10	836.08	0.01	0.28	1.11	0.23	0.02	121	482	354	0.07	0.25
52R-2, 10–11	836.10	0.07	0.40	0.36	0.28	0.03	142	128	406	0.15	1.11
52R-2, 134–135	837.34	0.04	0.45	0.09	0.11	0.04	409	81	383	0.08	5.00
53R-1, 102–103	845.12	0.06	0.26	0.00	0.02	0.02	1300	0	379	0.19	0.00
53R-3, 72–74	847.82	0.02	0.31	0.06	0.02	0.02	1550	300	376	0.06	5.16
53R-6, 123–125	852.83	0.00	0.00	49.00	0.00	0.00	0	0	290	0.00	0.00
54R-3, 140–150	875.90	0.01	0.37	0.02	0.03	0.03	1233	66	356	0.03	18.50
54R-4, 49–50	858.49	0.04	0.64	0.06	0.15	0.05	426	40	534	0.06	10.66
55R-2, 82–84	865.32	0.50	2.26	0.75	0.22	0.23	1027	340	487	0.18	3.01
57R-3, 110–115	885.80	0.05	0.01	0.20	0.03	0.00	33	666	264	0.83	0.05
57R-3, 140–150	886.10	0.01	0.00	1.11	0.03	0.00	0	3700	285	0.00	0.00
57R-7, 15–17	890.55	0.03	0.14	0.10	0.01	0.01	1400	1000	416	0.19	1.40
59R-3, 123–125	902.13	0.01	0.36	0.66	0.03	0.03	1200	2200	405	0.03	0.54
59R-3, 149–150	902.39	0.16	0.63	0.08	0.51	0.06	123	15	373	0.21	7.87
59R-4, 111–112	903.51	0.18	0.66	0.06	0.50	0.07	132	12	369	0.21	11.00
60R-2, 61–63	909.61	0.00	0.33	0.64	0.02	0.02	1650	3200	398	0.00	0.51
60R-3, 140–150	911.90	0.01	0.29	0.05	0.02	0.02	1450	250	448	0.03	5.80
60R-4, 0–1	912.00	0.05	0.57	0.00	0.05	0.05	1140	0	488	0.08	0.00
61R-5, 105–106	923.95	0.02	0.00	0.48	0.00	0.00	0	0	266	1.00	0.00
62R-3, 68–70	930.08	0.00	0.35	0.03	0.02	0.02	1750	150	389	0.00	11.66
62R-3, 84–85	930.24	0.02	0.10	0.20	0.00	0.01	0	0	391	0.17	0.50

Velocity

Compressional-wave velocity data, as determined with the Hamilton Frame apparatus, is shown in Figure 86. From this figure, one can observe an underlying trend of progressively increasing velocities from a value of approximately 1525 m/s in the calcareous ooze, near the seafloor sediment boundary, increasing to about 2010 m/s near the sediment basement boundary. Superimposed on this trend is a series of high- and low-velocity excursions. Higher values are associated with lithified claystone, chalk, or cemented sandstone, whereas low values are indicative of less lithified claystone, carbonates, or poorly cemented sandstone. The variability in the data is also, in part, a result of the sampling procedure followed. Samples were taken to be as representative as possible of the sediment section as a whole. In the case of a turbidite or debris-flow sequence, both the upper fine-grained and lower coarse-grained sequences were selected. Sample selection also depended upon the relative frequency, thickness, and homogeneity of a particular sequence; thin, unrepresentative lithologies were avoided. Basalt pebbles occurred frequently in the debris-flow sequences, and hence, were tested periodically. These materials were observed at 465.56, 635.33, and 763.34 mbsf and represent significant spikes in the data, as is shown in Figure 86.

A series of high-velocity peaks can be seen between 350 and 450 mbsf. These peaks appear to be superimposed on a slight velocity increase between 350 and 590 mbsf and closely correspond to intermediate-depth high-amplitude reflectors recorded on the seismic survey lines (see "Seismic Stratigraphy" section, this chapter). In addition, this section corresponds to the increased lithification of the sediments composing the turbidite and debris-flow sequences, as described in the previous section. A sharp decrease in velocity also occurs between 585.19 and 593.04 mbsf; this also corresponds to a low-amplitude reflector on the seismic profile. The index properties for this interval exhibit a significant variation, namely, an increase in porosity and water content and decrease in bulk density.

As an additional means of comparing the physical properties with the seismic data, an acoustic impedance plot (Fig. 86) has been created by multiplying the sediment bulk density by the corresponding velocity and plotting the result as a function of depth. Excluding the three high anomalous basalt pebble peaks at 465.56, 635.33, and 763.34 mbsf, one can more readily observe from this figure the possible occurrence of seismic reflec-

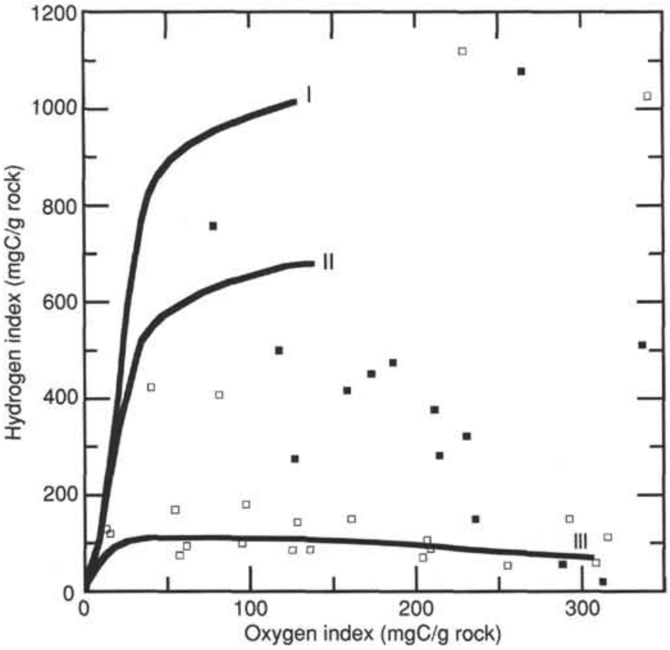

Figure 85. Van Krevelen plot, Site 765. Open squares indicate Cenozoic samples; solid squares indicate Cretaceous samples.

tors between 350 and 450 mbsf, along with the reflector at approximately 590 mbsf.

P-Wave Logger and GRAPE

P-wave logger velocities and GRAPE bulk densities are shown in Figure 87. *P*-wave velocity logging was performed on APC cores only; hence, no data are available below 152 mbsf. *P*-wave velocity data are consistent with those obtained using the Hamilton frame apparatus. However, note that these data had to be filtered to remove a corresponding series of low-velocity values that were associated with improper emplacement of the sample tube in the frame. A velocity on the order of 1525 m/s occurs in the calcareous ooze at the sediment/sea-bottom interface, and it increases linearly with depth to a value of approximately 1600 m/s at 152 mbsf. GRAPE bulk densities were obtained on both APC and XCB cores; hence, data are available to a depth of 340 mbsf. One can observe from Figures 86 and 87 that both the index properties and GRAPE bulk densities exhibit a great deal of variability with depth. This is to be expected, as the sediment column consists of turbidite sequences. The data also appear to indicate index-property bulk densities that are slightly higher than those obtained using the GRAPE apparatus, especially from about 150 to 340 mbsf.

Vane Shear Strength

Values of undrained shear strength were obtained using a four-bladed vane shear apparatus on samples taken from the APC and XCB cores. The resulting shear strengths are given in Table 28 and plotted as a function of depth in Figure 87.

The uppermost 80-m section indicates a fairly uniform increase in shear strength with depth, with a slope of about 0.7 kPa/m. As described earlier in the "Index Properties" section for this interval, Unit A consists primarily of a calcareous ooze. From 80 mbsf to the last sample tested at 299.67 mbsf, the data show a considerable amount of variability. This is a result of the presence of turbidite and debris-flow sequences. By extrapolating the shear strength slope of Unit A (0.7 kPa/m) to include the entire section, one can delineate the debris-flow sequences. From about 80 to 140 mbsf and again from 180 to 220 mbsf, a significant decrease in shear strength can be observed. These intervals consist of debris flows composed primarily of clays and calcareous ooze. The intervals from 140 to 180 mbsf and also from 220 to 263 mbsf show higher shear strengths, which are within the range of the aforementioned slope. These intervals consist of turbidite sequences composed primarily of clays with silt to sand bases. Below 263 mbsf, the samples often cracked during vane insertion, and testing was terminated below 300 mbsf.

Thermal Conductivity

Thermal conductivities given in Table 29 are shown in Figure 86G. Although the data exhibit a significant amount of variability, the general trend for thermal conductivity may be similar to that observed for sediment bulk densities, as described in the "Index Properties," this section. Namely, the thermal conductivity increases from approximately 0.9 to 1.3 W/m · K from the sediment/seafloor boundary to a depth of 100 mbsf. From 100 to 590 mbsf, thermal conductivities appear to increase slightly with depth. At a depth of 590 mbsf, the values decrease to about the same as those observed at 100 mbsf, namely, 1.3 W/m · K.

Conclusions

Sediment index properties, compressional-wave velocities, vane shear strengths, and thermal conductivities allow one to characterize the sediments at Site 765 into four physical property units. Unit A extends from the seafloor to 80 mbsf and consists predominantly of calcareous ooze with high water content. The physical properties change significantly with depth, but are consistent with normal compaction trends. Unit B includes the interval from 80 to 350 mbsf and is composed of turbidites and debris flows. Physical properties indicate normal compaction trends with depth, with the exception of the vane shear data. Variations in vane shear strength were found to correlate with the occurrences of turbidite or debris-flow sequences. Unit C extends from 350 to 590 mbsf and consists of lithified turbidite and debris-flow sequences. Physical properties data indicate a significant variation through this unit but are, for the most part, invariant with depth. Velocity spikes between 350 and 450 mbsf correlate with the high-amplitude reflectors observed in the seismic profiles. Unit D includes the interval from 590 to 896 mbsf and consists predominantly of a dark red claystone. This unit is distinguished by a significant change in physical properties at 590 mbsf. This boundary is also marked by a low-amplitude reflector in the seismic data. The unit shows normal compaction trends; however, numerical values of the physical properties data are approximately the same as those observed for a shallower unit, i.e., Unit B (80–350 mbsf).

BASEMENT LITHOSTRATIGRAPHY

Two of the holes drilled at Site 765 recovered volcanic basement; depths and drift information for these holes are given in Table 30. Basement was encountered in Hole 765C at 935.8 mbsf in Section 123-765-62R, CC. The hole was terminated at 963.9 mbsf (Core 123-765C-64R). Drift measurements at the base of the hole indicated a 10° deviation from vertical. Recovery averaged 31%, with Core 123-765C-63R having 60% recovery. Hole 765D was specifically designed as a deep basement penetration reentry site, and was cased with 11¾ in. (OD) casing to 8.4 m into basement. Basement was encountered in Hole 765D at 924 mbsf; drift shots showed the hole to be within 1° of vertical. The base of the casing shoe was located at 932.4 mbsf, and the top of the first core was at 947.9 mbsf; a 15-m "rathole" was left for cavings in the hole during the casing operation. Correcting for drift in Hole 765C, we observed approximately 15 m of overlap between the section drilled in Holes

Table 24. Gases in sediment samples, Site 765.

Core, section, interval (cm)	Depth (mbsf)	C_1 (ppm)	C_2 (ppm)	C_3 (ppm)	H_2S (ppm)	CO_2 (ppm)	CO	Code (ppm)	Other hydrocarbon gases (ppm)
123-765A-1H-4, 143–150	5.93	6.2	1.5	ND	ND	20,806		NG	
765A-1H-4, 145–150	5.95	4.8	ND					NG	
765B-1H-4, 143–150	5.93	7.8	ND	3.2	ND	34,029	6.8	NG	
765B-1H-4, 145–150	5.95	4.4	ND					HS	
765B-2H-4, 145–150	15.25	6.4	ND					HS	
765B-3H-4, 143–150	24.73	ND	ND	ND	40,647	8.5	NG		
765B-3H-4, 145–150	24.75	6.9	ND					HS	
765B-4H-4, 0–5	33.00	8.6	ND					HS	
765B-4H-4, 0–7	33.00	39.7	ND	24.1	30.3	33,233	10.3	NG	1-Pentene = 24.4, Propylene = 21.0, Cyclopentane = 11.0
765B-5H-4, 0–5	42.60	7.3	ND					HS	
765B-5H-4, 0–7	42.60	10.2	18.5	ND	ND	17,040		NG	Propylene = 3.0
765B-6H-4, 0–5	52.30	6.7	ND					HS	
765B-6H-4, 0–7	52.30	16.4	3.4	5.1	98.9	20,956	13.7	NG	
765B-7H-4, 0–5	61.90	8.2	ND					HS	
765B-7H-4, 0–7	61.90	4.4	ND	ND	ND	28,833		NG	
765B-8H-4, 0–7	71.60	5.5	4.6	ND	6.0	20,194	7.4	NG	
765B-9H-4, 0–5	81.30	8.6	ND					HS	
765B-9H-4, 0–7	81.30	16.6	ND	ND	26.2	19,966	4.3	NG	
765B-10H-4, 0–5	90.90	7.4	ND					HS	
765B-10H-4, 0–7	90.90	11.0	ND	3.8	ND	16,460	10.3	NG	
765B-11H-4, 0–5	100.50	8.3	ND					HS	
765B-11H-4, 0–7	100.50	10.8	ND	ND	ND	17,317	13.6	NG	
765B-12H-4, 0–5	110.10	7.9	ND					HS	
765B-12H-4, 0–7	110.10	17.1	ND	ND	ND	13,617	10.3	NG	
765B-13H-4, 0–5	119.70	7.5	ND					HS	
765B-13H-4, 0–7	119.70	18.0	ND	ND	ND	9,088	5.1	NG	
765B-14H-4, 0–5	129.30	5.8	ND					HS	
765B-14H-4, 0–7	129.30	2.2	ND	ND	ND	13,535	12.8	NG	
765B-15H-4, 0–7	139.00	6.6	ND	ND	ND	14,505	14.5	NG	
765B-15H-4, 0–7	139.00	7.6	ND					HS	
765B-16H-4, 0–7	148.70	6.7	ND					HS	
765B-16H-4, 0–7	148.70	12.1	ND	ND	ND	11,199	ND	NG	l-Butene = 2.1, *i*-Butane = 5.1
765B-17H-3, 143–150	158.33	ND	6.7	2.3	ND	13,936	ND	NG	
765B-17H-4, 0–5	158.40	7.4	ND					HS	
765B-18H-4, 0–5	167.50	6.4	ND					HS	
765B-18H-4, 0–7	167.50	2.2	ND	ND	ND	7,939	13.7	NG	*n*-Butane = 2.6
765B-19X-3, 143–150	177.73	13.3	ND	ND	ND	12,288	13.7	NG	Propylene = 3.4, l-Butene = 3.0
765B-19X-3, 145–150	177.75	4.4	ND					HS	
765B-20X-4, 0–7	187.50	ND	ND	ND	ND	5,423	11.1	NG	l-Butene = 1.5
765B-20X-4, 0–7	187.50	4.8	ND					HS	
765B-21X-3, 0–5	195.70	4.6	ND					HS	
765B-21X-3, 0–7	195.70	12.3	ND	8.5	ND	7,014	10.2	NG	
765B-22X-4, 0–5	206.90	4.9	ND					HS	
765B-22X-4, 0–7	206.90	13.7	ND	4.7	ND	6,439	17.1	NG	
765B-23X-2, 0–5	213.60	6.9	ND	ND	ND	3,571	12.8	NG	
765B-24X-4, 0–3	226.30	3.9	ND					HS	
765B-24X-4, 0–5	226.30	4.4	ND	ND	ND	4,757	ND	NG	*n*-Butane = 6.8
765B-26X-3, 143–150	245.63	ND	ND	ND	ND	82,088	ND	NG	
765B-26X-3, 145–150	245.65	4.8	ND					HS	
765B-27X-3, 0–5	252.90	3.2	ND					HS	
765B-27X-3, 0–7	253.90	6.6	ND	ND	ND	3,171	ND	NG	
765B-28X-2, 143–150	263.53	5.5	ND	ND	ND	865	ND	NG	
765B-28X-2, 145–150	263.55	2.7	ND					HS	
765B-29X-2, 0–5	271.70	2.8	ND					HS	
765B-29X-2, 0–7	271.70	19.1	ND	ND	ND	ND	3,787	6.0	*i*-Butane = 3.1
765B-30X-1, 100–105	280.90	3.7	ND					HS	
765B-31X-4, 0–5	294.10	4.7	ND					HS	
765B-31X-4, 0–7	294.10	ND	2.7	ND	14.1	3,665	2.6	NG	
765B-32X-2, 143–150	294.10	4.4	ND	ND	ND	2,748	6.8	NG	*i*-Butane = 2.9
765B-32X-2, 145–150	302.25	5.5	ND					HS	
765B-33X-4, 0–5	313.50	3.3	ND					HS	
765B-33X-4, 0–7	313.50	2.2	ND	ND	ND	4,147	ND	NG	
765B-34X-1, 139–146	320.09	5.5	ND	ND	ND	5,544	ND	NG	
765B-34X-1, 141–146	320.11	2.9	ND					HS	
765B-35X-2, 0–5	329.80	3.8	ND					HS	
765B-35X-2, 0–7	329.80	7.7	ND	ND	ND	5,352	2.6	ND	*i*-Butane = 2.0
765B-36X-2, 0–5	339.40	4.3	ND					HS	
765B-36X-2, 0–7	339.40	4.4	ND	ND	ND	3,411	6.8	NG	
765B-37X-2, 25–30	348.95	2.9	ND					HS	
765B-37X-2, 25–32	348.95	ND	ND	ND	ND	5,213	ND	NG	Propylene = 2.4
765B-38X-1, 0–5	357.10	4.3	ND					HS	
765B-38X-1, 0–7	357.10	20.6	ND	N	30.3	16,770	18.8	NG	
765B-39X-1, 79–86	367.49	14.2	2.2	1.6	ND	18,000	ND	NG	
765C-3R-3, 0–5	372.30	4.4	ND	ND	14.1	2,565	24.8	NG	

Table 24 (continued).

Core, section, interval (cm)	Depth (mbsf)	C_1 (ppm)	C_2 (ppm)	C_3 (ppm)	H_2S (ppm)	CO_2 (ppm)	CO	Code (ppm)	Other hydrocarbon gases (ppm)
765C-4R-3, 0–5	382.00	ND	ND	ND	ND	9,828	25.6	NG	
765C-6R-4, 0–5	402.80	6.6	ND	ND	ND	7,313	ND	NG	*i*-Hexane = 5.4, Cyclohexane = 70.0, *i*-Pentane = 4.6
765C-9R-3, 0–5	430.30	ND	ND	ND	14.1	7,556	5.9	NG	*n*-Hexane = 2.7, Methylcyclopentane = 5.5
765C-13R-1, 0–5	464.60	4.8	ND	ND				HS	
765C-13R-1, 0–5	464.60	7.7	ND	ND	ND	4,567	3.4	NG	
765C-14R-1, 0–5	474.10	3.6	ND	ND				HS	
765C-15R-1, 0–5	483.70	ND	3.8	2.6	ND	5,829	5.1	NG	*n*-Hexane = 6.2 Cyclohexane = 17.3 2-Methylepentane = 13.3
765C-15R-1, 0–5	483.70	5.4	ND	ND				HS	
765C-16R-1, 0–5	493.20	11.2	4.5	3.5				HS	
765C-17R-3, 0–5	505.40	3.1	ND	ND				HS	
765C-18R-4, 0–5	516.40	2.8	ND	ND				HS	
765C-19R-2, 0–5	522.80	3.1	ND	ND				HS	
765C-20R-1, 145–150	532.25	1.9	ND	ND				HS	
765C-21R-1, 0–5	540.40	2.2	ND	ND				HS	
765C-22R-3, 145–150	554.62	2.3	ND	ND				HS	
765C-22R-3, 145–150	554.62	3.8	ND	ND	ND	6,332	6.8	NG	
765C-23R-5, 55–60	566.25	2.3	ND	ND				HS	
765C-24R-4, 0–5	573.80	2.1	ND	ND				HS	
765C-24R-4, 0–5	573.80	4.9	ND	ND	ND	5,012	ND	NG	
765C-25R-4, 135–140	584.85	2.4	ND	ND				HS	
765C-26R-3, 135–140	592.58	2.3	ND	ND				HS	
765C-27R-1, 145–150	598.95	2.4	ND	ND				HS	
765C-28R-1, 145–150	608.45	2.7	ND	ND				HS	
765C-29R-2, 145–150	619.42	ND	ND	ND	ND	17,258	ND	NG	
765C-29R-2, 145–150	619.42	2.7	ND	ND				HS	
765C-30R-6, 99–104	634.28	2.5	ND	ND				HS	
765C-31R-3, 0–5	638.18	2.6	ND	ND				HS	
765C-32R-3, 0–5	647.90	2.7	ND	ND				HS	
765C-32R-3, 0–5	647.90	4.4	4.3	ND	12.1	8,506	ND	NG	
765C-33R-2, 0–5	656.18	3.2	ND	ND				HS	
765C-34R-2, 0–5	665.90	4.0	ND	ND				HS	
765C-35R-1, 145–150	675.55	7.7	ND	ND	ND	3,677	ND	NG	*i*-Butane = 1.6, Ethylene = 3.2
765C-35R-1, 145–150	675.55	2.5	ND	ND				HS	
765C-36R-5, 145–150	690.75	2.5	ND	ND				HS	
765C-37R-3, 110–115	697.10	ND	ND	ND	ND	6,264	7.7	NG	
765C-37R-3, 110–115	697.10	3.3	ND	ND				HS	
765C-38R-2, 145–150	705.45	4.0	ND	ND				HS	
765C-39R-3, 0–5	714.70	4.9	ND	ND				HS	
765C-40R-3, 145–150	725.35	8.4	ND	ND				HS	
765C-42R-4, 0–5	744.30	ND	ND	1.8	ND	975	ND	NG	
765C-42R-4, 0–5	744.30	5.6	ND	ND				HS	
765C-43R-6, 0–5	756.60	6.7	ND	ND				HS	
765C-44R-4, 0–5	763.00	8.7	ND	ND				HS	
765C-45R-5, 0–5	774.20	8.8	1.3	ND	ND	2,623	6.8	NG	*i*-Butane = 1.7, Propylene = 10.5, Cyclopentane = 1.0
765C-45R-5, 0–5	774.20	8.8	ND	ND				HS	
765C-46R-1, 145–150	779.25	8.3	ND	ND				HS	
765C-47R-4, 145–150	793.35	7.5	ND	ND				HS	
765C-48R-4, 0–5	801.40	8.1	ND	ND	ND	3,972	14.5	NG	
765C-48R-4, 0–5	801.40	8.8	ND	ND				HS	
765C-49R-4, 0–5	810.80	11.8	ND	ND				HS	
765C-40R-2, 145–150	818.55	9.1	ND	ND				HS	
765C-51R-5, 0–5	831.00	5.8	ND	ND				HS	
765C-51R-5, 0–5	831.00	11.3	2.8	ND	ND	9,817	ND	NG	Propylene = 3.5
765C-52R-2, 145–150	837.45	7.0	ND	ND				HS	
765C-53R-1, 0–5	844.10	16.6	2.2	ND	ND	1,159	6.8	NG	Methylcyclopentane = 17.7
765C-53R-1, 102–103	845.12	9.7	ND	ND				HS	
765C-54R-5, 0–5	859.41	7.5	ND	ND				HS	
765C-55R-3, 0–1	866.00	8.3	ND	ND				HS	
765C-57R-3, 110–115	885.80	6.0	ND	ND				HS	
765C-57R-3, 110–115	885.80	28.3	ND	ND	ND	1,643	ND	NG	l-Butene = 3.1, *i*-Butane = 1.5
765C-60R-4, 0–1	912.00	5.6	ND	ND				HS	
765C-60R-4, 0–1	912.00	12.3	ND	ND	ND	464	ND	NG	Propylene = 2.3, l-Pentene = 3.1, *i*-Butane = 2.0
765C-61R-2, 149–150	919.89	11.3	ND	ND				HS	

Table 25. Index properties and compressional-wave velocity of sediment samples from Hole 765A.

Core, section, interval (cm)	Depth (mbsf)	Bulk density (g/cm³)	Grain density (g/cm³)	Porosity (%)	Water content (%)	Velocity (m/s)
123-765A-1H-2, 78	2.28	1.46	2.29	83.3	139.8	1491
1H-4, 68	5.18	1.28	2.76	89.6	252.2	1526
1H-6, 68	8.18	1.56	2.46	76.6	101.4	1516

Note: Volumes determined using average sample diameter and height.

765C and 765D. Hole 765D was offset approximately 30 to 40 m from Hole 765C.

A total of 247 m of volcanic basement was cored in Hole 765D, resulting in a total penetration of 1194.9 mbsf, 270.9 m into volcanic basement. In all, 27 RCB cores were taken, with an average recovery of 31% (see Fig. 88A). Recovery was as low as 5% in Core 123-765D-4R, and as high as 112% in Core 123-765D-5R and 63% in Core 123-765D-24R. In the first five cores, recovery was highest where penetration rates were low (0.5 m/hr); these cores tended to constitute massive basalt intervals. However, this relationship was not maintained for the rest of the hole, despite penetration rates that varied from (0.25 to 0.54 m/hr). The caliper log indicated that certain intervals in the drill hole were as wide as 14 in. Although this may also be a function of lithology, the variation in width may be related to bit instability because no stabilizers were run in the drill string; this instability may be responsible for the abrasion and subsequent loss of core.

Relative to other deep basement holes, recovery is comparable to that for the upper 214 m basalt section in DSDP Hole 504B (about 35%; Shipboard Scientific Party, 1983), and is superior to that for the lowermost basalt and dike sections of Hole 504B (about 12%; Shipboard Scientific Party, 1988a), and significantly less than that for DSDP Holes 417 and 418A (about 80%; Shipboard Scientific Party, 1979a, 1979b). The lithologies and degree of alteration are comparable to those encountered in DSDP Holes 417 and 418A. In addition, drilling technology and bits used were comparable; thus, there is no obvious reason for the difference in recovery.

In addition to the volcanic basement cored in Hole 765C, a suite of volcanic pebbles was recovered in the sedimentary section. In total, at least 25 pebbles were encountered in cores, of which 10 were considered *in situ*, forming part of a mid-Tertiary conglomerate horizon in a debris flow (see "Sediment Lithostratigraphy" section, this chapter). The remaining volcanic pebbles were recovered on the top of cores and probably represent cavings. All pebbles obviously were transported from their place of origin, and provide some information as to the nature of volcanism on the Exmouth Plateau. Petrography and geochemistry of these pebbles are described in detail in the "Basement Petrography" section (this chapter).

In total, 22 igneous rock units were defined for Hole 765D and two units were defined for Hole 765C. The locations of the lithological unit boundaries are given in Table 31. These divisions were based on (1) lithologic characteristics, such as lava forms (pillows, thin flows, massive flows), and the presence of breccia (autoclastic or tectonic); (2) petrographic characteristics, such as the presence of phenocrysts and changes in degree of crystallinity and grain size; (3) geochemical characteristics, based on significant breaks in certain geochemical indexes with depth. No lithologic divisions were made on the basis of alteration, although the degree of alteration varied, depending on lithology, but not systematically with depth (see "Basement Alteration" section, this chapter).

The stratigraphic column for Holes 765C (>930 mbsf) and 765D are shown in Figure 88B. Variations of zirconium (ppm)

Table 26. Index properties and compressional-wave velocity of sediment samples from Hole 765B.

Core, section, interval (cm)	Depth (mbsf)	Bulk density (g/cm³)	Grain density (g/cm³)	Porosity (%)	Water content (%)	Velocity (%)
123-765B-1H-1, 96	0.96	1.26	2.79	92.9	311.2	1530
1H-3, 42	3.42	1.37	2.77	89.6	205.0	1525
1H-6, 61	8.11	1.33	2.48	91.9	244.5	1527
2H-1, 53	9.83	1.62	2.88	80.4	103.3	1523
2H-3, 65	12.95	1.36	2.50	84.6	175.7	1535
2H-6, 75	17.55	1.42	2.79	85.1	160.4	1530
3H-1, 83	19.63	1.51	2.66	77.3	110.0	1534
3H-4, 125	24.55	1.32	2.51	88.2	216.3	1544
3H-6, 22	26.52	1.55	2.69	73.2	93.4	1537
4H-2, 98	30.98	1.59	2.68	77.5	100.3	1537
4H-4, 115	34.15	1.49	2.73	83.9	137.0	1524
4H-6, 90	36.90	1.32	2.56	88.0	214.1	1535
5H-1, 119	39.92	1.35	2.50	89.4	209.8	1522
5H-4, 147	43.87	1.56	2.61	77.4	103.9	1526
6H-2, 102	50.32	1.55	2.63	73.3	94.2	1525
6H-4, 55	52.85	1.45	2.64	83.3	143.2	—
6H-1, 113	58.53	1.58	2.65	72.1	88.0	1482
7H-4, 65	62.55	1.68	2.67	63.8	63.8	1521
7H-6, 37	65.27	1.63	2.55	66.6	72.3	1556
8H-2, 49	69.09	1.61	2.71	73.2	87.7	1531
8H-5, 42	73.52	1.69	2.52	70.3	74.3	1534
8H-6, 107	75.67	1.65	2.46	64.6	67.0	1543
9H-2, 77	79.07	1.61	2.69	76.2	94.6	1498
9H-3, 67	80.47	1.67	2.61	65.0	66.7	1557
9H-6, 36	84.66	1.65	2.62	72.6	81.7	1537
10H-1, 98	87.38	1.65	2.62	68.7	74.1	1575
10H-2, 77	88.67	1.64	2.72	69.3	76.3	1590
10H-6, 87	94.77	1.71	2.62	64.8	63.4	1603
11H-1, 62	96.62	1.76	2.64	70.5	69.7	1534
11H-3, 92	99.92	1.95	2.70	71.9	60.7	1547
11H-5, 59	102.59	1.78	2.79	66.3	61.6	1604
12H-2, 117	108.27	1.68	2.92	69.1	73.0	1545
12H-3, 77	109.37	1.75	2.82	65.6	62.1	1547
12H-5, 78	112.38	1.71	2.64	67.2	67.2	1552
13H-3, 15	119.35	1.71	2.57	65.9	65.3	1554
13H-5, 133	122.53	1.82	2.58	62.9	54.8	1573
13H-6, 77	123.47	1.91	2.75	64.2	52.7	1592
14H-1, 76	125.56	1.85	2.71	66.1	57.9	1572
14H-4, 79	130.09	1.83	2.55	63.4	55.2	1571
14H-5, 68	131.48	1.83	2.75	65.3	57.7	1640
15H-1, 100	135.50	1.92	2.86	65.8	54.1	1558
15H-4, 84	139.84	1.79	2.64	62.4	55.8	1568
15H-6, 104	143.04	1.81	2.68	65.0	58.0	1618
16H-1, 28	144.48	1.73	2.73	65.2	62.7	1591
16H-3, 80	148.00	1.73	2.54	65.1	62.7	1574
16H-6, 50	152.20	1.70	2.53	63.7	62.3	1586
17H-1, 68	154.58	1.87	2.63	62.6	52.0	1580
17H-4, 80	159.20	1.81	2.80	61.7	53.5	1567
18H-2, 47	165.57	1.81	2.97	65.4	58.6	1565
18H-4, 97	168.47	1.73	2.45	60.7	56.2	1609
18H-6, 134	171.84	1.82	2.88	63.7	55.7	1593
19X-1, 40	173.70	1.69	2.62	63.6	62.5	1522
19X-2, 67	175.47	1.79	2.73	65.2	59.3	1588
19X-4, 123	179.03	1.92	2.82	56.0	42.8	1610
20X-3, 112	187.12	1.91	2.66	51.5	38.2	—
20X-4, 87	188.37	1.91	2.72	54.7	41.5	—
20X-5, 90	189.90	1.76	2.75	63.6	58.6	—
21X-1, 67	193.37	1.76	2.63	59.5	53.0	1586
21X-2, 60	194.80	1.85	2.78	60.1	50.1	1562
21X-3, 137	197.07	1.83	2.80	57.3	47.2	1596
22X-2, 80	204.70	1.77	2.64	61.2	55.0	1577
22X-3, 87	206.27	1.86	2.76	56.7	45.6	1601
22X-4, 60	207.50	1.94	2.67	54.2	40.2	—
23X-1, 31	212.41	1.98	2.65	60.0	45.0	1588
23X-2, 40	214.00	1.93	2.36	55.5	41.7	1590
24X-1, 64	222.44	1.95	2.63	60.0	46.0	1628
24X-2, 128	224.58	1.94	2.93	65.0	52.3	—
24X-4, 85	227.15	1.95	2.61	55.1	40.7	1648
25X-1, 50	232.00	1.95	2.81	55.0	40.8	1657
26X-2, 102	243.72	1.98	2.82	56.4	41.2	1624
26X-3, 13	244.33	2.04	2.85	55.4	38.6	1695
27X-1, 48	251.38	2.09	2.75	51.4	33.7	1679
27X-3, 64	254.54	1.93	2.61	53.6	39.7	1674
28X-1, 20	260.80	2.00	2.68	49.6	34.0	1691
28X-2, 90	263.00	1.87	2.63	57.8	46.2	1637
29X-1, 87	271.07	1.87	2.75	59.2	48.1	1626
30X-1, 35	280.25	1.79	2.72	64.5	58.5	1568
31X-2, 79	291.89	1.94	2.59	50.3	36.3	1693
31X-4, 10	294.20	2.00	2.85	54.0	38.3	1755
32X-1, 45	299.75	2.00	2.76	53.0	37.2	1679
32X-3, 29	302.59	2.02	2.69	49.4	33.4	1711
33X-1, 111	310.11	2.05	2.83	51.6	34.9	1660
33X-4, 84	314.34	2.02	2.78	51.2	35.0	1688
34X-1, 89	319.59	2.00	2.75	50.0	34.5	1673

Note: Tables 25, 26, and 27: owing to instrument error, values of "Bulk density" and "Porosity" printed here are incorrect. Corrected values will be published in the *Scientific Results* volume.

Table 26 (continued).

Core, section, interval (cm)	Depth (mbsf)	Bulk density (g/cm3)	Grain density (g/cm3)	Porosity (%)	Water content (%)	Velocity (%)
123-765B-34X-1, 98	319.68	2.00	2.75	50.1	34.5	—
35X-1, 110	329.40	2.07	2.81	48.3	31.4	1679
36X-2, 40	339.80	2.02	2.69	46.5	30.9	1631
37X-1, 42	347.92	2.02	2.77	47.1	31.3	1696
37X-CC, 56	350.43	2.22	2.71	41.3	23.6	2460
38X-1, 103	358.13	2.01	2.72	48.1	32.4	1688
38X-CC, 10	358.70	2.01	2.76	53.4	37.4	2062
39X-1, 32	367.02	1.94	2.64	53.5	39.5	—

and TiO_2 (wt%), used to define geochemical units, are displayed in Figure 88A.

Lithologic Summary

The entire volcanic section cored in Holes 765C and 765D comprises pillow basalts (54%), massive basalts (28%), brecciated pillow basalts (8%), autoclastic breccia (6%), and diabase (4%). The top of the section (Cores 123-765C-62R to -65R) is dominated by pillows having well-developed glassy margins. Similar, although more altered and brecciated, pillow units occur in the middle of the section (Cores 123-765D-9R to -22R) and near the base of the section (Cores 123-765D-25R and -26R). The top of Hole 765D is dominated by massive basaltic flows (Cores 123-765D-1R to -8R); massive flows occur again at the base of the hole in Cores 123-765D-23R to -25R and in Core 123-765D-27R. Two distinctly coarse-grained units, interpreted as massive flows or diabase sills, were recovered in Cores 123-765D-8R and -9R and in Core 123-765D-23R.

The entire section is moderately altered, with red-brown and green-yellow alteration fronts extending into the basalt along fractures composed of calcite, green celadonite, and iron-oxyhydroxides.

Hole 765C, Units 1 and 2, Aphyric Pillow Basalts

Three cores (Cores 123-765C-63R to -65R), plus the core-catcher sample in Core 123-765C-62R, penetrated a total of 28.1 m of aphyric pillow basalts in Hole 765C.

The contact with the overlying sediments was retrieved in Section 123-765C-62R, CC (Fig. 89). Pillow basalts are overlain by a sequence of red-brown calcareous and manganese-rich claystone, designated Subunit VIIB in the "Sediment Lithostratigraphy" section (this chapter). These sediments overlie bottle green hyaloclastite fragments cemented with sparry calcite; claystone fillings between the hyaloclastite confirm the interpretation of this zone as the original basalt/sediment contact. These fillings are provisionally dated as upper Berriasian to Valanginian (see "Biostratigraphy," section, this chapter). In Section 123-765C-62R, CC, carbonate alteration becomes more pervasive in the basalt toward the chilled contact overlain by sediment.

Both Units 1 and 2 comprise a sequence of pillow basalts. Individual pillows are recognized by fresh or devitrified glassy margins, or by grain size fining toward margins presumably lost during coring. The pillows average 30 to 40 cm in size, with the upper glassy chilled margins being up to 1.8 cm thick. Colors vary from dark gray at the base of the pillows to lighter blue-gray toward the top of the "fresh" pillow basalts. Altered pillows are gray-green to gray-brown. These pillows are fractured, and the fractures are filled with calcite, bottle-green celadonite, and brown and red iron-oxyhydroxides. In some instances, more than one generation of veining is evident (see "Basement Alteration" section, this chapter). Concentric alteration zones can be traced from the veins into the surrounding basalt. Nonetheless, when isolated from alteration veins, partially crystalline cores of pillows are commonly only slightly altered, and some glass has remained fresh even when in contact with veins.

Table 27. Index properties and compressional-wave velocity of sediment samples from Hole 765C.

Core, section, interval (cm)	Depth (mbsf)	Bulk density (g/cm3)	Grain density (g/cm3)	Porosity (%)	Water content (%)	Velocity (%)
123-765C-2R-1, 80	360.40	2.06	2.72	44.7	28.6	1839
2R-3, 47	363.07	2.36	2.84	34.0	17.3	2559
3R-1, 25	369.55	1.96	2.76	54.8	40.1	1998
3R-1, 111	370.41	2.04	2.66	46.9	30.9	1823
3R-2, 25	371.05	1.98	2.52	47.7	32.7	1799
3R-2, 40	371.20	1.93	2.69	55.4	41.5	1923
4R-1, 35	379.35	1.96	2.67	51.6	36.9	1830
4R-1, 118	380.18	2.34	2.71	26.1	12.9	3296
4R-2, 84	381.34	1.97	2.76	52.5	37.5	1980
4R-3, 58	382.58	2.18	2.66	35.5	20.0	2141
5R-1, 78	389.38	2.15	2.85	54.2	34.8	1845
5R-3, 28	391.88	2.04	2.66	50.4	34.0	1779
5R-3, 78	392.38	2.04	2.78	54.3	37.5	2161
6R-1, 89	399.19	2.27	2.81	46.6	26.6	1903
6R-3, 34	401.64	2.04	2.40	54.6	37.9	1814
6R-3, 45	401.75	2.04	2.66	56.4	39.6	1746
6R-3, 70	402.00	2.35	2.72	47.4	26.0	2336
7R-1, 109	409.09	2.08	2.64	47.0	30.1	1793
7R-2, 106	410.56	2.50	2.68	27.2	12.6	3228
7R-3, 34	411.34	2.05	2.57	53.2	36.3	1747
8R-1, 49	418.19	2.00	2.72	52.6	37.0	1766
8R-2, 133	420.53	2.59	2.63	26.0	11.5	3624
8R-3, 22	420.92	1.96	2.71	54.3	39.6	—
8R-4, 22	422.42	—	—	—	—	2134
8R-4, 71	422.91	2.09	2.57	44.2	27.7	1886
9R-1, 59	427.89	1.83	2.63	58.4	48.5	2148
9R-2, 112	429.92	2.02	2.58	58.7	42.4	1679
9R-3, 40	430.70	2.33	2.54	32.8	16.8	2979
9R-5, 60	433.90	1.97	2.52	57.3	42.5	1714
10R-2, 30	438.30	1.95	2.58	63.0	49.6	1990
10R-2, 47	438.47	2.08	2.65	45.1	28.5	1796
10R-4, 33	441.33	1.99	2.71	53.0	37.4	1906
10R-4, 112	442.12	—	—	—	—	1650
11R-1, 111	447.11	1.99	2.60	47.8	32.7	1825
11R-2, 91	448.41	2.37	2.76	29.9	14.9	2776
11R-3, 110	450.10	2.24	2.80	39.8	22.3	2475
11R-4, 116	451.66	1.69	2.61	65.6	66.0	1629
12R-1, 68	455.88	2.04	2.77	48.6	32.2	2075
12R-3, 85	459.05	2.26	2.72	39.1	21.5	2040
12R-4, 36	460.06	2.15	2.69	40.4	23.8	1887
12R-5, 67	461.87	2.03	2.63	45.9	30.2	2193
13R-1, 96	465.56	2.68	2.69	16.4	6.7	4670
13R-2, 127	467.37	2.14	2.75	40.0	23.7	2021
13R-3, 10	467.70	2.08	2.67	50.3	32.9	2003
14R-1, 59	474.69	2.13	2.73	46.2	28.5	1958
15R-1, 17	483.87	1.92	2.64	64.2	52.2	1741
16R-1, 103	494.23	2.27	3.12	51.8	30.5	1879
16R-2, 24	494.94	—	—	—	—	1871
16R-4, 50	498.20	2.33	3.06	34.4	17.8	2031
17R-1, 133	503.73	2.03	2.67	47.7	31.7	1800
17R-2, 109	504.99	1.99	2.63	52.8	37.3	—
17R-3, 40	505.80	2.22	2.74	44.4	25.8	1882
18R-1, 78	512.68	2.11	2.51	49.4	31.5	1854
18R-2, 48	513.88	1.98	2.64	56.2	41.0	1708
18R-3, 40	515.30	2.08	2.72	45.4	28.8	1907
19R-1, 55	521.85	2.06	2.66	53.4	36.2	1827
19R-2, 81	523.61	2.36	2.89	65.3	39.6	1808
19R-3, 119	525.49	2.22	2.65	50.0	29.9	2048
20R-1, 50	531.30	2.15	2.67	40.9	24.3	2033
20R-1, 94	531.74	2.37	2.83	42.5	22.5	2039
20R-2, 71	533.01	1.95	2.47	51.6	37.2	1823
21R-1, 15	540.55	2.29	2.80	42.5	23.5	2000
22R-1, 61	550.71	1.95	2.60	48.3	34.0	—
22R-1, 148	551.58	2.16	2.65	38.9	22.6	2004
22R-2, 102	552.62	1.91	2.56	52.0	38.5	1842
23R-4, 3	564.23	1.88	2.61	26.5	16.8	2023
23R-5, 3	565.73	2.59	2.64	41.3	19.5	2063
24R-1, 40	569.70	2.33	2.79	39.2	20.9	2010
24R-1, 146	570.76	2.25	2.71	38.9	21.5	2001
24R-3, 4	572.34	2.23	3.22	37.7	20.9	2091
25R-1, 37	579.37	2.34	2.77	37.0	19.4	2059
25R-3, 62	582.62	2.27	2.71	41.1	22.7	1952
25R-5, 19	585.19	2.25	2.67	41.5	23.3	1968
26R-4, 34	593.04	1.91	2.73	61.8	49.5	1655
26R-5, 37	594.12	1.88	2.55	60.8	49.5	1677
27R-1, 45	597.95	1.80	2.75	65.0	58.5	1632
27R-2, 18	599.25	1.87	2.63	59.9	48.9	1650
28R-1, 85	607.85	1.86	2.71	58.5	47.6	1680
28R-2, 97	609.47	1.99	2.71	59.0	43.7	1771
29R-1, 82	617.22	1.99	2.65	54.5	39.1	1775
29R-5, 35	622.97	1.93	2.59	52.6	38.7	1769
29R-6, 10	624.27	1.97	2.76	53.4	38.5	—
30R-2, 56	627.95	2.10	2.73	55.5	37.2	1781
30R-4, 107	631.39	1.82	2.58	57.0	47.1	1753
30R-6, 80	634.09	2.12	2.84	57.4	38.5	1868

Table 27 (continued).

Core, section, interval (cm)	Depth (mbsf)	Bulk density (g/cm³)	Grain density (g/cm³)	Porosity (%)	Water content (%)	Velocity (%)
123-765C-31R-1, 3	635.33	2.43	2.55	15.6	7.0	3549
31R-2, 74	637.45	2.06	2.67	47.7	31.1	1863
31R-3, 138	639.56	2.05	2.69	48.0	31.6	1882
32R-1, 77	645.77	2.15	2.72	49.2	30.6	1848
35R-1, 127	675.37	1.87	2.51	50.6	38.3	1823
35R-2, 94	676.54	1.94	2.59	51.7	37.4	1933
35R-3, 78	677.88	1.84	2.40	50.7	39.4	1890
35R-4, 41	679.01	1.93	2.46	49.9	35.9	1841
36R-2, 10	684.90	1.89	2.34	46.1	33.4	2315
36R-5, 120	690.50	1.97	2.53	49.2	34.4	1777
36R-6, 45	691.25	1.99	2.41	42.7	28.2	1676
37R-1, 107	694.07	1.83	2.51	58.4	48.6	1959
37R-2, 62	695.12	2.24	2.81	50.6	30.1	1888
37R-3, 96	696.96	2.12	2.58	46.3	28.8	1876
38R-1, 142	703.92	2.14	2.58	47.2	29.1	1949
38R-3, 47	705.97	2.03	2.28	43.6	28.2	2438
38R-5, 104	709.54	2.01	2.48	45.8	30.4	2035
38R-7, 7	711.57	2.06	2.60	50.0	33.2	1938
39R-1, 82	712.52	2.02	2.62	47.3	31.6	1876
39R-3, 51	715.21	1.82	2.41	53.5	43.1	2031
40R-2, 124	723.64	2.11	2.64	44.9	27.8	2017
40R-4, 22	725.62	2.13	2.79	56.6	37.4	1823
41R-1, 9	730.49	2.16	2.70	44.5	26.7	1553
42R-1, 46	740.26	2.02	2.62	52.3	36.0	1888
42R-2, 15	741.45	2.20	2.77	49.9	30.2	1578
42R-4, 59	744.89	2.06	2.77	53.0	35.7	1491
43R-2, 121	751.81	1.95	2.72	53.4	39.1	—
43R-4, 138	754.98	2.05	2.63	53.3	36.3	1776
43R-6, 52	757.12	2.01	2.77	52.7	36.7	1808
44R-2, 91	760.91	1.99	2.81	57.8	42.3	1762
44R-4, 34	763.34	2.64	2.69	17.7	7.4	2338
45R-1, 92	769.12	2.01	2.69	49.3	33.6	1829
45R-5, 70	774.90	2.00	2.69	50.8	35.3	1806
46R-1, 41	778.21	1.95	2.75	51.3	36.9	1772
46R-2, 36	779.66	2.05	2.86	50.4	33.8	1850
47R-1, 112	788.52	2.03	2.75	50.8	34.5	1848
47R-4, 32	792.22	2.02	2.67	48.3	32.3	1770
48R-1, 86	797.76	2.31	3.13	44.9	24.8	2028
48R-6, 127	805.67	2.11	2.74	44.8	27.8	1957
49R-1, 98	807.28	2.03	2.61	44.6	29.0	1907
49R-4, 82	811.62	2.06	2.64	46.0	29.7	1938
50R-2, 90	818.00	2.03	2.63	45.2	29.6	1941
50R-5, 38	821.98	2.22	2.93	41.8	23.9	1957
51R-1, 35	825.35	2.05	2.67	47.7	31.4	1929
51R-5, 5	831.05	2.10	2.66	42.1	25.8	2053
52R-2, 12	836.12	2.22	2.82	47.9	28.3	2023
25R-3, 102	838.52	2.19	2.74	49.0	29.9	2013
53R-1, 29	844.39	2.15	2.53	49.2	30.6	2520
53R-4, 26	848.86	2.43	2.72	36.5	18.2	2492
53R-7, 37	853.47	2.08	2.52	43.8	27.4	2084
54R-1, 109	854.59	2.14	2.70	44.5	27.1	2029
54R-4, 90	858.90	2.14	2.52	41.9	25.1	2181
55R-1, 107	864.07	2.08	2.70	47.7	30.6	1991
55R-3, 82	866.82	2.24	2.81	40.7	22.9	2044
56R-1, 67	873.17	2.21	2.70	46.5	27.5	2097
56R-2, 94	874.94	2.09	2.69	45.1	28.3	2003
57R-1, 6	881.76	2.05	2.68	47.3	30.9	1923
57R-3, 69	885.39	2.28	2.74	39.4	21.5	2147
58R-1, 90	892.10	2.25	2.66	37.7	20.7	2129
58R-4, 40	896.10	2.20	2.63	45.6	27.0	2010

Sparse phenocrysts of plagioclase and clinopyroxene are apparent. Very rare iddingsitized olivines are also identifiable. Larger phenocrysts and glomerocrysts are scattered throughout the pillows, which our evaluation of thin sections indicates to be xenocrysts (see "Basement Petrography" section, this chapter). Small vesicles (<1 mm) are filled with calcite and/or celadonite and are approximately 0.5% of the lava.

Units 1 and 2 are identical in lithology but were differentiated on the basis of a decrease in zirconium and titanium between Sample 123-765C-64R-1 (Piece 2 through Piece 3; Fig. 88). Further evidence for a unit change at this point comes from a magnetic polarity reversal: from reversed polarity in Piece 2 to normal polarity in Section 123-765C-64R-1 (Piece 3; see "Basement Paleomagnetism" section, this chapter).

Hole 765D, Units 1 and 2: Massive Aphyric Basalts

Cores 123-765D-1R and -2R constitute a series of massive basalt flows 1 to 2 m thick. Unit 1 in this hole overlaps the aphyric pillow basalt of Unit 2, recovered in Hole 765C. Hole 765D is located approximately 30 m from Hole 765C, suggesting lateral inhomogeneity between lithologies on the seafloor. As evident from Figure 88, the two lithologies are chemically similar, both the basalt from Unit 1 of Hole 765D and the basalt pillows from Unit 2 of Hole 765C being lower in zirconium and titanium than the basalt pillows of Unit 1 of Hole 765C. This implies that the pillowed unit and the massive flow may be associated with the same eruptive episode.

The contacts in the massive flows in Cores 123-765D-1R to -4R are not glassy and are recognized by a gradual change in crystallinity from medium- to fine-grained holocrystalline flow centers to chilled margins having a low degree of crystallinity. A brecciated chilled margin, which is invaded by calcite, is recognized between flows B and C in Section 123-765D-3R-1 at 80–82 cm; this contact has been tentatively interpreted as intrusive.

Rare plagioclase phenocrysts are present in the flows of Units 1 to 3, and vesicularity is <1%. Colors vary from gray for the fine-grained flow tops and bases to greener-gray for the flow centers.

Veins cut the flows with 45° to 80° dips and are filled with calcite, celadonite, and brown-red iron-oxyhydroxides. Orange and yellow-brown alteration fronts (halos) 3 to 4 cm wide extend from these veins into the basalts.

The division between Units 1 and 2 is based on a change in geochemical characteristics between Cores 123-765D-2R and -3R (Fig. 88). No other lithological differences are evident for these two units.

Unit 3: Massive Aphyric Basalt and Pillows

Unit 3 comprises a sequence of aphyric massive flows that are geochemically identical to those of Unit 2. They are, however, distinct in the presence of well-developed hyaloclastite zones between flows and intercalated horizons of pillow basalt (Fig. 90). The hyaloclastite contains droplets of fresh aphyric basalt glass. In general, the degree of alteration is lower in Unit 3 than that in Units 1 and 2.

Unit 4: Aphyric Pillow Basalts and Pillow Breccia

The hyaloclastite at the base of Core 123-765D-5R grades into a 3-m-thick sequence of pillow basalts that are intercalated with hyaloclastite having well-preserved glassy margins. Geochemically, the pillows of Unit 4 are identical to the massive basalt flows in Unit 3 and probably reflect the same eruptive episode (see Fig. 88). Rare plagioclase phenocrysts and scattered mafic phenocrysts, recognized in thin section as clinopyroxene, are present in these pillow lavas. Vesicles are approximately 1 mm in diameter and form <1% of the rock.

Unit 5: Massive Aphyric Basalt and Pillows

Basalts in Unit 5 are differentiated from those of Unit 4 by the lack of hyaloclastite and by their more massive appearance and interrelated pillows. A significant geochemical change characterizes this unit relative to Unit 4 and has been interpreted as reflecting a new eruptive unit.

Unit 6: Massive Aphyric Basalt

The basalts of Unit 5 are underlain by massive aphyric basalt flows of similar geochemistry. These flows are akin to those represented in Units 1 and 2. Yellow-brown and green-gray alteration zones halo calcite and celadonite veins. Fe-oxyhydroxide veins are less abundant than at higher levels in the section.

Unit 7: Aphyric Diabase

A medium-grained, aphyric massive diabase is present at the base of Core 123-765D-8R and the upper 1 m of Core 123-765D-9R. This unit is identifiable as a competent lithology of at least 15 m thickness on the sonic and resistivity logs (see

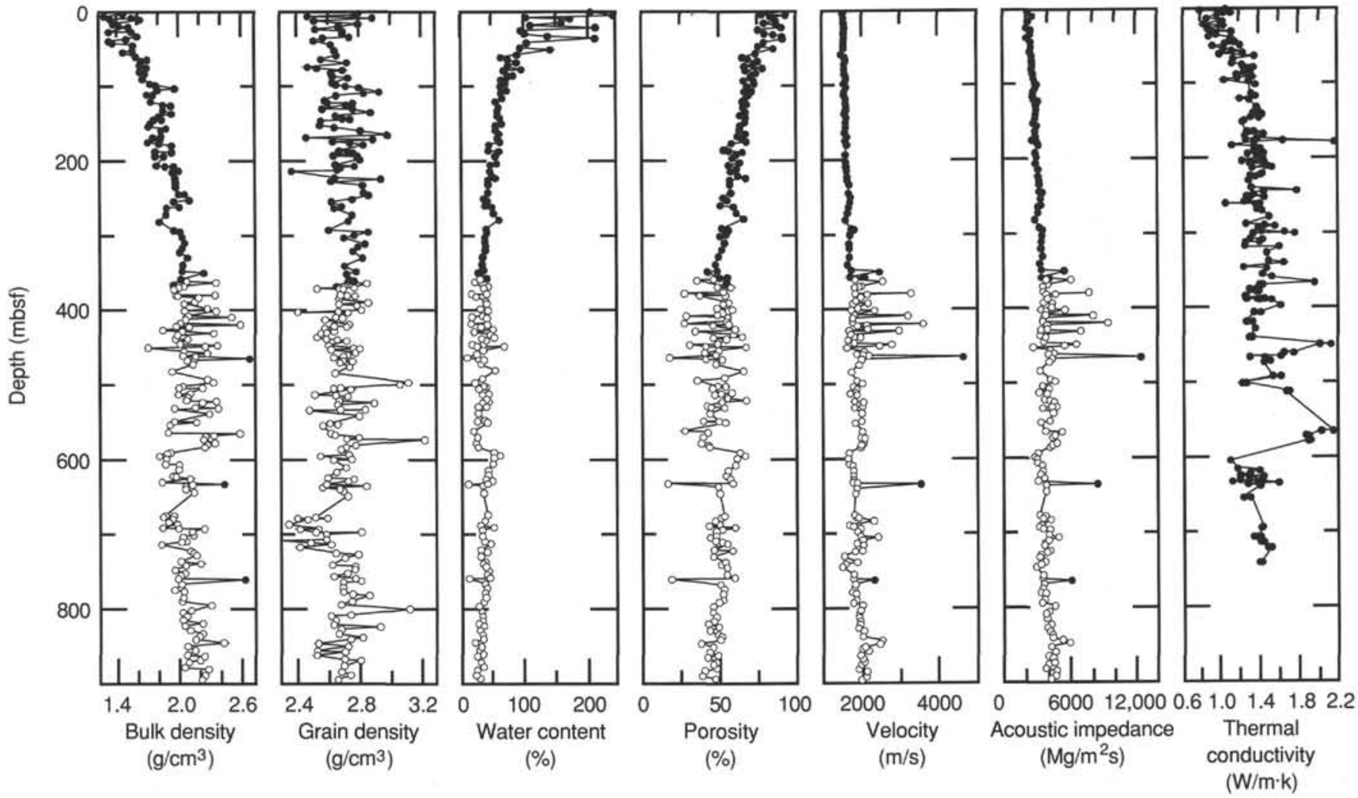

Figure 86. Physical-property data vs. depth for Site 765, including bulk and grain densities, water contents, porosity, compressional-wave velocity, acoustic impedance, and thermal conductivity. Solid circles represent values for basalt pebbles.

"Schlumberger Logs" section, this chapter). The contacts are not preserved. However, no obvious change in grain size occurs in the samples cored. The unit thus has been interpreted as a sill. The geochemical evidence for an intrusive relationship (Sample 123-765C-9R-1, 58–60 cm) is equivocal, as the unit does not significantly differ in zirconium and titanium from the massive basalt flows of Unit 6.

This diabase is gray-green where fresh, and pale reddish-brown and yellow-gray where altered. There are few veins in the diabase, compared to the massive flows.

Rare anhedral to subhedral phenocrysts of clinopyroxene are partially altered to clay minerals; the groundmass is subophitic.

Unit 8: Aphyric Pillow Basalt with Breccia Veins

This pillow basalt unit is differentiated from the underlying pillow units by the presence of pillow-basalt breccia cemented by calcite-filled net veins. Good examples can be seen in Intervals 123-765D-9R-1, 100–120 cm, -9R-2, 40–50 cm, and -9R-2, 90–95 cm. The base of this unit is also distinguished from the underlying pillows by a geochemical break (Fig. 88).

The pillows are light-gray, glassy, microcrystalline and fine-grained basalts. The veining is dominated by calcite, with minor celadonite and iron-oxyhydroxide. Bleached and reddish-brown alteration fronts extend into the basalts surrounding the veins. The fragments of basalt in the breccia do not display chilled margins, thus the breccia is interpreted as of tectonic origin, either by fracture infilling, or *in-situ* brecciation. Petrographically, the breccia fragments are identical to the unbrecciated pillow basalt.

Very small calcite- and celadonite-filled vesicles are present; no phenocrysts were observed.

Unit 9: Aphyric Pillow Basalt and Massive Basalt

The pillow basalts of Unit 9, in Core 123-765D-10R, are distinguished by their lack of brecciated veins and a total lack of phenocrysts (with the exception of the uppermost part of Unit 9). In these units, a gradual decline in zirconium and titanium is seen from Core 123-765D-19R with decreasing depth. This geochemical trend may reflect a change to more primitive magmas in the magma plumbing system (see "Basement Geochemistry" section, this chapter). The 65 m of pillow basalt composing this unit probably reflects periodic eruption of pillow lava. However, the only lithologic subdivision that can be made involves subtle changes in phenocryst content and the degree of autobrecciation.

Most of the pillows are sparsely phyric, with approximately 1% plagioclase phenocrysts and scattered clinopyroxene. Fresh to devitrified glass is preserved in the pillow margins, and pillow cores are fine-grained. Colors are dark to light gray. Green-brown alteration fronts follow celadonite and iron-oxyhydroxide-filled veins, and bleached alteration fronts are associated with calcite veins.

Unit 10: Moderately Plagioclase Phyric Pillow Basalt

Unit 10 is differentiated by the presence of a thin zone of moderately phyric pillow basalts. These are green-brown in color and are heavily veined and altered.

Units 11 to 13: Sparsely Phyric to Aphyric Pillow Basalt and Hyaloclastite

Unit 11 pillow basalts are identical in lithology to those of Unit 9. While few of the pillows were recovered intact, an average size of 30 cm represents a reasonable estimate. Throughout

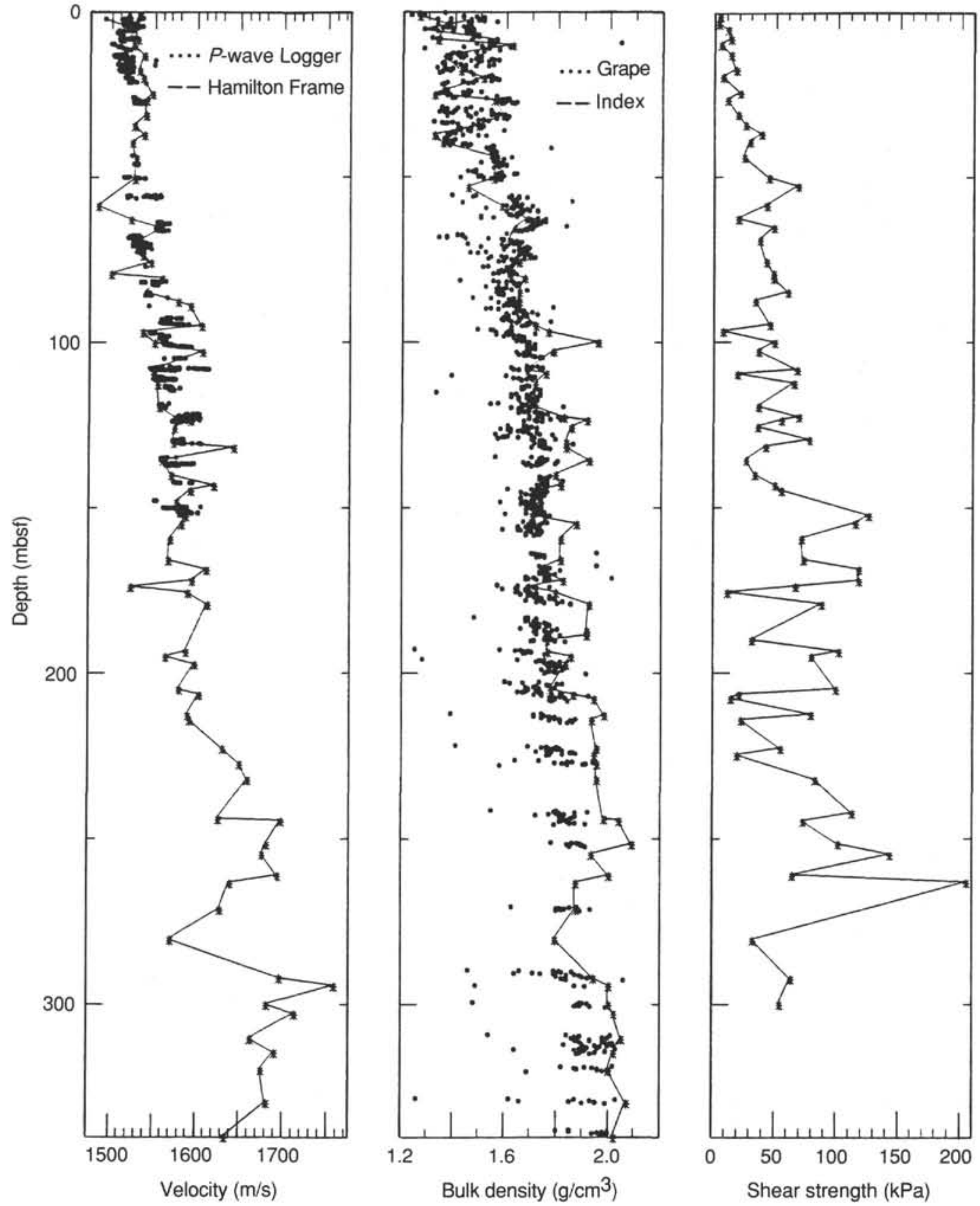

Figure 87. Compressional-wave velocity, bulk density, and shear strength vs. depth of samples from Holes 765A and 765B. Dotted data show *P*-wave logger velocities and GRAPE bulk densities.

Units 9 and 11, phenocryst content varies from sparsely phyric to aphyric. No change in phenocryst content was observed between the more evolved basalts of the lower units and the more primitive basalts of Unit 9.

Unit 12 is differentiated from the other pillow units by the presence of extensive zones of autobrecciation. Hyaloclastite breccia layers of up to 15 cm thick separate the pillow basalts (Fig. 91). The breccias contain fresh glass, devitrified glass, and glass totally altered to celadonite. An altered glass, in Sample 123-765D-16R-1, 39-41 cm, was analyzed from these breccias; the high LOI and K_2O content of this sample attests to the presence of celadonite.

The pillows are veined, and the hyaloclastites are cemented by calcite. Alteration veins of celadonite and iron-oxyhydroxides are comparable to the other pillow units.

Unit 13 is composed of pillow basalts, which are dominantly aphyric and exhibit similar lithological features to the pillows of Units 9 and 11.

Unit 14: Massive Aphyric Basalt Flow

In Section 123-765D-18R-1, we sampled a continous massive flow, which possibly extends as a single thick flow into Core 123-765D-17R. The lower contact of the flow is microcrystalline to glassy, and grain size coarsens toward the top of the core. A few sparse phenocrysts of plagioclase, altered olivine, and fresh clinopyroxene are present. The tops of this flow are characterized by subvertical fractures filled with calcite. Alteration is not extensive, but where veining is present, alteration fronts are comparable to those in other massive lava flows in the section.

Table 28. Vane shear strength data from sediment samples, Hole 765B.

Core, section, interval (cm)	Depth (mbsf)	Shear strength (kPa)
123-765B-1H-1, 100	1.00	3.70
1H-2, 87	2.37	0
1H-2, 95	2.45	0
1H-3, 47	3.47	2.40
1H-4, 73	5.23	10.20
1H-6, 63	8.13	12.20
1H-6, 73	8.23	0
2H-1, 50	9.80	4.30
2H-3, 62	12.92	12.60
2H-6, 71	17.51	16.90
3H-1, 80	19.60	6.30
3H-4, 120	24.50	20.30
3H-6, 20	26.50	10.00
4H-2, 103	31.03	18.30
4H-4, 112	34.12	24.40
4H-6, 95	36.95	37.90
5H-1, 125	39.35	28.40
5H-4, 134	43.94	23.40
6H-2, 98	50.28	43.70
6H-4, 51	52.81	67.20
7H-1, 120	58.60	41.90
7H-4, 73	62.63	18.90
7H-6, 45	65.35	47.80
8H-2, 57	69.17	36.50
8H-5, 50	73.60	0
8H-6, 102	75.62	41.60
9H-2, 86	79.16	47.40
9H-3, 74	80.54	47.40
9H-6, 45	84.75	59.10
10H-1, 103	87.43	32.80
10H-2, 85	88.75	0
10H-6, 82	94.72	44.50
11H-1, 55	96.55	6.60
11H-3, 100	100.00	48.10
11H-5, 69	102.69	35.00
12H-2, 123	108.33	66.40
12H-3, 84	109.44	18.20
12H-5, 84	112.44	64.20
13H-3, 120	119.40	35.00
13H-5, 130	122.50	67.80
13H-6, 72	123.42	54.00
14H-1, 70	125.50	35.00
14H-4, 7	129.37	76.60
14H-5, 65	131.45	41.60
15H-1, 95	135.45	25.50
15H-1, 80	139.80	32.80
15H-6, 100	143.00	48.90
16H-1, 40	144.60	54.00
16H-6, 55	152.25	124.70
17H-1, 64	154.54	113.80
17H-4, 75	159.15	70.70
18H-2, 43	165.53	72.20
18H-4, 94	168.44	116.70
18H-6, 140	171.90	116.70
19X-1, 48	173.78	65.60
19X-2, 60	175.40	10.90
19X-4, 130	179.10	86.80
20X-3, 118	187.18	3.70
20X-4, 83	188.33	3.70
20X-5, 84	189.84	30.60
21X-1, 63	193.33	100.50
21X-2, 67	194.87	78.60
21X-3, 132	197.02	6.60
22X-2, 75	204.65	98.30
22X-3, 96	206.36	20.40
22X-4, 56	207.46	13.80
23X-1, 39	212.49	78.00
23X-2, 35	213.95	21.80
24X-1, 72	222.52	53.90
24X-2, 122	224.52	18.90
24X-4, 81	227.11	0
25X-1, 47	231.97	81.50
26X-1, 81	242.01	112.10
26X-3, 38	244.58	72.10
27X-1, 45	251.35	100.50
27X-3, 69	254.59	142.70
28X-1, 16	260.76	63.70
28X-2, 86	262.96	204.70
30X-1, 41	280.31	31.80
31X-2, 84	291.94	62.50
32X-1, 38	299.68	53.50

Table 29. Thermal conductivity data for sediment samples from Holes 765A, 765B, and 765C.

Core, section, interval (cm)	Depth (mbsf)	Thermal conductivity (W/m · K)
123-765B-1H-1, 40	0.00	0.777
765A-1H-2, 40	1.50	0.812
765B-1H-2, 40	1.50	0.846
765B-1H-3, 40	3.00	0.892
765A-1H-3, 40	3.00	1.064
765A-1H-4, 40	4.50	0.791
765A-1H-5, 40	6.00	1.118
765B-1H-5, 40	6.00	1.054
2H-1, 40	9.30	0.973
2H-3, 40	12.30	0.973
2H-5, 40	15.30	0.874
2H-6, 40	16.80	0.911
3H-1, 40	18.80	1.030
3H-2, 40	20.30	0.896
3H-3, 40	21.80	0.837
3H-4, 40	23.30	1.035
4H-1, 50	28.50	0.895
4H-3, 50	31.50	1.118
4H-4, 50	33.00	0.916
4H-6, 50	36.00	0.963
5H-1, 40	38.10	0.891
5H-3, 40	41.10	1.115
5H-5, 40	44.10	1.095
5H-6, 40	45.60	1.151
6H-1, 40	47.80	1.053
6H-2, 40	49.30	1.213
6H-3, 40	50.80	0.926
6H-3, 40	50.80	0.926
6H-6, 40	55.30	1.040
7H-1, 40	57.40	1.126
7H-3, 40	60.40	1.231
7H-4, 40	61.90	0.990
7H-6, 40	64.90	1.350
8H-2, 40	68.60	1.125
8H-4, 40	71.60	1.123
8H-5, 40	73.10	1.122
9H-1, 45	76.80	1.225
9H-3, 45	79.80	1.341
9H-4, 45	81.30	1.259
9H-6, 45	84.30	1.245
10H-1, 40	86.40	1.306
10H-3, 40	89.40	1.176
10H-5, 40	92.40	1.328
10H-6, 40	93.90	1.174
11H-1, 40	96.00	1.041
11H-3, 40	99.00	1.293
11H-5, 40	102.00	1.362
11H-6, 40	103.50	1.283
13H-1, 60	115.20	1.312
13H-3, 60	118.20	1.351
13H-5, 60	121.20	1.199
13H-6, 60	122.70	1.298
15H-1, 51	134.50	1.371
15H-3, 51	137.50	1.372
15H-5, 51	140.50	1.340
15H-6, 51	142.00	1.428
16H-2, 50	145.70	1.307
16H-3, 50	147.20	1.393
16H-5, 50	150.20	1.242
16H-6, 50	151.70	1.219
18H-2, 50	165.10	1.278
18H-3, 50	166.00	1.337
18H-5, 50	169.00	1.433
18H-7, 50	172.00	1.244
19X-2, 30	174.80	1.375
19X-3, 30	176.30	1.250
19X-4, 30	177.30	2.146
19X-5, 30	179.30	1.337
20X-2, 37	184.50	1.113
20X-3, 37	186.00	1.338
20X-5, 37	189.00	1.396
20X-6, 37	190.50	1.337
21X-2, 50	194.20	1.435
21X-3, 50	195.70	1.276

Table 29 (continued).

Core, section, interval (cm)	Depth (mbsf)	Thermal conductivity (W/m · K)
123-765B-21X-4, 50	197.20	1.414
21X-5, 50	198.70	1.363
22X-1, 36	202.40	1.428
22X-3, 36	205.40	1.217
22X-4, 36	206.90	1.441
22X-5, 36	208.40	1.290
23X-1, 110	212.10	1.480
23X-1, 30	212.10	1.513
23X-2, 110	213.60	1.318
23X-2, 30	213.60	1.466
24X-1, 40	221.80	1.425
24X-2, 40	223.30	1.401
24X-3, 40	224.80	1.296
24X-4, 40	226.30	1.346
25X-1, 50	231.50	1.282
26X-1, 50	241.20	1.304
26X-3, 50	244.20	1.768
26X-4, 50	245.70	1.431
27X-1, 30	250.90	1.325
27X-2, 30	252.40	1.260
27X-3, 50	253.90	1.430
27X-3, 30	253.90	1.290
28X-1, 60	260.60	1.237
28X-1, 33	260.60	1.413
28X-2, 33	262.10	1.051
28X-3, 33	263.60	1.349
29X-1, 50	270.20	1.362
29X-1, 90	270.20	1.389
29X-2, 10	271.70	1.416
30X-1, 30	279.90	1.483
31X-1, 60	289.60	1.252
31X-2, 60	291.10	1.439
31X-3, 60	292.60	1.536
31X-4, 60	294.10	1.369
32X-1, 80	299.30	1.407
32X-1, 120	299.30	1.638
32X-2, 80	300.80	1.739
32X-3, 80	302.30	1.321
33X-1, 50	309.00	1.293
33X-2, 50	310.50	1.417
33X-4, 50	313.50	1.387
33X-5, 50	315.00	1.241
34X-1, 30	318.70	1.235
34X-2, 46	320.16	1.581
35X-1, 30	328.30	1.453
36X-1, 80	337.90	1.478
36X-2, 60	339.40	1.467
36X-3, 50	340.90	1.628
37X-1, 60	347.50	1.218
37X-2, 40	348.70	1.455
38X-1, 60	357.10	1.416
765C-2R-1, 31	359.60	1.510
2R-1, 31	359.60	1.530
765B-39X-1, 60	366.70	1.936
765C-3R-2, 34	370.80	1.410
3R-2, 34	370.80	1.380
765B-40X-1, 10	376.40	1.282
765C-4R-1, 120	379.00	1.350
4R-1, 120	379.00	1.370
765B-41X-1, 15	386.00	1.230
765C-5R-2, 79	390.10	1.350
5R-2, 91	390.10	1.430
5R-2, 110	390.10	1.244
5R-2, 91	390.10	1.360
5R-2, 96	390.10	1.503
6R-1, 91	398.30	1.590
6R-1, 91	398.30	1.570
7R-1, 18	408.00	1.390
7R-1, 18	408.00	1.320
8R-3, 8	420.70	1.250
8R-3, 8	420.70	1.310
9R-3, 88	430.30	1.340
9R-3, 88	430.30	1.330
10R-4, 38	441.00	1.300
10R-4, 38	441.00	1.280
11R-3, 102	449.00	2.100

Table 29 (continued).

Core, section, interval (cm)	Depth (mbsf)	Thermal conductivity (W/m · K)
123-765C-11R-3, 102	449.00	1.990
12R-5, 69	461.20	1.720
12R-5, 69	461.20	1.630
13R-2, 131	466.10	1.600
13R-2, 131	466.10	1.610
13R-3, 0	467.60	1.290
13R-3, 0	467.60	1.472
13R-3, 0	467.60	1.440
14R-1, 35	474.10	1.490
14R-1, 35	474.10	1.420
16R-1, 108	493.20	1.520
16R-1, 108	493.20	1.600
17R-1, 14	502.40	1.200
17R-1, 14	502.40	1.240
18R-2, 134	513.40	1.680
18R-2, 134	513.40	1.640
23R-5, 5	565.70	2.120
23R-5, 5	565.70	2.000
24R-3, 16	572.30	1.870
24R-3, 16	572.30	1.840
25R-1, 21	579.00	1.860
25R-1, 21	579.00	1.880
28R-1, 73	607.00	1.070
28R-1, 73	607.00	1.070
29R-2, 45	617.97	1.149
29R-4, 44	621.02	1.366
29R-6, 43	624.17	1.275
30R-2, 64	627.39	1.246
30R-2, 64	627.39	1.172
30R-3, 38	628.85	1.263
30R-3, 38	628.85	1.409
30R-6, 51	633.29	1.163
30R-6, 51	633.29	1.394
31R-1, 98	635.30	1.358
31R-1, 31	635.30	1.094
31R-2, 47	636.71	1.564
31R-3, 101	638.18	1.257
31R-4, 58	639.61	1.380
33R-2, 30	656.18	1.206
33R-2, 60	656.18	1.275
37R-3, 101	696.00	1.400
37R-3, 101	696.00	1.380
38R-5, 5	708.50	1.380
38R-5, 5	708.50	1.340
38R-5, 5	708.50	1.360
39R-3, 42	714.70	1.410
39R-3, 42	714.70	1.380
40R-2, 95	722.40	1.450
40R-2, 95	722.40	1.490
42R-3, 16	742.80	1.380
42R-3, 16	742.80	1.370

From Unit 14 to the bottom of the hole, saponite replaces celadonite as the dominant clay mineral (see "Basement Alteration" section, this chapter)

Geochemically, these massive flows are not significantly different from the pillow basalts in Units 13 to 9 above, and Unit 15 below.

Units 15 and 16: Aphyric Pillow Basalts

This sequence represents two units of monotonous pillow basalts, extending for 44 m (Section 123-765D-18R-3 through -23R-2). Despite a marked geochemical break at the base of Unit 15 (Core 123-765D-19R), no major lithologic changes are apparent. The pillows are aphyric and sometimes fresh and partly devitrified glass rinds have been preserved. Small brecciated horizons developed between some of the pillows. Poor to average recovery made identification of the size of the pillows difficult. Where bases and tops could be identified, the pillows are 30 to 40 cm thick. In two cases (Sections 123-765D-19R-1 and -22R-1),

Table 30. Depth information for Holes 765C and 765D.

Hole 765C		Hole 765D	
Seafloor:	5727.2 mbsl	Seafloor:	5624.3 mbsl
Basement:	935.8 mbsf	Basement:	924.0 mbsf
Bottom of hole:	963.9 mbsf	Bottom casing shoe:	932.4 mbsf
		Bottom 'rathole':	947.4 mbsf
Drift measurements		Top of first core:	947.9 mbsf
		Bottom of hole:	1194.9 mbsf
400 mbsf 4.0°			
580 mbsf 6.5°		Maximum drift	
777 mbsf 10.0°		1° between 0 and 1194.9 mbsf	
Recovery in basement: 31%		Recovery in basement: 31%	

thicker (60 to 80 cm) structures are identified; these may be thinner massive lavas than have been described above, or large pillows or tubes. These thicker structures are not extensive enough to differentiate as units.

As a whole, Unit 16 is remarkably coherent in geochemistry; this may indicate that the pillows represent a single eruptive episode.

Alteration remains comparable to that identified for the massive and pillowed lavas described above.

Units 17, 18, and 19: Massive Basalt Flows and Pillow Breccias

Section 123-765D-23R-1 marks a change to massive lava flows that are higher in zirconium and titanium than the pillows of Unit 16. Protrusions from Unit 16 intrude the upper part of Unit 17. These flows are sparsely plagioclase phyric and more vesicular than any of the overlying massive flows. The vesicles are up to 2 mm in size, and many are filled with calcite, saponite, and a white zeolite. Most vesicles outside the alteration halos remain unfilled or are lined with a thin layer of secondary minerals. The lava displays alteration fronts parallel to these veins comparable to those described for the massive lavas above.

Unit 17 is distinctly coarser-grained than the other massive flows described in Hole 765D. As for the diabase (Unit 7), no contacts are preserved, and one may consider Unit 17 to be a sill. However, there is no major geochemical break between Unit 17 and the underlying lavas; this favors an interpretation as a massive lava flow.

Unit 18 is a 1-m-thick zone of autoclastic flow-base and flow-top breccia with pillow basalt that separates Units 17 and 19. In Section 123-765D-24R-3, between 50 and 80 cm, angular devitrified glass fragments set in a calcite matrix grade into a hyaloclastite breccia; the latter has been injected by small pillow protrusions, which are chilled and exhibit classic onion-skin delaminations. Pieces of microcrystalline pillow basalt at the base of this hyaloclastite overlie a massive flow that is comparable (except for the presence of slightly more phenocrysts) to that described above for Unit 17.

Unit 19 is described as a massive flow, but it is considerably finer-grained than Unit 18. This flow contains rare plagioclase phenocrysts and has up to 5% vesicles. Apart from a greater vesicularity, the massive flows of Unit 19 are comparable to other fine-grained massive flows in Hole 765D.

Units 20 and 21: Brecciated Sparsely Phyric to Aphyric Pillow Basalts

The transition to Unit 20 represents a relatively abrupt change from massive lava to light gray pillow basalt. This difference is also reflected in the change in slope of the geochemical profile at approximately 1168 mbsf. All of these pillows are brecciated, with the breccia being best developed in Unit 21. The breccias are of tectonic origin, and extensive net-veining by calcite is evident. Spectacular examples can be found in Section 123-765D-25R-1 at 30 to 60 cm (Fig. 92) and in Section 123-765D-27R-1. Fragments do not show any chilled margins, but do display alteration fronts parallel to the fractures. Pillow margins are evident and preserve fresh and partially devitrified basaltic glass.

Breccia zones in Unit 21 are made up of broken pillow fragments cemented by calcite. These breccias show less distinct net-veining than those in Unit 20, and may represent cemented talus or fragments fallen into a fracture.

In the pillow lavas, plagioclase phenocrysts are rare and vesicles scarce. Veins are dominated by calcite, and alteration fronts result in bleached zones in the basalts.

Unit 22: Massive Aphyric Basalt Flows

The final unit cored in Hole 765D is a massive aphyric basalt. The flow displays a gradation from microcrystalline to fine-grained holocrystalline basalt from its margins to its center. Vesicles are comparable in size and abundance to those in Unit 17.

Alteration is identical to that described for massive lavas higher in the section, with the exception of iron-oxyhydroxides, which are less abundant at the base of the hole. All of the units described for Holes 765C and 765D are within a zone of low-temperature alteration.

BASEMENT PETROGRAPHY

This section is divided into two parts: Part 1 deals with the basalts that make up the acoustic basement and Part 2 deals with pebbles of volcanic rocks encountered at various levels in the sedimentary section.

Site 765 Basement

A total of 68 thin sections of the basement rocks obtained at Site 765 were described. Results of mineral identification and various petrographic determinations for these samples are listed in Table 32 and are summarized with lithostratigraphic information in Figure 93.

Phenocrysts

The basement rocks recovered in Holes 765C and 765D are predominantly aphyric, and phenocryst contents are 1 vol% or less in 60 out of 68 samples. Four samples are sparsely phyric (1.1% to 2.0%), two samples are moderately phyric (2.1% to 10.0%), and only two samples are highly phyric (12.8% and 31.3%). The "phenocrysts" (mostly plagioclase) in the highly phyric samples (Samples 123-765D-8R-1, 37–39 cm, and -23R-2, 64–66 cm) are actually coarse-grained subophitic patches representing a slow-cooling magma; they thus are different from phenocrysts in the glassy basalts. Plagioclase, clinopyroxene, and olivine appear as phenocrysts in decreasing order of abundance. Fifteen samples (23%) bear clinopyroxene phenocrysts with or without plagioclase phenocrysts. This is an unusually high frequency of clinopyroxene phenocrysts for ocean-floor basalts. Two samples are plagioclase-olivine-clinopyroxene-phyric, suggesting a cotectic composition for the magma. Thirty-one samples are purely plagioclase-phyric. Ten samples bear both olivine and plagioclase phenocrysts together, while purely olivine-phyric samples are absent. The remaining 12 samples are completely aphyric. The phenocryst assemblage changes with depth (Fig. 93). Clinopyroxene commonly appears in the upper part of the basement section (Cores 123-765C-62R to -65R and 123-765D-1R to -10R), but is rare in the lower part (Cores 123-765D-11R to -27R). In contrast, olivine phenocrysts are rare in the upper part, but more common in the lower part.

Plagioclase phenocrysts are generally 1 mm in size, subhedral and tabular, with simple Carlsbad or albite twinning and weak concentric compositional zoning. Their cores are mostly replaced by zeolite and/or clay minerals, although their rims

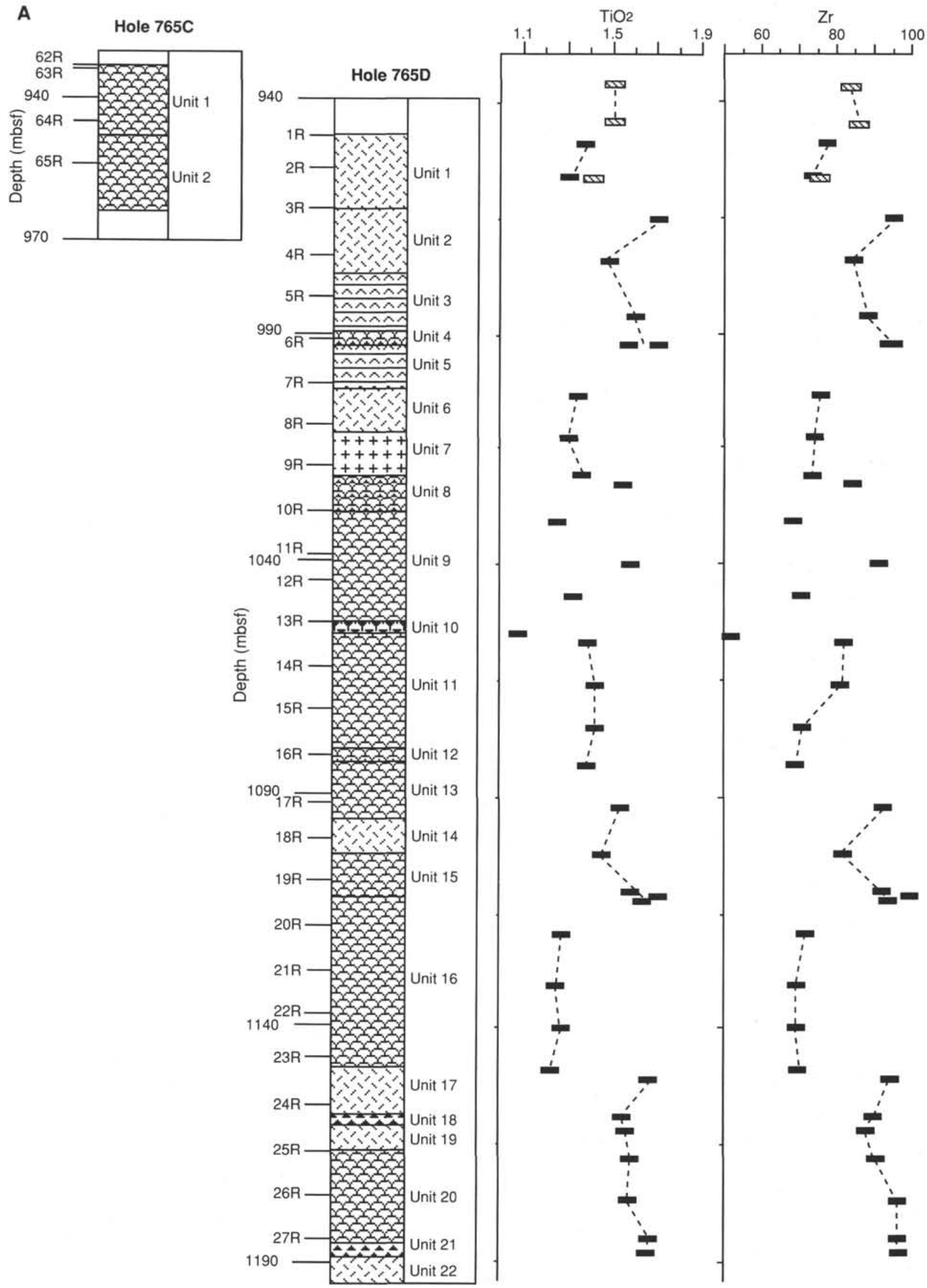

Figure 88. A. Variation in zirconium and TiO_2 (wt.5%) with depth in basaltic rocks in Hole 765D (solid bars) and Hole 765C (hatched bars). Samples belonging to a geochemical unit have been joined by lines. B. Lithostratigraphic column for basement section in Holes 765C and 765D. Scale is 1/1000.

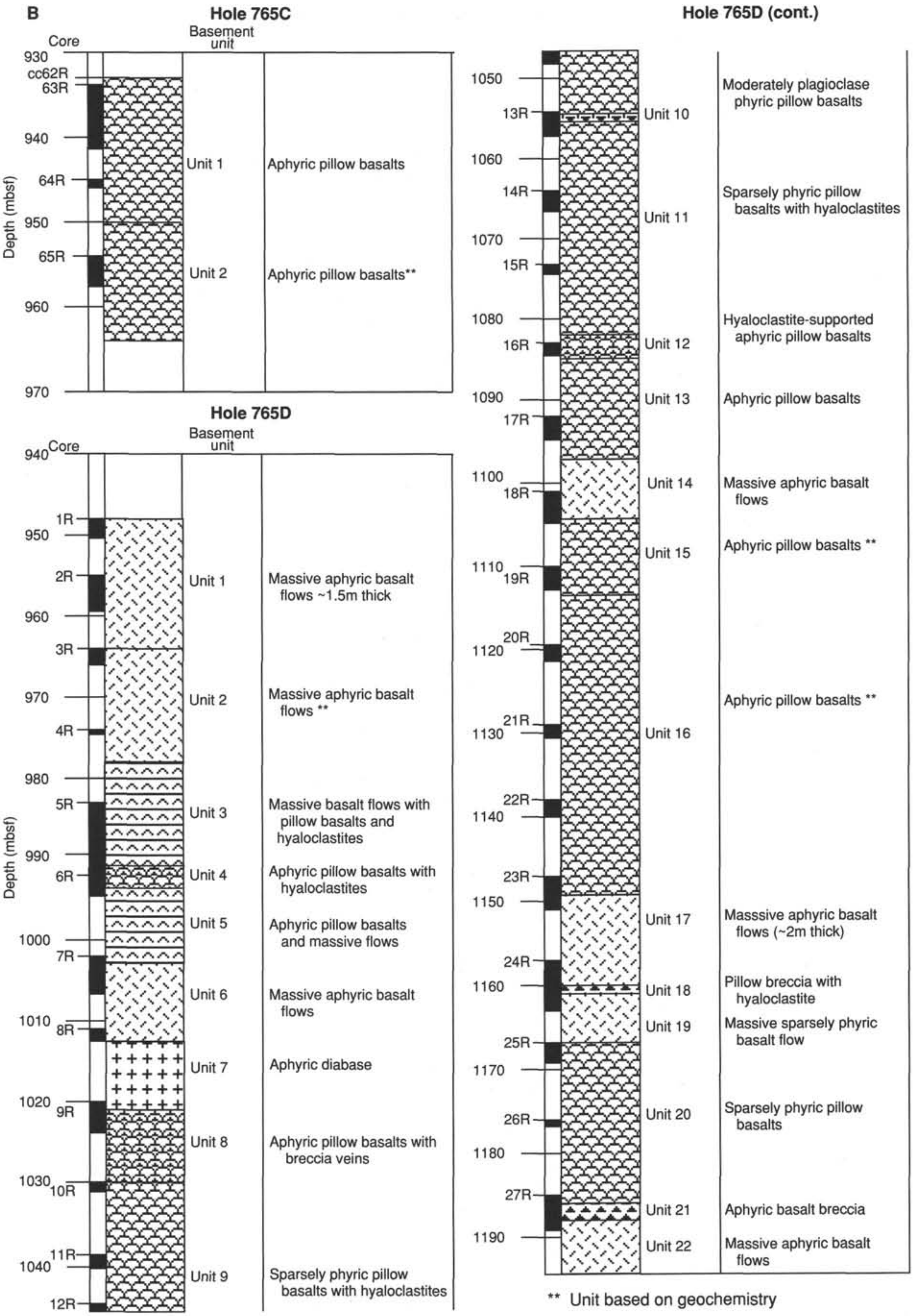

Figure 88 (continued).

Table 31. Limits and descriptions of lithologic units of Site 765 basement.

Hard rock lithologic unit	Description/sample (cm)
Hole 765C	
Unit 1	Aphyric pillow basalt
	(top) 123-765C-62R-4, 26 (Piece 1)
	(bottom) 765C-64R-1, 37 (Piece 2)
(A)	Hyaloclastite
	-62R-4, 26 (Piece 1)/-62R-4, 30 (Piece 1)
(B)	Altered pillow basalt
	-62R-CC, 0 (Piece 1A)/-62R-CC, 28 (Piece 1C)
(C)	Fresh pillow baslt
	-63R-1, 0 (Piece 1)/-63R-2, 10 (Piece 1)
(D)	Pillow basalt with hyaloclastite at the top
	-63R-2, 11 (Piece 2)/-63R-3, 118 (Piece 8B)
(E)	Pillow basalt with hyaloclastite at the top
	-63R-3, 119 (Piece 9)/-63R-5, 101 (Piece 11)
(F)	Massive basalt
	-64R-1, 0 (Piece 1)/-64R-1, 36 (Piece 2)
Unit 2	Aphyric pillow basalt
	(top) 765C-64R-1, 38 (Piece 3)
	(bottom) 765C-65R-2, 133 (Piece 10)
(A)	Massive basalt
	-64R-1, 38 (Piece 3)/-64R-1, 58 (Piece 3)
(B)	Pillow basalt
	-65R-1, 0 (Piece 1)/-65R-2, 102 (Piece 7)
(C)	Plagioclase-phyric pillow basalt
	-65R-2, 103 (Piece 8)/-65R-2, 113 (Piece 8)
(D)	Pillow basalt
	-65R-2, 114 (Piece 9A)/-65R-2, 134 (Piece 10)
Hole 765D	
Unit 1	Massive aphyric basalt
	(top) 765D-1R-1, 8 (Piece 3)
	(bottom) 765D-2R-4, 60 (Piece 7)
Flow A	-1R-1, 8 (Piece 3)/-1R-2, 117 (Piece 5)
Flow B breccia	-1R-2, 130 (Piece 7)/-2R-2, 69 (Piece 1E)
Flow C rubble	-2R-2, 82 (Piece 5A)/-2R-4, 5 (Piece 1)
Unit 2	Massive aphyric basalt
	(top) 765D-3R-1, 0 (Piece 1)
	(bottom) 765D-4R-1, 62 (Piece 8)
Flow A	-3R-1, 0 (Piece 1)/-3R-1, 54 (Piece 4C)
Flow B	-3R-1, 55, (Piece 5A)/-3R-1, 82 (Piece 5B)
Flow C	-3R-1, 83 (Piece 6A)/-3R-1, 140 (Piece 9)
Flow D	-3R-1, 141 (Piece 10)/-4R-1, 62 (Piece 8)
Unit 3	Massive aphyric basalt and pillows
	(top) 765D-5R-1, 0 (Piece 1)
	(bottom) 765D-5R-8, 25 (Piece 2)
Flow A (pillows)	-5R-1, 0 (Piece 1)/-5R-1, 62 (Piece 6C)
Flow B	-5R-1, 63 (Piece 7)/-5R-4, 20 (Piece 4)
Flow C (pillows)	-5R-4, 28 (Piece 6A)/-5R-4, 55 (Piece 7C)
Flow D	-5R-4, 56 (Piece 8)/-5R-8, 25 (Piece 2)
Unit 4	Aphyric pillow basalt and hyaloclastite
	(top) 765D-5R-8, 26 (Piece 3)
	(bottom) 765D-6R-1, 103 (Piece 8)
Unit 5	Aphyric massive basalt flows
	(top) 765D-6R-1, 105 (Piece 9)
	(bottom) 765D-7R-1, 72 (Piece 3)
Flow A	-6R-1, 105 (Piece 9)/-6R-2, 44 (Piece 3)
Flow B	-6R-2, 45 (Piece 4A)/-7R-1, 72 (Piece 3)
Unit 6	Massive aphyric basalt
	(top) 765D-7R-1, 73 (Piece 4)
	(bottom) 765D-8R-1, 90 (Piece 6)
Unit 7	Aphyric diabase
	(top) 765D-8R-1, 91 (Piece 7)
	(bottom) 765D-9R-1, 99 (Piece 11)
Unit 8	Aphyric pillow basalt with breccia veins
	(top) 765-9R-1, 100 (Piece 2A)
	(bottom) 765D-9R-3, 94 (Piece 10)
Unit 9	Aphyric pillow basalt and massive basalt
	(top) 765D-10R-1, 0 (Piece 1)
	(bottom) 765D-12R-2, 147 (Piece 16)
Unit 10	Moderately phyric pillow basalt
	(top) 765D-13R-1, 0 (Piece 1)
	(bottom) 765D-13R-1, 66 (Piece 6B)
Unit 11	Aphyric pillow basalt and hyaloclastite
	(top) 765D-13R-1, 67 (Piece 7)
	(bottom) 765D-15R-2, 44 (Piece 5)

Table 31 (continued).

Hard rock lithologic unit	Description/sample (cm)
Hole 765D	
Unit 12	Aphyric pillow basalt and hyaloclastite
	(top) 765D-16R-1, 0 (Piece 1A)
	(bottom) 765D-16R-1, 146 (Piece 13B)
Unit 13	Aphyric pillow basalt
	(top) 765D-16R-2, 0 (Piece 1)
	(bottom) 765D-17R-3, 72 (Piece 5)
Unit 14	Massive aphyric basalt flow
	(top) 765D-18R-1, 0 (Piece 1A)
	(bottom) 76D-18R-1, 129 (Piece 3)
Unit 15	Aphyric pillow basalts
	(top) 765D-18R-1, 130 (Piece 4)
	(bottom) 765D-19R-2, 138 (Piece 11)
Unit 16	Aphyric pillow basalts (partly intrusive into Unit 17)
	(top) 765D-20R-1, 0 (Piece 1)
	(bottom) 765D-23R-1, 94 (Piece 6)
Unit 17	Massive basalt flow and pillow breccia
	(top) 765D-23R-1, 95 (Piece 7)
	(bottom) 765D-24R-3, 43 (Piece 1C)
Flow A (vesicular)	-23R-1, 95 (Piece 7)/-23R-2, 115 (Piece 5B)
Flow B	-24R-1, 0 (Piece 1A)/-24R-3, 48 (Piece 2)
Unit 18	Massive basalt flow and pillow breccia
	(top) 765D-24R-3, 44 (Piece 2)
	(bottom) 765D-24R-3, 123 (Piece 9)
Unit 19	Massive basalt flow and pillow breccia
	(top) 765D-24R-4, 0 (Piece 1A)
	(bottom) 765D-24R-5, 92 (Piece 5)
Unit 20	Brecciated aphyric pillow basalt
	(top) 765D-25R-1, 0 (Piece 1)
	(bottom) 765D-27R-1, 25 (Piece 2)
Unit 21	Brecciated aphyric pillow basalt
	(top) 765D-27R-1, 26 (Piece 3)
	(bottom) 765D-27R-1, 108 (Piece 13)
Unit 22	Massive aphyric basalt
	(top) 765D-27R-1, 109 (Piece 14)
	(bottom) 765D-27R-3, 145 (Piece 16)

and groundmass plagioclase remain fresh. Clinopyroxene phenocrysts are approximately 0.5 mm in size and highly variable in shape: euhedral hexagons with remarkable sector and/or concentric zoning (Fig. 94); subhedral or anhedral irregular forms, or anhedral well-rounded forms with simple twinning (Fig. 94). These phenocrysts are augite with 2V(+) at 40°. Olivine phenocrysts have been mostly replaced by "iddingsite," green clay minerals, or calcite. They are up to 1 mm in size, and sometimes include tiny spinels, which are mostly replaced by hematite. Fresh euhedral olivine phenocrysts up to 1 mm in size and partly embayed by the surrounding glass occur in some pillow rims in the upper units of the basement (Samples 123-765C-63R-1, 122–124 cm, and -5R-1, 56–58 cm). These are forsterite with 2V(+) at 85°.

Groundmass

Regular variations of texture, crystallinity, and grain size of the groundmass are evident from the center to the margin of every pillow or lava flow in the recovered basement. The texture changes inward from glassy (Fig. 95, groundmass) through spherulitic and hyalo-ophitic (Fig. 94) to intersertal or intergranular. Sample 123-765D-5R-1, 56–58 cm, provides an excellent example of the textural change at a pillow rim. Some samples from pillow (or flow) margins show hyalopilitic texture with marked alignment of plagioclase laths and with their long axes parallel to flow lines. The thick flows or sills in Cores 123-765D-8R to -9R and in Core 123-765D-24R show a holocrystalline and subophitic texture with variolitic tendency (Fig. 96). The groundmass crystallinity ranges from 0% to 100%, with end-members represented by fresh glass at pillow rim and the holocrystalline diabase sill. Average grain size of plagioclase laths in the pillow (or thin flow) cores generally ranges from 0.1 to 0.3 mm, depending on the size of the pillow (or flow), but is not greater than 0.4 mm. Plagioclase laths in the thick flows or sills (>1 m) are coarser, and their average size ranges from 0.5 to 1.2 mm (Fig. 96).

Vesicularity is poor, and vesicles occupy less than 0.5 vol% in one-half of the samples. Samples containing more than 1 vol% vesicles constitute only 20% of the total. The most vesicular basalt occurs as a massive flow of Core 123-765D-27R, which includes 8 vol% vesicles. Some pillows (or thin flows) of Cores 123-765D-20R and -22R are also vesicular (4%–5%). Vesicles are filled by green clay minerals or calcite, and are sometimes filled by hematite near the oxidation halos along fractures. Vesicles in Section 123-765D-2R-2 are filled predominantly by zeolites. Vesicle-filling clays and zeolites often exhibit remarkable radial texture and concentric zonal structure. The center of large vesicles often remains void, especially in the massive flows in Cores 123-765D-23R and -27R. Sample 123-765D-23R-2, 64–66 cm, bears chondrulelike, spherical "segregation vesicles," 1 to 1.5 mm in size, closely resembling their counterparts reported from Atlantic ocean-floor basalts (Sato, 1978 and references therein). These vesicles are composed of brown iron- and titanium-rich clinopyroxene dendrites, with ilmenite and plagioclase needles showing marked quench texture. Many segregation vesicles had central voids that are now filled by pale green clay minerals.

Secondary minerals, which make up only a few percent of the rock, are green clay, calcite, zeolite, and hematite (or iron hydroxide) and replace plagioclase, olivine, glass, and mesostasis, as well as filling vesicles and fractures. The percentage of secondary minerals increases to 10% or 20% in alteration halos

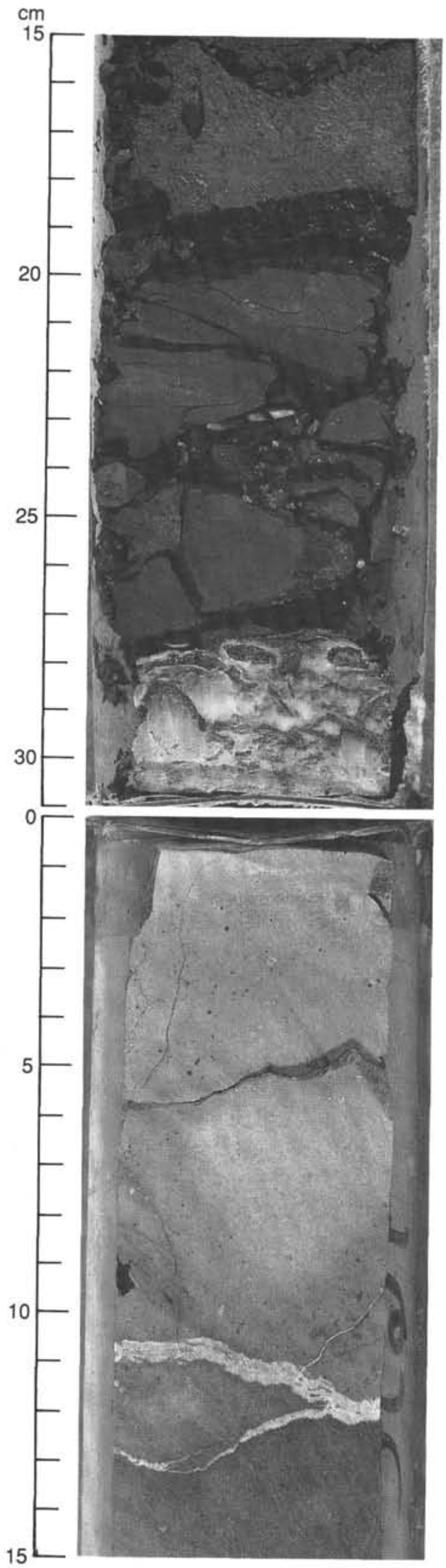

Figure 89. Contact of red-brown claystone with pillow basalt of Unit 1 in Hole 765C. The basalt is bleached by pervasive carbonate alteration and overlain by a hyaloclastite breccia. Note the alteration halo associated with horizontal calcite vein in the bottom of the picture (Intervals 123-765C-62R-4, 15–31 cm, and 123-765C-62R-CC, 1–15 cm).

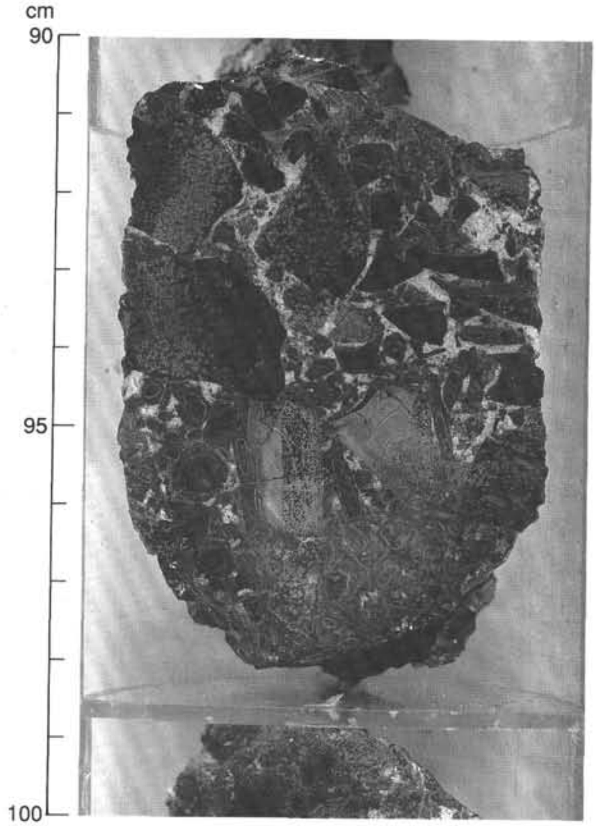

Figure 90. Hyaloclastite breccia, made up of fresh and partly devitrified glass with a sparry calcite cement (Interval 123-765D-5R-8, 90–100 cm).

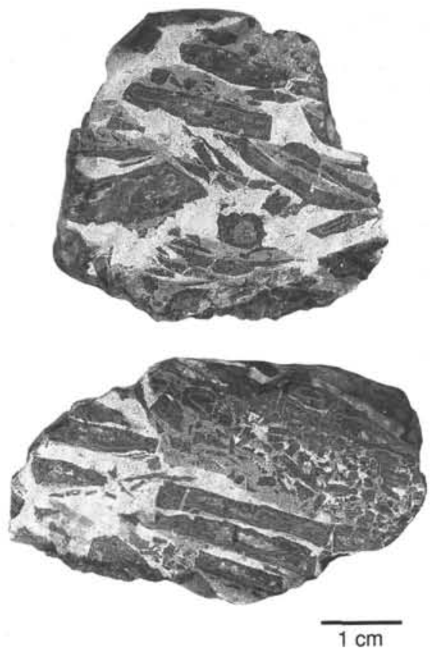

Figure 91. Hyaloclastite breccia, composed of partly divitrified glassy pillow fragments (elongate) and breccia fragments (angular). The fragments are cemented by sparry calcite, and the glass altered to a celadonite-smectite assemblage. Note that the pillow fragments represent "onion-skin" delamination from a pillow margin (Interval 123-765D-14R-1, 1–7 cm).

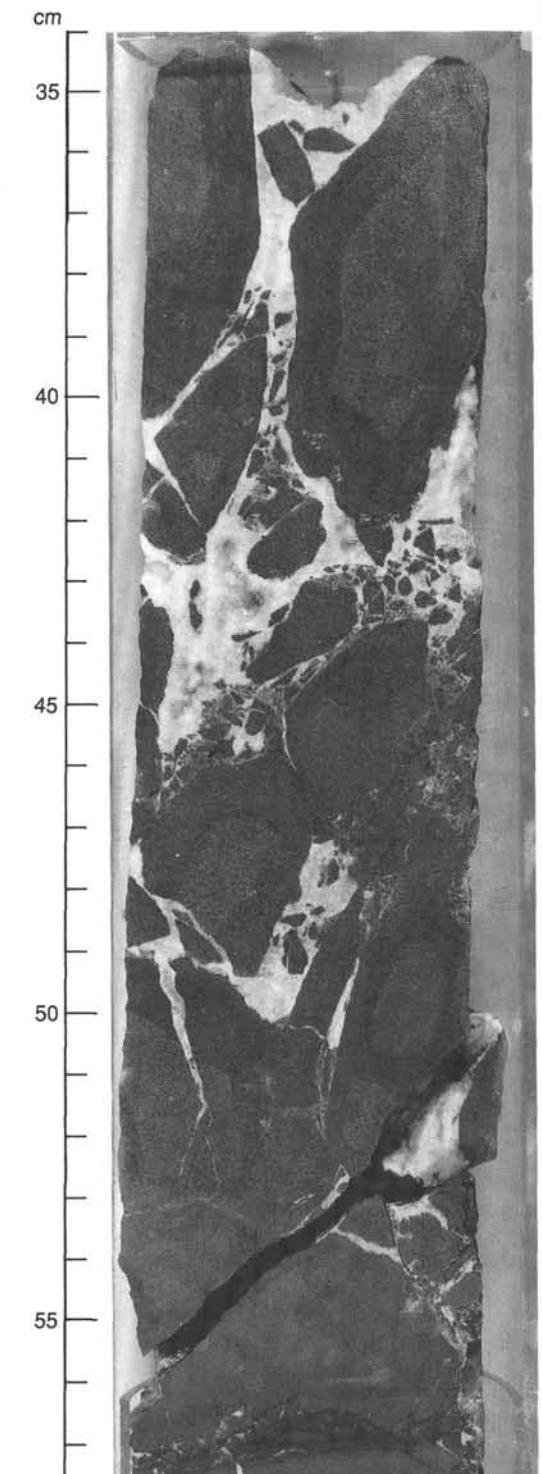

Figure 92. Tectonic breccia in pillow lavas. The brecciated pillow fragments did not exhibit chilled margins, and represent broken fragments in a fracture that have been cemented by calcite. Note the alteration fronts associated with the calcite pillow lava contacts (Sample 123-765D-25R-1, 34–59 cm).

along fractures. The topmost part of the basement (Section 123-765C-62R, CC) and some glassy fragments in hyaloclastites are 80% to 100% altered. Zeolite occurs as subhedral, bulky, optically isotropic crystals in a matrix of altered hyaloclastite (Samples 123-765D-6R-1, 16–18 cm, and -16R-1, 39–42 cm). Fracture-filling veins sometimes are zoned, with calcite occupying the center of the vein. Sample 123-765D-63R-4, 90–92 cm, a breccia vein in a pillow core, bears radial aggregates of length-slow chalcedony(?).

Xenocrysts and Xenoliths

Plagioclase xenocrysts, 2 mm in size, and gabbroic or diabasic xenoliths, 5 to 7 mm in size, frequently occur in the top part of the basement section (Cores 123-765C-63R, -1R, -2R, and -5R). Plagioclase xenocrysts generally exhibit remarkable concentric zoning and complex twinning, and sometimes occur as glomerocrysts. Their shape tends to be equant or thick tabular and different from thin tabular or bladed phenocrysts. Gabbroic xenoliths exhibiting coarse-grained cumulate texture are found in volcanic glass at a pillow rim (Sample 123-765C-63R-1, 122–124 cm). Small, anhedral clinopyroxene(?) crystals and basaltic glass fill the interstitial voids between 5-mm-sized, zoned, euhedral or subhedral plagioclase tablets (Fig. 95). These xenocrysts may simply be smaller fragments of such xenoliths. A diabase xenolith, 7 mm in size, was found in a glassy pillow margin (Sample 123-765C-2R-2, 88–90 cm). This xenolith is composed of a single clinopyroxene oikocryst that includes many euhedral plagioclase laths and exhibits a typical ophitic texture (Fig. 97). Some of the peripheral laths are detached from the xenolith and appear similar to ordinary phenocrysts. A similar ophitic "clot" was reported by Sato et al. (1978, p. 141) from the Mid-Atlantic Ridge, 14°N (DSDP Leg 46). The restricted occurrence of such xenocrysts and xenoliths in the topmost levels of the basement section (Fig. 93) suggests rapid and turbulent ascent of the magma through a mostly solidified magma chamber during the last stage of volcanism at this site.

Pebbles of Volcanic Rocks From the Sedimentary Section, Site 765

More than 100 pebbles of volcanic rocks were found in 23 out of 103 cores from the sedimentary section in Holes 765B and 765C. One basalt pebble was found in the top of Core 123-765D-1R with some sandstone pebbles. The position, occurrence, visual lithology, and microscopic features of these pebbles are listed in Table 33. A summary of petrographic data for 27 samples is given in Table 34, and geochemical data for five samples are presented in Table 35.

Occurrence

Pebbles of volcanic rocks are mostly 2 or 3 cm in size and subangular to well-rounded in form; the largest sample is 14 cm long and wider than the core barrel. All four pebbles in Hole 765B and pebbles from Hole 765C, Cores 123-765C-13R, -19R, -23R and -24R, indicate an apparent *in-situ* occurrence, as they are completely included in the sediments with molded contacts. The sediments, including the *in-situ* pebbles, range from Late Cretaceous to Pliocene in age. Most pebbles from the lower part of Hole 765C and the top of Hole 765D occur as drill breccia at the top of each core. The latter may have fallen from conglomerate beds situated in the upper sections of the hole and have no stratigraphic significance. A considerable number of these pebbles are well-rounded or subrounded, which suggests that their travel was either by subaerial river flow or by submarine turbidity flow. Pebbles of volcanic rocks are generally associated with pebbles of sedimentary rocks, such as sandstone (Sample 123-765B-11H-7, 23–24 cm), siltstone (Sample 123-765B-12H-1, 90–92 cm), ferruginous sandstone (Sample 123-765B-31X-1, 151–

Table 32. Petrographic data of basement basalts, Holes 765C and 765D.

Sample (core-section, cm)	Unit	Texture	Occurrence	Phenocrysts Ol (%)	Phenocrysts Pl (%)	Phenocrysts Cp (%)	Phenocrysts Sp (%)	Groundmass Crys (%)	Groundmass Size (mm)	Groundmass Relic	Altr. (%)	Vesicles (%)	Rem.
Hole 765C Basement basalts													
62R-4, 27–30	1	Gls	Hy	—	—	—	—	0	—	—	100	—	Vein
62R-CC, 1–3	1	Gls	PR	—	—	—	—	1	0.3	—	100	2.0	
62R-CC, 23–25	1	Hyo	PM	—	0.8	—	tr.?	5	0.2	—	97	2.0	
63R-1, 122–124	1	Gls	PR	0.3?	2.4	—	0.2	4	0.3	01, Cp Gl	77	0.5	Plxx XRF
63R-2, 111–114	1	Ins	PC	—	0.2	—	—	83	0.3	Cp	11	0.2	
63R-3, 133–135	1	Hyo	PM	—	0.2	0.2	—	3	0.2	Cp	2	1.0	
63R-4, 90–92	1	Ins	PB	—	—	—	—	55	0.3	Cp	5	0.7	Vein
63R-4, 97–99	1	Ins	PC	—	0.9	—	—	67	0.3	Cp	10	0.2	Plxx
64R-1, 2–4	1	Ins	PC	—	0.8	—	—	90	0.4	Cp	11	0.8	XRF
65R-1, 96–98	2	Ins	PC	—	0.7	0.1	—	35	0.3	Cp	—	5	0.5
65R-2, 106–108	2	Hyo	PB	—	0.2	0.2	—	4	0.3	Cp	12	0.6	XRF
65R-2, 130–132	2	Ing	PC	—	0.3	—	—	92	0.2	Cp	3	1.0	
Hole 765D Basement basalts													
1R-1, 106–108	1	Ing	FC	—	0.7	0.5	—	70	0.3	Cp	5	0.9	xx
2R-2, 31–33	1	Ing	FC	—	—	—	—	85	0.3	Cp	9	1.2	XRF Hem
2R-2, 88–90	1	Hyo	FM	—	0.5	1.0	—	17	0.1	Cp	6	0.4	xx
2R-3, 89–91	1	Ins	FC	—	0.5	1.0	—	50	0.1	Cp	6	0.9	Zeol
2R-4, 2–4	1	Gls	PR	—	0.2	—	—	5	0.1	Cp	22	1.0	Zeol
3R-1, 35–37	2	Ing	FC	—	—	0.5	—	70	0.3	Cp	6	0.4	XRF
4R-1, 35–37	2	Ins	FC	—	0.3	—	—	50	0.3	Cp	2	0.1	Vein XRF
5R-1, 56–58	3	Gls	PM	0.4	0.3	—	—	1	—	Ol	10	1.4	Spher
5R-3, 131–133	3	Ing	FC	—	0.3	—	—	70	0.2	Cp	13	—	XRF
5R-8, 117–120	4	Gls	PR	—	0.4	0.2	—	2	0.2	Cp	0	—	XRF spher
6R-1, 16–18	4	Gls	Hy	—	0.3	0.5	—	1	—	Cp	99	—	
6R-1, 49–51	4	Hyo	PC	—	—	—	—	6	0.2	Cp	4	0.2	XRF
7R-2, 9–11	5	Hyo	FC	—	0.5	—	—	6	0.2	Cp	4	1.2	XRF
8R-1, 37–39	6	[a]Ins	FC	—	[a]12.8	[a]1.0	—	50	0.3	Cp	5	1.6	Patchy
8R-1, 111–114	7	sOp	SC	—	—	—	—	100	1.2	Cp	2	—	
9R-1, 38–40	7	sOp	SC	—	—	—	—	100	1.2	Cp	7	—	
9R-1, 107–109	8	Hyo	FC	0.5?	tr.	—	—	26	0.3	Cp	1	0.5	
9R-3, 17–19	8	Hyo	FC	—	0.2	0.2	—	8	0.3	Cp	3	1.0	
10R-1, 81–83	9	Ins	PB	—	1.0	0.1	—	46	0.3	Cp	2	0.3	XRF
11R-1, 43–45	9	Ins	FC	—	0.5	—	—	29	0.3	Cp	12	0.4	Hem
12R-2, 13–15	9	Ins	FC	—	0.5	—	—	31	0.2	Cp	11	0.4	XRF
13R-1, 18–21	10	Hyp	FC	—	8.3	—	—	18	0.3	—	5	0.3	XRF
13R-3, 10–12	11	Gls	PM	—	1.0	—	—	4	0.2	Cp	3	0.6	XRF
14R-2, 51–53	11	Hyo	PC	—	0.5	—	—	22	0.3	Cp	8	0.3	XRF
15R-2, 17–20	11	Ins	FC	—	0.3	—	—	85	0.3	Cp	15	0.2	XRF
16R-1, 39–42	12	Gls	Hy	—	0.2	—	—	0	—	—	[b]100	—	XRF
16R-1, 58–60	12	Gls	PB	—	0.9	—	0.2?	3	0.1	(CP)	1	—	Spher.

153 cm), and clayey ironstone with 87 wt% Fe_2O_3 (Sample 123-765C-19R-1, 46–47 cm).

Visual Lithology

Pebbles of volcanic rocks are mostly yellow brown or red brown, and are fine-grained or microcrystalline; some are dark gray or grayish green and seem fresher than the brownish ones. These pebbles, especially the rounded ones, have a 5-mm-thick weathered crust of a more reddish color. Highly vesicular pebbles are rare, and no pebble has been cut by veins. The phyric and aphyric pebbles are about equal in number, and the phenocrysts are olivine and/or plagioclase. Except for one pebble of diabase, the pebbles are of low crystallinity.

Microscopic Observation

Results of petrographic observations are listed in Table 34. Despite strong weathering and/or alteration, original igneous textures are evident in all of the 27 thin sections. Hyalophitic and hyalopilitic textures of less than 20% crystallinity were observed in 12 samples, with one sample including fresh volcanic glass (Sample 123-765B-31X-1, 151–153 cm), 14 samples displaying an intersertal texture of 25% to 60% crystallinity, and one sample showing a holocrystalline, subophitic texture. Three samples exhibit variolitic tendency. Dominance of the low-crystallinity textures and the occurrence of fresh glass suggest their origin in submarine lava flows, probably pillow lavas or thin flows.

Olivine and plagioclase are the only observed phenocrysts. Clinopyroxene phenocrysts are absent. Tiny chromian spinel crystals are commonly included in olivine phenocrysts, but independent spinel microphenocrysts are rare. The volume of total phenocrysts is less than or equal to 1% in 17 samples, 1% to 2% in two samples, 2% to 5% in four samples, and 5% to 10% in four samples. Aphyric basalts are more abundant than sparsely phyric basalts.

Because of weathering, alteration, and low crystallinity, preservation of primary mineralogy is poor. Plagioclase is partly preserved in most samples, but relict spinel was found in only five samples. Clinopyroxene was observed in the groundmass of two samples and olivine in only one sample. Fresh spinel is transparent and brown, suggesting that it is poor in titanium and trivalent iron, as well as having a moderate chromium content. Groundmass clinopyroxene is colorless, suggesting its crystallization from subalkaline magma.

The percentage of alteration minerals is highly variable and averages 35%. Bright green, yellow green, or yellow brown clays

Table 32 (continued).

Sample (core-section, cm)	Unit	Tex-ture	Occur-rence	Phenocrysts Ol (%)	Pl (%)	Cp (%)	Sp (%)	Groundmass Crys (%)	Size (mm)	Relic	Altr. (%)	Vesi-cles (%)	Rem.
Hole 765D Basement basalts													
16R-2, 11–13	13	Ins	FC?	0.5	0.2	—	—	74	0.1	Cp	5	—	Patchy
17R-1, 37–39	13	Gls	PR?	0.3	0.5	0.2	—	3	0.1	Cp	1	0.6	Spher. XRF
17R-3, 9–11	13	Ins	PC	—	—	—	—	50	0.2	Cp	3	0.4	Patchy
18R-1, 3–7	14	sOp	FC	—	0.3	—	—	80	0.5	Cp	4	0.1	Patchy
18R-1, 112–114	14	Ins	FM	—	0.5	—	—	36	0.1	Cp	2	—	XRF
18R-1, 8–10	15	Hyo	FC	0.3	0.4	—	—	15	0.1	Cp	4	0.2	
19R-1, 51–52	15	Gls	PC	0.5	1.0	—	—	2	0.1	Cp	1	0.3	Spher. XRF
19R-1, 108–110	15	Ins	FC	—	0.2	—	—	75	0.2	Cp	5	0.9	XRF
19R-2, 32–34	15	Ing	FC	—	0.3	—	—	85	0.3	Cp	10	2.0	XRF
19R-2, 71–73	15	Ing	FC?	—	0.2	—	—	90	0.6	Cp	6	0.7	
20R-1, 14–16	16	Hyp	PM?	—	0.5	—	—	15	0.2	—	5	4.0	XRF
20R-1, 47–49	16	Ins	FC	0.2	0.5	0.3	—	54	0.2	Cp	4	—	
21R-1, 117–119	16	Ins	FC	—	0.4	—	—	28	0.2	Cp	2	0.1	XRF
21R-1, 86–89	16	Ins	FC	—	—	—	—	55	0.2	Cp	4	0.5	Patchy
22R-1, 83–85	16	Hyo	FC	—	0.4	—	—	22	0.3	Cp	8	5.0	
22R-1, 118–121	16	Ins	FC	—	0.3	—	—	44	0.2	Cp	2	0.6	XRF
22R-2, 37–39	16	Ins	FC	0.1	0.3	—	—	25	0.2	Cp	3	0.1	
22R-2, 40–42	16	Hyo	FM	0.1	0.7	—	—	3	0.1	—	1	0.2	
23R-1, 62–64	16	Hyo	PC	—	0.4	—	—	21	0.1	(Cp)	20?	0.2	XRF
23R-2, 64–66	17	Ins*	FC	—	[a]22.3	[a]9.0	—	49	0.5	Cp	3	1.5	Patchy segregation vesicles
23R-2, 97–100	17	Ins	FC	—	—	—	—	71	0.5	Cp	6	1.0	XRF
24R-2, 21–24	17	Ins	FC	—	—	—	—	97	0.8	Cp	5	0.4	XRF
24R-4, 93–95	17	Ins	FC	0.1	0.4	—	—	77	0.3	Cp	1	0.1	
24R-4, 106–109	19	Ins	FC	—	—	—	—	39	0.3	Cp	3	1.0	XRF
25R-2, 2–4	20	Hyo	FC	—	0.2	—	—	14	0.2	Cp	8	0.3	XRF
26R-1, 35–37	20	Ins	FC	0.1	0.1	—	—	40	0.2	Cp	20	0.1	XRF
27R-1, 4–6	20	Hyo	PB?	—	0.3	—	—	24	0.1	Cp	tr.	—	XRF
27R-2, 96–98	20	sOp	FC	—	0.7	—	—	85	0.4	Cp	13	1.0	XRF
27R-3, 54–55	20	Ing	FC	0.1	0.6	—	—	83	0.3	Cp	16	8.0	

[a]The crystals forming irregular subophitic patches represent early crystllization stages and are different from phenocrysts in the other samples.

[b]Altered glass fragments completely replaced by clays occupy 80% of the rock. Matrix is complsed of cubic zeolite (10%), clays (8%), and calcite (2%).

Explanations. Texture: Gls = Glassy, Hyp = Hyalopilitic, Ing = Intergranular, V = Variolitic, Hyo = Hyalo-ophitic, Ins = Intersertal, sOp = Subophitic, G = Glomeroporphyritic. Occurrence: In = *in situ* in sediments, Hy = Hyaloclastite, PM = Pillow margin, BP = Pillow breccia, FM = Massive flow margin, DB = Drill breccia on top of core, PC = Pillow cire, PR = Pillow rum, FC = Massive flow center, SC = Sill center. Minerals: Ol = Olivine, Cp = Clinopyroxene, Gl = Fresh volcanic glass, Pl = Plagioclase, Sp = Spinel. Plagioclase remains in almost all samples and is not listed as a relic. Percentage represents original unaltered state and includes pseudomorphs. Veins are excluded from total, while vesicles are included. Miscellaneous: Altr = Alteration minerals, Crys = Crystallinity, XRF = XFR analysis available, Spher. = Spherulitic, Vein = Calcite veins dominant, xx = Xenocrysts, Zeol = Vesicles filled with zeolite, Hem = Vesicles filled with hematite or iron hydroxide.

replace volcanic glass, olivine, and groundmass clinopyroxene. Vesicles generally occupy less than 3% (average 1.4%) of the rock and are filled mainly by clay minerals and rarely by calcite. Plagioclase is partly replaced by zeolite and/or sericitic clays. Olivine and spinel is sometimes replaced by "iddingsite" and hematite.

Geochemistry

Five samples were analyzed for major elements, and four samples also were analyzed for trace elements. Results are listed in Table 35. Four samples are basaltic, with SiO_2 content ranging from 48 to 50 wt%, while one sample is andesitic (SiO_2 = 54 wt%). The basalts contain very high Al_2O_3 (19–21 wt%), in spite of their low contents of plagioclase phenocrysts. These basalts are mostly corundum-normative. Two basalts (Samples 123-765C-13R-1, 101–103 cm, and -17R-1, 8–10 cm) have relatively low Fe_2O_3* (9–10 wt%) and high MgO (6 wt%) with low FeO*/MgO (1.4) and are comparable to MORB. They resemble MORB also in terms of high chromium (600 ppm) and nickel (360 ppm), as well as moderate TiO_2 (1.0 and 1.5 wt%), low K_2O (0.14 and 0.42 wt%) and low P_2O_5 (<0.1 wt%). However, the other two basalts are probably fractionated MORB (Samples 123-765C-13R-2, 39–42 cm, and -20R-1, 5–10 cm) and have high Fe_2O_3* (12 and 13 wt%), low MgO (5 and 1 wt%), and high FeO*/MgO (2.2 and 10.7 wt%). They are rich in TiO_2 (1.6 and 1.8 wt%), K_2O (2.0 and 2.9 wt%), and P_2O_5 (0.18 and 0.90 wt%). One of them is relatively rich in chromium (ppm) and nickel (ppm), while the other is poor in these elements (269 and 84 ppm, respectively). The "andesite" (Sample 123-765C-36R-1, 20–22 cm) contains high Al_2O_3 (21 wt%) and K_2O (3.1 wt%), and is poor in MgO (1.3 wt%). Its high FeO*/MgO (7.1 wt%) and TiO_2 (1.6 wt.%) clearly distinguish it from calc-alkali andesites, and suggest an affinity with "oceanic" andesite suites. The rock is poor in nickel (102 ppm) but relatively rich in chromium (429 ppm). Trace elements, such as zirconium (64–121 ppm) and yttrium (22–65 ppm) have a reasonable concentration range for oceanic magmas, and increase regularly with decreasing nickel and chromium. The pebbles are distinctly higher in strontium (187–267 ppm) than the adjacent basement basalts (average 89 ppm with standard deviation of 34 ppm), and plot in the area between ocean island tholeiites and MORBs in terms of zirconium vs. strontium (Fig. 98). Their niobium/yttrium ratios are restricted (0.5 to 0.9) and intermediate to the values for N- and T-MORBs. However, their zirconium/yttrium ratios (1.8 to 3.6) are comparable to all types of MORB, and some ocean island tholeiites. Moreover, the basalt and andesite pebbles are dis-

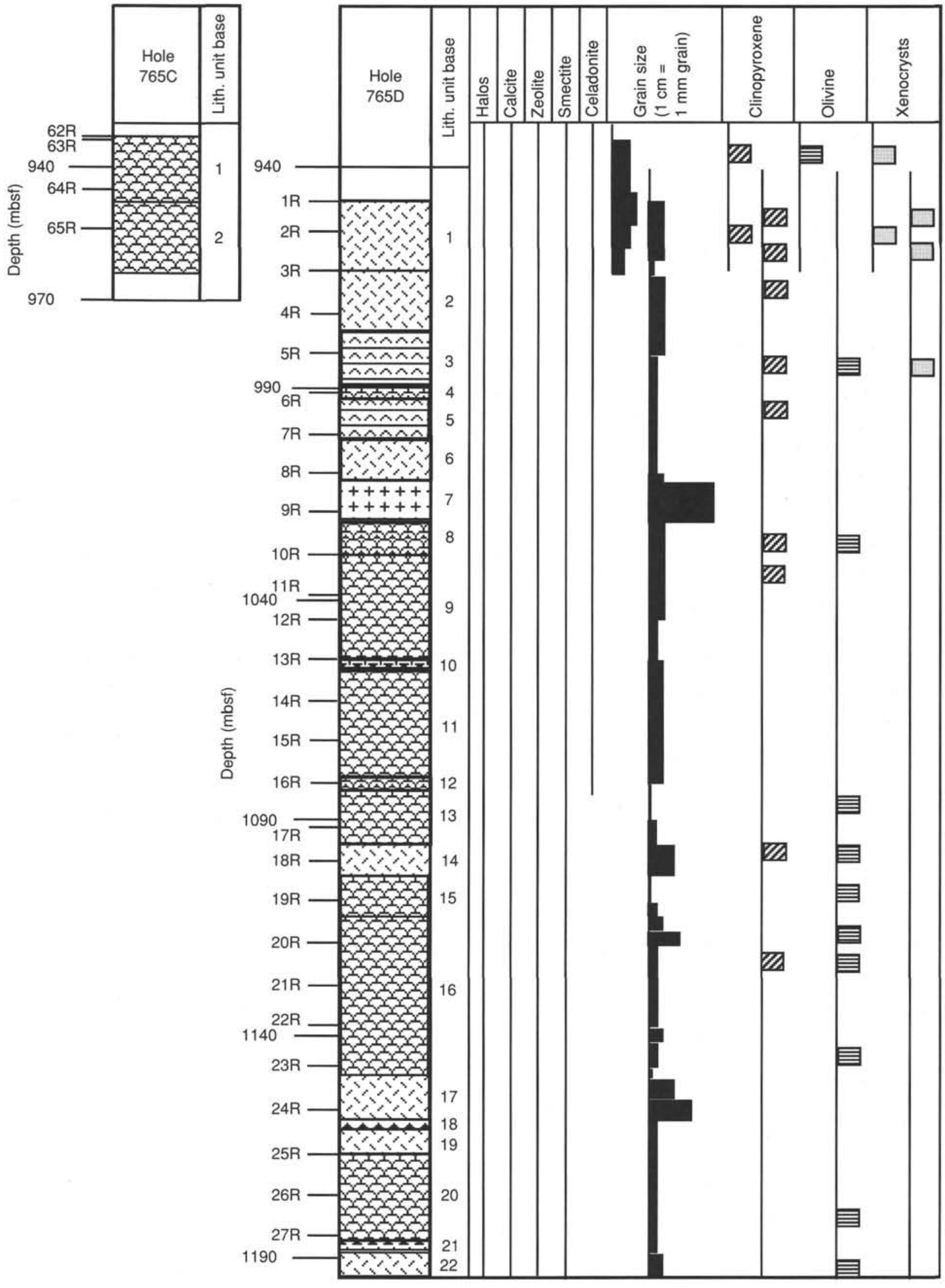

Figure 93. Graph of mineral identification and petrographic determination of thin sections, Site 765.

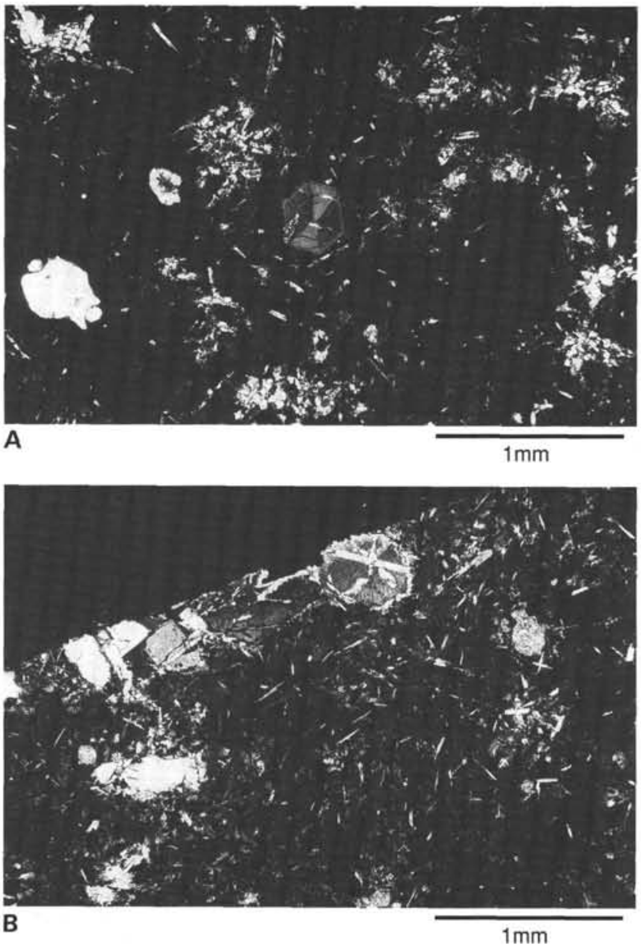

Figure 94. A. Sample 123-765C-65R-2, 106–108 cm, in thin section. Sector-zoned augite phenocryst in glassy basalt, crossed nicols. B. Sample 123-765C-63R-3, 133–135 cm, in thin section. Twinned augite phenocryst in glassy basalt, crossed nicols.

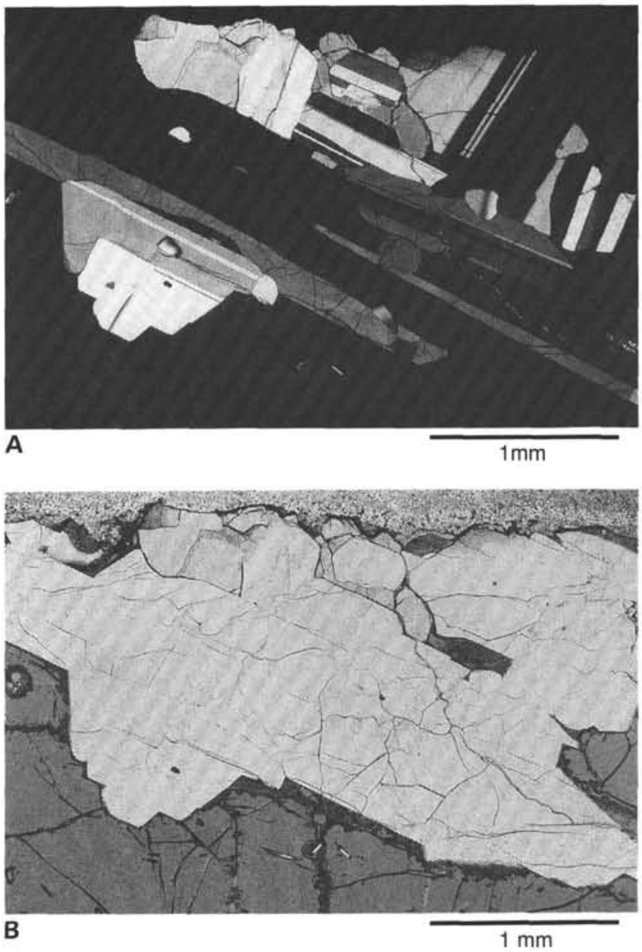

Figure 95. A. Sample 123-765D-63R-1, 122–124 cm, in thin section. Gabbro xenolith in basaltic glass, crossed nicols. B. Same sample, open nicols.

tinctly higher in nickel and chromium than the basement basalts with equivalent TiO_2 abundances (Fig. 99).

The data above indicate that the basalt and andesite pebbles represent a primitive MORB-type magma, but are enriched in TiO_2, zirconium, and incompatible elements relative to Site 765 basalts. The unusually high Al_2O_3 and strontium may be either original or alteration features; the former hypothesis is favored for the Al_2O_3 abundances. Concentration of rubidium is 35 to 50 times higher than that in N-MORB and may have been introduced during low-temperature alteration.

Discussion

Site 765 is situated at the exit of several submarine canyons cutting the Exmouth and Wombat plateaus. The pebbles of volcanic and sedimentary rocks may have been readily eroded and transported from outcrops on the wall of the canyons by turbidity currents or debris flows. Note, however, that no basaltic rocks have been recovered from dredge sampling on the western wall of the Swan Canyon, which faces Site 765 (Von Stackelberg et al., 1980). Furthermore, pebbles of trachyte (or mugearite) and alkali rhyolite, which would be comparable to lithologies dredged from the northern side of the Wombat Plateau, have not been found from any stratigraphic level in Site 765. The petrographic and geochemical studies above reveal the presence of primitive MORB among the basaltic pebbles at Site 765, and suggest that their provenance is in the continent/ocean transitional realm. Basement outcrops in the Argo Abyssal Plain between the mouth of Swan Canyon and Site 765 may be the source of the pebbles. Basement highs evident as tilted blocks on *Atlantis II* seismic profile Line 93-14 at the exit of the Swan Canyon may have been exposed during the Late Cretaceous and Tertiary, when these pebbles were eroded. The pebbles of differentiated MORB and oceanic andesite further suggest that the rock suites related to the oceanic island volcanism or the early rifting event may also outcrop in the vicinity.

BASEMENT ALTERATION

This section is divided into two parts: Part 1 deals with the basaltic basement of Holes 765C and 765D, and Part 2, with the igneous pebbles from the sedimentary section of Holes 765B and 765C.

Part 1. Basaltic Basement

The basement rocks recovered from Site 765 are slightly to moderately altered and are typical of low-temperature alteration in the brownstone facies of ocean-floor metamorphism. These rocks exhibit numerous single and multiple oxidation halos that mantle veins filled with iron-oxyhydroxides, celadonite, saponite, calcite, and zeolites, in single- or multiple-layered relationships. Cross-cutting vein relationships are also apparent in some areas of the core. The intensity of alteration varies on a scale of

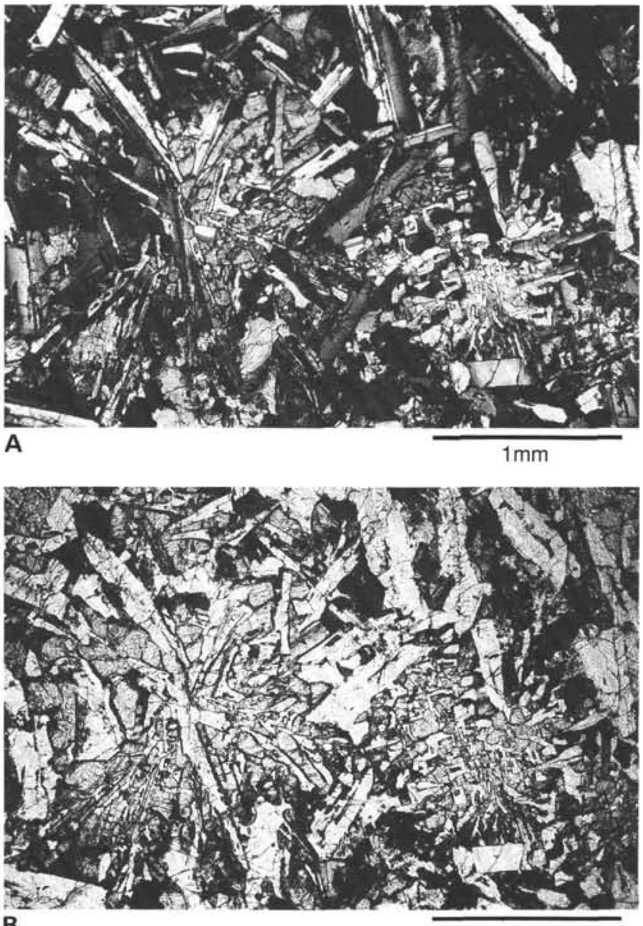

Figure 96. A. Sample 123-765D-8R-1, 111–114 cm, in thin section . Diabase sill, crossed nicols. B. Same sample, open nicols.

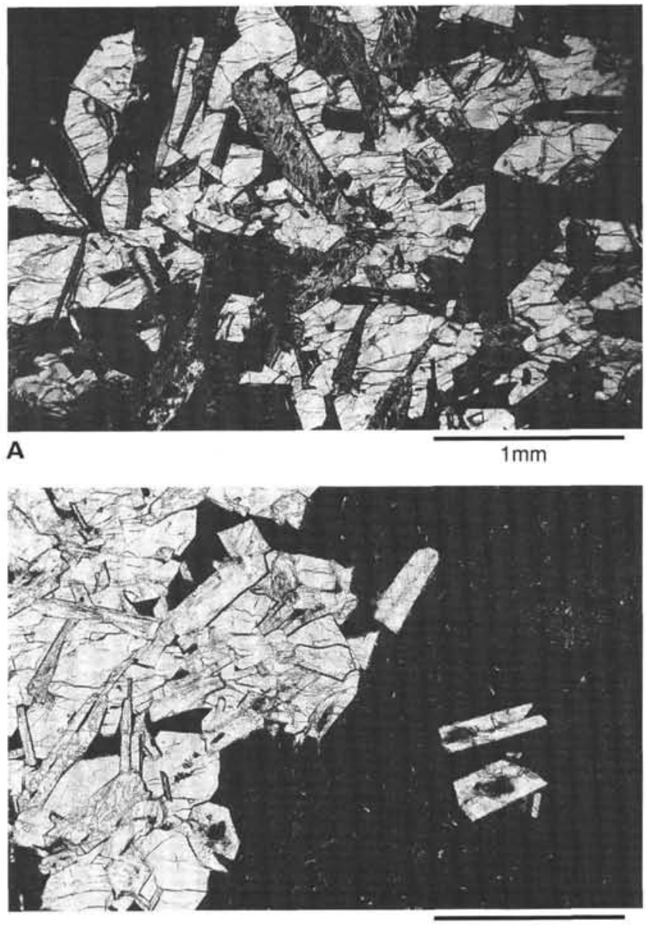

Figure 97. A. Sample 123-765D-2R-2, 88-90 cm, in thin section. Diabase xenolith in glassy basalt, crossed nicols. B. Same sample, open nicols.

centimeters to meters; from zones of hyaloclastite breccias completely replaced by clay minerals to pillow margins containing fresh glass. Clay minerals are the only secondary phase to show a systematic change with depth.

Figure 93 depicts the distribution of secondary minerals in Holes 765C and 765D.

The characteristics of the oxidation halos, veins, hyaloclastite and tectonic breccias, and vesicle and cavity fillings are described below; this is followed by a description of the alteration stratigraphy.

Oxidation Halos

Oxidation halos occur throughout the basement, but are less common lower in the section. They vary in thickness from a few millimeters to several centimeters; there is no systematic variation in width downhole. The halos can be simple or complex (Figs. 100 to 104), but form by the same basic process: namely, fluids that permeate outward from fractures into the body of the rock, replacing primary minerals and precipitating secondary minerals. Oxidation halos may contain 10% to 20% secondary minerals, compared with a few percent in the "fresh" rock away from fractures. Each halo consists of several zones; the number and combinations of the zones differ between halos. The basic sequence from "fresh" rock farthest from a fracture toward a fracture is as follows:

Zone 1: A dark band with sharp outer contact marks the outermost extent of the alteration front and is up to several millimeters thick. The fracture side of this band is diffuse and grades into Zone 2.

Zone 2: An irregular layer of orange and red staining of varying thickness that in turn grades into Zone 3. This staining results from the presence of iron oxyhydroxide, which discolors primary minerals and precipitates in cavities in the rock.

Zone 3: A dark gray or black zone adjacent to the fracture that may contain isolated areas of orange staining. Overprinting of one or more halos can create a series of colored bands adjacent to a fracture (Figs. 100 to 103).

If alteration was particularly pervasive and intense, the rock may have been altered pervasively to a light gray before development of the basic oxidation halo (Fig. 104); usually the background rock is dark gray (Fig. 100). In some cases, Zone 3 may be absent and the orange-red of Zone 2 abuts the fracture; Zone 3 only develops when the oxidized band has moved away from the fracture and into the rock.

Veins

Calcite and clay minerals are the dominant vein components throughout the basement, with lesser zeolites present in pillow margins and hyaloclastite breccias. Veins can be filled by a sin-

Table 33. Petrographic data of basement basalts, Holes 765B, 765C, and 765D.

Core, section, interval (cm)	Occurrence	Hand specimen	Thin section
123-765B-7H-1, 72–74	*in situ*	Pyrite-rich clast in pebbly to boulder conglomerate, 4.5 m thick.	Aphyric, intersertal basalt with relict augite.
11H-7, 23–24	*in situ*	Sandstone or volcanic rock in a conglomerate bed, 4 m thick.	Fine sandstone.
12H-1, 90–92	*in situ*	Pebble of coarse-grained volcanic rock, 3 cm in size, occurring in ooze.	Moderately plagioclase, olivine-phyric, hyalo-ophitic basalt with relict spinel.
12H-2, 78–79	*in situ*	Siltstone (volcanic rock?) pebble in a disturbed calcareous clay bed.	Very fine sandstone
22X, CC 40–42	*in situ*	Volcanic fragment in a conglomerate bed with *Inoceramus* fragments.	Spa. plagioclase-phyric, hyalo-ophitic basalt with relict augite.
30X-1, 149–150	*in situ*	Volcanic rock (rhyolite).	Ferruginous clayey fine sandstone or sandy ironstone.
31X-1, 151–153	*in situ*	Brown fine-grained pebble (siltstone) in pebbly mudstone.	Sparsely plagioclase-phyric, hyalo-ophitic basalt.
123-765C-13R-1, 16		Angular, black, fine-grained volcanic rock, 1 cm size.	Drill breccia.
13R-1, 23–28	drill bit	Angular, black, fine-grained volcanic rocks, 2 cm and 3 cm size.	
13R-1, 94–96	*in situ*	Boulder of olivine-phyric basalt, at least 14 cm size and wider than the core barrel.	Moderately olivine-phyric, intersertal basalt.
13R-2, 30	*in situ*	Red-brown weathered aphyric basalt.	
13R-2, 39–42	*in situ*	Angular, greenish dark gray, olivine-phyric basalt pebble, 4.5 cm size.	Moderately olivine-pyric (glomero-porphyritic), hyalo-ophitic basalt with relict spinel.
13R-3, 27–28	*in situ*	Angular yellow brown basalt pebble, 1 cm in size.	
15R-1, 1–3	drill bit	Angular, dark brownish gray, aphyric basalt pebble, 4×2 cm in size.	Aphyric intersertal basalt.
15R-1, 3–6	drill bit	Subangular, light greenish gray, sparsely olivine-phyric basalt, 4 cm in size.	Sparsely ol-phyric intersertal or hyalo-ophitic basalt.
16R-1, 6–10	drill bit	Angular, light gray/brown, weathered, sparsely oliving-phyric basalt(?), 4 cm in size.	Sparsely olivine-plagioclase-phyric, variolitic/hyalo-ophitic basalt with relict spinel and olivine.
17R-1, 6–8	drill bit	Angular, dark gray, sparsely olivine-phyric basalt pebble, 2.5×1.5 cm in size.	Sparsely plagioclase-olivine-phyric, intersertal/variolitic basalt.
17R-1, 8–10	drill bit	Subangular, dark gray green, sparsely olivine-phyric basalt, 3×2.5 cm in size.	Aphyric, intersertal/variolitic basalt.
19R-1, 46–47	*in situ*	Subangular, brown, glassy, vesicular volcanic rock, 4 cm in size	Aphyric glassy basalt.
		XRF analysis of this sample revealed that it is not a volcanic glass but an ironstone. Chemical data for major elements: SiO_2 = 7.5%, TiO_2 = 0.2%, Al_2O_3 = 1.1%, Fe_2O_3 = 86.5%, MnO = 0.1%, MgO = 0.4%, CaO = 0.2%, Na_2 = 0.1%, K_2O = 0.2%, P_2O_5 = 1.14%, LOI = 11.3%. For trace elements: Cr = 2.1 ppm, Ni = 18.9 ppm, Rb = 3.5 ppm, Ba = 21 ppm, Nb = 3.4 ppm, Ce = 24 ppm, Sr = 43 ppm, V = 189 ppm, Zr = 0 ppm, Y = 6.0 ppm, Zn = 85 ppm, Cu = 33 ppm.	
19R-1, 85–86	*in situ*	Angular, yellowish brown, medium-grained diabase, 4.5×3.5 cm in size.	Sparsely olivine-plagioclase-phyric subophitic basalt.
19R-1, 119–120	*in situ*	Well rounded, brown, vesicular, very fine-grained, aphyric basalt or andesite.	Sparsely plagioclase-olivine-phyric intersertal basalt with relict spinel.
19R-2, 123–124	*in situ*	Angular, dark gray, very fine-grained, aphyric volcanic rock (basalt?), 4×2 cm in size.	Aphyric hyalo-ophitic basalt.
19R-2, 124–125	*in situ*	Subrounded, yellowish brown, altered, very fine-grained, aphyric basalt, 3 cm in size.	Moderately plagioclase-phyric, hyalo-ophitic basalt.
20R-1, 0–2	drill bit	Sandstone?	Coarse sandstone rich in angular claystone fragments.
20R-1, 2–5	drill bit	Sandstone?	Disturbed siltstone.
20R-1, 3–5	drill bit	Basaltic rock.	Sparsely plagioclase-phyric, intersertal/hyalo-ophitic basalt.
20R-1, 5–10	drill bit	Altered basalt.	Sparsely plagioclase-phyric intersertal/hyalo-ophitic basalt.
20R-1, 6–7	drill bit	Basaltic rock.	Aphyric intersertal basalt with relict augite.
20R-1, 8–10	drill bit	Altered basalt.	Aphyric basalt, hyalopilitic.
23R-CC, 13–17	*in situ*	Subgrounded, grayish green, altered, sparsely vesicular, fine-grained, sparsely pyroxene-phyric basalt, 6×4.5 cm size, with brown weathered margins. The vesicles are filled with chlorite(?).	Aphyric altered intersertal/hyalo-ophitic basalt.
24R-3, 134–136	*in situ*	Basaltic rock, 3×5.5 cm in size.	Sparsely olivine-plagioclase-phyric intersertal basalt.
31R-1, 4–8	drill bit	Red brown, very fine grained basaltic rock.	Aphyric intersertal/variolitic basalt.
31R-1, 6–13	drill bit	Yellow brown, fine-grained, highly olivine-phyric basalt.	
36R-1, 18–42	drill bit	Eleven pebbles of light olive, weathered, aphyric basalt. One fresh pebble is plagioclase-phyric. 4.5×5.5 to 1×1 cm in size.	
(20–22)		Moderately olivine-plagioclase-phyric, intersertal basalt.	(XRF analysis revealed that this sample is an oceanic andesite.)
(43–45)		Altered aphyric intersertal basalt (andesitic?).	
(52–54)		Aphyric hyalo-ophitic basalt.	

Table 33 (continued).

Core, section, interval (cm)	Occurrence	Hand specimen	Thin section
123-765C-37R-1, 26–34	drill bit	Five pebbles of yellow brown, weathered, aphyric basalt, 5×3 to 1×1.5 cm in size.	
39R-1, 6–8	drill bit	Occurrence not clear.	Moderately plagioclase-phyric, glomeroporphyritic/intersertal basalt (possibly andesitic).
40R-1, 0–12	drill bit	Ten pebbles of yellow brown, weathered, aphyric basalt, less than 2×3 cm in size.	
41R-1, 0–13	drill bit	"Mixed pebbles, mainly basalts, subrounded to subangular" (from visual core description).	
42R-1, 0–20	drill bit	About 30 pebbles of basaltic rocks (80%), white chert (10%), green mudstone (5%), and iron ore-bearing sediment (5%).	
43R-1, 24–28	drill bit	Four pebbles of basaltic rocks, 2 cm in size.	
44R-1, 0–12	drill bit	Seven pebbles of basaltic rocks, 3 cm in size. One basalt(?) pebble is extremely glassy with vesicles elongated along flow lines. It is also possible that this is an ironstone pebble.	
45R-1, 0–4	drill bit	Mixed pebbles of claystone and volcanics.	
62R-1, 0–10	drill bit	Two pebbles of fine-grained basaltic rocks, 5×2 and 2.5×1 cm in size.	Altered aphyric intersertal basalt.
123-765D-1R-1, 6–8	drill bit	Well-rounded pebble of dark gray, moderately olivine-phyric basalt, 3.5×2.5 cm in size, occurring with a white sandstone pebble at the top of the core.	

Table 34. Petrographic data of sedimentary pebbles of volcanic rocks encountered at Site 765.

				Phenocrysts				Groundmass					
Core, section, interval (cm)	Unit	Texture	Occurrence	Ol (%)	Pl (%)	Cp (%)	Sp (%)	Crys (%)	Size (mm)	Relict	Altr. (%)	Vesicles (%)	Rem.
Hole 765B Basalt pebbles													
7H-1, 72–75	1A	Ins	In	—	0.5	—	—	48	0.2	Cp	12	3.0	
12H-1, 90–92	1B	Hyo	In	1.3	4.0	—	tr.	13	0.1	Sp	9	9.5	
28X-CC, 34–36	2A	Hyo	In	—	1.0	—	—	16	0.4	Cp?	3	1.0	
31X-1, 151–153	2A	Hyo	In	—	2.5	—	—	5	0.4	Gl	3	2.0	Plxx
Hole 765C Basalt pebbles													
13R-1, 94–96	3A	Ins	In	7.5	—	—	0.3	50	0.5	—	31	tr.	XRF
13R-2, 39–42	3A	Hyo	In	5.1	0.3	—	tr.	20	0.2	Sp	25	—	XRF
15R-1, 1–3		Ins	DB	0.2	—	—	—	60	0.4	—	50	1.0	
15R-1, 3–6		Ins	DB	1.0	—	—	—	50	0.3	—	45	1.0	
16R-1, 6–10		HyoV	DB	0.6	0.5	—	tr.	15	0.3	01Sp	95	1.5	
17R-1, 1–6		Ins	DB	2.0	0.5	—	—	45	0.5	—	60	1.0	
17R-1, 8–10		InsV	DB	—	—	—	—	46	0.3	—	40	1.5	XRF
19R-1, 85–86	3B	sOp	In	0.5	0.5	—	—	100	0.2	—	63	—	
19R-1, 119–120	3B	Ins	In	0.5	0.4	—	tr.	30	0.2	Sp	30	3.0	
19R-2, 123–124	3B	Hyo	In	—	0.2	—	—	20	0.2	—	5	3.0	Plxx
19R-2, 124–124	3B	Hyo	In	0.1	5.2	—	—	10	0.1	—	10	1.0	
20R-1, 3–5		Hyo	DB	—	0.8	—	—	15	0.1	—	9	0.2	
20R-1, 5–10		Hyo	DB	—	2.0	—	—	20	0.2	—	20	2.0	XRF
20R-1, 6–7		Ins	DB	—	0.4	—	—	35	0.2	Cp	10	0.8	
20R-1, 8–10		Hyp	DB	—	0.2	—	—	23	0.1	—	13	0.5	
23R-CC, 12–14	3D	Hyo	In	—	0.2	—	0.4?	20	0.1	—	97	1.0	
24R-3, 125–127	3D	Ins	In	0.4	0.6	—	—	52	0.3	—	65	0.4	
31R-1, 4–8		InsV	DB	0.1	0.4	—	—	45	0.4	—	36	0.4	
36R-1, 20–22		Ins	DB	0.5	4.0	—	—	40	0.2	—	40	0.2	XRF
36R-1, 43–45		Ins	DB	—	—	—	—	45	0.2	—	65	1.0	
36R-1, 52–54		Hyo	DB	0.1	0.2	—	—	10	0.3	—	15	0.6	
39R-1, 1–6		InsG	DB	0.3	4.8	—	—	25	0.1	—	40	0.2	
62R-1, 1–3		Ins	DB	—	—	—	—	50	0.2	—	50	1.0	

See Table 32 for explanation of terms.

gle phase or by several different phases in layers (e.g., Fig. 100 at 50–54 cm) or (fill the vein) chaotically (e.g., Fig. 101 at 68–75 cm). Cross-cutting vein relationships also occur; (in these cases) veins filled with clay minerals cut calcite veins (Fig. 100 at 35–38 cm), calcite veins cut veins filled by clay minerals, and veins without associated oxidation halos dissect veins with oxidation halos (e.g., Fig. 100 at 50 cm and Fig. 101 at 80 cm). Where clay minerals and calcite are present in the same vein, calcite is generally the last phase to precipitate; there are, however, a few examples of veins with late-stage clay minerals precipitated interior to the calcite (Fig. 100). The high frequency of fractures containing late-stage calcite suggests that many veins were reopened after circulating fluids had changed composition. In the oxidation halos, veins often have walls coated with red iron-oxyhydroxides, with later green clay minerals ± calcite filling their centers.

Hyaloclastite and Tectonic Breccias

Hyaloclastite breccias recovered from the pillow units contain fresh glass, but generally the high porosity and high fluid flux associated with these areas have resulted in some of the most intense alteration found in the basement. Individual glass fragments have been altered to clay minerals of varying shades of green and exhibit well-developed liesegang structures (Figs. 90 and 91). The hyaloclastites are often cemented by clay minerals, but can be intensely veined by calcite with minor phillipsite.

Several areas in the core are tectonized with broken angular rock fragments cemented by a network of calcite veins (Figs. 92 and 105). Clays are absent from these veins; the event that caused the fracturing was most likely coincident with the calcite veining seen elsewhere and is presumably a late-stage event.

Vesicle and Cavity Fillings

Basalts from Site 765 are variably vesicular. The type, quantity, and relationships of the secondary minerals that fill vesicles are related to their position in relation to veins and alteration halos. Near veins, vesicles tend to be completely filled, and farther away may be partly empty. The secondary minerals that fill vesicles are often identical to those that fill fractures; like veins, rims are generally coated by green clay minerals with calcite and/or zeolites centers (Fig. 106). Within oxidation halos, the vesicle rims are typically composed of iron-oxyhydroxides.

Alteration Stratigraphy

Figure 93 shows the variation in basement alteration mineralogy at Site 765; Holes 765C and 765D have been combined for this figure. The vertical lines delineate the large-scale distribution of secondary minerals; on a local scale, some secondary minerals may be absent, but this probably reflects slight variations in the local conditions of alteration. Orange and red alteration halos in the rock, containing iron-oxyhydroxides, are present throughout the basement. These halos can vary in intensity and width from section to section, although their general distribution indicates that the entire basement at Site 765 was subjected to oxidative alteration processes. Calcite is abundant as a vein-filling mineral throughout the hole; the sediment/basement contact in Hole 765C is represented by a hyaloclastite cemented by sparry calcite; calcite veins are present all the way to the lowermost cores. Calcite is a late-stage secondary mineral; it fills and seals veins previously coated by clay minerals and fills the centers of clay-coated vesicles in the rock. Calcite is the only phase to cement the tectonic breccias in Core 123-765D-27R and in several hyaloclastite breccia samples. Zeolites occur throughout the hole as veins within pillow margins, within hyaloclastites, and as the fillings to vesicles in several lithologic units, particularly in Units 17, 18, and 19. These may be a late-stage secondary mineral.

Clay minerals are the only secondary phase to show stratification in Site 765. Clay minerals filling veins from several locations in Holes 765C and 765D were identified by XRD. Most of the clay minerals displayed basal peaks between 12 and 15 Å; these expanded to 17 Å on glycolation. This is typical of the mineral saponite (a type of smectite), a characteristic low-temperature alteration phase in oceanic basalts. Significantly, however, a number of samples exhibited the 10-Å peak of celadonite, a characteristic mineral of low-temperature alteration under oxidizing conditions. The transition from samples containing both saponite and celadonite to samples containing only saponite (i.e., no 10-Å peaks) occurs in Core 123-765-16R (Fig. 93). The change in clay mineralogy identified by XRD is supported by thin section observations; the upper section of the hole contains a bright green clay mineral with the optical characteristics of celadonite, whereas in the lower section of the hole, the clay minerals are more yellow green and brownish-green and more characteristic of saponite. Bulk rock geochemical evidence discussed below, also reflects this change in clay mineralogy with depth.

Bulk Alteration Geochemistry

Thirty-seven samples of the basaltic basement at Site 765 were analyzed for major and trace elements by XRF. Most of the geochemical variation in these samples may be interpreted in terms of igneous differentiation (see "Basement Geochemistry" section, this chapter). This is not surprising, since we tried to sample the least-altered portions of each basalt lithology. However, even in these fairly fresh samples, some elements show variations that reflect alteration. The distribution of the alkali elements, K_2O and rubidium, may reflect the changing clay mineralogy with depth. The K_2O and rubidium abundances in the basalts decrease at about 1080 mbsf (Fig. 107), and this is the depth near which assemblages containing celadonite give way to assemblages containing only the alkali-poor smectite and saponite. Other elements show variations that do not reflect specific phase boundaries, but simply reflect the increasing extent of alteration of the basalts. Alteration of basalt on the seafloor takes place primarily through hydration and carbonation reactions. The weight percent LOI of the basalts is largely a measure of the total H_2O and CO_2 contents, and thus a fairly good indication of the progress of these alteration reactions. There is no systematic relationship between LOI and depth in the Site 765 basement (Fig. 108), which suggests that alteration is variable on a small scale. However, a few elements tend to correlate with LOI. There is a sporadic increase in CaO and decrease in MgO with increasing LOI (Fig. 109). The increase in CaO with LOI is most likely coupled to calcite, which is present to some extent in all basement samples. The decrease in MgO with LOI may be due to leaching during alteration. Note that the variations in CaO and MgO at low LOI values ($<1\%$) are consistent with igneous differentiation, and thus these basalts preserve systematics indicative of both their igneous and alteration histories.

Part 2. Igneous Pebbles

A series of igneous pebbles was recovered from the sediment section in Holes 765B and 765C. All of these exhibit varying degrees of oxidative alteration (see Fig. 93, "Basement Petrography" section, this chapter) manifested as yellow- and red-brown rims. The centers of less-altered pebbles are grayish green. Primary mineral preservation is poor; bright green (celadonite?), yellow-green, and yellow-brown clay minerals (saponite) are common. Olivine is replaced by iron oxyhydroxide, and plagioclase is partly altered to zeolites. Vesicles are generally filled with clay minerals, but some have calcite centers. These pebbles appear to be from one or more basement outcrops that underwent similar low-temperature alteration to the basement at Site 765. Additional shore-based microprobe studies of the clay minerals and zeolites will help to confirm this.

Conclusions

The basement alteration at Site 765 is characterized by the presence of celadonite + saponite + phillipsite + calcite. This is the characteristic mineral assemblage of low-temperature brownstone facies metamorphism as defined by Cann (1979); there is no evidence for high-temperature chloritic alteration at Site 765. The style of alteration at Site 765 is similar to that described from several other DSDP and ODP holes drilled in the upper oceanic crust (see review in Adamson and Richards, 1990)

Table 35. XRF analyses of basalt and andesite pebbles in sediment samples, Site 765.

Core, section, interval (cm)	Depth (mbsf)	SiO_2 (wt%)	TiO_2 (wt%)	Al_2O_3 (wt%)	Fe_2O_3 (wt%)	MnO (wt%)	MgO (wt%)	CaO (wt%)	Na_2O (wt%)	K_2O (wt%)	P_2O_5 (wt%)
123-765C-13R-1, 101–103	465.6	48.77	1.06	18.86	10.13	0.14	6.90	10.56	2.71	0.14	0.05
13R-2, 39–42	466.5	49.82	1.81	19.08	12.06	0.05	5.05	5.95	2.78	1.82	0.18
17R-1, 8–10	502.5	49.73	1.49	21.25	8.95	0.06	5.97	7.53	3.39	0.42	0.08
20R-1, 5–10	530.8	49.93	1.59	18.56	13.07	0.04	1.20	6.86	2.62	2.67	0.90
36R-1, 20–22	683.5	54.34	1.61	20.42	10.09	0.05	1.28	5.48	3.40	2.86	0.18

of a variety of different ages (110 m.y. at Sites 417 and 418, Shipboard Scientific Party, 1979a, 1979b; <100,000 yr at Site 648, Shipboard Scientific Party, 1988).

Low-temperature oxidative alteration affects the upper oceanic crust immediately after formation. Circulating fluids rich in oxygen form the oxidation halos characteristic of this facies and so apparent in the basement of Site 765. The first mineral to form is generally an iron-oxyhydroxide that stains primary phases and that forms layers in vesicles and cavities. The clay mineral that forms at this time is a potassium-rich saponite (termed "protoceladonite"—a clay mineral having chemistry and optical properties of celadonite but without a 10-Å peak when X-rayed—see review in Adamson and Richards, 1990) or a dioctahedral celadonite. This may fill empty or previously iron-oxyhydroxide-coated vesicles in a layered relationship. Scattered late influx of the fluids responsible for precipitating the iron-oxyhydroxides can form additional red layers within the green clay minerals, or create entirely overprinted oxidation halos. Multiple oxidation halos, such as at Site 765, suggest reopening of previously sealed fractures, possibly as the crust moved off axis. The last alteration event to affect the basement at Site 765 was the precipitation of calcite and, locally, zeolites in veins and vesicles; this event was more pervasive in nature and affected areas of rock isolated from fractures. However, even this event was insufficiently intense, or too short-lived, to fill all vesicles in some of the less-fractured and coarser-grained lithological units at the site. The precipitation of calcite in cross-cutting veins, and as the cement in breccia zones void of clay, suggests that this was the result of a tectonic event (or events) that occurred after the crust had been sealed to oxidative alteration and after the circulating fluid chemistry changed.

The pebbles recovered from the sediment sections in Holes 765B and 765C are strongly oxidized, suggesting that they were exposed on the seafloor for a considerable time before being buried to any great depth. Further shore-based investigations will be necessary to see whether these pebbles underwent higher temperature *in-situ* alteration before being deposited in the area of Site 765.

BASEMENT GEOCHEMISTRY

The major- and trace-element analyses presented in this section were determined on board *JOIDES Resolution* during Leg 123 by XRF. Details of the analytical techniques used are given in the "Explanatory Notes" chapter (this volume). Analytical results for the MORB standard AII-92-29-1A and the Leg 123 inter-laboratory standard are presented in Table 36. Results of major-element analyses for basement basalts recovered at Site 765 are listed in Table 37, and trace-element XRF analyses are in Table 38. The geochemical results for volcanic pebbles recovered in the sedimentary section are presented in the "Basement Petrography" section, this chapter.

Major Elements

The average composition and standard deviation of 38 basement samples are shown and are compared below with an average composition of basalts dredged from the active Mid-Indian Ocean Ridge (MIOR) (see caption of Fig. 110 for data sources).

Major Elements

The average composition and standard deviation of 38 basement samples are shown and are compared below with an average composition of basalts dredged from the active Mid-Indian Ocean Ridge (MIOR) (see caption of Fig. 110 for data sources).

	SiO_2	TiO_2	Al_2O_3	Fe_2O_3	MnO	MgO	CaO	Na_2O	K_2O	P_2O_5
Site 765										
Ave.	50.01	1.47	14.47	12.17	0.21	6.79	11.81	2.25	0.47	0.12
(wt%)	0.92	0.15	0.80	0.14	0.04	0.85	0.92	0.28	0.32	0.02
MIOR basalt										
	51.22	1.22	15.98	9.12	0.16	8.07	11.43	2.92	0.15	0.16
	0.96	0.22	1.14	1.39	0.03	0.98	0.87	0.55	0.12	0.08

The basement at Site 765 is clearly basaltic, with compositions of about 50 wt% SiO_2 and 7 wt% MgO. These compositions are readily identified as MORBs by their moderate TiO_2 (1.5 wt%) and very low P_2O_5 (0.1 wt%). CIPW norms reveal that these basement basalts are predominantly olivine tholeiites, with less than 11 wt% normative olivine. Ten samples are quartz normative, and one highly altered hyaloclastite (with 12 wt% LOI) is nepheline-normative (Sample 123-765D-16R-1, 39–41 cm). Alteration has the effect of decreasing the normative silica value.

The effects of alteration on geochemistry are discussed in "Basement Alteration" section, this chapter. However, the effect of alteration on important geochemical indexes, such as FeO*/MgO, are evident in Figure 110, by comparing samples having <1 wt% LOI with those having >1 wt% LOI. MgO is clearly lost in the most altered samples. Changes in Fe_2O_3 are less evident, while the most altered samples are generally enriched in Fe_2O_3*. The combination of these changes leads to a marked increase in FeO*/MgO with alteration. Similarly, K_2O abundances increase with increasing alteration. Even the K_2O abundances in the freshest samples are considered as suspect; evaluation of large ion lithophile element abundances in these basalts must await analysis of the fresh glass recovered at intervals throughout the section.

When compared with average MIOR basalts, Site 765 basalts are 2 wt% lower in Al_2O_3, 3 wt% higher in Fe_2O_3*, and 0.3 wt% higher in TiO_2. FeO*/MgO ranges from 1.1 to 2.4, with an average of 1.67 ± 0.34; this value is considerably higher than the average MIOR basalt (FeO*/MgO, 1.08). The high Fe_2O_3 and low Al_2O_3 indicate that these tholeiites have evolved relative to MIOR basalt.

The evolved nature of the Site 765 magmas relative to MIOR basalts is further demonstrated in Figure 110. In these diagrams, major oxides are plotted vs. TiO_2, which is used as a fractionation index. The Site 765 basalts plot at the high TiO_2, fractionated end of each variation diagram. Therefore, in the context of their higher Fe_2O_3 and lower MgO and Al_2O_3, the Site 765 basalts simply represent a fractionated end-member of a continuum from the recent primitive basalt compositions erupted at the MIOR axes.

Table 35 (continued).

Total (wt%)	LOI (wt%)	Nb (ppm)	Zr (ppm)	Y (ppm)	Sr (ppm)	Rb (ppm)	Zn (ppm)	Cu (ppm)	Ni (ppm)	Cr (ppm)	V (ppm)	Ce (ppm)	Ba (ppm)
99.32	2.20	2.1	64.9	22.0	244.9	1.4	80.5	80.4	354.8	641.6	251.8	3.7	10.2
98.58	3.64	3.2	109.4	36.2	360.9	35.5	188.8	52.2	202.1	592.3	242.1	16.2	23.4
98.87	3.16												
97.45	3.00	3.2	120.2	60.3	280.7	42.2	111.4	63.3	82.8	283.5	201.1	16.6	40.6
99.71	2.35	2.7	122.2	32.5	196.8	48.7	93.8	67.6	101.6	429.7	231.2	14.8	16.6

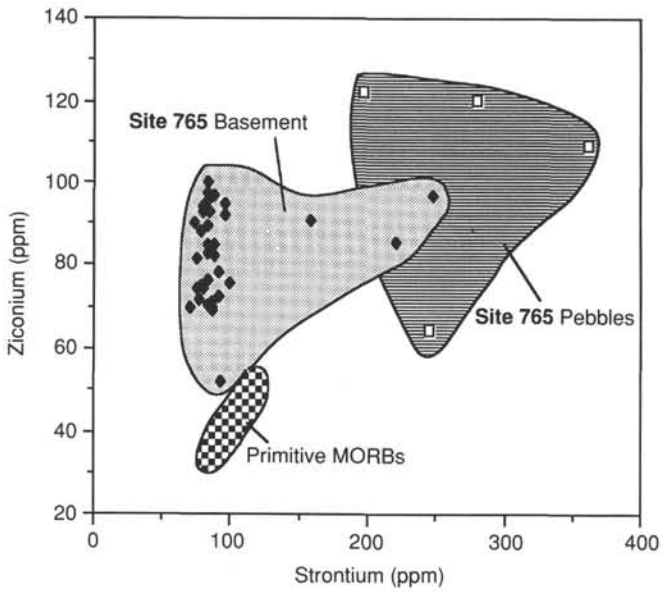

Figure 98. Diagram of zirconium and strontium, indicating basalt and andesite pebbles in the sedimentary section at Site 765. Primitive MORB values are from Sun et al., 1979.

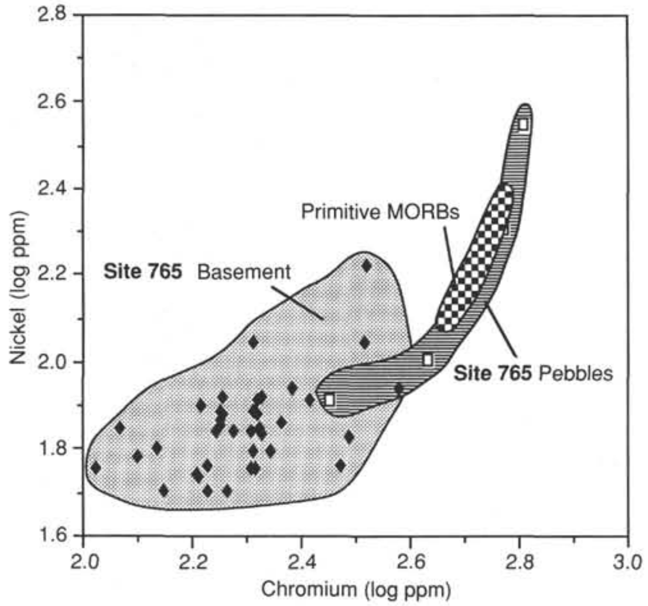

Figure 99. Diagram of chromium vs. nickel abundance (log ppm) in basalt and andesite pebbles from the sedimentary section at Site 765. Refer also to Table 35.

In general, with the exception of Al_2O_3 in two samples, DSDP Site 261 basalts are more comparable to MIOR basalts, but these plot at the evolved end of this data set. Two titanium-rich samples, interpreted as a late "alkalic" sill at Site 261 (Robinson and Whitford, 1974), are not plotted in these diagrams; these samples contain as much as 3.5 wt% TiO_2 and are highly fractionated with respect to other MIOR basalts.

The positive correlation of TiO_2 with Fe_2O_3 indicates that these lavas have not fractionated titanomagnetite. This is also demonstrated in Figure 111, where TiO_2 is also shown to correlate with zirconium; the latter is highly incompatible during magmatic evolution. Nonetheless, the Site 765 basalts are significantly different from the MIOR basalts in terms of titanium and zirconium. As evident from the position of the Site 765 basalts in the Al_2O_3 vs. zirconium diagram (Fig. 111), this difference may be related to lower zirconium contents for the Site 765 basalts than would be expected, given the evolved nature of the Site 765 magmas.

As discussed in the "Basement Lithostratigraphy" section (this chapter), zirconium and titanium can be used to define a series of geochemical cycles within Hole 765D. Both titanium and zirconium are reasonably inert to alteration effects, and these cycles are considered to represent fluctuations in the compositions of the magma erupted at the surface. Changes in abundances of Al_2O_3, SiO_2, CaO, and Na_2O relative to zirconium variation are shown in Figure 112. With magmatic evolution Al_2O_3 and CaO exhibit a marked decrease. For SiO_2 and Na_2O, although trends are less evident, both appear to be stable, or increase slightly, with increasing zirconium. Fe_2O_3* and MgO are not shown, but when the least-altered samples are selected, these elements show an increase and decrease, respectively.

As shown above, all of the Site 765 lavas are evolved relative to MIOR basalts. Little olivine was observed in thin section, and the main phenocryst phases are plagioclase and clinopyroxene (see "Basement Petrography" section, this chapter). The decrease in Al_2O_3, CaO, and MgO are consistent with plagioclase and clinopyroxene fractionation. Furthermore, xenocrysts of both minerals are common in the basalts at the top of the section, indicating that these magmas may have disrupted plagioclase and clinopyroxene cumulates prior to eruption.

Thus, the geochemical cycles represented by variations of zirconium and titanium may represent intercalation of magmas that underwent a different extent of fractional crystallization. The stratigraphic changes are less evident for the major elements, probably because of "noise" associated with alteration, the more compatible behavior of most major elements, and the possible inclusion of nonequilibrium phenocrysts. However, a significant change in Fe_2O_3 and presence of quartz-normative rocks, in addition to a decrease in the abundance of clinopyroxene phenocrysts and plagioclase and clinopyroxene xenocrysts, were observed below Core 123-765D-7R. These changes may indicate a substantial difference in magma composition, upon which the more subtle variations in titanium and zirconium are superimposed.

The position of the Site 765 lavas with respect to the MIOR basalts may be taken to indicate that these lavas evolved along a

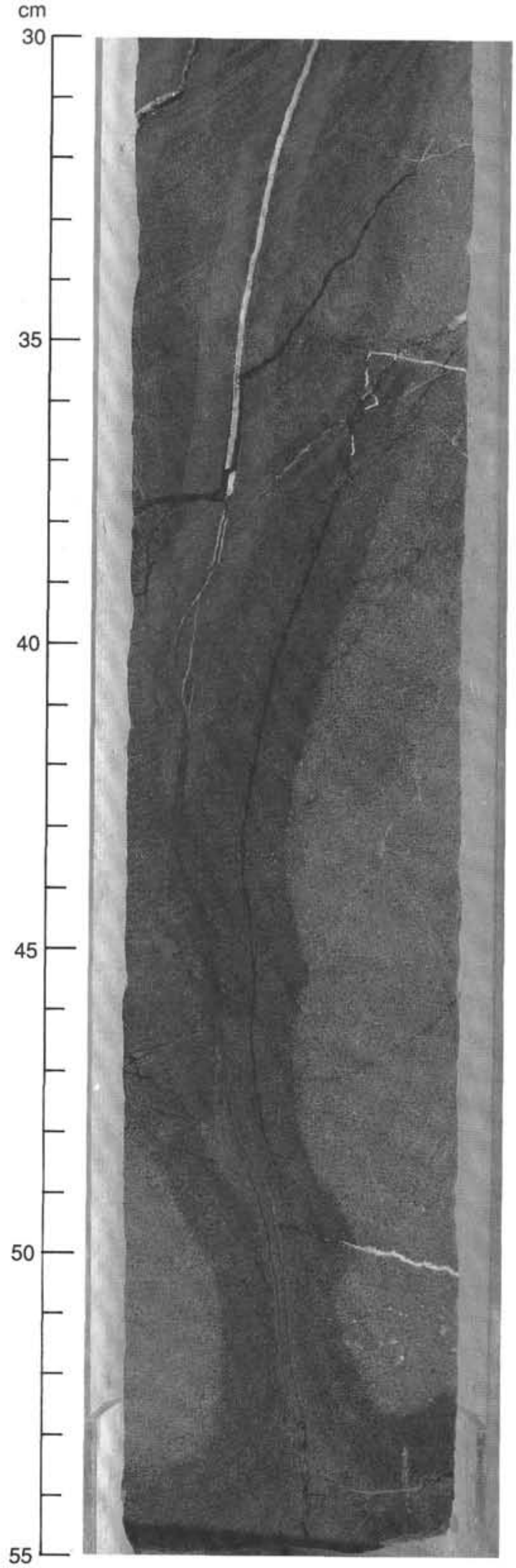

Figure 100. Multiple-phase oxidation halos in Interval 123-765D-2R-1, 30–55 cm. A late-stage clay mineral vein cuts a mixed clay mineral and calcite vein at 38 cm. Late-stage calcite veins at 35 and 50 cm have no associated oxidation halo.

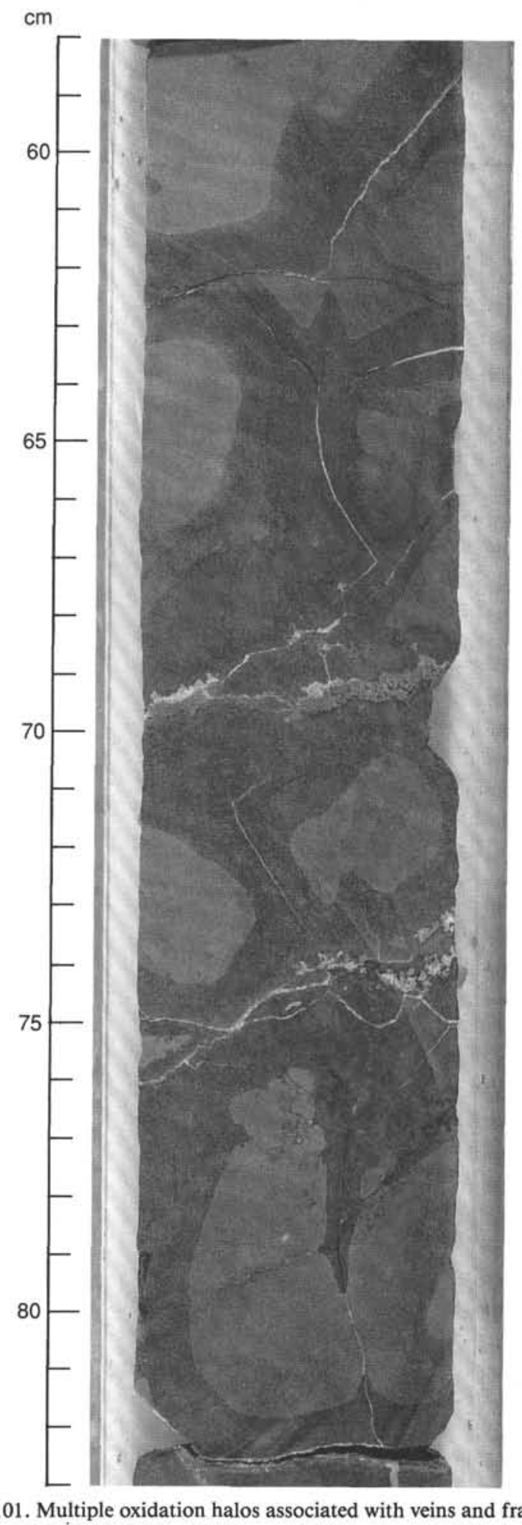

Figure 101. Multiple oxidation halos associated with veins and fractures in Interval 123-765D-2R-3, 58–83 cm. Calcite veins are late-stage and are not necessarily associated with oxidation halos, e.g., 79–82 cm.

low-pressure cotectic defined by the trends in Figure 110. The evolved position of the Site 765 basalts thus may be consistent with fractionation of an assemblage dominated by plagioclase and clinopyroxene and poor in olivine. However, as shown in Figure 113, Na_2O and CaO abundances, although somewhat scattered are, respectively, lower and higher than MIOR basalts.

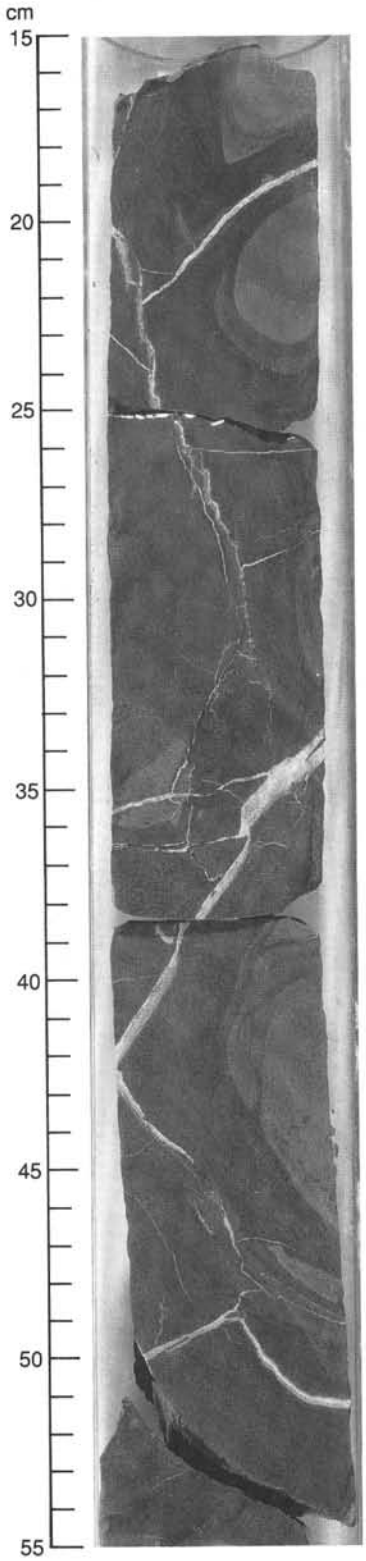

Figure 102. Multiple oxidation halos associated with calcite and clay mineral veins in Interval 123-765D-2R-3, 15–55 cm. The best multiple oxidation halos are at 18–28, 28–33, and 38–44 cm.

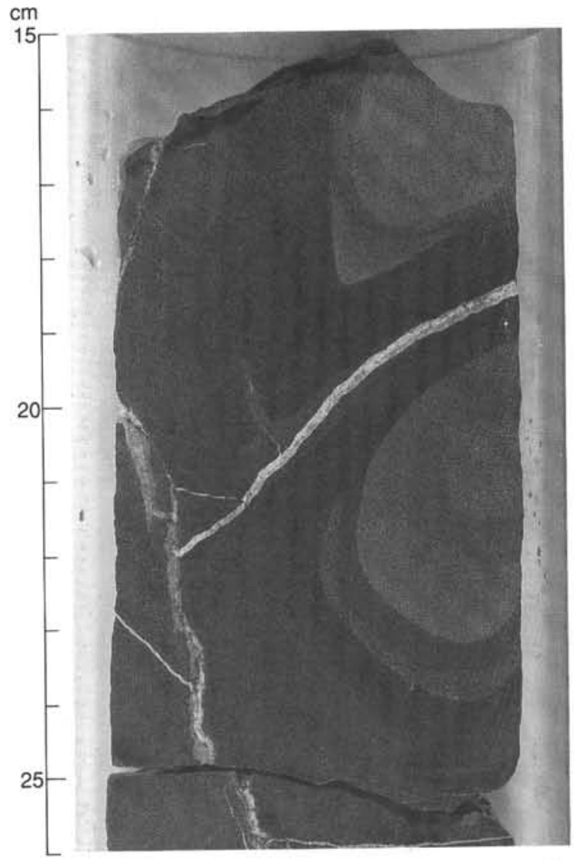

Figure 103. Close-up of the area at 15–26 cm in Figure 102. Multiple oxidation halos overprint the rock emanating from the calcite- and clay-mineral-filled veins (Interval 123-765D-2R-3, 15–26 cm).

This contrasts with the trends of Fe_2O_3*, MgO, and Al_2O_3, which suggest a continuum with MIOR basalts. CaO obviously has decreased during fractional crystallization, and Na_2O may have increased or perhaps remained relatively unchanged, due to fractional crystallization of a mineral assemblage having a distribution coefficient of near unity. Thus, the Site 765 magmas would, on first evaluation, appear to be related to Ca-rich and Na-poor magmas relative to MIOR basalts. Such a relationship may reflect greater degrees of melting in the mantle, which yielded the Site 765 basalts.

Trace Elements

Trace-element XRF analyses of the basement basalts are given in Table 38. Results for the MORB standard AII-92-29-1A and the Leg 123 inter-laboratory standard are listed in Table 36.

The average analysis for Site 765 basalts is given below and compared with an MIOR basalt average (see caption of Fig. 110 for data sources).

Rb	Ba	Nb	Ce	Sr	Zr	V	Y	Cr	Ni	Zn	Cu
Site 765 basalt (ppm)											
9.1	9.3	2.1	8.2	94.3	83.9	386	35.9	206	73.5	99	71.5
5.6	13.7	0.4	3.1	36.1	11.2	35	4.4	60	21	11	21
MIOR basalt (ppm)											
2.2	16.2	2.61	12.8	140	95	250	29	355	125	77	63
2.2	9	1.05	6.1	26	18	60	7	85	26	18	13

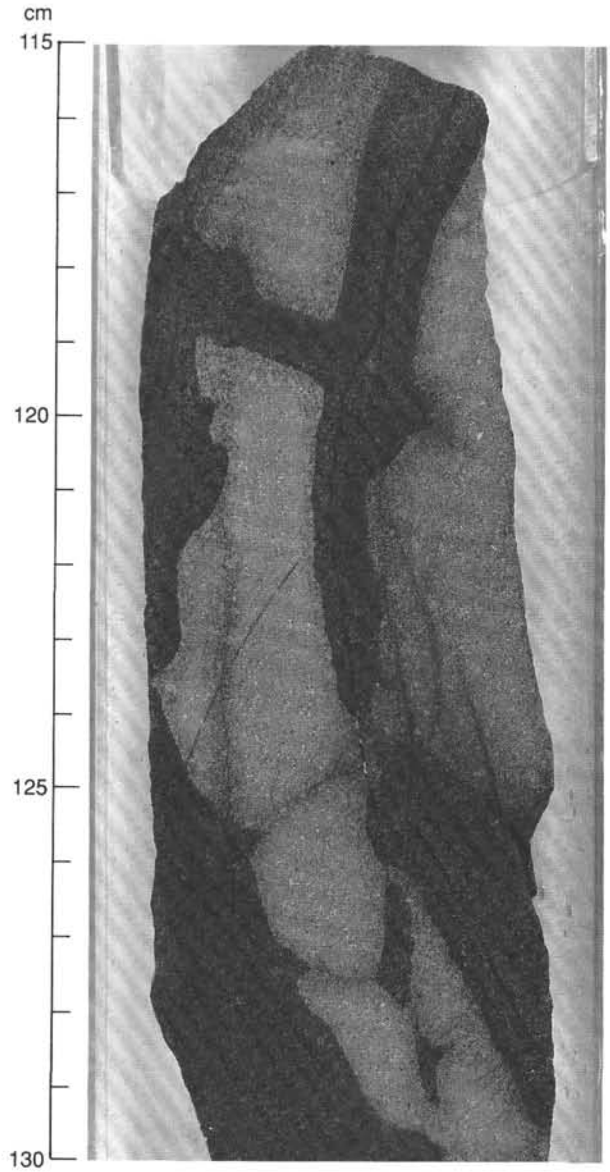

Figure 104. The entire rock has been pervasively altered to a pale gray, with later oxidation bands developed parallel to veins (Interval 123-765D-19R-2, 115–130 cm).

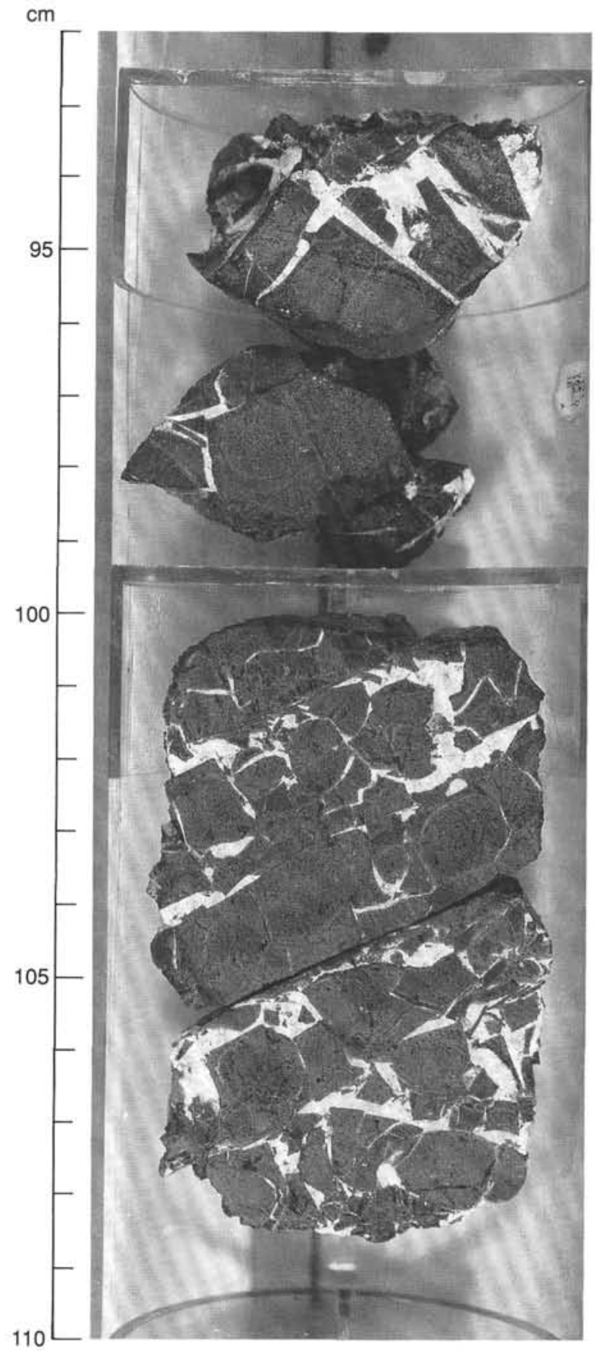

Figure 105. Calcite-cemented breccia. Note the absence of clay minerals in these veins (Interval 123-765D-13R-1, 92–110 cm).

All of the Site 765 basalts analyzed have been altered to a variable extent, and the abundances of the most lithophile trace elements, such as rubidium and barium, undoubtedly have been changed as a result of low-temperature alteration. The MIOR basalt average has been calculated for fresh lavas from the ridge axis and is representative of primary elemental abundances. Comparisons for these elements must await the results of trace elements on the fresh glass samples recovered at Site 765. Nonetheless, the evolved nature of the Site 765 basalts relative to the MIOR basalt average is evident from the trace-element abundances of elements that are less susceptible to alteration. The high vanadium contents are consistent with the high TiO_2 abundances, and the low chromium and nickel are indicative of extensive fractionation of mafic minerals. The lower stronium values for Site 765 may be indicative of extensive plagioclase fractionation.

Selected trace elements are plotted vs. zirconium as a fractionation index in Figure 114. Systematic increases in yttrium, cesium, and nubium relative to zirconium define trends following constant ratios of approximately 2.1, 40, and 8.5, respectively. This indicates that these elements are incompatible with the mineral phases being removed during fractionation. The constant ratios for all basalt samples implies that the magmas are cogenetic and simply related by fractional crystallization. Based on this limited data set, there is no reason to invoke geochemical changes related to different degrees of partial melting, or to mantle heterogeneity to explain the variations in trace elements between Site 765 basalts.

The chromium and nickel contents of the basement basalts exhibit a variation that would be expected if the phenocryst assemblage was dominated by clinopyroxene, rather than by olivine. Nickel and chromium are plotted vs. zirconium in Figure

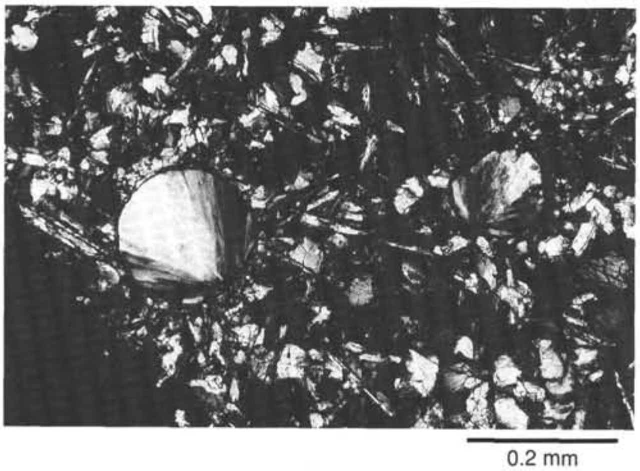

Figure 106. Zeolite-filled vesicles in basalt (Sample 123-765D-2R-3, 89–91 cm; crossed nicols).

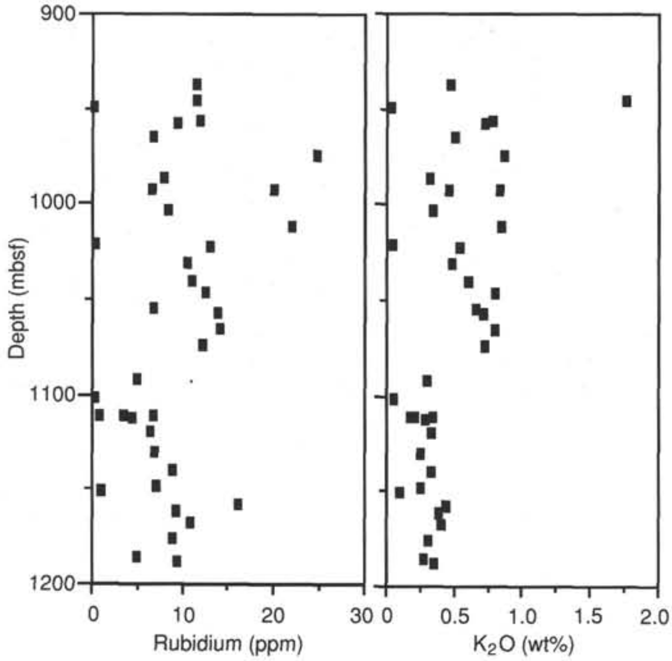

Figure 107. K_2O and rubidium variations with depth in Site 765 basalts. Concentrations of both K_2O and rubidium are lower below 1070 mbsf, which corresponds to the disappearance of celadonite in the alteration mineral assemblage.

114. Chromium decreases more rapidly than nickel for the Site 765 basalts. This trend is opposite that typically observed in MORBs, where nickel decreases more rapidly than chromium. This clearly indicates that nickel-consuming olivine fractionation is not an important differentiation process for Site 765 basalts, but that chromium-consuming clinopyroxene fractionation is dominant; this interpretation is supported by the abundance of clinopyroxene phenocrysts. Zinc abundances are higher than average MIOR basalts and increase with fractionation in Site 765 basalts; zinc thus must be largely incompatible with the fractionating assemblage. Copper abundances are comparable to those of the average MIOR basalt and exhibit no consistent trends with fractionation.

Zirconium, yttriuim, and niobium abundances of Site 765 basalts have been compared with MIOR basalts and Site 261 ba-

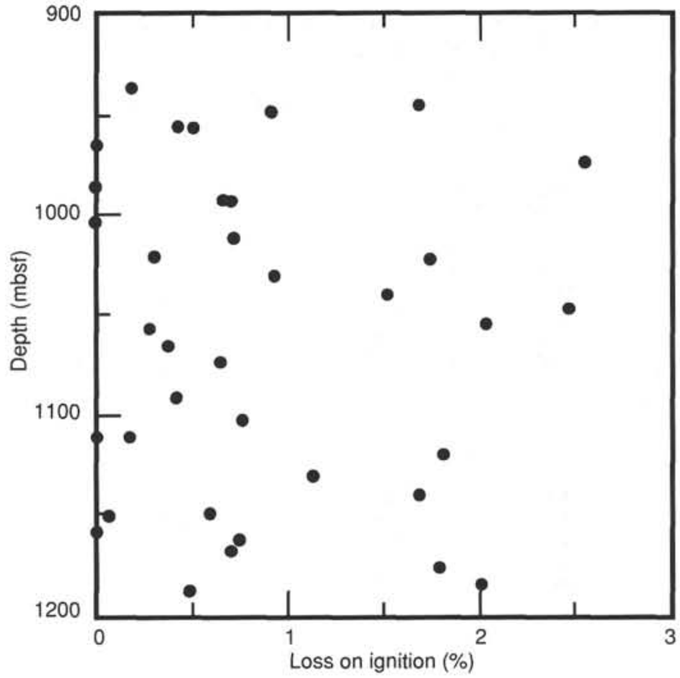

Figure 108. Loss on ignition (LOI) vs. depth for Site 765 basalts. LOI is a good measure of the extent of alteration of samples. LOI varies randomly with depth in these samples.

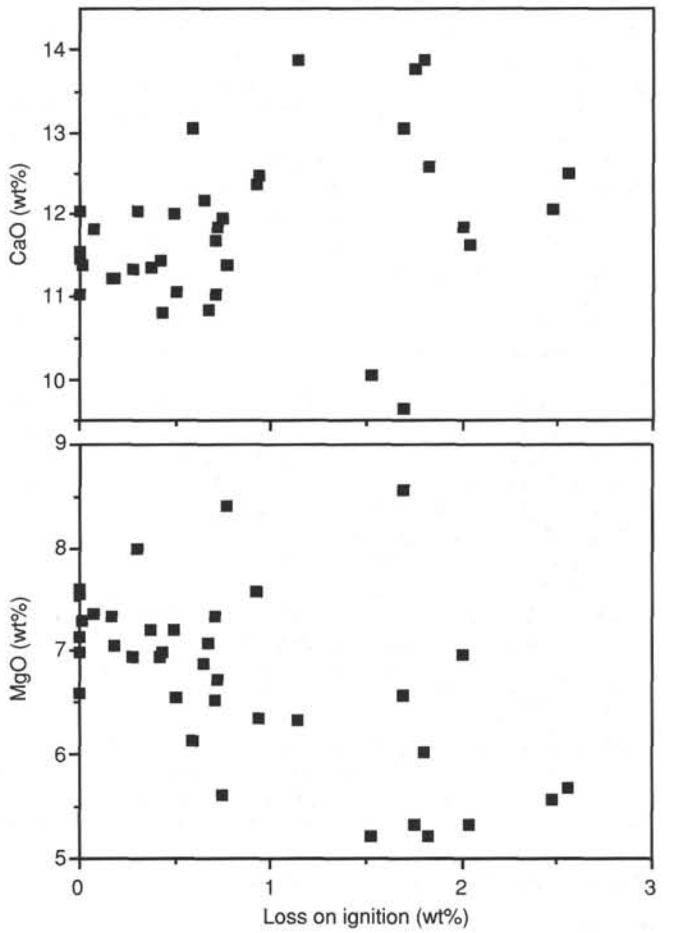

Figure 109. CaO and MgO vs. loss on ignition (LOI) in Site 765 basalts. There is a general increase in CaO and decrease in MgO with LOI.

Table 36. Analytical data and standard deviations (MORB from Hole 765 andLeg 123 standard).

	Leg 123		Sample 123-765D-19R-1, 72–78 cm
Major elements (wt%)			
SiO_2	49.51	±0.20	50.99
TiO_2	1.85	±0.01	1.63
Al_2O_3	15.53	±0.13	14.35
Fe_2O_3	10.83	±0.15	10.13
MnO	0.18	±0.01	0.20
MgO	7.50	±0.22	7.69
CaO	11.09	±0.04	11.78
Na_2O	3.1	±0.12	2.53
K_2O	0.17	±0.01	0.17
P_2O_5	0.15	±0.01	0.15
	N = 13		
Trace elements (ppm)			
Nb	3.1	±0.2	2.2
Zr	129	±2.9	96
Y	40	±0.5	43
Sr	126	±1.0	83
Rb	1.0	±0.4	0.9
Zn	86	±1.2	106
Cu	62	±0.6	118
Ni	105	±1.1	78
Cr	239	±5.9	207
V	302	±4.1	380
Ce	17	±2.6	14
Ba	6.7	±5.5	2
	N = 7		

salts in Figure 114. Given the evolved nature of the Site 765 basalts, and the predicted incompatible element behavior of zirconium, yttrium, and niobium, if the Site 765 magmas were simply fractionated basalts derived from a mantle source similar to that of MIOR basalts, they should define similar ratios with generally higher total abundances for these elements. This is clearly not the case. Yttrium values are significantly higher than MIOR basalts, which is consistent with the more evolved nature of the Site 765 magmas, while both zirconium and niobium are comparable to the less-evolved MIOR basalts. Thus, Site 765 basalts have a low zirconium/yttrium value of 2.1, compared with a value of approximately 3.0 for MIOR basalts. Zirconium/niobium values are approximately 40 in both Site 765 and MIOR basalts.

When considering the parental magmas for these suites, one must "back-fractionate" the data to a predetermined major element composition. While it is beyond our scope to quantify the fractionation process, it is evident even without rigorously back-fractionating the compositions of trace elements that the Site 765 magmas are abnormally low in both niobium and zirconium relative to modern MIOR basalts. One possible interpretation, which may be consistent with the arguments cited above for high CaO and low Na_2O magmas, is that the low zirconium and niobium abundances reflect extensive mantle melting at the time of formation of the Site 765 magmas. Why yttrium abundances do not reflect this process is unclear.

The trace-element data base for Sites 261 and 260 is limited. Site 261 basalts have slightly lower zirconium/yttrium values, a result of higher yttrium abundances. Two analyses of Site 260 basalts give zirconium/yttrium values of 3 to 3.4, values more comparable to those of modern MIOR basalts. However, both Site 260 and 261 basalts are more comparable to MIOR basalts than Site 765 basalts in terms of major elements.

Summary

Abundances of both major and the most compatible trace elements are consistent with cotectic control of the Site 765 basalt compositions. MIOR basalts and Site 765 basalts fall on a single liquid line of descent; the Site 765 magmas are more evolved than MIOR magmas, and their fractionating assemblage was dominated by plagioclase and clinopyroxene.

At least five geochemical units can be defined at Site 765. These represent the eruption of successive pulses of magma that underwent a different extent of crystal fractionation.

Significant differences are evident between Site 765 magmas and MIOR magmas for incompatible trace-element ratios, such as zirconium/yttrium and yttrium/niobium. These differences probably reflect different mantle source regions for these magmas.

CaO, Na_2O (possibly Fe_2O_3*), zirconium, and niobium abundances reflect a higher extent of melting for the Site 765 magmas than for modern MIOR basaltic magmas.

BASEMENT PALEOMAGNETISM

Analyses

Archive halves of basement basalt cores from Holes 765C and 765D were measured using a pass-through cryogenic magnetometer at natural remanent magnetization (NRM) and at alternating field (AF) demagnetization steps of 10, 15, and 20 mT. An additional 11 whole-round blocks, taken from cores of Hole 765D for strain measurements, were demagnetized and measured in the same way.

Discrete samples were measured for five minicores taken from the last four cores of Hole 765C (Samples 123-765C-62R, CC, 23–25 cm; -63R-2, 111–113 cm; -63R-4, 97–99 cm; -64R-1, 14–16 cm; and -65R-1, 96–98 cm), and 35 samples from the 27 cores of Hole 765D. These discrete samples were subjected to eight steps of AF demagnetization treatments from 2, 4, 8, 10, 12, 15, 20, and 25 mT, and measured after each step with a Minispin spinner magnetometer. Because of iron hydroxides in weathered portions, preliminary thermal demagnetizations were performed for several selected samples using a Schonstedt TSD-1 thermal demagnetizer. Thermal treatments of 200°C and, for some samples, 250°C were used to remove any secondary magnetic component carried by such iron hydroxides, which have a Curie temperature of between 60° to 170°C (Tarling, 1983). The result for each discrete sample was plotted onto vector (Zijderfeld) and stereographic plots to examine its magnetic stability upon AF and thermal demagnetizations.

Magnetic susceptibility was measured for archive halves and for discrete samples using a Bartington MSB1 susceptibility meter. Susceptibility of the archive halves were measured every 10 cm, skipping layers composed of rubble.

Magnetic Properties

Intensities of NRM of basalts from Site 765 range from 60 to 6000 mA/m, with the majority falling between 200 to 1000 mA/m. Stepwise AF demagnetizations of archive blocks and discrete samples generally indicate low magnetic coercivities with mean destructive field (MDF) values, at which the intensity of magnetization decreases to one-half the NRM intensity, which is less than 15 mT. This coercivity varied with the lithology. Fine-grained basalt generally had a lower coercivity than coarse-grained basalt. In particular, 10 of the 35 minicores from Hole 765D have MDF intensities of less that 5 mT. Nine of these 10 samples were taken from massive basalt flows.

In contrast, a fine-grained basalt sample (Sample 123-765C-62R-CC, 23–25 cm) taken about 25 cm below the chill margin of the uppermost pillow flow, displayed a stable reversed-polarity magnetization having an MDF value of about 16 mT (Fig. 115A). Irrespective of the difference in coercivity, almost all of the samples exhibit stable magnetic behavior, as indicated by the linear decay of magnetic vectors toward the origin of vector plots or stable directions displayed in stereographic plots (Fig. 115B).

Table 37. XRF concentrations of major-element oxides in basement samples, Site 765.

Core, section, interval (cm)	Depth (mbsf)	SiO_2 (wt%)	TiO_2 (wt%)	Al_2O_3 (wt%)	Fe_2O_3 (wt%)	MnO (wt%)	MgO (wt%)	CaO (wt%)	Na_2O (wt%)	K_2O (wt%)	P_2O_5 (wt%)	Total (wt%)	LOI
123-765C-													
63R-1, 122–124	937.0	49.62	1.50	14.06	13.53	0.24	7.06	11.22	2.05	0.47	0.09	99.83	0.18
64R-1, 2–6	945.3	50.57	1.50	14.47	10.80	0.18	8.56	9.65	2.22	1.76	0.09	99.80	1.69
65R-2, 106–110	957.2	50.11	1.41	14.64	13.30	0.22	6.56	11.06	2.43	0.72	0.09	100.54	0.51
123-765D-													
1R-1, 94–96	948.8	50.19	1.37	14.30	11.67	0.20	7.59	12.36	2.15	0.03	0.09	99.98	0.92
2R-2, 41–43	956.5	50.64	1.35	13.89	12.68	0.21	6.99	10.80	2.80	0.78	0.11	100.26	0.43
3R-1, 33–35	964.7	50.41	1.64	13.96	11.89	0.23	6.99	11.50	2.56	0.50	0.15	99.84	0.00
4R-1, 35–37	974.0	49.00	1.48	13.34	14.03	0.28	5.68	12.50	2.33	0.86	0.12	99.61	2.56
5R-3, 131–133	986.1	49.77	1.56	13.73	12.49	0.25	7.61	11.54	2.16	0.32	0.12	99.55	0.00
5R-8, 117–120	992.0	49.38	1.65	13.99	13.71	0.29	7.08	10.83	2.26	0.46	0.14	99.80	0.67
6R-1, 52–54	992.9	49.33	1.56	13.65	14.04	0.35	6.52	11.03	2.04	0.83	0.13	99.49	0.71
7R-2, 9–11	1003.5	50.68	1.35	14.60	11.07	0.18	7.56	12.04	2.08	0.34	0.11	100.01	0.00
8R-1, 63–65	1012.1	50.51	1.31	14.22	11.66	0.17	6.73	11.86	2.17	0.84	0.09	99.56	0.72
9R-1, 58–60	1021.5	50.53	1.37	14.16	11.76	0.17	7.99	12.05	2.04	0.04	0.11	100.22	0.30
9R-4, 32–34	1022.7	50.64	1.54	14.94	10.14	0.16	5.33	13.77	2.33	0.54	0.12	99.51	1.75
10R-1, 81–83	1031.0	49.35	1.27	15.45	12.27	0.26	6.36	12.48	1.69	0.48	0.11	99.71	0.94
11R-1, 73–75	1040.1	48.74	1.57	15.12	14.91	0.19	5.21	10.04	2.73	0.60	0.12	99.22	1.53
12R-2, 15–18	1046.7	48.44	1.33	15.83	13.03	0.24	5.57	12.08	1.97	0.80	0.14	99.44	2.47
13R-1, 19–21	1054.6	49.46	1.10	17.39	11.62	0.13	5.32	11.62	2.32	0.66	0.06	99.68	2.04
13R-3, 10–12	1057.4	49.80	1.41	13.89	13.12	0.21	6.95	11.33	2.25	0.71	0.11	99.77	0.28
14R-2, 51–53	1065.7	49.83	1.42	13.93	12.68	0.21	7.20	11.37	2.24	0.80	0.11	99.78	0.37
15R-2, 14–17	1074.6	50.19	1.42	14.83	11.53	0.18	6.89	12.17	1.84	0.72	0.11	99.89	0.65
16R-1, 39–41	1082.9	48.73	1.39	12.58	13.46	0.06	7.37	11.67	1.84	2.26	0.04	99.38	12.30
17R-1, 37–39	1092.0	50.44	1.53	14.41	11.92	0.18	6.94	11.45	2.22	0.30	0.13	99.51	0.42
18R-1, 112–114	1102.2	50.75	1.45	15.40	10.04	0.16	8.42	11.39	2.52	0.05	0.11	100.29	0.77
19R-1, 51–52	1110.8	49.77	1.57	13.80	12.67	0.22	7.33	11.22	2.28	0.34	0.12	99.31	0.17
19R-1, 72–78	1111.0	50.99	1.63	14.35	10.13	0.20	7.69	11.78	2.53	0.17	0.15	99.62	15.01
19R-1, 108–110	1111.4	50.93	1.69	13.90	10.92	0.20	7.30	11.38	2.63	0.21	0.14	99.30	0.01
19R-2, 32–34	1111.9	52.89	1.62	14.19	9.81	0.20	7.14	11.47	2.76	0.28	0.13	100.48	0.00
20R-1, 15–17	1119.6	48.01	1.28	15.71	14.08	0.17	5.22	12.58	2.13	0.33	0.12	99.62	1.82
21R-1, 117–119	1130.2	49.59	1.25	14.86	11.88	0.23	6.34	13.88	1.86	0.25	0.09	100.24	1.14
22R-1, 118–121	1139.8	48.85	1.28	15.03	12.32	0.24	6.58	13.05	1.86	0.33	0.10	99.65	1.69
23R-1, 62–64	1148.9	49.83	1.24	15.15	10.92	0.17	6.13	13.04	2.53	0.25	0.09	99.35	0.59
23R-2, 97–100	1150.3	51.81	1.65	14.15	10.14	0.19	7.37	11.82	2.42	0.10	0.14	99.78	0.07
24R-2, 21–24	1158.6	49.62	1.54	13.04	15.37	0.22	6.59	11.04	1.87	0.44	0.13	99.85	0.00
24R-4, 106–109	1161.9	49.92	1.56	13.62	14.10	0.21	5.62	11.95	2.30	0.38	0.13	99.78	0.75
25R-2, 2–4	1167.9	50.24	1.57	14.44	11.13	0.18	7.33	11.68	2.78	0.40	0.12	99.86	0.71
26R-1, 35–37	1176.4	48.76	1.56	14.16	12.35	0.21	6.02	13.86	2.22	0.31	0.13	99.58	1.80
27R-1, 4–6	1185.4	50.23	1.65	14.91	11.46	0.24	6.96	11.86	2.22	0.27	0.13	99.92	2.01
27R-2, 96–98	1187.5	50.55	1.64	14.17	11.40	0.20	7.21	12.02	1.87	0.35	0.13	99.53	0.49

LOI = Loss on inignition.

Where present, secondary components are commonly removed by AF demagnetization of 10 to 15 mT. For example, Sample 123-765D-3R-1, 35–37 cm, has a strong overprint of normal polarity, which is removed by 8 to 10 mT demagnetization to reveal a stable reversed polarity (Fig. 115C).

All five discrete samples from Hole 765C and the five uppermost samples from Hole 765D were subjected to thermal demagnetization at 200°C following AF demagnetization at 26 mT. This level of thermal demagnetization exceeds the Curie point of iron hydroxide (goethite) alteration minerals, but should have minimal affect on iron-titanium oxides. This thermal treatment rendered a slight decrease (less than 20%) in magnetic intensity, but did not cause any significant change in direction. Therefore, the primary iron-titanium oxides have not been completely replaced by iron hydroxides like goethite, which suggests that the characteristic magnetization carried is mainly titanomagnetite or titanomaghemite, as commonly contained in oceanic basalts (e.g., Hamano et al., 1980).

A similar rapid intensity decrease upon AF demagnetization, but with good directional stability, was also reported for Upper Jurassic(?) to Lower Cretaceous basalt samples recovered at nearby DSDP Sites 259, 260, and 261 of Leg 27 (McElhinny, 1974).

Magnetic Stratigraphy

Hole 765C

Basalt basement of Cores 123-765C-62R and 123-765C-63R has reversed polarity, while Core 123-765C-65R and most of the cores of Hole 765D have normal polarity (Fig. 116). Intervening Core 123-765C-64R, which consists of one short section (58 cm long) of three pieces, exhibits different polarities before and after AF demagnetizations. The NRM of this section displays a normal polarity as a whole, but, with progressive AF demagnetization, the inclinations of the upper two pieces (40 cm long) change to downward inclinations, indicating reversed polarity. Some portions of these pieces displayed shallow positive inclinations only after a demagnetization of 25 mT; the lowest piece preserved negative inclinations, indicating normal polarity. The rapid change in inclination of the upper part of Core 123-765C-64R was also supported by progressive AF demagnetization of a discrete sample taken 14 cm from the top of Section 123-765C-64R-1; for this sample, the initial steep upward inclination of −62.8° changed to −11.7° after a demagnetization of 25 mT. The anomalously shallow negative (partly positive) inclinations of the upper part of Core 123-765C-64R may indicate an intermediate earth magnetic field during the transition from normal

Table 38. XRF concentrations of trace elements in basement samples, Site 765.

Core, section, interval (cm)	Nb (ppm)	Zr (ppm)	Y (ppm)	Sr (ppm)	Rb (ppm)	Zn (ppm)	Cu (ppm)	Ni (ppm)	Cr (ppm)	V (ppm)	Ce (ppm)	Ba (ppm)
123-765C-												
63R-1, 122–124	2.2	84.3	36.5	84.8	11.5	107.3	61.0	125.3	418.9	5.3	3.9	
64R-1, 2–6	2.2	85.6	34.9	220.8	11.4	96.6	31.0	71.2	117.6	354.8	7.6	54.9
65R-2, 106–110	2.4	75.8	34.0	99.1	9.4	97.3	74.2	62.8	204.7	403.7	8.0	38.9
123-765D-												
1R-1, 94–96	1.9	78.1	34.5	91.0	0.1	86.5	80.9	69.1	213.5	376.7	5.4	3.2
2R-2, 41–43	1.6	74.2	31.9	75.3	11.8	86.9	44.3	63.1	221.1	366.8	7.0	59.7
3R-1, 33–35	2.8	96.0	42.1	84.3	6.7	112.1	49.6	55.6	160.7	441.0	13.9	26.0
4R-1, 35–37	1.9	85.2	36.6	82.6	24.7	91.9	103.3	54.4	163.1	401.0	9.0	3.2
5R-3, 131–133	2.5	89.2	39.6	82.8	7.9	105.8	73.9	79.8	164.3	395.0	10.3	1.1
5R-8, 117–120	3.0	94.8	37.4	95.8	6.6	106.1	69.7	64.0	136.8	406.9	13.2	13.4
6R-1, 52–54	1.9	95.8	38.9	85.6	20.0	103.5	68.4	51.1	140.2	402.1	12.2	−4.2
7R-2, 9–11	1.6	76.3	33.9	82.8	8.3	91.3	88.6	111.8	327.9	368.4	9.1	6.7
8R-1, 63–65	2.0	74.9	30.4	78.5	22.0	80.4	37.8	67.4	306.1	341.6	6.6	7.4
9R-1, 58–60	2.1	74.3	33.7	79.5	0.4	81.1	82.3	81.6	260.7	365.5	8.1	7.6
9R-4, 32–34	2.0	84.8	35.6	87.9	12.9	85.5	26.2	69.3	175.5	352.7	12.1	0.1
10R-1, 81–83	2.0	69.1	32.4	87.0	10.5	96.1	77.9	58.2	294.9	418.6	3.7	7.8
11R-1, 73–75	2.3	92.0	41.7	95.5	11.0	119.4	81.3	57.1	105.6	519.9	10.4	0.7
12R-2, 15–18	1.7	71.4	29.0	87.1	12.4	99.1	48.1	50.3	183.4	396.9	0.8	14.1
13R-1, 19–21	1.3	52.2	25.6	93.4	6.7	84.7	92.7	87.3	380.9	394.5	2.6	2.3
13R-3, 10–12	1.9	82.7	35.1	82.6	13.8	97.3	69.5	57.4	207.5	368.1	11.1	9.8
14R-2, 51–53	2.5	81.8	33.6	75.0	14.1	92.8	69.6	57.2	202.9	360.4	7.8	5.9
15R-2, 14–17	2.2	71.6	34.8	76.5	12.1	96.2	73.4	87.4	242.3	355.3	8.5	0.2
16R-1, 39–41	1.5	69.6	16.9	70.4	40.2	77.0	89.7	71.6	178.2	139.6	5.1	27.8
17R-1, 37–39	2.1	93.0	38.2	84.8	5.0	93.7	96.0	69.2	202.8	380.2	9.2	6.5
18R-1, 112–114	2.3	82.3	36.3	88.7	0.3	90.4	69.3	165.8	331.7	388.7	8.3	2.3
19R-1, 51–52	2.6	92.7	37.9	79.6	6.7	102.5	75.8	77.5	206.2	393.7	10.4	8.0
19R-1, 72–78	2.2	95.7	43.1	83.2	0.9	106.8	118.0	77.7	207.3	380.1	12.7	1.8
19R-1, 108–110	2.6	100.3	42.7	83.1	3.5	122.9	52.4	83.4	213.0	453.9	11.5	8.1
19R-2, 32–34	2.8	94.3	40.6	80.5	4.4	96.0	43.1	82.6	208.5	354.1	10.5	11.5
20R-1, 15–17	1.7	72.3	30.9	91.8	6.4	105.2	67.1	70.3	211.7	440.9	5.7	5.1
21R-1, 117–119	2.0	70.1	30.0	86.0	6.9	94.1	83.7	70.0	189.1	359.3	4.5	0.0
22R-1, 118–121	1.6	69.9	29.0	84.9	8.8	93.8	83.5	73.4	179.5	382.3	5.3	4.3
23R-1, 62–64	1.3	70.3	28.7	82.6	7.1	95.2	84.4	83.5	180.3	347.4	6.0	0.0
23R-2, 97–100	1.9	95.0	40.9	81.0	1.0	120.7	121.7	77.2	178.9	356.8	11.2	11.9
24R-2, 21–24	2.5	90.4	40.2	73.6	16.0	86.3	77.2	51.0	168.8	384.9	7.5	4.3
24R-4, 106–109	1.7	88.3	38.1	77.7	9.2	93.4	57.7	58.1	168.9	381.4	5.7	0.9
25R-2, 2–4	2.4	91.0	37.9	158.7	10.8	119.8	59.7	73.1	230.9	359.3	6.9	10.8
26R-1, 35–37	2.4	96.8	36.0	87.4	8.9	97.5	73.1	75.8	181.3	383.6	4.7	4.3
27R-1, 4–6	2.1	96.8	39.5	247.3	5.0	111.8	55.8	75.9	207.9	357.6	10.2	4.3
27R-2, 96–98	1.9	97.4	41.9	83.3	9.3	105.9	77.7	111.4	205.7	363.7	9.5	8.2

to reversed polarity or incomplete demagnetization. In contrast, the discrete samples of the upper reversed-polarity cores and the lower normal-polarity cores displayed stable magnetic behaviors. This polarity change is perhaps the result of the location of Site 765 on the landward edge of reversed-polarity anomaly "M-26." In the magnetic anomaly transition zone, one would expect the uppermost flows to have erupted during the reversed-polarity chron over earlier flows, formed during the preceding normal-polarity chron.

Hole 765D

Only three cores from Hole 765D did not display a predominance of normal polarity. Cores 123-765D-3R, -21R, and -25R exhibit distinct reversed polarities throughout (Fig. 116). Although there are some reversely magnetized pieces scattered within the other cores of normal polarity, these were probably accidentally inverted or are short pieces having no up/down orientation. The reversed magnetizations of the three cores listed above were confirmed by measuring discrete samples. Such brief and frequent intervals of apparent polarity changes, which would imply an extended history of basalt eruptions, are not compatible with models of ocean crust formation at rift zones. Possible explanations for such anomalous intervals of opposing polarity include (1) partial thermal remagnetization during later hydrothermal activity, (2) accidental inversion of entire sections of these cores during the curatorial preparation process, and (3) persistent overprints of secondary chemical magnetization.

There may be two more narrow, reversed-polarity zones in Cores 123-765D-14R and -25R, but these are regarded with suspicion because of the lack of supporting evidence from discrete-sample measurements.

Mean Inclinations

Table 39 is a preliminary interpretation of paleomagnetic data from long cores, special blocks, and discrete samples. All inclinations and associated lithological information are illustrated in Figure 116.

The arithmetic mean inclination of basalt cores from Hole 765C is 46°, which is comparable to the mean inclination of sediments above them (42°; see "Sediment Paleomagnetism" section, this chapter). The similar mean inclinations for basalts and overlying sediments suggest that post-depositional "inclination error" from compaction processes is not significant for these reddish pelagic sediments. The lower portion of Hole 765C deviates 11° from vertical; therefore, mean inclinations may include an error of the same amount. Correction for hole deviation magnitude and direction, and more careful demagnetization treatments and statistical analysis, are required for discrete samples from these cores.

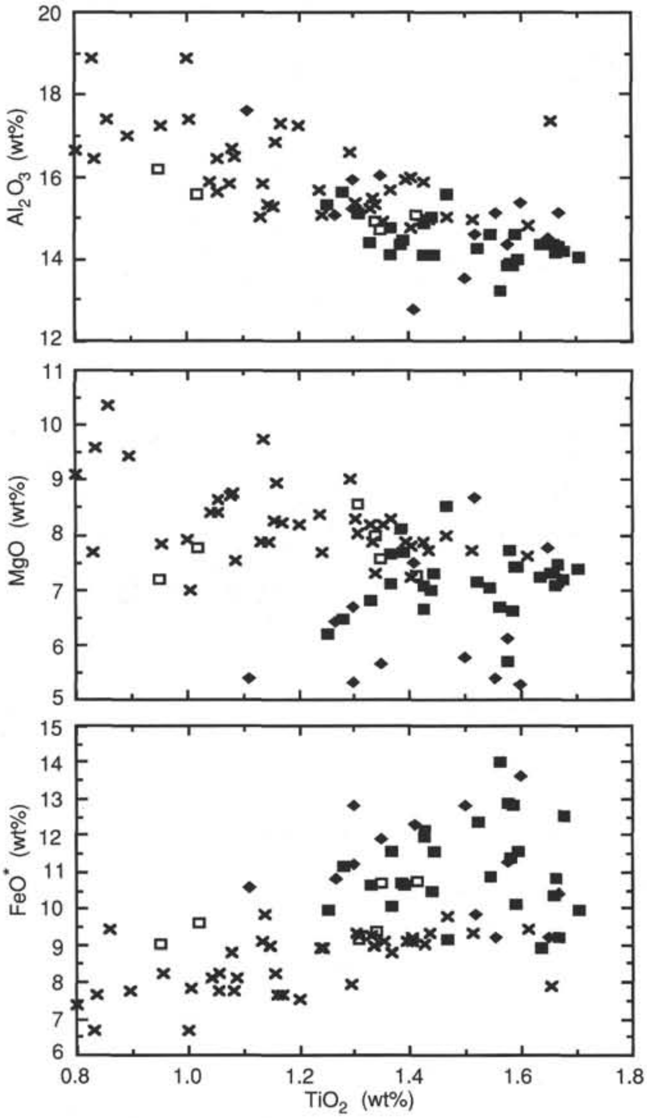

Figure 110. Diagrams of variations of element oxides. Squares = "freshest" samples (<1 wt% LOI); diamonds = "most altered" samples (>1 wt% LOI). DSDP Site 261 = open squares. Mid-Indian Ocean Ridge (MIOR) basalts = crosses. MIOR data were compiled from Frey et al. (1977), Price et al. (1986), Dosso et al. (1988), and Humler and Whitechurch (1988).

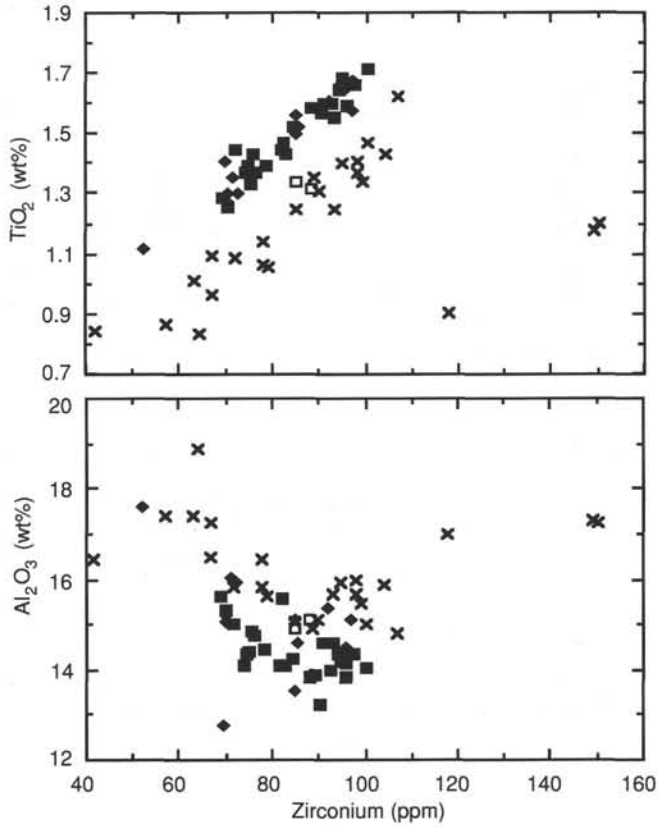

Figure 111. Al_2O_3 and TiO_2 variations vs. zirconium for Site 765, DSDP Site 261 and MIOR basalts. Symbols and data sources as in Figure 110.

Inclinations of Hole 765D are slightly steeper than those of Hole 765C. Although inclinations of the upper seven cores of Hole 765D display a high degree of scatter, the average inclination seems to be about 55°. This inclination agrees with that of Hole 765C after adding a hole-deviation correction of approximately 10°.

Regardless of their polarities, the inclinations of Cores 123-765D-9R through -14R are well grouped between 60° and 70°. Inclinations of similar value also were reported for basalts recovered at Site 261 of DSDP Leg 27 (McElhinny, 1974), although only nine samples were available from the site. The corresponding paleolatitude estimated from these preliminary mean inclinations of Hole 765D is between 41° and 54°.

Below Core 123-765D-14R, inclinations are much steeper, with average values between 70° and 80°. Such steep inclinations, which would imply very high paleolatitudes of more than 60°S, are not compatible with the predicted paleolatitudes of Site 765 (see "Background and Introduction" chapter, this volume), or with the results from the upper portion of Hole 765D. One explanation is that the lower portion of Hole 765D penetrated a block that rotated in the rift zone, after which it was overlain by basaltic flows.

In general, inclination data do not display clusters of values that can be used to infer eruption intervals during different stages of secular variation.

Susceptibility

Figure 117 is a summary of susceptibility measured for long cores of Holes 765C and 765D. The extremely low susceptibilities at the top (926.4–931.0 mbsf) correspond to sediments just above the basement. The majority of basalts have volume susceptibilities between 1 to 3 × 10^{-3} cgs (Gauss/Oersted), comparable to or slightly higher than those of typical oceanic basalts (e.g., Bryan and Juteau et al., 1988). Strong susceptibilities of more than 4 × 10^{-3} cgs were obtained from Core 123-765D-24R at about 1160 mbsf, within massive basalt flow. The second coarsest grain size and the highest iron content of this basalt core (see "Basement Petrography" section, this chapter) are considered as responsible for this unusually strong magnetic susceptibility.

BASEMENT PHYSICAL PROPERTIES

Introduction

The physical properties determined from basement rocks at Site 765 on the Argo Abyssal Plain include compressional-wave velocity (as measured using a Hamilton Frame velocimeter), in-

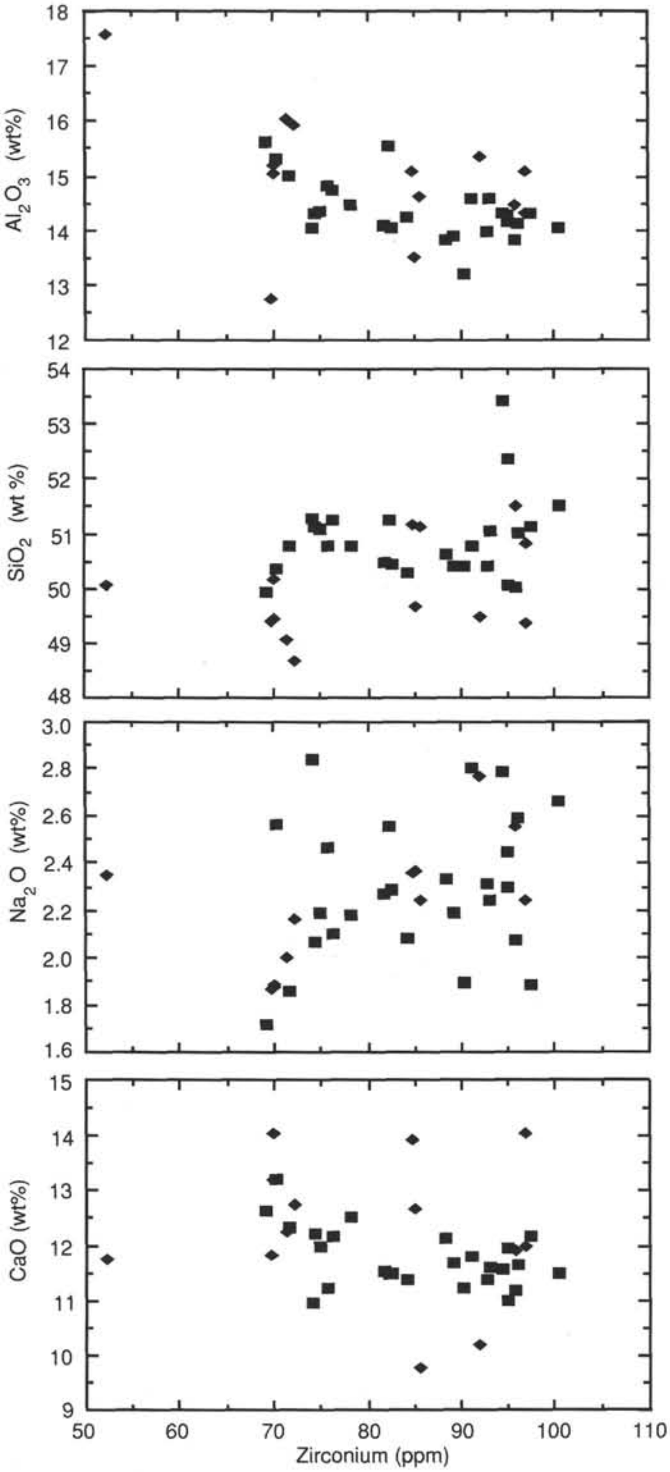

Figure 112. Variations of major elements vs. zirconium for Site 765. Zirconium represents an index of degree of fractionation for these basalts.

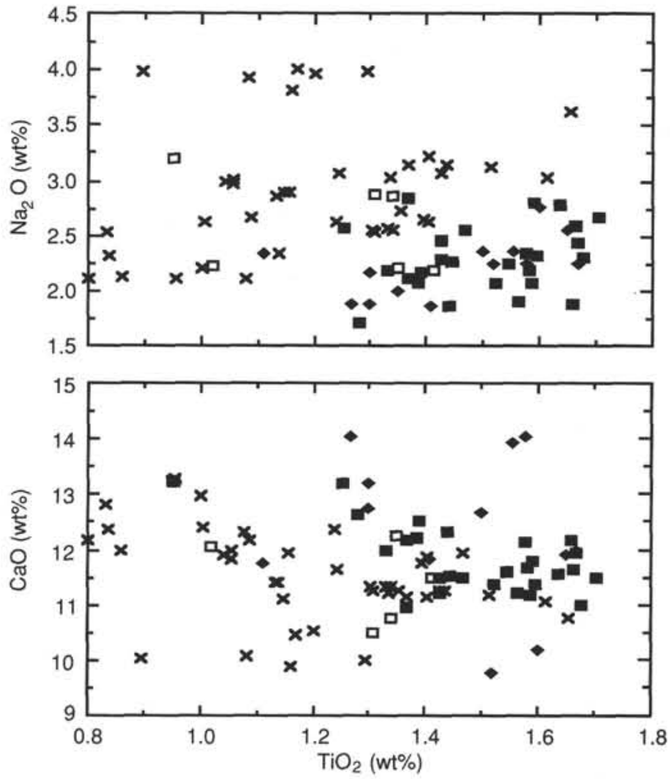

Figure 113. CaO and Na_2O in Site 765 basalts relative to MIOR and DSDP Site 261 basalts. Symbols as in Figure 110.

dex properties (i.e., bulk density, grain density, porosity, and water content, as determined by a pycnometer and balance), and thermal conductivity. Four holes (Holes 765A through 765D) were cored at Site 765. Specific details concerning coring procedures and depths can be found in the "Operations" section (this chapter). Velocities and index properties were measured on samples from each core. Values of various physical-property measurements are listed in Tables 40 and 41, and variations of these properties with depth are illustrated in Figure 118.

Results

Index Properties

Bulk density, grain (or matrix) density, porosity, and water content (dry basis) of the samples from Hole 765D are listed in Table 40 and plotted relative to depth in Figure 118A-D. The unit, in terms of index properties, is fairly homogeneous and is composed primarily of pillow basalts and massive basalt flows. Bulk and grain densities, for the unit as a whole, have average values of 2.85 ± 0.06 g/cm^3 and 2.93 ± 0.07 g/cm^3, respectively. Water content and porosity data exhibit a higher degree of variability, but also appear to remain relatively constant with depth and have values of 1.5 $\pm$ 0.8 % and 4.0 ± 2.2%, respectively. A significant increase in water content and porosity occurred at 994 and 1005 mbsf. The rocks tested appeared lighter in color and had a much coarser grain structure when compared with other samples for the unit. A significant variation in the index properties occurs at 1162 mbsf. The sample does not appear to be significantly different from the surrounding material, namely, dark fine-grained basalt; therefore, these data are believed to be suspect.

When reducing the physical properties data, we found that the difference between the wet and dry volumes was often less than the accuracy of the pycnometer. The problem became manifest in a significant number of instances where dry volume was found to exceed the wet volume. Thus, when calculating index properties, the wet or total volume was determined using an averaged sample diameter and height, as measured to the nearest 0.002 cm by a set of calipers. This volume, along with the wet and dry weights, was used to develop the phase relationships, hence, the index properties for the basement rock.

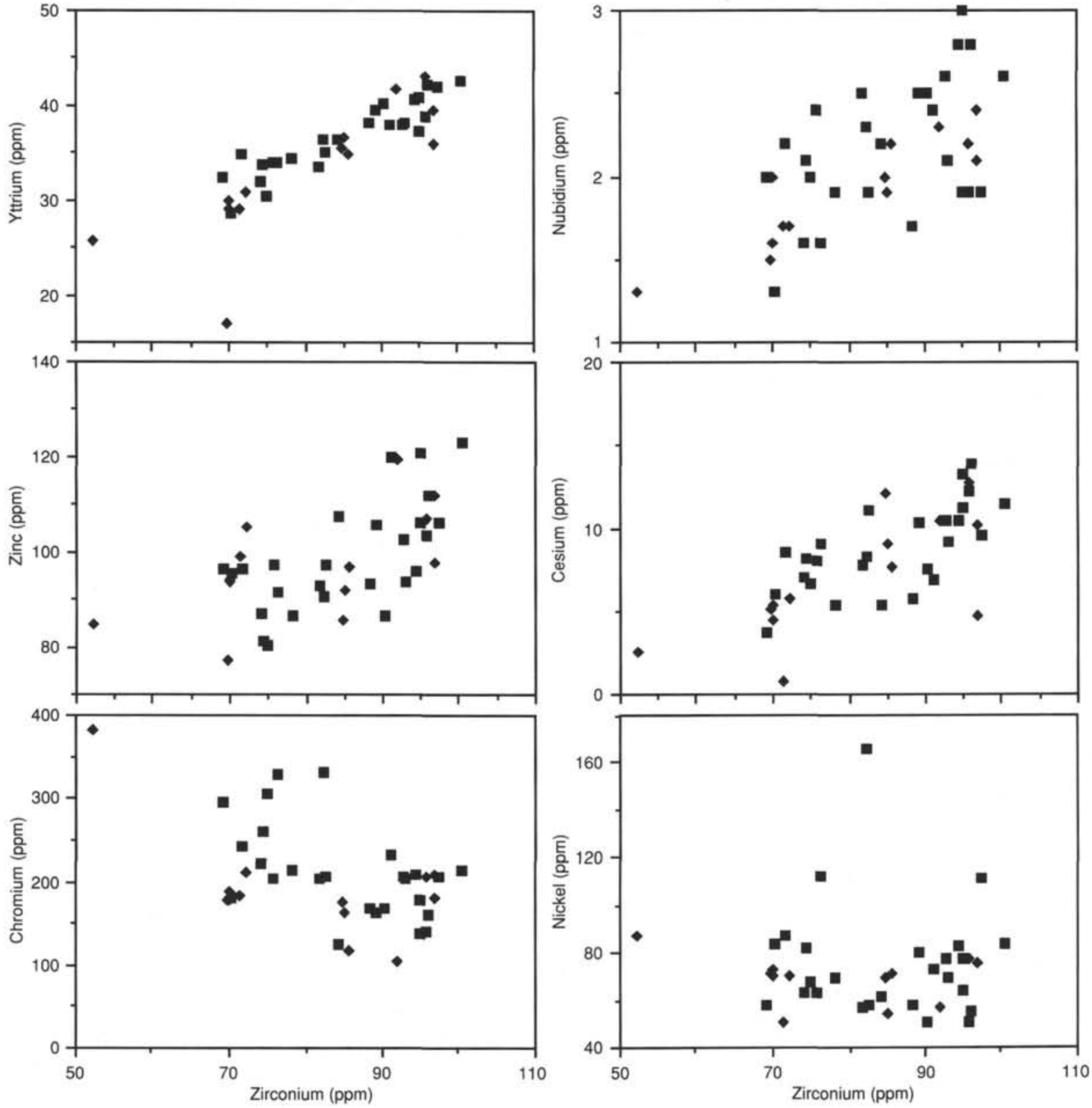

Figure 114. Trace-element variations for Site 765 with respect to zirconium as an index of fractionation.

Velocity

Compressional-wave velocity data, as determined with the Hamilton Frame apparatus, are shown in Figure 118E. From this figure one observes that the velocity remains relatively constant throughout the basement rock, with a value of 5500 m/s. Noticeable velocity reductions can be seen at 994, 1005, and 1140 mbsf. The first two depths correspond to intervals in which the index properties also showed considerable variation. This is attributed to changes in rock characteristics, as described in the above section. The third velocity reduction at 1140 mbsf corresponds to an interval in which a number of calcite veins were observed.

As an additional means of comparing index properties with velocity data, an acoustic impedance plot (Fig. 118F) was created by multiplying the basement rock bulk density by the corresponding velocity and plotting the result as a function of depth.

Thermal Conductivity

Thermal conductivities given in Table 41 are shown in Figure 118G. Although the data exhibit a significant amount of variability (± 0.14 W/m · K), thermal conductivity appears to be invariant with depth, with an average value of 1.67 W/m · K.

Conclusions

Basement index properties, compressional-wave velocities, and thermal conductivities remain relatively constant throughout the section. The grain or matrix density for the basalt is 2.93 $\pm$ 0.07 g/cm^3. The average water content and porosity are low, with values of 1.5% and 4.0%, respectively. The average compressional-wave velocity for the section is 5500 m/s. Noticeable variations in index properties and velocities can be attributed to degree of crystallinity, rock composition, and calcite veins. Such variations were observed at 994, 1005, and 1140 mbsf. Thermal

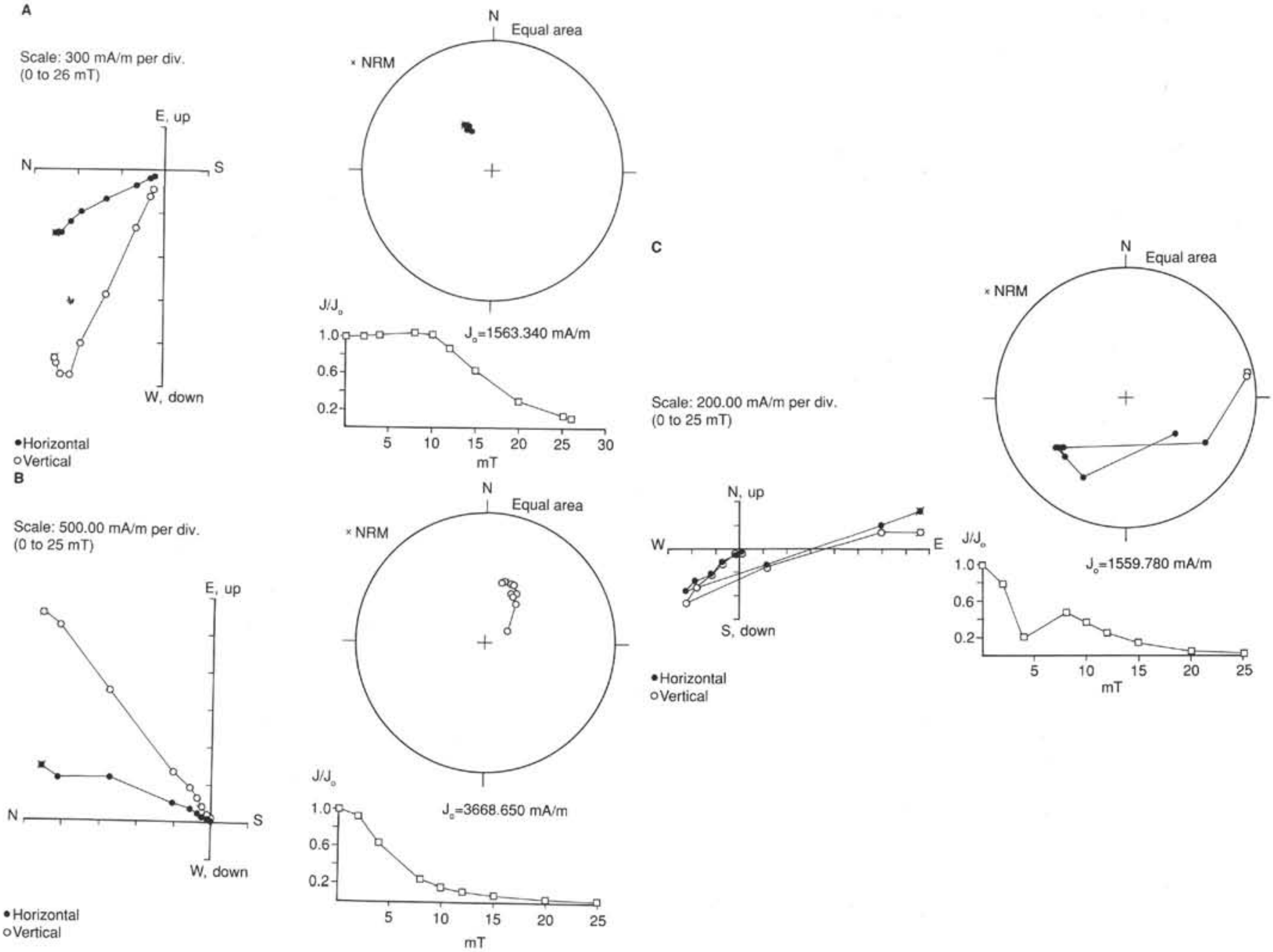

Figure 115. A. Vector (Zijderveld) and equal-area stereographic plots of progressive AF magnetization for a discrete sample of reverse polarity (Sample 123-765C-62R-CC, 23–25 cm). B. Vector (Zijderveld) and equal-area stereographic plots of progressive AF demagnetization for a normally magnetized sample (123-765D-8R-1, 37–39 cm), showing the typical rapid decrease in intensity and good stability in direction of basalt samples from Site 765. C. Vector (Zijderveld) and equal-area stereographic plots of progressive AF demagnetization for a reversely magnetized sample (Sample 123-765D-3R-1, 35-37 cm), showing the removal of a strong overprint of normal polarity to obtain a characteristic magnetization of reversed polarity.

conductivity data appear to be invariant with depth, with an average value of 1.67 W/m · K, but vary considerably.

BASEMENT STRESS MEASUREMENTS

Anelastic Strain Recovery Experiments

Introduction

The underlying basis of the anelastic strain recovery experimental procedure and of the subsequent preliminary analysis is that a volume of rock will, upon being released from its *in-situ* stress environment, expand in the direction of and in proportion to the magnitudes of the maximum and minimum horizontal and vertical *in-situ* stresses. One assumes that the rock sample is homogeneous and will expand elliptically across its section and uniformly along its length. By measuring physical changes in the shape of the samples at three or more pre-determined positions across its diameter, the orientation and magnitude of the resultant strain recovery ellipsoid can be calculated. By subsequently relating these results to the elastic characteristics of the rock, the *in-situ* stress field can be determined.

None of the sediment cores recovered from Holes 765A, 765B, and 765C were sufficiently lithified to be suitable for anelastic strain recovery experiments. Therefore, the first sample for this work was taken from the first full basement core from Hole 765C (Core 123-765C-63R). The subsequent relatively poor recovery of concomitant whole-round rock cores resulted in only 10 additional samples being taken from Hole 765D before drilling terminated.

Sample Selection and Experimental Procedure

Whole-round samples were taken within a few minutes of removal from the core barrel and replaced in the core liners by corresponding lengths of styrofoam. Because core recovery averaged about 31%, it was difficult to establish exactly where in the rock column a particular rock sample was from and thus to estimate the elapsed time between the cutting of that sample and its arrival on deck. However, as the time between cores was usually about 6 hr and samples were taken from as near the bottom of the core as possible, the elapsed time was probably no more than 3 hr. The samples taken varied in length from about 156 to 251 mm and were generally about 56 mm in diameter.

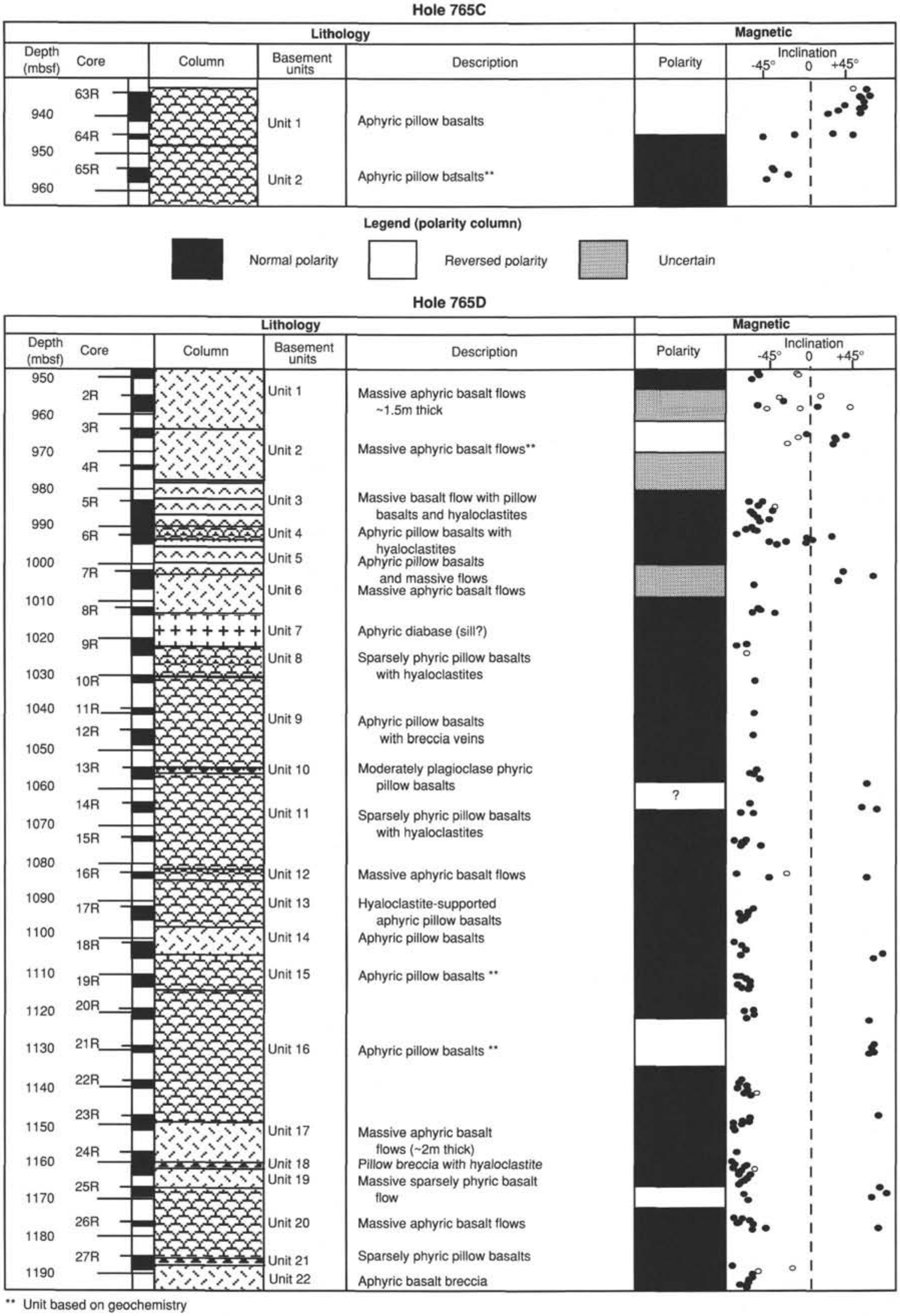

Figure 116. Stratigraphic plot of magnetic inclinations of basalts (Table 39) with interpretation of possible polarity zones. Inclination values from magnetically unstable samples are indicated by open circles. Polarity zone interpretations do not include single samples with apparent opposite polarities because such anomalous blocks may have been inadvertently inverted. Lithologic column and units are from "Basement Lithostratigraphy" section (this chapter).

Table 39. Magnetic inclinations of basalt long-core pieces, whole-round blocks, and discrete samples.

Core, section, interval (cm)	Long-core incl. (°)	Special blocks incl. (°)	Special blocks decl. (°)	Discrete samples incl. (°)
Hole 765C				
62R, CC, 0–30	+45 (inaccurate)			
23–25				+60.4
63R-1, 18–39	+64.4			
63R-2, 15–35	+55.5			
34–54		+52.3	218.7	
111–113				+57.9
129–149	+54.2			
63R-3, 33–42	+36.0			
132–150	+52.5			
63R-4, 0–12	+30.5 (inaccurate)			
27–48	+53.7			
Lower blocks — odd shallow inclinations, etc.				
97–99				+19.6
63R-5 — Anomalous behavior				
64R-1, 0–21	−43.9			
	[25 mT = +5, 26 mT = +25 = wierd]			
14–16				−17.3
27–39	+46.0			
42–54	−49.4			
65R-1, 15–45	−39.2			
96–98				−37.5
126–138	−22.3			
65R-2, 54–87	−46.6			
Average basalt =	45.7			38.5
vs				
Average sediment =	42			
Hole 765D				
1R-1, 36–60	−56.0			
66–150	−53.2			
106–108				−14.6 (unstable)
113–115				−12.5 (unstable)
1R-2, 0–39	−62.8 (inaccurate)			
2R-1, 12–27	+11.4			
33–54	−33.6 (same block as above!)			
60–99	−27.6			
2R-2, 3–66	−56.5			
31–33				+44.0 (unstable)
2R-3, 3–12	+6.4			
18–129	−11.9 (R trend)			
88–90				−46.5 (unstable)
3R-1, 9–30	−3.3			
33–39	−13.6 (R trend)			
35–37				+38.3
48–54	+26.2			
57–78	+26.3			
81–105	+8.2 (25 mT = +25)			
107–125		−23.8	22.6 (R trend)	
5R-1, 12–27	−64.1			
16–18				−49.5
72–144	−55.7			
118–120				−33.7 (unstable)
5R-2, 0–114	−39.9			
5R-3, 0–117	−62.6			
5R-5, 3–66	−58.4			
61–63				−43.5
69–96	−54.9			
102–144	−53.1			
5R-6, 0–108	−61.2			
110–129		−56.0	319.9	
5R-7, 27–45	−60.2			
51–72	−68.5			
81–114	−69.1			
5R-8, 0–18	−77.9			
102–111	+24.6 (with chill margin)			
6R-1, 42–57	−2.7			
108–132	+0.9			
135–147	−3.3			
6R-2, 0–18	−26.9			
21–33	−35.2			
30–32				−43.1

[Core 123-765D-7R has unknown Up/Down orientations on all blocks]

Table 39 (continued).

Core, section, interval (cm)	Long-core incl. (°)	Special blocks incl. (°)	Special blocks decl. (°)	Discrete samples incl. (°)
Hole 765D				
7R-1, 138–140				+35.5
7R-2, 122–124				+60.7
7R-3, 48–50				−59.2
90–110		+28.5	54.1	
8R-1, 21–30	−54.5			
33–57	−63.0			
37–39				−55.7
60–75	−36.5			
9R-1, 0–102	−78.6			
38–40				−67.0
9R-3, 17–19				−67.6 (unstable)
10R-1, 116–118				−58.9
11R-1, 45–47				−59.4
12R-1, 55–57				−60.6
13R-1, 18–30	−56.4			
18–20				−63.4
107–125		−58.8	86.6	
126–147	−53.5			
13R-3, 18–30	+60.8			
14R-1, 9–11				−63.5 (inverted?)
21–33	+55.8			
75–96	+71.6			
14R-2, 18–30	−59.5			
39–66	−73.6			
15R-1, 57–66	−79.1			
102–114	−70.8			
117–129	−72.6			
15R-2, 0–12	−51.0			
15–24	−73.4			
26–28				−67.2
16R-1, 33–42	−25.0 (spawled pillow rinds)			
58–60				−77.2
16R-2, 0–6	+61.4			
36–51	−52.6			
17R-1, 60–90	−59.7			
17R-2, 0–12	−65.9			
42–51	−76.5			
90–114	−66.1			
123–141	−72.6			
17R-3, 3–33	−74.3			
13–15				−69.6
18R-1, 0–102	−80.1			
99–101				−72.6
18R-2, 0–18	−67.9			
57–69	+76.8			
18R-3, 37–54		−74.6	260.0	
78–80				+66.4
19R-1, 0–33	−73.5			
57–84	−77.2			
98–100				−68.5
114–126	−66.5			
19R-2, 0–27		−76.8	165.9	
30–42	−64.3			
38–40				−65.2
87–102	−72.4			
20R-1, 30–51	−69.7			
47–49				−59.7
66–78	−66.5			
77–99		−67.4	210.5	
111–117	+62.3			
21R-1, 84–93	+68.5			
86–88				+67.2
114–126	+65.5			
132–141	+63.2			
22R-1, 0–45	−72.6			
51–78	−74.8			
81–99	−76.3			
96–98				−67.0
117–138	−64.3			
22R-2, 0–16		−69.2	354.1	
36–42	−56.0 (inaccurate)			
69–78	−62.4			
23R-1, 9–36	+73.5			
99–105	−63.3			
138–147	−64.2			

Table 39 (continued).

Core, section, interval (cm)	Long-core incl. (°)	Special blocks incl. (°)	Special blocks decl. (°)	Discrete samples incl. (°)
Hole 765D				
23R-2, 0–15	−81.2			
18–33	−71.7			
54–69	−70.9			
65–67				−73.3
81–93	−81.0			
96–114	−80.1			
24R-1, 6–120	−77.9			
24R-2, 0–48	−83.1			
51–129	−79.4			
24R-3, 3–45	−80.4			
33–35				−67.8
60–75	−68.1 (with chill margin)			
114–123	−58.7 (inaccurate)			
24R-4, 3–24	−72.9			
95–97				−75.3
102–123	−75.8			
126–144	−62.8			
24R-5, 0–12	−66.5			
18–36	−69.3			
45–69	−72.6			
73–90		−74.0	349.5	
25R-1, 18–27	+73.9			
36–57	−66.5 (inverted?)			
99–117	+80.7			
25R-2, 0–18	+66.9			
11–13				−64.5
24–33	−63.3 (unreliable orientation)			
54–63	+84.0			
26R-1, 0–18	−79.1			
24–51	−71.2			
28–30				−62.3
60–69	−76.4			
73–92		−74.9	293.0	
99–111	−60.4			
117–129	+72.7			
26R-2, 24–30	−61.5			
93–99	−46.6			
27R-1, 0–21	−81.2			
45–51	−17.9 (pillow breccia)			
99–108	−56.5 (pillow breccia)			
27R-2, 0–48	−59.0			
54–93	−61.2			
96–126	−64.1			
27R-3, 0–15	−65.6			
18–27	−67.2			
39–60	−74.0			
69–81	−66.8			

On arrival in the laboratory, each sample was marked with a scribe line for orientation purposes, and 1-mm-diameter holes were drilled at positions relative to the scribe line commensurate with the TΔ configuration for transducer location. One longitudinal and four axial transducers were set in place and adjusted to be nominally within the center of their measurement range before the complete assembly was placed in a thermally insulated container and immersed in silicon fluid. The transducer control unit was interfaced with a Compaq Portable 386 microcomputer that acted as a data logger. Data were captured directly into a Lotus 123 spreadsheet using Lotus Measure as the communication software. Control parameters were set to recover data once every minute for all the samples, except for the first, which was set for every 2 min. Following each cycle of data capture, the complete spreadsheet file was recorded on hard disc to counter potential data loss (e.g., from power failures). Once operating in the data capture mode, instruments could be left unattended for about 24 hr, at which time the internal memory would be exhausted and, if necessary, a new file could be

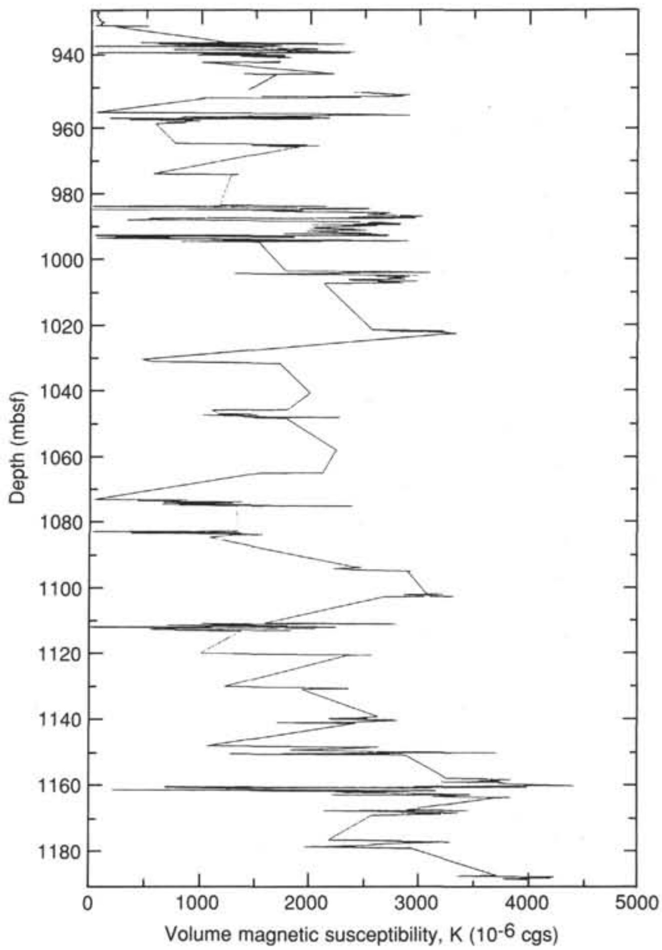

Figure 117. Plot of susceptibility vs. depth of cores from Holes 765C and 765D.

initiated to continue with the measurements. At any time the data collection mode could be interrupted to allow graphical presentation of the results to date to be presented on the screen. This allowed us to assess progress of the experiment. The amount of time for preparing each sample and setting up equipment before measuring was generally about 40 min.

Equipment for measuring stress relaxation of the core performed without fault, and silicon fluid prevented the sample from drying out during measurement periods. The thermal insulation afforded by the immersion of the sample within silicon fluid inside an insulated container restricted temperature drift during experimental periods to a maximum of 0.8°C, but usually to within 0.3°C. Even so, the response of the transducer across the glass ceramic disk indicated that for some of the experiments, there was a slight drift during the first minutes of measurement, while thermal stability was being established. The effects of this drift can be removed at a later stage of data processing.

Although no core orientation device was used during drilling, the mean magnetic declination of each sample, with respect to the scribe line and relative to the position of magnetic north during the Earliest Cretaceous, was achieved by measuring paleomagnetism. This inclination could then be related to today's north (Embleton, 1981) to within ±30°, which subsequently allowed us to deduce the orientation of the maximum stress direction.

Table 40. Index properties and compressional-wave velocity of samples from Holes 765C and 765D.

Core, section, interval (cm)	Depth (mbsf)	Bulk density (g/cm^3)	Grain density (g/cm^3)	Porosity (%)	Water content (%)	Velocity (m/s)
123-765C-63R-2, 23	937.47	—	—	—	—	5341
765C-63R-4, 133	941.54	—	—	—	—	5952
765C-64R-1, 48	945.78	—	—	—	—	5067
765C-65R-1, 27	954.97	—	—	—	—	6267
765C-65R-2, 40	956.5	—	—	—	—	5260
765D-1R-1, 113	949.03	2.84	2.93	4.6	1.7	5578
2R-2, 31	956.40	2.96	2.99	1.6	0.6	6148
2R-3, 88	958.04	2.79	2.87	2.5	0.9	5893
3R-1, 35	964.75	2.85	2.93	4.0	1.5	5495
5R-1, 16	983.36	2.85	2.91	3.5	1.3	5552
5R-1, 118	984.38	2.90	2.97	3.5	1.3	5952
5R-5, 61	988.77	2.86	2.93	3.6	1.3	5292
6R-2, 30	994.20	2.76	2.92	8.0	3.1	2785
7R-1, 138	1003.38	2.95	2.99	2.3	0.8	5936
7R-2, 122	1004.68	2.76	2.90	7.6	2.9	4955
7R-3, 48	1005.36	2.76	2.90	7.3	2.8	4883
8R-1, 37	1011.87	2.86	2.95	4.2	1.5	5550
9R-1, 38	1021.28	2.86	2.90	2.3	0.8	5859
9R-3, 17	1024.01	2.90	2.96	3.1	1.1	5563
10R-1, 116	1031.36	2.84	2.91	4.0	1.5	5551
11R-1, 45	1039.85	2.92	2.96	2.1	0.7	5792
12R-1, 55	1045.65	2.77	2.84	3.7	1.4	5160
13R-1, 18	1054.58	2.77	2.85	4.1	1.5	5073
14R-1, 9	1063.99	2.89	2.92	1.8	0.7	5410
15R-2, 26	1074.76	2.87	2.91	2.4	0.9	5377
16R-1, 58	1083.08	2.84	2.89	2.3	0.9	5528
17R-3, 13	1094.67	2.84	2.94	5.2	1.9	4903
18R-1, 99	1102.09	2.93	2.97	2.0	0.7	5907
18R-3, 78	1103.92	2.86	2.93	3.8	1.4	5041
19R-1, 98	1111.28	2.85	2.95	5.2	1.9	4814
19R-2, 38	1111.98	2.87	2.96	4.3	1.6	5481
20R-1, 47	1119.97	2.82	2.88	3.0	1.1	5194
21R-1, 86	1129.86	2.79	2.86	3.6	1.3	5193
22R-1, 96	1139.56	2.72	2.83	6.1	2.3	4406
23R-2, 65	1149.95	2.85	2.92	4.0	1.5	4598
24R-1, 13	1157.23	—	—	—	—	5669
24R-3, 33	1160.00	2.92	2.99	3.5	1.2	5284
24R-4, 95	1161.85	2.98	3.27	13.0	4.6	5883
25R-2, 11	1168.04	2.85	2.89	2.0	0.7	5675
26R-1, 28	1176.28	2.87	2.93	3.4	1.2	5349

Table 41. Thermal conductivity data, Hole 765D.

Core, section, interval (cm)	Depth (mbsf)	Thermal conductivity (W/m · K)
123-765D-1R-1, 52	948.42	1.7350
1R-1, 52	948.42	1.7250
1R-2, 52	949.92	1.7250
2R-2, 0	956.09	1.1050
2R-3, 95	958.11	1.6700
3R-1, 33	964.73	1.6950
4R-1, 30	974.00	1.6100
5R-1, 133	984.53	1.6750
5R-5, 29	988.45	1.7550
5R-7, 129	992.29	1.7600
6R-1, 0	992.40	1.6750
7R-1, 81	1002.81	1.6900
8R-1, 28	1011.78	1.7700
9R-1, 72	1021.62	1.8400
9R-1, 72	1021.62	1.8400
10R-1, 64	1030.84	1.5800
11R-1, 90	1040.30	1.5900
12R-1, 26	1045.36	1.6900
15R-1, 55	1073.55	1.5550
17R-2, 103	1094.16	1.6950
18R-1, 10	1101.20	1.8300
19R-1, 114	1111.44	1.5000
20R-2, 71	1121.71	1.6350
21R-1, 113	1130.13	1.7550
22R-1, 15	1138.75	1.6900
23R-2, 20	1149.50	1.7250
24R-4, 42	1161.32	1.7400
25R-1, 125	1167.75	1.7650
26R-2, 92	1178.42	1.4250
27R-2, 40	1186.95	1.7250

Preliminary Results

Initial results from a preliminary assessment of our data are shown in Table 42. This table indicates how we computed the magnitudes of vertical and maximum and minimum horizontal strains, the orientation of the maximum strain relative to modern north, and elapsed time from the beginning of strain-relief monitoring to full relaxation of the sample. Also shown in Figure 119 are plots of computed vertical and maximum and minimum horizontal strain-relief curves for Samples 123-765C-63R-2, 34–54 cm; -765D-3R-1, 110–125 cm; and -765D-20R-1, 77–99 cm. A more comprehensive and complete analysis of these data will be conducted as part of our shore-based studies, together with instrument drift corrections of raw data. Thus, these results are subject to change. However, some interesting and unexpected trends are apparent. The most startling result is from Sample 123-765D-7R-3, 90–110 cm (labeled Bas 4) from 1005.78 mbsf, where the strain relief was large, consistently negative in all three directions, and continued to relax for more than 3 days. The next three samples exhibit a high-to-low maximum horizontal strain recovery trend, with zero to low minimum horizontal strain recovery values, while the last four samples show a similar trending pattern. Orientation results indicate a relatively wide scatter.

Interpretation of these data will require further analysis, but two potential explanations warrant closer attention and a detailed comparison with borehole logging and hydrofracture experimental results. First, the upper 240 m of basement rocks can be subdivided into several distinct stress provinces, and second, the anelastic stress relaxation of these particular basalt samples was particularly influenced by the calcitic cleavage planes (albeit well-cemented) cutting through the rock fabric.

In-Situ Stress Directions

Introduction

The *in-situ* stress measurement program planned for Leg 123 was partially successful. Two openhole borehole televiewer (BHTV) runs (932–1156 mbsf) were conducted approximately 3 days apart within the basalt section of Hole 765D. The first BHTV run recorded reasonable images of what we think is stress-induced wellbore breakouts. The second run produced a log of lesser quality because the logging tool used smaller centralizer springs.

Efforts to measure *in-situ* stress magnitudes, using the hydraulic fracturing technique, were aborted after several unsuccessful attempts to inflate the straddle packers. When the packers were tested and examined on deck, we discovered that the inflation ports had been filled to compaction with basalt cuttings. Failure of the packers to inflate was caused by a combination of our placing the packers near the bottom of the hole, where the cuttings had accumulated, and errors in setting up the packer before lowering it into the hole. See the "Operational Reports" section (this chapter) for further details. Fractures within the cores were mapped on mylar sheets prior to sawing the samples in half. This information will quantify the distribution, dip angle, and fracture type (i.e., open vs. healed) and later will be incorporated with paleomagnetic and BHTV data.

Borehole Televiewer

The BHTV is an ultrasonic, high-resolution logging tool used to measure wellbore breakouts, fractures, and other lithostratigraphic features. Stress-induced wellbore breakouts are localized zones of shear failure due to compressive stress concentrations exceeding the compressive strength of the rock. Under these conditions, the breakout orientation will develop in the direction of the least principal horizontal stress. See the "Explanatory Notes" chapter (this volume) for details of the BHTV.

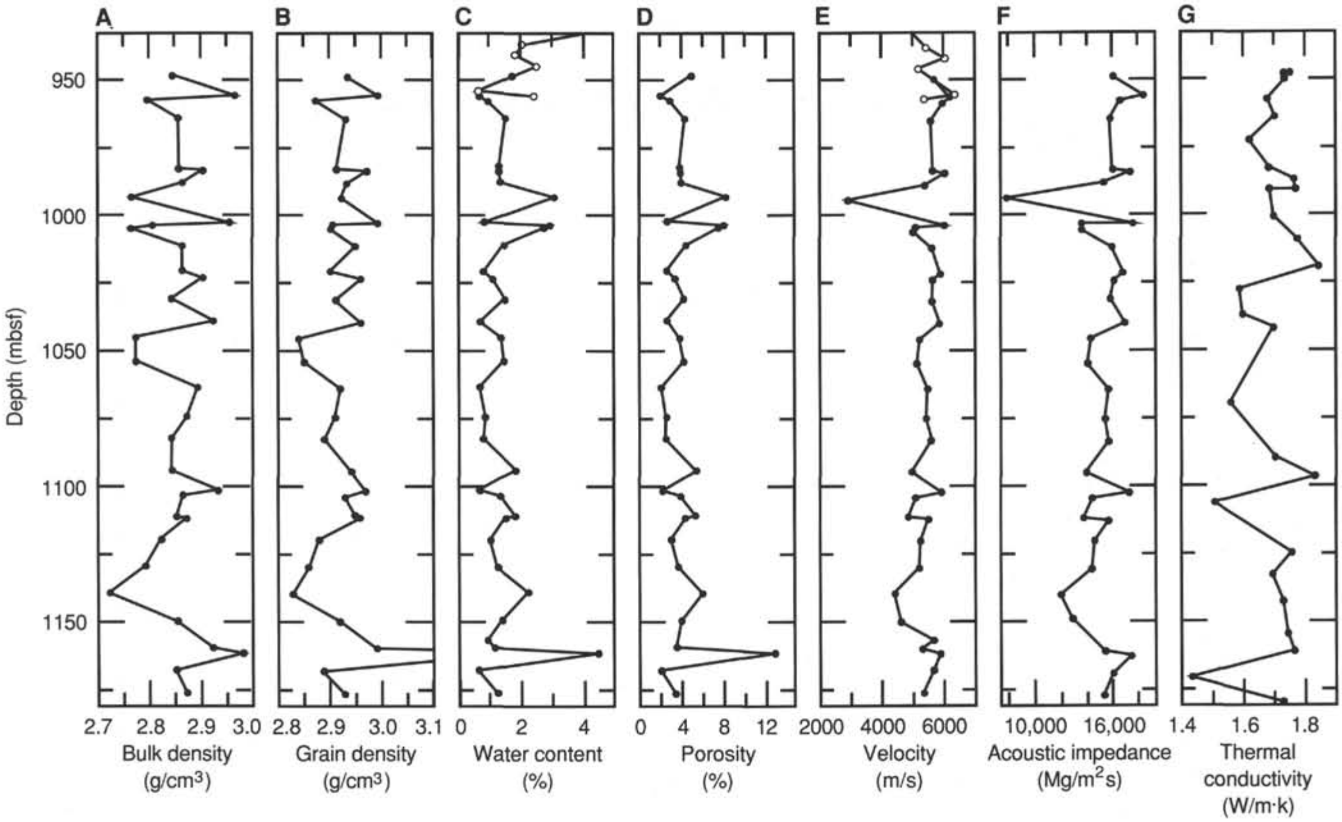

Figure 118. Physical properties of basement rocks, Holes 765C and 765D, vs. depth of samples. A. Bulk density. B. Grain density. C. Water content (Hole 765D only). D. Porosity (Hole 765D only). E. Compressional-wave velocity. F. Acoustic impedance. G. Thermal conductivity (Hole 765D only).

Table 42. Preliminary results of anelastic strain recovery experiments conducted on basalt samples from Holes 765C and 765D.

Core, section, interval (cm)	Depth (mbsf)	Final Hmax (μe)	Principal Hmin (μe)	Strain vert (μe)	Orientation (degrees)	Elapse time[a] (hr)
Bas 1 123-765C-63R-2, 34–54	937.58	35.2	−47.9	0.7	119 ± 30	38.6
Bas 2 765D-3R-1, 110–125	965.47	59.0	−32.4	60.7	38 ± 30	22.5
Bas 3 765D-5R-6, 110–129	990.76	−6.3	−13.8	6.2	44 ± 30	11.6
Bas 4 765D-7R-3, 90–110	1005.78	−67.2	−200.5	−99.1	3 ± 30	79.5
Bas 5 765D-13R-1, 31–50	1054.71	46.3	0	−2.6	24 ± 30	25.0
Bas 6 765D-18R-3, 37–54	1103.51	20.8	−13.1	19.1	2 ± 30	11.5
Bas 7 765D-19R-2, 0–27	1111.60	12.8	0	6.1	107 ± 30	5.7
Bas 8 765D-20R-1, 77–99	1120.27	153.0	−22.2	32.3	71 ± 30	46.3
Bas 9 765D-22R-2, 0–16	1138.60	75.1	−3.9	17.5	59 ± 30	20.3
Bas 10 765D-24R-5, 73–90	1163.09	32.7	3.1	22.5	113 ± 30	19.9
Bas 11 765D-26R-1, 73–92	1176.73	22.6	8.6	15.5	74 ± 30	9.9

[a] From onset of strain relief monitoring.

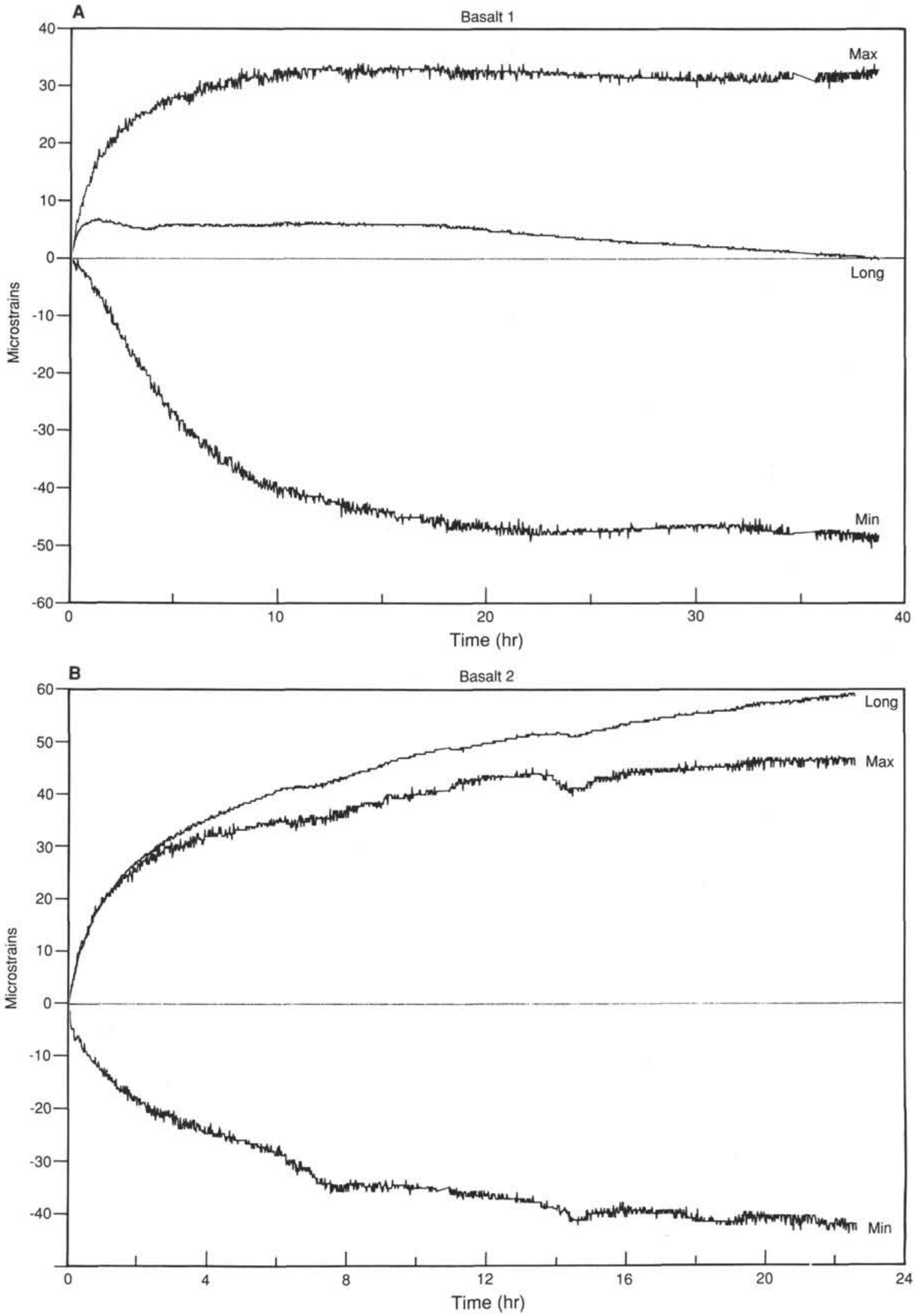

Figure 119. A. Strain-relief curves of maximum and minimum horizontal and vertical strains for Interval 123-765C-63R-2, 34–54 cm. B. Strain-relief curves of the maximum and minimum horizontal and vertical strains for Interval 123-765D-3R-1, 110–125 cm. C. Strain-relief curves of the maximum and minimum horizontal and vertical strains for Interval 123-765D-20R-1, 77–99 cm.

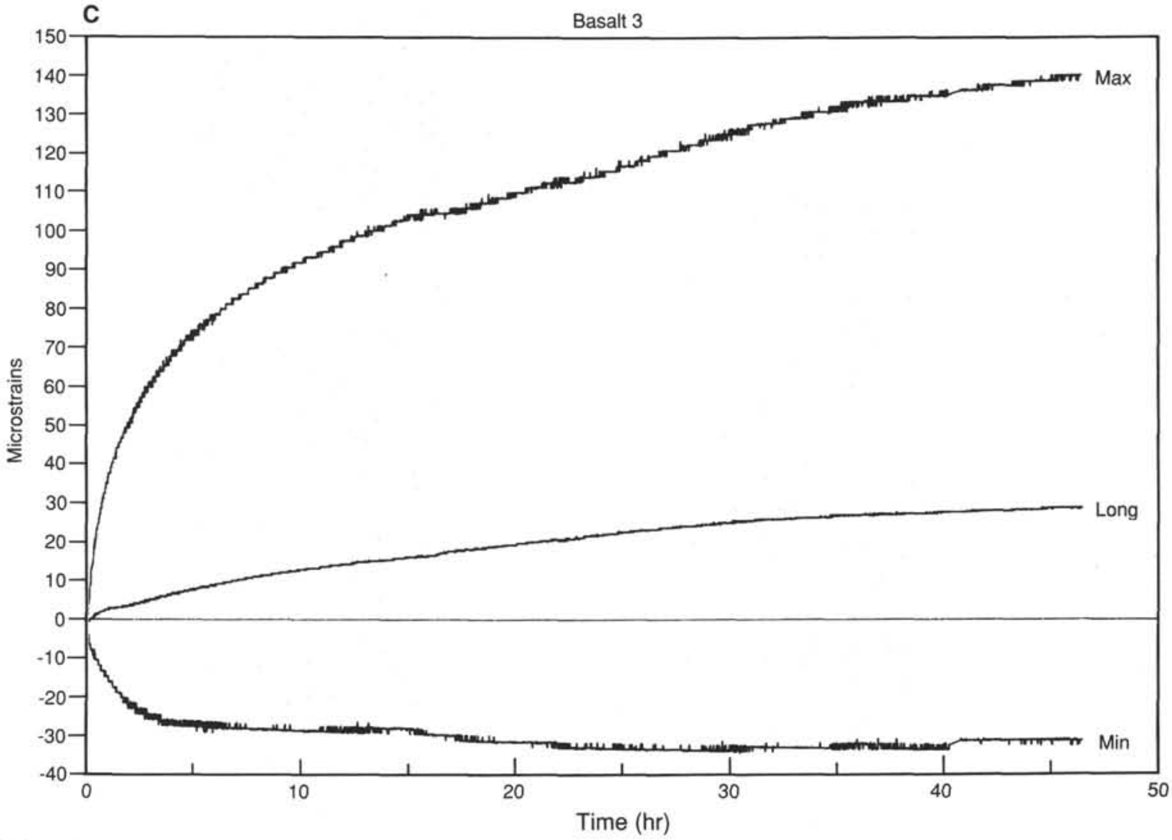

Figure 119 (continued).

Results

The first BHTV log was run on 12 October 1988. Attached at the base of the BHTV was a new temperature logging tool. At about 2000 meters below rig floor (mbrf), as the tool was being lowered down through the pipe, the BHTV's compass and rotation mechanism began to malfunction. The tool was retrieved and replaced with a backup BHTV. Curiously, the second tool behaved in a similar manner. Once the tool was in the open hole, however, the problem disappeared, suggesting that the pipe was affecting the performance of the magnetometer. The tool performed satisfactorily, except for a problem with "stick-slipping." Stick-slipping is caused by using springs that are too stiff, which causes the tool to remain stationary while scanning the same section of the borehole. After several seconds, the tool is suddenly jerked upward, skipping a few centimeters and resulting in a discontinuous image of the borehole wall. The second BHTV log was run on 16 and 17 October 1988, but with a smaller set of centralizer springs and without a temperature tool. We anticipated that the smaller centralizers would reduce the likelihood of the tool's stick-slipping. Unfortunately, the tool was greatly off center because the smaller centralizers over-compensated for the slipping effect.

Polaroid images collected from the two BHTV runs show that the basement section of Hole 765D (932.7–1156.0 mbsf) was marked by varying degrees of hole elongation (presumably breakouts), pillow basalts, massive flows, and fracturing (Fig. 120). Image processing of these data will enhance these apparent features. Precise orientations of BHTV records are not available at this time. However, during several pre-log calibration runs of the BHTV performed from the ship's fantail, the tool appeared to be triggering near true magnetic north. This suggests that the left- and right-hand sides of the Polaroids are reading magnetic north. From left to right, the directions should be approximately north-east-south-west-north.

We found that the degree of breakout development was a function of the magnitude of the differential stresses and the strength of the basaltic material. Therefore, because the apparent breakouts observed within the basement column are not continuous, several processes may be operating in this area, such as (1) the differential stresses are highly variable or (2) the compressive strength of the basalts varies with depth. If one assumes that the stress field is continuous with depth, with no well-pronounced stress provinces, the varied character of the apparent breakouts may be a manifestation of preexisting fractures or fault boundaries, and/or changes from a massive basalt section (i.e., smaller breakouts) to a more altered rock (i.e., larger breakouts). However, if the constitution of the rock mass remains nearly uniform with depth over the interval analyzed and changes with depth in breakout patterns do occur, there may be isolated stress provinces within this small vertical section of the oceanic crust. This may explain the anomalous data point observed near 1005 mbsf during the anelastic strain recovery experiment (see "Fracture Analysis" section, this chapter).

Figure 120 is a typical representation of the data collected in Hole 765D. The interval between 1005 and 1011 mbsf indicates that this section is marked by higher reflectivity and thus less extensive breakouts. In this example, the breakouts appear to be one-sided; this is an occasionally observed phenomenon that may be related to irregularities in the rock formation or may be an artifact of the decentralized tool. Processing these data will clarify the matter. Although the section is highly reflective (sug-

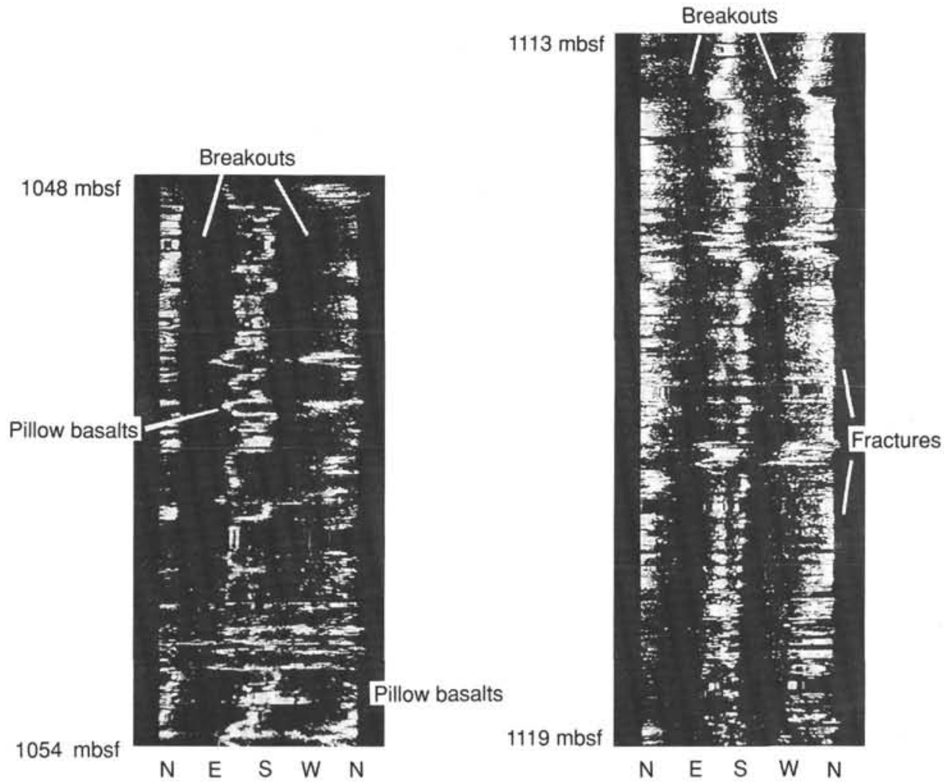

Figure 120. Mosaic of two sections of borehole televiewer data collected in the basalt section of Hole 765D. These Polaroid images are show features that may be stress-induced breakouts, pillow basalts, and/or fractures.

gesting competent rock), there still appears to be an abundance of fractures that continues upsection in photos not shown. The interval between 1048 and 1054 mbsf (Fig. 120) is an example showing the apparent breakouts that trend approximately east-west. The width of these breakouts approaches the maximum aperture observed in Hole 765D. The oblate features, such as those shown near the center of the photo, are widespread and, in fact, may be the edges of pillow basalts. In this example, these features appear to be approximately 30 cm in diameter. In the interval between 1113 and 1119 mbsf (Fig. 120), the tool may have encountered drilling-induced artifacts. These artifacts may be due to pipe scraping the borehole wall in a deviated hole. Three-component magnetometer data from the general purpose inclinometer tool (GPIT), run on the lithodensity tool string, will be used to determine inclination of the holes inclination.

Fracture Analysis

Introduction

The major objective of this study is to address the possible relationship between preexisting fractures and the present and/or paleo stress regime. To understand the processes associated with the formation of fractures, joints, and other extensional features, orientations of structures observed in the cores were constructed. Tracings of these features were constructed from 27 cores within the 948- to 1195-mbsf interval. The core exhibited an abundance of through-going fractures, with dips ranging from 15° to 90°. Some of these fractures were filled with either calcite, smectite, or other clay alteration minerals, of varying degrees. Some fractures were hairline cracks, possibly induced during drilling. Overall, these fractures are systematically oriented, with the highest population of fractures falling near 45° with respect to vertical (Fig. 121). These tracings will be compared with the processed images of the BHTV (see "Borehole Televiewer" section, this chapter).

Methodology

Tracing was done on a continuous piece of clear shrink tubing wrapped around specimens that were larger than 10 cm long. The up-direction and the saw-cut line were carefully annotated on each piece. The top of the core was annotated by hole number and letter, section number, and piece number. Calcite-filled fractures were differentiated between other fractures that were open or healed with other secondary minerals. Voids were outlined and appropriately annotated. Fracture dips were estimated on through-going fractures and rounded to the nearest 5°. Post-cruise processing will incorporate core orientation data collected from paleomagnetic and BHTV data.

Results

Figure 121 is a digitized example of fracture tracings taken from Core 123-765D-5R. Overall, the predominate dip angle is near 45°, with additional nodes near 30° and 60° (Figs. 120, 122, 123, and 124). It is interesting to speculate about the possible relationship between the predominant dip angle observed in these oceanic basalts and the structural fabric observed along oceanic spreading centers; namely, the documentation of normal faults dipping 45° from direct observations, high-resolution sonar, and earthquake focal mechanisms. Assuming no major tectonic overprinting occurred, we may be able to determine independently the original spreading direction for this section of the Indian plate. Post-cruise processing will include a comparison of the traced fractures with those observed using the BHTV, after BHTV data have been digitized.

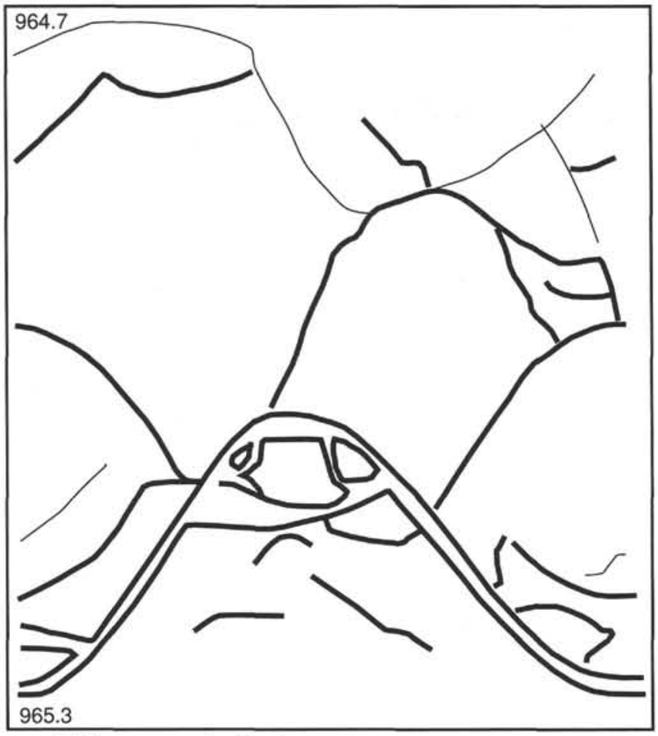

Figure 121. Digitized plot of fracture tracings from Section 123-765D-3R-1 from 964.7 to 965.3 mbsf. The fractures are hairline cracks (thin lines) with moderate amounts of secondary mineralization and open (thick lines) calcite-filled fractures.

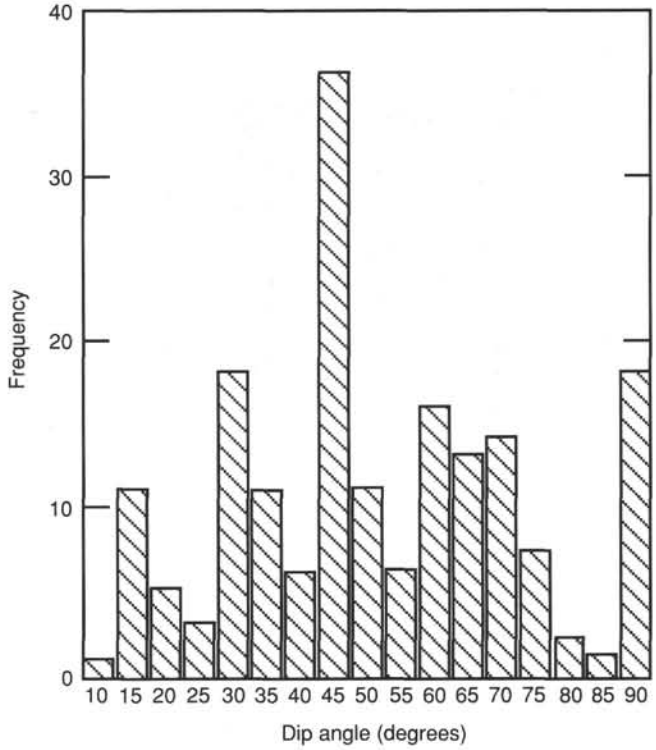

Figure 122. Plot of the number of fractures vs. fracture dip with respect to vertical. The peak at about 45° may be the dominant dip angle for this section of the oceanic crust. Other nodes may be associated with fracture plays off the 45° structures or other fractures exhibiting different coefficients of friction.

SCHLUMBERGER LOGS

Hole 765C

Introduction

A list of logging tool and curve abbreviations used in this chapter is presented in Table 43. The initial plans for Site 765 called for three Schlumberger tool strings to be run over the full hole length (Downhole Measurements Panel recommendation 1987/24). Holes 765A and 765B (APC and XCB holes) reached 173 and 395 mbsf, respectively, and we decided not to log these holes. Hole 765C was drilled to 949 mbsf. Using rotary coring, we covered sections from 350 to 949 mbsf, which took 10 days to core. Seawater was used as drilling fluid, with Driscol added in 25-bbl batches at the end of each core run to act as a sweep mud; batch density was 8.9 lb/gal (1.07 g/cm^3). Monitoring of the shale stability during coring using Baroid's capillary suction test (CST; Wilcox et al., 1984) indicated that shales should be stabilized by adding KCl before logging. On the basis of the Baroid CST, 5% KCl (18 lb/bbl) was added to the mud during hole conditioning. About 0.3% barite was added to bring the mud weight to 9.5 lb/gal (1.14 g/cm^3). The salinity of the conditioning mud was 47,500 ppm, and the mud cake (derived from a filter press test at 100 psi) was 8 mm thick. In view of the long period of time during which the hole was exposed to seawater and physical damage the formation sustained during 10 days of drilling, hole stability problems were to be expected in zones of swelling clays that were indicated by the CST. The CST results are shown in Figure 125. The principal zones of instability were, as expected: (1) above 180 mbsf; (2) between 450 and 580 mbsf; and (3) below 620 mbsf. We decided to set the base of the drill pipe at 180 mbsf to avoid problems with the upper clays, and to log as far as possible without the "sidewall entry sub" (SES) below this depth. From sea bed to 180 mbsf, we would be unable to obtain a gamma-ray spectrometry log through the drill pipe. The first run, with the seismic stratigraphy string (SS), encountered a bridge at 480 mbsf, and after several attempts to get through the bridge with a core barrel, we decided to pull out of the hole and run in again with the SES installed. After installation of the SES, two further runs were obtained in the open hole, from 524 to 647 mbsf and from 662 to 740 mbsf. A recurrent problem was the blocking of the end of drill pipe with sediment while penetrating bridges. The use of the mechanical bit release leaves four radial slots about 20 cm above the end of pipe. The presence of these slots prevented effective flushing of the end of the pipe with drilling fluid, and the resultant plug of sediment prevented the logging tool from emerging into the open hole on several occasions. This problem effectively negates the advantage of using the SES in soft sediment. Therefore, we find it difficult to recommend that the SES should be run with the mechanical bit release in sediment that is likely to enter the end of drill pipe when pushing through bridges.

After penetrating a bridge below 774 mbsf, it proved impossible to clear the end of pipe, and rather than risk cable damage, we decided to pull out of the hole and run the lithoporosity string without the SES, in the clear section between 158 mbsf and 466 mbsf. We accomplished this without problems. In anticipation of being able to run the geochemical logging tool (GLT) in casing with no tool joint attenuation problems, we decided not to run the GLT in Hole 765C. Data obtained during the various runs are summarized in Tables 44 and 45. Abbreviations used in the tables are listed in Table 43.

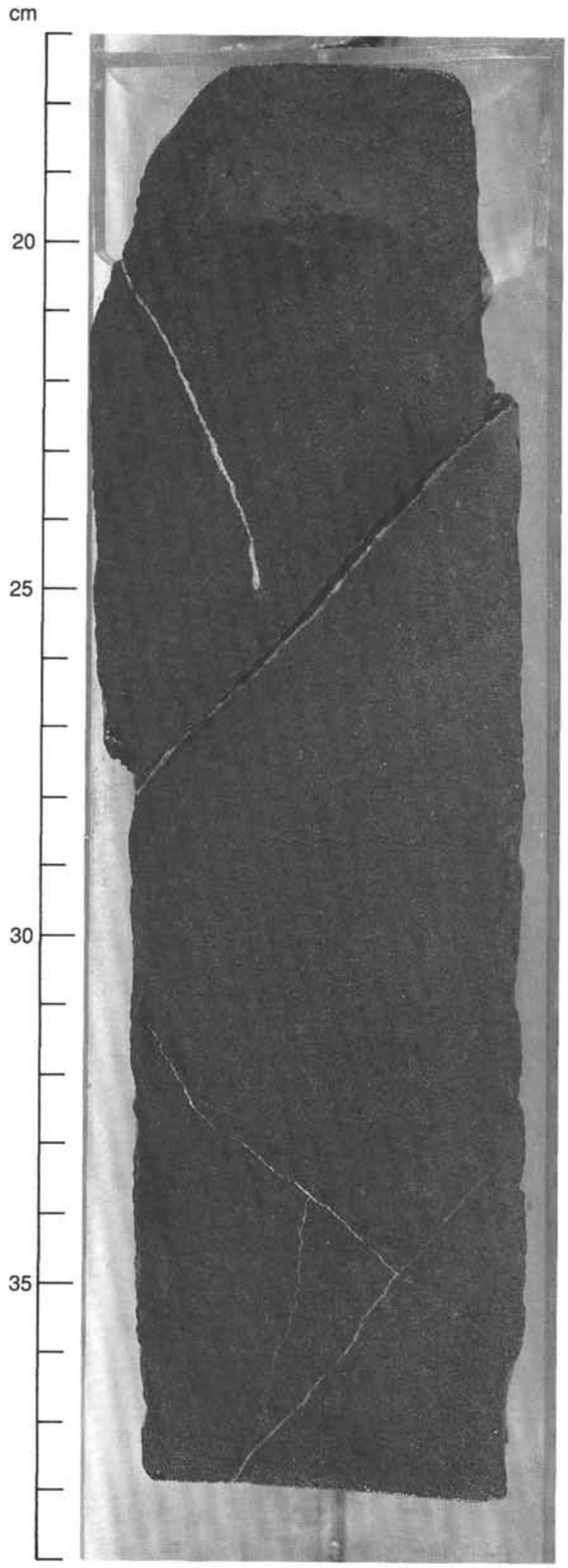

Figure 123. Close-up of Interval 123-765D-24R-5, 17–39 cm. Saw cut was made to show true dip angle. This particular core sample is a typical representation of fracture dip angle and the level of calcite-filling observed at this site. Note the conjugate fractures dipping about 45°.

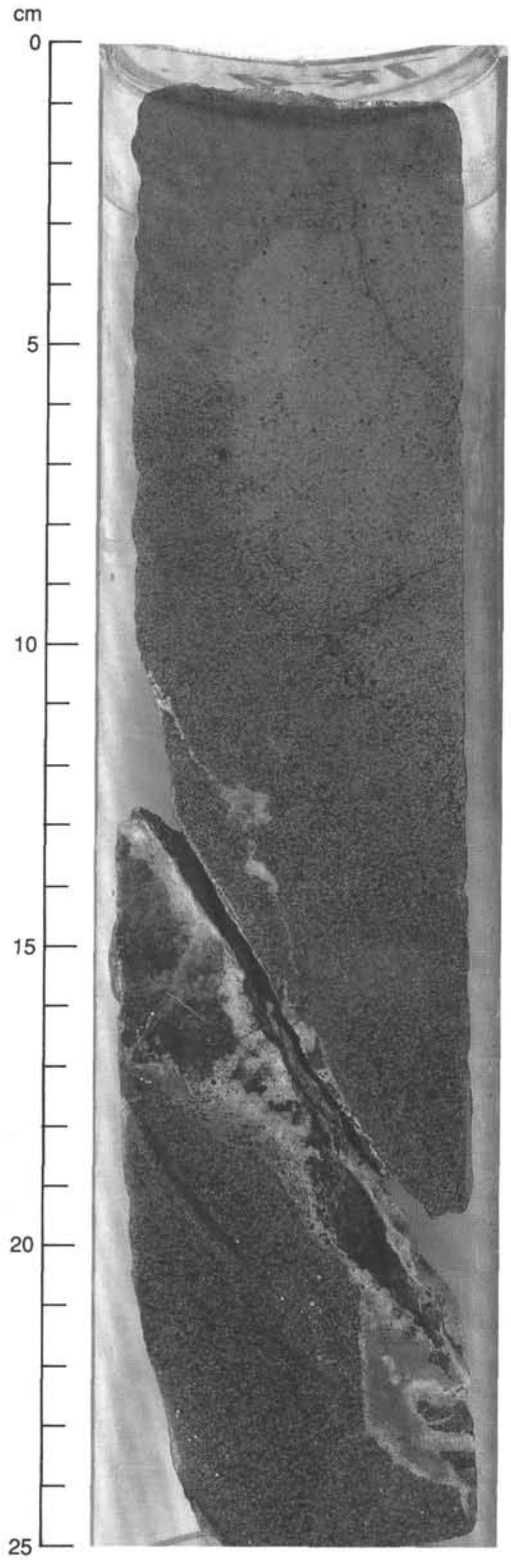

Figure 124. Close-up of Interval 123-765D-7R-4, 0–25 cm. Saw cut was made to show true dip angle. In some cases, fractures may have been major conduits for low-temperature hydrothermal activity. In this example, veins are filled with a combination of calcite and smectite mineralization. Note the dark alteration halo that extends to the left out to 10 cm.

Table 43. Abbreviations used in site summary and data acquisition tables.

1. Measurements

CCA	GST calcium measurement
CCHL	GST chlorine measurement
CFE	GST iron measurement
CGR	Natural gamma-ray radiation minus uranium contribution (API units)
CHY	GST hydrogen measurement
CSI	GST silica measurement
CSUL	GST sulfur measurement
DRHO	Difference between long- and short-spaced source-receiver pair response from the density tool
DTLF	Acoustic transit time (far spacing) (μs/ft)
DTLN	Acoustic transit time (near spacing) μs/ft)
ENPH	Epithermal neutron porosity (free hydrogen index)
HD	Hole diameter from the mechanical caliper (in.)
IDPH	Deep induction resistivity (ohm-m)
IHV	Integrated hole volume (in.^{3})
IIR	GST iron indicator ratio
IMPH	Medium depth induction resistivity (ohm-m)
ITT	Integrated transit time (ms)
LIR	GST lithology indicator ratio
NPHI	Thermal neutron porosity (total [including bound] hydrogen index)
PEF	Photoelectric factor (barns/electron)
PIR	GST porosity indicator ratio
POTA	Potassium content from gamma-ray spectrometry
RHOB	Bulk density (g/cm^3)
SELU	Spherically focused induction resistivity (shallow depth) (ohmm)
SGR	Total natural gamma radiation (0.2 to 3.0 MeV) (API units)
SIR	GST salinity indicator ratio
THOR	Thorium content from gamma-ray spectrometry (ppm)
URAN	Uranium content from gamma-ray spectrometry (ppm)

2. Quality

G	Good
M	Moderate
P	Poor
A	Attenuated (in pipe)

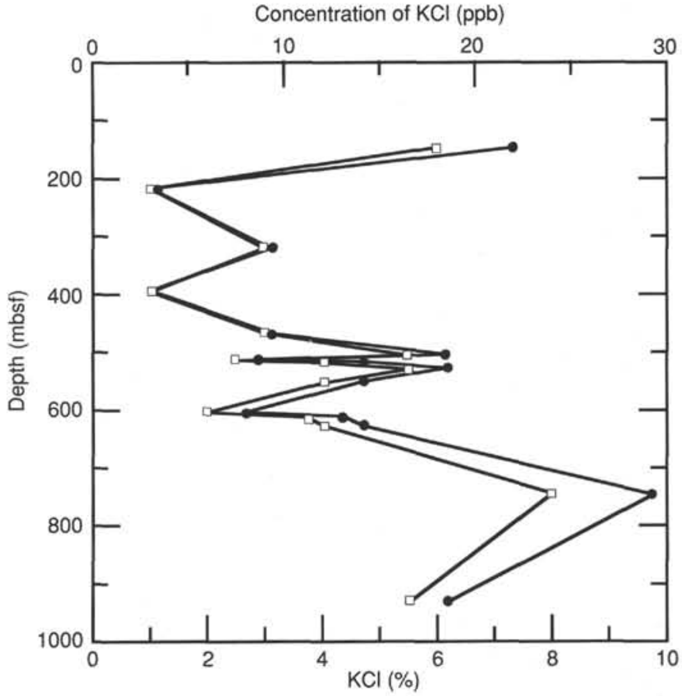

Figure 125. Plot of results of Baroid capillary suction test for identifying swelling clays in Hole 765C.

Table 44. Quality of data acquired using seismic stratigraphy string in Hole 765C.

Depth (mbsf)	Sonic			Resistivity			Gamma spectrometry					Hole geometry	
	DTLF	DTLN	ITT	IDPH	IMPH	SFLU	SGR	CGR	POTA	THOR	URAN	HD	IHV
0 to 182 (in pipe)							A	AP	AP	AM	AM	G	G
182 to 386 (open hole)	G	G	G	G	G	P	G	P	P	M	M	G	G
386 to 524 (in pipe)							A	A	AM	AM	AM	G	G
524 to 647 (open hole)	G	G	G	G	G	M	G	G	G	G	G	G	G
647 to 662 (in pipe)							A	A	A	A	A	G	G
662 to 740 (open hole)	G	G	G	G	G	M	G	G	G	G	G	G	G

Table 45. Quality of data acquired using lithoporosity string in Hole 765C.

Depth (mbsf)	Compensated neutron		Lithodensity			Gamma spectrometry				
	ENPH	NPHI	RHOB	DRHO	PEF	SGR	CGR	POTA	THOR	URAN
0 to 158 (in pipe)	AM	AP				A	A	A	A	A
158 to 466 (open hole)	M	G	M	G	G	G	G	G	G	G

Log Quality

Borehole Conditions and Caliper Measurements

Depth Matching. Logging tools were zeroed at the mud line using the spectral gamma-ray tool (SGR). Despite this control, a depth mismatch of 4.4 m occurred between the SS and lithoporosity depths. We assumed that the lithoporosity depth was accurate, and 4.4 m was subtracted from the SS depths for later processing. The accompanying figures are depth corrected, but correlation with core depths proved difficult at this stage because of poor core recovery. However, the depths of coarse nannofossil ooze at the base of graded sections ties in well with both log suites. On this basis, we consider that the log depths (as presented in the accompanying diagrams) at present are not more than 1 m different from core depths, although more detailed work is necessary to confirm this.

The SGR correlation coefficient traces from the two logging runs was 0.69, indicating an acceptable depth match.

Hole Size. The caliper tool measured 1.46 in. too high, according to calibration in drill pipe (true ID = 4.3 in. in 5-in. pipe and 4.5 in. in 5.5-in. pipe). The logging scientists corrected calibrations before the logs were further processed, but not before Schlumberger cyber service unit (CSU) corrections were made during logging. This will affect CSU borehole corrections of density, neutron, and gamma logs. We assumed that the caliper tool responded linearly above the 4 in. diameter, but because the tool cannot be calibrated with rings this is uncertain. Later runs in 10.88-in. casing suggest that the response is linear, at least to this diameter. Maximum caliper extension is 15.9 in. The caliper values on field tapes have not been corrected.

Hole rugosity was sufficient to cause cycle skipping on more than one sonic receiver channel in several locations. Using a sonic reprocessing program, the velocity curve displayed in Plate 2 (back pocket foldout) has been processed to remove bad channel data. The density log has also been affected greatly by hole conditions, with DRHO often reading large negative values, a sign of poor data quality in light mud (Bateman, 1985, p.164).

Nuclear Effects

The addition of barite and KCl to stabilize the hole during the first SS run affected the natural gamma-ray spectrometry tool (NGT) responses. All the gamma spectrometer potassium windows (W1NG, W2NG and W3NG) were affected by the 5% KCl (18 ppb) added to the conditioning mud. The hole was flushed with seawater during subsequent attempts using the SES, and the latter two SS runs and the lithoporosity run are not noticeably affected by KCl or barite (but more detailed analysis may show some residual affects). During the first SS run, a KCl correction was applied to the NGT readings by the normal CSU algorithm. This correction proved excessive in practice, leading to negative potassium values. Data were reprocessed with the KCl correction removed, at which point the values had the same range as the NGT potassium values derived from the lithoporosity run over the same interval, although the correlation between runs is low. The field tape values still have the original KCl correction applied to the recorded K (POTA) values. The lithodensity log will be affected by the presence of both residual barite in the mud cake and residual KCl in the invaded fluids. The density log also was affected because the lithoporosity string does not carry a caliper tool. The only hole size correction that can be made to these readings in real time is a static bit-size correction, which can lead to errors of up to 0.02 g/cm^3 in log readings. Although this is substantially less than the total probable error for this tool, a back-calculation of the raw bulk-density (RHOB) reading and subsequent caliper correction using the SS caliper was conducted before plotting back-pocket Plate 2 and the calculation of M and N values (Burke et al., 1976).

Sonic Log

The sonic log reading was checked in free drill pipe both before and after the run, where it gave values of 57 μs/ft (±2). As mentioned above, the presence of cycle skipping was noted at 543, 546, 559 to 569, 676, 679, 709, and 712 mbsf (corrected depth). These depths correspond to high caliper readings. The sonic waveforms were not examined at the well-site but will be studied later onshore. In general, the near and far detectors track well (correlation coefficient, r = 0.86), and the crossplot readings are consistent. The velocity values plotted in back-pocket Plate 2 are derived from the Lamont-Doherty Geological Observatory sonic reprocessing program.

Natural Gamma-Ray Spectrometry

The NGT tool was run on both the SS and lithoporosity strings. These strings were deliberately run at the same logging speed of 300 m/hr to enable direct comparison of the gamma-ray spectra in both open hole and drill pipe. Because of variation in pipe position for each of the runs, we were able to obtain spectra over the same section in both open hole and drill pipe, enabling us to correct for the attenuation of gamma rays caused by drill-pipe wall thickness. There are four attenuation conditions to be considered: (1) wall thickness of 5-in. drill pipe; (2) wall thickness of 5.5-in. drill pipe; (3) drill pipe tool joint thickness; (4) wall thickness of 8-in. drill collar. We were able to correct the effect of each by using regression equations derived from crossplots of the open hole and in-pipe versions of each section. The values plotted in back-pocket Plate 2 are corrected values from the NGT run using the GLT string. Correlation between depth-corrected SGR from the two different strings is generally acceptable (correlation coefficient, r = 0.69). Estimates of the K content from both runs correlate poorly; the problem is probably a combination of variable KCl content and hole geometry.

Density Log

The DRHO curve is a measure of log quality. Values recorded from Hole 765C are about −0.2, indicating rather mediocre log quality in a seawater gel mud with effectively no barite. The lack of caliper on the modified lithodensity (LDT) tool meant that a static correction for bit size was applied in the CSU software. This was removed during post-processing, and the caliper measurement from the SS string was applied to the back-calculated raw RHOB values. The values of density and porosity calculated using a matrix density of 2.71 g/cm^3 track the thermal neutron porosity reasonably well in these carbonate sediments (correlation coefficient, r = 0.6), although the density-derived porosity values are about 10% too high in crossplots. At the 50% to 60% porosities that can be found in most of the Miocene carbonates, the RHOB value reads about 0.2 g/cm^3 too low. This agrees with the difference between physical-property bulk density and log-derived bulk density. Additional evidence indicating the need for correction comes from the M-N crossplot (Schlumberger chart CP-8 [Schlumberger Chart Book, 1987]), where the uncorrected M and N values fall in unlikely positions on the crossplot. After correction (increase) of RHOB by 0.2 g/cm^3, values are more understandable in terms of an undercompacted calcareous ooze section. The density curve plotted in back-pocket Plate 2 was corrected as described above.

Photoelectric Factor

Photoelectric values range from three to five, and crossplots of the photoelectric factor (PEF) vs. potassium and thorium/potassium give reasonable clay types. PEF values at the top and base of the lithoporosity tool string run (above 180 mbsf and below 460 mbsf) have lower values that are more characteristic of swelling smectitic clays, as would be anticipated from the results of the CST.

Neutron Logs

Thermal neutron porosity values (NPHI) recorded by the neutron porosity tool (CNT-G) agree reasonably well with physical-property values in a visual plot, although the actual correlation coefficient is low ($r = 0.4$), probably reflecting the need for better core-log depth matching. Epithermal neutron porosity values read about 20 porosity units higher than thermal neutron values. This is probably the result of ineffective excentralization of the CNT-G part of the lithoporosity tool string in the ODP configuration, where because of the restrictions imposed by the drill-pipe ID, the bow springs are significantly weaker than usual for this tool. Epithermal neutron values are more sensitive to hole rugosity than the dual detector thermal neutron values, and should be corrected for hole rugosity using the caliper from the SS string before being used further.

Resistivity Logs

Hole conditions were not optimal for induction logging. The R_{mf}/R_w (mud filtrate resistivity to formation fluid resistivity) ratio is about 1.0; the drilling fluid was seawater. Spherically focused induction resistivity logs (SFLU) suffered from intermittent failure during all runs. The de-spiked log is of limited value, and probably should not be used for further analyses. Deep and medium induction resistivities track well (correlation coefficient, $r = 0.83$) with no apparent quality problems. Resistivity-porosity crossplots indicate resistivity formation factor constants of $a = 1$ and $m = 0.8$ for the Miocene section covered by the SS string.

Results

The most complete log coverage is over Miocene lithologic Subunits IIC, IIB, and IIA. Coverage by the SS string alone extends from the top of the early Aptian to the basal Oligocene (lithologic Subunits VA to IIIA).

Lithologic Unit II (age = late to early Miocene)

Subunit IIA (189.1–379.0 mbsf). Subunit IIA is dominated by graded sequences of calcareous sediment of pelagic origin (see "Sediment Lithostratigraphy" section, this chapter). The graded sequences have a basal lithology of calcareous foraminiferal ooze with quartz sand. The grain size of the basal units is fine to medium sand, fining upward to clay or silt size. The sequence thickness varies from 5 to 200 cm in the cores. The average $CaCO_3$ content is 70%. The color is greenish gray.

Subunit IIB (379.0–459.9 mbsf). Subunit IIB is composed of graded sequences 2 to 165 cm thick. There are intervals of nannofossil chalk, and 6- to 20-cm claystones with dolomite. The dolomite reaches 30% in some samples.

Subunit IIC (459.9–474.1 mbsf). The graded upper part of Subunit IIC is predominantly chalk. The lower part is conglomeratic, with a matrix support of clayey chalk. A wide variety of pebble lithologies was recorded, including basalt and Jurassic silty claystone. Pebble diameters ranged up to 8.5 cm.

The upper lithologic unit boundaries proposed above are not immediately identifiable on the logs. The thorium/uranium ratio log, shown in back-pocket Plate 2, was plotted so that values of more than 2.0 were shaded black. This value is often used as a dividing line between more oxidized (>2.0) and reduced (<2.0) sediments (Doveton et al., 1988). The curve shows an asymmetric form that changes frequency and amplitude at the base of a 12-m asymmetric unit at 269 mbsf. The section above this point is dominated by high-amplitude, low-frequency log oscillations. Below 269 mbsf, this asymmetric curve has a lower amplitude and higher frequency down to 379 mbsf. Here, the frequency changes again, and a petrophysical unit boundary appears to correspond to the boundary between Subunits IIA and IIB. There is too short an interval below the proposed Subunit IIB/IIC boundary to comment on any change of log signature. Examination of the continuous *M-N* plot, shown in Figure 126, indicates that the compaction trend (change in width of the shaded area) is broadly continuous but has some significant anomalies. The *M* value is defined as:

$$M = \frac{(\text{fluid transit time} - \text{formation transit time})}{(\text{formation bulk density} - \text{fluid density})} \times 0.01,$$

and the *N* value is defined as:

$$N = \frac{(1.0 - \text{formation neutron porosity})}{(\text{formation bulk density} - \text{fluid density})},$$

(Burke et al., 1976). The *M* value assumes a linear transit time to porosity relationship, which Raymer et al. (1980) showed empirically was invalid for high-porosity sediments. This nonlinearity can be used to advantage in the continuous *M-N* plot where, although *N* values remain stable at around 0.55 (typical shale value), the *M* value in undercompacted sediments is depressed from its theoretical value. As the sediment becomes progressively compacted, the *M* value tends toward its theoretical shale value of 0.65. Offset scales are used to give an immediate visual impression of the degree of compaction (the shading between curves approaches zero for fully compacted shales). Breaks in sedimentation show up as sharp gradient changes in the shaded area. In Figure 126, there is a marked break at 269 mbsf that corresponds to the change in thorium/uranium ratio character. There may be another distinct petrophysical unit from 300 to 383 mbsf, where a mineralogy change seems to dominate the compaction trend. This might be caused by either an increase in silica or an increase in calcite (or both) relative to the undercompacted clay components. The low *M* values indicate that the physical response of lithologic Unit II is dominated by grain size and compaction effects, rather than mineralogy. One would not expect the *N* value to change in carbonates, but the *M* value should be over 0.75 in a fully compacted chalk.

Although one is tempted to associate the asymmetry in the spectrometer ratio data with the graded sequences noted in core descriptions, caution should be exercised. The combination of mineralogy, compaction, and grain-size components in the log signature need further study before one can make a definitive correlation. However, a first-order agreement of the low thorium/uranium values (<2.0) and the bases of some of the larger graded sequences was noted. These also correspond to high uranium/potassium ratio values, and a curve (such as that displayed in Fig. 127) could be generated if both potassium and thorium increase toward the tops of the graded sequence while uranium is depleted.

Lithologic Units III and IV and Subunit VA (age = Eocene to early Aptian)

Log coverage in these units was limited to the SS string. The base of Subunit IIIA is not sufficiently well represented to enable one to identify a log break. There is a distinctive log break between Subunits IIIB and IIIC at 560 mbsf. The boundary between the claystones of Subunit IIIC and the zeolitic claystones of Subunit VA appears to occur at 594 mbsf, based on gamma-ray resistivity and velocity signatures. Subunit IIIC is characterized by high-amplitude log variation and higher velocities. Subunit IVA is relatively homogeneous in character with lower velocities, lower resistivities, and high natural gamma-ray radiation (70 API units). The boundary with Subunit IVB is clearly

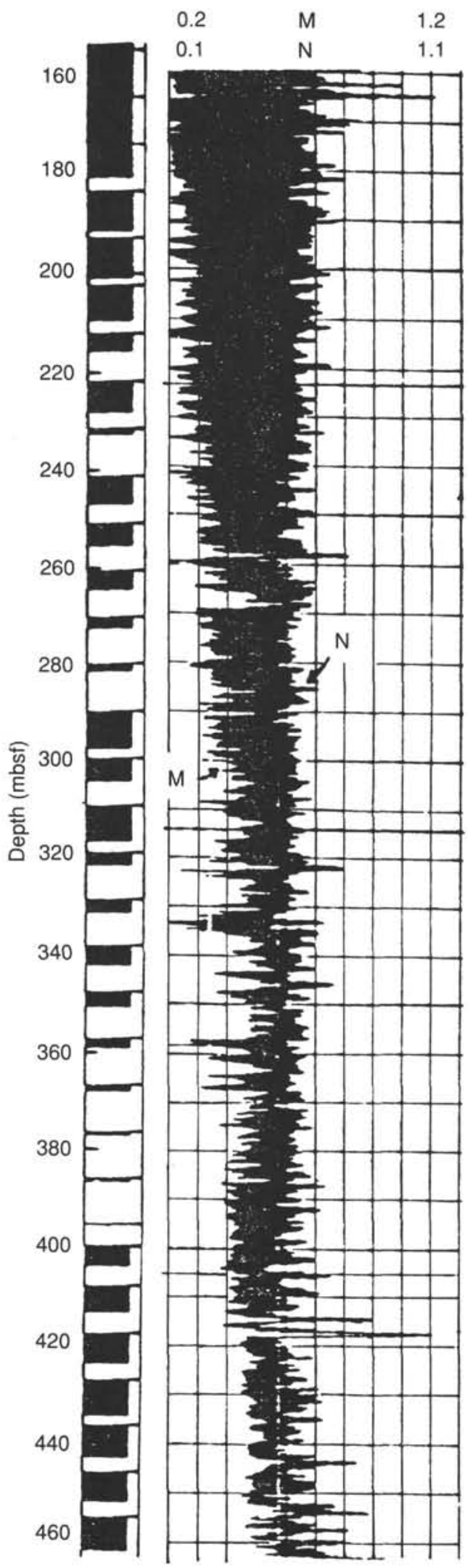

Figure 126. Plot of depths of M and N in Hole 765C.

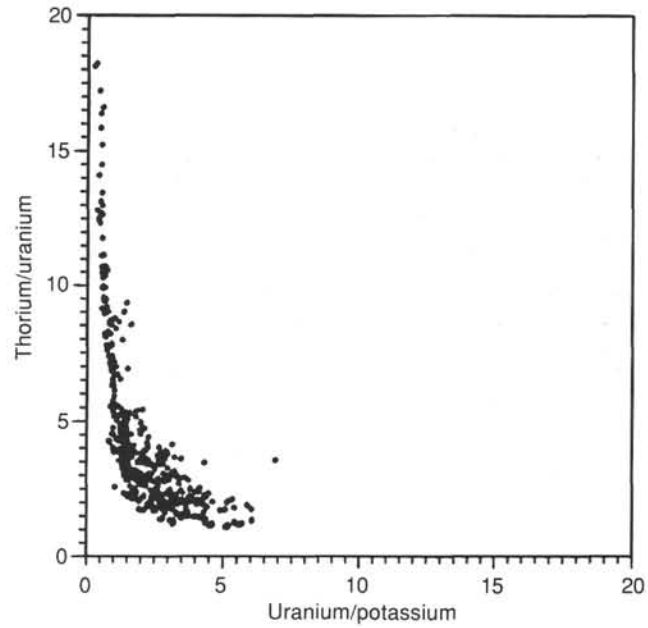

Figure 127. Cross plot of thorium/uranium vs. uranium/potassium for Miocene interval, 160 to 460 mbsf, in Hole 765C.

marked at 608.5 mbsf, but there appears to be evidence for another petrophysical subunit from 608.5 to 618 mbsf that is characterized by higher velocities and lower gamma-ray values. The rest of Subunit IVB (down to the end of the log data at 638 mbsf) may be gradational with velocity and resistivity increasing with depth, while gamma-ray values remain high at 70 API. Unfortunately, the Albian/Aptian boundary is not covered by logs because of poor hole conditions. The petrophysical boundaries between Aptian Subunits IVC, IVD, and VA are not clear. There might be petrophysical subunit boundaries at 680, 700, and 720 mbsf that may correspond to the lithologic boundaries.

Hole 765D

Introduction

Hole 765D is situated about 20 to 30 m from Hole 765C. Our aim at the site was to case the sediment section of the hole to provide a higher annular velocity for cuttings from the basalt section and to drill 250 m of basalt. Thus, the casing shoe was placed 4.8 m below the sediment/basalt interface, across which a full suite of logs was not possible. The hole was cased from the seafloor to 933 mbsf with 11.75-in. OD casing (weight 54 lb/ft, grade K55) with an ID of 10.88 in. The casing sequence is shown in the "Operations" section, (this chapter). A "rathole" 15.2 m deep was drilled below the casing shoe, and more than one annular volume of cement was pumped into the rathole and the casing-borehole annulus.

Operations

The first Schlumberger string run in the hole was the SS tool string, during which run the drill pipe was held at 55 mbsf. After zeroing the tool string at the seafloor, the casing shoe was found at 932 mbsf. The SS string reached TD at 1180 mbsf, and the basalt section was logged upward at a speed of 300 m/hr to a depth of 852 mbsf. The string was then lowered to 900 mbsf, and the resistivity channels disallowed. The cased section to 450 mbsf then was logged at 300 m/hr to allow us to acquire an extra set of NGT data through casing for statistical purposes.

Our aim for sonic logging in the cased hole was to use the difference between the zones showing free-pipe slowness (57 μs/ft) and zones showing cycle skipping for identifying regions of better casing-to-formation or casing-to-cement bonding for the vertical seismic profiling (VSP) experiment. A cement bond log (CBL) would have been preferable, but was not available on board the *Resolution*. A slow logging speed was chosen so as to remove one of the sources of variability in the count statistics of the gamma-ray spectrometer (all NGT runs on Hole 765C had been at 300 m/hr). At 450 mbsf the speed was increased to 900 m/hr to the seafloor. The GLT was the second suite of logs run in Hole 765D. This tool was calibrated in the washout below the casing shoe so as not to saturate a viable formation. TD was found at 1165.8 mbsf during this run. From 1165.8 to 1024 mbsf, logging speed was 100 m/hr. This speed was increased at 1024 mbsf to 150 m/hr, and data were acquired up to 169 mbsf where, for some unknown reason, the string stuck in casing. The tool eventually came free and was retrieved normally in good condition. There were no indications as to the possible reason for this sticking.

The third Schlumberger suite of logs was the lithoporosity string. To avoid possible problems in the casing at 169 mbsf, the drill pipe was lowered to 870 mbsf before logging. The logging depth was zeroed at the casing shoe at 933 mbsf. TD was reached at 1157 mbsf, and the basalt section was logged up at 300 m/hr. At the casing shoe, all channels apart from the CNT-G and NGT were disallowed, and speed was increased to 500 m/hr. The cased section was logged to the seafloor, giving a complete neutron porosity section through casing alone to 870 mbsf and through pipe and casing from 870 to 0 mbsf. Existing neutron and spectrometer data from openhole logs in Hole 765C from 160 to 475 mbsf will provide a means of calculating attenuation constants for these logs, enabling us to get complete coverage from the seafloor to 1140 mbsf through the sediment/basalt interface and up through the sediment column.

Data obtained during the various runs are summarized in the Tables 46 to 48.

Log Quality

Depth Matching

Logging tools were zeroed at the mud line using the SGR. Depths on the geochemical string matched depths from logging runs in Hole 765C, and these depths were used as reference depths. Corrections required to the other strings were as follows: (1) seismic stratigraphy, 0 to 552 feet below seafloor (fbsf), $\pm$4.0 ft; 552.5 to 1620.5 fbsf, $\pm$ 7 ft; 1621 to 1699.5 fbsf, $\pm$7.5 ft; 1700 to 2306.5 fbsf, $\pm$8.5 ft; 2307 fbsf to TD, $\pm$8 ft; (2) lithoporosity, 2 to 700 fbsf, $\pm$4 ft; 700.5 to 1907 fbsf, $\pm$7 ft; 1907.5 fbsf to TD, $\pm$8 ft. Corrections were made before conversion to meters below seafloor and before plotting for Plate 2. Values on the field tapes and prints have not been corrected. Correlation with driller's depth at the casing shoe is good, and at present, there is no reason to propose a core-depth to log-depth shift. This may change with more detailed examination of core data.

Hole Size

The caliper tool measured 1.4 in. too high, according to calibration in casing (true ID of 10.88 in. in 11.75-in. casing). The logging scientist made corrections before further log processing, but not before CSU corrections were made during logging. This will affect borehole corrections made to density, neutron, and gamma logs. We assume that the caliper tool responded linearly above the 4-in. diameter, but because the tool cannot be calibrated with rings, this is not certain. Later runs in 10.88-in. casing suggest that the response is linear, at least to this diameter. Maximum caliper extension is 15.9 in.

Digital enhancement of the BHTV images can produce a caliper log. This log will be included in future reprocessing of logs affected by hole size over sections covered by the BHTV.

Nuclear Effects

Corrections of density logs have also been affected because the lithoporosity string does not carry a caliper tool. The only

Table 46. Quality of data acquired using seismic stratigraphy string in Hole 765D.

Depth (mbsf)	Sonic			Resistivity			Gamma spectrometry					Hole geometry	
	DTLF	DTLN	ITT	IDPH	IMPH	SFLU	SGR	CGR	POTA	THOR	URAN	HD	IHV
55 to 933 (in casing)	A	A					AG	AG	AG	AG	AG	G	G
933 to 1180 (open hole)	G	G	G	G	G	P	G	G	G	G	G	G	G

Table 47. Quality of data acquired using the lithoporosity string in Hole 765D.

Depth (mbsf)	Compensated neutron		Lithodensity			Gamma spectrometry				
	ENPH	NPHI	RHOB	DRHO	PEF	SGR	CGR	POTA	THOR	URAN
0 to 870 (in casing and pipe)		AG				AM	AM	AM	AM	AM
870 to 933 (in casing and pipe)		AG				AM	AM	AM	AM	AM
933 to 1154 (open hole)	G	G	G	G	G	G	G	G	G	G

Table 48. Quality of data acquired using the geochemical string in Hole 765D.

Depth (mbsf)	Geochemical										Gamma spectrometry				
	LIR	SIR	PIR	CSUL	CFE	CCHL	CFE	CCA	CSI	ALU	SGR	CGR	POTA	THOR	URAN
0 to 55 (in casing and pipe)	G	G	G	G	G	G	G	G	G	G	G	G	G	G	G
55 to 933 (in casing)	G	G	G	G	G	G	G	G	G	G	G	G	G	G	G
933 to 1180 (open hole)	G	G	G	G	G	G	G	G	G	G	G	G	G	G	G

hole-size correction that can be made to these readings in real time is a static correction of bit size. For logging in Hole 765D, the static hole size used was 8 in., which means, in effect, that RHOB values were not corrected for hole size. This can lead to errors of up to 0.02 g/cm^3 in log readings. The RHOB plot shown in back-pocket Plate 2 was not corrected for hole size.

Sonic Log

The sonic log reading was checked in free drill pipe both before and after its run, where it gave values of about 57 μs/ft. In the cased hole section, the tool recorded 57 μs/ft over some sections, 70 μs/ft over other sections, a cycle skipped over much of the remaining section below 570 to 750 mbsf, and complete loss of signal from 750 mbsf to the casing shoe at 933 mbsf. This was interpreted as indicating that the top of good cement was at 750 mbsf, channeling to 570 mbsf, and much free casing, with occasional formation contact above 570 mbsf. We expected that the VSP signal would deteriorate in zones having a "free pipe" indication, and would have higher energy in zones of cycle skipping. Initial examination of the VSP results failed to confirm this interpretation, possibly because the increase uphole of signal energy dominated the response characteristics.

Velocities derived from measuring cores for physical properties in the basalts agree well with velocities from the sonic log, and apparently, no systematic shift is required (back-pocket Pl. 2). Velocities shown in Plate 2 are derived from reprocessed sonic data using median slowness. The sonic values on field tapes and prints were not altered.

Natural Gamma-Ray Spectrometry Log

The NGT tool was run on all strings. A logging speed of 300 m/hr was used for the SS and lithoporosity strings, whereas the geochemical string was run at 150 m/hr. This enabled us to compare the gamma-ray spectra both in the open hole and in the casing with the casing and the drill pipe. Because of the variation in pipe position during these runs, we were able to obtain spectra over the same section of hole in both a cased hole and in the cased hole with pipe, enabling us to correct for attenuation of gamma rays from several thicknesses of steel pipe, as discussed for Hole 765C. At the present stage of processing, the multiplicative attenuation factors appear to be (1) SGR, 1.9; (2) potassium, 1.8; (3) thorium, 3.0; and (4) uranium, 1.0. Uranium values do not appear to be affected markedly by the presence of casing, and most of the variation can be accounted for by count rate statistics. A comparison of the three NGT runs in casing shows that the best correlation of depth-corrected values is between the total gamma values on the geochemical and SS strings. These have a correlation coefficient of 0.71. Values from the lithoporosity string (run after the activation from the aluminium clay tool [ACT]) exhibit poor correlations (about 0.4). Detailed examination of spectrometer results from the three logs show that (as expected) spectrometer window 4 values were most heavily affected by the neutron activation.

Density Log

The DRHO (density quality) curve is near zero, with some high positive values associated with larger hole diameters. This is a normal response in borehole fluids having no barite added and indicates a good quality log. A comparison with core-derived physical properties (back-pocket Pl. 2) indicates that no systematic shift in density values is required in the basalt section. Core values agree well with log values.

Photoelectric Factor

A lack of barite in this section of Hole 765D should mean that PEF values will not need correction.

Neutron Logs

Thermal neutron porosity values (NPHI) recorded by the CNT-G tool do not agree reasonably with physical property values in the basalts. Log values typically show a porosity of more than 17%, as opposed to typical core values of 5%. There are several possible causes for this. The dominance of vugular and fracture porosity in the basalts will cause log values to be read as indicating more fracture and vesicle porosity than the small core fragments, but in this case, velocity and density values should show equivalent systematic differences, which these values do not. The lithoporosity tool was run after the activation tool, which affected the CNT-G tool. The dominant influence is the matrix density used for porosity calculation, which will be significantly higher in basalt than the value of 2.71 that was used to calculate values in sediments. The epithermal neutron porosity values read consistently lower than the thermal neutron values (3 to 4 porosity units less), indicating reasonable log quality, in addition to probable dominance of thermal neutron readings by fracture porosity.

Before being used further, both neutron values should be corrected for hole rugosity using the corrected caliper from the SS string.

Resistivity Logs

Hole conditions were not optimal for induction logging. The ratio of mud filtrate resistivity to formation fluid resistivity (R_{mf}/R_w) is about 1.0, and drilling fluid used was seawater. The spherically focused induction resistivity log (SFLU) did not produce reliable results. The deep and medium induction resistivities track well with no apparent quality problems.

Results

Cased-Hole Section

NGT data supports the comments made concerning the Hole 765C. In addition, because of the continuous spectrometer data through the cased section, one can examine more general trends. Figure 128 shows a preliminary subdivision of the sediment section into 10 petrophysical units on the basis of total gamma-ray

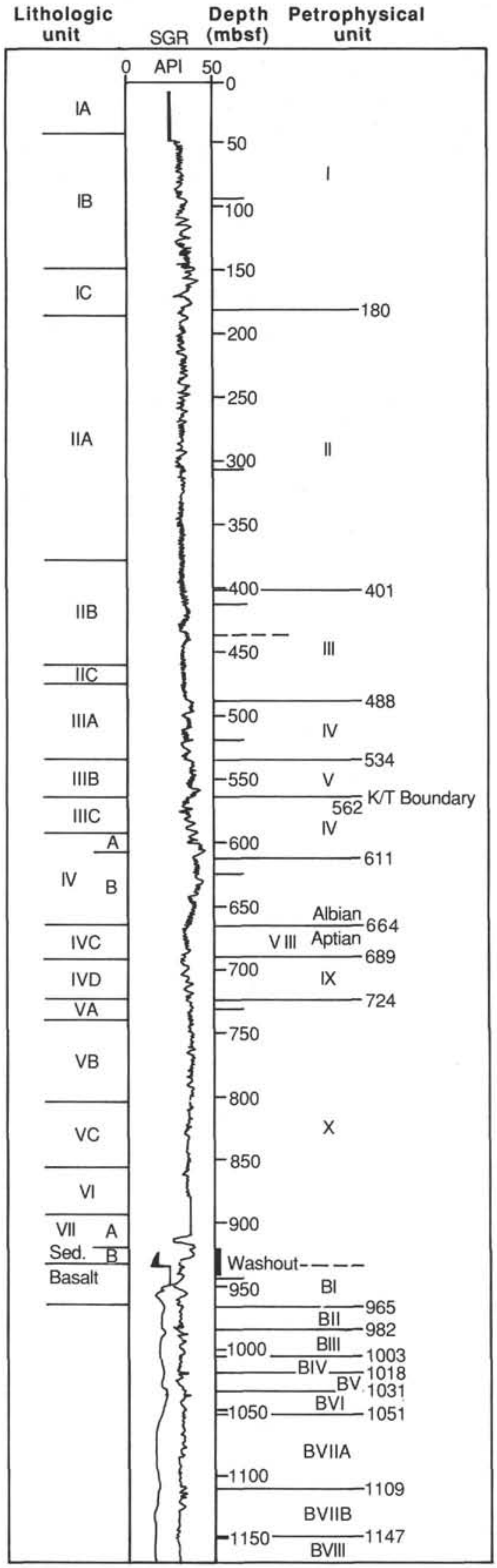

Figure 128. Plot of depths of preliminary petrophysical unit boundaries in Hole 765D.

activity. There is general agreement with lithologic subdivision, but a more detailed quantitative stratigraphic subdivision will be conducted later on the basis of all available geochemical log data. The increase in gamma rays at the K/T boundary is not quite as marked here as it was for Leg 122 Sites 762 and 763, but it remains a notable feature. The relatively low total gamma-ray response in petrophysical Units 8 and 9 correspond to the high sedimentation rate exhibited in lithologic Subunits IVC and IVD in the Aptian.

Petrophysical Unit 7 (611–664 mbsf; corresponding to the Albian lithologic Subunit IVB) has a very distinctive potassium and thorium/potassiium signature, with the potassium content increasing relative to uranium and thorium. This could indicate more illitic clays than are found in the rest of the sediment section. The sediment/basalt interface is obscured by the casing shoe and a washout behind casing (923–933 mbsf).

Basalt Section

The basalt section was logged openhole, and a full suite of logs was obtained from 940 to 1155 mbsf. The basal 40 m was covered by fill and could not be logged.

The basalt section was preliminarily subdivided into eight petrophysical units on the basis of available log data.

Petrophysical Unit 1 (932–965 mbsf). The top of this unit is obscured by washouts and the casing shoe, but Unit 1 has deep fractures and alteration zones of low resistivity and density alternating with zones of very high density and resistivity. The difference between the thermal and epithermal neutron porosities in this unit is about 8 p.u. *K* values are also high. This unit corresponds to basement Unit 1.

Petrophysical Unit 2 (965–982 mbsf). Unit 2 is a higher porosity unit (25% to 30% log porosity), relatively homogeneous and has lower potassium values.

Petrophysical Unit 3 (982–1003 mbsf). This unit has similar petrophysical characteristics as basement Unit 1 and large fractures and alteration zones. Epithermal neutron values are greater than thermal neutron values within these zones, probably as a response to washouts. Resistivity tool logs depict large shoulder effects over these areas, indicating that these are relatively thin conductive zones (?seawater). Thorium/uranium and thorium/potassium ratios are low throughout the basalt section in comparison to the sediment section above, but basement Unit 3 has extremely low values.

Petrophysical Unit 4 (1003–1018 mbsf). A relatively homogeneous unit with lower porosity and increased density, Unit 4 corresponds to basement Units 6 and 7. The unit has high resistivities (1000–2000 ohm) and velocities (5900 m/s). Petrophysical Unit 4 also has high calcium and low chlorine values, with low potassium at the base.

Petrophysical Unit 5 (1018–1031 mbsf). Unit 5 has a petrophysical signature similar to Unit 2. Potassium values are about 0.5 wt%, log porosity is about 25% to 30%, and bulk density increases from 2.5 g/cm^3 at the base to 2.85 g/cm^3 at the top of the unit.

Petrophysical Unit 6 (1031–1051 mbsf). Low resistivity (10 ohm), high log porosity (50%), and low velocities (4000 m/s) characterize Unit 6. The unit corresponds to basement Unit 9 and has potassium values up to 1%. Total gamma rays increase here to 30 API units. Unit 6 may be heavily fractured or altered in narrow zones. This is one of the units exhibiting a phase difference between deep and medium resistivity curves, which we interpret as indicating dipping fractures or alteration zones that intersect the borehole in this region (e.g., back-pocket Pl. 1 at 1038 and 1043 mbsf). Crossplots of deep vs. medium resistivity curves over short intervals show Lissajou figures that can be used to indicate both the regions of dipping fractures and the dips. These features will be studied further in the future.

Petrophysical Unit 7 (1051–1147 mbsf, Subunit 7A ([1051–1109 mbsf]; Subunit 7B [1109–1147 mbsf]). Unit 7 has been identified as having essentially consistent log response characteristics, although it can be subdivided into two similar sections. Each section or subunit shows that potassium increases upward, from less than 0.5% at the base to 1% at the top. A zone of deep fracturing or alteration from 1109 to 1116 mbsf marks the boundary between the subunits. Velocity is about 5050 m/s, and the bulk density is about 2.7 g/cm^3. Velocity and density do not show any marked trends. Any variation appears to be chemical, rather than physical. Log porosity is about 28%.

Petrophysical Unit 8 (below 1147 mbsf). Unit 8 is just noticeable at the end of the logged section; it corresponds to basement Unit 17. The few meters of log that were obtained show steady values. Velocity is 5500 m/s, bulk density is 2.83 g/cm^3, resistivity is 70 ohm, and log porosity is 26%.

SEISMIC STRATIGRAPHY

Site Selection

The final location of Site 765 (originally designated AAP1B) was proposed in a revision of ODP Proposal 121B that was submitted to the JOIDES Planning Committee (PCOM) in May 1986 (von Rad et al., 1986). The site was developed following two successful site survey cruises (Legs 55 and 56) that were conducted aboard the Australian Bureau of Mineral Resources (BMR) research vessel *Rig Seismic* during March through May 1986. Parts of these two cruises were devoted to searching for specific sites without safety hazards on the Exmouth Plateau and Argo Abyssal Plain. Six detailed areas were investigated with multifold and singlefold seismic surveys and dredge hauls. The northern part of the Exmouth Plateau and adjacent Argo Abyssal Plain were surveyed during the second part of Leg 56, which included 8 days of seismic and 7 days of dredging (Fig. 129). Multifold data were collected in both detailed surveys at specific areas of interest and regional tie lines. This program included a grid of lines at the proposed Site AAP1B and two long regional lines out to and back from the area (Lines 56/22 and 56/24; Fig. 129). Details of this survey are presented in a BMR cruise report (Exon and Williamson, 1988).

The grid of multifold seismic data collected in the AAP1B area consisted of the northeast end of regional Line 56/22, three short segments across the site area (56/23A, 56/23B, and 56/23C), and the northern end of regional line 56/24 (Fig. 130). A few other BMR and Shell Oil Company seismic lines in the area allowed for the reconstruction of a generalized map of total sediment thickness (Exon and Williamson, 1988; von Rad et al., 1986). The final location for Site AAP1B was along line 56/23C, near the intersection with line 56/22 in an area of maximum sediment thickness and a water depth of 5740 m (Figs. 130 and 131).

The seismic line across the proposed site (Fig. 131) shows an approximately 900-m-thick sedimentary section overlying a strong, smooth, gently dipping reflector inferred to be the top of Upper Jurassic oceanic crust. The site lies between two basement faults, indicated by diffraction hyperbola. Based on tentative correlation with DSDP Site 261, approximately 320 km to the north, cruise scientists postulated that the sedimentary section consisted of Cenozoic ooze overlying Upper Cretaceous through Upper Jurassic clays and claystones (Fig. 131). Our major objectives at this site were to study (1) the Late Jurassic through Early Cretaceous eastern Tethys paleocirculation and paleoecology, (2) the age of Indian Ocean M-series magnetic anomalies, and (3) the subsidence history of the oldest oceanic site adjacent to the Northwest Australian margin (von Rad et al., 1986).

Further support for drilling in the southwest Argo Abyssal Plain was provided by a second proposal submitted to JOIDES by Gradstein (1986). In addition to more detailed stratigraphic and paleoceanographic objectives related to Site AAP1B, Gradstein (1986) proposed a companion site (AAP2) located just to the northwest along *Atlantis II* line 93-14 (Fig. 132), at proposed marine magnetic anomaly M-25. This transect of two stratigraphically staggered Jurassic sites had as its principal objectives: (1) high-resolution, multiple biomagnetostratigraphy, particularly at and below M-25; (2) a three-dimensional, quantitative distribution model of microfossils needed in paleoenvironmental reconstructions, paleogeography, and stratigraphy, particularly of the equatorially oriented Mesozoic world ocean system between the (proto) Atlantic and (super) Pacific; and (3) comparison of seismic stratigraphy between the deep Argo Abyssal Plain and the adjacent Exmouth Plateau.

Finally, PCOM decided that only one site in the Argo Abyssal Plain would be required to accomplish most of the major stratigraphic objectives outlined in the drilling proposals discussed above. In addition, the same site, by drilling deeper into basement, could be used to address several basement objectives, such as providing a global geochemical reference hole in old oceanic crust as well as a site for hydrofracture experiments to determine crustal stresses. The final site selected was that of AAP1B (Fig. 131), which then became the prime site for Leg 123 and was designated as Site 765 (Fig. 132).

Approach to Site

The approach to Site 765 was made by intersecting BMR site survey line 56/22 at its northeast end and then by paralleling it southwest on a course 224° to the site area (Fig. 132). During this run, singlefold seismic data was continually collected at a speed of approximately 5.5 kt, and a sonobuoy also was recorded. The final location of the site was selected by comparing the analog seismic record displayed on the Raytheon recorder (Fig. 133) with the multifold seismic record (Fig. 134). A beacon was dropped at 1830L (local time) after first recognizing the gentle structural rollover in the sediments above a basement fault block, and then the smooth, gently-dipping, high-amplitude basement reflection (Figs. 133 and 134). The ship then made a broad turn and passed back over the site area on a reciprocal course to obtain a second crossing before securing the seismic system at 1935L (Figs. 132 and 133). The final site was located at the intersection of BMR Lines 56/22 and 56/23C, just 0.25 mi southeast of the originally planned Site AAP1B. Site 765 is centered in the middle of the area having maximum sediment thickness (Fig. 130) and is characterized by a smooth, gently-dipping basement reflection (Figs. 133 and 134). Final position of the site, determined by averaging numerous satellite fixes after site occupation, was 15°58.55′S, 117°34.51′E.

Data Base

A preliminary seismic stratigraphic framework for the Site 765 area was established using, primarily, the grid of multifold seismic data collected during the BMR site survey cruise. The lines available to Leg 123 through the ODP Data Bank were the northeast end of Line 56/22 plus the three short segments of Line 56/23 (A, B, and C; Fig. 132). These lines have been fully processed. One set of lines was displayed with automatic gain control (AGC) applied; these lines were used in Figures 134 through 136. Recording parameters, the processing sequence, and the display parameters for these lines are shown in Table 49. Preliminary interpretation of these sequences was guided by the additional singlefold seismic data in the region, including *JOIDES Resolution* Line 1, shot while approaching the site (Fig. 132).

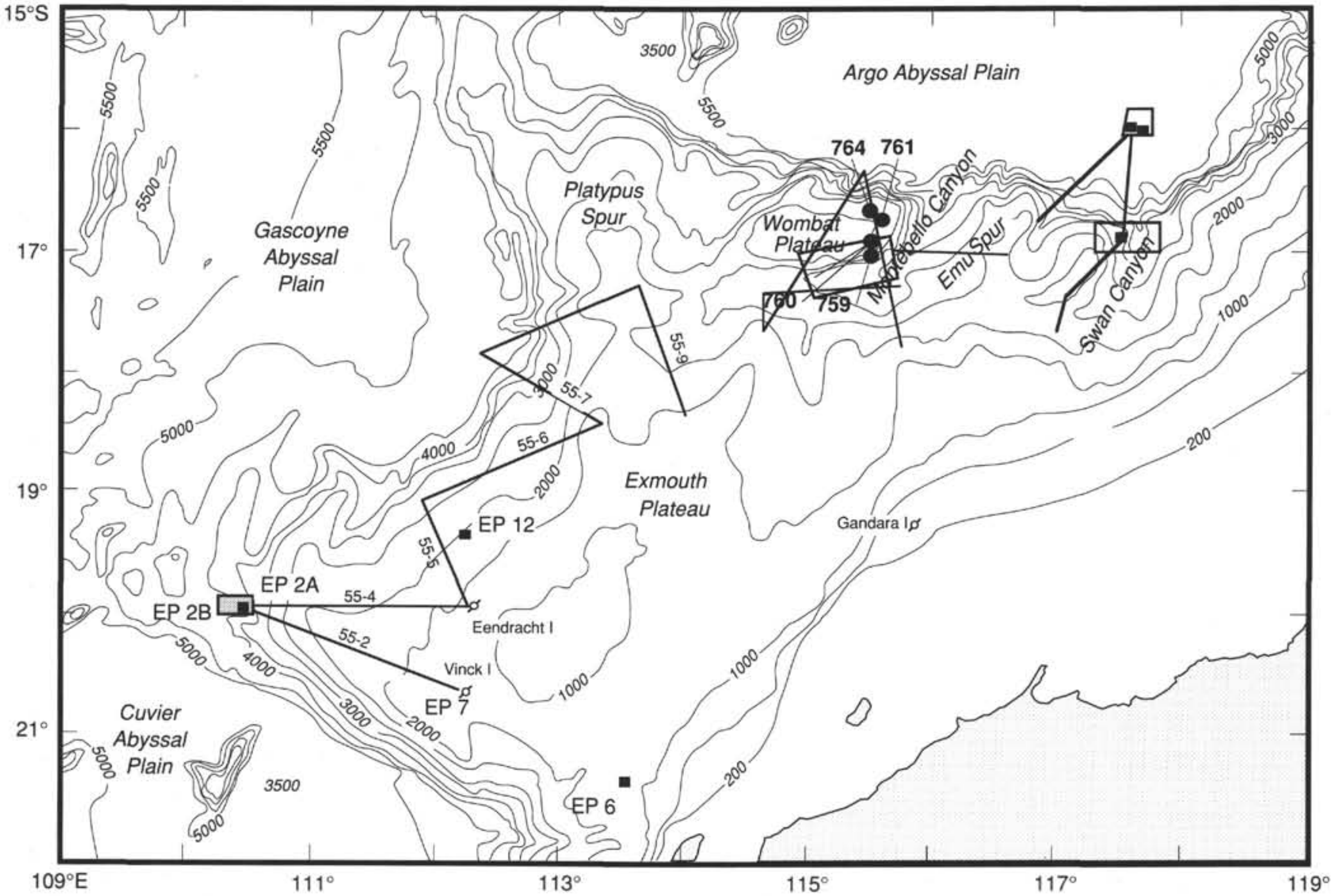

Figure 129. Bathymetric map of Exmouth Plateau area showing location of site surveys conducted during Australian BMR *Rig Seismic* cruises 55 and 56 (1986). Proposed Site AAPIB is located in the southern Argo Abyssal Plain (from Exon and Williamson, 1988).

Seismic Sequences

The stratigraphic section lying above the high-amplitude reflection (inferred as the top of oceanic basement) was subdivided into seven seismic sequences, based on standard seismic stratigraphic procedures. Since this is an abyssal site, not all sequence boundaries displayed disconformable relationships, and in some cases, the boundaries were based primarily on reflection amplitude, reflection continuity, and vertical changes in seismic character. Each of the seven sequences is described briefly below.

Sequence 1

Sequence 1 extends from the seafloor down approximately 0.1 s to 7.694 s at Site 765 (Fig. 134; all times are in two-way traveltime). This sequence is characterized by several parallel, continuous, high-amplitude reflections, followed by a low-amplitude, discontinuous reflection at the base (Fig. 134). Its lower boundary is an irregular, channeled erosional surface exhibiting subtle truncation of reflections below and onlap above (Figs. 135 and 136). The unit thins by onlap to the southwest along line 56/22, where a lower discontinuous part is absent (Fig. 136).

Sequence 2

Sequence 2 occurs between approximately 7.694 and 7.802 s at Site 765 (Fig. 134). The sequence is almost uniformly thick over most of the area, except in the southwest along Line 56/22, where it thickens as the upper boundary becomes more concordant and less eroded (Fig. 136). The lower boundary is characterized by several cycles of onlap to the east within the site survey area along Lines 56/22 (Fig. 136) and 56/23B. This onlap pattern also can be seen regionally from the singlefold seismic data; in particular, from the *Conrad* Line 1403 that crosses the basin in a northeast-southwest direction just south of the site (Fig. 132). This line shows the flat-lying Sequences 1 and 2 onlapping the gently dipping beds of the underlying Sequence 3 along both the eastern and western flanks of the basin. Thus, the boundary represents an important change in sedimentation pattern in the southern Argo Basin. Over most of the site area, the seismic reflections are parallel, have variable, high-to-moderate amplitude, and moderate-to-high continuity. However, to the southwest, along line 56/22, reflections become more discontinuous and slightly hummocky (Fig. 136), suggesting a sedimentary facies change in this direction.

Sequence 3

Sequence 3 occurs between 7.802 and 7.912 s at Site 765 (Fig. 134). Reflections below the upper boundary are concordant and do not show truncation locally. Reflections within the sequence are generally parallel-to-subparallel, have variable moderate-to-low amplitude, and have only moderate continuity (Figs. 135 and 136). In a few areas, some gently mounded configurations can be seen. To the southwest, the reflections become more discontinuous and are similar to Sequence 2 described above (Fig. 136). Although in the site area the limits of the lower boundary are concordant, this boundary was selected as a sequence boundary because (1) it separates two units having slightly different seismic facies; (2) it forms a continuous reflection that

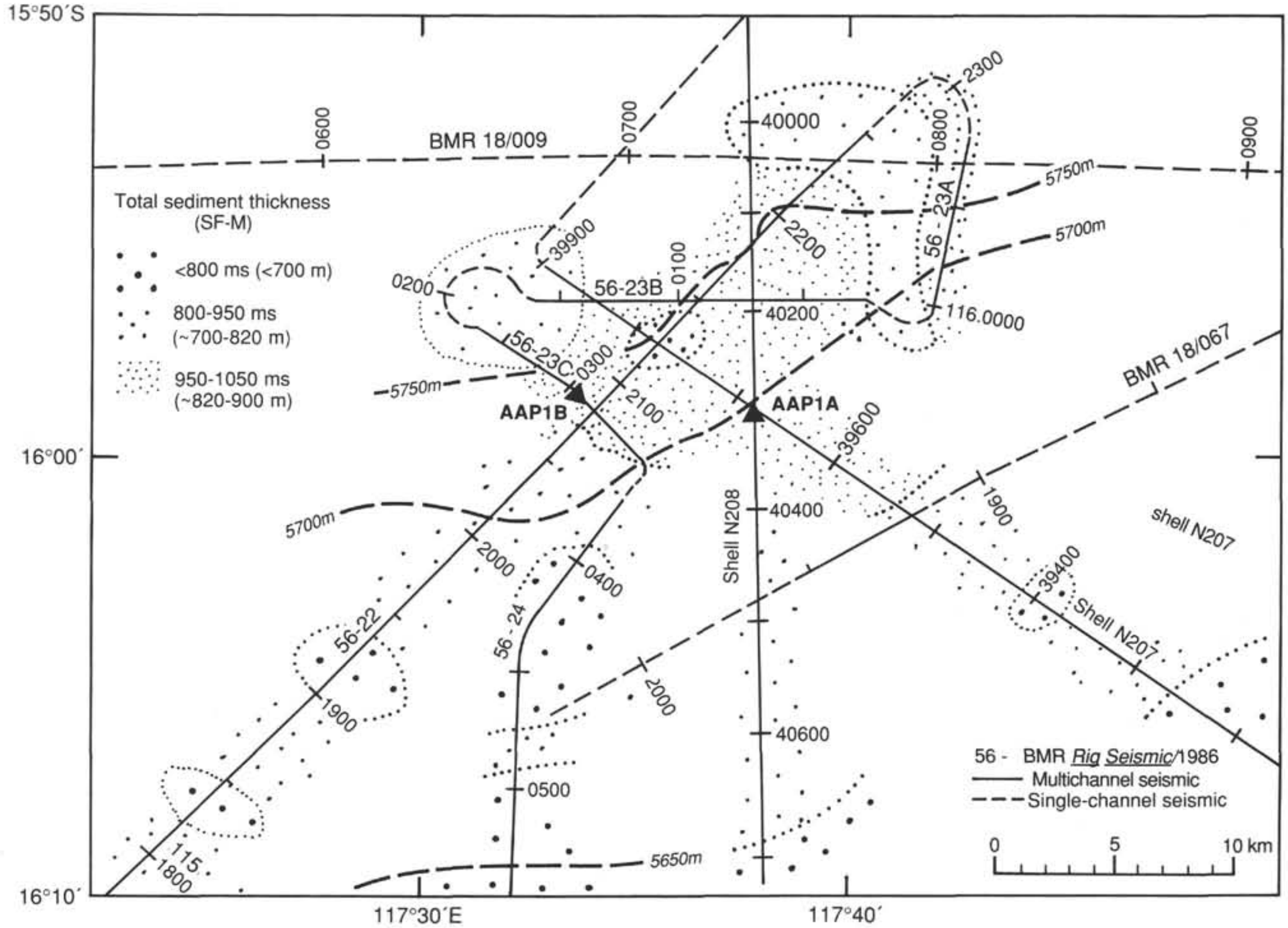

Figure 130. Detailed map of Site 765 (AAPIB) area showing location of BMR multifold seismic lines plus additional BMR and Shell lines used to determine estimated total sediment thickness (in two-way traveltime) and proposed location of Site 765. Bathymetry in meters (from Exon and Williamson, 1988; von Rad et al., 1986).

can be correlated regionally; and (3) it is characterized by onlap and truncation along the basin margins, as is evident from the regional singlefold seismic lines.

Sequence 4

Sequence 4 is approximately 0.12 s thick at Site 765 (7.912 to 8.038 s; Fig. 134) and remains uniformly thick across the site survey area (Figs. 135 and 136). Internally, the sequence is characterized by parallel-to-subparallel, generally low-amplitude reflections having moderate-to-high continuity (Figs. 135 and 136). The beds above and below the lower boundary are concordant, but the boundary is marked by an abrupt change from low- to high-amplitude reflections. Although this increase in amplitude probably reflects a geological change, the boundary may not represent a true sequence boundary; no obvious disconformable relationships were recognized either at the site area or along the adjacent margins on the singlefold lines. In fact, to the north, higher amplitude reflections appear above the boundary, suggesting more of a lateral facies change, i.e., a regional change in turbidite facies or a diagenetic change (see below).

Sequence 5

This sequence consists of a group of four to five parallel, high-amplitude reflectors lying between 8.038 and 8.130 s at Site 765 (Fig. 134). These reflections have a high continuity, and the unit itself has a uniform thickness across the site area. The lower boundary is the lowermost high-amplitude, continuous reflection. It is a prominent unconformity characterized by erosional truncation of gently folded beds of the underlying sequence (Fig. 136).

Sequence 6

This sequence extends from 8.130 to 8.246 s at Site 765 (Fig. 134) and maintains a uniform thickness over most of the site area (0.11–0.12 s). Exceptions are in areas of small faults and gentle folds that seem to affect only this sequence and the underlying Sequence 7, e.g., on the flanks of Site 765 on Line 56/22 (Figs. 134 and 136). Here, the upper part of the sequence has been gently truncated by erosion, thinning the sequence to about 0.08 to 0.09 s. The sequence itself consists of two parts, an upper low-amplitude zone with one high-amplitude reflection in the middle, and a lower zone characterized by two large, high-amplitude positive peaks (a doublet) separated by a large negative peak. In a few places, a smaller positive peak appears between the two larger peaks, separating the negative peak. At the lower boundary, there is again some gentle erosional truncation at the crest of gentle folds and faults in the underlying sequence, e.g., just southwest of Site 765 on Line 56/22 (Fig. 136). The truncation at both the upper and lower boundaries of this sequence, above gentle folds and small faults, suggests reactivation of basement faults just prior to, and just after, the deposition of this sequence. As no apparent onlap occurs above each boundary, erosion must have completely planed off the sequence prior to deposition of the overlying sediments.

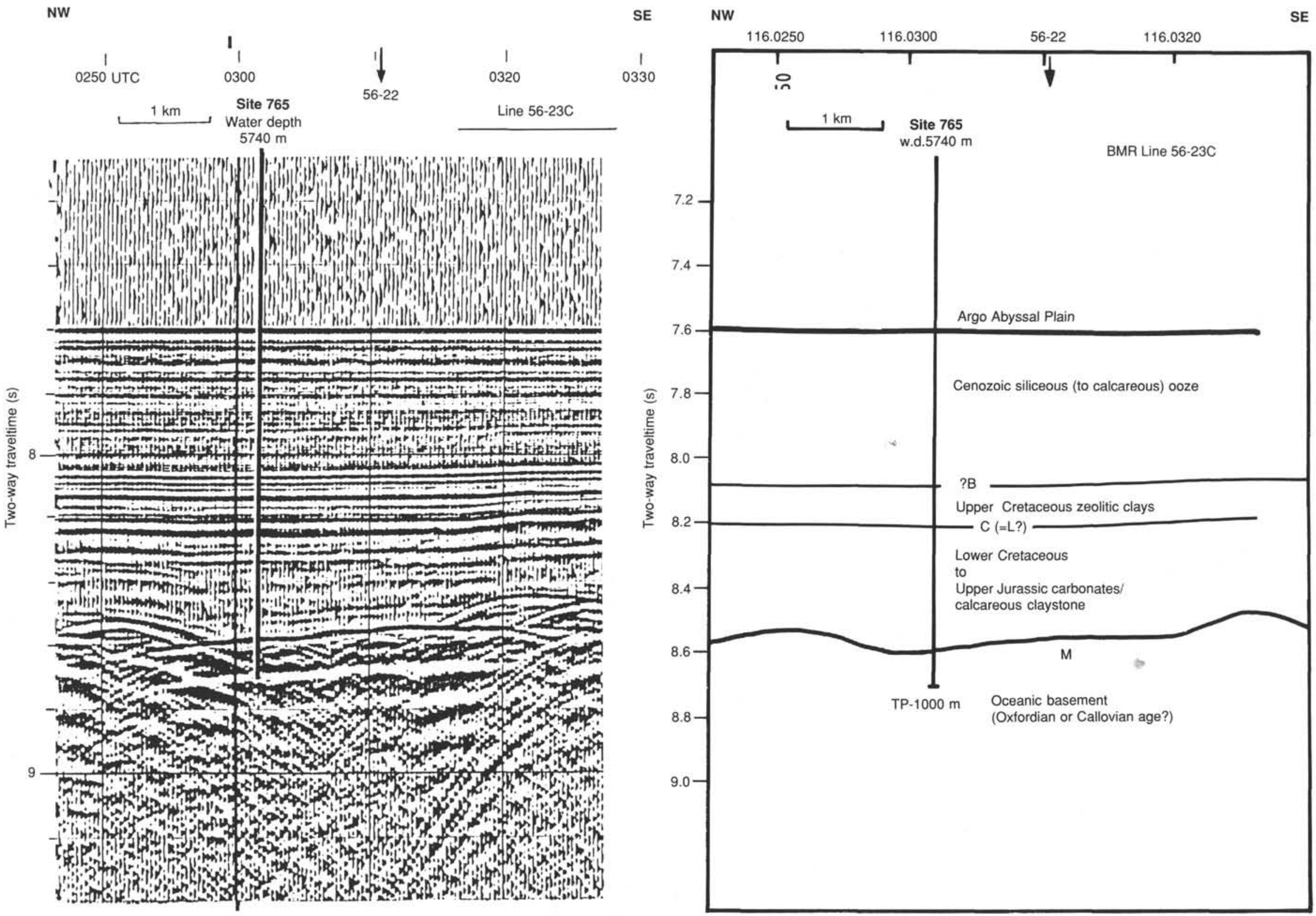

Figure 131. Portion of BMR multifold seismic Line 56/23C across proposed Site 765 near intersection with BMR Line 56/22. Preliminary interpretation of geology based on tentative correlation with DSDP Site 261, located 320 km to the north (from Exon and Williamson, 1988; von Rad et al., 1986).

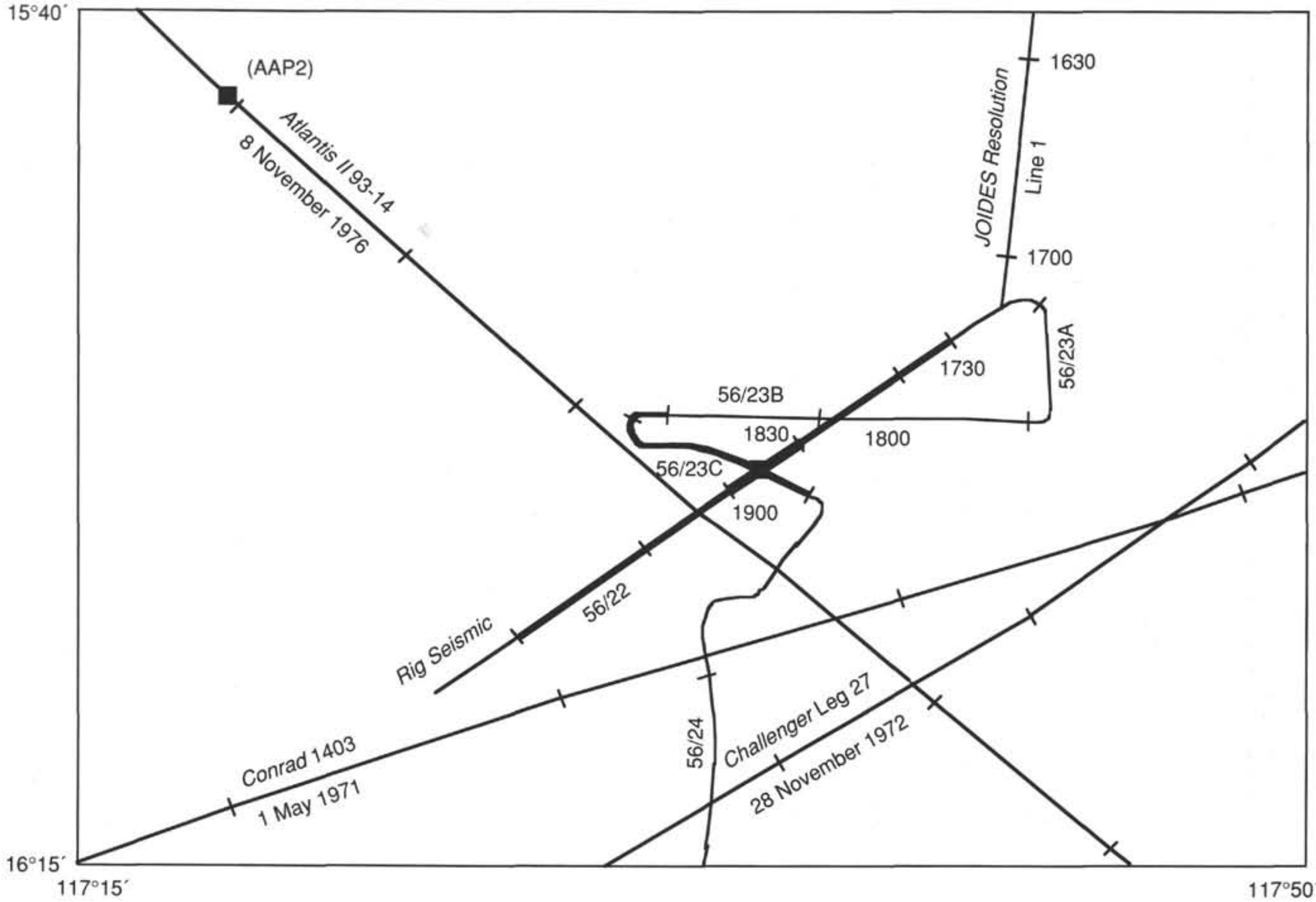

Figure 132. Track chart of BMR site survey lines (56/22, 56/23A–23C, and 56/24), as well as other available singlefold seismic data in the region. Shown are locations of Site AAPIB proposed by von Rad et al. (1986) and Gradstein (1986), as well as Site AAP2 proposed by Gradstein (1986). Location of Site 765 is at intersection of Lines 56/22 and 56/23C. Locations of Figures 134 through 136 and track of *JOIDES Resolution* (Line 1) during approach to Site 765 also are indicated.

Sequence 7

The lowermost Sequence 7 is the thickest by far. Its upper boundary is the unconformity at the base of the high-amplitude doublet described above, while its base is the prominent, high-amplitude reflection that corresponds to the top of acoustic basement (top oceanic crust). This boundary extends from 8.246 to 8.560 s at Site 765 (0.32 s thick; Fig. 134). The unit varies considerably in thickness. In a few places, it thins slightly from the top as a result of erosional truncation. The main thinning, however, appears to be at the base of the section because of the onlap onto basement. This is particularly significant along Line 56/22, southwest of the drill site, where the sequence thins to about 0.2 s over a basement high (Fig. 136). A similar relationship is seen on line 56/23C, south of the drill site (Fig. 135). The irregular basement throughout the site area is caused by numerous small faults that are characterized by offsets of the basement reflection and numerous diffractions. Local relief on basement is as much as 0.2 s along Line 56/22 from the site to approximately 10 km southeast of the site. Internally, most of the sequence is characterized by moderately continuous, subparallel, low-amplitude reflections. There is a persistent band of slightly higher amplitude reflections about one-quarter of the way down in the unit (about 8.30–8.33 s at Site 765; Fig. 134), and a few slightly higher amplitude reflections toward the base of the unit (about 8.50 s at Site 765; Fig. 134). These reflections are not continuous enough to allow for further subdivision of the unit. To the southeast along Line 56/22, Sequence 7 thins and also changes facies. Here, the reflections become subparallel and more discontinuous, and there does appear to be several unconformable surfaces within the sequence (Fig. 136). As mentioned above, Sequence 7 appears to be gently folded and, in places, faulted above some of the basement fault blocks. Because no obvious depositional thinning or thickening occurs across these faults, this relationship suggests reactivation of basement structures after deposition of the sequence.

Correlation With Site 765

Incomplete sonic logs, plus a large discrepancy between *P*-wave velocities measured in the laboratory and shown on the sonic logs in the upper part of the hole, make it difficult to calculate reliable interval velocities for the seismic sequences from these data (see "Sediment Physical Properties" and "Schlumberger Logs" sections, this chapter, for a description of these data). Consequently, this makes it difficult to produce an accurate depth vs. two-way traveltime plot for correlating seismic sequences with coring and logging results. However, we were able to correlate an approximate of these data (Fig. 137). This correlation, referred to in the following discussions as Interpretation A, is based on (1) estimated but reasonable interval velocities for each sequence; and (2) significant changes in lithology, paleontology, and physical properties that might be producing re-

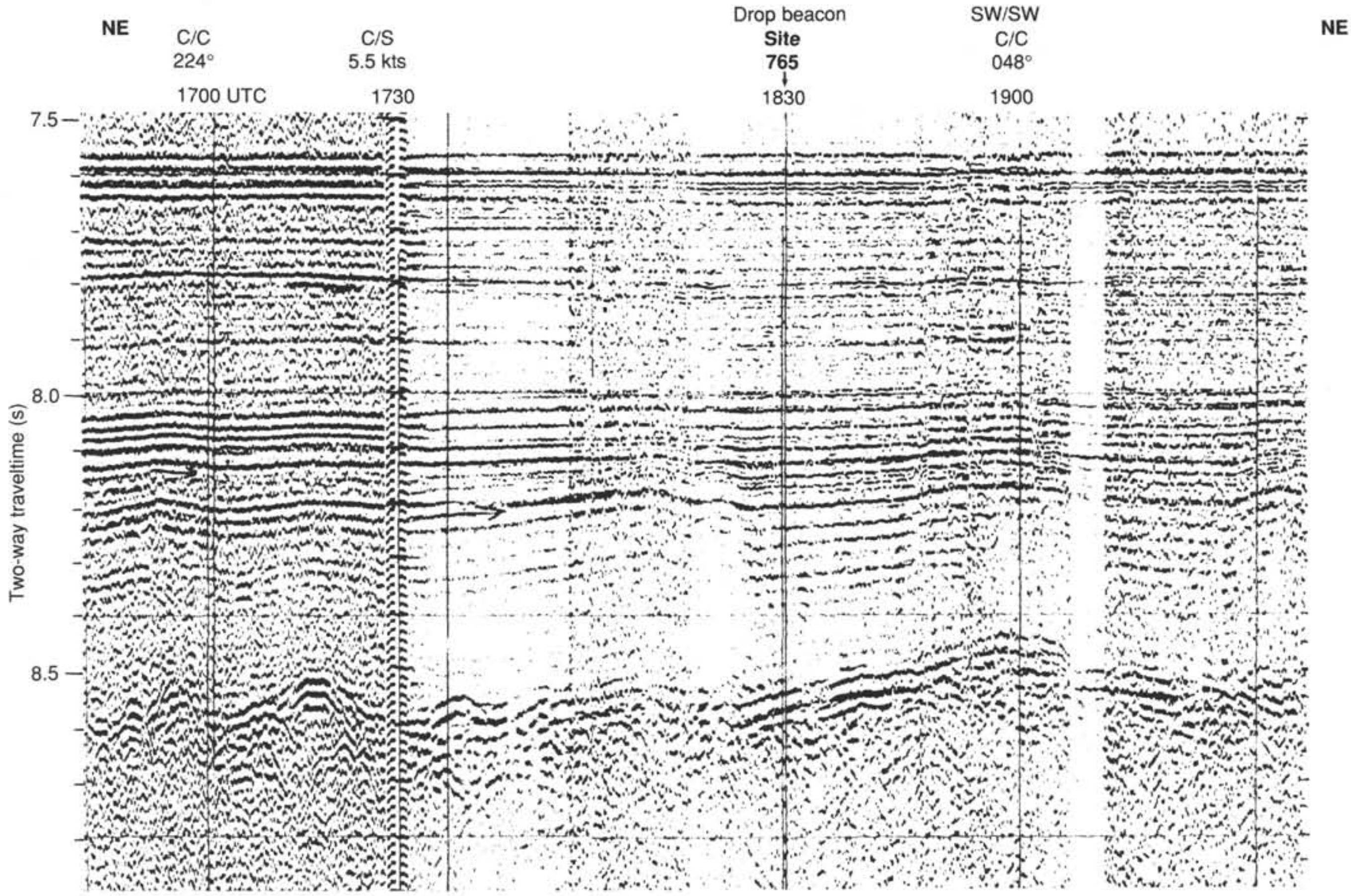

Figure 133. Analog record of singlefold seismic Line 1 collected aboard *JOIDES Resolution* during approach to Site 765. Beacon was dropped at 1830 UTC.

flections at each sequence boundary, as well as internally within each sequence.

After making Interpretation A, results of the VSP experiment became available (see "Vertical Seismic Profiling" section, this chapter). A traveltime vs. depth plot derived from first arrivals of the downgoing wavefields was used to calculate the depths to the sequence boundaries on the multifold seismic line at Site 765 (Fig. 138). These boundaries differ somewhat from those of Interpretation A and thus are referred to as Interpretation B. Both interpretations are presented here and are discussed briefly below. Each will be evaluated in more detail post-cruise.

Sequence 1—Interpretation A

If 0.11 s is used for the thickness and 1550 m/s for the interval velocity (approximate average of velocities measured in the laboratory), then the thickness of Sequence 1 is approximately 85 m. This depth may correlate with the base of the Pleistocene (Fig. 137). Even though the seismic data suggest an erosional unconformity, there is no designated lithologic unit boundary here. A very slight increase occurs in measured velocity, however, as well as an interval showing redeposition of Pliocene strata at this level. There also is a large increase in magnetic susceptibility beginning between 90 and 104 m, which may reflect this break. Sequence 1 appears to correspond to Pleistocene calcareous turbidites.

Sequence 1—Interpretation B

VSP data suggest a depth of 82 m (Fig. 138) similar to Interpretation A, and thus, the same discussion above applies here.

Sequence 2—Interpretation A

Sequence 2 is 0.108 s thick, which corresponds to 84 m if a 1600 m/s interval velocity is used. This places the lower boundary at about 169 mbsf, which correlates almost exactly with the major biostratigraphic break or hiatus between the upper Pliocene and upper Miocene at 170 mbsf; this break occurs in between the closest lithologic changes identified (lithologic Subunit IB/IC, and lithologic Unit I/II boundaries; Fig. 137). This boundary is, however, near a major decrease in magnetic susceptibility at 176 mbsf. The presence of onlap at this boundary suggests the possibility of a hiatus. Thus, correlation with the biostratigraphic break seems the most reasonable, and the sequence is considered to represent upper Pliocene clayey calcareous turbidites, slumps, and debris flows (Fig. 137). Clay in the sequence probably produces the variable high- to low-amplitude character of the unit. The facies change to the southwest (noted on Line 56/22) may reflect more disorganized facies, such as fan channels, slumps, and debris flows.

Sequence 2—Interpretation B

The depth of 189 mbsf does correlate with the major lithologic change at the lithologic Unit I/II boundary (Fig. 138). As above, this sequence corresponds to Pliocene clayey calcareous turbidites and debris flows of the lower part of lithologic Unit I.

Sequence 3—Interpretation A

Using a spread of velocities between 1650 and 1900 km/s, the thickness of Sequence 3 ranges from 91 to 105 m, making

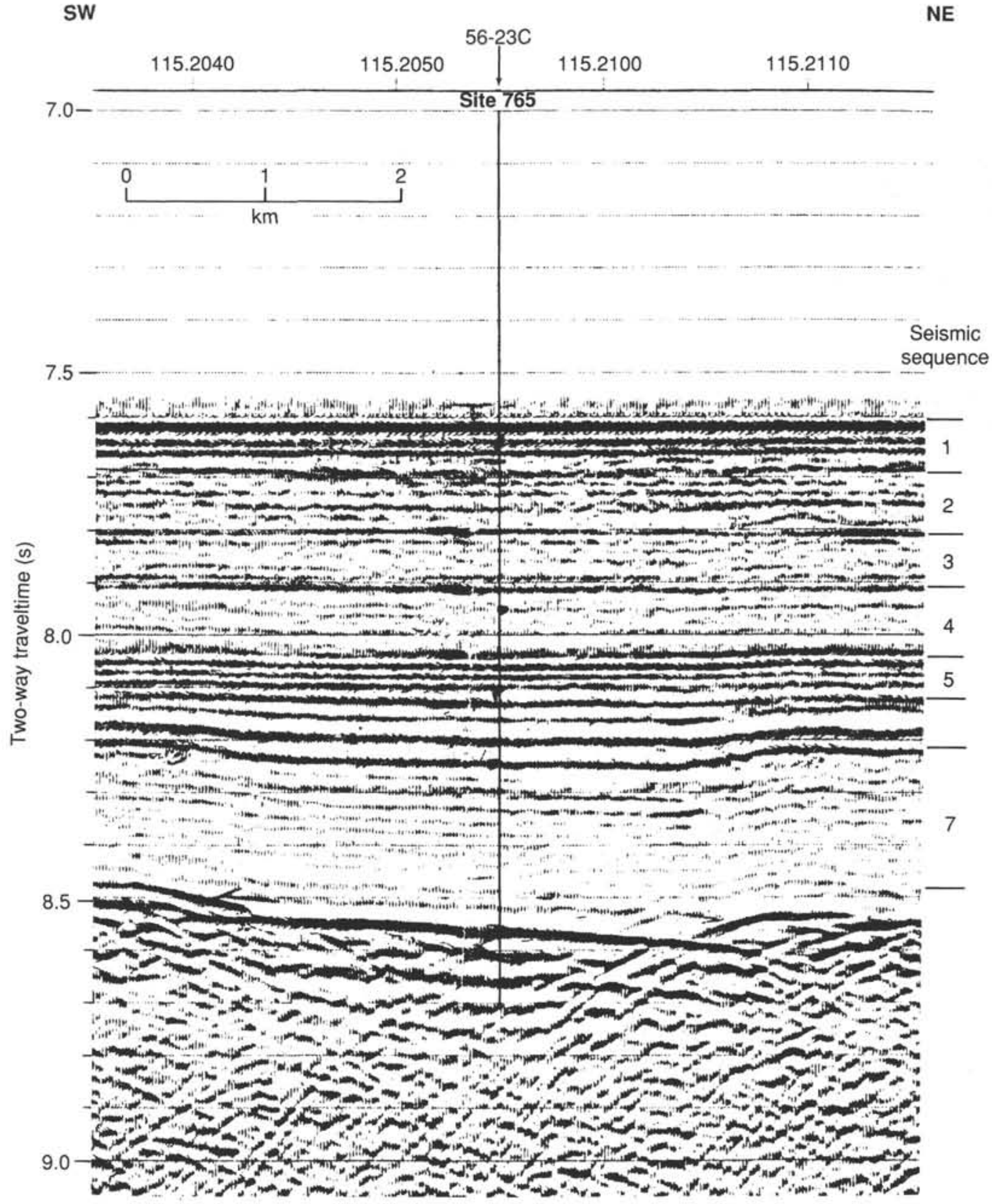

Figure 134. Portion of BMR multifold seismic Line 56/22 across Site 765 at intersection with Line 56/23C. Preliminary seismic sequences 1 through 7 are identified in the site area (see Table 49 for recording parameters, processing sequence, and display parameters; see Fig. 132 for location).

the lower boundary between 260 and 275 mbsf. No obvious lithologic, biostratigraphic, or magnetic susceptibility boundaries occur here (Fig. 137), but a few minor velocity changes on both velocity logs may be producing the reflections at the boundary. These may be recording slightly higher velocities because of an increase in lithification of the calcareous turbidites from ooze to chalk, as noted in Cores 123-765B-27R and -28R. A large positive velocity increase at 268 mbsf on the sonic log was arbitrarily picked as the boundary, because it is midway between the ranges of depths. This depth gives a reasonable interval velocity of 1800 m/s. The lower boundary occurs within the middle of the late Miocene, making Sequence 3 correspond to upper Miocene calcareous turbidites (Fig. 137). The generally lower amplitude reflections of this sequence, compared with Sequence 2 above, may reflect the overall decrease in clay content. The more uniform lithology should produce less impedance contrasts. Again, the facies change to the southwest may be reflecting a change to more disorganized debris flows.

Sequence 3—Interpretation B

This interpretation also suggests that Sequence 3 correlates with upper Miocene calcareous turbidites (Fig. 138). There is no obvious lithologic break, and as discussed above, the lower boundary may be reflecting a diagenetic change.

Sequence 4—Interpretation A

If an average interval velocity of 1850 m/s is used for Sequence 4, the 0.12 s thickness converts to 111 m, placing the lower boundary at 379 mbsf (Fig. 137). This depth corresponds to the boundary between lithological Subunits IIA and IIB, but

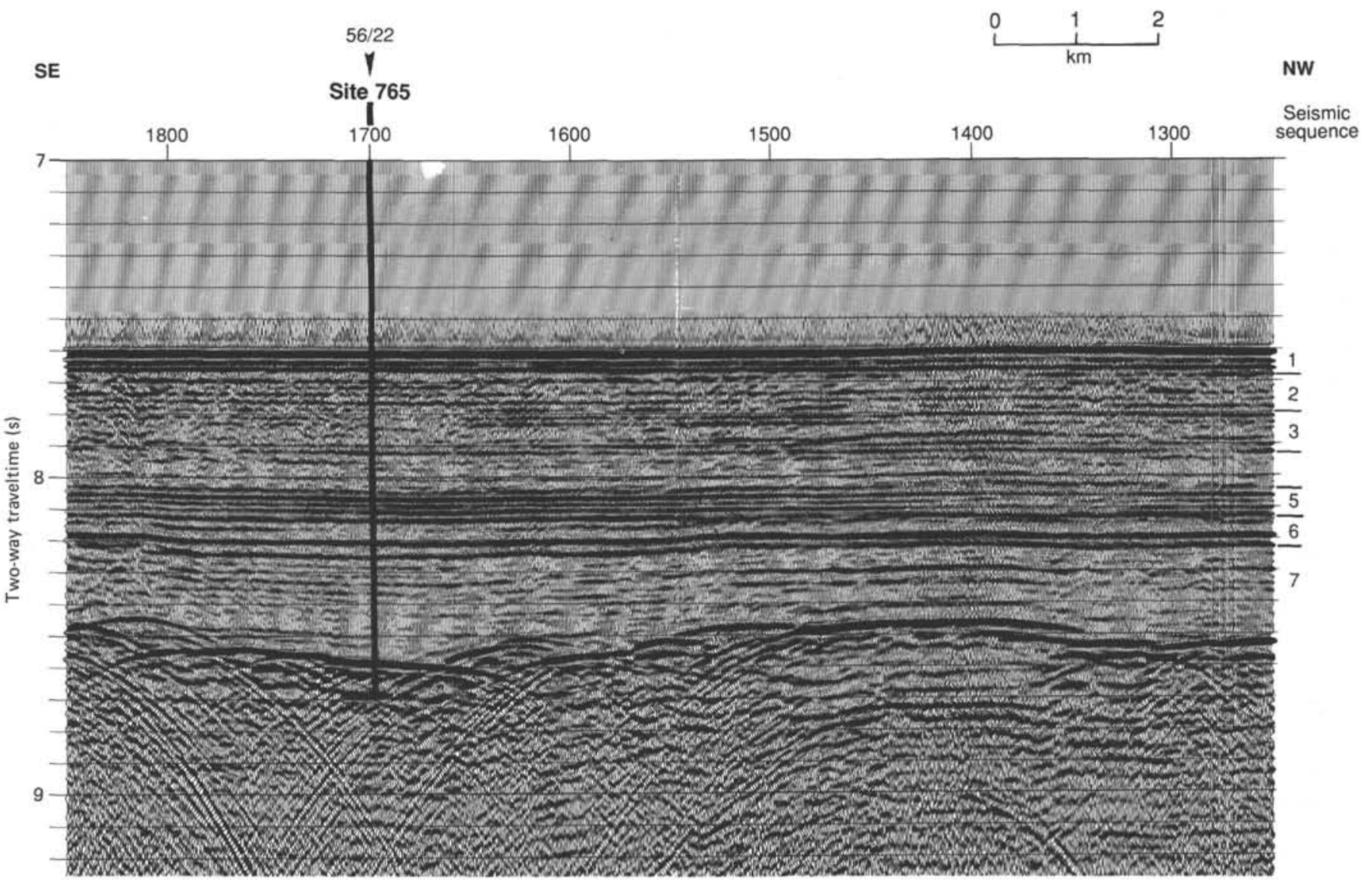

Figure 135. BMR multifold seismic Line 56/23C across Site 765 showing seismic sequences identified in site area (see Table 49 for recording parameters, processing sequence, and display parameters; see Fig. 132 for locations).

does not correspond to any major biostratigraphic break. Thus, Sequence 4 corresponds to middle through upper Miocene calcareous turbidites. Again, the uniform calcareous lithology probably does not produce any major impedance changes and thus is responsible for the generally low amplitudes of the unit.

Sequence 4—Interpretation B

This interpretation places Sequence 4 within the middle Miocene turbidite section, spanning the boundary between lithologic Subunits IIA and IIB (Fig. 138). As discussed above, the generally low-amplitude facies corresponds to the uniform calcareous lithology.

Sequence 5—Interpretation A

The increase in high-amplitude reflections in Sequence 5 probably corresponds to the increase in clay content, as well as an increase in lithification of lithologic Subunit IIB, which would produce more impedance contrasts (Fig. 138). This is supported by the significant change to the widely variable velocities measured in the laboratory at about this depth. Corresponding sonic velocities are missing for most of the section. The sequence is 0.09 s thick, which corresponds to 95 m using an interval velocity of 2100 m/s. This is a reasonable velocity, based on an average of the measured velocities. This places the base of the unit at 474 mbsf, which corresponds to the base of lithologic Subunit IIC (i.e., the base of a large debris flow unit). This boundary also corresponds to a major biostratigraphic break in the upper lower Miocene as well as a major change in physical properties. This includes a reversal to more uniformly measured velocities and a significant increase in magnetic susceptibility; the latter probably reflects an increase in clay content. As this sequence boundary is a major regional seismic unconformity, correlation with this major break in sedimentation seems reasonable. Thus, Sequence 5 apparently corresponds mainly to the middle Miocene calcareous turbidites of lithologic Subunits IIB and IIC. As mentioned in the previous section, high-amplitude reflections appear above this unit farther north, suggesting more clayey turbidites in the unit above or possibly more lithification of turbidites higher in the section. Thus, the upper boundary may be more of a lithologic change than a regional sequence boundary.

Sequence 5—Interpretation B

At this point, the two interpretations begin to diverge somewhat. Interpretation B places the upper boundary within the lower part of the middle Miocene calcareous turbidites (middle of lithologic Subunit IIB; Fig. 138). The debris flow unit (lithologic Subunit IIC) may correspond to the next lower high-amplitude reflection at 8.06 s. Thus, the lower boundary unconformity correlates with the major biostratigraphic gap between the Oligocene and Eocene in lithologic Subunit IIIA, which seems reasonable geologically. The group of high-amplitude reflections of Sequence 5 corresponds mainly to the clayey, more condensed Oligocene through lower Miocene section, including the debris-flow unit.

Sequence 6—Interpretation A

Sequence 6 correlates with the 134 m of condensed Upper Cretaceous through lower Tertiary section corresponding to lithologic Unit III and Subunit IVA. This sequence is 0.11 s thick,

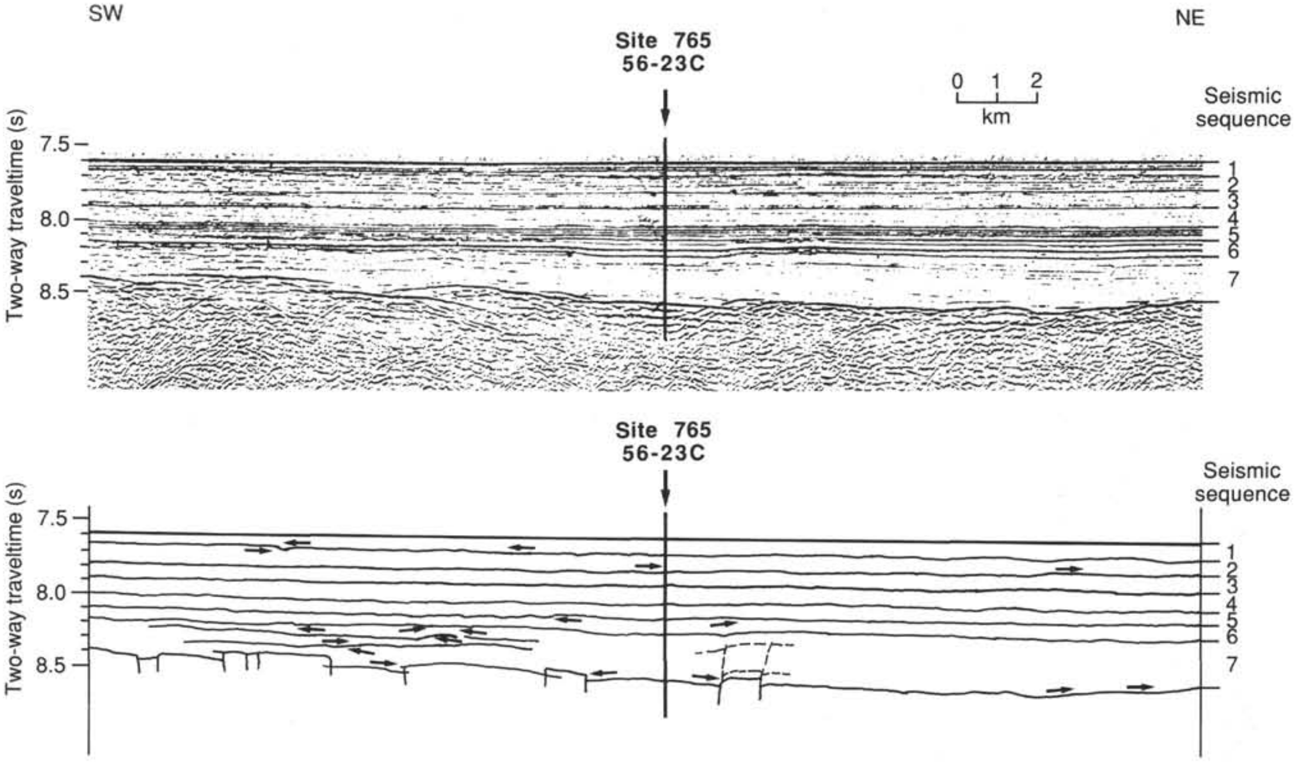

Figure 136. BMR multifold seismic Line 56/22 across Site 765. Line drawing shows interpretation of seismic sequences 1 through 7, including disconformable relationships at sequence boundaries (see Table 49 for recording parameters, processing sequence, and display parameters; see Fig. 132 for locations).

Table 49. Recording parameters, processing sequence, and display parameters of BMR multifold site-survey seismic data, Lines 56/23 and 56/22, Site 765.

Recording parameters (Exmouth Plateau survey, 1986; stack section with AGC)

Vessel:	*Rig Seismic*	Date recorded:	April 1985
Ship speed:	5.5 kt	Shot interval:	50 m
Source:	2 × 8 air guns	Source depth:	8 m
Group length:	50 m	Nominal cable length:	10 m
Number of traces:	48	Leading trace:	1
CDP spacing:	25 m	Coverage:	24-fold
Near offset:	222 m	Maximum offset:	2572 m
Sample rate:	2 ms	Record length:	7500 ms
Data recording format:	BMR SEG 1600 BPI tape		

Processing sequence

1. Geometry definition
2. Reformat to disco interval format
3. Resample to 4 ms
4. Static correction applied
5. F-K shot records
6. Velocity analysis
7. Spike edit
3. Spherical divergence correction
9. Spike deconvolution 100-point operator
10. Normal moveout correction
11. Inside trace mute to attenuate multiple
12. Stack 24-fold
13. Predictive deconvolution 50-point operator. 20-point gap
14. Time-gated bandpass filter: WB to WB + 1500 ms 15-60 Hz; WB + 3000 ms to end data 8-35 Hz
15. AGC with 500 ms gate

Display parameters

Trace density:	15.7 traces/cm
Time scale:	10 cm/s
Polarity:	Normal
Display gain:	0.75
Horizontal scale:	1:39,400 (1 cm = about 394 m)
Display date:	December 1987

This seismic section was processed at the Seismic Processing Centre of the Bureau of Mineral Resources (BMR), Geology and Geophysics Division of Marine Geoscience and Petroleum Geology, Canberra, Australia, by M. Swift.

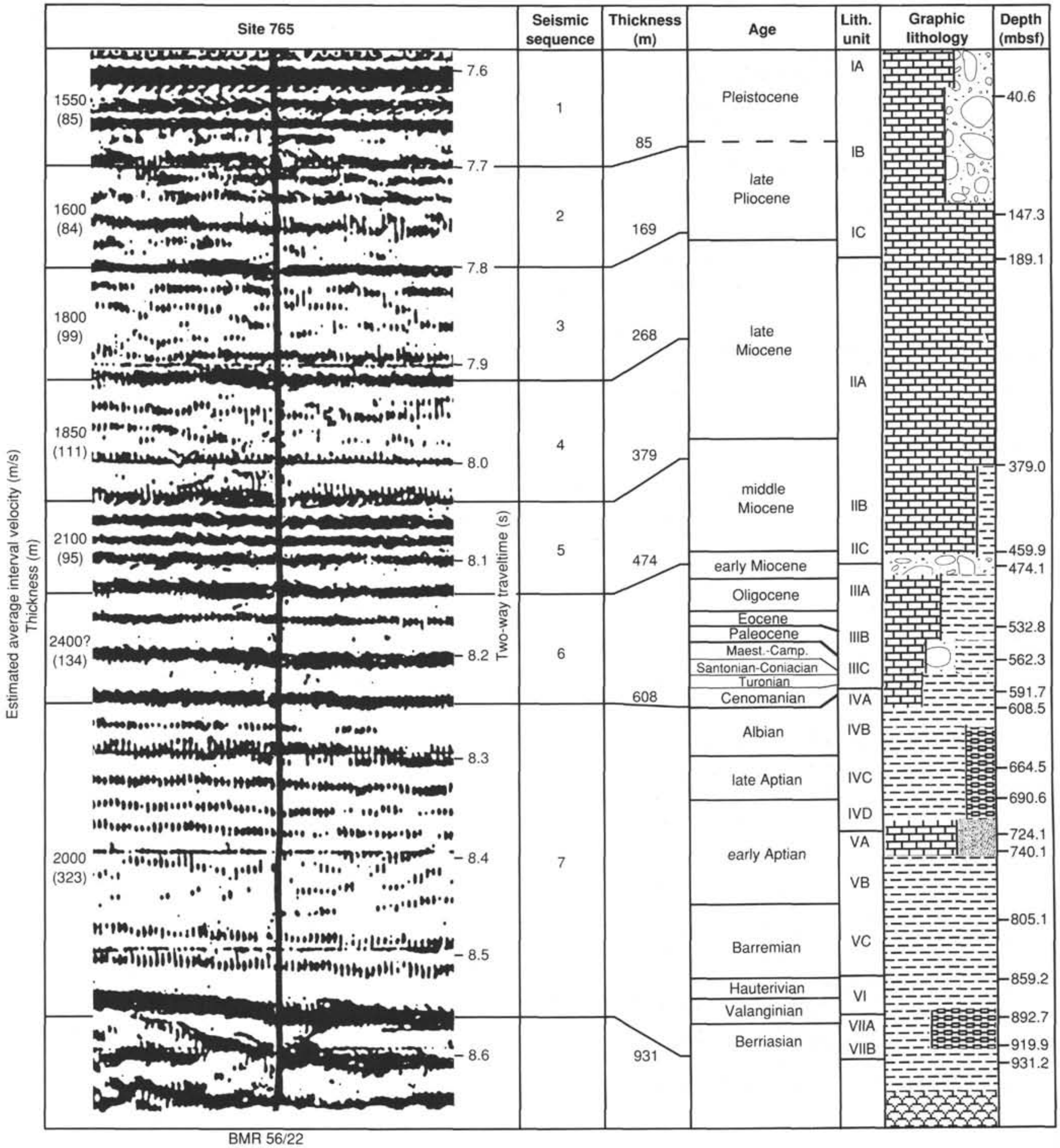

Figure 137. Tentative correlation (Interpretation A) of seismic sequences with drilling results, based mainly on geologic inferences plus average velocities estimated, in part, from measured *P*-wave velocities and sonic logs.

which requires an interval velocity of approximately 2400 m/s (Fig. 137). This value is somewhat high, as measured velocities are considerably lower. Sonic velocities were not measured in most of this interval, although the uppermost part of the middle sonic-log segment does suggest higher velocities. This correlation is based mainly on (1) equating the upper boundary unconformity with the major lithology break at the base of the debris flows discussed above, and (2) equating the lower boundary with the break at the base of lithologic Subunit IVA at 608 mbsf. The clayey lithologic Subunit IVA represents a significant decrease in velocity for both velocity data sets. The major negative reflection peak in the middle of the doublet at the base of the sequence thus is probably a response to the velocity decrease. Therefore, the unconformable lower boundary was placed near the base of lithologic Subunit IVA, where velocity again increases. This boundary also corresponds to a major biostrati-

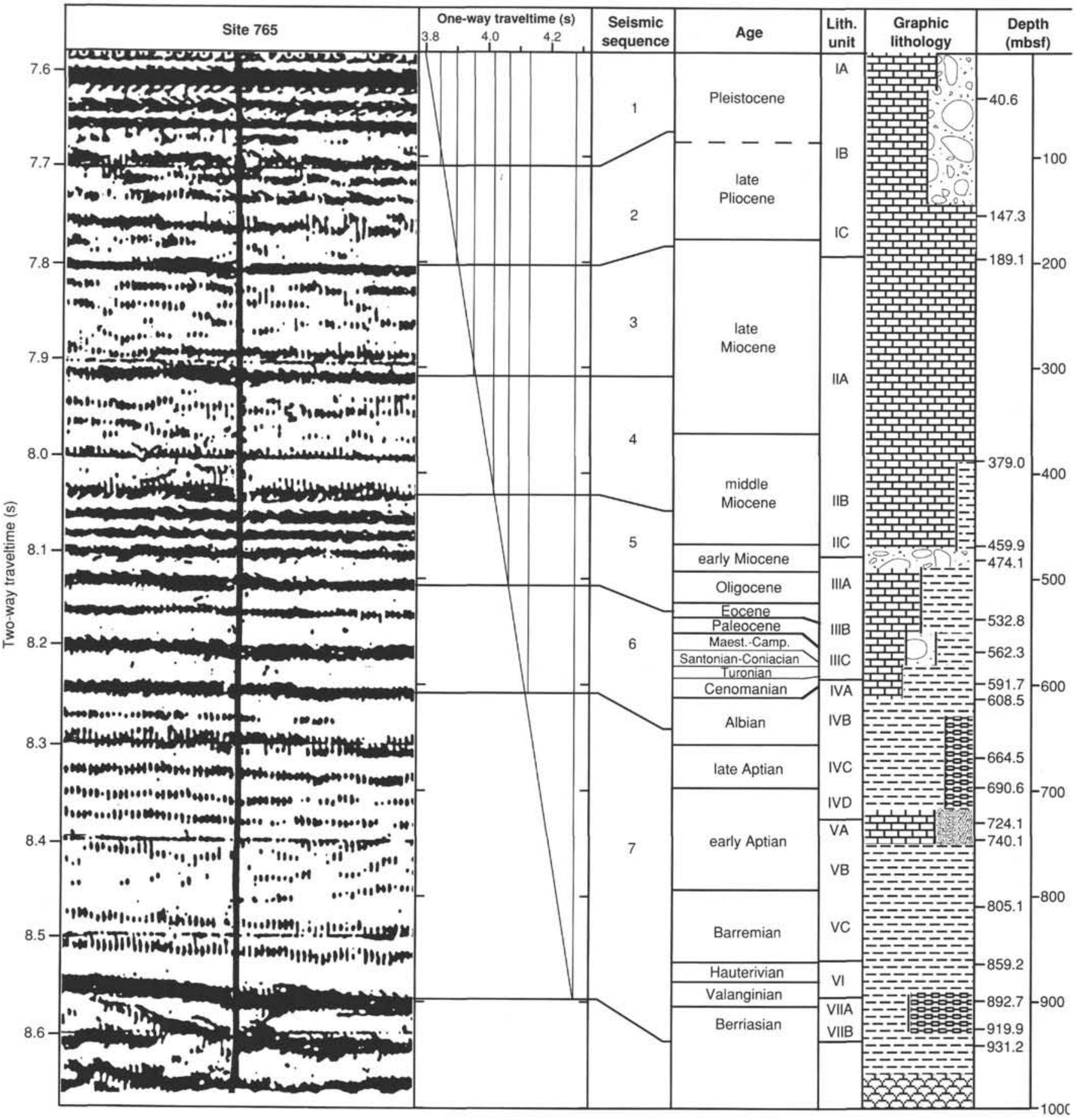

Figure 138. Tentative correlation (Interpretation B) of seismic sequences with drilling results, based on traveltime vs. depth curve determined from VSP experiment.

graphic break (Fig. 137). The truncation of this unit at the upper boundary suggests uplift and reactivation along basement faults during the Miocene.

Sequence 6—Interpretation B

Interpretation B suggests that Sequence 6 corresponds mainly to the condensed Upper Cretaceous-lower Cenozoic section, i.e., older than above (Fig. 138). The major lithological break at the lithologic Unit III/IV boundary may be the upper high-amplitude reflection of the doublet at 8.2 s. The unconformable lower boundary occurs within the lower Albian. The more widely spaced high- and low-amplitude reflections of this sequence may correspond to the alternating calcareous and clayey units. This interpretation alleviates forcing the higher velocities for the sequence and also suggests termination of faulting by the Eocene instead of the Miocene.

Sequence 7—Interpretation A

Sequence 7 corresponds to the thick Lower Cretaceous section (lithologic Subunits IVB through IVD, and Units V, VI, and VII; Fig. 137). A thickness of 0.32 s corresponds to a 323-m thickness if an interval velocity of 2000 m/s is used. This is a reasonable velocity and corresponds closely with an average velocity determined from both measured values and sonic logs. The uniform clayey lithologies and the general lack of higher velocity carbonates probably explain the overall low-amplitude reflection character of this sequence. The slightly higher amplitude zones, toward the top and bottom of the sequence, may correspond to the local increases in carbonate noted for lithologic Subunit IVC and Unit VI. Again, the truncation at the top of the sequence above basement blocks and faults suggests reactivation of these faults during the late Early Cretaceous.

Sequence 7—Interpretation B

Sequence 7 also corresponds to the Lower Cretaceous section as described above, but is not so thick a section (Fig. 138).

VERTICAL SEISMIC PROFILING

Introduction

Vertical seismic profiling (VSP) is a downhole geophysical experiment that involves clamping a geophone or seismometer in a borehole at different depths and recording the seismic wavefield generated from a source at the surface (Fig. 139). This technique bridges the gap between surface reflection work and well logs. It allows one to measure directly the *in-situ* behavior of a wavefield generated by standard seismic sources as they propagate through the earth's crust surrounding the borehole. This technique is used extensively in the petroleum exploration industry and is beginning to be used regularly during ODP operations.

There are two basic variations in the technique, depending on the location of the source. If a source is near the borehole and does not move during the experiment, the experiment is described as a zero-offset VSP (Fig. 139). If the source is at varying distances from the borehole, then the experiment is termed an offset VSP. The first technique allows one to examine the structure immediately surrounding the borehole. It is effective in structurally simple settings for producing a direct tie between the drilled section, logged properties, and surface seismics. The second technique allows one to investigate the medium at some distance from the borehole. It is used effectively to investigate structurally complex settings and requires a second platform to be used as a source. Only the first method was used during Leg 123 at Site 765.

During the VSP experiment, a seismometer in the borehole records both the direct, downgoing waves as well as any upgoing waves reflected from interfaces (impedance changes) below the clamping depth (Figs. 139 and 140). Processing techniques can be used to separate the downgoing from the upgoing wavefields, thus helping to eliminate noise, such as interbed multiples (Fig. 140). Analysis of these wavefields allows one to study in detail the change of seismic wavetrains with depth. Acoustic properties of rocks then can be linked directly to and interpreted in terms of the subsurface lithology. Some scientific applications and advantages of the zero offset VSP experiment, such as that conducted during Leg 123, are described briefly below:

1. Depth vs. arrival time data from the downgoing wavefield provides a direct tie between the drilled section and the surface seismic records. Accurate depths to specific seismic sequences and their boundaries can be determined, and thus, one can analyze what physical changes in rock properties are responsible for the observed reflection character of the sequences and their boundaries.
2. Correlation to key reflections with the borehole can be verified by extrapolating the upgoing wavefield of the reflections downward to where they intersect the same phase point on the downgoing first arrivals (Fig. 140).
3. In many cases, the seismogram produced by VSP can provide a better alternative to a synthetic seismogram produced by a sonic log, as it more nearly approximates arrival times and wave shapes of the surface recorded reflection record.
4. Interval velocities of the section drilled (sediments and oceanic crust) can be determined by calculating the difference in arrival times of the direct downgoing wave between receiver depths. This velocity information can be correlated with borehole lithology and is important for understanding the physical properties of the rocks drilled. These data supplement and provide more accurate velocity data than sonic logs.
5. An accurate correlation between drill site and seismic data maximizes drilling results by allowing one to extrapolate results regionally, beyond the site area.
6. These techniques can be used to image interfaces and structure beneath the borehole and to predict the depths to deeper reflections, often ahead of the bit.
7. By using a three-component geophone, both *P*-wave and *S*-wave data can be obtained for a more detailed analysis of rock properties and lithology.
8. Downgoing wavefields can be used to define more accurately deconvolution operators for attenuating multiples in further processing of the upgoing VSP reflection data, as well as to reprocess surface seismic data.
9. VSP, unlike a sonic log, can be run in either a cased or uncased borehole.

Since 1961, borehole seismic experiments have been conducted as part of ocean drilling (at DSDP and ODP) with varying degrees of success. A brief history and summary of these experiments is included in a recent workshop report about vertical seismic profiling (Mutter and Balch, 1988). Prior to Leg 123, five experiments had been conducted, including an offset experiment during Leg 102 and conventional zero-offset VSPs during Legs 104, 111, and 118. Increased use of conventional zero-offset VSP at ODP is the result of several factors, including (1) a more routine use of VSPs in industry; (2) drilling deeper holes with good accompanying seismic data for regional extrapolation; and (3) a greater appreciation in the scientific community for the value of downhole logging. All of these previous experiments addressed problems related specifically to oceanic crust.

Site 765 provided ODP the first opportunity to conduct a conventional zero-offset VSP in a thick sedimentary section with closely spaced clampings specifically meant for stratigraphic analyses. The excellent multifold seismic data collected by the Australian BMR allowed us to develop a detailed seismic stratigraphic framework for the thick sedimentary section in the Argo Abyssal Plain at the site area (see "Seismic Stratigraphy" section, this chapter). Thus, one of the primary scientific objectives of this VSP experiment was the detailed correlation of borehole results with the defined seismic sequences. This should allow for a more complete extrapolation of drilling results throughout the Argo Abyssal Plain using existing seismic data. The end result will be a more complete interpretation of the depositional and structural history of the Argo Abyssal Plain as well as the adjacent Exmouth Plateau margin.

Understanding the nature and origin of oceanic crust in the southeastern Argo Abyssal Plain is another important problem addressed at Site 765. The site is located near a complex continent/ocean boundary in one of the oldest areas of Indian Ocean crust. Thus, another major objective of the VSP experiment was to obtain detailed velocity and structural information from the upper part of the oceanic crust for comparison with drilling results. The experiment also will allow us to image subcrustal reflections and structure below the borehole.

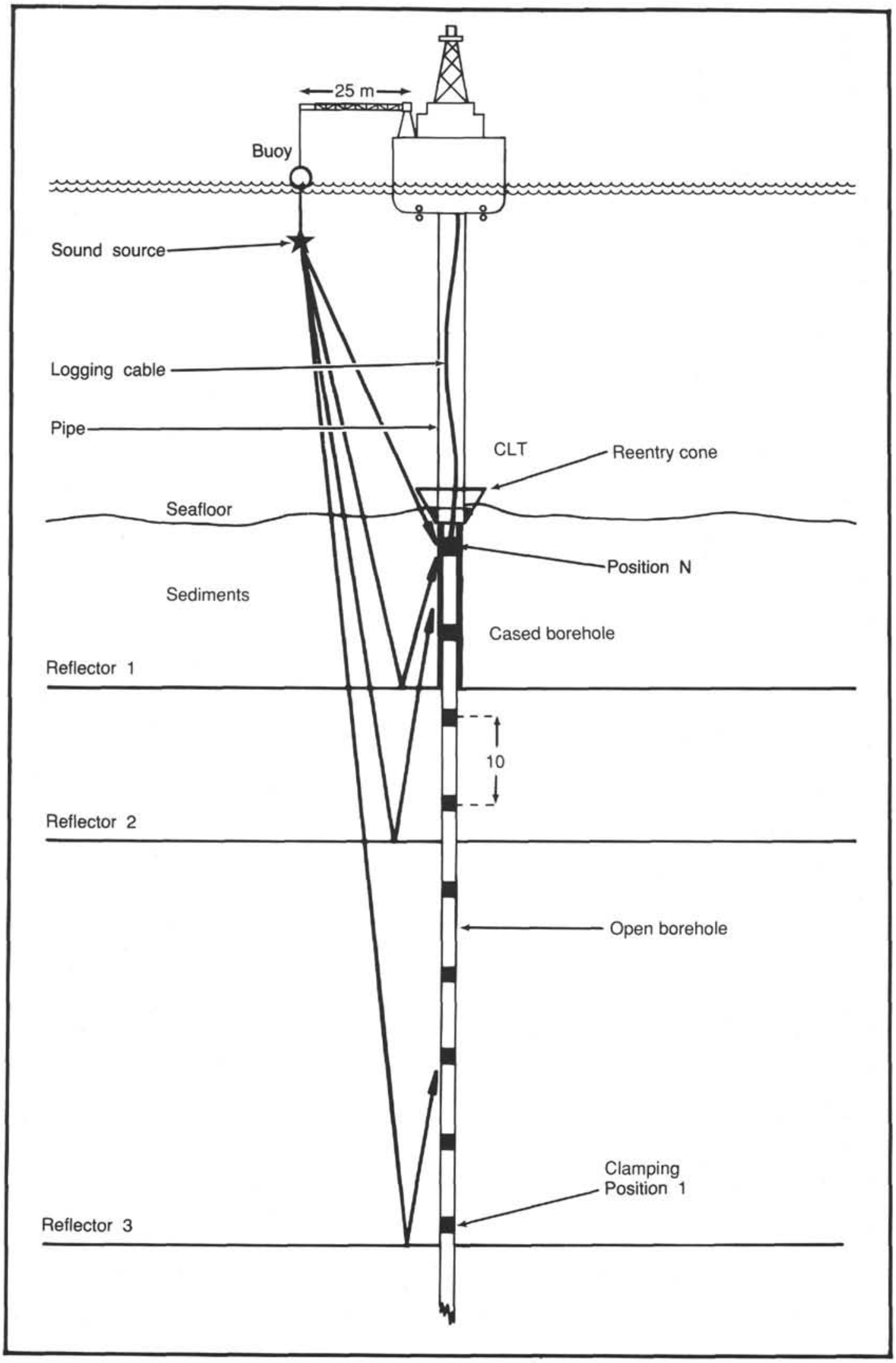

Figure 139. Schematic diagram of configuration of zero-offset VSP experiment conducted either in cased or uncased hole. CLT is casing landing tool for helping to secure drillpipe to the reentry cone (from Shipboard Scientific Party, 1988).

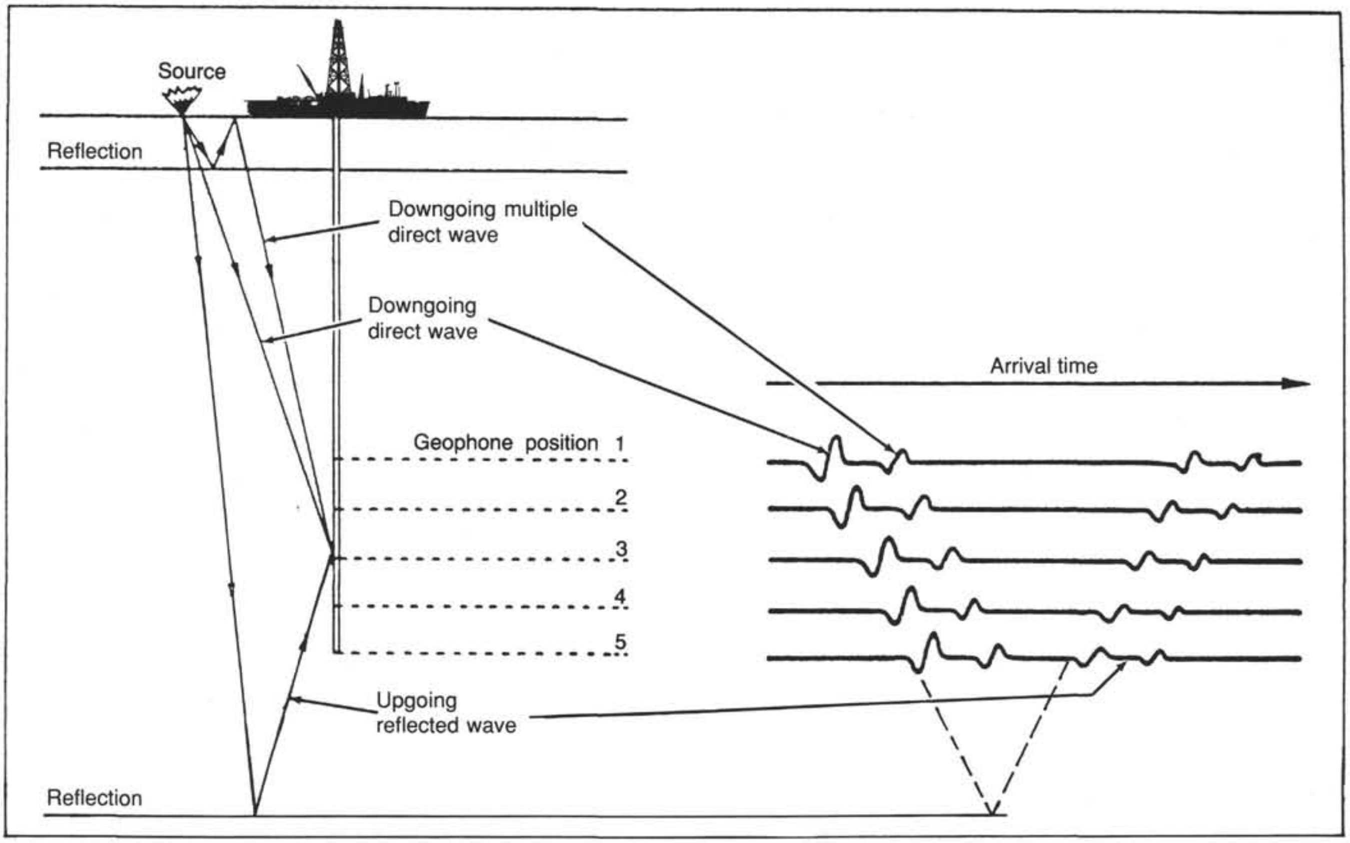

Figure 140. Diagram illustrating principles of zero-offset VSP experiment. Seismogram shows downgoing wavefields received at each geophone position plus upgoing wavefields from deeper reflection (modified from Schlumberger, 1987).

Finally, the VSP data at Site 765 (particularly with additional processing) will provide information about the physical properties of rocks through study of particle motion and downhole seismic attenuation. This will allow for direct comparisons with properties measured aboard the *Resolution*, as well as from the geophysical logs. These data also can be used to compare velocity information determined from three varying methods, shipboard measurements, sonic logs, and sonobuoys, thus providing an excellent direct comparison of the three methods. In addition, the experiment will provide us an opportunity to test the effectiveness of shooting through casing, especially a long casing string, where bonding between the casing and borehole might be a problem.

Acquisition System and Methods

The receiver used for the VSP experiment during Leg 123 is a Geospace wall-lock seismometer provided by Woods Hole Oceanographic Institution (WHOI). Two similar but slightly different tools were available, which are designated as the "new tool" and the "old tool," based on their relative age. These tools contain three sets of two 4.5-Hz geophones, each wired in series and orthogonally configured with two components in the horizontal plane and one in the vertical plane. These geophones have a flat response at 4.5 to 100 Hz. The tools contain a three-channel preamplifier that can be remotely stepped through gain-setting increments from 0 up to 72 dB. After pre-amplication, three voltage signals are carried via the seven-conductor, 9-km-long logging cable to the winch aft of the pipe racker. Optimally, signals are sent up the logging cable with a maximum amplitude of 25 V peak to peak. From the winch, signals are patched into the data acquisition system in the Underway Geophysics Laboratory (UGL). During operation, the tool is clamped to the borehole or casing using an arm that is activated from a control box in the winch hut. This arm sits at a 45° angle to the two horizontal geophones. Receiver depths (depth below rig floor) are read from the Schlumberger meter wheel attached at the logging winch. In addition to the three seismic signals, a source monitor signature is received on an AQ-1 hydrophone suspended about 250 mbsl from the starboard taut-line mooring boom abeam the moon pool. This signature, which also can be used to process seismic data later, is received with a pre-amplication gain of 20 dB before being sent to the UGL's data acquisition system.

Two separate seismic sources were used in the experiment: (1) a 400-in.^{3} water gun (SSI P400 Model 2) and (2) a 1000-in.^{3} air gun (Bolt Model PAR 1500), both operated with approximately 1800 to 1900 psi so as to not damage the thruster seals. The water gun provides higher frequency energy for better resolution of a shallower sedimentary section, while the larger air gun provides lower frequency energy for penetration into both the deeper sedimentary section and the basement. These guns were suspended vertically from a pair of Norwegian floats having vent ports at 6.7 and 4.6 m below sea level (air gun was deepest; Fig. 141). Gun depths were selected from the experience and tests conducted during previous legs, particularly Leg 118. A blast phone attached between guns was used to detect the shot instant. Buoys were moored to the aft port crane, 36 m aft of the drill string and 39 m to the port of the *Resolution*'s centerline. The guns were not fired simultaneously; at each receiver clamping depth, alternate sequences of air- and water-gun shots were fired (see below).

Three seismic signals plus the source monitor were recorded digitally at 1000 Hz (1 ms sample rate) using the HIGHRES logging program installed on a Masscomp M-50 minicomputer located in the UGL. Digital data were written on nine-track mag-

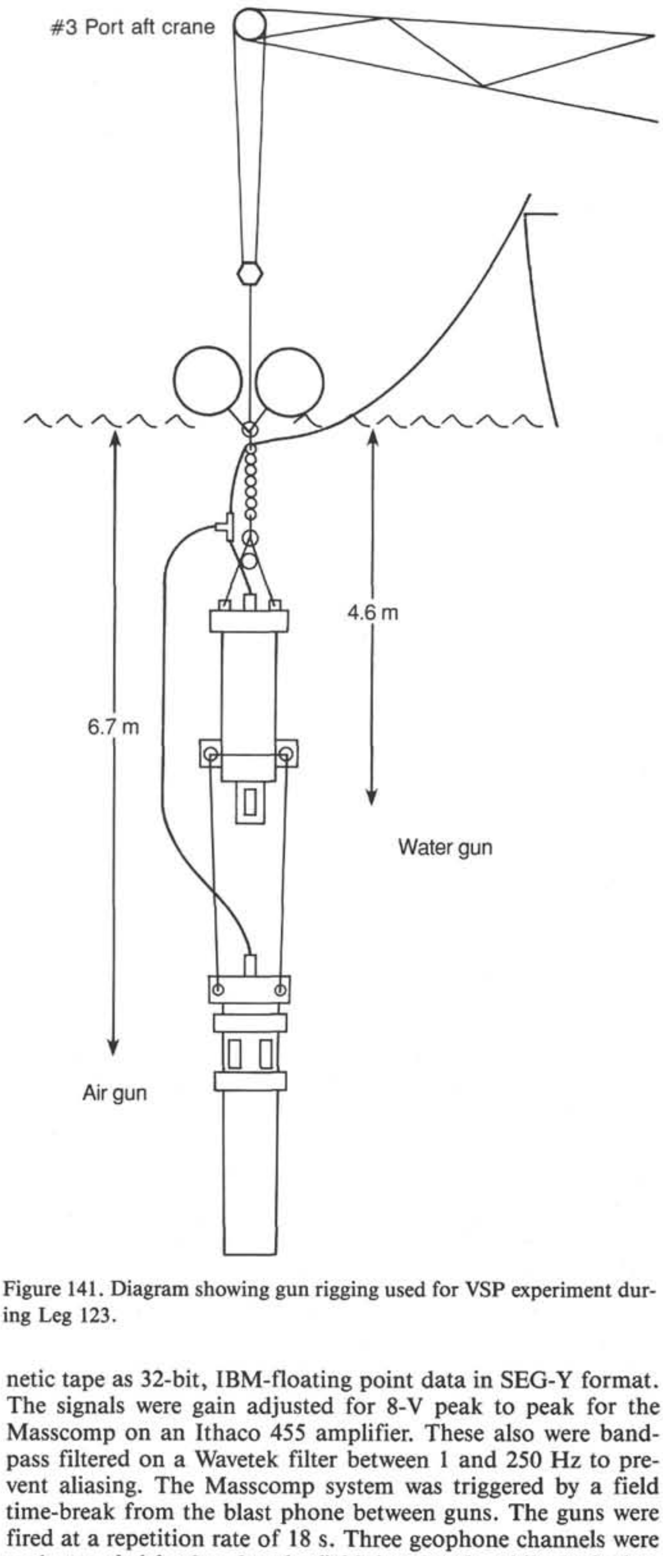

Figure 141. Diagram showing gun rigging used for VSP experiment during Leg 123.

netic tape as 32-bit, IBM-floating point data in SEG-Y format. The signals were gain adjusted for 8-V peak to peak for the Masscomp on an Ithaco 455 amplifier. These also were band-pass filtered on a Wavetek filter between 1 and 250 Hz to prevent aliasing. The Masscomp system was triggered by a field time-break from the blast phone between guns. The guns were fired at a repetition rate of 18 s. Three geophone channels were each recorded for 9 s after the field time-break, while the hydrophone was recorded for 1 s.

All four seismic channels, the blast phone's field time-break, and a time code were recorded on an eight-channel Hewlett-Packard 0.25-in. tape recorder (Model 3968A). These analog signals were recorded as a backup in case the Masscomp system did not work. Before signals went to the tape recorder, they were gain adjusted so as not to exceed 1.5 V peak to peak on attenuators provided by WHOI. An analog monitor record for the air-gun shots at most of the stations was displayed on one of the Raytheon recorders in the UGL.

Field Experiment

The actual VSP field experiment during Leg 123 began at approximately 1600L on 12 October and continued until 1600L on 13 October. While rigging up the tool to the logging cable, we set the drill pipe down on a paddle-style casing landing tool (CLT) at the reentry cone. The weight of the drill pipe down against the CLT was supposed to help secure the pipe and minimize noise from the pipe banging against the casing. In addition, the drill pipe was connected to the drilling heave compensator to reduce the effect of ship's motion during the logging run. (The weather was excellent with only a gentle southerly wind and gentle seas.) The sedimentary section was enclosed in casing, which extended 5 m below the sediment/basement contact. The bottom of the hole was open to basement.

First, the new tool was connected to the logging cable, the clamping arm tested, and then the tool was struck with a small bar to monitor the seismic signal in the UGL. There, signals were observed on an oscilloscope. A poor signal on the vertical as well as one of the horizontal channels, plus significant background noise, prompted our decision to switch to the old tool. Similar tests with this tool indicated an acceptable signal, although considerable background noise still existed. This tool then was lowered to about 700 mbrf in the pipe, clamped, and the guns fired to test the signal. Noise dominated the signal again, and we decided to move the tool to a lower position. While trying to lower the tool, we discovered that it had stuck in the pipe for no apparent reason at about 800 mbrf. After trying to work the tool loose, we decided to crimp the logging wire with the Kinley crimper. Just before we sent the crimper down, the tool worked itself free and was brought up the hole. We saw no damage to the tool or cable and discovered that a bolt from the cable wiper at the rig floor had fallen into the pipe, causing the tool to jam in the pipe.

In the meantime, the new tool was checked out and some wires were replaced, and so we decided to connect it back to the logging cable. An acceptable, but again noisy, signal was monitored on the scope; hence, we decided to run the tool to the bottom of the open hole in basement to test the signal in a quieter environment. After several clamping attempts, we successfully established a clamp at about 1143 mbsf. Both guns were fired, but no seismic signal was observed on the scope above the background noise. After several other unsuccessful attempts to clamp and record in basement, our time began to run short, so we decided to pull the tool up into the casing base at the bottom of the sedimentary section.

Our first clamping in casing at 915 mbsf was successful, and we observed the first reliable seismic signals on the scope, even though background noise continued. Again, because time was running short, we decided to continue the experiment upward from this point using a 12-m clamping schedule. The routine consisted of shooting enough shots with each gun to observe about four to five "good" shots. Good was defined as a clean first-arrival signal with no significant noise bursts either just before, during, or about 5 s following the return. Because of continued noise, a considerable number of shots often were needed before five good shots could be recorded. Shooting depths and shots recorded at each depth for each source are summarized in Table 50.

Signal strength increased as the experiment continued uphole, but the pace was slow. This slowness was caused by three factors:

1. The HIGHRES recording program continued to fail while shooting, especially when turning the guns off and on when

Table 50. Summary of all shots collected at each depth, separated by source.

Depth (mbsf)	Air gun	Water gun
1158	0004–0020	0021–0031
1143	0109–0114	0056–0069
1131		0122–0243
915	0299–0305, 0322	0318–0321
903	0355–0368	
891	0376–0382	0383–0389
879	0418–0429	0390, 0430–0440
867	0454–0467	0473
852	0510–0522	0523–0540
839	0589–0598, 0604–0605	0599–0603
827	0636–0644	0645–0650
812	0697–0730	0732–0738
800	0773–0781	0763–0772
790	0813–0817	0805–0812
775	0906–0916	0893–0905, 0917
760	0943–0950	0931–0942
746	0993–1003	0984–0992
718	1038–1043	1029–1037
691	1084–1095	1071–1083
662	1117–1124	1110–1116
634	1160–1171	1140–1159
607	1210–1224	1188–1209, 1225
578	1262–1273	1246–1261
551	1314–1317	1303–1305, 1318–1319
523	1352–1361	1342–1351
494	1413–1426	1395–1412
466	1451–1460	1436–1450
438	1480–1493	1468–1479
414	1517–1532	1504–1516, 1533
396	1588–1599, 2487–1491	1568–1587, 2480–1248, 2492
369	1619–1632, 2507	1610–1618, 2502–2506
341	1707–1717, 2526–2608	1673–1700, 2515–2525
315	1747–1757	1724–1747
313	2635–2648	2649–2653
284	1804–1809, 2672–2679	1793–1803, 2661–2671
270	1841, 1945–1965, 2327–2345, 2694–2702	1838–1840, 1926–1944 2685–2693
244	2346–2355	2356–2366
214	2393–2405	2379–2393
196	2425–2433	2413–2424
143		2733–2757
129	2758–2767	2768–2781
99	2790–2794	2782–2784

changing clamping depths. The system often would take several minutes to come back up. Finally, it was decided to leave the guns cycling while moving stations, which cut down considerably on the number of failures.

2. Noise continued to plague the experiment throughout. The noise usually occurred as short or long bursts, and often lasted many seconds at a time. Although we never positively identified the cause, it probably was pipe noise that was generated either from the rig floor or by pipe banging or moving in the casing or at the reentry cone, although the pipe already sat in the reentry cone. The noise also may have been caused by minor tool slippage. As noted above, it was difficult to find a window between the noise to record good shots, and often it took several minutes to record four to five good shots.

3. Most of the time we were unable to clamp the tool at the desired position. During operation, the tool was dragged to the next higher location with the clamping arm extended. This saved clamping time, but it often took 5 to 10 min for the winch operator to set the tool in casing. Using pipe joints for clamping locations helped.

These three combined delays forced us to take 10 to 20 min between stations.

As the experiment proceeded uphole, time was short. At 746 mbsf, we decided to double the station spacing to about 24 m to finish the experiment on time. During the morning of 13 October, the seismic signal began to weaken, as observed on the Raytheon recorder. At first, we thought that this resulted from a zone of poor sediment-casing coupling, but finally the computer went down because it was not getting a start signal from the guns. We then discovered that the water gun was leaking badly. The guns were pulled, the water gun was repaired quickly, and shooting continued. Several of the previous stations having weak signals were re-occupied. During this time, the overall signal became much quieter for no explainable reason. After skipping over the area where a previous logging tool had been stuck, shooting continued up to the end of the drill pipe, which was suspended 84 mbsf. At this point, the noise reappeared, thus, the last few shots contain no usable data. Shooting was completed at 1610L. Overall, 39 stations were occupied in the casing between 915 and 99 mbsf, while usable data were recorded between 915 and 196 mbsf. The tool was back on deck by 1830L, and all systems were secured.

Results of Shipboard Processing

Preliminary processing of VSP data collected was performed onboard the *JOIDES Resolution*. First, the digital data produced by the Masscomp computer in SEG-Y format was converted to ROSE single-shot file format (La Traille, 1983) to allow for further processing using the shipboard VAX 11/750 computer with software developed by WHOI. Next, shots sorted by depth and gun type (Table 50) were displayed for visual inspection (Fig. 142). Noisy traces were eliminated, and only good traces were stacked (5-deep) to produce individual traces for each gun at each depth (Fig. 142). The good shots used to stack are listed in Table 51. These final stacked traces were then displayed together vs. depth as a seismogram for each gun (Figs. 143 and 144). A trace normalization was applied to the individual traces.

In addition, first arrivals were selected for each stacked trace by eye using a cursor on the computer screen video display, and a smoothed traveltime vs. depth curve was produced (Fig. 145). Three different places (1, 4, and 5) along the first arrival wave were chosen (Fig. 145). The collected data will be further processed and refined post-cruise.

Conclusions

Preliminary conclusions of the VSP experiment are summarized below:

1. For the first time, a successful conventional zero-offset VSP experiment was conducted aboard the *JOIDES Resolution* in a thick sedimentary section using a close clamping spacing. A total of 39 stations were occupied between 915 and 99 mbsf.

2. The experiment showed the feasibility of conducting VSP through casing, even though bonding between casing and borehole was not ideal, and it was difficult and time consuming to clamp the tool in casing.

3. Extreme pipe noise plagued the experiment throughout, although the drill pipe was set in a CLT at the reentry cone and the drillfloor heave compensator was engaged. Although the exact origin of the noise is unknown, we suspect that the 80 m of drill pipe extending below the re-entry cone may have been hitting the casing, causing the noise. This prevented our collecting usable data in the upper part of the hole and probably was responsible for the bursts of noise throughout the experiment. In future VSP experiments in casing, care should be taken to secure the pipe at its end, as well as at the reentry cone, perhaps with packers.

4. Apparently, no seismic returns from below the top of basement were observed or recorded, possibly because of a combination of noise, poor clamping, and lack of seismic energy to pen-

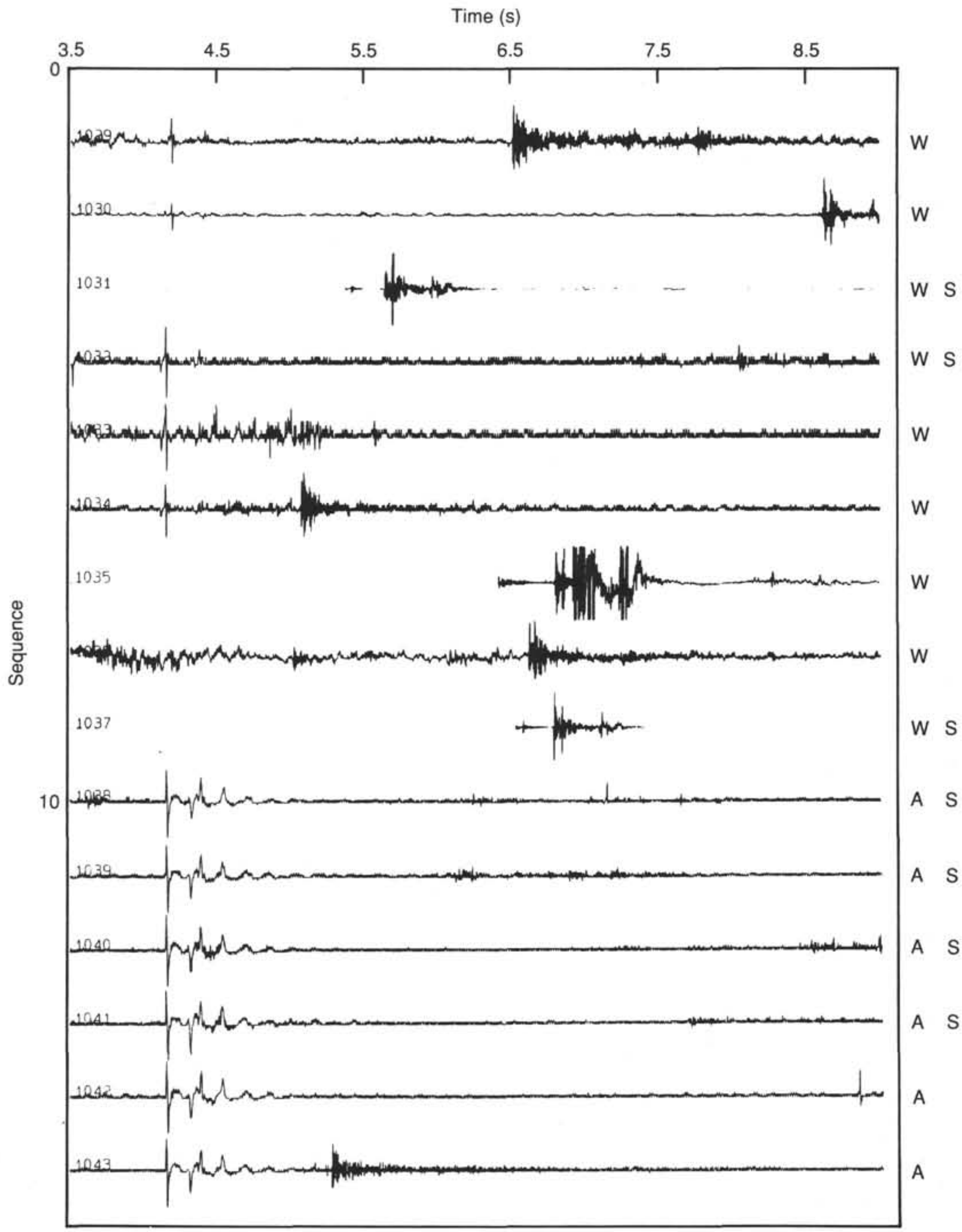

Figure 142. Plot showing all air gun (A) and water gun (W) shots recorded at 718 mbsf from vertical geophone. This is an example of the plots used for visual inspecting traces to decide whether to save for stacking (S) or to eliminate.

etrate basement at such water depths and in sediments that thick. Further processing will be necessary to confirm this.

5. Preliminary stacks for both the air and water guns show no obvious upgoing reflections in the sedimentary section. This may result from the increased spacing between stations in the upper part of the hole, which reduced resolution. This increased spacing was required because of the limited time available for conducting the experiment. Further processing, including separation of the upgoing and downgoing wavefields, will be necessary for evaluation of upgoing reflections.

6. No obvious upgoing wavefields were observed from within the basement below the clamping depths. The only obvious upgoing reflection on the record is from the top of basement itself (Figs. 143 and 144).

7. The effectiveness of the air gun vs. the water gun in resolving reflections is inconclusive. Further processing and separation of the upgoing from the downgoing wavefields will be necessary.

8. This experiment, along with other velocity information gathered at this site (such as sonic logs, laboratory measurements, and sonobuoys) will provide a unique comparison of the various techniques for obtaining velocity data at a well site.

9. The downgoing first arrival provides depth vs. traveltime plots that can be used for correlating seismic sequences with the

Table 51. Summary of all "good" shots stacked to create new stacked trace, by source.

Shot stacked	Depth (mbsf)	Air gun	Water gun
1	915	0299–0302, 0322	0321
2	903	0355, 0357, 0460, 0361, 0362, 0366, 0369	
3	891	0376, 0378, 0382	0385, 0388
4	879	0421, 0424, 0427	0431, 0436, 0437
5	867	0455, 0562–0464	
6	852	0510, 0511, 0518, 0520–0522	0531, 0532, 0537–0539
7	839	0592–0596	0600, 0602–0604
8	827	0637–0640, 0642, 0644	0647, 0650
9	812	0698, 0699, 0703, 0705, 0722, 0828, 0729, 0731	0734–0737
10	800	0775–0777, 0780	0765, 0766, 0770–0772
11	790	0813–0816	0807, 0809–0811
12	775	0914, 0915	0893, 0896, 0898, 0905, 0917
13	760	0944, 0945, 0947, 0949	0931, 0936, 0939, 0940
14	746	0995, 0998, 0999	0984, 0987, 0989
15	718	1038–1041	1031, 1032, 1037
16	691	1084, 1086, 1092, 1094	1079, 1081
17	662	1117, 1118, 1121–1123	1110, 1112, 1113
18	634	1161, 1170, 1171	1143, 1148, 1151, 1156
19	607	1212, 1215, 1223, 1224	1192, 1199, 1202, 1203, 1207
20	578	1263, 1267, 1272	1248, 1253, 1254, 1258
21	551	1314, 1316, 1317	1303, 1305, 1318
22	523	1353, 1355, 1356, 1360, 1361	1342, 1345–1348
23	494	1413, 1414, 1422, 1424, 1425	1399, 1408
24	466	1452, 1456, 1459	1437–1439, 1442, 1446, 1448, 1449
25	438	1482, 1486, 1489, 1492	1471, 1473, 1478
26	414	1518–1521, 1529–1532	1513–1516
27	396	2488–1491	2480, 2481, 2483–2486, 2492
28	369	2507	2502–2506
29	341	2600–2603, 2605, 2606, 2608	2517, 2519, 2520, 2525
30	313	2636, 2637, 2643–2645	2649, 2653
31	284	2572–2675, 2678, 2679	2662, 2665, 2667, 2670, 2671
32	270	2692–2699, 2701	2685–2687, 2691
33	244	2346, 2349–2352, 2354, 2355	2361, 2363–2365
34	214	2396, 2401–2404	2379–2381, 2383
35	196	2426, 2427, 2430–2432	2419, 2421–2424
38	99	2792–2794	

borehole (Fig. 145). See the "Seismic Stratigraphy" section (this chapter) for how Figure 145 was used to correlate seismic sequence boundaries with the multifold seismic line at Site 765. This correlation will allow us to extrapolate the borehole information regionally, especially along the new *JOIDES Resolution* seismic Line 1, collected during Leg 123 between DSDP Site 261 and ODP Site 765 (see "Underway Geophysics" chapter, this volume).

HEAT FLOW MEASUREMENTS

Introduction

The temperature logging tool (TLT) was used successfully once in Hole 765C and three times in Hole 765D. The TLT was pressure activated at about 200 mbsf (5528 mbrf), logging in the open hole in the sediment section of Hole 765C (180–480 mbsf) and in the open hole in the basalt section and within casing in Hole 765D. In Hole 765C, the TLT was attached to the bottom of the Schlumberger SS tool string. In Hole 765D, the TLT was attached to the bottom of the SS, the LDT combinations, and the BHTV. The TLT measured temperature and hydrostatic pressure as a function of time. The two thermistors located in the tool measured the stable and short-term thermal characteristics of the hole. If fluid flow were occurring somewhere within Hole 765D (see "Permeability Measurements" section, this chapter), it may be possible to determine one or more locations on the basis of thermal perturbations in TLT data.

Depths in the temperature profiles shown in Figure 146 were computed from pressure data measured by the TLT. The pressure-to-depth conversion assumed hydrostatic pressure using a density of 1.02 g/cm^3 for seawater at about 0°C. This pressure-to-depth conversion scheme is the reason for the high-frequency noise seen in the data. These depths are strictly estimates and thus should not be used for exact depth correlations. Depths will be more accurately determined when the elapsed time data from the TLT is merged with elapsed time data from the Schlumberger logs.

The equilibrium thermal gradient can be determined using at least two temperature logging passes. In practice, the slower and more accurate up-going logs are used for caculating temperatures. In the case of Hole 765C, where there was only one log, it may be necessary to use both the upgoing and downgoing runs to help constrain the problem.

Hole 765C Results

Only one TLT run was performed in this hole because of poor hole conditions. The run took place shortly after drilling and circulation had been completed. Although two Schlumberger log runs were performed in this hole, we decided to save the only tool on board ship for the basement hole to avoid the risk of losing the TLT during SES operations. Fluids circulated in the process of using the SES may also have affected temperatures, making it more difficult to extract the thermal gradient. Because it takes a minimum of two log runs to determine the equilibrium temperature profile, one may be able to use both the downgoing (not shown in Fig. 146) and upgoing logs to calculate the thermal gradient during post-cruise processing. Results do indicate, however, that the tool was operating correctly (Fig. 146).

Hole 765D Results

The TLT was used three times in Hole 765D, and the SS, LDT, and the BHTV. The Schlumberger SS and LDT runs were conducted with no thermal disturbances from water circulation. Shortly after fluid was circulated into the hole, we ran the BHTV log. A comparison of Figures 146C with 146D reflects the decrease in temperature caused by adding cool water into the hole. Irrespective of when the logs were run, the temperature profile is consistent, especially within the basalt section (Figs. 146B, 146C, and 146D). Temperature profiles indicate several interesting trends. The data show a slight decrease in temperature at about 1050 mbsf for all three profiles, suggesting the occurrence of fluid flow in the hole. A small temperature increase occurs at about 450 mbsf. Curiously, these temperatures were measured in casing (Figs. 146B through 146D). At about 950 mbsf, a marked decrease in temperature occurs near the casing shoe and the sediment/basement interface (Figs. 146B, 146C, and 146D).

The temperature increase at 1050 mbsf suggests that the hole may have intersected a zone of preexisting fractures that provided a conduit for fluid flow. Correlation of temperature data with other data sensitive to *in-situ* fracturing will be conducted later. For instance, temperature data will be correlated with zones of hydrothermal alteration as evidenced in cores (see "Basement Alteration" section, this chapter) and chemical variations within the geochemical and gamma-ray spectroscopy logs (see "Schlumberger Logs" section, this chapter). Fracture mapping using the BHTV and direct sampling from cores also will be correlated with temperature data (see "Stress Measurements" section, this chapter).

The source of cool fluids near the casing shoe is unclear. Fluids from overlying sediments may be percolating downward along preexisting fractures, along drilling-induced fractures, or along the hole itself, indicating incomplete cementing. Apparently, the permeability (Fig. 147) observed in this hole is consistent with the thermal perturbations seen in the basement section.

Only preliminary estimates for crustal heat flow in the basalts are possible at this time. Five days following the comple-

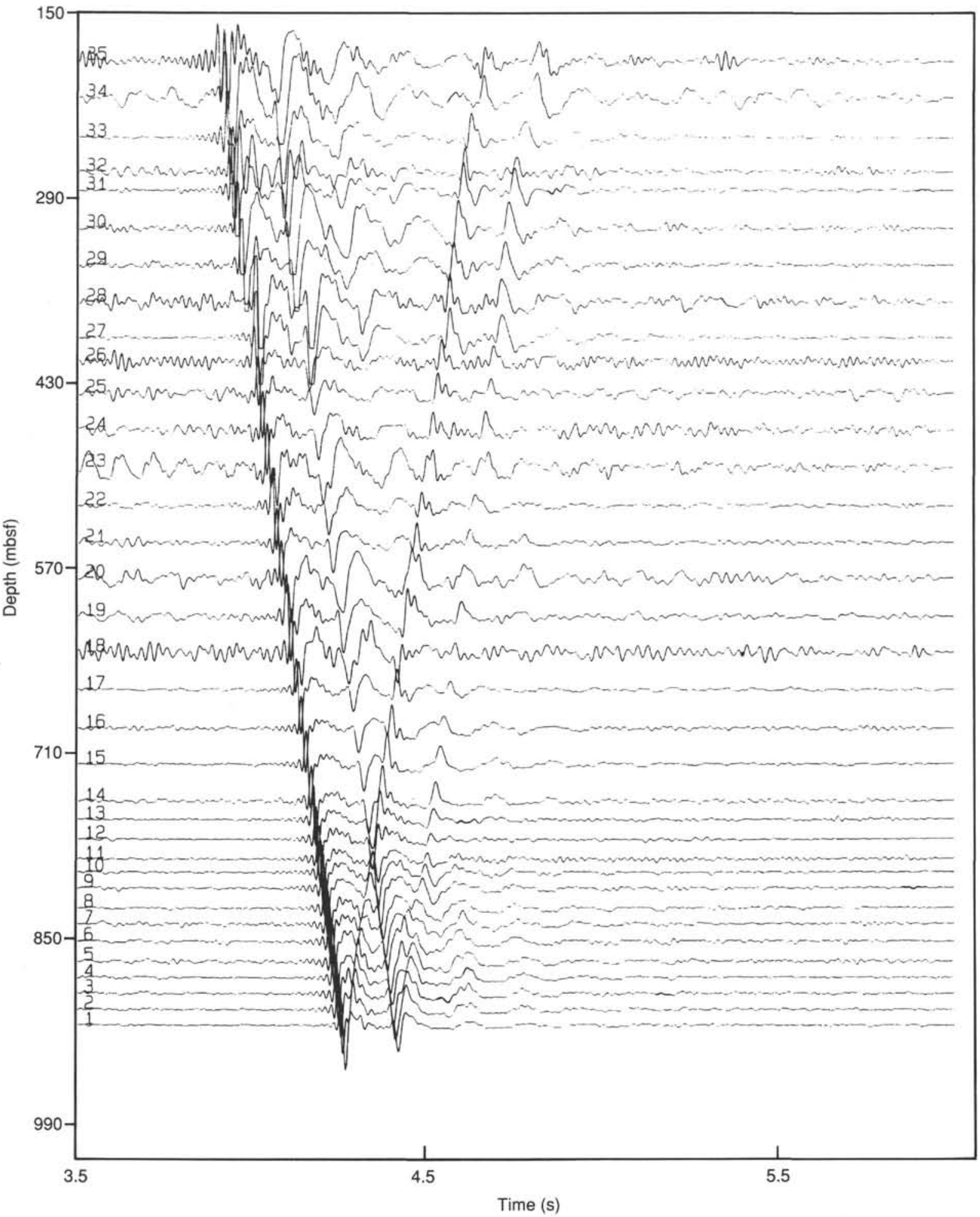

Figure 143. Preliminary seismogram of stacked traces from air-gun shots between 196 and 915 mbsf from vertical geophones. Obvious are first arrival of downgoing wavefield plus upgoing reflection from sediment/basement interface. Data have been bandpass-filtered between 5 and 55 Hz. Data need further processing and application of static shifts to align traces.

tion of drilling and fluid circulation, the 1195 m drilled at Hole 765D had a bottom temperature of about 38.9°C. This equates to a thermal gradient of about 32°C/km, which is normal for oceanic crust in this type of setting. The heat flow for this area is approximately 55 mW/m^2, using an average thermal conductivity value of 1.7 W/m · K (See "Physical Properties" section, this chapter). Exact information about equilibrated thermal gradient and thermal conductivity awaits further computation. For the thermal gradient, these computations include the cooling rate, which can be determined by comparing the three temperature profiles. Using information from both the geochemical and petrophysical logs, it is possible to compute a continuous ther-

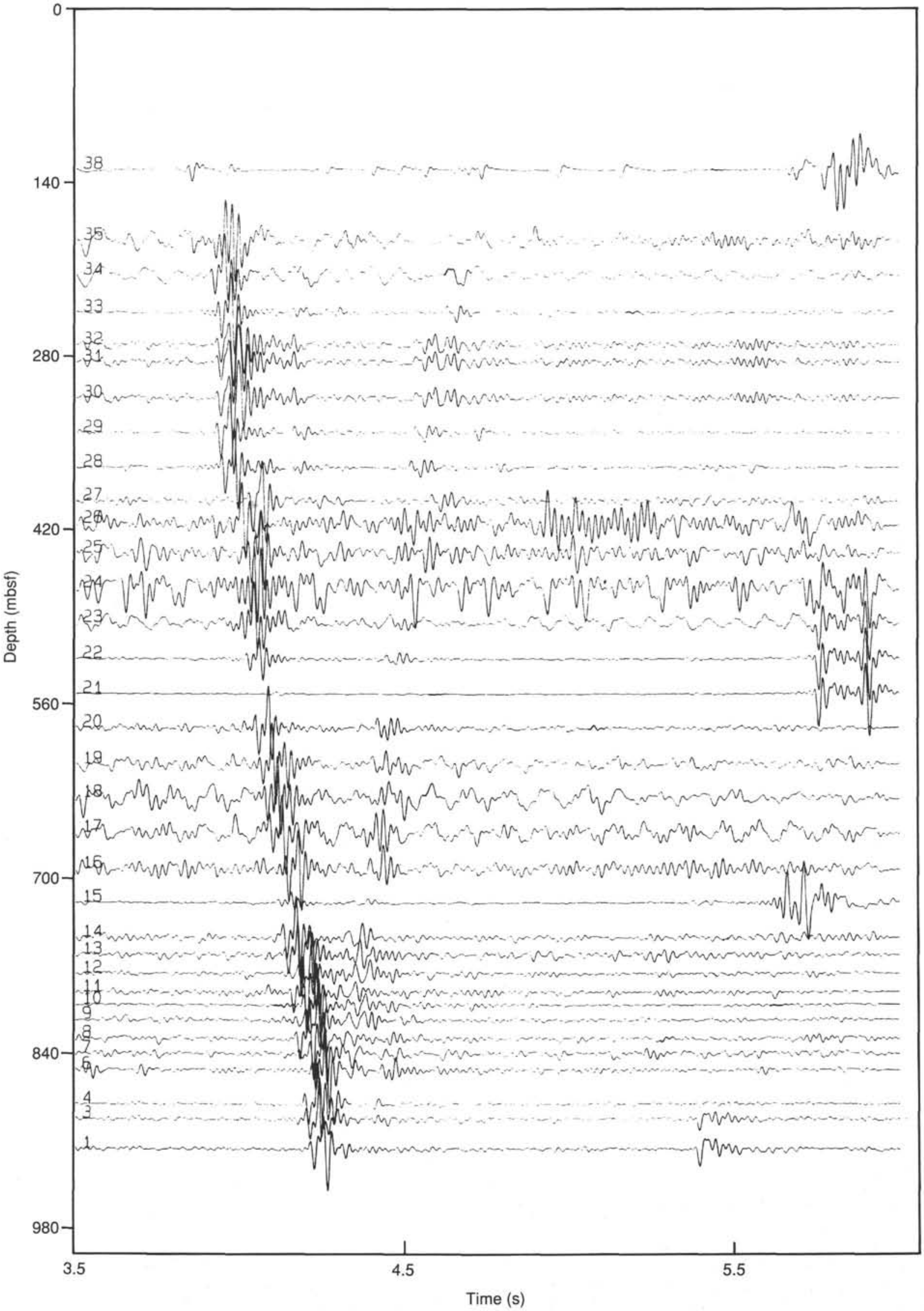

Figure 144. Preliminary seismogram of stacked traces from water-gun shots between 196 and 915 mbsf from vertical geophones. Data have been bandpass-filtered between 5 and 55 Hz. Data need further processing and application of static shifts to align traces.

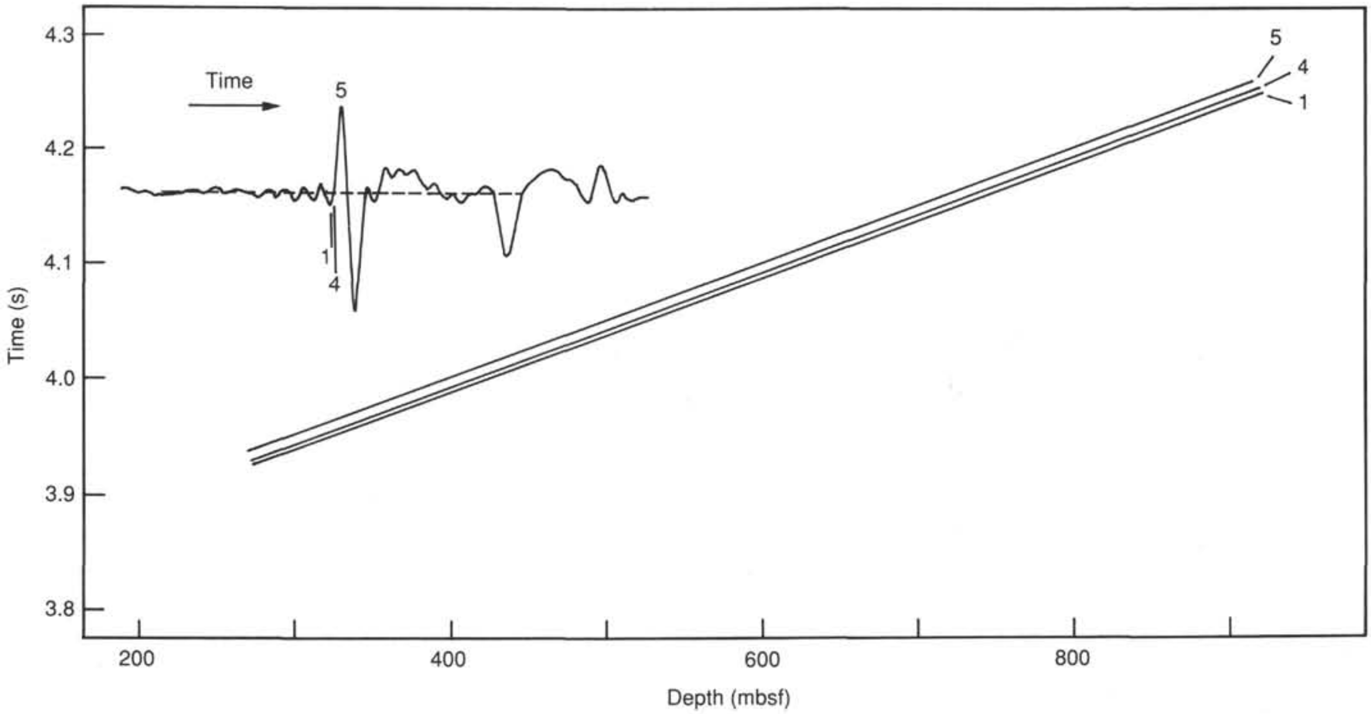

Figure 145. Smoothed plot of first arrival traveltimes vs. depth from air-gun data plotted in Figure 142. Location of picks 1, 4, and 5 (used for plot) are shown on waveform.

mal conductivity log. The final product should be a heat flow log as a function of depth.

PERMEABILITY MEASUREMENTS

Introduction

Our objective for collecting permeability measurements at Hole 765D was to determine the hydrologic properties of this ancient oceanic crust. Analysis of the calcite- and/or smectite-filled fractures observed within the cores (See "Alteration" section, this chapter), the pervasive occurrence of fractures in the BHTV records (see "Stress Measurements" section, this chapter), and temperature perturbations in the temperature data (see "Heat Flow Measurements" section, this chapter) together suggest that fluid flow played an active role in the past, and possibly into the present. Preliminary results from a pressure decay curve during pulse testing suggest that the crust in this locality may be permeable. Unfortunately, the opportunity to quantify permeability more accurately using the Tam drilling packer was aborted when the packers failed during a constant-flow test.

Results

A 13-hr test was conducted on 14 October 1988, after the Schlumberger logging suites, VSP, and BHTV runs had been successfully completed. The packers were initially set in casing at 869 mbsf to determine bulk permeability of the entire openhole section, as well as to test integrity of the drilling packer before its being lowered to an openhole section. Our first attempt to inflate the packer failed because the go-devil was dressed with incorrect shear pins. The go-devil was re-dressed with the proper sized pins and re-deployed. Under normal conditions, shearing of pins in the go-devil will produce an instantaneous pulse test that can be used for permeability studies. Unfortunately, there was insufficient weight on the packer to hold back this sudden increase in pressure, and the packer moved uphole about 10 m. A pressure pulse test was conducted, followed by a rapid pressure decay (Fig. 147). A second pulse test duplicated the previous results, ensuring that the packer was set. In a case such as this, the magnitude of permeability can be roughly estimated using the shape of the pressure decay curve. However, a more accurate approach would be to conduct a constant-flow test. While pumping fluids into the hole, pressures below the packer increased rapidly enough to move both the packer and the pipe compensator up about 30 m (Fig. 147 at 13.5 min). At the time, we believed that the packer was still in good condition, and we decided to lower the packer to 1156 mbsf to test the lowermost section of the hole. However, efforts to inflate the packer at this new depth were unsuccessful. To save our remaining time for a hydrofrac experiment with straddle packers, we decided to pull out of the hole and to switch packers.

Figure 147 depicts a surface pressure vs. time record of the two pulse tests conducted at 869 mbsf. The rapid pressure decay after peaks at 6 and 9 min indicates that fluid either flowed into the formation along fractures, around the cement in the casing, or leaked past the packer. Results are inconclusive, and further analysis will be necessary. We intend to review the Kuster downhole pressure records, surface pressure records, flow rates, and heave compensator weight indicators from the TOTCO system to determine if, in fact, the formation is permeable. In addition, thermal perturbations in the temperature profiles (see "Heat Flow Measurements" section, this chapter) will be used to isolate any zones of fluid flow. If fluids were flowing past the cement, implying incomplete cementing, waveforms from the sonic log (see "Schlumberger Logs" section, this chapter) should be highly attenuated if cement was lacking.

SUMMARY AND CONCLUSIONS

Operations

During Leg 123, three holes were drilled at Site 765 in a water depth of 5720 m. A total of 935.6 m of sediment was penetrated in Holes 765B and 765C. Hole 765C was continued for

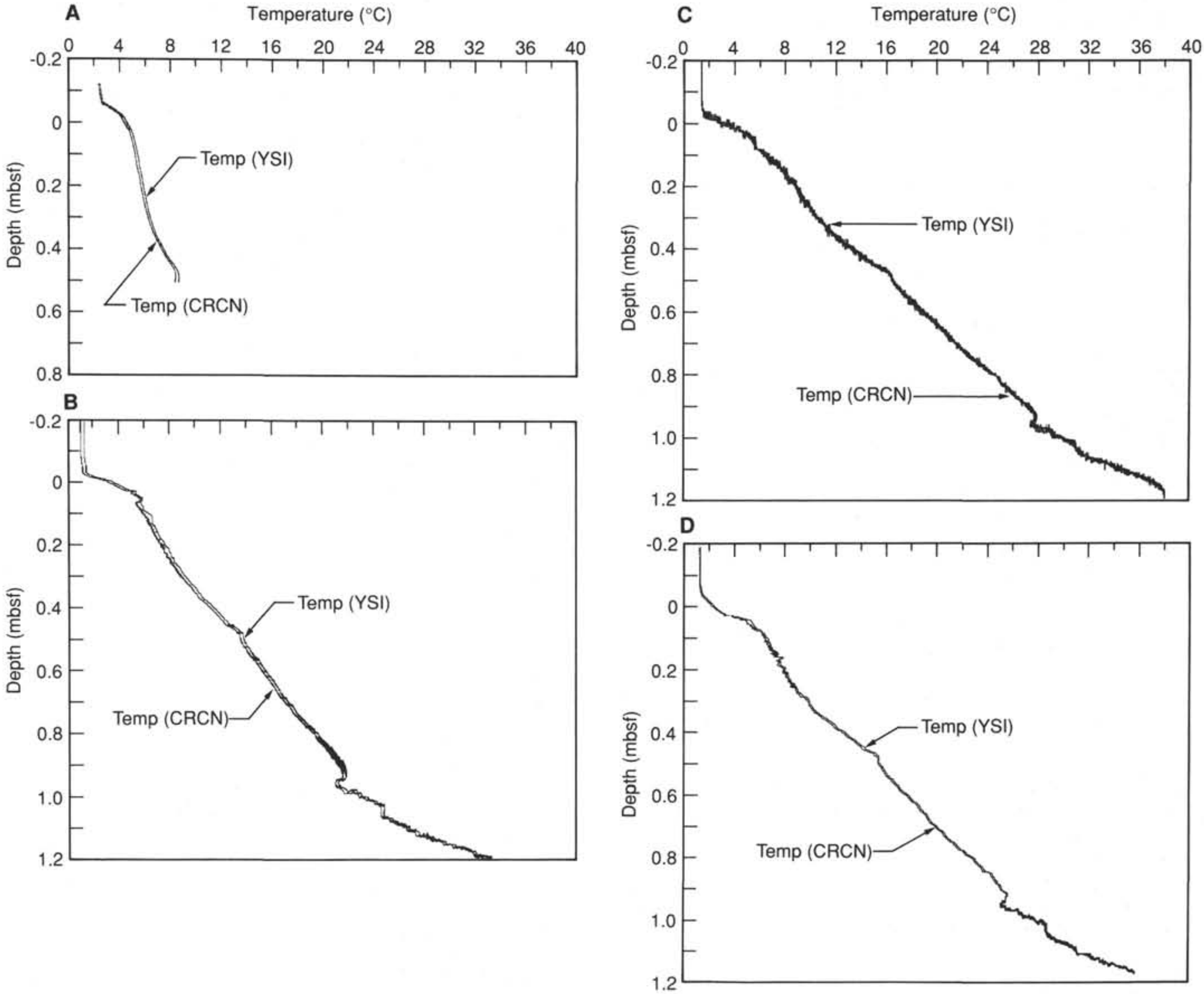

Figure 146. A. Profile of temperature vs. depth from Hole 765C, collected during the Schlumberger SS logging run. Only upgoing log is shown. B. Profile of temperature vs. depth from Hole 765D, collected during the Schlumberger SS logging run. Only upgoing log is shown. C. Profile of temperature vs. depth from Hole 765D, collected during the Schlumberger LTD logging run. Only upgoing log is shown. D. Profile of temperature vs. depth from Hole 765D collected during the BHTV logging run. Only the upgoing log is shown.

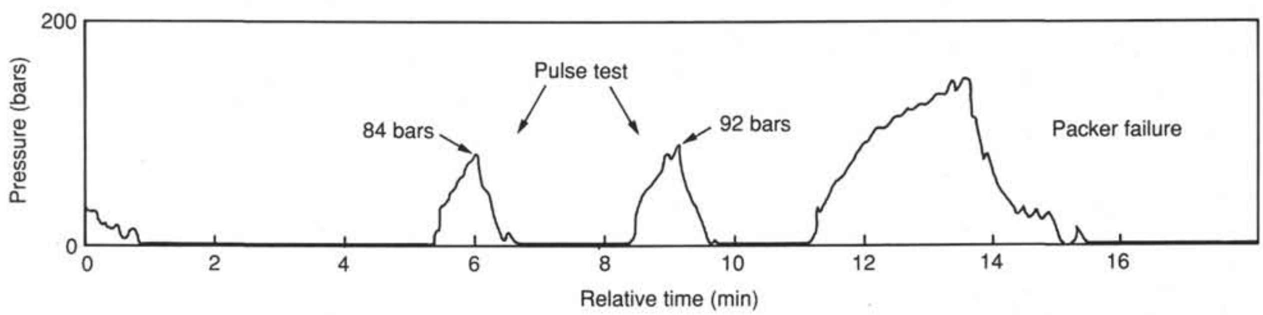

Figure 147. Record of pressure vs. time of pulse test at 869 mbsf. Rapid pressure decay after pulse tests at 6 and 9 min indicate formation permeability. Rapid pressure decay in third cycle results from shutting off rig pump when packer began sliding uphole. Test interval = 326 m.

30 m farther into basaltic basement. Hole 765D was cored to 950 m, lined with a steel casing, and cemented into basement. Drilling into basement penetrated a total of 270 m of fresh and altered basalt. Logging and geophysical experiments were conducted openhole in Hole 765C, through casing in Hole 765D, and with open basement in Hole 765D.

Biostratigraphy

Calcareous nannofossil biostratigraphy was applied successfully to the interval from 0 to 720 mbsf, which includes zones of Pleistocene to Aptian age. Assemblages are generally abundant and moderately to well-preserved. Despite the reworked nature of most of the calcareous deposits, a stratigraphically correct succession of nannofloras was observed. The interval from 721 to 892 mbsf yielded an impoverished flora of Barremian to Valanginian age. The species composition of these assemblages is quite different from those recorded from the Mediterranean area. The basal interval (sedimentary Unit VIIB; 920–930 mbsf) yielded an etched, monospecific assemblage of the species *Watznaueria manivitae*.

Planktonic foraminiferal biostratigraphy was applied to the interval from 0 to 777 mbsf, which includes Holocene to Aptian sequences. The Neogene interval (0–480 mbsf) contains a diverse fauna typical of the tropical Indo-Pacific. A large part of the Neogene is represented; however, a significant faunal break can be seen in Core 123-765B-18H, where the lower Pliocene sequence may be missing. The Paleogene succession is condensed and includes the interval between approximately 490 and 560 mbsf. In general, recovered Oligocene assemblages are well-preserved and diverse; however, the Eocene fauna is poorly preserved and contains few identifiable forms. Poorly preserved Upper Cretaceous microfaunas have been recovered from a condensed sequence between approximately 566 and 594 mbsf. Lower Cretaceous (Aptian-Albian) planktonic foraminiferal assemblages are scattered in the interval from 600 to 777 mbsf and are dominated by primitive *Hedbergella*. Evidence for reworking of planktonic foraminiferal assemblages occurs throughout the hole. Paleogene and Upper Cretaceous specimens are encountered throughout the Miocene. Reworking is conspicuous in some Oligocene samples, where Upper Cretaceous and lower to middle Eocene foraminifers are common. Many of the Upper Cretaceous samples contain specimens reworked from the Albian to Coniacian.

Cenozoic and Upper Cretaceous deep-water benthic foraminifers in Holes 765B and 765C repesent mainly sorted, displaced assemblages from bathyal depths. There is no evidence of displaced assemblages from neritic depths. Lower Cretaceous benthic foraminiferal assemblages consist of *in-situ* abyssal forms dominated by agglutinated species. These assemblages resemble Upper Cretaceous abyssal assemblages described from Leg 27 sediments; however, Lower Cretaceous abyssal agglutinated assemblages have never been fully described. The biostratigraphy of Cretaceous deep-water benthic foraminifers compares well with the reported ranges in the Atlantic and Tethys regions, with the exception of several abyssal agglutinated species that first occur at older levels in Hole 765C than their reported ranges in the Alps.

Dinoflagellate cysts were recovered from the Neogene and Lower Cretaceous. It is difficult to compare the Neogene assemblages with known zonations, but the Lower Cretaceous assemblages do allow for accurate age assignment, using Australian margin zonations, between the Albian and upper Berriasian.

Abundant and well-preserved Quaternary radiolarians recovered from the uppermost nine cores of Hole 765B provide us with a detailed upper Quaternary biostratigraphy. These assemblages are characteristic of the low-latitude Indian Ocean.

For the first time in the Southern Hemisphere, a complete sequence of Neocomian (upper Berriasian to Aptian) radiolarian assemblages was recovered. It provides a detailed biostratigraphy, which is difficult to correlate with the Tethyan radiolarian biostratigraphy because of scarce common markers. Rapidly evolving, low-diversity radiolarian assemblages recovered from radiolarite layers in the lower part of Hole 765C have been interpreted as upwelling faunas displaced from the continental escarpment toward the basin. Assemblages recovered from claystones and chalks of the same interval are scarce, have low diversity, and were interpreted as indicative of a restricted oceanic environment.

Sedimentology

Site 765 provided more than a few sedimentological surprises:

1. The domination of the Lower Cretaceous and Cenozoic sediments by carbonate turbidites. These are composed of pelagic grains, deposited for the most part below 2000 m, and redeposited as turbidites of 10 cm to more than 5 m thick. Many exhibit sedimentary structures typical of siliciclastic turbidites. Markov chain analysis indicates that mixed carbonate-siliciclastic turbidite sequences exist at this site.
2. No true black shales were found. Some dark gray claystones of Aptian age were interbedded with lighter colored claystones, but these do not exhibit the diagnostic features of true black shales (fissility, abundant pyrite, extremely dark color, and high organic content). However, these dark gray claystones do contain somewhat more organic carbon than do other sediments at Site 765.
3. Rhodochrosite is common in the Lower Cretaceous sediments at Site 765 and has two modes of occurrence: (1) as silt- to sand-sized micronodules that constitute laminated or graded layers commonly a few millimeters to a few centimeters thick or which combine to form concretions up to a few centimeters wide; and (2) as silt-sized micronodules dispersed in a claystone matrix. Occurrence 2 was interpreted as representing authigenic *in-situ* formation of rhodochrosite, whereas Occurrence 1 may indicate reworking of rhodochrosite-bearing clays by bottom currents, with the concentration of rhodochrosite micronodules in traction deposits.
4. The lowest sedimentary unit at Site 765 is dominated by thinly laminated calcareous fragment claystones, which contain locally as much as 50% silt- to sand-sized calcite particles, most of which have been interpreted as "*Inoceramus*" prisms. These brown sediments do not resemble any other sediments found at the site. The basal sediments consist of noncalcareous silty claystones, similar in color to the calcareous claystones overlying them. These sediments, a red clay matrix containing a hyaloclastic basalt breccia, directly overlie volcanic basement without apparent drilling disturbance or hiatus, a red clay matrix containing a hyaloclastic basalt breccia.
5. Twenty layers of bluish-gray smectitic clays, ranging in thickness from less than a centimeter to about 10 cm, occur in the Lower Cretaceous sediments at Site 765. These clays have been tentatively interpreted as bentonites, and are of about the same age as clays (also interpreted as bentonites) that were found during Leg 122 on the Wombat Plateau.

Paleomagnetics

1. A complete M-sequence from M0 through M13 will probably be obtained from Site 765 from red mudstones displaying excellent magnetic properties.
2. These will be the first Southern Hemisphere Early Cretaceous magneto-biostratigraphic correlations.
3. Reversed-polarity chron M"-1" of late Aptian age was documented at Site 765.

4. Site 765 drilled the edge of a marine magnetic anomaly; therefore, the uppermost basalt flows as observed have reversed polarity, whereas the lower flows have normal polarity.

5. During the Early Cretaceous, these sites were located approximately 15° south of their present latitudes.

6. Systematic susceptibility measurements performed at close-spaced intervals provide an excellent means to identify (1) lithologic changes within a core and (2) stratigraphic trends at a hole.

Organic Geochemistry

1. The Cenozoic and Mesozoic sedimentary column is dominated by turbidite deposition, and the high concentrations of calcium carbonate (up to 80 wt%) in the sediments is largely due to redeposition. Erratic variations in carbonate contents (often between 0 and 80 wt%) that appeared in the record, generated from routine core sampling, were found to occur over distances of less than 1 m upon detailed sampling of two turbidite sequences from the Cenozoic section. The base of the turbidite is enriched in carbonate. Low carbonate contents indicate periods of hemipelagic deposition below the CCD with bioturbation and dissolution of underlying turbidite tops.

2. Sedimentary TOC contents are highest in near-surface sediments (about 1.5 wt%) and decrease erratically with increasing sediment depth. These erratic variations reflect the influence of turbidites, while the systematic decrease with increasing depth results from microbial decomposition of the labile (probably marine) organic carbon. Minimum TOC concentrations were found between 500 and 600 mbsf. TOC contents increase with increasing depth in Mesozoic sediments and are higher (up to 1.0 wt% TOC) in dark claystones, compared with green and red claystones. One isolated sample (1 cm thick) had a TOC content of 5 wt%. Rock-Eval pyrolysis indicates that the organic matter in Cenozoic sediments is mixed marine and terrestrial organic carbon, but Mesozoic sediments contain primarily terrestrial organic carbon. Results are compatible with the idea that a large proportion of the TOC preserved in sediments at Site 765 is derived from turbidites, which originate from the shallow-water continental margin.

Inorganic Geochemistry

Interstitial-Water Chemistry and Sediment Mineralogy

Interstitial-water (IW) chemistry studies at Site 765 revealed two distinct intervals that are separated by an order-of-magnitude increase in the sedimentation rate. The upper interval (0–484.9 mbsf) exhibits chemical trends that reflect organic matter degradation by sulfate-reducing bacteria, including depletion of sulfate and an increase in alkalinity, phosphate, and ammonium. The increase in alkalinity results in precipitation of diagenetic carbonates: dolomite, rhodochrosite, ankerite, and possibly calcite. IW trends in the lower interval (below 484.9 mbsf) are far less obvious. Sulfate and magnesium both increase, a result of lower organic matter contents and no dolomite precipitation. The most puzzling aspect of the lower interval is the unusually low-salinity values, especially the sharp chloride gradients observed. Although IW chemistry may have been diluted by simple freshwater, the source of this freshwater is problematic. No other pelagic basins are known to have such low salinity.

Geochemical Reference Site

One of the objectives of Leg 123 was to establish Site 765 as a geochemical reference hole for understanding geochemical fluxes between earth's crust and mantle that occur at subduction zones. Drilling at Site 765 penetrated more than 900 m of sediment and more than 250 m of the underlying basaltic basement. Thus, the recovered cores represent a reference section for the abyssal sediments and oceanic crust of the Argo Abyssal Plain, which is rapidly being consumed at the Indonesian trench. Indeed, the abyssal sediments and Lower Cretaceous basement of Site 765 are typical of many crustal sections approaching trenches today. The majority of these oceanic sections constitute oceanic crust of Cretaceous or older age and pelagic sediments typical of abyssal plains. However, Site 765 is not strictly representative of, for example, the open abyssal plains of the mid-Pacific Ocean, which are far removed from terrigenous influx. Site 765 is situated on oceanic crust adjacent to the Australian continental margin and thus constitutes sediments having a high terrigenous component and higher than abyssal sedimentation rates. In addition, although the basaltic basement of Site 765 may be clearly identified as typical of mid-ocean ridges, it is unusually fractionated and may represent an unusually high-degree mantle melt. These factors also may reflect the special tectonic setting of Site 765, which is adjacent to a continental margin. Therefore, although Site 765 is certainly representative of the Argo Abyssal Plain crust and is grossly representative of many crustal sections approaching trenches, it also represents an end-member section—the first crust formed and last crust consumed in the birth and demise of an ocean basin.

Preliminary chemical data about Site 765 sediments and basalts obtained by shipboard XRF analysis suggest that the actual exercise of constructing a geochemical reference section may be fairly straightforward. The sediment geochemistry is remarkably variable, even on the scale of a meter. However, most of the variability is a result of simple mixing between three end-members: biogenic calcium carbonate, biogenic silica, and a terrigenous clay-rich component that has remained remarkably similar through time. For almost any given metal, a single number may be extracted from the data to represent the terrigenous component, and the resulting geochemical variability in the sediment is largely due to dilution by metal-poor biogenic components. Therefore, although variability is extreme, it may be described simply. Sediment geochemistry is largely dependent upon composition of a single terrigenous component.

The second part of establishing a geochemical reference section is to describe basement chemistry and the fluxes involved during seafloor alteration of the basalts. The unaltered basalts of Site 765 may be related to each other, largely by crystal fractionation of a single parental magma. Alteration of the basalts, although not extreme, is typical of low-temperature seafloor alteration. Chemical alteration of these basalts is largely associated with secondary mineralization developed in fractures and vesicles and may be variable on a small scale. Thus, basement geochemistry is characterized by a relatively simple igneous differentiation trend overprinted by the growth of secondary minerals on a variable scale. Quantifying the extent of alteration of these basalts and extrapolating this information from the upper 250 m down through the rest of the oceanic crust may prove to be the most difficult part.

The ultimate goal of this study is to extract not only a single average composition for the entire site, but also to understand the processes responsible for the geochemical variability preserved throughout an entire crustal section. The geochemistry of the 130-m.y. crustal section of Site 765 (1) is fairly straightforward to describe, (2) will provide a useful data base for comparison to other geochemical reference sites established in the future, and (3) will serve as a first step in understanding the chemical composition and variability of material that has been recycled back into the mantle at subduction zones.

Oceanic Basement

The excellent degree of preservation of the volcanics, with the common presence of fresh volcanic glass, makes this site ideal for studying ancient oceanic mantle reservoirs.

Lavas are evolved relative to MIOR basalts and are characterized by plagioclase and clinopyroxene phenocryst assemblages with little or no olivine; such assemblages are rare in MORB magmas.

Both major-element and the most compatible trace-element abundances are consistent with co-tectic control of the Site 765 basalt compositions. MIOR basalts and Site 765 basalts fall on a single liquid line of descent; the Site 765 magmas are more evolved than MIOR magmas, and their fractionating assemblage was dominated by plagioclase and clinopyroxene.

At least five geochemical units can be defined at Site 765. These represent the eruption of successive pulses of magma having undergone a different extent of crystal fractionation.

Significant differences are evident between Site 765 and MIOR magmas for incompatible trace-element ratios, such as zirconium/yttrium and yttrium/niobium. These differences probably reflect different mantle source regions for these magmas.

Abundances of CaO, Na_2O, (possibly Fe_2O_3*), zirconium, and niobium reflect a higher extent of melting for the Site 765 magmas than for modern MIOR basaltic magmas.

Physical Properties

Sediment physical properties at Site 765 allow one to characterize the sediments into three basic units. Unit A extends from the seafloor to 80 mbsf and consists predominantly of calcareous ooze. Significant changes can be observed in the physical properties, but these are consistent with normal compaction trends for a marine sediment. Unit B includes the interval from 80 to 350 mbsf and is composed of sediments derived from turbidites and debris flows. Physical properties showed normal compaction trends, with the exception of vane shear strength, which exhibited large variations that were found to correlate with the occurrence of turbidite and debris-flow sequences. Unit C, which extends from 350 to 590 mbsf, consisted of lithified turbidite and debris-flow sequences. Physical properties exhibited a significant amount of variation through the unit because of lithology and for the most part, were invariant with depth. Two significant velocity peaks were observed at 350 and 450 mbsf that correlate with high-amplitude reflectors observed in seismic data. Porosities increased significantly, while velocities decreased. The boundary is also marked by a low-amplitude reflector in the seismic data. Unit C exhibits normal compaction trends; however, the physical properties are more consistent with those observed for a much shallower depth, i.e., Unit B (80–350 mbsf).

Physical properties of the basement rock remained relatively constant throughout the section. Porosity and water content are low; whereas, bulk and grain densities increase significantly. Compressional-wave velocities also increase significantly. Variations in these velocities were found to correlate to changes in rock composition and the occurrence of calcite intrusions.

Petrophysical Logging

A geochemical reference for the subduction of old oceanic crust of relatively fast spreading rates (Site 765) was successfully sampled with a nearly complete Schlumberger suite of geochemical and petrophysical logs. This suite included velocity, density, porosity, spectrometry data, and high-resolution geochemical logs.

Basement stress measurements were collected successfully using a borehole televiewer imaging device and a recently applied anelastic strain-recovery method. Data from the borehole televiewer strongly suggest that Site 765 is situated in an area undergoing high differential stresses, as evidenced by the pervasive occurrence of stress-induced breakouts. Based on only preliminary analysis, the breakouts are trending east-west, implying north-south compression in this section of the Indian plate as it approaches the Java Trench to the north.

Fracture permeability was detected within the basalt section, based on results from a packer experiment and high-resolution temperature profiles. Fracture/alteration zones were observed in cores and were detected using the natural gamma-ray spectrometry tool. Fractures were later imaged downhole with the borehole televiewer.

Detailed mapping of fractures, joints, and other extensional features observed in the cores reveals a predominant structural trend of about 45° with respect to vertical. Orientations of this structural fabric using the televiewer and paleomagnetic data may independently document the paleospreading direction, assuming that the 45° fabric represents dips in the direction of seafloor spreading.

Geophysics

A successful VSP experiment at Site 765 provided the necessary tie between drilling results and regional seismic data. This will allow for regional extrapolation of drilling results throughout the Argo Abyssal Plain and onto the adjacent Exmouth Plateau margin, which will provide a better documentation of the stratigraphic and tectonic evolution of the region.

A long, regional seismic line collected between DSDP Site 261 and ODP Site 765 during the transit across the Argo Abyssal Plain suggests several interesting stratigraphic and structural relationships:

1. Major reactivation of basement fault blocks occurred in late Early Cretaceous to early Late Cretaceous time, deforming and uplifting the thick Lower Cretaceous section.
2. Some minor reactivation of faults continued into the early Tertiary over the area of oceanic crust.
3. Large, high-relief, asymmetrical basement blocks south of Site 261 may represent fracture zones. Major middle to Late Cretaceous tectonic activity also occurred along these blocks and is characterized by growth faults along the flanks and uplift and folding of the Lower Cretaceous section over the blocks. These blocks are progressively onlapped and then capped by the thick Cenozoic turbidite section drilled at Site 765. Continued minor faulting and folding along the crests of these blocks involved beds as young as Miocene and explain the transparent "diapirs" or "chimneys" noted in earlier surveys of the Argo Abyssal Plain.
4. Regional uplift of the Lower to Upper Cretaceous section in the Site 261 area is characterized by onlap of the Miocene and older turbidites, explaining the absence of the earlier Cenozoic section at Site 261.

Preliminary analysis of the available seismic data in the Site 765 area suggests north-east trending basement features, which tends to support a north-west opening direction for the Argo Abyssal Plain.

There is excellent correlation between seismic sequences at Site 766 and lithologic and biostratigraphic units. The lower sandstone/siltstone unit (Subunit IIIB) has a wedge-shaped geometry that thickens to the southwest and onlaps the underlying faulted basement, suggesting a local source to the southwest. A short seismic survey just to the southwest of the site indicates that Subunit IIIB has been downfaulted along the adjacent margin. The sequences drilled appear to correlate with sequences on the adjacent plateau that can be correlated with Site 762 along BMR Line 55/4. These correlations suggest wedges of sediments that are (1) younger (late Valanginian through Hauterivian) than the distal Barrow Group drilled at Sites 762/763 and (2) may have a possible source from a local landmass.

Future Operations at Hole 765D

Hole 765D was left cased to 932 mbsf and is the deepest cased hole in ocean crust on the seafloor. The casing shoe is set in basalt, and pipe is cemented for at least the lower 200 m. Approximately 15 m of fill was left in the hole after operations terminated on 17 October 1988. Hole deviation was less than 1° from vertical. As such, Hole 765D represents a deep-ocean laboratory ready for future drilling projects. The volcanics drilled are reasonably fresh, and the base of the hole should be near the transition from "brownstone" alteration to subgreenschist alteration. Recovery was stable at the base of the hole at 30% to 40%; high-speed diamond drilling technology might increase this rate of recovery. Given the present drilling limits of the *JOIDES Resolution*, a further penetration of 1 to 1.5 km might be possible.

REFERENCES

Adamson, A. C., and Richards, H. G., 1990. Low-temperature alteration of very young basalts from ODP Hole 648B: Serocki volcano, Mid-Atlantic Ridge. *In* Detrick, R., Honnorez, J., Bryan, W. B., Juteau, T., et al., *Proc. ODP, Sci. Results*, 106/109: College Station, TX (Ocean Drilling Program), 181–194.

Apthorpe, M., 1988. Cainozoic depositional history of the North West Shelf. *In* Purcell, P. G., and Purcell, R. R. (Eds.), *The North West Shelf, Australia*. Proc. Pet. Expl. Soc. Aust. Symp., 55–84.

Backhouse, J., 1988. Late Jurassic and Early Cretaceous Palynology of the Perth Basin, Western Australia. *Bull. Geol. Surv. West. Aust.*, 135.

Barrett, T. J., 1982. Stratigraphy and sedimentology of Jurassic bedded chert overlying ophiolites in the Northern Apennines, Italy. *Sedimentology*, 29:353–373.

Bateman, R. M., 1985. *Log Quality Control*: Boston (Inter. Human Resour. Dev. Corp.).

Baumgartner, P. O., 1984. A Middle Jurassic-Early Cretaceous low-latitude radiolarian zonation based on Unitary Associations and age of Tethyan radiolarites. *Eclogae Geol. Helv.*, 77:729–836.

________, 1987. Age and genesis of Tethyan Radiolarites. *Eclogae Geol. Helv.*, 80:831–879.

Berggren, W. A., 1969. Cenozoic chronostratigraphy, planktonic foraminiferal zonation and the radiometric time scale. *Nature*, 224: 1072–1075.

Berggren, W. A., Kent, D. V., and Flynn, J. J., 1985a. Jurassic to Paleogene: Part 2, Paleogene geochronology and chronostratigraphy. *In* Snelling, N. J. (Ed.), *The Chronology of the Geologic Record*. Geol. Soc. (London) Mem., 10:141–195.

Berggren, W. A., Kent, D. V., and van Couvering, J. A., 1985b. The Neogene: Part 2, Neogene geochronology and chronostratigraphy. *In* Snelling, N. J. (Ed.), *The Chronology of the Geologic Record*. Geol. Soc. (London) Mem., 10:211–260.

Berner, R. A., 1970. The sedimentary formation of pyrite. *Am. J. Sci.*, 268:1–27.

Blow, W. H., 1969. Late Middle Eocene to Recent planktonic foraminiferal biostratigraphy. *In* Brönnimann, P., and Renz, H. H. (Eds.), *Proc. 1st Int. Conf. Planktonic Microfossils*, 1:199–422.

Bolli, H. M., and Saunders, J. B., 1985. Oligocene to Holocene low latitude planktonic foraminifera. *In* Bolli, H. M., Saunders, J. B., and Perch-Nielsen, K. (Eds.), *Plankton Stratigraphy*: Cambridge (Cambridge Univ. Press), 155–262.

Bolli, H. M, Saunders, J. B., and Perch-Nielsen, K., 1985. Comparison of zonal schemes for different fossil groups. *In* Bolli, H. M., Saunders, J. B., and Perch-Nielsen, K. (Eds.), *Plankton Stratigraphy*: Cambridge (Cambridge Univ. Press), 3–10.

Bown, P. R., Cooper, M.K.E., and Lord, A. R., 1988. A calcareous nannofossil biozonation scheme for the early to mid Mesozoic. *Newsl. Stratigr.*, 20:91–114.

Bukry, D., 1973. Low-latitude coccolith biostratigraphic zonation. *In* Edgar, N. T., Saunders, J. B., et al., *Init. Repts. DSDP*, 15: Washington (U.S. Govt. Printing Office), 685–703.

Burke, J. A., Campbell, R. L., and Schmidt, A. W., 1976. The litho-porosity crossplot. *Log Analyst*, Nov.-Dec.

Cann, J. R., 1979. Metamorphism in the ocean crust. *In* Talwani, M., Harrison, C. G., and Hayes, D. E. (Eds.), *Deep Drilling Results in the Atlantic Ocean: Ocean Crust*: Washington (Am. Geophys. Union, Geodynamics Project), 48:230–238.

Cant, D. J., and Walker, R. G., 1976. Development of a braided fluvial facies model for the Devonian Battery Point Sandstone, Quebec. *Can. J. Earth Sci.*, 13:102–119.

Caron, M., 1985. Cretaceous planktonic foraminifera. *In* Bolli, H. M., Saunders, J. B., and Perch-Nielsen, K. (Eds.), *Plankton Stratigraphy*: Cambridge (Cambridge Univ. Press), 17–86.

Carr, T. R., 1982. Log-linear models, Markov chains and cyclic sedimentation. *J. Sediment. Petrol.*, 52:905–912.

Channell, J.E.T., Lowrie, W., and Medizza, R., 1979. Middle and Early Cretaceous magnetic stratigraphy from the Cismon section, Northern Italy. *Earth Planet. Sci. Lett.*, 42:153–166.

Claypool, G. A., and Kvenvolden, K. A., 1983. Methane and other hydrocarbon gases in marine sediment. *Annu. Rev. Earth Planet. Sci.*, 11:299–327.

Cooper, M.K.E., 1984. Nannofossils across the Jurassic/Cretaceous boundary in the Tethyan Realm. *Int. Symp. Jurassic Stratigr.*, 2:429–443.

Crame, A., and Howlett, P., 1988. Fossil bearing strata from the Tithonian-Valanginian interval of the Antarctic peninsula. *Bull. Br. Antarctic Surv*.

Davis, J. C., 1973. *Statistics and Data Analysis in Geology*: New York (Wiley).

de Raaf, J.F.M., Reading, H. G., and Walker, R. G., 1965. Cyclic sedimentation in the Lower Westphalian of North Devon, England. *Sedimentology*, 4:1–52.

Detrick, R., Honnorez, J., Bryan, W. B., Juteau, T., et al., 1990. *Proc. ODP, Sci. Results,* 106/109: College Station, TX (Ocean Drilling Program).

Dosso, L., Bougault, H., Beuzart, P., Calvez, J.-Y., and Joron, J.-L., 1988. The geochemical structure of the South East Indian Ridge. *Earth Planet. Sci. Lett.*, 88:47–49.

Doveton, J. H., et al., 1988. The use of color coded crossplots in log analysis. *Trans. Soc. Prof. Well Log Analysts*.

Duff, P. McL. D., Hallam, A., and Walton, E. K., 1967. *Cyclic Sedimentation: Developments in Sedimentology* (Vol. 10): Amsterdam (Elsevier).

Embleton, B.J.J., 1981. A review of the paleomagnetism of Australia and Antarctica. *In* McElhinny, M. W., and Valencio, D. (Eds.), *Paleoreconstruction of the Continents*: Washington (Am. Geophys. Union), 77–92.

Espitalié, J., Madec, M., and Tissot, B., 1977. Source Rock characterization method for petroleum exploration. *Proc. Annu. Offshore Technol. Conf.*, 3:439–443.

Exon, N. F., and Williamson, P. E., 1988. *Rig Seismic Research Cruise 7 and 8, Sedimentary Basin Framework of the Northern and Western Exmouth Plateau*. Bur. Miner. Resour. Austral. Record, 30.

Frey, F. A., Dickey, J. S., Jr., Thompson, G., and Bryan, W. B., 1977. Eastern Indian Ocean DSDP sites: correlations between petrology, geochemistry and tectonic setting. *In* Heirtzler, J. R., Bolli, H. M., Davies, T. A., Saunders, J. B., and Sclater, J. G. (Eds.), *Indian Ocean Geology and Biostratigraphy*: Washington (Am. Geophys. Union), 189–257.

Fullerton, L. G., Sager, W. W., and Handschumacher, D. W., 1989. Late Jurassic-Early Cretaceous evolution of the eastern Indian Ocean adjacent to Northwest Australia. *J. Geophys. Res.*, 94:2937–2953.

Gartner, S., Jr., 1977. Calcareous nannofossil biostratigraphy and revised zonation of the Pleistocene. *Mar. Micropaleontol.*, 2:1–25.

Geroch, S., and Nowak, W., 1984. Proposal of zonation for the late Tithonian-late Eocene, based upon arenaceous foraminifera from the outer Carpathians, Poland. *Benthos '83: 2nd Int. Symp. Benthonic Foraminifera*, 225–239.

Gieskes, J. M., 1981. Deep-sea drilling interstitial waters: implications for chemical alteration of the oceanic crust, Layers I and II. *Soc. Econ. Paleontol. Mineral. Spec. Publ.*, 31:49–167.

________, 1983. The chemistry of interstitial waters of deep-sea sediments: interpretation of deep-sea drilling data, *In* Riley, J. P., and Chester, R. (Eds.), *Chemical Oceanography* (Vol. 8): London (Academic Press), 222–269.

Gingerich, P. D., 1969. Markov analysis of cyclic alluvial sediments. *J. Sediment. Petrol.*, 39:330–332.

Gradstein, F. M., 1978. Biostratigraphy of Lower Cretaceous Blake Nose and Blake-Bahama Basin foraminifera, DSDP Leg 44, western North

Atlantic Ocean. *In* Benson, W. E., Sheridan, R. E., et al., *Init. Repts. DSDP*, 44: Washington (U.S. Govt. Printing Office), 663–701.

———, 1986. *Jurassic Paleoenvironment and Stratigraphy, Argo Abyssal Plain*. JOIDES ODP Proposal 240/B (updated July, 1986).

Hamano, Y., Nishitani, T., and Kono, M., 1980. Magnetic properties of basalt samples from Deep Sea Drilling Project Holes 417D and 418A. *In* Donnelly, T., Francheteau, J., Bryan, W., Robinson, P., Flower, M., Salisbury, M., et al., *Init. Repts. DSDP*, 52: Washington (U.S. Govt. Printing Office), 1391–1405.

Harper, C. W., Jr., 1984. Improved methods of facies sequence analysis. *In* Walker, R. G. (Ed.), *Facies Models* (2nd ed.), Geosci. Can. Reprint Ser., 1:10–13.

Hein, R. J., and Karl, S. M., 1983. Comparisons between open ocean and continental margin chert sequences. *In* Iijima, A., Hein, J. R., and Siever, R. (Eds.), *Siliceous Deposits in the Pacific Region*: Amsterdam (Elsevier), 25–43.

Heirtzler, J. R., Cameron, P., Cook, P. J., Powell, T., Roeser, H. A., Sukardi, S., and Veevers, J. J., 1978. The Argo Abyssal Plain. *Earth Planet. Sci. Lett.*, 41:21–31.

Helby, R., Morgan, R., and Partridge, A. D., 1987. A palynological zonation of the Australian Mesozoic. *Mem. Assoc. Austral. Paleontol.*, 4:1–94.

Hilde, T.W.C., Isezaki, N., and Wageman, J. M., 1976. Mesozoic seafloor spreading in the North Pacific. *In* Woolard, G. P., Sutton, G. H., Manghnani, M. H., and Moberly, R. (Eds.), *Geophysical Monograph 19, The Geophysics of the Pacific Ocean Basin and it Margins*: Washington (Am. Geophys. Union), 205–226.

Humler, E., and Whitechurch, H., 1988. Petrology of basalts from the Central Indian Ridge (lat. 25°23′S, long. 70°04′E): estimates of frequencies and fractional volumes of magma injection in a two layered reservoir. *Earth Planet. Sci. Lett.*, 88:160–181.

Jarrard, R. J., 1974. Paleomagnetism of some Leg 27 sediment cores. *In* Veevers, J. J., Heirtzler, J. R., et al., *Init. Repts. DSDP*, 27: Washington (U.S. Govt. Printing Office), 415–423.

Jenkyns, H. C., and Winterer, E. L., 1982. Paleoceanography of Mesozoic ribbon radiolarites. *Earth Planet. Sci. Lett.*, 60:351–375.

Kastner, M., 1979. Silica polymorphs. *In* Burns, R. G. (Ed.), *Marine Minerals* (Vol. 6): Miner. Soc. Am. Rev. Miner., 99–111.

Katz, B. J., 1983. Limitations of Rock Eval pyrolysis for typing organic matter. *Org. Geochem.*, 4:195–199.

Keating, B. H., and Helsley, C. E., 1978a. Magnetostratigraphic studies of Cretaceous sediments from DSDP Site 369. *In* Lancelot, Y., Seibold, E., et al., *Init. Repts. DSDP*, Suppl. to Vols. 38, 39, 40, and 41: Washington (U.S. Govt. Printing Office), 983–986.

———, 1978b. Paleomagnetic results from DSDP Hole 391C and the magnetostratigraphy of Cretaceous sediments from the Atlantic Ocean floor. *In* Benson, W. E., Sheridan, R. E., et al., *Init. Repts. DSDP*, 44: Washington (U.S. Govt. Printing Office), 523–528.

Kennett, J. P., and Srinivasan, M. S., 1983. *Neogene Planktonic Foraminifera, a Phylogenetic Atlas*: Stroudsburg, PA (Hutchinson Ross).

Khramov, A. N., 1982. *Paleomagnetologia*: Leningrad (Nedra).

Kono, M., 1980a. Paleomagnetism of DSDP Leg 55 basalts and implications for the tectonics of the Pacific plate. *In* Jackson, E. D., Koizumi, I., et al., *Init. Repts. DSDP*, 55: Washington (U.S. Govt. Printing Office), 737–752.

———, 1980b. Statistics of paleomagnetic inclination data. *J. Geophys. Res.*, 85:3878–3882.

Krasheninnikov, V. A., 1974. Upper Cretaceous benthonic agglutinated foraminifera, Leg 27, Deep Sea Drilling Project. *In* Veevers, J. J., Heirtzler, J. R., et al., *Init. Repts. DSDP*, 27: Washington (U.S. Govt. Printing Office), 631–661.

Langmuir, C. H., and Natland, J., 1986. *Drilling Old Ocean Crust at Convergent Margins: Argo Abyssal Plain and Western Pacific*. JOIDES Proposal 267/F (updated December 1986).

Larson, R. L., 1975. Late Jurassic sea floor spreading in the eastern Indian Ocean. *Geology*, 3:69–71.

La Traille, S. L., 1983. Archiving and exchange of a computerized marine seismic database: the ROSE data archive system. *Hawaii Inst. Geophys. Data Report* 43.

Lowrie, W., Channell, J.E.T., and Alvarez, W., 1980. A review of magnetic stratigraphy investigations in Cretaceous pelagic carbonate rocks. *J. Geophys. Res.*, 85:3597–3605.

Lowrie, W., and Heller, F., 1982. Magnetic properties of marine limestones. *Rev. Geophys. Space Phys.*, 20:171–192.

Martini, E., 1971. Standard Tertiary and Quaternary calcareous nannoplankton zonation. *In* Farinacci, A. (Ed.), *Proc. 2nd Planktonic Conf.*, 2:739–785.

McCave, 1979. *In* Tucholke, B. E., Vogt, P. E., et al., *Init. Repts. DSDP*, 43: Washington (U.S. Govt. Printing Office).

McElhinny, M. W., 1974. Paleomagnetism of basalt samples, Leg 27. *In* Heirtzler, J. R., Veevers, J. J., et al., *Init. Repts. DSDP*, 27: Washington (U.S. Govt. Printing Office), 403–404.

Miall, A. D., 1973. Markov chain analysis applied to an ancient alluvial plain succession. *Sedimentology*, 20:347–364.

Morgan, G. E., 1979. Paleomagnetic results from DSDP Site 398. *In* Sibuet, J.-C., Ryan, W.B.F., et al., *Init. Repts. DSDP*, 47 (Pt. 2): Washington (U.S. Govt. Printing Office), 599–611.

Moullade, M., 1984. Intéret des spetits foraminifères benthiques "profonds" pour la biostratigraphie et l'analyse des paleoenvironnements océaniques Mésozoiques. *In* Oertli, H. J. (Ed.), 2nd Int. Symp. Benthic Foraminifera, "Benthos '83," Pau, France (1983), 429–464.

Munsell Soil Color Charts, 1975. Munsell (Baltimore).

Mutter, J. C., and Balch, A., 1988. *Vertical Seismic Profiling (VSP) and the Ocean Drilling Program (ODP): Report of a Workshop*: Washington (Joint Oceanographic Inst.).

Mutterlose, J., 1986. Belemnites from the Orville Coast (eastern Antarctica) and their paleobiogeographic significance. *Bull. Br. Antarctic Surv.*

Ogg, J. G., 1981. Sedimentology and paleomagnetism of Jurassic pelagic limestones [Ph.D. dissert.]. Scripps Institution of Oceanography, Univ. of California, San Diego.

———, 1986. Paleolatitudes and magnetostratigraphy of Cretaceous and lower Tertiary sedimentary rocks, Deep Sea Drilling Project Site 585, east Mariana Basin, western Central Pacific. *In* Moberly, R., Schlanger, S. O., et al., *Init. Repts. DSDP*, 89: Washington (U.S. Govt. Printing Office), 629–646.

———, 1987. Early Cretaceous magnetic polarity time scale and the magnetostratigraphy of Deep Sea Drilling Project Sites 603 and 534, western Central Atlantic. *In* Sheridan, R. E., Gradstein, F. M., et al., Init. Repts. DSDP, 93: Washington (U.S. Govt. Printing Office), 849–880.

———, 1988. Early Cretaceous and Tithonian magnetostratigraphy of Galicia margin (Ocean Drilling Program Leg 103). In Boillot, G., Winterer, E. L., Meyer, A., et al., *Proc. ODP, Sci. Results*, 103: College Station, TX (Ocean Drilling Program), 659–682.

Okada, H., and Bukry, D., 1980. Supplementary modification and introduction of code numbers to the "Low-latitude coccolith biostratigraphic zonation" (Bukry, 1973; 1975). *Mar. Micropaleontol.*, 5: 321–325.

Perch-Nielsen, K., 1985. Cenozoic calcareous nannofossils. *In* Bolli, H. M., Powers, D. W., and Easterling, R. G., 1982. Improved methodology for using embedded markov chains to describe cyclical sediments. *J. Sediment. Petrol.*, 52:913–923.

Pessagno, E. A., and Blome, C. D., 1986. Faunal affinities and tectonogenesis of Mesozoic rocks in the Blue Mountain Province of eastern Oregon and western Idaho. *In* Vallier, T. L., and Brooks, H. C. (Eds.), *Geology of the Blue Mountains Region of Oregon, Idaho and Washington*. U.S. Geol. Surv. Prof. Paper 1435, 65–78.

Peters, K. E., 1986. Guidelines for evaluating petroleum source rock using programmed pyrolysis. *AAPG Bull.*, 32:318–329.

Price, R. C., Kennedy, A. K., Riggs-Sneering., M., and Frey, F. A., 1986. Geochemistry of basalts from the Indian Ocean triple junction: implications for the generation and evolution of Indian Ocean ridge basalts. *Earth Planet. Sci. Lett.*, 78:379–396.

Raymer, L. L., Hunt, E. R., and Gardner, J. S., 1980. An improved sonic transit time-to-porosity transform. *Trans. Soc. Prof. Well Log Analysts*.

Read, W. A., 1969. Analysis and simulation of Namurian sediments in Central Scotland using a Markov process model. *Math. Geol.*, 1: 199–219.

Robinson, P. T., and Whitford, D. J., 1974. Basalts from the Eastern Indian Ocean, DSDP Leg 27. *In* Veevers, J. J., Heirtzler et al., *Init. Repts. DSDP*, 27: Washington (U.S. Govt. Printing Office), 551–559.

Roth, P., 1978. Jurassic and Lower Cretaceous calcareous nannofossils in the western North Atlantic (Site 534): biostratigraphy, preservation, and some observations on biogeography and paleoceanography. *In* Sheridan, R. E., Gradstein, F. M., et al., *Init. Repts. DSDP*, 76: Washington (U.S. Govt. Printing Office), 587–621.

Sanfilippo, A., and Riedel, W. R., 1985. Cretaceous Radiolaria. *In* Bolli, H. M., Saunders, J. B., and Perch-Nielsen, K. (Eds.), *Plankton Stratigraphy*: Cambridge (Cambridge Univ. Press), 573–630.

Sanfilippo, A., Westberg-Smith, M. J., and Riedel, W. R., 1985. Cenozoic Radiolaria. *In* Bolli, H. M., Saunders, J. B., and Perch-Nielsen, K. (Eds.), *Plankton Stratigraphy*: Cambridge (Cambridge Univ. Press), 631–712.

Sato, H., 1978. Segregation vesicles and immiscible liquid droplets in ocean-floor basalt of Hole 396B, IPOD/DSDP Leg 46. *In* Dmitriev, L., Heirtzler, J., et al., *Init. Repts. DSDP*, 46: Washington (U.S. Govt. Printing Office), 283–297.

Sato, H., Aoki, K., Okamoto, K., and Fujita, B., 1978. Petrology and chemistry of basaltic rocks from Hole 396B, IPOD/DSDP Leg 46. *In* Dmitriev, L., Heirtzler, J., et al., *Init. Repts. DSDP*, 46: Washington (U.S. Govt. Printing Office), 115–141.

Saunders, J. B., and Perch-Nielsen, K. (Eds.), *Plankton Stratigraphy*: Cambridge (Cambridge Univ. Press), 427–554.

Schaaf, A., 1985. Un nouveau canevas biochronologique du Crétacé inférieur et moyen: les biozones à Radiolaires. *Sci. Géol. Bull. Strasbourg*, 38(3):227–269.

Schott, M., 1984. Mikrofaziell-multivariate Analyse einer rhato-liassischen Karbonatplattform in den Nordlichen Kalkalpen. *Facies*, 11: 229–280.

Sclater, J. G., Meinke, L., Bennett, A., and Murphy, C., 1985. The depth of the ocean through the Neogene. *In* Kennett, J. P. (Ed.), *The Miocene Ocean*. Geol. Soc. Am. Mem., 163:1–19.

Schlumberger, 1987. *Log Interpretation Principles/Applications*. Houston, TX (Schlumberger Educ. Serv.).

Selley, R. C., 1970. Studies of sequence in sediments using a simple mathematical device. *Q. J. Geol. Soc. London*, 125:557–581.

Shipboard Scientific Parties, 1979a. Site 417. *In* Donnelly, T., Francheteau, J., Bryan, W., Robinson, P., Flower, M., Salisbury, M., et al., *Init. Repts. DSDP*, 51–53: Washington (U.S. Govt. Printing Office), 23–350.

Shipboard Scientific Parties, 1979b. Site 418. *In* Donnelly, T., Francheteau, J., Bryan, W., Robinson, P., Flower, M., Salisbury, M., et al., *Init. Repts. DSDP*, 51–53: Washington (U.S. Govt. Printing Office), 351–626.

Shipboard Scientific Party, 1983. Sites 501 and 504: Sediments and ocean crust in an area of high heat flow on the southern flank of the Costa Rica Rift. *In* Cann, J. R., Von Herzen, R. P., White, G. M., et al., *Init. Repts. DSDP*, 69: Washington (U.S. Govt. Printing Office), 31–173.

Shipboard Scientific Party, 1986. Site 462. *In* Moberly, R., Schlanger, S. O., et al., *Init. Repts. DSDP*, 89: Washington (U.S. Govt. Printing Office), 179–184.

Shipboard Scientific Party, 1988a. Site 504: Costa Rica Rift. *In* Becker, K., Sakai, H. et al., *Proc. ODP*, 111: College Station, TX (Ocean Drilling Program), 35–251.

Shipboard Scientific Party, 1988b. Site 648. *In* Detrick, R., Honnorez, J., Bryan, W. B., Juteau, T., et al., *Proc. ODP*, *Init. Repts.*, 106/109: College Station, TX (Ocean Drilling Program), 35–134.

Sissingh, W., 1977. Biostratigraphy of Cretaceous calcareous nannoplankton. *Geol. Mijnbouw*, 56:37–65.

Sliter, W. V., 1980. Mesozoic foraminifers and deep-sea benthic environments from Deep Sea Drilling Project Sites 415 and 416, eastern north Atlantic. *In* Lancelot, Y., Winterer, E. L, et al., *Init. Repts. DSDP*, 50: Washington (U.S. Govt. Printing Office), 353–428.

Stam, B., Gradstein, F. M., Lloyd, P., and Gillis, D. 1986. Algorithms for porosity and subsidence history. *Comput. Geosci.*, 13:317–349.

Steiner, M. B., 1977. Magnetization of Jurassic red deep sea sediments in the Atlantic (DSDP Site 105). *Earth Planet. Sci. Lett.*, 35:205–214.

Steinhausen, D., and Langer, K., 1977. *Clusteranalyse*: Berlin (de Gruyter).

Stover, L. E., and Partridge, A. D., 1973. Tertiary and Late Cretaceous spores and pollen from the Gippsland Basin, Southeastern Australia. *Proc. R. Soc. Victoria*, 85:237–286.

Sun, S.-S., Nesbitt, R. W., and Sharaskin, A. Y., 1979. Geochemical characteristics of mid-ocean ridge basalts. *Earth Sci. Planet. Lett.*, 44:119–138.

Tarling, D. H., 1983. *Palaeomagnetism. Principles and Applications in Geology, Geophysics and Archaeology*: New York (Chapman and Hall).

Thierstein, H. R., 1973. Lower Cretaceous calcareous nannoplankton zonation. *Abh. Geol. Bundesanst.*, 29:1–52.

Toumarkine, M., and Luterbacher, H., 1985. Paleocene and Eocene planktonic foraminifera. *In* Bolli, H. M., Saunders, J. B., and Perch-Neilson, K. (Eds.), *Plankton Stratigraphy*: Cambridge (Cambridge Univ. Press), 87–154.

Tucholke, B. E., Vogt, P. R., et al., 1979. *Init. Repts. DSDP*, 43: Washington (U.S. Govt. Printing Office).

Vandenberg, J., and Wonders, A.A.H., 1980. Paleomagnetism of late Mesozoic pelagic limestones from the Southern Alps. *J. Geophys. Res.*, 85:3623–3627.

van Morkhoven, F.P.C.M., Berggren, W. A., and Edwards, A. S., 1986. Cenozoic cosmopolitan deep-water benthic foraminifera. *Bull. Cent. Rech. Explor.-Prod. Elf-Aquitaine, Mem.*, 11.

Veevers, J. J., Heirtzler, J. R., et al., 1974. *Init. Repts. DSDP*, 27: Washington (U.S. Govt. Printing Office).

Veevers, J. J., Tayton, J. W., and Johnson, B. D., 1985. Prominent magnetic anomaly along the continent-ocean boundary between the northwestern margin of Australia (Exmouth and Scott Plateaus) and the Argo Abyssal Plain. *Earth Planet. Sci. Lett.*, 72:415–426.

Vincent, E., 1977. Indian Ocean Neogene planktonic foraminiferal biostratigraphy and its paleoceanographic implications. *In* Heirtzler, J. R., Bolli, H. M., Davies, T. A., Saunders, J. B., and Sclater, J. G. (Eds.), *Indian Ocean Geology and Biostratigraphy*: Washington (Am. Geophys. Union), 469–584.

Vogt, P. R., and Einwich, A. M., 1979. Magnetic anomalies and seafloor spreading in the western North Atlantic, and a revised calibration of the Keathley (M) geomagnetic reversal chronology. *In* Tucholke, B. E., Vogt, P. R., et al., *Init. Repts. DSDP*, 43: Washington (U.S. Govt. Printing Office), 857–876.

von Rad, U., and Exon, N. F., 1982. Mesozoic-Cenozoic sedimentary and volcanic evolution of the starved passive continental margin off northwest Australia. *In* Watkins, J. S., and Drake, C. L. (Eds.), *Studies in Continental Margin Geology.* AAPG Mem., 34:253–281.

von Rad, U., Exon, P., Williamson, P., and Boyd, R., 1986. *ODP Leg Off NW Australia-Argo Abyssal Plain-Exmouth Plateau.* JOIDES Proposal 121B (revised, May 1986).

von Rad, U., Haq, B., and Leg 122 Shipboard Scientific Party, in press. From Gondwana to Australia: rifting, paleoenvironment and sea level. *Nature.*

von Rad, U., Haq, B., Gradstein, F., Ludden, J., and O'Connell, S., 1988, Legs 122 and 123 Scientific Prospectus, Exmouth Plateau and Argo Basin. ODP Sci. Prospectus Nos. 22 and 23: College Station, TX (Ocean Drilling Program).

von Rad, U., and Rösch, H., 1972. Mineralogy and origin of clay minerals, silica and authigenic silicates in Leg 14 sediments. *In* Hayes, D. E., Pimm, A. C., et al., *Init. Repts. DSDP*, 14: Washington (U.S. Govt. Printing Office), 727–746.

von Stackelberg, U., Exon, N. F., von Rad, U., Quilty, P., Shafik, S., Beiersdorf, H., Seibertz, E., and Veevers, J. J., 1980. Geology of the Exmouth and Wallaby Plateaus off northwest Australia: sampling of seismic sequences. *BMR J. Aust. Geol. Geophys.*, 5:113–140.

Walker, R. G., 1979. General introduction: facies and facies models. *In* Walker, R. G. (Ed.), *Facies Models*: Geosci. Can. Reprint Ser., 1: 1–7.

________, 1984. General introduction: facies, facies sequences and facies models. *In* Walker, R. G. (Ed.), *Facies Models*: Geosci. Can. Reprint Ser., 1:1–9.

Wensink, H., Hartosukohardjo, S., and Kool, K., 1987. Paleomagnetism of the Nakfunu Formation of Early Cretaceous age, Western Timor, Indonesia. *Geol. Mijnbouw*, 66:89–99.

Whelan, J. K., and Hunt, J. M., 1980. C_1-C_7 volatile organic compounds in sediments from Deep Sea Drilling Project Legs 56 and 57, Japan Trench. *In* Scientific Party, *Init. Repts. DSDP*, 56, 57 (Pt. 2): Washington (U.S. Govt Printing Office), 1349-1365.

Wilcox, R. D., Fisk, J. V., Jr., and Corbett, G. E., 1984. Filtration method characterizes dispersive properties of shales. Proc. Soc. Pet. Engrs. 59th Annu. Tech. Conf. (Houston), Pap. SPE 13162.

Williams, G. L., and Bujak, J. P., 1985. Mesozoic and Cenozoic dinoflagellates. *In* Bolli, H. M., Saunders, J. B., and Perch-Neilson, K. (Eds.) *Plankton Stratigraphy*: Cambridge (Cambridge Univ. Press), 847–964.

Ms 123A:104

NOTE: All core description forms ("barrel sheets") and core photographs have been printed on coated paper and bound as Secton 3, near the back of the book, beginning of page 355.

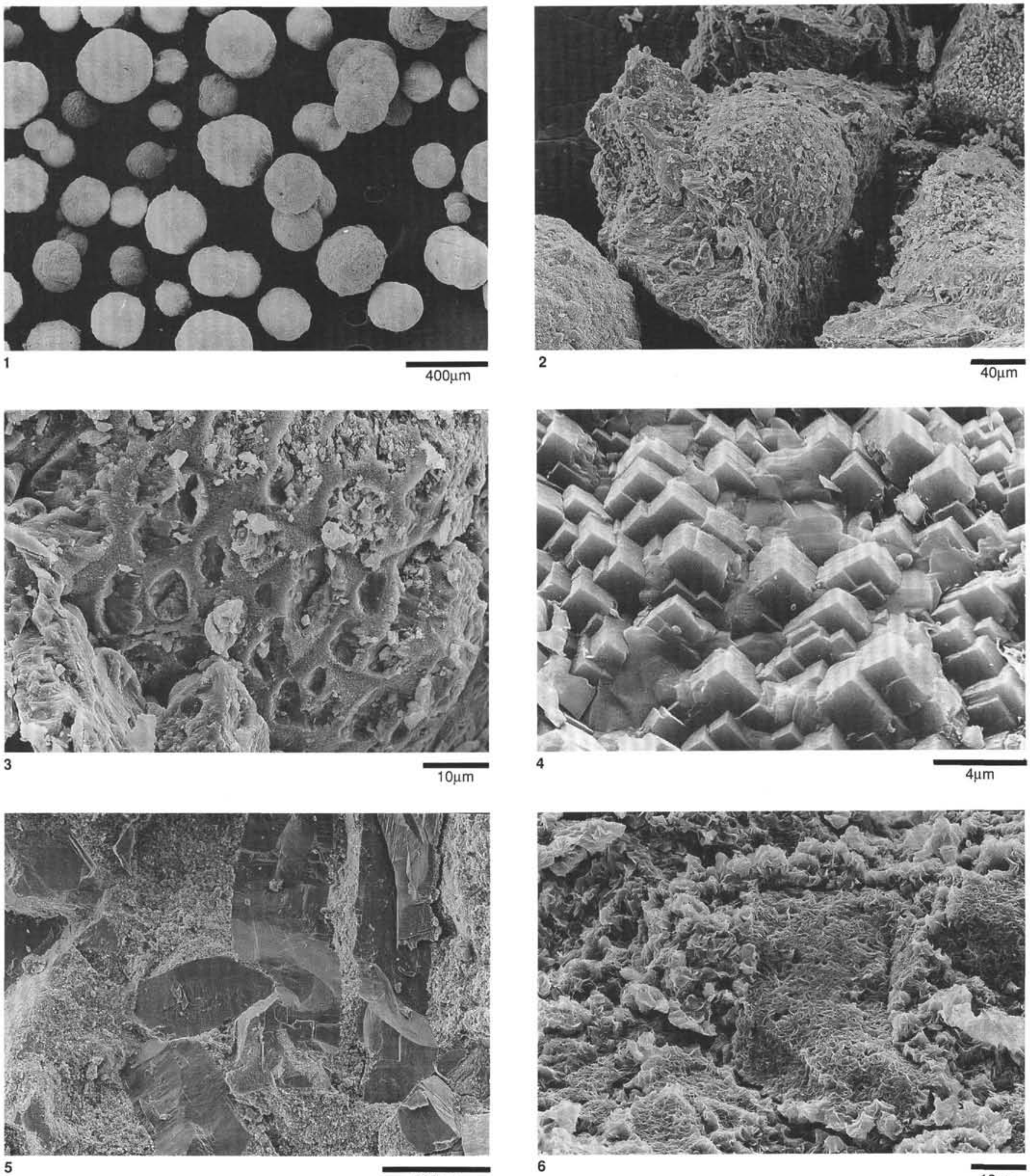

Plate 1. **1.** Rhodochrosite micronodules (washing residue). The micronodules form either as single spheres or as agglomerates of spheres. **2.** (Close-up of Fig. 1) Broken micronodule showing images of microfossils (radiolarians and diatoms) forming the nuclei of these nodules. Radiolarian in center has been replaced by rhodochrosite. **3.** (Close-up of Fig. 2) Skeletal structure of radiolarian in rhodochrosite micronodule. The skeleton has been entirely replaced by rhodochrosite, preserving the original skeletal structure. **4.** Close-up of the surface of a rhodochrosite nodule consisting of crystal growth faces. **5.** Large authigenic barite crystals growing in silicified clay matrix. Closely associated are spherical rhodochrosite micronodules (not visible on photograph). **6.** Sediment is made of 100% smectite. Rectangular feature in center is explained as a pseudomorph of smectite after a ?mafic mineral.

Summary Log for Site 765C

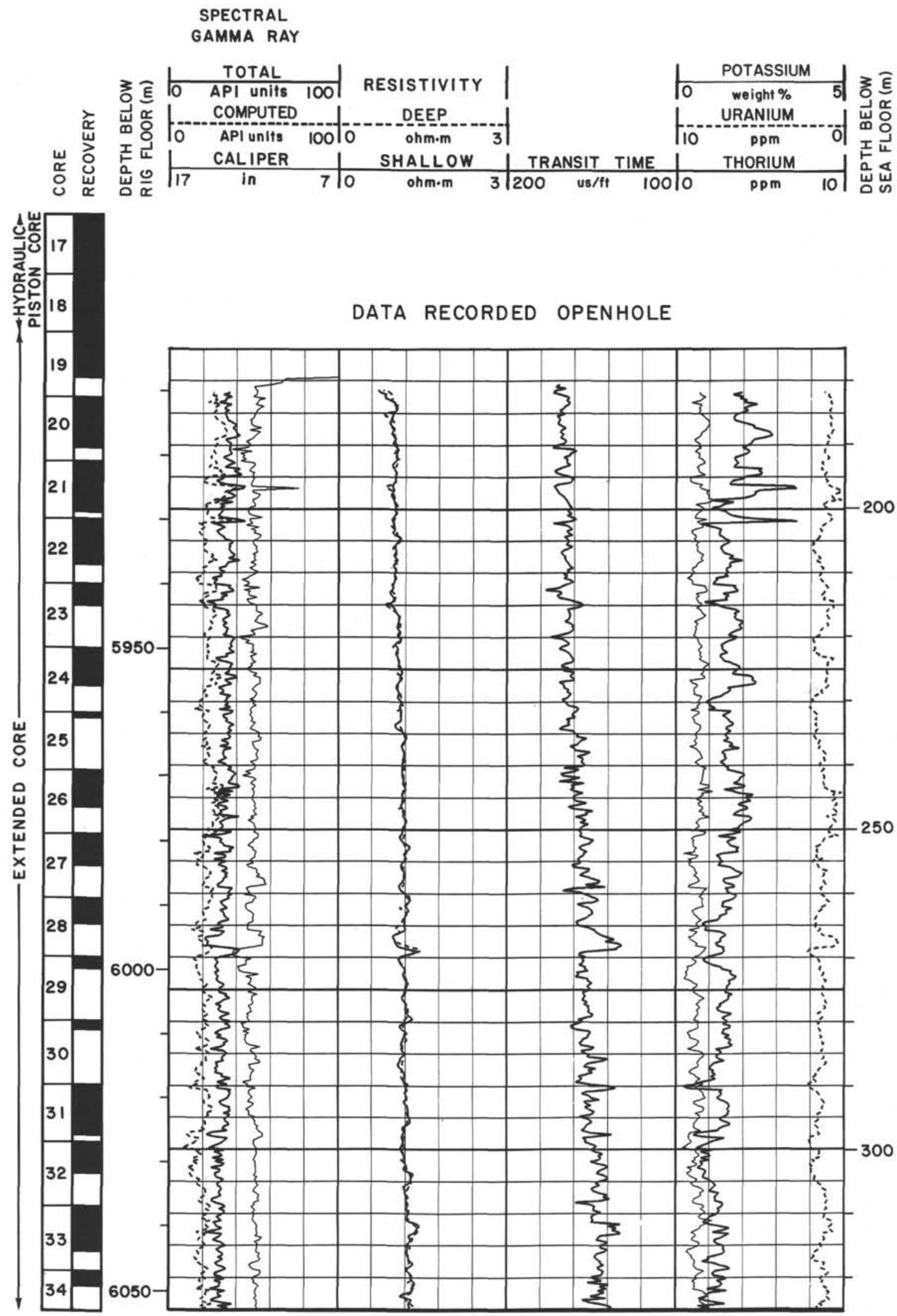

Summary Log for Site 765C (continued)

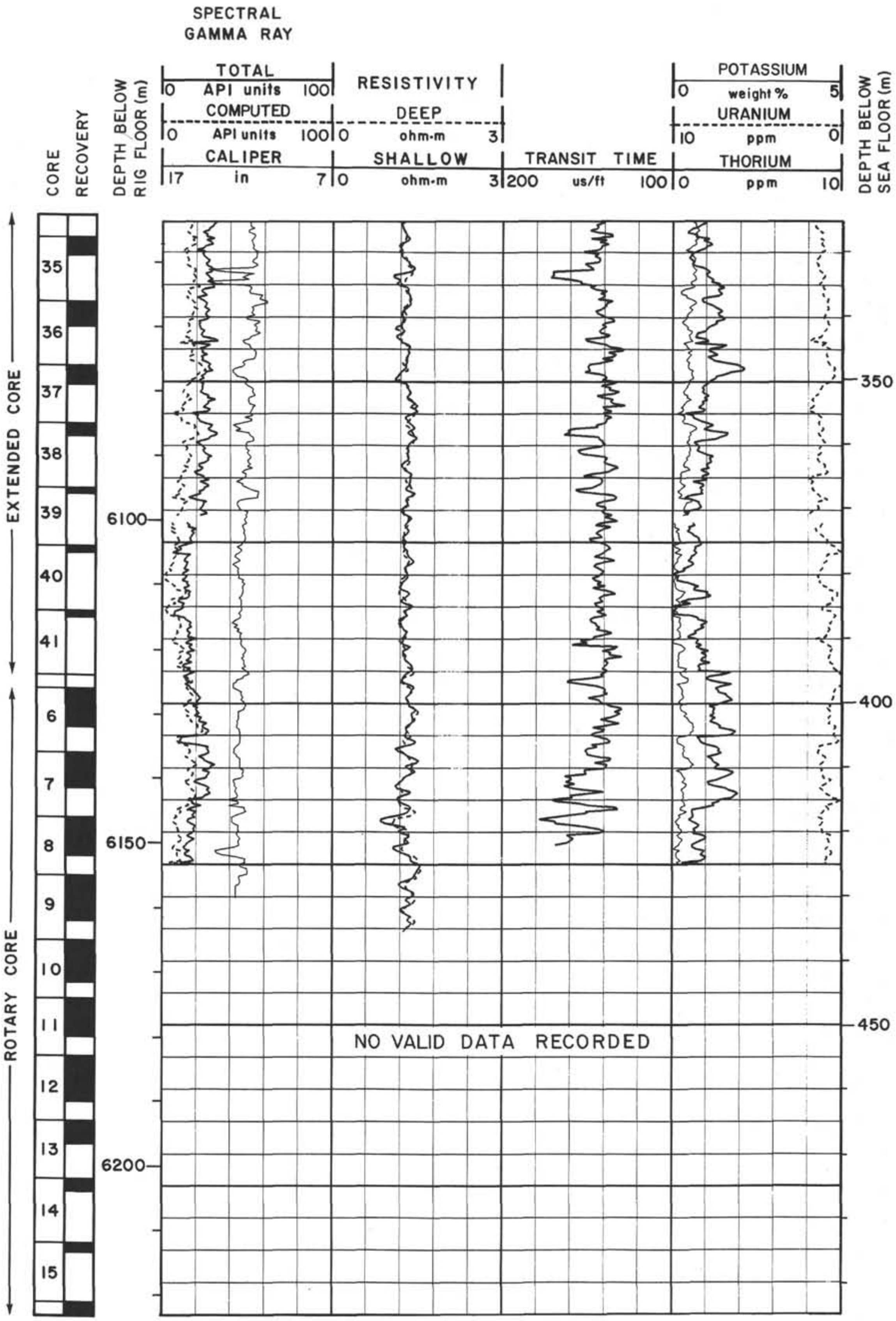

Summary Log for Site 765C (continued)

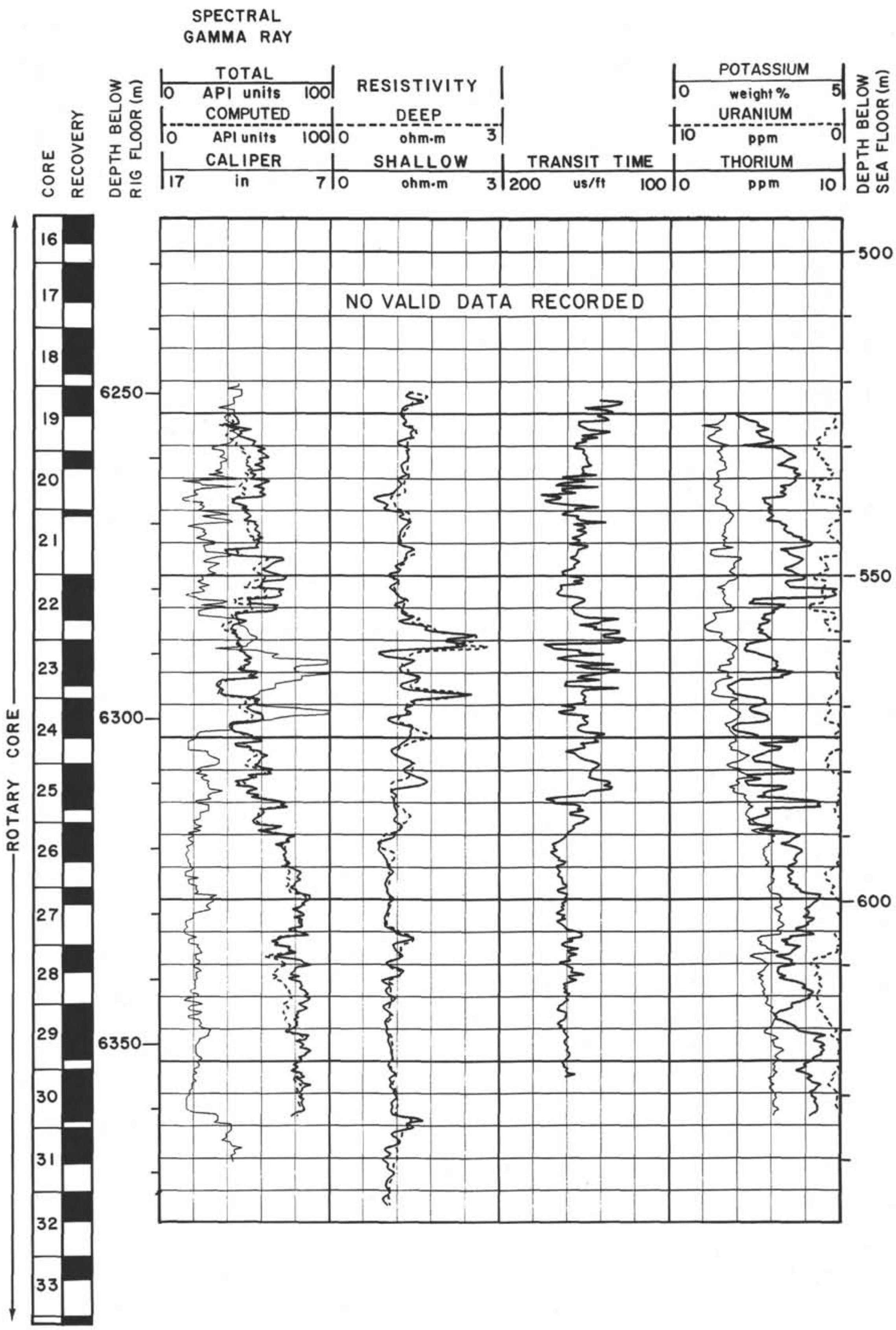

Summary Log for Site 765C (continued)

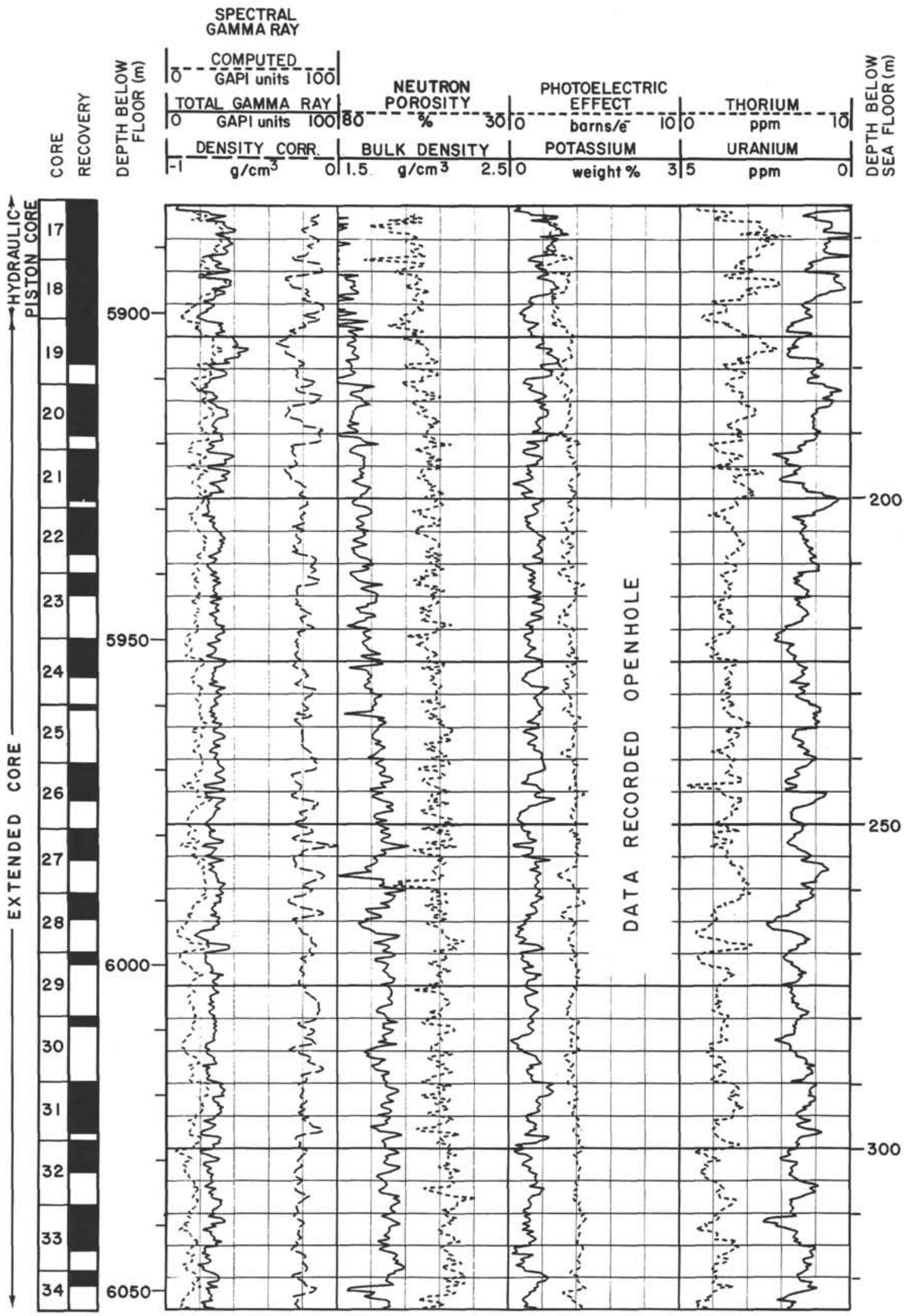

Summary Log for Site 765C (continued)

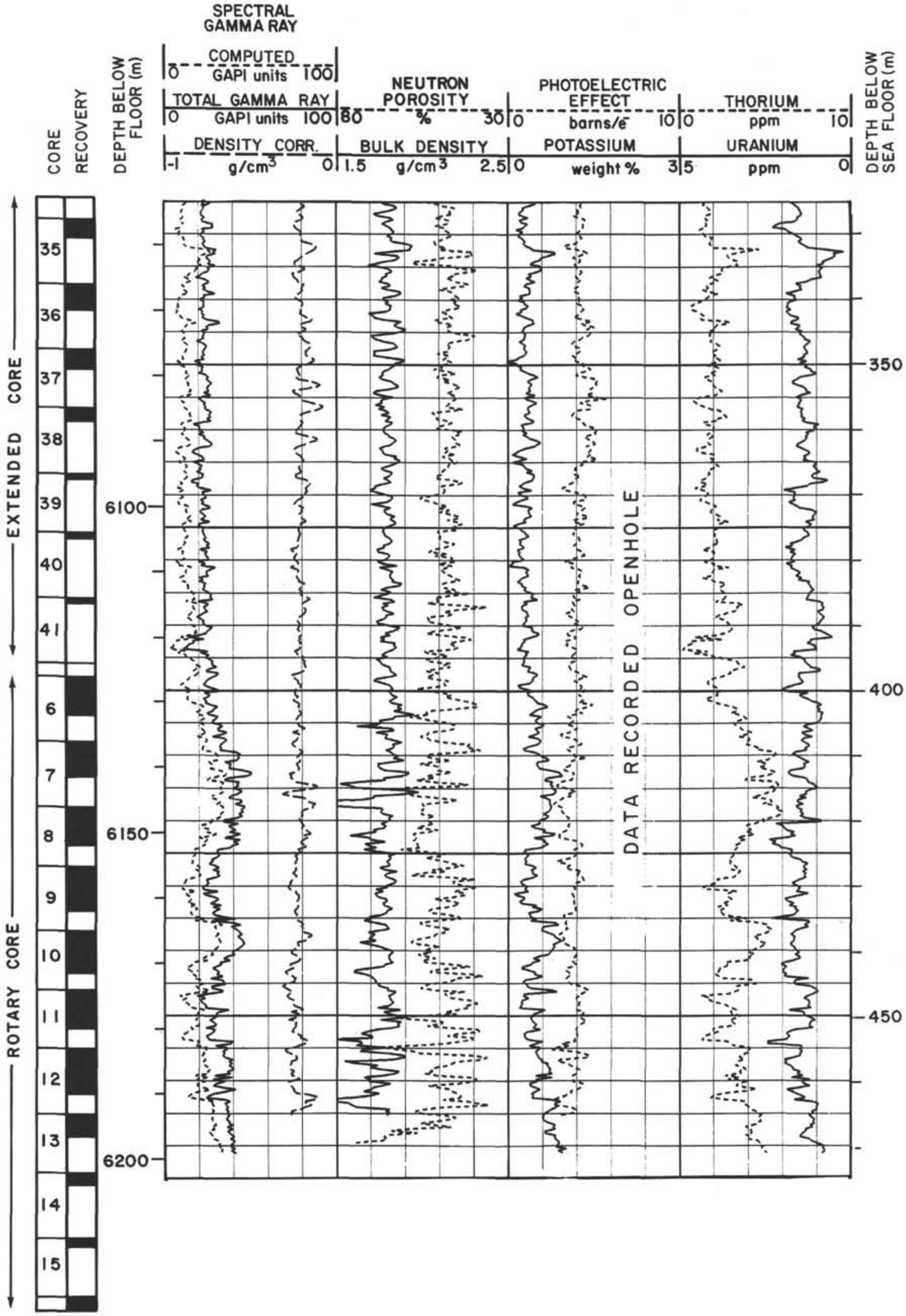

Summary Log for Site 765D

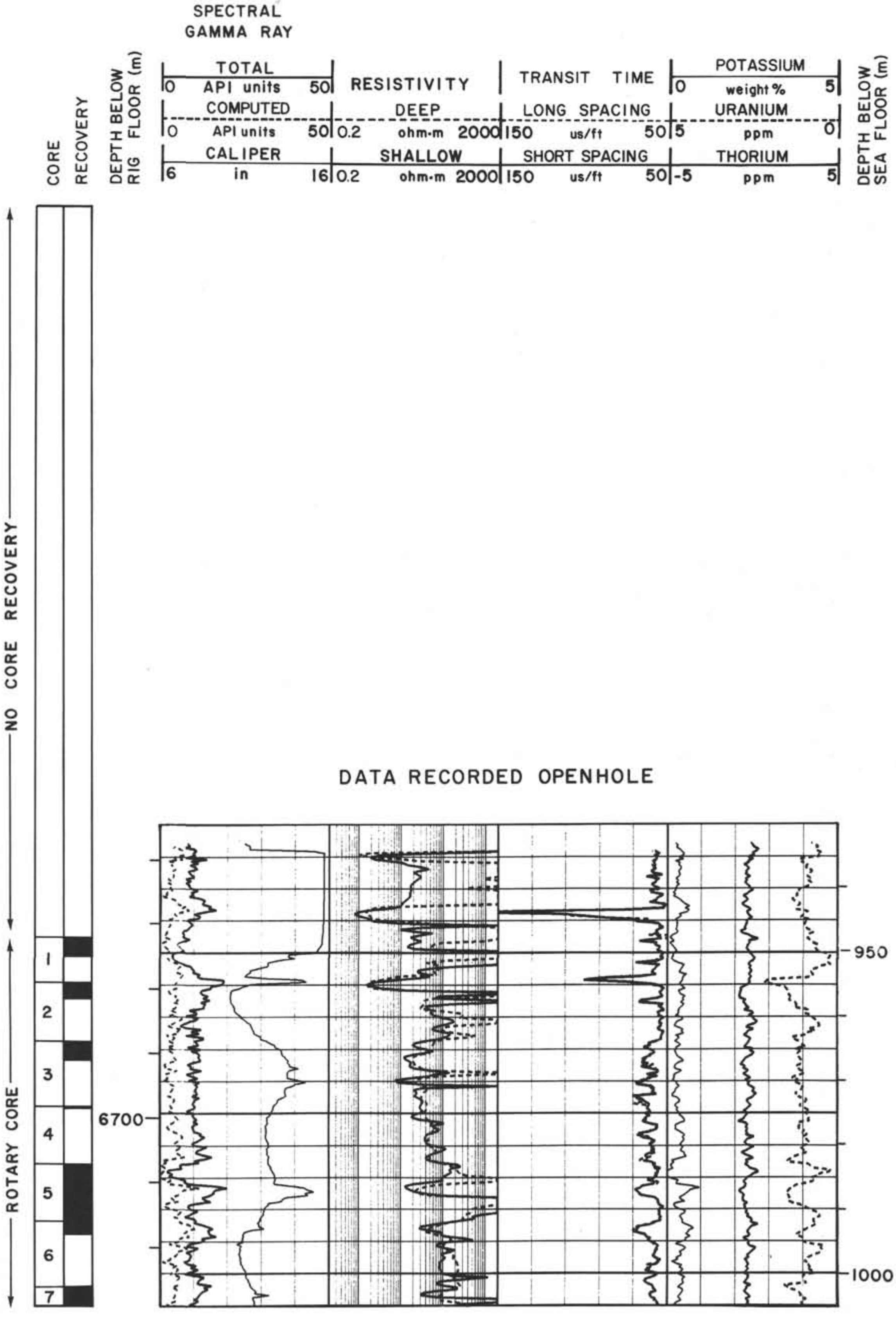

Summary Log for Site 765D (continued)

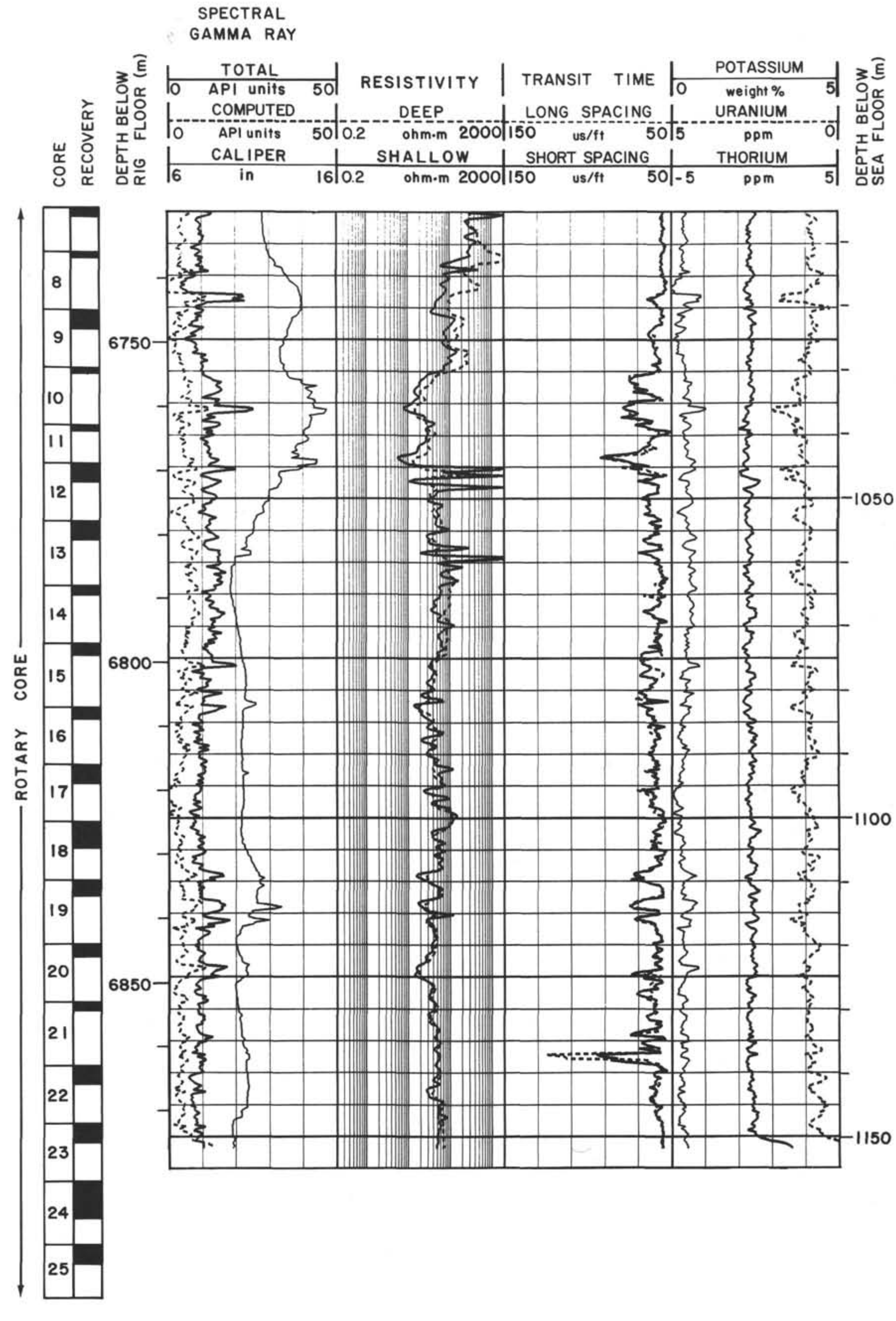

Summary Log for Site 765D (continued)

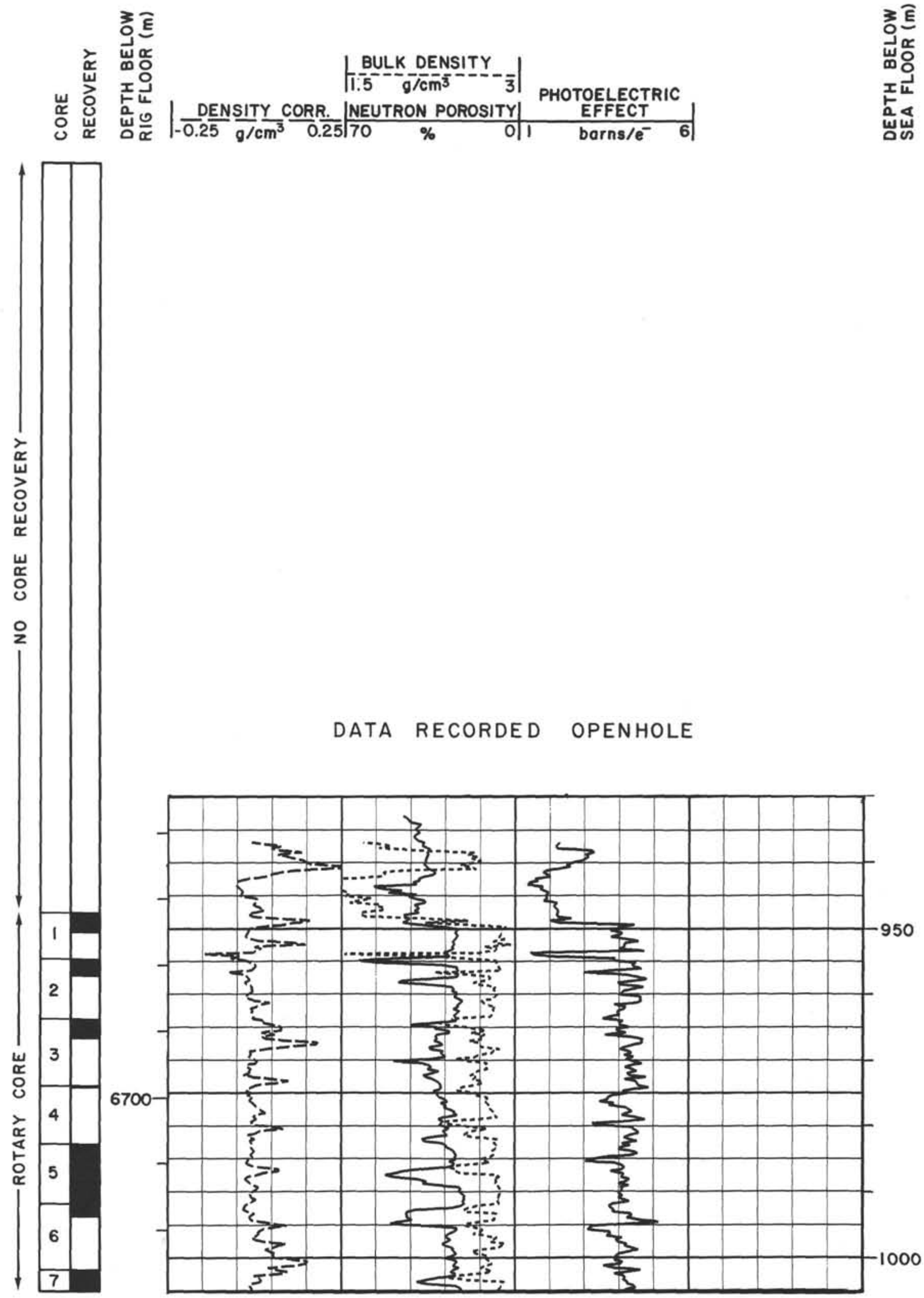

Summary Log for Site 765D (continued)

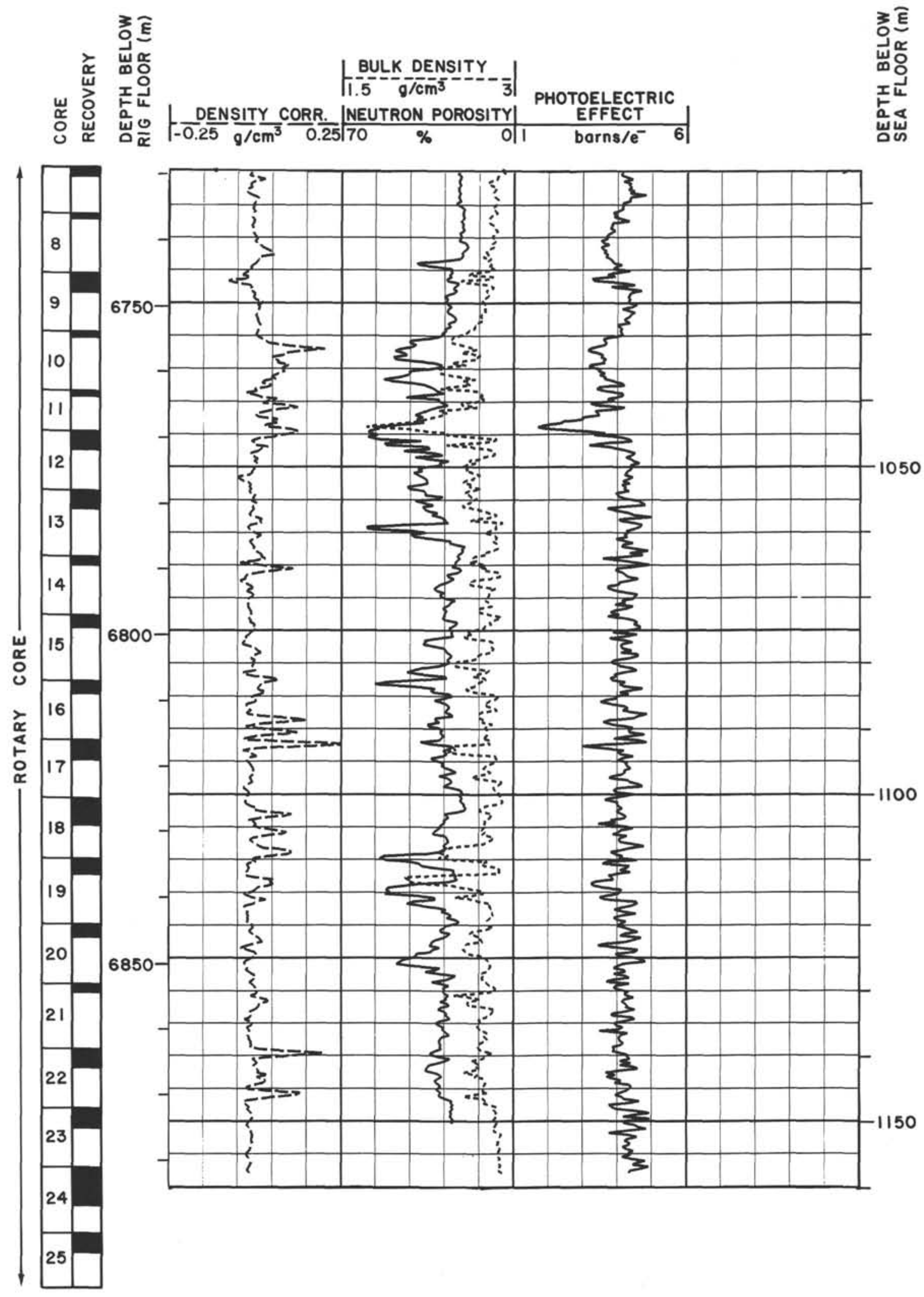

Summary Log for Site 765D (continued)

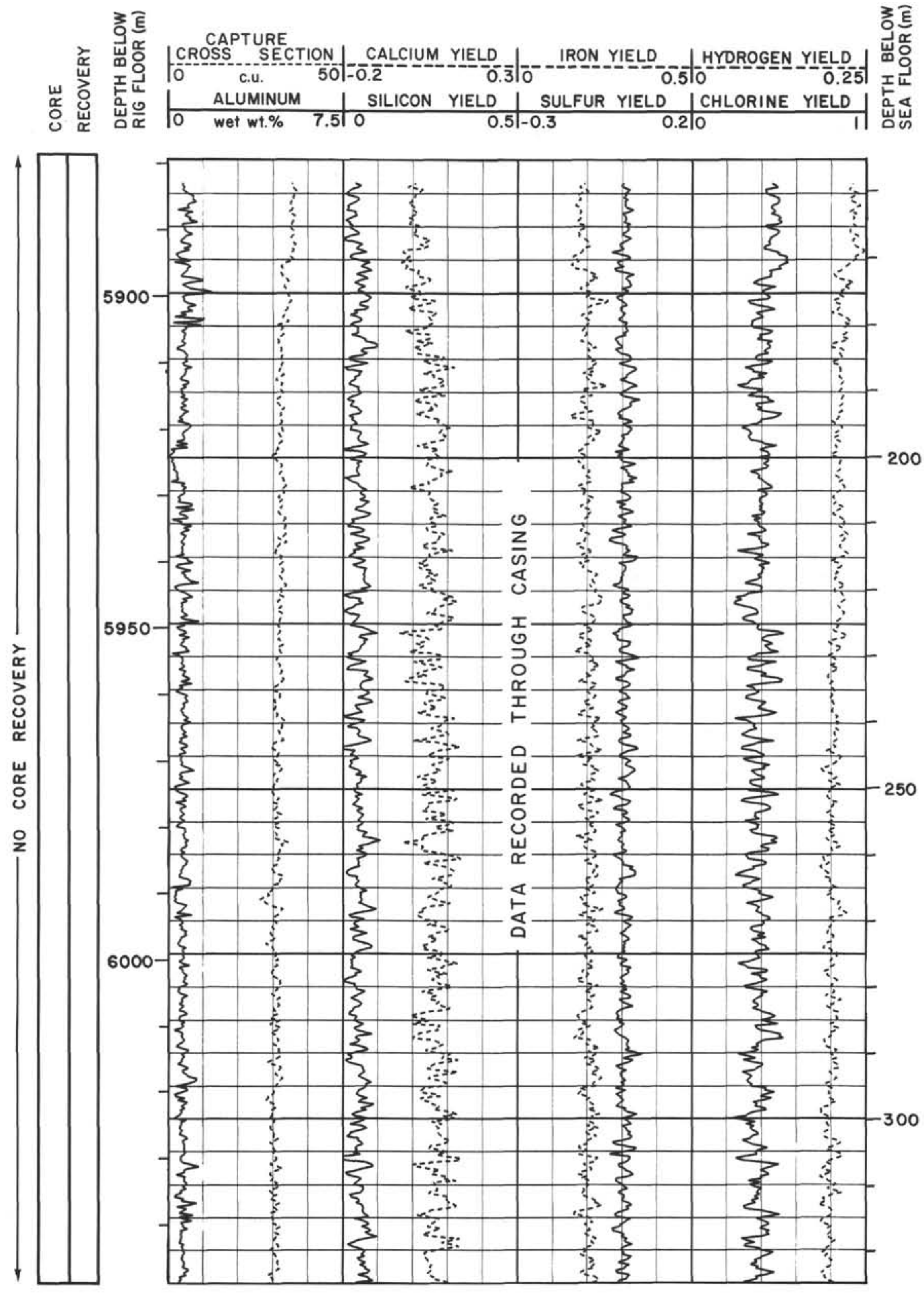

Summary Log for Site 765D (continued)

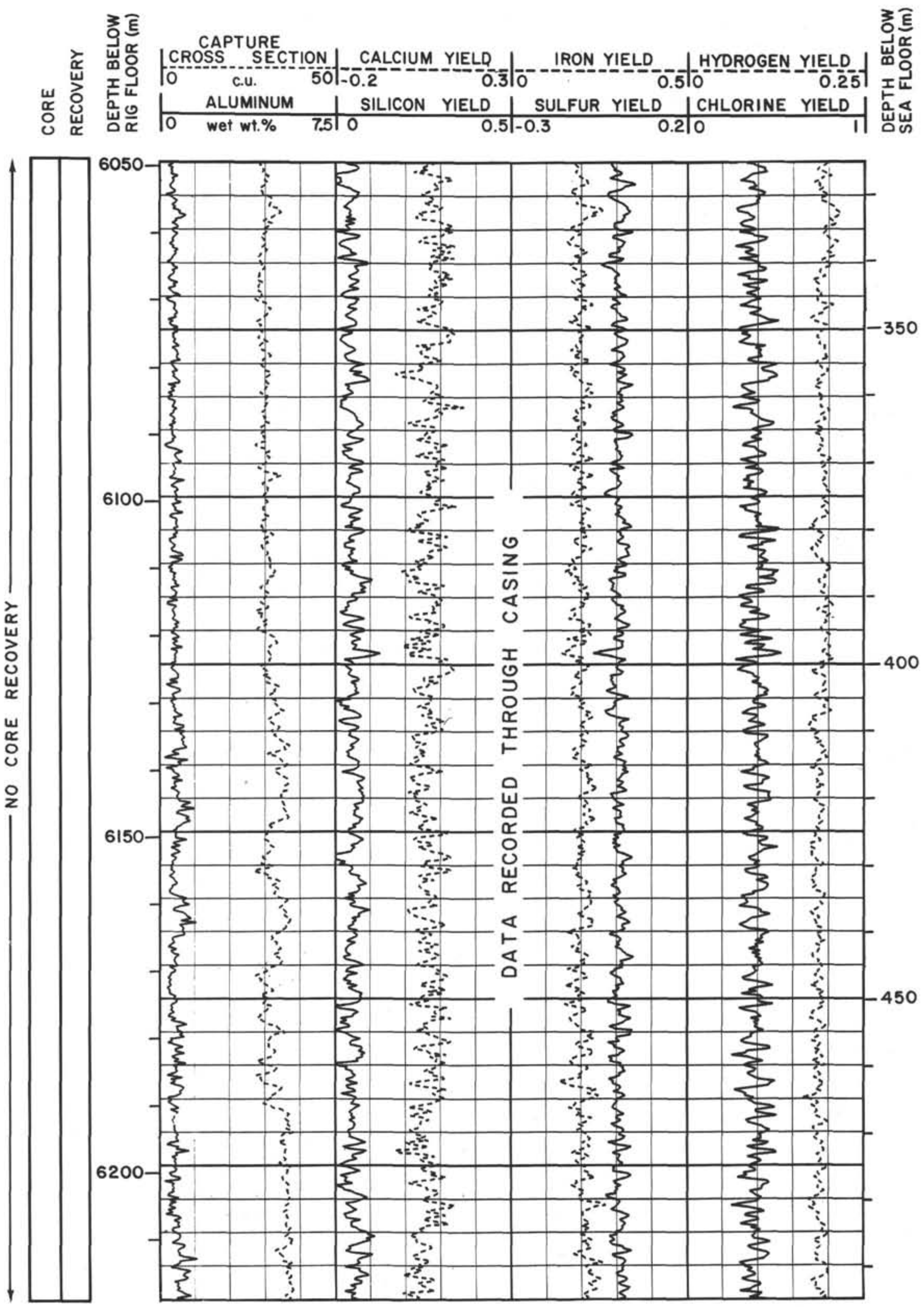

Summary Log for Site 765D (continued)

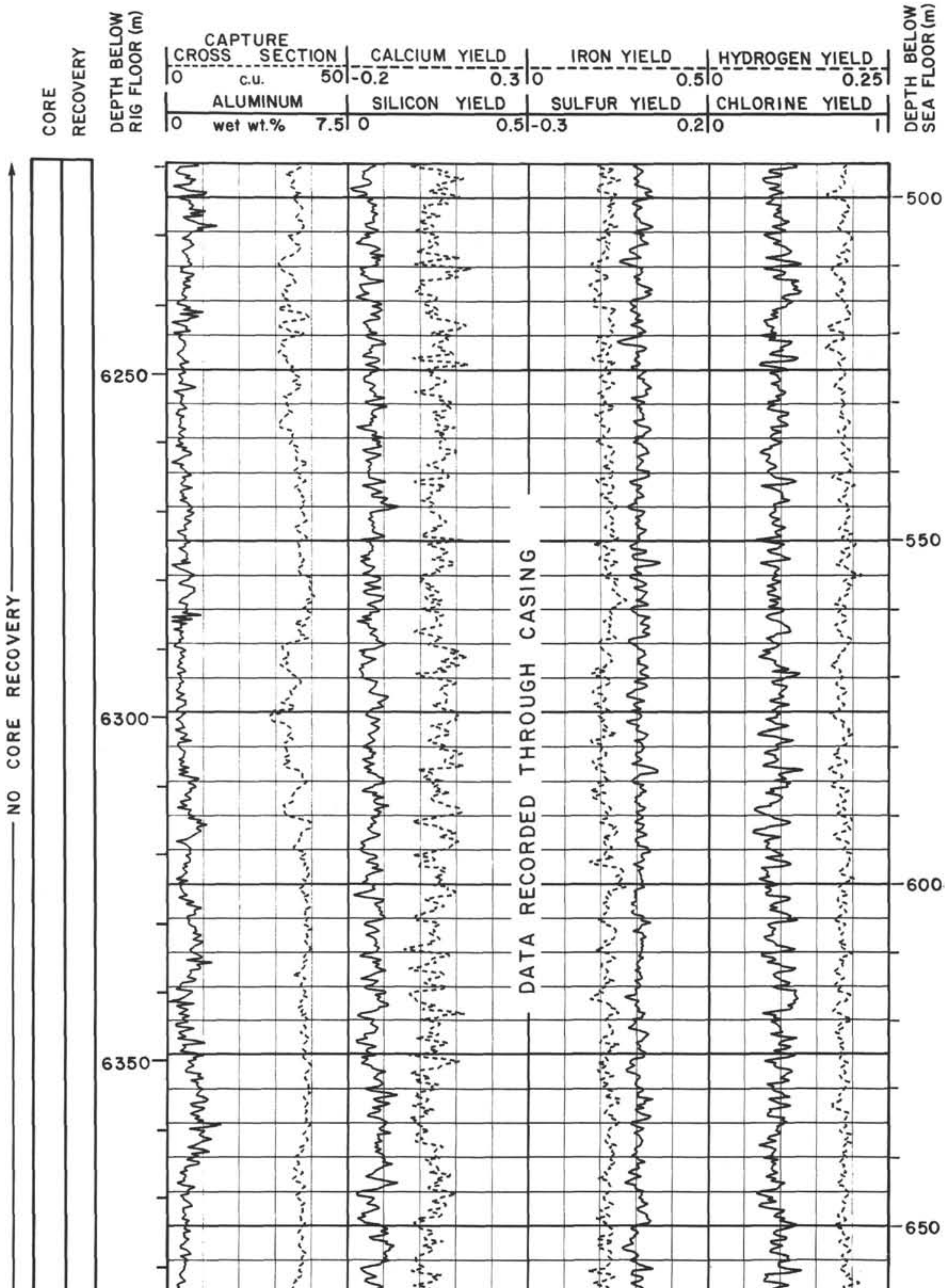

Summary Log for Site 765D (continued)

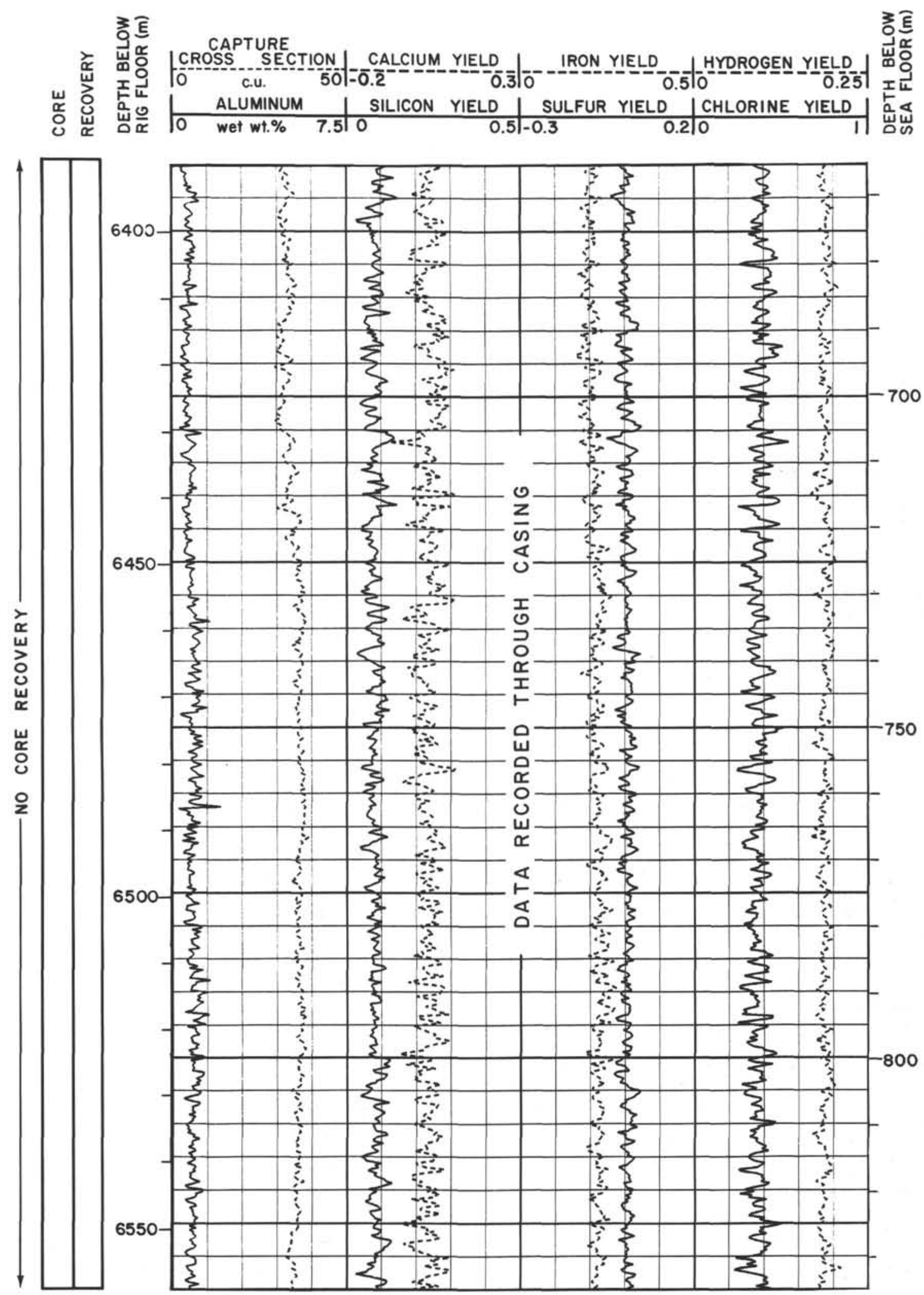

Summary Log for Site 765D (continued)

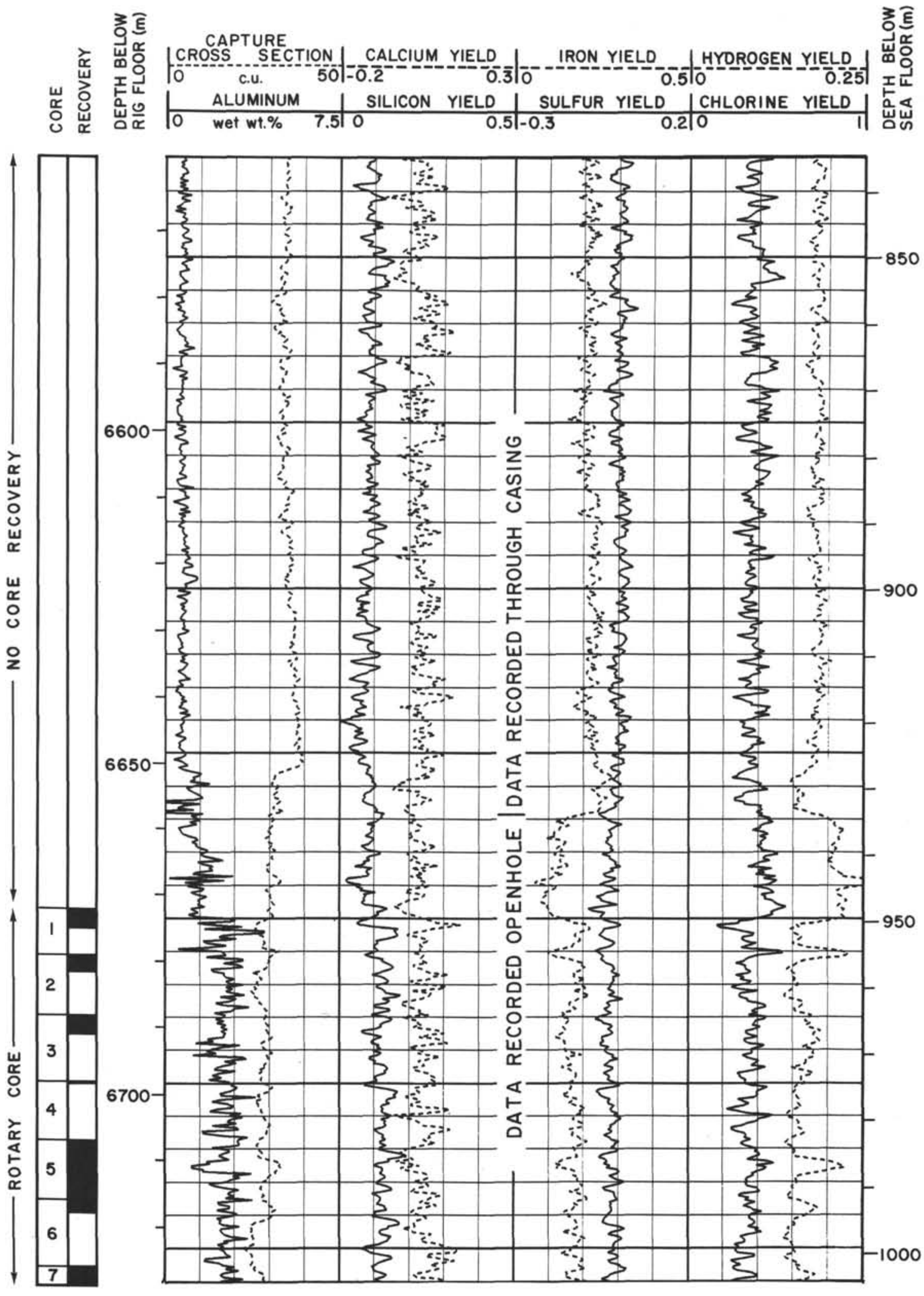

Summary Log for Site 765D (continued)